TOPOLOGICAL PHOTONICS

EDITED BY: Xiaoyong Hu, Cuicui Lu, Guancong Ma and Yulan Fu
PUBLISHED IN: Frontiers in Physics

frontiers Research Topics

ISSN 1664-8714
ISBN 978-2-88976-527-0
DOI 10.3389/978-2-88976-527-0

About Frontiers

Frontiers is more than just an open-access publisher of scholarly articles: it is a pioneering approach to the world of academia, radically improving the way scholarly research is managed. The grand vision of Frontiers is a world where all people have an equal opportunity to seek, share and generate knowledge. Frontiers provides immediate and permanent online open access to all its publications, but this alone is not enough to realize our grand goals.

Frontiers Journal Series

The Frontiers Journal Series is a multi-tier and interdisciplinary set of open-access, online journals, promising a paradigm shift from the current review, selection and dissemination processes in academic publishing. All Frontiers journals are driven by researchers for researchers; therefore, they constitute a service to the scholarly community. At the same time, the Frontiers Journal Series operates on a revolutionary invention, the tiered publishing system, initially addressing specific communities of scholars, and gradually climbing up to broader public understanding, thus serving the interests of the lay society, too.

Dedication to Quality

Each Frontiers article is a landmark of the highest quality, thanks to genuinely collaborative interactions between authors and review editors, who include some of the world's best academicians. Research must be certified by peers before entering a stream of knowledge that may eventually reach the public - and shape society; therefore, Frontiers only applies the most rigorous and unbiased reviews.
Frontiers revolutionizes research publishing by freely delivering the most outstanding research, evaluated with no bias from both the academic and social point of view. By applying the most advanced information technologies, Frontiers is catapulting scholarly publishing into a new generation.

What are Frontiers Research Topics?

Frontiers Research Topics are very popular trademarks of the Frontiers Journals Series: they are collections of at least ten articles, all centered on a particular subject. With their unique mix of varied contributions from Original Research to Review Articles, Frontiers Research Topics unify the most influential researchers, the latest key findings and historical advances in a hot research area! Find out more on how to host your own Frontiers Research Topic or contribute to one as an author by contacting the Frontiers Editorial Office: frontiersin.org/about/contact

TOPOLOGICAL PHOTONICS

Topic Editors:
Xiaoyong Hu, Peking University, China
Cuicui Lu, Beijing Institute of Technology, China
Guancong Ma, Hong Kong Baptist University, China
Yulan Fu, Beijing University of Technology, China

Citation: Hu, X., Lu, C., Ma, G., Fu, Y., eds. (2022). Topological Photonics. Lausanne: Frontiers Media. doi: 10.3389/978-2-88976-527-0

Table of Contents

frontiers | Frontiers in Physics

EDITORIAL
published: 14 June 2022
doi: 10.3389/fphy.2022.953407

Editorial: Topological Photonics

Xiaoyong Hu[1], Guancong Ma[2]*, Cuicui Lu[3]* and Yulan Fu[4]**

[1]State Key Laboratory for Mesoscopic Physics and Department of Physics, Collaborative Innovation Center of Quantum Matter and Frontiers Science Center for Nano-Optoelectronics, Beijing Academy of Quantum Information Sciences, Peking University, Beijing, China, [2]Department of Physics, Hong Kong Baptist University, Kowloon Tong, Hong Kong SAR, China, [3]Laboratory of Advanced Optoelectronic Quantum Architecture and Measurements of Ministry of Education, Beijing Key Laboratory of Nanophotonics and Ultrafine Optoelectronic Systems, School of Physics, Beijing Institute of Technology, Beijing, China, [4]Institute of Information Photonics Technology and School of Physics and Optoelectronics, Faculty of Science, Beijing University of Technology, Beijing, China

Keywords: topological photonic, topological photonic insulator, topological acoustics, non-Hermitian topological systems, topological quantum photonics, topological photonic devices

Editorial on the Research Topic

Topological Photonics

As one of the research frontiers of photonics in recent years, topological photonics plays an essential role in fields of both fundamental physics and device applications. Topological photonics provides a new and robust platform to study the interactions between light and matter based on a topological degree of freedom, which has triggered the discovery of a kaleidoscope of new physical effects and new device applications. These findings are bringing substantial potential in transformative technologies.

The purpose of this Research Topic is to systematically reflect on the latest research progress of topological photonics, and promote the development of topological photonics in new directions. The scope of the Research Topic includes design, fabrication, and measurement of photonic topological insulators, synthetic dimensions, non-Hermitian topological photonics, high-order topological states, quantum topological photonics, topological microwaves, topological acoustics, and their applications.

This Research Topic includes nine original research articles and five review articles covering fundamental physics and device applications of topological photonics. The nine original research articles report the latest research progress and direction of topological photonics. Yuan et al. reported a novel design strategy for constructing optical topological cavities using photonic crystals (Yuan et al.), which could provide valuable guidance when constructing topological optical devices. Jia et al. reported the fabrication of a pseudospin-dependent topological acoustic insulator by using hexagonal rods (Jia et al.), which could offer useful reference when constructing multi-functional acoustic devices. Li et al. reported the fabrication of two-dimensional acoustic higher-order topological insulators, and demonstrated the coupling effects of topological corner modes (Li et al.), which provided a new platform for the study of high-order topological photonics and non-Hermitian physics. Lai et al. reported the construction and characterization of tunable topological surface states of three-dimensional acoustic crystals (Lai et al.), where various multi-functional topological acoustic devices could be realized. Peng et al. reported the theoretical results of the properties of topological one-way edge states in an air-hole honeycomb gyromagnetic photonic crystal biased by an external magnetic field (Peng et al.), which may open a new door towards the observation of nontrivial edge states. Elshahat and Lu reported a unidirectional and bidirectional rainbow trapping, realized based on trapping a chirped photonic crystal as a sandwich between two edge states (Elshahat and Lu), which provided a new way to construct topological nanophotonic devices. Liao et al. reported an equivalent circuit model for topological engineering of the iso-frequency contours in connection-type metamaterials (Liao et al.), which may provide a new pathway for the realization of novel nanophotonic devices. Zhao et al. reported the theoretical finding

OPEN ACCESS

Edited and reviewed by:
Lorenzo Pavesi,
University of Trento, Italy

****Correspondence:***
Xiaoyong Hu
xiaoyonghu@pku.edu.cn
Guancong Ma
phgcma@hkbu.edu.hk
Cuicui Lu
cuicuilu@bit.edu.cn
Yulan Fu
fuyl@bjut.edu.cn

Specialty section:
This article was submitted to Optics and Photonics, a section of the journal Frontiers in Physics

Received: *26 May 2022*
Accepted: *31 May 2022*
Published: *14 June 2022*

Citation:
Hu X, Ma G, Lu C and Fu Y (2022) Editorial: Topological Photonics. Front. Phys. 10:953407. doi: 10.3389/fphy.2022.953407

of multiple one-way edge modes in sonic crystals with large Chern numbers (Zhao et al.), and the realization of acoustic diodes by joining sonic crystals with different Chern numbers. This work offers a new route for the realization of novel acoustic non-reciprocal devices. Li et al. reported the realization of multiport routing of topologically optical transport based on the merging of valley-dependent edge states and second-order corner states (Li et al.), which provided a valuable reference for the realization of topological photonic integrated circuits.

Review articles are indispensible for both the specialists and beginners engaged in the field of topological photonics. We are excited that this Research Topic includes a high-quality collection of in-depth reviews. Xie et al. give a systematical review of topological semimetal phases in artificial photonic microstructures and their applications in coupling spin-polarized electromagnetic waves, anomalous reflection, vortex beams generation, bulk transport, and non-Hermitian effects (Xie et al.). This article will promote the study of higher-order topological semimetals and their applications. Jiang et al. provide an in-depth review of recent progress in the chiral topological quantum interface (Jiang et al.), which will be a valuable reference for the research of quantum topological photonics. Luo et al. offer a systematical and in-depth review of Hermitian and non-Hermitian Dirac-like cones in photonic and phononic structures (Luo et al.), which would promote the research of non-Hermitian topological photonics and phononics. Wang et al. give a comprehensive review of fundamentals and applications of topological polarization singularities (Wang et al.), which will help to improve the applications of topological photonics in fields of optical communication, biosensing, and so on. Haixiao Wang et al. offer a review of the all-dielectric topological photonic crystals from the aspect of topological phases (Wang et al.), which will surely improve the developments of all-dielectric topological photonics.

The topic of "Topological Photonics" has brought rich physical phenomena, and will stimulate more interest due to the unique properties of topological protection. We believe that this Research Topic will provide valuable guidance for the future research direction and applications of topological photonics. Both new physics and various new kinds of functional nanophotonic devices and chips will be expected to be realized based on topological photonics in the near future. Last but not least, we wish to express our sincere gratitude towards all the excellent scientists, including authors and reviewers, whose invaluable contributions made this Research Topic a reality.

AUTHOR CONTRIBUTIONS

All authors listed have made a substantial, direct, and intellectual contribution to the work and approved it for publication.

Conflict of Interest: The authors declare that the research was conducted in the absence of any commercial or financial relationships that could be construed as a potential conflict of interest.

Publisher's Note: All claims expressed in this article are solely those of the authors and do not necessarily represent those of their affiliated organizations, or those of the publisher, the editors and the reviewers. Any product that may be evaluated in this article, or claim that may be made by its manufacturer, is not guaranteed or endorsed by the publisher.

frontiers in Physics

ORIGINAL RESEARCH
published: 07 June 2021
doi: 10.3389/fphy.2021.697719

Construction of Optical Topological Cavities Using Photonic Crystals

Meng Yuan[1], *Tao Xu*[1,2] *and Zhi Hong Hang*[1,3]*

[1]School of Physical Science and Technology and Collaborative Innovation Center of Suzhou Nano Science and Technology, Soochow University, Suzhou, China, [2]Shenzhen Kuang-Chi Institute of Advanced Technology, Shenzhen, China, [3]Institute for Advanced Study, Soochow University, Suzhou, China

A novel design of the Fabry–Pérot optical cavity is proposed, utilizing both the topological interface state structures and photonic bandgap materials with a controllable reflection phase. A one-to-one correspondence between the traditional Fabry–Pérot cavity and optical topological cavity is found, while the tunable reflection phase of the photonic crystal mirrors provides an extra degree of freedom on cavity mode selection. The relationship between the Zak phase and photonic bandgap provides theoretical guidance to the manipulation of the reflection phase of photonic crystals. The dispersions of interface states with different topology origins are explored. Linear interfacial dispersion emerging in photonic crystals with the valley–spin Hall effect leads to an extra $n = 0$ cavity mode compared to the Zak phase–induced deterministic interface states with quadratic dispersion. The frequency of the $n = 0$ cavity mode is not affected by the cavity length, whose quality factor can also be tuned by the thickness of the photonic crystal mirrors. With the recent help of topology photonics in the tuning reflection phase and dispersion relationship, we hope our results can provide more intriguing ideas to construct topological optical devices.

Keywords: photonic crystal, topological interface states, reflection phase, Zak phase, valley–spin Hall effect

OPEN ACCESS

Edited by:
Guancong Ma,
Hong Kong Baptist University, China

Reviewed by:
Xueqin Huang,
South China University of Technology, China
Meng Xiao,
Hong Kong University of Science and Technology, China

***Correspondence:**
Zhi Hong Hang
zhhang@suda.edu.cn

Specialty section:
This article was submitted to Optics and Photonics, a section of the journal Frontiers in Physics

Received: *20 April 2021*
Accepted: *17 May 2021*
Published: *07 June 2021*

Citation:
Yuan M, Xu T and Hang ZH (2021) Construction of Optical Topological Cavities Using Photonic Crystals. Front. Phys. 9:697719. doi: 10.3389/fphy.2021.697719

INTRODUCTION

In 2008, Haldane and Raghu [1, 2] introduced topology to photonics, opening a brand-new research direction in the realm of photonics: topological photonics [3, 4]. Various topological invariants, having been applied to topological insulators, can also be used to characterize the properties of photonic bulk bands. When two optical materials, characterized by different topological properties, are placed in proximity, robust edge states emerge along their interfaces which could accommodate backscattering-immune electromagnetic propagations. After the first demonstration of a unidirectional optical waveguide [5], the Chern number, as the quantized flux of the Berry curvature through the whole Brillouin zone (BZ), has triggered various designs in electronic [6], photonic [7–9], and cold atom [10] systems. The Zak phase [11], a one-dimensional (1D) geometric phase, was also found to be capable of describing bulk photonic band properties [12]. It was further extended to two-dimensional (2D) and deterministic waveguiding in both acoustic and photonic systems [13–16]. Different from the systems characterized by the Chern number, that time reversal symmetry is broken; the inverted symmetry breaking results in a sign opposite to that of the Berry curvature near the two inequivalent BZ corners where the valley Chern number [17–19] can be defined and unidirectional valley pseudospin propagation was observed [20–23]. With the help of these topologically induced unidirectional electromagnetic propagations, various novel designs, such as optical delay lines [24], valley couplers [25], and nonlinear optical devices [26], have been

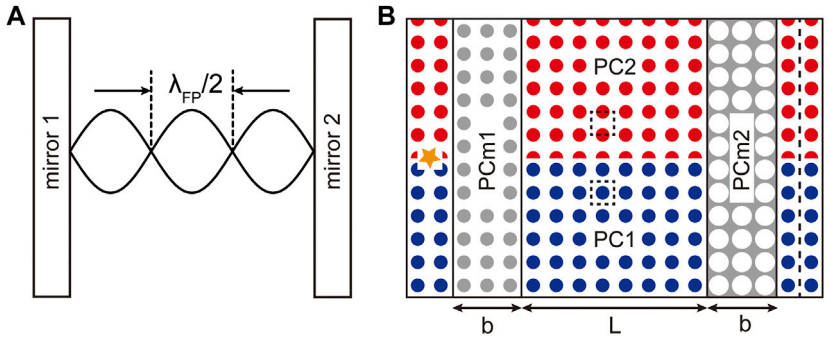

FIGURE 1 | (A) Sketch of a traditional FP cavity. Light of wavelength λ_{FP} will exist in such a cavity. **(B)** The schematic diagram of OTC type **I** constructed by 2D PCs. PC1 and PC2 are with different Zak phases where interface states are induced along their interface within the common photonic bandgap of PCm1 and PCm2 (in gray). Two PC mirrors are considered to replace the original reflecting mirrors.

successfully demonstrated. Moreover, major research attention has also been devoted to laser operations, employing the topological interface states [27–33]. Different topological interface state designs, based on mechanisms such as the Su–Schrieffer–Heeger (SSH) model [27, 28], magneto-optical effect [29], coupled ring–resonator array [30], spin Hall effect [31], and valley–spin Hall effect [32], have been applied to increase the total emission power in topological cavities and maintain a stable single-mode emission of the whole system. Topological bulk lasing is also possible by engineering band-inversion–induced reflection [33].

In a traditional laser, the Fabry–Pérot (FP) cavity, in which photons bounce back and forth in the lasing medium between two parallel plane mirrors (as shown in **Figure 1A**), is an important component to provide light energy feedback. Furthermore, it also plays an important role in frequency selection. In this article, we extend the study of topological photonics to the design of the FP laser cavity by using 2D topological photonic crystals (PCs). Different from previous studies where only topologically induced interface modes were employed, we also design the reflection mirrors of PCs based on topological photonics. By assembling different PCs with topologically induced interface states and different PC mirrors with different reflection properties, we can construct optical topological cavities (OTCs) with tunable properties. Two different types of OTCs, based on different topological interface states, are designed and compared with the physics discussed below. The PC-based reflection mirrors also provide a degree of freedom for mode selection, and an efficient approach to tune the cavity fidelity is also discussed.

DESIGNS AND RESULTS

Optical Topological Cavity Type I

As shown in **Figure 1A**, a traditional FP cavity is composed of parallel cavity mirrors and a lasing medium in between. The laser wavelength λ_{FP} to be selected depends on the distance between the two cavity mirrors: $n\lambda_{FP}/2 = L_{cavity}$, where L_{cavity} is the distance between the two mirrors and n indicates its index. Our construction principle for OTCs is to use topologically induced interface states to replace the lasing medium and PC mirrors to replace the cavity mirrors. A scheme of OTC type I is depicted in **Figure 1B**. In OTC type I, the Zak phase–induced interface states are employed where PC2 is the counterpart of the cylinder-arrayed PC1 with a shifted lattice [15]. The cavity length L is defined as the number of columns of PCs used. Photonic bandgap materials will serve as reflecting mirrors, and as an example, mutually inverted 2D PCs with thickness b are used as illustrated in gray. Other PC mirrors can also be considered. In this work, we carry out numerical simulations using the finite element method [34] to study the properties of such OTCs. A point source (denoted as an orange star in **Figure 1B**) is used to excite the cavity modes, and its transmission spectrum is obtained by a line integral along the black dotted line on the right side of the cavity. Within the gap frequencies of PC mirrors, the peaks existing in the transmission spectrum denote the cavity modes excited.

Here, we consider the transverse magnetic (TM, with electric field E_Z along cylinder axis) polarization. The calculated photonic band diagrams of the PC1 and PC2 are shown in **Figure 2A**. PC2 (in red) is identical to PC1 (in blue) of a square array of dielectric cylinders except that its unit cell is shifted by half a lattice constant a along the y direction. The radius of cylinders for PC1 and PC2 is $r_1 = 0.282a$. In **Figure 1B**, colored regions (red, blue, and gray) indicate where dielectric materials with $\varepsilon_{diel} = 10.5$ are used and air is assumed in other regions. With identical unit cells, PC1 and PC2 possess the same band diagram with a common bandgap above the first photonic band. It is discussed and experimentally verified [15, 16] that the Zak phase of the first band is inverted between PC1 and PC2; thus, an interface state would emerge if PC1 and PC2 are assembled, as shown in the black line in **Figure 2B**. Here, we consider a supercell with 15 unit cells of both PCs, and periodic boundaries are applied along both the x and y directions. Electromagnetic waves will propagate along the interface within the frequency range between 0.2521 and $0.3021c/a$. The major physical reason that the interface state shall arouse along the interface is that the reflection phase $\varphi_{PC1(2)}$ on PC1(2) is of a different sign, and when $\varphi_{PC1} + \varphi_{PC2} = 0$, an interface state emerges [15]. The reflection phase of PCs plays a

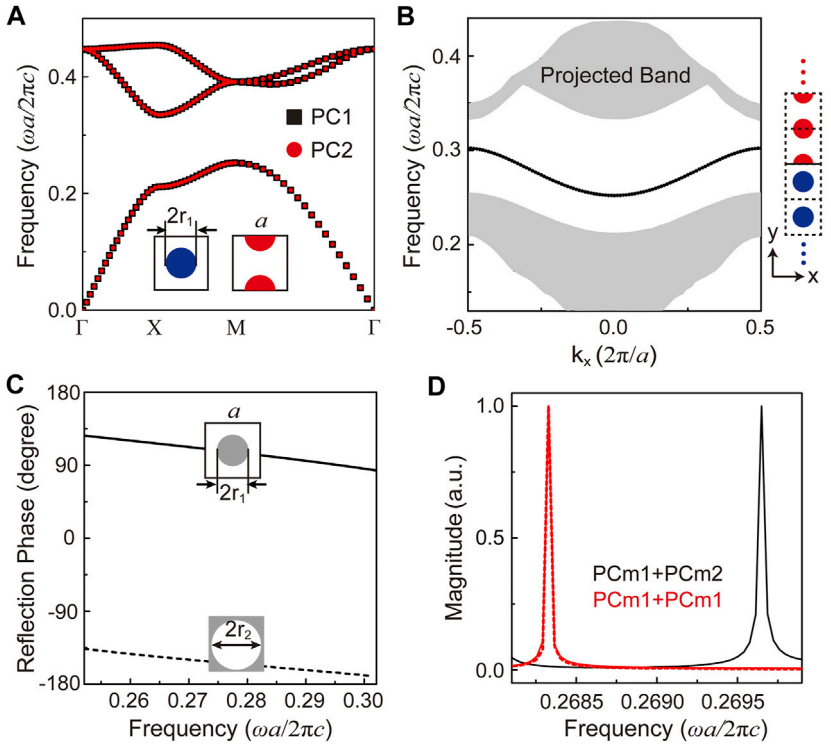

FIGURE 2 | (A) TM photonic band diagrams of PC1 and PC2 with shifted lattice. **(B)** Calculated projected band structure with a supercell of PC1 and PC2 assembled along the *y* direction. The folded bulk bands of PC1 and PC2 are painted in gray, and the interface state is in black. **(C)** The reflection phases upon PC mirrors. **(D)** By changing PC mirrors, the cavity mode frequency will change. Red lines indicate the scenario where PCm1 serves as both cavity mirrors, and the black line indicates the scenario where PCm1 and PCm2 serve as the two cavity mirrors, respectively. A slab of effective parameters ε = −2.8 and μ = 1.2 with a reflection phase 113.578°is also considered to replace PCm1, whose reflection phase is the same as that of PCm1 at 0.2683 *c/a*.

key role in the emergence of such an interface state. Will the reflection phase play a role similar to that of the PC mirrors? PCm1 is chosen to be the same as PC1, and its reflection phase is calculated to be between 83.551 and 126.542°, within the frequency range of the interface state dispersion. If we consider a similar cylinder-in-air geometry and at the first photonic bandgap, we shall obtain a reflection phase with similar values. On the contrary, as discussed in Huang et al. [14], an inverted PC, with air holes in a dielectric slab, will have inverted the Zak phase as well as the reflection phase at the photonic gap above the first band. In other words, the reflection on an inverted PCm2 constructed by drilling air holes of radius $r_2 = 0.473a$ in the dielectric slab will be totally different from that with cylinder-in-air geometry, where its calculated reflection phase is found between −170.309 and −136.291°, as shown in **Figure 2C**. OTC type I is thus constructed with the Zak phase–induced interface as the lasing medium and PCs with inverted structures as mirrors, as depicted in **Figure 1B**. In **Figure 2D**, the calculated transmission spectrum of OTC type I is plotted with the cavity length $L = 11a$ and mirror thickness $b = 3a$. A cavity mode, peaked at 0.2696 *c/a*, is excited. What if PC mirrors are changed? By replacing PCm2 back to PCm1, an obvious shift of the cavity mode is acquired.

In the studies of traditional FP cavities, the reflection phase of mirrors has never been considered. The major reason is that in a traditional FP cavity, metallic mirrors are considered with a 180° reflection phase. During the back-and-forth bouncing between these two mirrors, no phase accumulation will occur. On the contrary, although total reflection occurs on PCm1/PCm2, the frequency shift we observe shall correspond to their different reflection phases. Electromagnetic waves propagate along the interface and then bounce back on one PC mirror with the accumulated phase and propagate again along the interface. Thus, the FP condition of a cavity shall be revised as

$$\varphi_{\mathrm{PCm1}} + \varphi_{\mathrm{PCm2}} + 2k(\omega)L = 2n\pi, \tag{1}$$

where $\varphi_{\mathrm{PCm1\,(2)}}$ is the reflection phase on PCm1(2) in the radian unit, $k(\omega)$ is the wave number (in the unit of 2π/2) of the interface state at different frequency ω, L is the length of the OTC, and n is an integer. **Eq. 1** can be easily reduced to the FP condition if inserting $\varphi_{\mathrm{PCm1}} = \varphi_{\mathrm{PCm2}} = \pi$ and $k(\omega) = 2\pi/\lambda_{\mathrm{FP}}$. From **Eq. 1**, we can easily see that using PC mirrors will provide an effective approach to tune the reflection phases and the mode to be selected. However, the precise verification of **Eq. 1** is not straightforward as both the reflection phases of PCs and the dispersion of the interface states are frequency dependent. As total reflection occurs here for PC mirrors, a simpler approach is to replace PC mirrors with effective medium slabs with a single negative value of permittivity/permeability, where the arbitrary

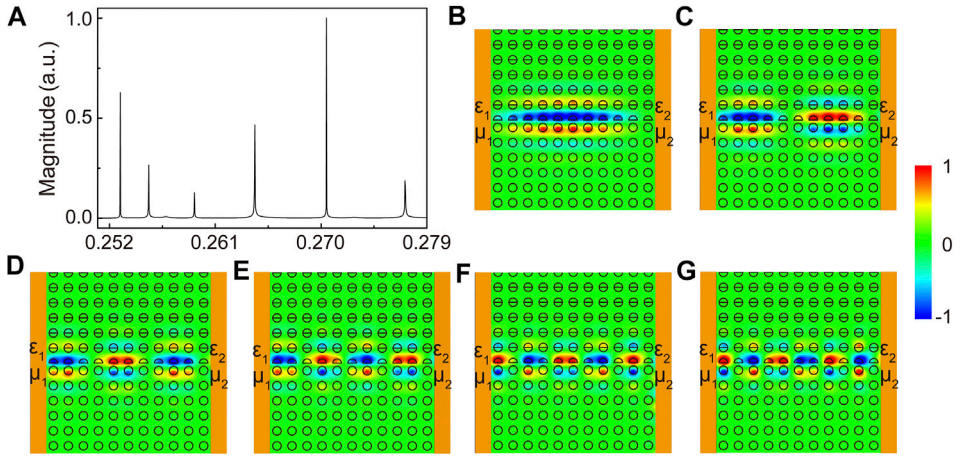

FIGURE 3 | (A) The calculated transmission spectrum with PC mirrors replaced by single negative effective medium slabs. **(B–G)** Simulated E_Z field distributions at 0.2529, 0.2553, 0.2592, 0.2644, 0.2705, and 0.2771 *c*/*a*.

TABLE 1 | Cavity modes at length $L = 11a$.

n	f(c/a)	k(π/a)	k$'$ (π/a)	2 *kl*
1	0.2529	0.090	0.091	1.988π
2	0.2553	0.182	0.182	4.000π
3	0.2592	0.273	0.272	5.999π
4	0.2644	0.363	0.364	7.997π
5	0.2705	0.454	0.455	9.986π
6	0.2771	0.544	0.545	11.968π

reflection phase can be tuned. As shown in the dashed line in **Figure 2D**, by replacing PCm1 with a slab with $\varepsilon = -2.8$, $\mu = 1.2a$, whose reflection phase is the same as that of PCm1 at the frequency 0.2683 *c*/*a*, a nearly identical spectrum is obtained, indicating the validity of our effective slab model. We thus can verify **Eq. 1** through numerical simulations by various slabs with tunable reflection phases. We change PCm1 to slab1 with $\varepsilon_1 = -3$, $\mu_1 = 2$ and PCm2 to slab2 with $\varepsilon_2 = 3$, $\mu_2 = -2$, and their reflection phase sum is $\varphi_{m1} + \varphi_{m2} = 0$. The slab thickness is *a*. As can be found in **Figure 3A**, multiple cavity modes are excited in OTC type I with $L = 11a$. The corresponding mode profiles (normalized to its own maximal intensity) can be found in **Figures 3B–G** at the frequencies 0.2529, 0.2553, 0.2592, 0.2644, 0.2705, and 0.2771 *c*/*a*, respectively. Red (blue) color indicates that the electric field is of positive (negative) value, which bears great similarity to the first of the sixth-order FP modes. It is the fifth-order FP mode that we achieved, as shown in **Figure 2D**.

Further analysis is conducted as shown in **Table 1**. We can find its corresponding wave number *k* at the transmission spectrum peak frequency in our calculated dispersion, as shown in **Figure 2B**. Thus, the total phase accumulation 2 *kl* with $\varphi_{m1} + \varphi_{m2} = 0$ is very close to the corresponding *n* multiplied by 2π. For comparison, we can also obtain the corresponding wave number k' by the fast Fourier transformation of the corresponding electric field distribution as shown in **Figures 3B–G**, where good consistency can be found with our dispersion readout.

Optical Topological Cavity Type II

Using Zak phase–induced interfaces, we have successfully constructed OTC type I and discovered the role PC mirrors play in the mode selection. As various applications have been demonstrated utilizing the unidirectional interface states induced by the valley-spin Hall effect, we extend our work to construct OTC type II by using valley-spin Hall PCs. By introducing sublattice symmetry breaking into the honeycomb lattice PC [25], unidirectional interface states are induced and adopted to construct OTC type II. We consider PC3 and PC4 with inverted inversion symmetry. Here, three honeycomb lattices are considered as an enlarged hexagonal unit cell, with six dielectric cylinders with permittivity $\varepsilon'_{diel} = 7.5$ inside, as depicted in the inset of **Figure 4A**. If all six cylinders are of the same radius, with such an enlarged unit cell, the Dirac cones originally at BZ boundaries (K and K' points) of the honeycomb lattice will be folded to the BZ center (Γ point) to form a doubly degenerate Dirac cone. If neighboring cylinders are of different radii ($r_3 = 0.176a'$ and $r_4 = 0.147a'$, where a' is the side length of the hexagon unit cell), a bandgap opens in the calculated TM photonic band diagrams of PC3 and PC4, as shown in **Figure 4A**. PC3 and PC4 are of an identical unit cell but cylinders of radius r_3 are swapped with those of r_4. Assembling PC3 and PC4 along the lattice armchair orientation will give rise to unidirectional interface states, with the calculated interface dispersions (in green and orange) shown in **Figure 4B**. Here, we consider a supercell (shown in the right panel) consisting of five unit cells for both PC3 and PC4, with periodic boundary conditions applied along the *x* direction and scattering boundary conditions applied along the *y* direction. Interface states corresponding to valley pseudospins up (in green) intercross those of pseudospin down (in orange) linearly at Γ point, which is very different from the Zak phase–induced interface state, as shown in **Figure 2B**. A major difference between OTC type I and type II is that the

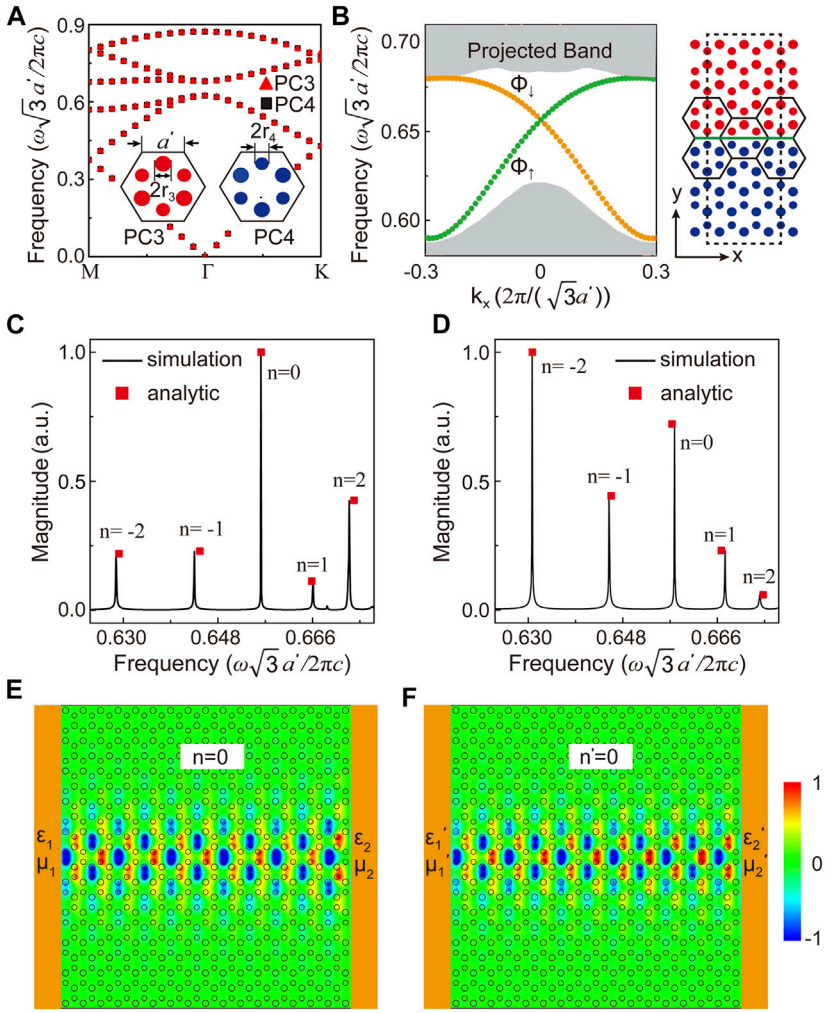

FIGURE 4 | (A) Calculated bulk TM photonic band diagrams of PC3 and PC4. As the diameters of cylinders in a unit cell are not identical in both PC3 and PC4 ($r_3 = 0.176a'$, $r_4 = 0.147a'$, and $\varepsilon'_{diel} = 7.5$), a photonic bandgap appears by sublattice symmetry breaking. **(B)** The projected band structure consists of five unit cells for both PC3 and PC4 along the *y* direction, shown in the right panel. The folded bulk bands belonging to PC3 or PC4 are painted in gray, whereas the two topological interface bands are shown by yellow dots. **(C,D)** The received transmission spectra for different effective medium slabs ($\varepsilon_1 = -5$, $\mu_1 = 1$; $\varepsilon_2 = 5$, $\mu_2 = -1$ and $\varepsilon'_1 = -6$, $\mu'_1 = 1$; $\varepsilon'_2 = 1.5$, $\mu'_2 = -1$) serving as two cavity mirrors, respectively. **(E,F)** Simulated E_Z field distributions of $n = 0$ and $n' = 0$ modes at 0.6562 and 0.6579 *c/a* (normalized to its own maximal intensity).

interface states are with linear or quadratic dispersion, which leads to their different performance, as we shall elaborate later.

We have shown in the previous section that using an effective medium slab can explain the role of PC mirrors in constructing an OTC, and thus, a pair of effective medium mirrors with zero total-reflecting phases is first considered here to construct OTC type II with $\varepsilon_1 = -5$, $\mu_1 = 1$ and $\varepsilon_2 = 5$, $\mu_2 = -1$. In **Figure 4C**, we show the calculated transmission spectrum through this OTC, where multiple peaks, inferring multiple cavity modes, are obtained. For comparison, as shown in **Figure 4D**, the spectrum of another set of slab mirrors, with $\varepsilon'_1 = -6$, $\mu'_1 = 1$ and $\varepsilon'_2 = 1.5$, $\mu'_2 = -1$ is considered with $\varphi_{m1} + \varphi_{m2} = 0.189\pi$, where all modes shift to higher frequency. But a detailed analysis from **Eq. 1** reveals some new physics. Instead of all-positive mode indices found in OTC type I, negative indices are also possible in OTC type II, as derived from **Eq. 1**. The field profiles of mode ± 1 (± 2) are very similar to each other and bear similarity to **Figures 3B and C**. Here, the corresponding analytical mode index is achieved by finding wave number k from **Eq. 1** and its readout of the frequency from the valley pseudospin up dispersion. Moreover, an extra $n = 0$ mode emerges. As can be seen in **Figure 4E**, the mode is almost homogenous along the whole interfacial region except for some variations in one unit cell, inferring no phase accumulation for electromagnetic waves during interfacial propagation.

The unidirectional property of valley–spin Hall interface states provides a totally different picture of the electromagnetic wave propagation inside OTC type II. As our source is on the left side of the OTC, only the valley pseudospin up state (the green-colored

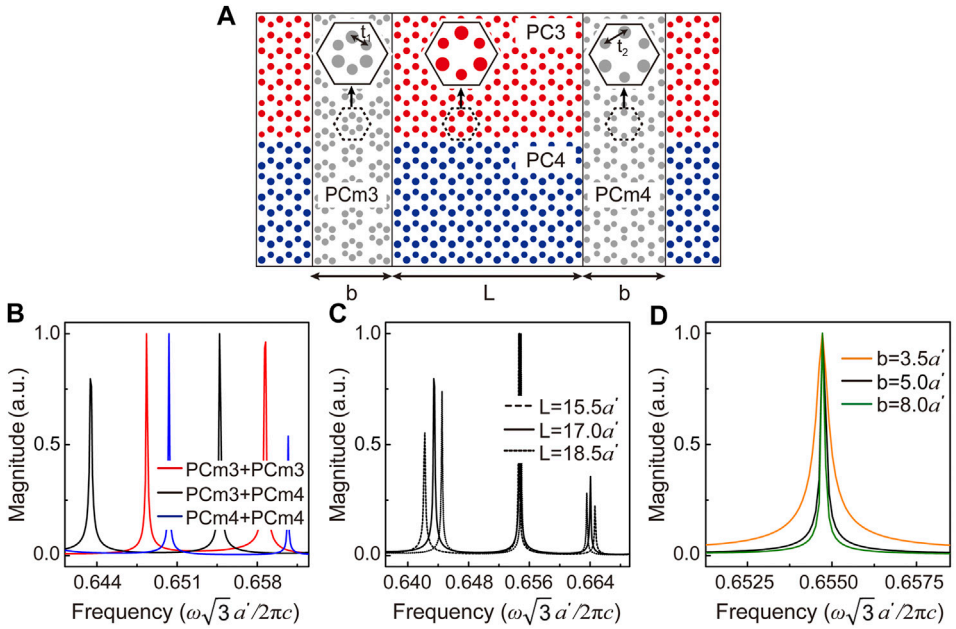

FIGURE 5 | (A) Schematics of OTC type II and 2 PC cavity mirrors. PCm3 (PCm4) is considered with a shrunken (expanded) lattice compared to the PC structure considered at the interface region. **(B)** The mode selection of different PC mirror configurations. **(C)** The received transmission spectra with different cavity lengths. **(D)** By tuning the thickness of PC mirrors, the cavity fidelity will be enhanced (b = 3.5a', Q = 1333.20; b = 5a', Q = 3418.46; and b = 8a', Q = 4830.43).

dispersion in **Figure 4B**) is excited to propagate rightward, whose wave number is decided by the corresponding frequency. With its linear dispersion, both positive and negative values of the wave number are possible and correspond to different frequencies. When bounced on the right mirror, the pseudospin up state must be flipped to the pseudospin down state as for the unidirectional property and a change of dispersion occurs. However, although the sign of the wave number changes accordingly, as for leftward propagation, further phase accumulation will occur to satisfy the FP condition as shown in **Eq. 1**. The phenomenon will be identical if the source is put on the right side of the OTC with an identical transmission spectrum to be received on the left side of the OTC. However, if the leftward propagation valley pseudospin down state is considered first, which is the case with source on the right, mode index n will be reversed such that the sequence of the peaks shall read as 2, 1, 0, −1, and −2, as in **Figures 4C and D**, respectively. This is quite different from OTC type I with a Zak phase–induced interface state with only positive indices. With its quadratic dispersion, the frequency with wave number k is the same as that of $-k$ and thus positive and negative indices are degenerate to each other.

The absence of n = 0 mode in OTC type I can also be understood from their dispersion difference. Although k = 0 (at Γ point) is possible for the Zak phase–induced interface state, time reversal symmetry requires that its dispersion be quadratic, whose group velocity is zero there. This slow light will not be physical and will not appear in our calculated spectrum. On the contrary, the finite group velocity of the linear dispersion of the valley–spin Hall effect at Γ point allows its emergence.

Knowing the physics of OTC type II, we can construct it using PC structures. We consider PC mirrors with deformed honeycomb lattice, where the positions of the six cylinders in PC3 and PC4 are changed. When the six cylinders in one unit cell are moved closer to the center of the unit cell, decreasing the intercylinder distance, a shrunken-latticed PCm3 is constructed where its expanded counterpart is considered as PCm4, both shown in gray in **Figure 5A**. The lattice deformation not only provides an extra mechanism for the bandgap opening of the linear dispersion of two interface states [35], but also leads to the quantum spin Hall effect of photonic crystals [36, 37]. With the bandgap of the interfacial state dispersion, PCm3 and PCm4 can serve as the PC mirrors for OTC type II. Of course, other honeycomb structures can be introduced as PC mirrors whose photonic bandgap frequency overlaps with the linear interfacial dispersion of the valley–spin Hall effect in the PC we design. The introduction of lattice deformation is the easiest approach (though not of the easiest geometry) to guarantee the bandgap with matched lattice. With the same dielectric material considered, this 2D design can be further extended to photonic slab geometry. The intercylinder distance is t_1 = 0.594a' for PCm3 and t_2 = 0.645a' for PCm4, and thus, they are with a common bandgap but different bulk topological properties. We thus can obtain the transmission spectra through OTC type II as illustrated in **Figure 5A**, and the results are shown in **Figures 5B–D**. By considering different PC mirror configurations, the obvious frequency shift of cavity modes can be achieved. The frequency shift is a consequence of the reflection phase difference between PCm3 and PCm4. It is totally understandable because of the different topological bulk

properties (Z_2 topological invariant) for expanded and shrunken lattices. In both OTC type I and type II, the use of PC mirrors with different reflection phases is an efficient approach to select the mode to be excited. From **Eq. 1** and the traditional FP cavity, the cavity mode will also be dependent on the cavity length L, except for the $n = 0$ mode, which only exists in OTC type II. As can be seen in **Figure 5C**, the frequency of the $n = 0$ mode remains at the frequency of 0.6548 c/a with different cavity lengths considered, but the frequency difference between other peaks becomes smaller for a longer cavity. Here, PCm3 and PCm4 are considered as cavity mirrors on either side. Mode fidelity is also a key property of optical cavities. The quality (Q) factor, the full-width half maximum of the $n = 0$ mode can be largely enhanced if the PC mirror thickness is increased. Although the results are obtained with cavity length $L = 17a^{'}$, as the frequency of the $n = 0$ mode is not sensitive to cavity length, the tuning of quality factor can be applied to other cavity designs.

DISCUSSION AND CONCLUSION

In summary, we extend the study of topology photonics to the construction of OTCs. Different topological invariants have been utilized for the generation of robust topological interface states with various applications triggered. Following the theoretical derivation based on the Zak phase and valley–spin Hall effect of light, respectively, different topologically induced interface states are designed and introduced in the construction of OTC type I (PCs with shifted lattice) and OTC type II (honeycomb lattice with broken inversion symmetry). Although one-to-one correspondence between a traditional FP optical planar mirror cavity and OTCs can be found, the quadratic interface dispersion in OTC type I and the linear interface dispersion in OTC type II govern the totally different mode selection criteria in the two OTCs. Negative and zeroth mode indices appear for OTC type II, solely because of its linear dispersion with topological origin. The zeroth mode maintains a constant working frequency irrespective of the length of the cavity.

We also extend the study of topological invariants to the design of the reflection phase in an OTC. We find that the reflection phase of PC mirrors adopted in the construction of OTC plays a key role in mode selection and will be essential when designing an OTC working at one particular frequency. The change of the topological invariant indicates a topology phase transition which also accompanies a dramatic reflection phase change at the associated photonic bandgap, which is verified for PC mirrors based on the Zak phase and quantum spin Hall effect. This new design principle to tune the reflection phase of PCs will help the future development of optical devices.

DATA AVAILABILITY STATEMENT

The original contributions presented in the study are included in the article/Supplementary Material, and further inquiries can be directed to the corresponding author.

AUTHOR CONTRIBUTIONS

ZH conceived the idea and wrote part of the manuscript. MY performed the numerical simulations and wrote part of the manuscript. MY and TX analyzed the results and prepared the figures. All authors have given approval to the final version of the manuscript.

FUNDING

This work is supported by the National Natural Science Foundation of China (Grant No. 11874274) and a project funded by the Priority Academic Program Development of Jiangsu Higher Education Institutions (PAPD). The authors are also grateful for the support from Jiangsu Key Laboratory of Thin Films and Jiangsu Key Lab of Advanced Optical Manufacturing Technologies.

ACKNOWLEDGMENTS

The authors would like to acknowledge Hua Jiang for his kind suggestions.

REFERENCES

1. Haldane FDM, and Raghu S. Possible Realization of Directional Optical Waveguides in Photonic Crystals with Broken Time-Reversal Symmetry. *Phys Rev Lett* (2008) 100:013904. doi:10.1103/PhysRevLett.100.013904
2. Raghu S, and Haldane FDM. Analogs of Quantum-Hall-Effect Edge States in Photonic Crystals. *Phys Rev A* (2008) 78:033834. doi:10.1103/PhysRevA.78.033834
3. Khanikaev AB, and Shvets G. Two-dimensional Topological Photonics. *Nat Photon* (2017) 11:763–73. doi:10.1038/s41566-017-0048-5
4. Ozawa T, Price HM, Amo A, Goldman N, Hafezi M, Lu L, et al. Topological Photonics. *Rev Mod Phys* (2019) 91:015006. doi:10.1103/RevModPhys.91.015006
5. Wang Z, Chong Y, Joannopoulos JD, and Soljačić M. Observation of Unidirectional Backscattering-Immune Topological Electromagnetic States. *Nature* (2009) 461:772–5. doi:10.1038/nature08293
6. Sheng DN, Weng ZY, Sheng L, and Haldane FDM. Quantum Spin-Hall Effect and Topologically Invariant Chern Numbers. *Phys Rev Lett* (2006) 97:036808. doi:10.1103/PhysRevLett.97.036808
7. Poo Y, Wu R, Lin Z, Yang Y, and Chan CT. Experimental Realization of Self-Guiding Unidirectional Electromagnetic Edge States. *Phys Rev Lett* (2011) 106:093903. doi:10.1103/PhysRevLett.106.093903
8. Skirlo SA, Lu L, and Soljačić M. Multimode One-Way Waveguides of Large Chern Numbers. *Phys Rev Lett* (2014) 113:113904. doi:10.1103/PhysRevLett.113.113904
9. Skirlo SA, Lu L, Igarashi Y, Yan Q, Joannopoulos J, and Soljačić M. Experimental Observation of Large Chern Numbers in Photonic Crystals. *Phys Rev Lett* (2015) 115:253901. doi:10.1103/PhysRevLett.115.253901
10. Price HM, Zilberberg O, Ozawa T, Carusotto I, and Goldman N. Measurement of Chern Numbers through Center-of-Mass Responses. *Phys Rev B* (2016) 93:245113. doi:10.1103/PhysRevB.93.245113
11. Zak J. Berry's Phase for Energy Bands in Solids. *Phys Rev Lett* (1989) 62:2747–50. doi:10.1103/PhysRevLett.62.2747

12. Xiao M, Ma G, Yang Z, Sheng P, Zhang ZQ, and Chan CT. Geometric Phase and Band Inversion in Periodic Acoustic Systems. *Nat Phys* (2015) 11:240–4. doi:10.1038/NPHYS3228
13. Yang Y, Huang X, and Hang ZH. Experimental Characterization of the Deterministic Interface States in Two-Dimensional Photonic Crystals. *Phys Rev Appl* (2016) 5:034009. doi:10.1103/PhysRevApplied.5.034009
14. Huang X, Yang Y, Hang ZH, Zhang ZQ, and Chan CT. Geometric Phase Induced Interface States in Mutually Inverted Two-Dimensional Photonic Crystals. *Phys Rev B* (2016) 93:085415. doi:10.1103/PhysRevB.93.085415
15. Yang Y, Xu T, Xu YF, and Hang ZH. Zak Phase Induced Multiband Waveguide by Two-Dimensional Photonic Crystals. *Opt Lett* (2017) 42:3085–8. doi:10.1364/OL.42.003085
16. Zhao W, Xu YF, Yang Y, Tao Z, and Hang ZH. Multiband Acoustic Waveguides Constructed by Two-Dimensional Phononic Crystals. *Appl Phys Express* (2020) 13:094001. doi:10.35848/1882-0786/abafc7
17. Ma T, and Shvets G. All-Si valley-hall Photonic Topological Insulator. *New J Phys* (2016) 18:025012. doi:10.1088/1367-2630/18/2/025012
18. Dong J-W, Chen X-D, Zhu H, Wang Y, and Zhang X. Valley Photonic Crystals for Control of Spin and Topology. *Nat Mater* (2017) 16:298–302. doi:10.1038/NMAT4807
19. Yan M, Lu J, Li F, Deng W, Huang X, Ma J, et al. On-chip valley Topological Materials for Elastic Wave Manipulation. *Nat Mater* (2018) 17:993–8. doi:10.1038/s41563-018-0191-5
20. Ye L, Yang Y, Hong Hang Z, Qiu C, and Liu Z. Observation of valley-selective Microwave Transport in Photonic Crystals. *Appl Phys Lett* (2017) 111:251107. doi:10.1063/1.5009597
21. Gao F, Xue H, Yang Z, Lai K, Yu Y, Lin X, et al. Topologically Protected Refraction of Robust Kink States in valley Photonic Crystals. *Nat Phys* (2018) 14:140–4. doi:10.1038/NPHYS4304
22. Shalaev MI, Walasik W, Tsukernik A, Xu Y, and Litchinitser NM. Robust Topologically Protected Transport in Photonic Crystals at Telecommunication Wavelengths. *Nat Nanotech* (2019) 14:31–4. doi:10.1038/s41565-018-0297-6
23. He X-T, Liang E-T, Yuan J-J, Qiu H-Y, Chen X-D, Zhao F-L, et al. A Silicon-On-Insulator Slab for Topological valley Transport. *Nat Commun* (2019) 10:872. doi:10.1038/s41467-019-08881-z
24. Mittal S, Fan J, Faez S, Migdall A, Taylor JM, and Hafezi M. Topologically Robust Transport of Photons in a Synthetic Gauge Field. *Phys Rev Lett* (2014) 113:087403. doi:10.1103/PhysRevLett.113.087403
25. Yang Y, Jiang H, and Hang ZH. Topological Valley Transport in Two-Dimensional Honeycomb Photonic Crystals. *Sci Rep* (2018) 8:1588. doi:10.1038/s41598-018-20001-3
26. Smirnova D, Leykam D, Chong Y, and Kivshar Y. Nonlinear Topological Photonics. *Appl Phys Rev* (2020) 7:021306. doi:10.1063/1.5142397
27. St-Jean P, Goblot V, Galopin E, Lemaître A, Ozawa T, Le Gratiet L, et al. Lasing in Topological Edge States of a One-Dimensional Lattice. *Nat Photon* (2017) 11:651–6. doi:10.1038/s41566-017-0006-2
28. Parto M, Wittek S, Hodaei H, Harari G, Bandres MA, Ren J, et al. Edge-mode Lasing in 1D Topological Active Arrays. *Phys Rev Lett* (2018) 120:113901. doi:10.1103/PhysRevLett.120.113901
29. Bahari B, Ndao A, Vallini F, El Amili A, Fainman Y, and Kanté B. Nonreciprocal Lasing in Topological Cavities of Arbitrary Geometries. *Science* (2017) 358:636–40. doi:10.1126/science.aao4551
30. Zhao H, Miao P, Teimourpour MH, Malzard S, El-Ganainy R, Schomerus H, et al. Topological Hybrid Silicon Microlasers. *Nat Commun* (2018) 9:981. doi:10.1038/s41467-018-03434-2
31. Bandres MA, Wittek S, Harari G, Parto M, Ren J, Segev M, et al. Topological Insulator Laser: Experiments. *Science* (2018) 359:eaar4005. doi:10.1126/science.aar4005
32. Zeng Y, Chattopadhyay U, Zhu B, Qiang B, Li J, Jin Y, et al. Electrically Pumped Topological Laser with valley Edge Modes. *Nature* (2020) 578:246–50. doi:10.1038/s41586-020-1981-x
33. Shao Z-K, Chen H-Z, Wang S, Mao X-R, Yang Z-Q, Wang S-L, et al. A High-Performance Topological Bulk Laser Based on Band-Inversion-Induced Reflection. *Nat Nanotechnol* (2020) 15:67–72. doi:10.1038/s41565-019-0584-x
34. *Comsol Multiphysics, v5.4* (https://cn.comsol.com)
35. Yang Y, Jia Z, Wu Y, Xiao R-C, Hang ZH, Jiang H, et al. Gapped Topological Kink States and Topological Corner States in Honeycomb Lattice. *Sci Bull* (2020) 65:531–7. doi:10.1016/j.scib.2020.01.024
36. Wu L-H, and Hu X. Scheme for Achieving a Topological Photonic crystal by Using Dielectric Material. *Phys Rev Lett* (2015) 114:223901. doi:10.1103/PhysRevLett.114.223901
37. Yang Y, Xu YF, Xu T, Wang H-X, Jiang J-H, Hu X, et al. Visualization of a Unidirectional Electromagnetic Waveguide Using Topological Photonic Crystals Made of Dielectric Materials. *Phys Rev Lett* (2018) 120:217401. doi:10.1103/PhysRevLett.120.217401

Conflict of Interest: The authors declare that the research was conducted in the absence of any commercial or financial relationships that could be construed as a potential conflict of interest.

frontiers in Physics

ORIGINAL RESEARCH
published: 28 September 2021
doi: 10.3389/fphy.2021.762567

Pseudospin-dependent Acoustic Topological Insulator by Sonic Crystals With Same Hexagonal Rods

Ding Jia[1,2], *Shuai Gu*[1], *Shuai Jiang*[1], *Yong Ge*[1], *Shou-qi Yuan*[1] *and Hong-xiang Sun*[1,3]*

[1]*Research Center of Fluid Machinery Engineering and Technology, School of Physics and Electronic Engineering, Jiangsu University, Zhenjiang, China,* [2]*School of Computer Science and Communications Engineering, Jiangsu University, Zhenjiang, China,* [3]*State Key Laboratory of Acoustics, Institute of Acoustics, Chinese Academy of Sciences, Beijing, China*

We report the experimental and numerical realization of a pseudospin-dependent acoustic topological insulator based on two sonic crystals constructed by the same regular hexagonal rods. Based on the zone folding mechanism, we obtain double Dirac cones with a four-fold deterministic degeneracy in the sonic crystal, and realize a band inversion and topological phase transition by rotating the rods. We observe the topologically protected one-way sound propagation of pseudospin-dependent edge states in a designed topological insulator composed of two selected sonic crystals with different rotation angles of the rods. Furthermore, we experimentally demonstrate the robustness of topological sound propagation against two types of defects, in which the edge states are almost immune to backscattering, and remain pseudospin-dependent characteristics. Our work provides a diverse route for designing tunable topological functional sound devices.

Keywords: sonic crystal, acoustic topological insulator, pseudospin, dirac cone, acoustics

OPEN ACCESS

Edited by:
Guancong Ma,
Hong Kong Baptist University, Hong Kong, SAR China

Reviewed by:
Yugui Peng,
Cuny Advanced Science Research Center, United States
Yun Jing,
The Pennsylvania State University (PSU), United States
Wen-Jie Chen,
Hong Kong University of Science and Technology, Hong Kong, SAR China

***Correspondence:**
Hong-xiang Sun
jsdxshx@ujs.edu.cn

Specialty section:
This article was submitted to Optics and Photonics, a section of the journal Frontiers in Physics

Received: *22 August 2021*
Accepted: *15 September 2021*
Published: *28 September 2021*

Citation:
Jia D, Gu S, Jiang S, Ge Y, Yuan S-q and Sun H-x (2021) Pseudospin-dependent Acoustic Topological Insulator by Sonic Crystals With Same Hexagonal Rods. Front. Phys. 9:762567. doi: 10.3389/fphy.2021.762567

INTRODUCTION

In the past few years, acoustic topological insulators (ATIs) have become a hot topic in the area of acoustics for its great potential applications, such as acoustic-noise reduction [1], acoustic beam splitter [2] and acoustic communications [3]. However, the intrinsic difference between electrons and acoustics poses a challenge to realize a spin-like degree of freedom for acoustics due to the longitudinal polarization characteristics of sound. To overcome it, four types of ATIs have been proposed successively. To mimic the quantum Hall effect and break time-reversal symmetry, topologically protected edge states were observed in acoustic waveguides by introducing circular flowing air [4–9]. Later, analogous Floquet ATIs were proposed based on coupled acoustic trimers or strong coupling ring resonator waveguides [10–13]. Moreover, to realize acoustic valley Hall (AVH) states, the nonzero Berry curvature located near the valley K/K′ was obtained by breaking mirror or inversion symmetry, and valley-projected topological edge states were observed at the interface between two sonic crystals (SCs) with distinct AVH phases [14–28]. Furthermore, to mimic quantum spin Hall states in acoustics, the SCs with C_6 crystal symmetry were introduced to realize artificial pseudospins-1/2 states by hybridizing degenerate modes [29–39]. Generally, the observed double Dirac cones are accidental degeneracy in these pseudospin-dependent ATIs, and the sizes or shapes of rods in the SCs are different, which is still a challenge for practical applications.

Recently, by introducing the zone folding mechanism, a type of pseudospin-dependent ATI without depending on a fixed filling ratio was proposed [30, 31], in which the observed double Dirac cones were a deterministic degeneracy. These types of pseudospin-dependent ATIs were designed by fictitious soft metamaterial rods [30] and three circular rods with different radius [31], and the

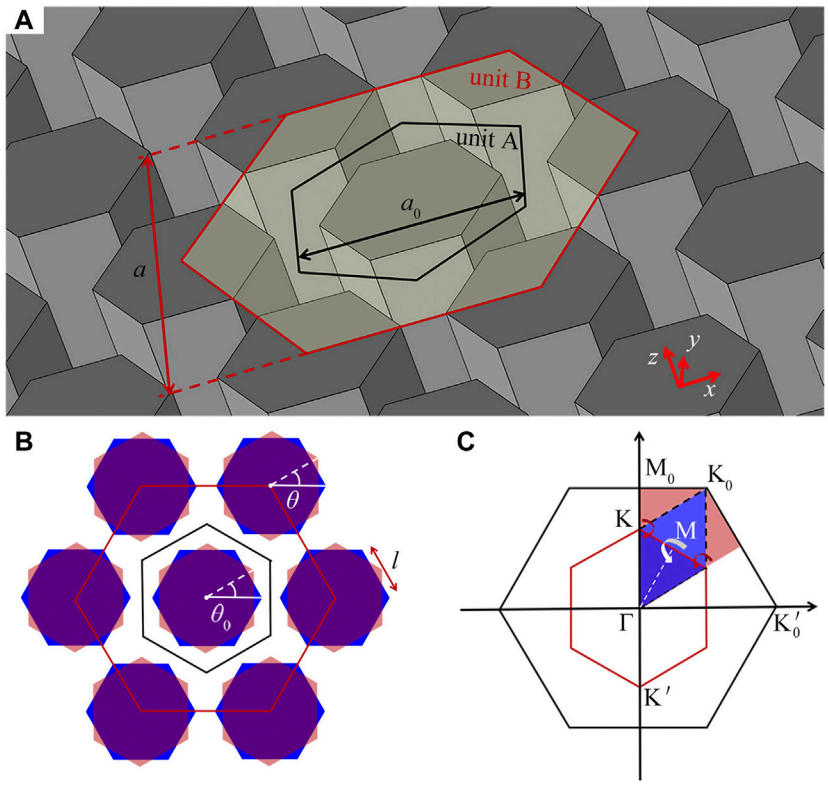

FIGURE 1 | (A) Schematic of an airborne SC composed of regular hexagonal rods. Black and red open regular hexagons refer to the units A and B with the lattice constants a_0 and a, respectively. **(B)** Schematic of the unit B with two types of configurations. Red regular hexagons exhibit its rotation state, and the parameters θ_0 and θ are the rotation angles of a central rod and six surrounding rods, respectively. Blue regular hexagons represent its riginal configuration ($\theta_0 = \theta = 0^\circ$). **(C)** Schematic of the folding mechanism of the BZs for the units A and B, corresponding to the black and red open regular hexagons, respectively.

complex structures greatly limit their applications. Based on the SCs composed of same rods, the experimental realization of the pseudospin-dependent ATIs with a deterministic degeneracy is still a challenge.

In this work, we propose a pseudospin-dependent ATI constructed by two airborne SCs which consist of the same rods. Based on the zone folding mechanism, we obtain double Dirac cones with the deterministic degeneracy, and realize a band inversion by simply rotating the rods in the SCs. Moreover, we design an ATI composed of two SCs with different rotation angles of the rods, and observe a one-way sound propagation of topological edge states. Finally, we experimentally demonstrate the robustness of the topologically protected sound propagation against two types of defects of a disorder and a bend.

RESULTS AND DISCUSSIONS

Figure 1A shows an airborne SC composed of regular hexagonal rods with the side length $l = 14.4$ mm. The proposed SC can be described by the unit A or B, in which the lattice constants of the units A and B are $a_0 = 30$ mm and $a = 30\sqrt{3}$mm, respectively. By simply rotating these rods, we obtain another type of SC composed of the unit B (shown in **Figure 1B**), in which the rotation angles of a central rod and six surrounding rods are θ_0 and θ, respectively. **Figure 1C** shows the folding mechanism of the Brillouin zones (BZs) for the units A and B. In the BZ, the point K_0 with high symmetry of the unit A can be folded into the point Γ of the unit B. Here, we use the COMSOL Multiphysics software to numerically simulate propagation characteristics of sound. The regular hexagon rods are fabricated with polymethyl methacrylate (PMMA), which is used to meet the condition of sound hard boundary in numerical models. The material parameters are adopted as follows: the density $\rho = 1180$ kg/m^3, the longitudinal wave velocity $c_l = 2730$ m/s and the transversal wave velocity $c_t = 1430$ m/s for PMMA; the density $\rho_0 = 1.18$ kg/m^3 and sound velocity $c_0 = 346$ m/s for air.

Figures 2A, B show the dispersion relations of the units A and B in the SC-I ($\theta_0 = 0^\circ$ and $\theta = 0^\circ$), respectively. As shown in **Figure 2A**, there exists a Dirac cone with the two-fold degeneracy at the point K_0 for the unit A, which is attributed to its C_{6v} symmetry. However, for the unit B, we observe double Dirac cones with a four-fold deterministic degeneracy at the point Γ (**Figure 2B**). The dispersion characteristics of both units agree well with the folding of the BZ.

Figures 2C,D show the dispersion relations of the unit B in the SC-II ($\theta_0 = 30^\circ$ and $\theta = 0^\circ$) and SC-III ($\theta_0 = 0^\circ$ and $\theta = 30^\circ$), respectively, in which the four-fold degeneracy is broken, and is divided into a double two-fold degeneracy (p and d types) for both cases. We can see that the bands of the d type are above the p

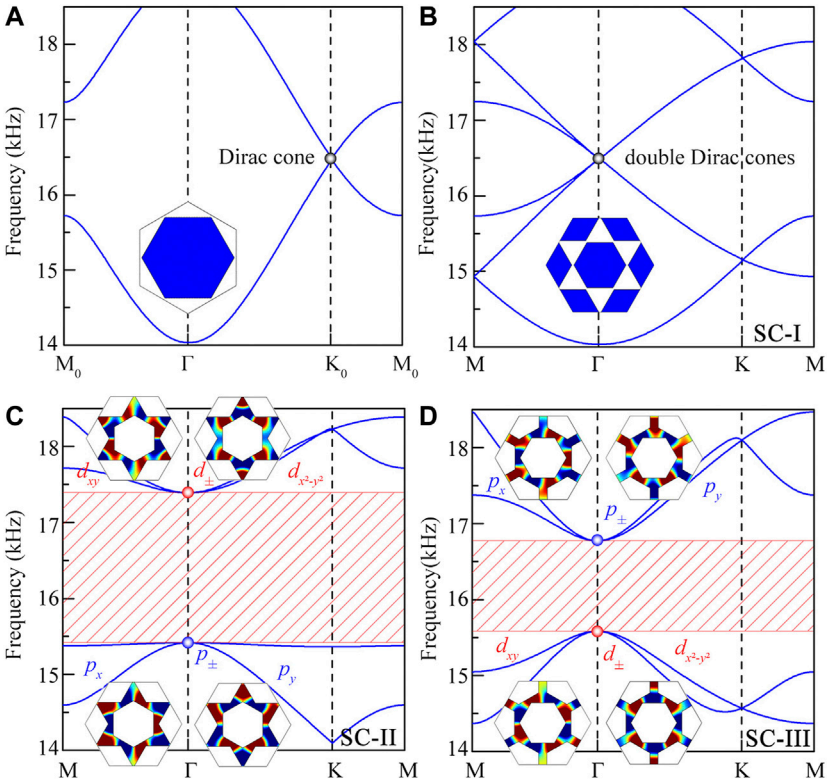

FIGURE 2 | Dispersion relations of the units **(A)** A and **(B)** B in the SC-I ($\theta_0 = 0^o$ and $\theta = 0^o$), and of the unit B in the **(C)** SC-II ($\theta_0 = 30^o$ and $\theta = 0^o$) and **(D)** SC-III ($\theta_0 = 0^o$ and $\theta = 30^o$). Black dots in **Figures 2A,B** represent the Dirac points. Eight insets in **Figures 2C,D** are the simulated pressure eigenfunctions of the pseudospin dipolar (p_x and p_y) and quadrupolar modes (d_{xy} and $d_{x^2-y^2}$) at the BZ center (red and blue dots) of the SC-II and SC-III, respectively.

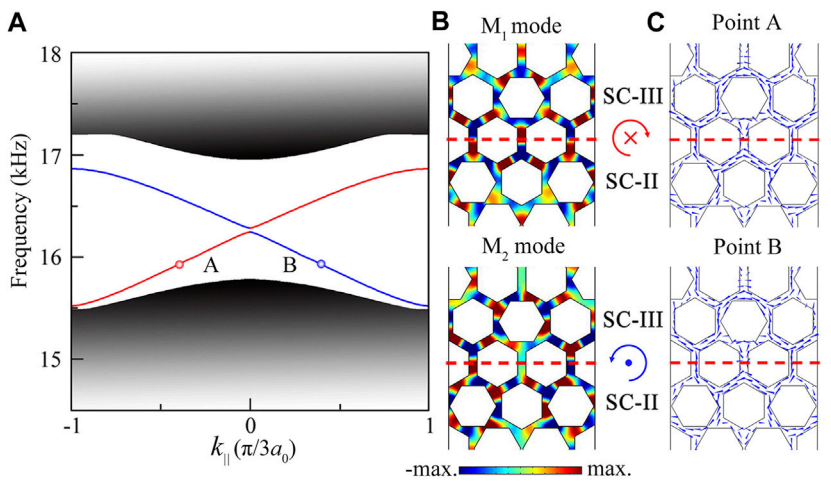

FIGURE 3 | (A) Dispersion relations of the ATI composed of the SC-II and SC-III. **(B)** Simulated pressure eigenfunctions (M_1 and M_2 modes) of the supercell at the point A ($k_{||} = -0.4$). **(C)** Simulated acoustic energy flow of the pseudospin-dependent edge states at the points A and B ($k_{||} = 0.4$). Red dashed lines refer to the domain wall of the ATI.

type in the SC-II (**Figure 2C**), while the bands of the *p* type are above the *d* type in the SC-III. The phenomenon of band inversion arises from the increasing coupling strength between the hexagonal rods by changing the values of θ_0 and θ. Additionally, the pressure eigenfunctions of the dipolar (p_x and p_y) and quadrupolar (d_{xy} and $d_{x^2-y^2}$) modes which

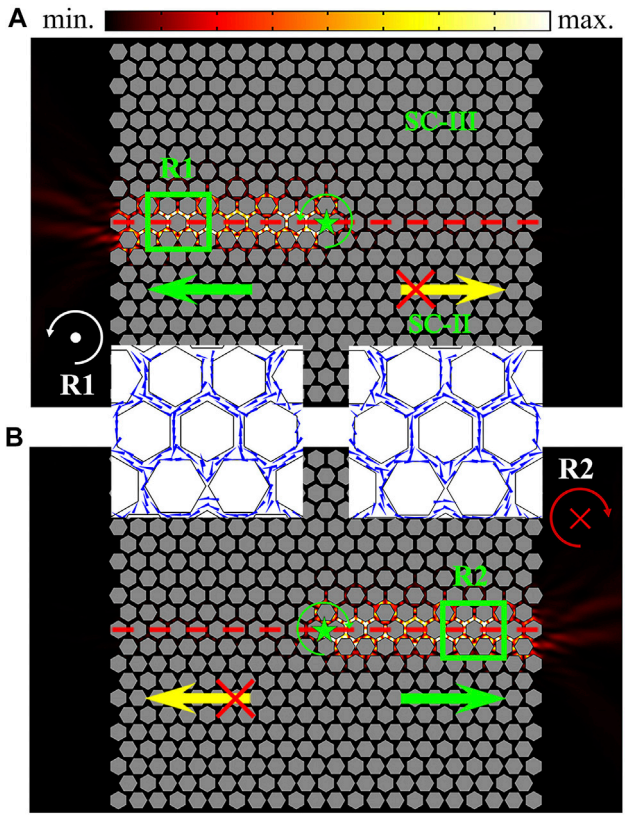

FIGURE 4 | Simulated intensity distributions in the ATI at 16.0 kHz (within the bulk band gap). Two types of chiral sound sources (green stars) with the opposite chirality (green circular arrows) are placed at the center of the domain wall, realizing one-way sound propagation towards the **(A)** left and **(B)** right sides along the domain wall. Red dashed lines represent the domain wall, and blue arrows in the zooms R1 and R2 refer to the direction of energy flow.

correspond to the blue and red dots are displayed in eight insets of **Figures 2C,D**, further showing a typical characteristic of the band inversion. Additionally, we also calculated the Chern numbers of SC-II and SC-III based on the Wilson-loop method (shown in the supplementary material), which further verify that both SCs have different topological phases. Here, it is worth mentioning that the pseudospin-1/2 modes of sound are the basis for imitating quantum spin Hall effect in acoustics, which can be realized by hybridizing both modes p and d as $p_{\pm} = (p_x \pm ip_y)/\sqrt{2}$ and $d_{\pm} = (d_{x^2-y^2} \pm id_{xy})/\sqrt{2}$.

Figure 3A shows the dispersion relations of the designed ATI composed of the SC-II and SC-III, in which the SC-III is placed on the upside of the SC-II. We observe a pair of edge states (red and blue solid lines) in the overlapped bulk band gap of both SCs, which is located at the domain wall between the SC-II and SC-III. Here, the group velocity of the edge states is determined by the slope of the bands (red and blue solid lines), and thus the edge states have the same acoustic velocity, but propagate in the opposite directions. Moreover, it is obvious that there exists a mini gap located between the bands of two edge states, which mainly arises from the reduction of the C_{6v} point group symmetry at the domain wall between SC-II and SC-III. **Figure 3B** shows the eigen-modes for the real (M_1) and imaginary (M_2) parts of the edge state at the point A. The edge states at the points A and B can be obtained by hybridizing the modes M_1 and M_2 as the forms of M_1+iM_2 and M_1-iM_2, respectively. To further exhibit the pseudospin-dependent characteristics, we simulate the distributions of energy flow around the domain wall of a supercell at the points A and B (shown in **Figure 3C**). We find that there exist energy vortexes around the domain wall, and the chirality of the vortex is clockwise at the point A, but is anticlockwise at the point B, which corresponds to the pseudospin− (red circular arrow) and pseudospin+ (blue circular arrow), respectively.

Next, we simulate the pseudospin-dependent one-way propagation of sound in the ATI composed of the SC-II and SC-III, in which the intensity distributions excited by two types of chiral sources (green stars) with the opposite chirality at 16.0 kHz are shown in **Figure 4**. The chiral sources are realized by six point sound sources arranged in a circular array with different initial phase delays, which are placed at the center of the domain wall. As shown in **Figure 4A**, when the chirality of the source is anticlockwise, the edge state propagates toward the left side along the domain wall with almost negligible backscattering. In addition, it is found from the zoom of R1 that, the chirality of the energy vortex remains the same during its propagation along the domain wall, which further demonstrates the one-way propagation of the pseudospin + edge state. However, when the chirality of the source is clockwise, the pseudospin edge state is excited and propagates toward the right side. Therefore, we demonstrate the one-way sound propagation of the pseudospin-dependent edge states.

To demonstrate the robustness feature of the pseudospin-dependent edge states, we separately introduce two kinds of defects (a lattice disorder and a bend) around the domain wall of the ATI. **Figure 5A** shows the photograph of the sample without the defects. The description of experimental set-up is displayed in the supplementary material. **Figures 5B–D** show the simulated intensity distributions in the ATIs without defects and with the defects of a disorder and a bend, respectively, in which a point source is placed at the left side of the domain wall. Meanwhile, the measured intensity distributions in the scanning region (green open rectangle) are shown at the right side. We find that the smooth propagations of the pseudospin edge states still exist with both types of defects (**Figures 5C,D**), and the corresponding intensity distributions are almost the same as those in **Figure 5B**. The experimental results agree well with the simulations. Beyond that, in the zooms of R3-R5 (**Figures 5B–D**), the chirality of edge states is not affected by both defects, showing high robustness of the pseudospin-dependent edge states.

Finally, to demonstrate the topologically protected sound propagation, we also experimentally measure the transmission spectra for the three types of ATIs in **Figures 5B–D**, which is shown in **Figure 6**. Note that the transmittance spectra for the three cases are almost the same, especially in the overlapped bulk band gap (black shaded region). Therefore, we further experimentally demonstrate the robustness of the pseudospin-dependent edge states.

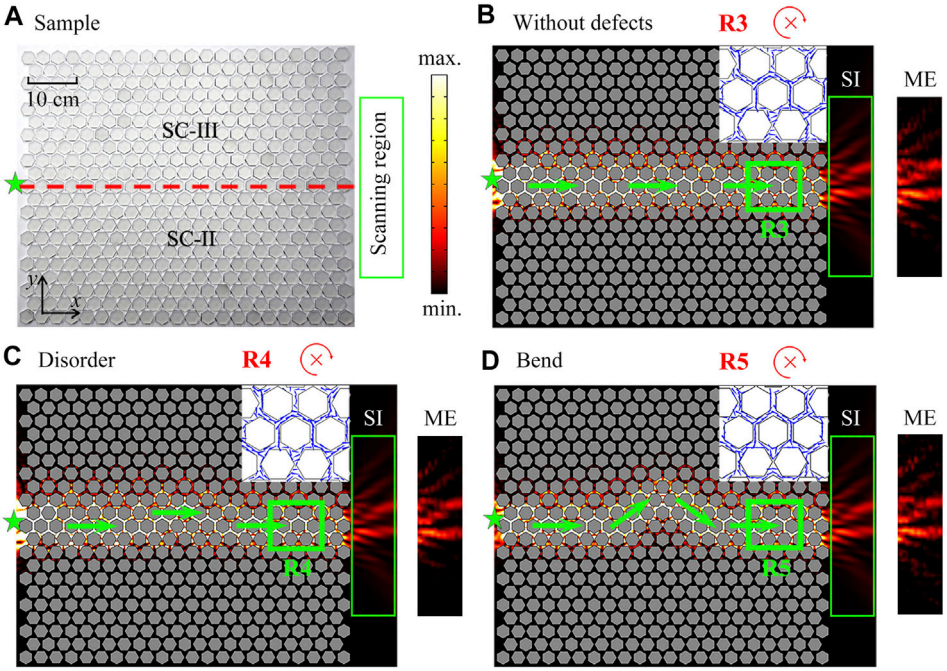

FIGURE 5 | (A) Photograph of an ATI without defects. Green stars and red dashed lines represent the point sound source and domain wall, respectively. Green open rectangle is the scanning region in the measurement. Simulated (SI) and measured (ME) distributions of intensity field in the ATIs with three different configurations at 16.0 kHz, corresponding to **(B)** without defects, with **(C)** a lattice disorder and **(D)** a bend around the domain wall. Green arrows are the propagation paths of sound in the ATIs. Blue arrows in the zooms R3-R5 represent direction of energy flow.

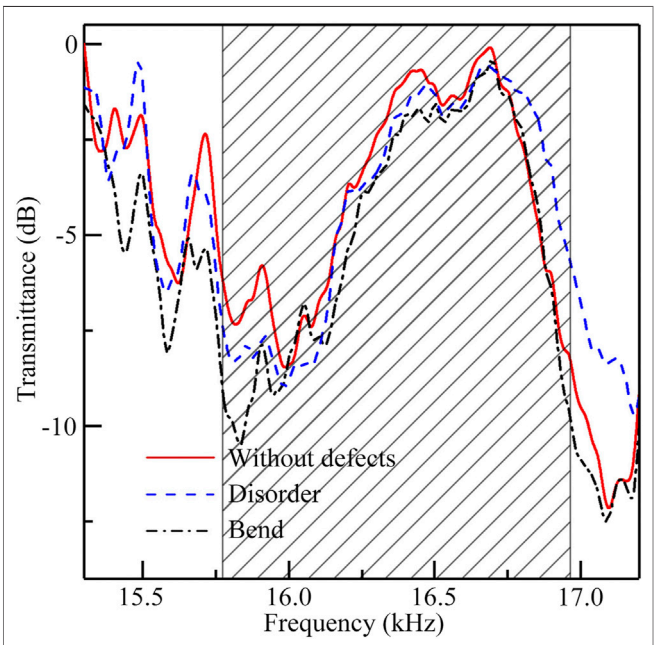

FIGURE 6 | Measured transmittance spectra of the ATIs with and without defects. Black shaded region represents the overlapped bulk band gap.

CONCLUSIONS

In conclusion, we have demonstrated a pseudospin-dependent ATI composed of two SCs with the same regular hexagonal rods. The results show that, by using the zone folding mechanism, the double Dirac cones with a four-fold deterministic degeneracy are observed in the SC, and the band inversion is realized by rotating the rods. Moreover, the ATI composed of two SCs with different rotation angles of the rods is designed, and the one-way sound propagation of the pseudospin-dependent edge states excited by the chiral sound sources in the ATI is observed. Furthermore, by measuring the transmission spectra in the ATIs with and without defects, the robustness of sound propagation against two types of defects (a lattice disorder and a bend) is demonstrated. The simulated and measured results agree well with each other. Our work opens a new venue to design tunable pseudospin-dependent ATIs with various functionalities and applications.

DATA AVAILABILITY STATEMENT

The original contributions presented in the study are included in the article/**Supplementary Material**, further inquiries can be directed to the corresponding author.

AUTHOR CONTRIBUTIONS

All authors listed have made a substantial, direct, and intellectual contribution to the work and approved it for publication.

FUNDING

This work was supported by the National Natural Science Foundation of China (Grant Nos. 11774137, 51779107 and 12174159), the China Postdoctoral Science Foundation (Grant No. 2020M671351), and the Postdoctoral Research Funding Program of Jiangsu Province (Grant No. 2021K567C).

SUPPLEMENTARY MATERIAL

The Supplementary Material for this article can be found online at: https://www.frontiersin.org/articles/10.3389/fphy.2021.762567/full#supplementary-material

REFERENCES

1. He C, Ni X, Ge H, Sun X-C, Chen Y-B, Lu M-H, et al. Acoustic Topological Insulator and Robust One-Way Sound Transport. *Nat Phys* (2016) 12:1124–9. doi:10.1038/nphys3867
2. Ye L, Qiu C, Lu J, Wen X, Shen Y, Ke M, et al. Observation of Acoustic valley Vortex States and valley-chirality Locked Beam Splitting. *Phys Rev B* (2017) 95(17):174106. doi:10.1103/physrevb.95.174106
3. Zhang Z, Tian Y, Wang Y, Gao S, Cheng Y, Liu X, et al. Directional Acoustic Antennas Based on Valley-Hall Topological Insulators. *Adv Mater* (2018) 30(36):1803229. doi:10.1002/adma.201803229
4. Yang Z, Gao F, Shi X, Lin X, Gao Z, Chong Y, et al. Topological Acoustics. *Phys Rev Lett* (2015) 114(11):114301. doi:10.1103/physrevlett.114.114301
5. Khanikaev AB, Fleury R, Mousavi SH, and Alù A. Topologically Robust Sound Propagation in an Angular-Momentum-Biased Graphene-like Resonator Lattice. *Nat Commun* (2015) 6:8260. doi:10.1038/ncomms9260
6. Ni X, He C, Sun X-C, Liu X-p., Lu M-H, Feng L, et al. Topologically Protected One-Way Edge Mode in Networks of Acoustic Resonators with Circulating Air Flow. *New J Phys* (2015) 17(5):053016. doi:10.1088/1367-2630/17/5/053016
7. Chen ZG, and Wu Y. Tunable Topological Phononic Crystals. *Phys Rev Appl* (2016) 5(5):054021. doi:10.1103/physrevapplied.5.054021
8. Ding Y, Peng Y, Zhu Y, Fan X, Yang J, Liang B, et al. Experimental Demonstration of Acoustic Chern Insulators. *Phys Rev Lett* (2019) 122:014302. doi:10.1103/PhysRevLett.122.014302
9. Gao P, Zhang ZW, and Christensen J. Sonic valley-Chern Insulators. *Phys Rev B* (2020) 101(2):020301. doi:10.1103/physrevb.101.020301
10. Fleury R, Khanikaev AB, and Alù A. Floquet Topological Insulators for Sound. *Nat Commun* (2016) 7:11744. doi:10.1038/ncomms11744
11. He C, Li Z, Ni X, Sun X-C, Yu S-Y, Lu M-H, et al. Topological Phononic States of Underwater Sound Based on Coupled Ring Resonators. *Appl Phys Lett* (2016) 108:031904. doi:10.1063/1.4940403
12. Peng Y-G, Qin C-Z, Zhao D-G, Shen Y-X, Xu X-Y, Bao M, et al. Experimental Demonstration of Anomalous Floquet Topological Insulator for Sound. *Nat Commun* (2016) 7:13368. doi:10.1038/ncomms13368
13. Wei Q, Tian Y, Zuo SY, Cheng Y, and Liu XJ Experimental Demonstration of Topologically Protected Efficient Sound Propagation in an Acoustic Waveguide Network. *Phys Rev B* (2017) 95:094305. doi:10.1103/physrevb.95.094305
14. Lu J, Qiu C, Ye L, Fan X, Ke M, Zhang F, et al. Observation of Topological valley Transport of Sound in Sonic Crystals. *Nat Phys* (2016) 13:369–74. doi:10.1038/nphys3999
15. Lu J, Qiu C, Deng W, Huang X, Li F, Zhang F, et al. Valley Topological Phases in Bilayer Sonic Crystals. *Phys Rev Lett* (2018) 120:116802. doi:10.1103/physrevlett.120.116802
16. Zhang ZW, Tian Y, Cheng Y, Wei Q, Liu XJ, and Christensen J. Topological Acoustic Delay Line. *Phys Rev Appl* (2018) 9(3):034032. doi:10.1103/physrevapplied.9.034032
17. Yang Y, Yang Z, and Zhang B. Acoustic valley Edge States in a Graphene-like Resonator System. *J Appl Phys* (2018) 123(9):091713. doi:10.1063/1.5009626
18. Wen X, Qiu C, Lu J, He H, Ke M, and Liu Z. Acoustic Dirac Degeneracy and Topological Phase Transitions Realized by Rotating Scatterers. *J Appl Phys* (2018) 123(9):091703. doi:10.1063/1.5004073
19. Zhang Z, Cheng Y, and Liu X. Achieving Acoustic Topological valley-Hall States by Modulating the Subwavelength Honeycomb Lattice. *Sci Rep* (2018) 8:16784. doi:10.1038/s41598-018-35214-9
20. Xie BY, Liu H, Cheng H, Liu ZY, Chen SQ, and Tian JG. Acoustic Topological Transport and Refraction in a Kekulé Lattice. *Phys Rev Appl* (2019) 11:044086. doi:10.1103/physrevapplied.11.044086
21. Zhu ZX, Huang XQ, Lu JY, Yan M, Li F, Deng WY, et al. Negative Refraction and Partition in Acoustic Valley Materials of a Square Lattice. *Phys Rev Appl* (2019) 12:024007. doi:10.1103/physrevapplied.12.024007
22. Shen Y, Qiu C, Cai X, Ye L, Lu J, Ke M, et al. Valley-projected Edge Modes Observed in Underwater Sonic Crystals. *Appl Phys Lett* (2019) 114:023501. doi:10.1063/1.5049856
23. Shan Q, Yu D, Li G, Yuan L, and Chen X. One-way Topological States along Vague Boundaries in Synthetic Frequency Dimensions Including Group Velocity Dispersion (Invited). *Pier* (2020) 169:33–43. doi:10.2528/pier20083101
24. Tian Z, Shen C, Li J, Reit E, Bachman H, Socolar JES, et al. Dispersion Tuning and Route Reconfiguration of Acoustic Waves in valley Topological Phononic Crystals. *Nat Commun* (2020) 11:762. doi:10.1038/s41467-020-14553-0
25. Zhao W, Xu Y, Yang Y, Tao Z, and Hang ZH. Multiband Acoustic Waveguides Constructed by Two-Dimensional Phononic Crystals. *Appl Phys Express* (2020) 13:094001. doi:10.35848/1882-0786/abafc7
26. Wang M, Zhou W, Bi L, Qiu C, Ke M, and Liu Z. Valley-locked Waveguide Transport in Acoustic Heterostructures. *Nat Commun* (2020) 11:3000. doi:10.1038/s41467-020-16843-z
27. Yu L, Xue H, and Zhang B. Antichiral Edge States in an Acoustic Resonator Lattice with Staggered Air Flow. *J Appl Phys* (2021) 129:235103. doi:10.1063/5.0050645
28. Jia D, Ge Y, Xue H, Yuan S-q., Sun H-x., Yang Y, et al. Topological Refraction in Dual-Band valley Sonic Crystals. *Phys Rev B* (2021) 103:144309. doi:10.1103/physrevb.103.144309
29. Mei J, Chen Z, and Wu Y. Pseudo-time-reversal Symmetry and Topological Edge States in Two-Dimensional Acoustic Crystals. *Sci Rep* (2016) 6:32752. doi:10.1038/srep32752
30. Zhang Z, Wei Q, Cheng Y, Zhang T, Wu D, and Liu X. Topological Creation of Acoustic Pseudospin Multipoles in a Flow-free Symmetry-Broken Metamaterial Lattice. *Phys Rev Lett* (2017) 118:084303. doi:10.1103/PhysRevLett.118.084303
31. Deng Y, Ge H, Tian Y, Lu M, and Jing Y. Observation of Zone Folding Induced Acoustic Topological Insulators and the Role of Spin-Mixing Defects. *Phys Rev B* (2017) 96:184305. doi:10.1103/physrevb.96.184305
32. Yves S, Fleury R, Lemoult F, Fink M, and Lerosey G. Topological Acoustic Polaritons: Robust Sound Manipulation at the Subwavelength Scale. *New J Phys* (2017) 19(7):075003. doi:10.1088/1367-2630/aa66f8
33. Chen JJ, Huang HB, Huo SY, Tan ZH, Xie XP, Cheng JC, et al. Self-ordering Induces Multiple Topological Transitions for In-Plane Bulk Waves in Solid Phononic Crystals. *Phys Rev B* (2018) 98(1):014302. doi:10.1103/physrevb.98.014302

34. Jia D, Sun H-x., Xia J-p., Yuan S-q., Liu X-j., and Zhang C. Acoustic Topological Insulator by Honeycomb Sonic Crystals with Direct and Indirect Band Gaps. *New J Phys* (2018) 20:093027. doi:10.1088/1367-2630/aae104
35. You B, Dong M, Zhou J, and Xu H. Performance Improvement and Antenna Design of Left-Handed Material Units Based on Topological Deformations. *Pier* (2019) 165:13–33. doi:10.2528/pier19011603
36. Lee T, and Iizuka H. Bragg Scattering Based Acoustic Topological Transition Controlled by Local Resonance. *Phys Rev B* (2019) 99(6):064305. doi:10.1103/physrevb.99.064305
37. Ma G, Xiao M, and Chan CT. Topological Phases in Acoustic and Mechanical Systems. *Nat Rev Phys* (2019) 1:281–94. doi:10.1038/s42254-019-0030-x
38. Wang B, Huang Q, Chen K, Zhang J, Kurczveil G, Liang D, et al. Modulation on Silicon for Datacom: Past, Present, and Future (Invited Review). *Pier* (2019) 166:119–45. doi:10.2528/pier19102405
39. Ji CY, Zhang Y, Liao Y, Zhou X, Jiang JH, Zou B, et al. Fragile Topologically Protected Perfect Reflection for Acoustic Waves. *Phys Rev Res* (2020) 2(1): 013131. doi:10.1103/physrevresearch.2.013131

Conflict of Interest: The authors declare that the research was conducted in the absence of any commercial or financial relationships that could be construed as a potential conflict of interest.

Publisher's Note: All claims expressed in this article are solely those of the authors and do not necessarily represent those of their affiliated organizations, or those of the publisher, the editors and the reviewers. Any product that may be evaluated in this article, or claim that may be made by its manufacturer, is not guaranteed or endorsed by the publisher.

frontiers in Physics

ORIGINAL RESEARCH
published: 26 October 2021
doi: 10.3389/fphy.2021.770589

Measurement of Corner-Mode Coupling in Acoustic Higher-Order Topological Insulators

Xiao Li[1,2,3‡], *Shiqiao Wu*[2†‡], *Guanqing Zhang*[2], *Wanzhu Cai*[4], *Jack Ng*[1] *and Guancong Ma*[2*]

[1]Department of Physics, Southern University of Science and Technology, Shenzhen, China, [2]Department of Physics, Hong Kong Baptist University, Kowloon Tong, China, [3]Department of Physics, The Hong Kong University of Science and Technology, Hong Kong, China, [4]Guangzhou Key Laboratory of Vacuum Coating Technologies and New Energy Materials, Siyuan Laboratory, Department of Physics, Jinan University, Guangzhou, China

OPEN ACCESS

Edited by:
Yiqi Zhang,
Xi'an Jiaotong University, China

Reviewed by:
Haoran Xue,
Nanyang Technological University, Singapore
Yihao Yang,
Zhejiang University, China
Daohong Song,
School of Physics, Nankai University, China

***Correspondence:**
Guancong Ma
phgcma@hkbu.edu.hk

[†]**Present address:**
Shiqiao Wu,
School of Physical Science and Technology, Soochow University, Suzhou, China

[‡]These authors have contributed equally to this work

Specialty section:
This article was submitted to Optics and Photonics, a section of the journal Frontiers in Physics

Received: 04 September 2021
Accepted: 07 October 2021
Published: 26 October 2021

Citation:
Li X, Wu S, Zhang G, Cai W, Ng J and Ma G (2021) Measurement of Corner-Mode Coupling in Acoustic Higher-Order Topological Insulators. Front. Phys. 9:770589. doi: 10.3389/fphy.2021.770589

Recent developments of band topology have revealed a variety of higher-order topological insulators (HOTIs). These HOTIs are characterized by a variety of different topological invariants, making them different at a fundamental level. However, despite such differences, the fact that they all sustain higher-order topological boundary modes poses a challenge to phenomenologically tell them apart. This work presents experimental measurements of the coupling effects of topological corner modes (TCMs) existing in two different types of two-dimensional acoustic HOTIs. Although both HOTIs have a similar four-site square lattice, the difference in magnetic flux per unit cell dictates that they belong to different types of topologically nontrivial phases—one lattice possesses quantized dipole moments, but the other is characterized by quantized quadrupole moment. A link between the topological invariants and the response line shape of the coupled TCMs is theoretically established and experimentally confirmed. Our results offer a pathway to distinguish HOTIs experimentally.

Keywords: topological corner modes, higher-order topological insulators, phononic crystals, tightbinding model, green's function

INTRODUCTION

The recent development of topological band theory has revealed the existence of higher-order topological insulators (HOTIs) [1–5]. An important hallmark of such HOTIs is the existence of $(D-n)$ -dimensional topological boundary modes, where D is the dimensionality of the system, and $n \in (1, D]$ is an integer. Thanks to the development of classical wave crystals, HOTIs have not only been observed in solid-state electronics but also in photonic crystals [6–12], sonic crystals [13–19], and elastic-wave crystals [20, 21].

For HOTIs with two real-space dimensions, the higher-order topological boundary modes are zero-dimensional modes localized at the corners of the lattice. These topological corner modes (TCMs) can be protected by a variety of topological invariants, such as quantized dipole moments [9, 10, 22], quantized quadrupole moments [1, 23, 24], combinations of first Chern numbers [17], etc. However, although their topological protection can be revealed by theoretical computation of the topological invariants, it is difficult to distinguish them from an observational point of view.

A previous theoretical study has analyzed the finite-size effect on neighboring TCMs in a 2D HOTI [25]. By comparing two different types of topologically nontrivial square-lattice HOTIs—a topological dipole insulator (TDI) wherein the dipole moments are quantized and a topological

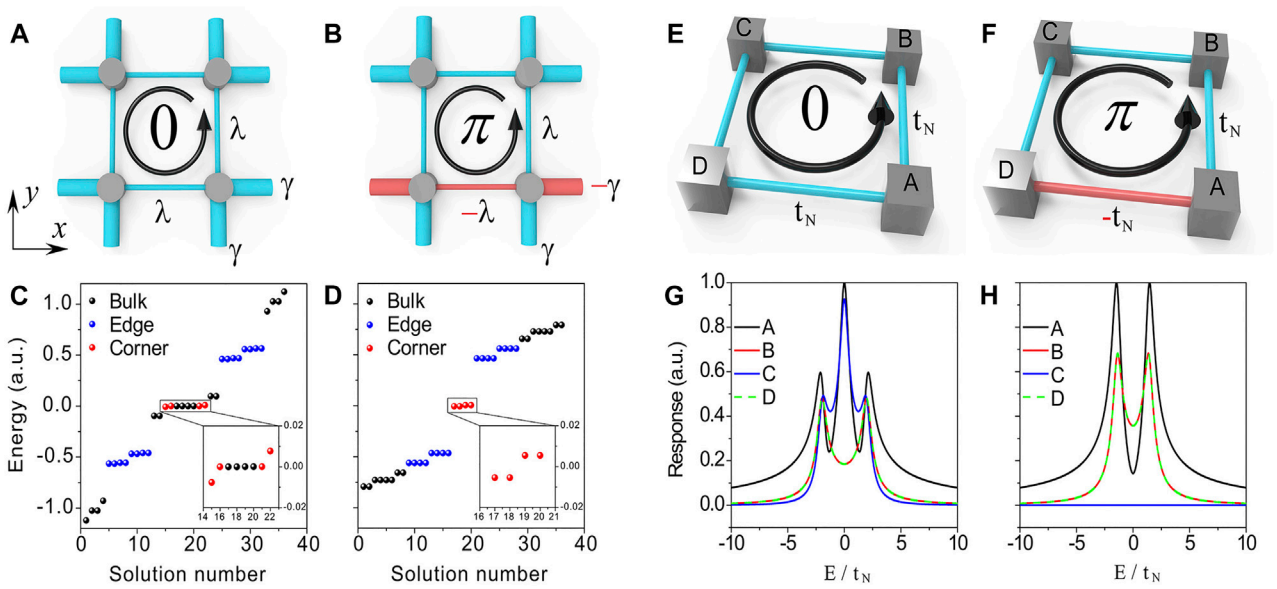

FIGURE 1 | The unit cell of the TDI **(A)** and TQI **(B)**, where the thin and thick tubes denote the intracell (λ or $-\lambda$) and intercell (γ or $-\gamma$) hopping, respectively. **(C–D)** The bulk (black points), edge (blue points), and corner (red points) modes of a 3×3 lattice of the TDI **(C)** and TQI **(D)**, where $\lambda = 0.1$ and $\gamma = 0.5$. **(E–F)** Schematic drawings of a corner-mode Hamiltonian for the TCMs of the TDI **(E)** and TQI **(F)**. The gray boxes represent the TCMs. The blue and red tubes respectively represent positive and negative edge hopping. **(G–H)** The corner responses with excitation at corner A. Here, $\eta = 0.4$.

quadrupole insulator (TQI) with a quantized quadrupole moment, it was shown that the TCMs' spectral responses split, and the line shapes are associated with the topological characteristics of the HOTI. As such, the spectral responses of the coupled TCMs are an observable effect, by which the underlying topological nature can be phenomenologically revealed.

THEORETICAL CONSTRUCT

For the sake of completeness, we first briefly summarize the important theoretical background. A complete theoretical analysis can be found in Ref. [25]. Here, the TDIs and TQIs are both based on the extensions of the 1D Su-Schrieffer-Heeger (SSH) model, and we show the unit-cell structures for the 2D TDI and TQI in **Figure 1A,B**, respectively. The strengths of the staggered nearest couplings along x and y directions are denoted as intracell λ (thin tubes) and intercell γ (thick tubes) hopping. For the TDI, all hopping coefficients are on the same sign so that the net magnetic flux in a plaquette is zero. For the TQI, the hopping coefficients can take opposite signs, as indicated by the red tubes in **Figure 1B**. The resultant net magnetic flux is π. When $|\lambda/\gamma| < 1$, both systems are in the topologically nontrivial phase and have topological edge modes and TCMs, as shown in **Figures 1C,D**.

For a $N \times N$ TDI lattice, the corresponding Hamiltonian can be written as

$$H^{TDI} = I_{2N\times 2N} \otimes H_x^{SSH} + H_y^{SSH} \otimes I_{2N\times 2N}, \tag{1}$$

with

$$H_x^{SSH} = H_y^{SSH} = H^{SSH} = \lambda \sum_{m=1}^{N} (|m, B\rangle\langle m, A| + |m, A\rangle\langle m, B|) + \gamma \sum_{m=1}^{N-1} (|m+1, A\rangle\langle m, B| + |m, B\rangle\langle m+1, A|), \tag{2}$$

where $I_{2N\times 2N}$ is a $2N \times 2N$ identity matrix, $\otimes$ denotes Kronecker product, and $|m, A\rangle$ and $|m, B\rangle$ denote states of the left and right atoms, respectively, in the mth unit cell for a 1D SSH chain model. For a $N \times N$ TQI, the Hamiltonian is

$$H^{TQI} = I_{2N\times 2N} \otimes \sigma_3 \otimes H_x^{SSH} + H_y^{SSH} \otimes I_{2N\times 2N} \otimes \sigma_0, \tag{3}$$

where σ_0 is a 2×2 identity matrix, and σ_3 is the z-component of the spin-1/2 Pauli matrices.

We plot the eigenvalues of **Eq. 1**, **3** in **Figures 1C,D**, respectively. The parameters are set as $\lambda = 0.1$, $\gamma = 0.5$, and $N = 3$. The bulk, edge, and corner modes are marked by black, blue, and red points, respectively. In both cases, four TCMs are found. As seen in the insets, the four TCMs are not degenerate. This is because, in a finite-sized lattice, the edges can provide coupling to neighboring TCMs [25]. For the TDI, the TCMs split into three clusters, with the two modes in the middle being degenerate. The two degenerate TCMs are still pinned at zero energy because of chiral symmetry. For the TQI, it can be proved that all eigenstates, including bulk modes and TCMs, are at least doubly degenerate [25, 26]. Therefore, the TCMs are divided into two doubly degenerate clusters, which are symmetric about zero energy. The finite-sized coupling effect can be captured by a four-state effective Hamiltonian with the four TCMs as the basis, which reads

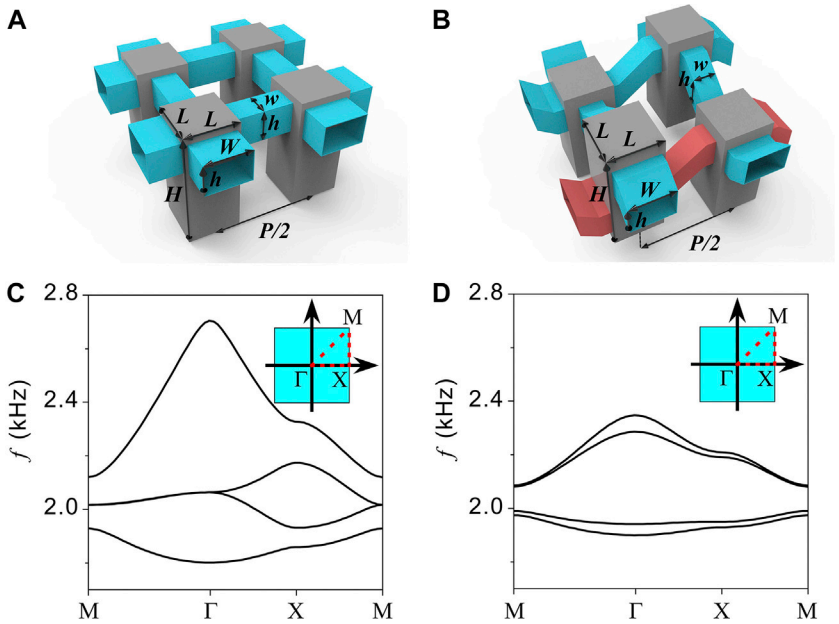

FIGURE 2 | (A–B) The designs of phononic crystal unit cells of the TDI **(A)** and TQI **(B)**. **(C–D)** The band structures of the TDI **(C)** and TQI **(D)**. The inset in each plot denotes the first Brillouin zone.

$$H_{corner}^{TDI} = \begin{pmatrix} 0 & t_N & t_N & 0 \\ t_N & 0 & 0 & t_N \\ t_N & 0 & 0 & t_N \\ 0 & t_N & t_N & 0 \end{pmatrix}, \tag{4}$$

for the TDI, and

$$H_{corner}^{TQI} = \begin{pmatrix} 0 & t_N & t_N & 0 \\ t_N & 0 & 0 & t_N \\ t_N & 0 & 0 & -t_N \\ 0 & t_N & -t_N & 0 \end{pmatrix}, \tag{5}$$

for the TQI. Here, $t_N = a_1 b_N \lambda (-\lambda/\gamma)^{N-1}$, where a_m (b_m) denotes the strength of the eigenstate $|m, A\rangle$ ($|m, B\rangle$) of H^{SSH}. Since $|\lambda/\gamma| < 1$, t_N is vanishing for large N. These models are schematically shown in **Figures 1E,F**. Note that similar to their respective unit cells, there is a magnetic flux of 0 and π in the TDI and TQI-corner models, respectively. From **Eqs. 4**, **5**, we can use a Green's function to describe the spectral responses of the coupled TCMs

$$\hat{G}(E) = \sum_{j=1}^{4} \frac{|\phi_j\rangle\langle\phi_j|}{E - E_j + i\eta t_N}, \tag{6}$$

where E_j is the eigenvalue and $|\phi_j\rangle$ is the eigenvector, and η accounts for any dissipative effect in the system. When excited at corner $|m\rangle$, the response at the corner $|n\rangle$ will be $G_{m,n}(E) = \langle m|\hat{G}(E)|n\rangle$. When excited at corner A, the responses at each corner are shown in **Figure 1G** for the TDI, and **Figure 1H** for TQI. It is seen that the spectral responses are different for the TDI and TQI. Particularly, the TDI responses can split into three peaks when measured at corners A and C, and the TQI response vanishes when measured at C. Such distinctions are an important manifestation of the quantized magnetic fluxes in the systems, which can be used as experimental evidence to distinguish the two classes of HOTIs.

EXPERIMENTAL RESULTS

We next present the designs of phononic crystals to realize both the TDI and TQI. The unit cells are shown in **Figures 2A,B**, respectively. The gray blocks denote the acoustic cavities, whose first-order resonance fulfills the role of the on-site orbital. The cavities have a height of H = 80mm and a width of L = 35mm, and they are coupled by tubes that facilitate the hopping terms. For the TDI, the widths of the intracell and intercell coupling tubes are w = 17mm and W = 30mm, respectively. They are connected at a vertical position with the height being the same h = 21mm. The lattice constant is a = 150mm. The design of the TQI is different because we need to realize hopping terms with a negative sign. To achieve this, we connect the top of one cavity to the bottom of the designated neighbor using a bent tube (red in **Figure 2B**). The blue tubes which facilitate positive hopping are also bent in the same manner so that all tubes have the same length. The positions of the cavities are staggeredly elevated so that the lengths of the intracell or intercell coupling tubes are the same. We use COMSOL Multiphysics to compute the band structures of the two types of unit cells. The medium inside the cavity and coupling tubes is air with a mass density of 1.23 kg/m^2 and a sound speed of $343 \times (1 + 0.005i)$ m/s, where the imaginary part denotes losses. The results are respectively shown in **Figures 2C,D**, where four bands are seen for both cases.

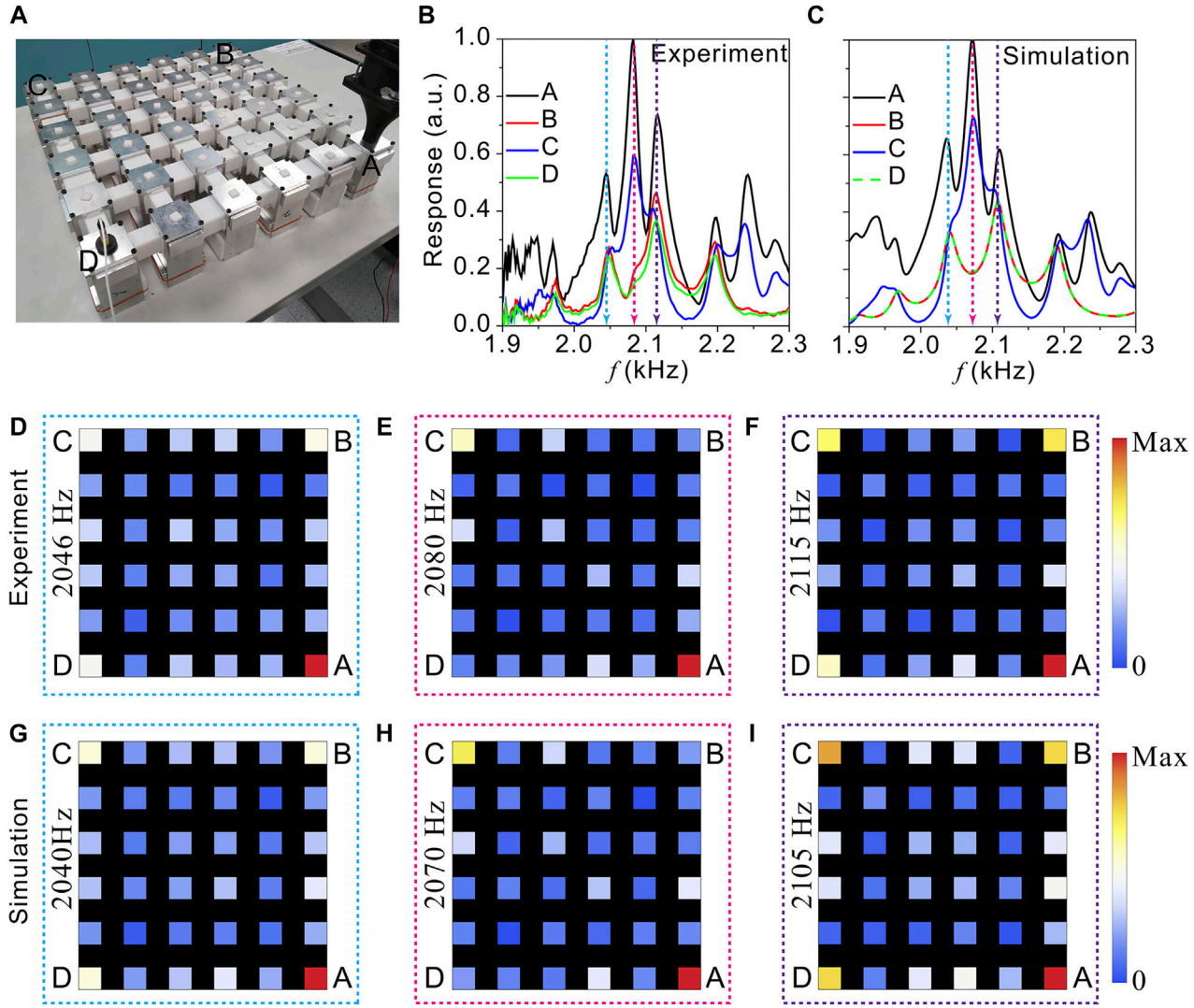

FIGURE 3 | (A) A photograph showing the fabricated TDI phononic crystal. **(B–C)** Measured **(B)** and simulated **(C)** corner responses. **(D–F)** Measured responses at the frequencies corner-mode resonant peaks: **(D)** 2046Hz, **(E)** 2080Hz, **(F)** 2115 Hz. **(G–I)** Simulated responses at the frequencies corner-mode resonant peaks: **(G)** 2040Hz, **(H)** 2070Hz, **(I)** 2105 Hz.

Based on these two designs, we have fabricated the phononic crystals. The cavities are machined from aluminum alloy and the coupling tubes are 3D printed using photosensitive resin. The photographs of the TDI and TQI configurations are shown in **Figure 3A**, **4A**, respectively. Both lattices are 3×3 in size, containing a total of 36 cavities. At the top of the cavities, we drilled a small hole (covered with a small white plug), where a sound signal is sent or a probe can detect the acoustic signal inside the cavity. We excite corner A with a loudspeaker, as shown in **Figure 3A**, **4A**. Then, we used a microphone to obtain the spectral response field in every cavity. For the TDI lattice, the responses measured at corners A, B, C, D are shown in **Figure 3B**. In the predicted frequency regime, i. e., 2,050–2,150 Hz, a three-peak response line shape is seen for both the spectra measured at corners A and C. And two-peak line shape is seen for corners B and D. These results agree well with the theoretical prediction by the tight-binding model (**Figures 1C,G**). To confirm that these responses are due to the coupled TCMs, we have measured the pressure responses in all cavities at the frequencies of the response peaks. The results are shown in **Figures 3D–F**. Clearly, the spatial distributions are strongly localized at the corners, which is a signature characteristic of TCMs. We have further verified the responses in numerical simulations. The results in **Figure 3C,G–I** also show excellent agreement with the experiment.

Similar experiments were performed for the TQI lattice. In **Figure 4B**, two response peaks are identified in the bulk gap (2,000–2,150 Hz) for the spectra measured at corners A, B, D. Also, the response at corner C is significantly weaker. These observations again align with the prediction (**Figures 1D,H**) and simulations (**Figure 4C**). We further confirm in the measured (**Figures 4D,E**) and simulated (**Figures 4F,G**) spatial maps that the response peaks are indeed due to the TCMs.

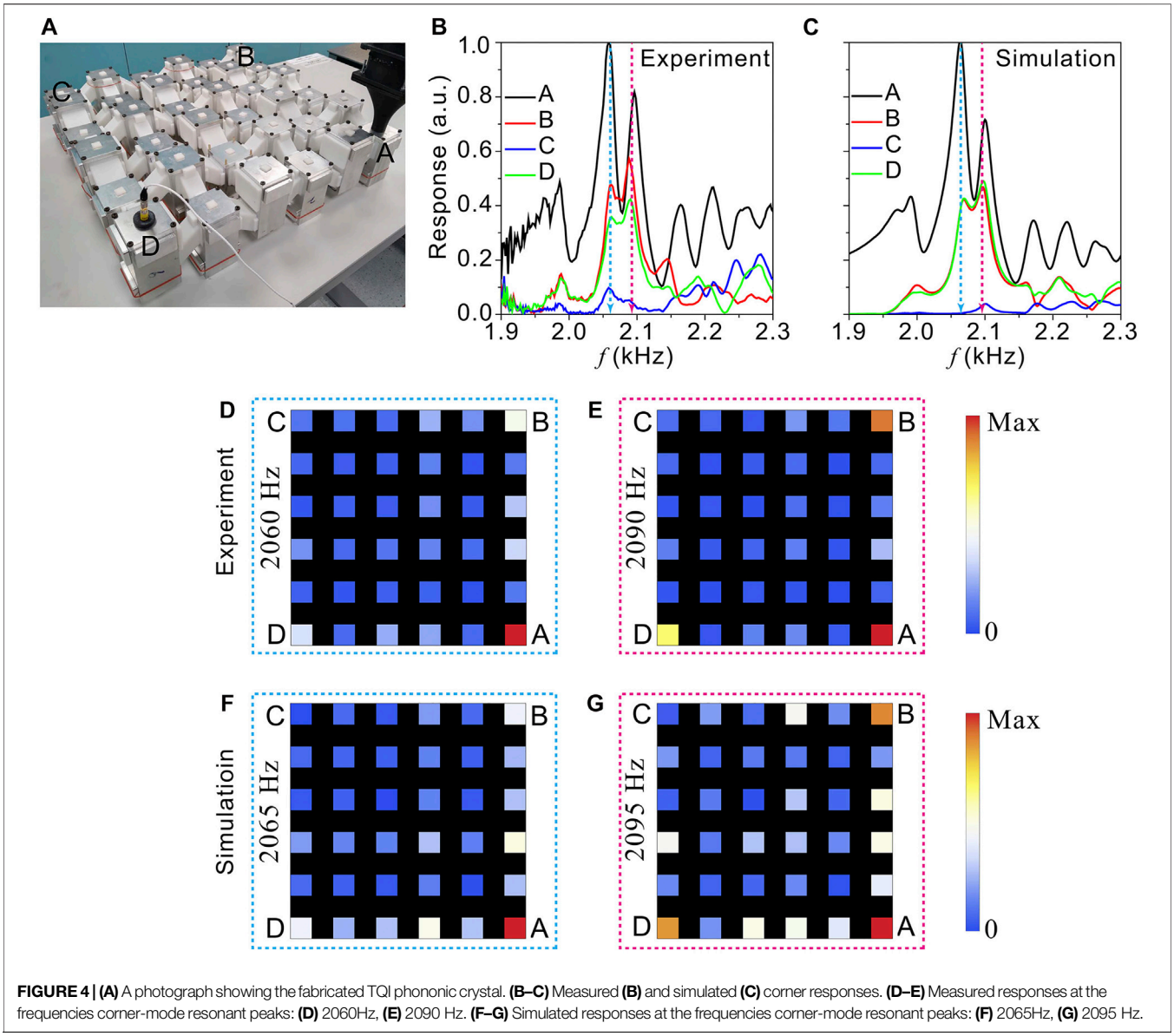

FIGURE 4 | (A) A photograph showing the fabricated TQI phononic crystal. **(B–C)** Measured **(B)** and simulated **(C)** corner responses. **(D–E)** Measured responses at the frequencies corner-mode resonant peaks: **(D)** 2060Hz, **(E)** 2090 Hz. **(F–G)** Simulated responses at the frequencies corner-mode resonant peaks: **(F)** 2065Hz, **(G)** 2095 Hz.

CONCLUSION

In summary, we have experimentally observed the coupling effects of TCMs in two different types of acoustic HOTIs. The measured line shapes of the corner responses agree excellently with a previous theoretical study, which confirms that the topological properties of the HOTIs can indeed influence the coupling effects of TCMs. Therefore, the corner responses can serve as an experimental hallmark to separate HOTIs of different classes. It is interesting to further the study by investigating the coupling effects in other types of HOTIs such as a Kagome lattice [4], honeycomb lattice [20], etc. On the other hand, the coupled higher-order topological modes can be a useful starting point for higher-order non-Hermitian physics [27, 28]. They may also find applications such as topological wave and light confinement [13, 29] and topological lasing [30, 31].

DATA AVAILABILITY STATEMENT

The raw data supporting the conclusion of this article will be made available by the authors, without undue reservation.

AUTHOR CONTRIBUTIONS

XL and SW performed numerical simulations and designed the experiment. XL, SW, GZ carried out the measurements. All authors

analyzed and discussed the results. XL and GM wrote the manuscript with inputs from others. GM initiated and supervised the research.

FUNDING

This work was supported by Hong Kong Research Grants Council (12302420, 12300419, 22302718, and C6013-18G), National Natural Science Foundation of China (11922416, 11802256), and Hong Kong Baptist University (RC-SGT2/18-19/SCI/006).

ACKNOWLEDGMENTS

The authors thank Weiwei Zhu for the discussions.

REFERENCES

1. Benalcazar WA, Bernevig BA, and Hughes TL. Quantized Electric Multipole Insulators. *Science* (2017) 357:61–6. doi:10.1126/science.aah6442
2. Benalcazar WA, Bernevig BA, and Hughes TL. Electric Multipole Moments, Topological Multipole Moment Pumping, and Chiral Hinge States in Crystalline Insulators. *Phys Rev B* (2017) 96:245115. doi:10.1103/physrevb.96.245115
3. Schindler F, Cook AM, Vergniory MG, Wang Z, Parkin SSP, Bernevig BA, et al. Higher-order Topological Insulators. *Sci Adv* (2018) 4:eaat0346. doi:10.1126/sciadv.aat0346
4. Ezawa M. Higher-Order Topological Insulators and Semimetals on the Breathing Kagome and Pyrochlore Lattices. *Phys Rev Lett* (2018) 120: 026801. doi:10.1103/PhysRevLett.120.026801
5. Xie B, Wang HX, Zhang X, Zhan P, Jiang JH, Lu M, et al. Higher-order Band Topology. *Nat Rev Phys* (2021) 1-13. doi:10.1038/s42254-021-00323-4
6. Peterson CW, Benalcazar WA, Hughes TL, and Bahl G. A Quantized Microwave Quadrupole Insulator with Topologically Protected Corner States. *Nature* (2018) 555:346–50. doi:10.1038/nature25777
7. Mittal S, Orre VV, Zhu G, Gorlach MA, Poddubny A, and Hafezi M. Photonic Quadrupole Topological Phases. *Nat Photon* (2019) 13:692–6. doi:10.1038/s41566-019-0452-0
8. Noh J, Benalcazar WA, Huang S, Collins MJ, Chen KP, Hughes TL, et al. Topological protection of Photonic Mid-gap Defect Modes. *Nat Photon* (2018) 12:408–15. doi:10.1038/s41566-018-0179-3
9. Chen X-D, Deng W-M, Shi F-L, Zhao F-L, Chen M, and Dong J-W. Direct Observation of Corner States in Second-Order Topological Photonic Crystal Slabs. *Phys Rev Lett* (2019) 122:233902. doi:10.1103/physrevlett.122.233902
10. Xie B-Y, Su G-X, Wang H-F, Su H, Shen X-P, Zhan P, et al. Visualization of Higher-Order Topological Insulating Phases in Two-Dimensional Dielectric Photonic Crystals. *Phys Rev Lett* (2019) 122:233903. doi:10.1103/physrevlett.122.233903
11. El Hassan A, Kunst FK, Moritz A, Andler G, Bergholtz EJ, and Bourennane M. Corner States of Light in Photonic Waveguides. *Nat Photon* (2019) 13: 697–700. doi:10.1038/s41566-019-0519-y
12. Zhang L, Yang Y, Lin ZK, Qin P, Chen Q, Gao F, et al. Higher-Order Topological States in Surface-Wave Photonic Crystals. *Adv Sci (Weinh)* (2020) 7:1902724. doi:10.1002/advs.201902724
13. Xu C, Chen Z-G, Zhang G, Ma G, and Wu Y. Multi-Dimensional Wave Steering with Higher-Order Topological Phononic Crystal. *Sci Bull* (2021) 66: 1740–5. doi:10.1016/j.scib.2021.05.013
14. Xue H, Yang Y, Gao F, Chong Y, and Zhang B. Acoustic Higher-Order Topological Insulator on a Kagome Lattice. *Nat Mater* (2019) 18:108–12. doi:10.1038/s41563-018-0251-x
15. Ni X, Weiner M, Alù A, and Khanikaev AB. Observation of Higher-Order Topological Acoustic States Protected by Generalized Chiral Symmetry. *Nat Mater* (2019) 18:113–20. doi:10.1038/s41563-018-0252-9
16. Zhang X, Wang H-X, Lin Z-K, Tian Y, Xie B, Lu M-H, et al. Second-order Topology and Multidimensional Topological Transitions in Sonic Crystals. *Nat Phys* (2019) 15:582–8. doi:10.1038/s41567-019-0472-1
17. Chen ZG, Zhu W, Tan Y, Wang L, and Ma G. Acoustic Realization of a Four-Dimensional Higher-Order Chern Insulator and Boundary-Modes Engineering. *Phys Rev X* (2021) 11(1):011016. doi:10.1103/physrevx.11.011016
18. Chen ZG, Wang L, Zhang G, and Ma G. Chiral Symmetry Breaking of Tight-Binding Models in Coupled Acoustic-Cavity Systems. *Phys Rev Appl* (2020) 14(2):024023. doi:10.1103/physrevapplied.14.024023
19. Serra-Garcia M, Peri V, Süsstrunk R, Bilal OR, Larsen T, Villanueva LG, et al. Observation of a Phononic Quadrupole Topological Insulator. *Nature* (2018) 555:342–5. doi:10.1038/nature25156
20. Fan H, Xia B, Tong L, Zheng S, and Yu D. Elastic Higher-Order Topological Insulator with Topologically Protected Corner States. *Phys Rev Lett* (2019) 122(20):204301. doi:10.1103/physrevlett.122.204301
21. Wu Q, Chen H, Li X, and Huang G. In-plane Second-Order Topologically Protected States in Elastic Kagome Lattices. *Phys Rev Appl* (2020) 14(1): 014084. doi:10.1103/physrevapplied.14.014084
22. Xie B-Y, Wang H-F, Wang H-X, Zhu X-Y, Jiang J-H, Lu M-H, et al. Second-order Photonic Topological Insulator with Corner States. *Phys Rev B* (2018) 98(20):205147. doi:10.1103/physrevb.98.205147
23. Qi Y, Qiu C, Xiao M, He H, Ke M, and Liu Z. Acoustic Realization of Quadrupole Topological Insulators. *Phys Rev Lett* (2020) 124(20):206601. doi:10.1103/physrevlett.124.206601
24. Xue H, Ge Y, Sun H-X, Wang Q, Jia D, Guan Y-J, et al. Observation of an Acoustic Octupole Topological Insulator. *Nat Commun* (2020) 11:2442. doi:10.1038/s41467-020-16350-1
25. Zhu W, and Ma G. Distinguishing Topological Corner Modes in Higher-Order Topological Insulators of Finite Size. *Phys Rev B* (2020) 101(R):161301. doi:10.1103/physrevb.101.161301
26. Zhao YX, Huang Y-X, and Yang SA. Z2 -projective Translational Symmetry Protected Topological Phases. *Phys Rev B* (2020) 102:161117. doi:10.1103/physrevb.102.161117
27. Ding K, Ma G, Xiao M, Zhang ZQ, and Chan CT. Emergence, Coalescence, and Topological Properties of Multiple Exceptional Points and Their Experimental Realization. *Phys Rev X* (2016) 6:021007. doi:10.1103/physrevx.6.021007
28. Tang W, Jiang X, Ding K, Xiao Y-X, Zhang Z-Q, Chan CT, et al. Exceptional Nexus with a Hybrid Topological Invariant. *Science* (2020) 370:1077–80. doi:10.1126/science.abd8872
29. Ota Y, Liu F, Katsumi R, Watanabe K, Wakabayashi K, Arakawa Y, et al. Photonic crystal Nanocavity Based on a Topological Corner State. *Optica* (2019) 6:786. doi:10.1364/optica.6.000786
30. Kim H-R, Hwang M-S, Smirnova D, Jeong K-Y, Kivshar Y, and Park H-G. Multipolar Lasing Modes from Topological Corner States. *Nat Commun* (2020) 11:5758. doi:10.1038/s41467-020-19609-9
31. Han C, Kang M, and Jeon H. Lasing at Multidimensional Topological States in a Two-Dimensional Photonic Crystal Structure. *ACS Photon* (2020) 7: 2027–36. doi:10.1021/acsphotonics.0c00357

Conflict of Interest: The authors declare that the research was conducted in the absence of any commercial or financial relationships that could be construed as a potential conflict of interest.

Publisher's Note: All claims expressed in this article are solely those of the authors and do not necessarily represent those of their affiliated organizations, or those of the publisher, the editors and the reviewers. Any product that may be evaluated in this article, or claim that may be made by its manufacturer, is not guaranteed or endorsed by the publisher.

frontiers in Physics

ORIGINAL RESEARCH
published: 08 November 2021
doi: 10.3389/fphy.2021.789697

Tunable Topological Surface States of Three-Dimensional Acoustic Crystals

Hua-Shan Lai, Yu-Li Xu, Bo He, Xiao-Chen Sun, Cheng He* and Yan-Feng Chen**

National Laboratory of Solid State Microstructures and Department of Materials Science and Engineering, Nanjing University, Nanjing, China

Topological design for band structures of artificial materials such as acoustic crystals provides a powerful tool to manipulate wave propagating in a robust and symmetry-protected way. In this paper, based on the band folding and breaking mechanism by building blocks with acoustic atoms, we construct a three-dimensional topological acoustic crystal with a large complete bandgap. At a mirror-symmetry domain wall, two gapped symmetry and anti-symmetry surface states can be found in the bandgap, originated from two opposite Su-Schrieffer-Heeger chains. Remarkably, by enforcing a glide symmetry on the domain wall, we can tune the original gapped surface states in a gapless fashion at the boundaries of surface Brillouin zone, acting as omnidirectional acoustic quantum spin Hall effect. Our tunable yet straightforward acoustic crystals offer promising potentials in realizing future topological acoustic devices.

Keywords: topological material, three-dimensional acoustic crystal, topological surface state, band folding, interface glide symmetry

OPEN ACCESS

Edited by:
Guancong Ma,
Hong Kong Baptist University, Hong Kong SAR, China

Reviewed by:
Weiyin Deng,
South China University of Technology, China
Jie Ren,
Tongji University, China

****Correspondence:***
Xiao-Chen Sun
xcsun@nju.edu.cn
Cheng He
chenghe@nju.edu.cn
Yan-Feng Chen
yfchen@nju.edu.cn

Specialty section:
This article was submitted to Optics and Photonics, a section of the journal Frontiers in Physics

Received: *05 October 2021*
Accepted: *22 October 2021*
Published: *08 November 2021*

Citation:
Lai H-S, Xu Y-L, He B, Sun X-C, He C and Chen Y-F (2021) Tunable Topological Surface States of Three-Dimensional Acoustic Crystals. Front. Phys. 9:789697. doi: 10.3389/fphy.2021.789697

INTRODUCTION

In the past decades, the cross-disciplinary science of topology in mathematics and solid-state material in physics has led to a prosperous research field, *i.e.*, topological physics [1, 2]. The well-known cases are the family of quantum Hall effect [1, 3] and topological insulators [4, 5]. One of the most intriguing characters is the topologically robust boundary states protected by their bulk topology [6]. In 2008, Haldane and Raghu made a crucial claim that topology is an intrinsic feature of periodic Bloch waves independent of the statistical difference between fermions and bosons [7, 8], extending the scope of topological physics from electronic to classical-wave systems, such as photonic crystal and acoustic crystal (AC). The advantages of classical-wave systems in studying topological behaviors come from their flexible structures, less complicated samples, and more accessible measurements [9–12]. Since then, there have been enormous works focusing on the classical-wave analogs of topological phases, ranging from one-dimensional (1D) to three-dimensional (3D) and even higher synthetic dimensions [13–22]. These topological models provide unprecedented ways to manipulate waves with robust and symmetry-protected manners. For example, the localized zero-dimensional (0D) bound states in 1D Su-Schrieffer-Heeger (SSH) chains can support extremely enhanced field intensity [13], and the 1D chiral edge states in two-dimensional (2D) Chern insulators can support backscattering-immune one-way boundary transport [20]. Compared to 1D and 2D topological phases, 3D topological phases can efficiently manipulate waves in multiple dimensions [23–27]. Nevertheless, despite many works on 3D acoustic semimetals [28–38], the studies on 3D acoustic topological insulators are insufficient [39, 40].

In general, the topology of band structure space originates from its nontrivial geometry phase, *e.g.*, Zak phase in 1D [41] or Berry phase in 2D [2], which is ill-defined at the degenerated point.

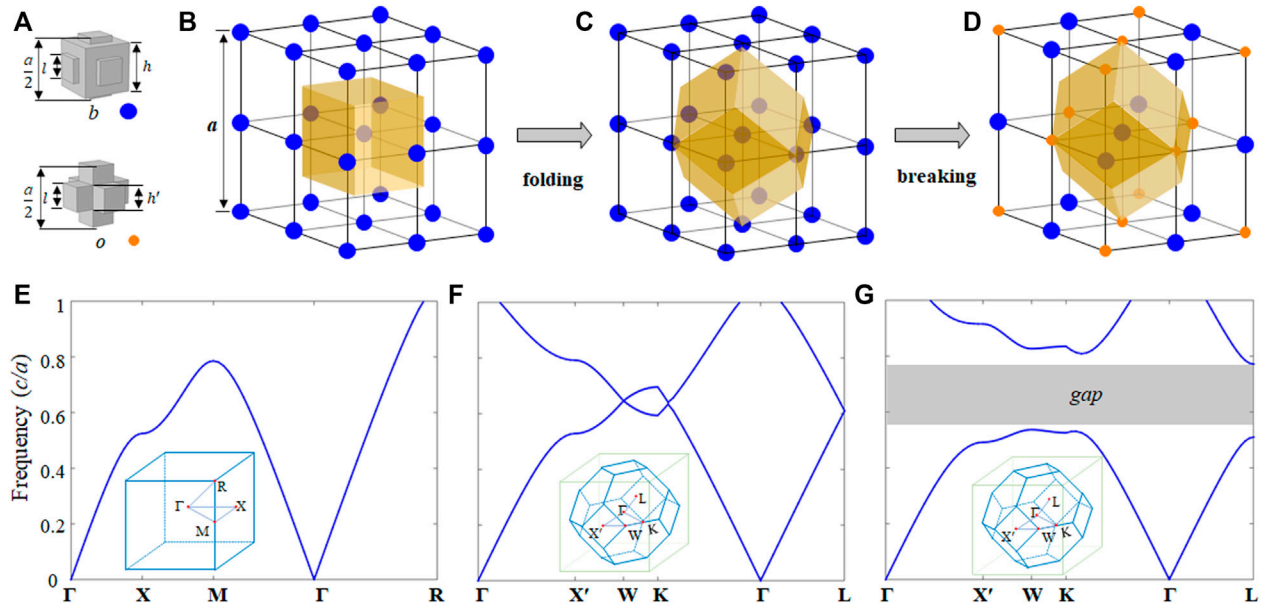

FIGURE 1 | Band folding and breaking in a 3D AC. **(A)** Two different acoustic atoms *b* (blue ball) and *o* (orange ball) with air cavity-tube structures. The structure parameters are $h = 0.4a$, $l = h' = 0.2a$ **(B)** Simple cubic structure with identical *b* atoms, where the primitive unit cell is cubic structure denoted by yellow area **(C)** Doubling case with the unit cell enlarged to a rhombic dodecahedral shape **(D)** Breaking the *a*/2 spatial translation symmetry by replacing the nearest neighbors with *o* atoms. **(E–G)** Bulk band structures corresponding to **(B–D)**, where the insets show the first BZs.

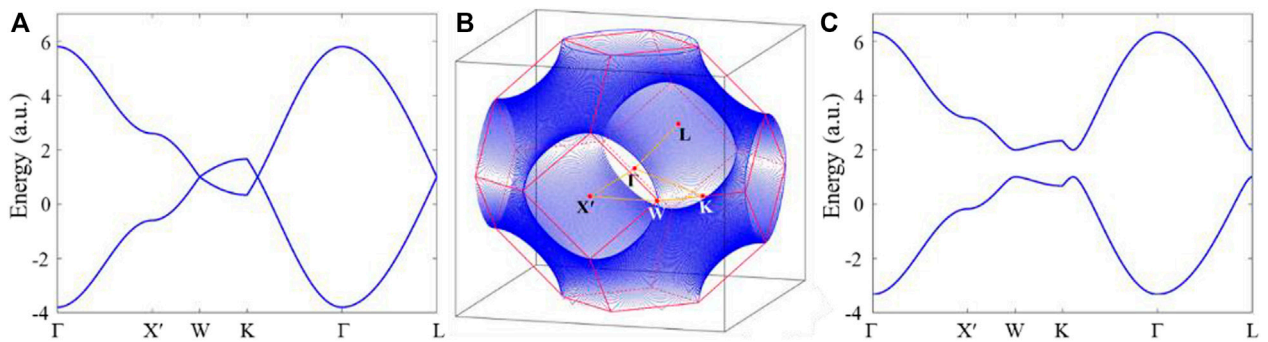

FIGURE 2 | Bulk band structures via TBA. **(A)** Band structures with $m_1 = m_2 = 1$, $t = 0.8$ **(B)** A 3D view of nodal plane in the 3D BZ. **(C)** Complete bandgap case of the NaCl-like AC when $m_2 = 2$.

In other words, the degenerated point of band structure might be the phase transition point between trivial phase and some topological phase. An excellent way to realize topological insulators is to lift band degeneracy by breaking symmetries. One can lift the linear or quartic band degenerated point by either breaking time-reversal symmetry to obtain 2D quantum Hall effect [42], or breaking spatial symmetry to 2D topological valley [43] and quantum spin Hall effect [44]. Regarding the construction of degeneracy by building symmetries, there are mainly three approaches. The first one is to resort to group theory, creating a high symmetric structure with 2D irreducible representation such as E in C_{3v} [43] or C_{4v} [45] lattices. This kind of band degeneracy requires careful lattice optimization to obtain favorite dispersion and eliminate the influence of other bands. The second one is to construct accidental band degeneracy relying on elaborately designed parameters [46]. Last but not least, the band folding mechanism increases symmetries by enlarging the primitive unit cell. For example, with in-plane 2D folding, four-fold degeneracy can be constructed using a triple unit cell three times larger than the primitive one [44, 47]. Likewise, with out-of-plane 1D folding, two two-fold Weyl points can reshape into one four-fold Dirac degeneracy [40, 48]. Thus, extending the band

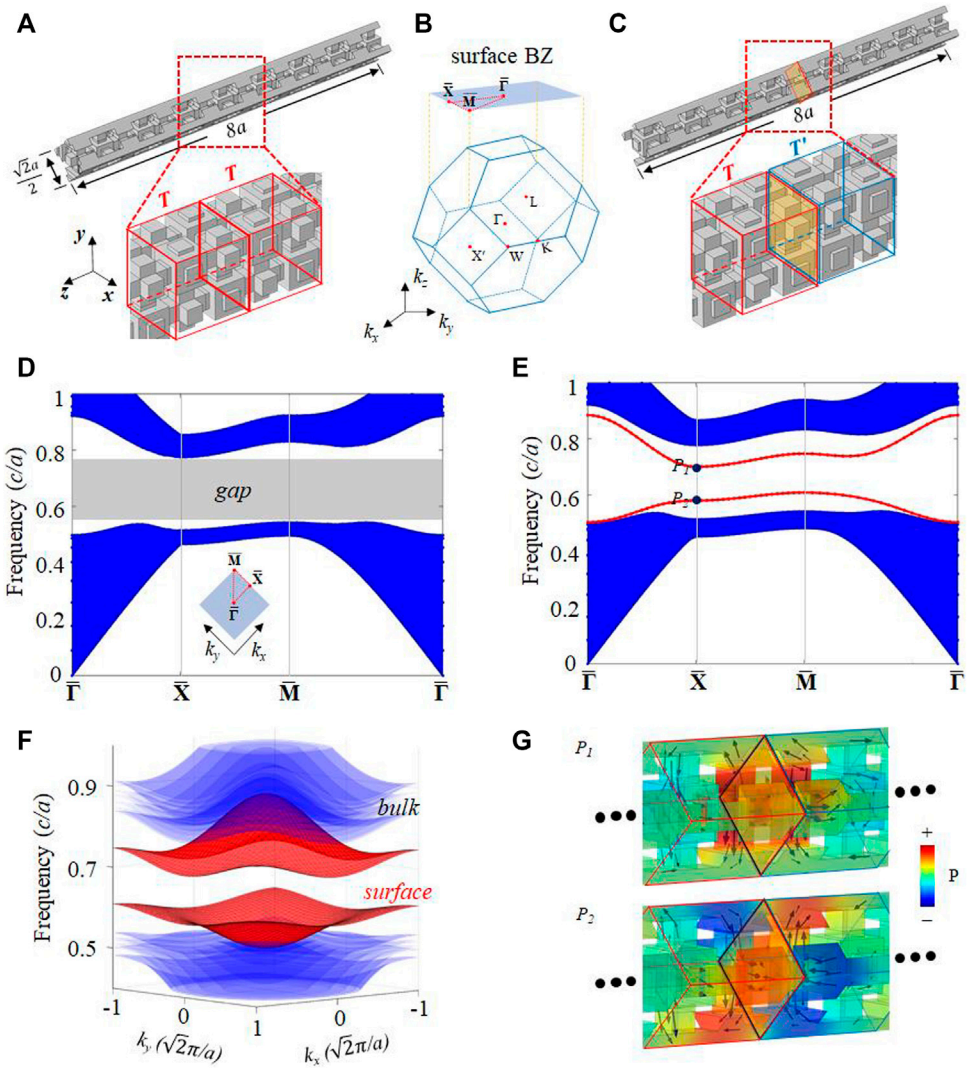

FIGURE 3 | Surfaces states on the mirror-symmetry domain wall. **(A)** Supercell configuration without domain wall. **(B)** The bulk BZ and (001) surface BZ. **(C)** Supercell configuration with a mirror-symmetry domain wall. **(D-E)** Projected band structures on (001) surface corresponding to **(A)** and **(C)**, respectively. **(F)** 3D view of surface states in **(E)**. **(G)** Acoustic field distributions at points P_1 and P_2 in **(E)**, where black arrows represent the directions of energy flow.

folding and breaking mechanism to a 3D Brillouin zone (BZ) would bring us a convenient way to realize topological insulators in 3D ACs.

In this paper, we propose a 3D AC with tunable topological surface states based on the 3D band folding and breaking mechanism. We start from one simplest 3D AC structure with a simple cubic lattice by building blocks. By doubling the unit cell in real space, the first isolated band of AC is folded in a 3D BZ, forming two-fold band degeneracy with a nodal plane. Then, we break the band degeneracy with a NaCl-like AC structure to get a large 3D complete bandgap. We can also obtain tunable topological surface states in the bandgap upon different symmetries of domain walls, *e.g.*, mirror or glide symmetry. Our model shows the controllable and reconfigurable abilities of topological sound transport on a 2D plane.

Band Folding and Breaking in a 3D AC

To begin with, we try to construct an AC by building blocks, using two acoustic cavity-tube structures as shown in **Figure 1A**. The structure parameters are $h = 0.4a$, $l = h' = 0.2a$, where a is the lattice constant. These two cavities having different resonant frequencies act as two different acoustic atoms, represented by b and o. The connecting tubes act as the hopping of neighboring atoms. Thus, as shown in **Figures 1B–D**, a simple cubic lattice AC can be built using identical b-type acoustic atoms, where the primitive unit cell only contains one atom. Using band folding and breaking mechanism, we can double the primitive unit cell in real space with two atoms to create band degeneracy. Then, we break such degeneracy by replacing the nearest neighbors to be o-type acoustic atoms with a NaCl-like structure. Accordingly, their band structures will experience a

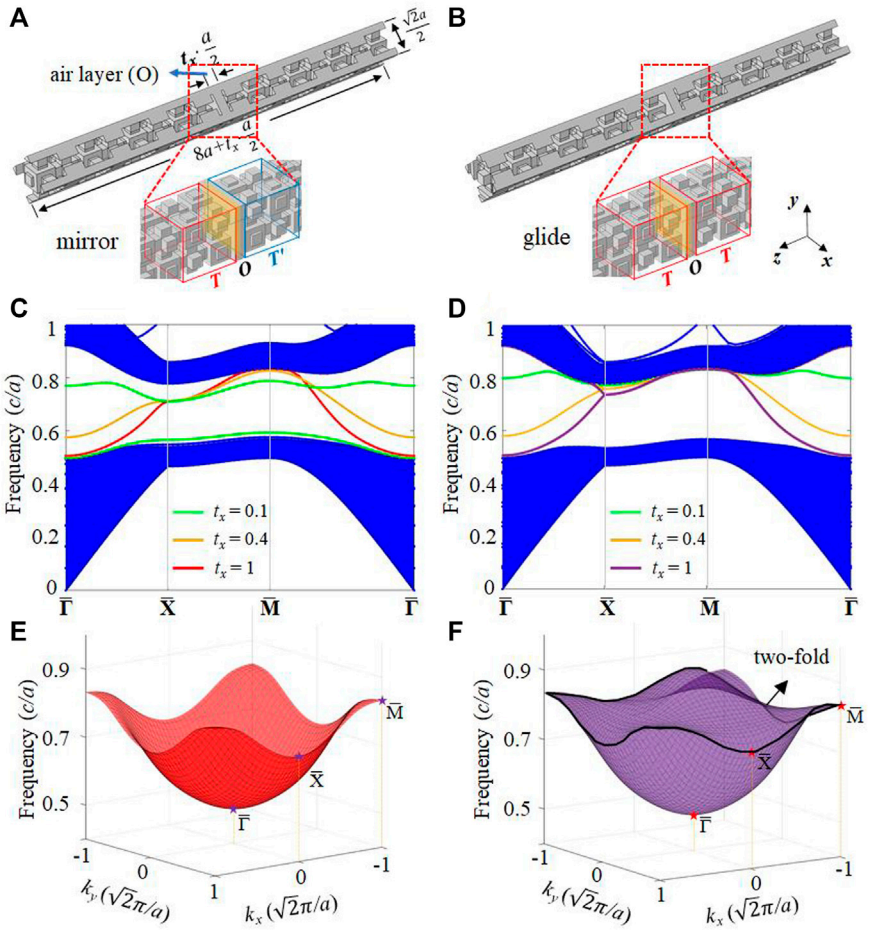

FIGURE 4 | Tunable surfaces states on different symmetries of domain walls. **(A)** Mirror-symmetry domain wall with a $t_x a/2$-thickness air layer at the interface (T-O-T' configuration). **(B)** Glide-symmetry case (T-O-T configuration). **(C-D)** Projected band structures under various thicknesses of air layers corresponding to **(A–B)**. The green, orange, and red lines represent t_x = 0.1, 0.4, and 1, respectively **(E-F)** 3D views of surface states in **(C–D)** when t_x = 1.

folding and breaking process to open a 3D complete bulk bandgap (**Figures 1E–G**). Here, we only focus and operate on the first band of such AC. In **Figure 1C**, the unit cell is chosen to be rhombic dodecahedral geometry which is twice large as that of a simple cubic case, associating with a half volume of bulk BZ in **Figure 1F**. The band degeneracy originates from additional symmetries in this non-primitive unit cell. In other words, the cubic BZ is folded into a truncated octahedral BZ in 3D.

We resort to the tight-binding approximation (TBA) method to further illustrate the degeneracy created by band folding. The TBA model can well describe our cavity-tube structure with definite local resonance and hopping effect. Considering two acoustic atoms (b and o) in a rhombic dodecahedral unit cell, the Bloch Hamiltonian on the basis of sublattices is:

$$H(k) = \begin{pmatrix} m_1 & H_{AB} \\ H_{AB}^{*} & m_2 \end{pmatrix}$$

where $H_{AB} = 2t[\cos(ak_x/2) + \cos(ak_y/2) + \cos(ak_z/2)]$, Bloch wavevector $\boldsymbol{k} = (k_x, k_y, k_z)$, a represents the lattice constant, t represents the nearest-neighbor hopping, and m_1 (m_2) represents the onsite energy of the sublattice b (o). The results are shown in **Figures 2A,C**. In identical atoms case ($m_1 = m_2 = 1$), the band structure possesses a two-fold degenerated nodal plane in the first 3D BZ, which is similar to the Fermi surface of copper (Cu). Then, we can lift the nodal plane to open a 3D complete bulk bandgap by changing $m_2 = 2$, corresponding to the broken half-lattice symmetry with a NaCl-like AC in **Figure 1D**.

In our model, the moderate structure parameters already ensure a large complete bandgap with a relative bandwidth of 36%, which facilities the propagation and manipulation of acoustic surface states. Increasing the contrast ratio of two acoustic atoms will bring a broader bandgap. The nodal plane in **Figure 2B** resembles a sphere with a nearly identical amplitude of Bloch vectors. It implies that the broken half-lattice symmetry would have almost the same effect on the band degeneracy along all directions, which minimizes the directional bandgap overlap

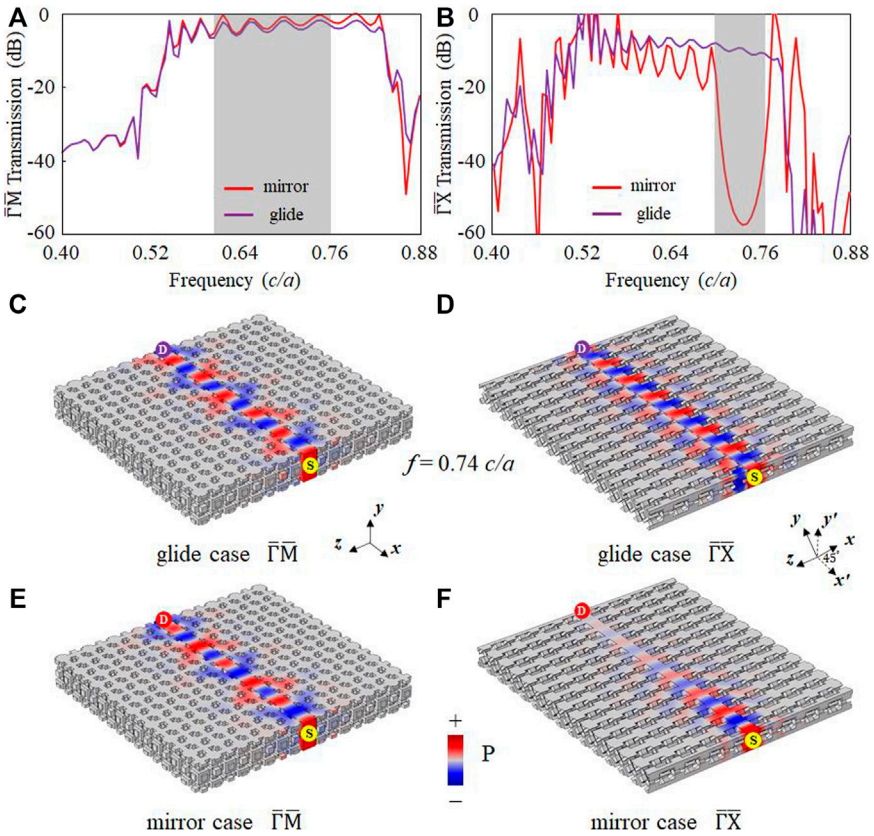

FIGURE 5 | Acoustic transmission spectra. **(A)** ΓM̄-direction transmission spectra on mirror- and glide-symmetry domain walls. The shadow area represents the complete bulk bandgap. **(B)** ΓX̄-direction transmission spectra, where the shadow area represents the directional surface bandgap of the mirror case. **(C-F)** Acoustic field distributions at a frequency of 0.74 *c/a*.

to guarantee a large 3D complete bandgap. In this work, the numerical results are calculated using a finite element method software package (COMSOL Multiphysics). The density and velocity are chosen to be 1.25 kg/m^3 and 343 m/s, respectively.

Tunable Topological Surface States on Different Domain Walls

Then, we focus on the surface states on the (001) surface, the same as those on (100) or (010) surfaces. **Figure 3A** is a supercell configuration without a domain wall along the *z*-direction. A periodical segment is denoted by T. **Figure 3B** shows the surface BZ. A typical domain wall can be introduced by adding a mirror symmetry at the interface with a T-T' configuration, where segment T' is the mirror counterpart of T (**Figure 3C**). Due to the equivalence of each principal axis in a cubic lattice, T and T' also possess a relative *a*/2 shift along *x*- or *y*-direction. **Figure 3D** is the projected band structure without the domain wall, where the 3D complete bandgap agrees with **Figure 1G**. For the case of the mirror-symmetry domain wall, two gapped surface states in the bulk bandgap can be found (**Figure 3E**).

These two surface states on the mirror-symmetry domain wall can be taken as an extension of two bound states of two *z*-direction SSH chains in the k_{xy} plane. Here, we can exchange the onsite and hopping terms and denote the original connecting tube as *u*. Then, the cuboid supercell is composed of a pair of SSH chains, as $(\cdots\frac{u}{2}\overset{o}{\leftrightarrow}u\overset{b}{\leftrightarrow}\frac{u}{2})$-$(\frac{u}{2}\overset{b}{\leftrightarrow}u\overset{o}{\leftrightarrow}\frac{u}{2}\cdots)$ and $(\cdots\frac{u}{2}\overset{b}{\leftrightarrow}u\overset{o}{\leftrightarrow}\frac{u}{2})$-$(\frac{u}{2}\overset{o}{\leftrightarrow}u\overset{b}{\leftrightarrow}\frac{u}{2}\cdots)$ along the *z*-axis. Each chain gives one bound state at the domain wall according to 1D SSH with different Zak phases on each side of the interface [41, 49]. In a 3D case, these two 0D bound states extend to two 2D surface states with dispersion under the coupling of two chains in the k_{xy} plane. Along the boundaries of surface BZ, the in-plane (k_{xy} plane) coupling is missing. Therefore, two surface states are separated. As in-plane coupling increases from BZ boundary to center, these two surface states will gradually merge into bulk bands in opposite directions, forming two inverted bowl shapes (**Figure 3F**). Due to the mirror symmetry M_z: $(x, y, z) \rightarrow (x, y, -z)$ relative to the interface, two surface states can also be classified into symmetry and anti-symmetry modes. Moreover, the interface is an anti-phase boundary formed by shifting a portion of the crystal lattice as

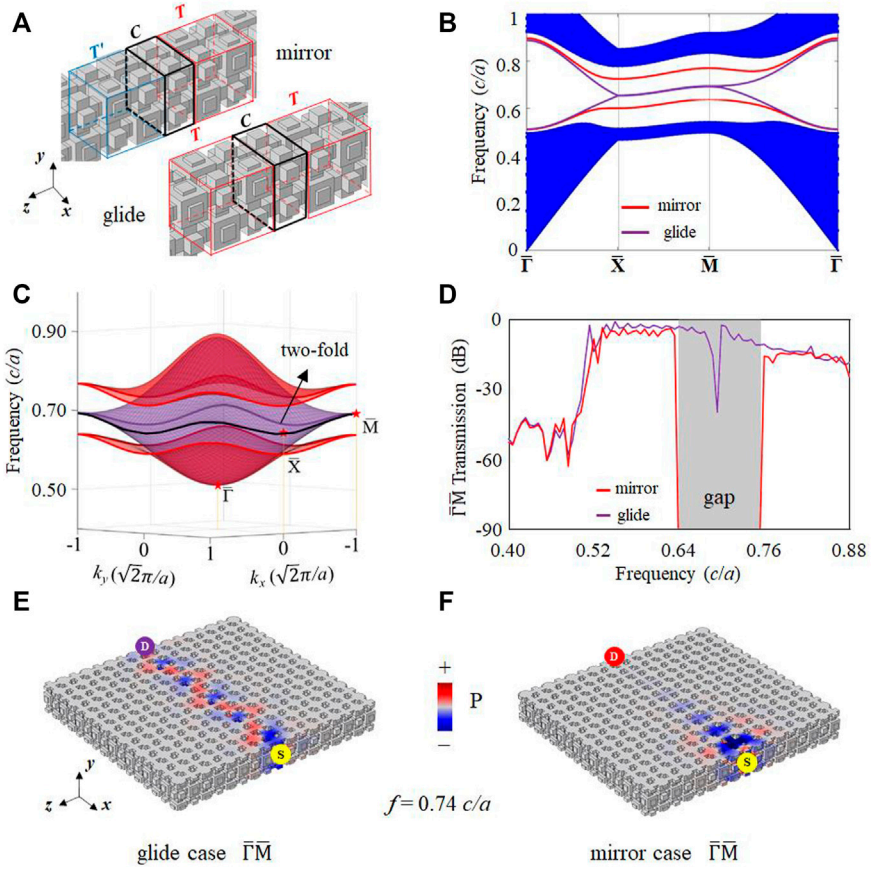

FIGURE 6 | Tunable surface states with modified interface layer. **(A)** Supercells of mirror and glide cases. The interface with uniform *o*-type acoustic atoms (denoted as C). **(B)** Projected band structure. The red (purple) line represents the mirror (glide) case **(C)** A 3D view of surface states. **(D)** Γ̄M̄-direction transmission spectra. The shadow area represents the surface bandgap of the mirror case **(E-F)** Acoustic field distributions at a frequency of 0.74 *c*/*a*.

well, which can support pseudospin-momentum locking [50, 51]. The acoustic pseudospin can be defined by the rotating direction of the energy flow [52–55]. The acoustic field distributions of anti-symmetry surface mode P_1 and symmetry mode P_2 at $\bar{X}$ point, with counter-rotation of energy flow (black arrows), are presented in **Figure 3G**.

Besides the mirror-symmetry domain wall, our model can possess a glide-symmetry domain wall as well. Here, we consider an additional air layer (O) with a thickness of $t_x a/2$ added on both mirror-symmetry and glide-symmetry domain walls (**Figures 4A,B**). As the thickness parameter (t_x) increases from 0.1 to 1, for the mirror-symmetry case (T-O-T' configuration), the anti-symmetry mode gradually emerges into bulk bands, and the symmetry one has a blue shift connecting the upper bulk band (**Figure 4C**). On the other hand, for the glide-symmetry case (T-O-T configuration), the surface states are always two-fold degenerated at the boundaries of surface BZ (**Figure 4D**). Such band degeneracy is the consequence of glide symmetries [56–58], *i.e.*, G_x: $(x, y, z) \rightarrow G(-x, y + a/2, z)$ and G_y: $(x, y, z) \rightarrow G(x + a/2, -y, z)$. The 3D views of surface states with $t_x = 1$ are plotted in **Figures 4E,F**.

These flexible and tunable surface states can be used to realize reconfigurable directional acoustic filters. For example, the surface states have directional surface bandgap along $\bar{\Gamma}\bar{X}$ direction in the mirror-symmetry case, which is different from the glide-symmetry case with gapless surface states. Their transmission spectra are shown in **Figures 5A,B**. In a wide frequency window from 0.58 to 0.76 *c*/*a*, $\bar{\Gamma}\bar{M}$ transmission spectra maintain a high valve for both two cases. However, $\bar{\Gamma}\bar{X}$ transmission is forbidden for the mirror-symmetry case in the frequency window from 0.70 to 0.76 *c*/*a*, but allowed for the glide-symmetry case. The acoustic field distributions at a frequency of 0.74 *c*/*a* in **Figures 5C–F** match well with projected band structures and transmission spectra. It should be noticed that T and T' are the same structures, only possessing a relative *a*/2 shift along the *x*- or *y*-direction. That means we can efficiently turn on/off sound transport by simply tuning the relative displacement between left-side and right-side ACs in the experiment.

Omnidirectional Acoustic Quantum Spin Hall Effect

In addition to the directional surface bandgap, we can also construct a complete surface bandgap by modifying the interface. In **Figure 6A**, we elaborately tune the aforementioned air-interface layer to another modified interface layer C with $a/2$ thickness composed of uniform o-type acoustic atoms. The mirror symmetry and glide symmetries still sustain in T-C-T' and T-C-T configuration, respectively. The projected band structures are shown in **Figure 6B**. A complete surface bandgap is constructed for the mirror-symmetry case, forbidding surface sound transport in all directions. For the glide-symmetry case, the surface states at the boundaries of the surface BZ are still degenerated but with flat dispersion.

In the glide-symmetry case, two SSH chains can be described as modified $(\cdots\frac{o}{2}\overset{u}{\leftrightarrow}b\overset{u}{\leftrightarrow}\frac{o}{2})$-$(\frac{b}{2}\overset{u}{\leftrightarrow}o\overset{u}{\leftrightarrow}\frac{b}{2}\cdots)$ and $(\cdots\frac{b}{2}\overset{u}{\leftrightarrow}o\overset{u}{\leftrightarrow}\frac{b}{2})$-$(\frac{o}{2}\overset{u}{\leftrightarrow}b\overset{u}{\leftrightarrow}\frac{o}{2}\cdots)$ along the z-axis. The interface is chosen to be identical o-type acoustic atoms. Like two unmodified chains in the mirror-symmetry case (T-T' configuration), each modified chain also gives one bound state. Around the surface BZ center with strong in-plane (k_{xy} plane) coupling, these two bound states lift in both cases. However, the situation is different at the surface BZ boundaries without in-plane coupling. The additional glide symmetry (T-C-T configuration) guarantees two-fold degeneracy, forming two buckled bowl-shaped fashion (**Figure 6C**). In each k_y (or k_x) slice, these two degenerate surface states turn into a pair of helical edge states, which implies that such glide-symmetry domain wall can act as an omnidirectional acoustic quantum spin Hall layer on a 2D plane [46, 59].

The simulated transmission spectra for both mirror-symmetry and glide-symmetry cases are shown in **Figure 6D**, consisting of their gapped and gapless surface states. The corresponding acoustic field distributions at a frequency of 0.74 c/a are shown in **Figures 6E,F**. Note that there is a slight dip at a frequency of 0.70 c/a due to the linear degeneracy, resembling the ballistic transport of sound at the surface Dirac point [60, 61].

CONCLUSION

To conclude, we construct a sizeable topological bandgap in an AC by building blocks based on a 3D band folding and breaking mechanism. By adjusting the interface symmetries of domain walls, we realize various kinds of topological surface states to turn on/off sound transport efficiently. The omnidirectional acoustic quantum spin Hall layer can be achieved under a glide-symmetry domain wall as well. Compared to 1D edge states in 2D models, these tunable surface states show great potentials in manipulating acoustic signals in multiple directions. Our simple yet flexible 3D AC may provide a route of realizing tunable acoustic devices such as acoustic filters on a 2D plane.

DATA AVAILABILITY STATEMENT

The raw data supporting the conclusion of this article will be made available by the authors, without undue reservation.

AUTHOR CONTRIBUTIONS

CH and Y-FC conceived the idea and supervised the project. H-SL, Y-LX, and BH performed the numerical simulations. H-SL and X-CS did the theoretical analysis. H-SL wrote the article.

FUNDING

The work was jointly supported by the National Key R&D Program of China (Grant No. 2017YFA0305100) and the National Natural Science Foundation of China (Grant Nos. 52022038, 11874196, 11890700, and 51721001).

REFERENCES

1. Klitzing Kv., Dorda G, Pepper M. New method for high-accuracy determination of the fine-structure constant based on quantized Hall resistance. *Phys Rev Lett* (1980) 45:494–7. doi:10.1103/PhysRevLett.45.494
2. Berry MV. Quantal phase factors accompanying adiabatic changes. *Proc R Soc Lond A* (1984) 392:45–57. doi:10.1098/rspa.1984.0023
3. Bernevig BA, Hughes TL, Zhang S-C. Quantum spin Hall effect and topological phase transition in HgTe quantum wells. *Science* (2006) 314: 1757–61. doi:10.1126/science.1133734
4. Hatsugai Y. Chern number and edge states in the integer quantum Hall effect. *Phys Rev Lett* (1993) 71:3697–700. doi:10.1103/PhysRevLett.71.3697
5. Kane CL, Mele EJ. Quantum spin Hall effect in graphene. *Phys Rev Lett* (2005) 95:226801. doi:10.1103/PhysRevLett.95.226801
6. Thouless DJ, Kohmoto M, Nightingale MP, den Nijs M. Quantized Hall conductance in a two-dimensional periodic potential. *Phys Rev Lett* (1982) 49: 405–8. doi:10.1103/PhysRevLett.49.405
7. Haldane FDM, Raghu S. Possible realization of directional optical waveguides in photonic crystals with broken time-reversal symmetry. *Phys Rev Lett* (2008) 100:013904. doi:10.1103/PhysRevLett.100.013904
8. Raghu S, Haldane FDM. Analogs of quantum-Hall-effect edge states in photonic crystals. *Phys Rev A* (2008) 78:033834. doi:10.1103/PhysRevA.78.033834
9. Huber SD. Topological mechanics. *Nat Phys* (2016) 12:621–3. doi:10.1038/nphys3801
10. Ozawa T, Price HM, Amo A, Goldman N, Hafezi M, Lu L, et al. Topological photonics. *Rev Mod Phys* (2019) 91:015006. doi:10.1103/RevModPhys.91.015006
11. Lu L, Joannopoulos JD, Soljačić M. Topological states in photonic systems. *Nat Phys* (2016) 12:626–9. doi:10.1038/nphys3796
12. Ma G, Xiao M, Chan CT. Topological phases in acoustic and mechanical systems. *Nat Rev Phys* (2019) 1:281–94. doi:10.1038/s42254-019-0030-x
13. Xiao M, Ma G, Yang Z, Sheng P, Zhang ZQ, Chan CT. Geometric phase and band inversion in periodic acoustic systems. *Nat Phys* (2015) 11:240–4. doi:10.1038/nphys3228
14. Yang Z, Gao F, Shi X, Lin X, Gao Z, Chong Y, et al. Topological acoustics. *Phys Rev Lett* (2015) 114:114301. doi:10.1103/PhysRevLett.114.114301
15. Xiao M, Chen W-J, He W-Y, Chan CT. Synthetic gauge flux and Weyl points in acoustic systems. *Nat Phys* (2015) 11:920–4. doi:10.1038/nphys3458

16. Deng W, Huang X, Lu J, Peri V, Li F, Huber SD, et al. Acoustic spin-Chern insulator induced by synthetic spin-orbit coupling with spin conservation breaking. *Nat Commun* (2020) 11:3227. doi:10.1038/s41467-020-17039-1
17. Deng Y, Oudich M, Gerard NJ, Ji J, Lu M, Jing Y. Magic-angle bilayer phononic graphene. *Phys Rev B* (2020) 102:180304. doi:10.1103/PhysRevB.102.180304
18. Yang Y, Lu J, Yan M, Huang X, Deng W, Liu Z. Hybrid-Order Topological Insulators in a Phononic Crystal. *Phys Rev Lett* (2021) 126:156801. doi:10.1103/PhysRevLett.126.156801
19. Chen Z-G, Zhu W, Tan Y, Wang L, Ma G. Acoustic Realization of a Four-Dimensional Higher-Order Chern Insulator and Boundary-Modes Engineering. *Phys Rev X* (2021) X11:011016. doi:10.1103/PhysRevX.11.011016
20. Wang Z, Chong Y, Joannopoulos JD, Soljačić M. Observation of unidirectional backscattering-immune topological electromagnetic states. *Nature* (2009) 461:772–5. doi:10.1038/nature08293
21. Khanikaev AB, Fleury R, Mousavi SH, Alù A. Topologically robust sound propagation in an angular-momentum-biased graphene-like resonator lattice. *Nat Commun* (2015) 6:8260. doi:10.1038/ncomms9260
22. Xu C, Chu H, Luo J, Hang ZH, Wu Y, Lai Y. Three-Dimensional Electromagnetic Void Space. *Phys Rev Lett* (2021) 127:123902. doi:10.1103/PhysRevLett.127.123902
23. He H, Qiu C, Ye L, Cai X, Fan X, Ke M, et al. Topological negative refraction of surface acoustic waves in a Weyl phononic crystal. *Nature* (2018) 560:61–4. doi:10.1038/s41586-018-0367-9
24. Xu C, Chen Z-G, Zhang G, Ma G, Wu Y. Multi-dimensional wave steering with higher-order topological phononic crystal. *Sci Bull* (2021) 66:1740–5. doi:10.1016/j.scib.2021.05.013
25. Lu J, Huang X, Yan M, Li F, Deng W, Liu Z. Nodal-Chain Semimetal States and Topological Focusing in Phononic Crystals. *Phys Rev Appl* (2020) 13:054080. doi:10.1103/PhysRevApplied.13.054080
26. Zhang X, Xie B-Y, Wang H-F, Xu X, Tian Y, Jiang J-H, et al. Dimensional hierarchy of higher-order topology in three-dimensional sonic crystals. *Nat Commun* (2019) 10:5331. doi:10.1038/s41467-019-13333-9
27. He C, Yu S-Y, Wang H, Ge H, Ruan J, Zhang H, et al. Hybrid acoustic topological insulator in three dimensions. *Phys Rev Lett* (2019) 123:195503. doi:10.1103/PhysRevLett.123.195503
28. Li F, Huang X, Lu J, Ma J, Liu Z. Weyl points and Fermi arcs in a chiral phononic crystal. *Nat Phys* (2017) 14:30–4. doi:10.1038/nphys4275
29. Ge H, Ni X, Tian Y, Gupta SK, Lu M-H, Lin X, et al. Experimental Observation of Acoustic Weyl Points and Topological Surface States. *Phys Rev Appl* (2018) 10:014017. doi:10.1103/PhysRevApplied.10.014017
30. Xie B, Liu H, Cheng H, Liu Z, Tian J, Chen S. Dirac points and the transition towards Weyl points in three-dimensional sonic crystals. *Light Sci Appl* (2020) 9:201. doi:10.1038/s41377-020-00416-2
31. Yang Y, Sun H-x., Xia J-p., Xue H, Gao Z, Ge Y, et al. Topological triply degenerate point with double Fermi arcs. *Nat Phys* (2019) 15:645–9. doi:10.1038/s41567-019-0502-z
32. Luo L, Wang H-X, Lin Z-K, Jiang B, Wu Y, Li F, et al. Observation of a phononic higher-order Weyl semimetal. *Nat Mater* (2021) 20:794–9. doi:10.1038/s41563-021-00985-6
33. Wei Q, Zhang X, Deng W, Lu J, Huang X, Yan M, et al. Higher-order topological semimetal in acoustic crystals. *Nat Mater* (2021) 20:812–7. doi:10.1038/s41563-021-00933-4
34. Cheng H, Sha Y, Liu R, Fang C, Lu L. Discovering Topological Surface States of Dirac Points. *Phys Rev Lett* (2020) 124:104301. doi:10.1103/PhysRevLett.124.104301
35. He H, Qiu C, Cai X, Xiao M, Ke M, Zhang F, et al. Observation of quadratic Weyl points and double-helicoid arcs. *Nat Commun* (2020) 11:1820. doi:10.1038/s41467-020-15825-5
36. Yang Y, Xia J-p., Sun H-x., Ge Y, Jia D, Yuan S-q., et al. Observation of a topological nodal surface and its surface-state arcs in an artificial acoustic crystal. *Nat Commun* (2019) 10:5185. doi:10.1038/s41467-019-13258-3
37. Huang X, Deng W, Li F, Lu J, Liu Z. Ideal Type-II Weyl Phase and Topological Transition in Phononic Crystals. *Phys Rev Lett* (2020) 124:206802. doi:10.1103/PhysRevLett.124.206802
38. Deng W, Huang X, Lu J, Li F, Ma J, Chen S, et al. Acoustic spin-1 Weyl semimetal. *Sci China Phys Mech Astron* (2020) 63:287032. doi:10.1007/s11433-020-1558-8
39. He C, Yu S-Y, Ge H, Wang H, Tian Y, Zhang H, et al. Three-dimensional topological acoustic crystals with pseudospin-valley coupled saddle surface states. *Nat Commun* (2018) 9:4555. doi:10.1038/s41467-018-07030-2
40. He C, Lai H-S, He B, Yu S-Y, Xu X, Lu M-H, et al. Acoustic analogues of three-dimensional topological insulators. *Nat Commun* (2020) 11:2318. doi:10.1038/s41467-020-16131-w
41. Zak J. Berry's phase for energy bands in solids. *Phys Rev Lett* (1989) 62:2747–50. doi:10.1103/PhysRevLett.62.2747
42. Wang Z, Chong YD, Joannopoulos JD, Soljačić M. Reflection-free one-way edge modes in a gyromagnetic photonic crystal. *Phys Rev Lett* (2008) 100:013905. doi:10.1103/PhysRevLett.100.013905
43. Lu J, Qiu C, Ye L, Fan X, Ke M, Zhang F, et al. Observation of topological valley transport of sound in sonic crystals. *Nat Phys* (2017) 13:369–74. doi:10.1038/nphys3999
44. Wu L-H, Hu X. Scheme for achieving a topological photonic crystal by using dielectric material. *Phys Rev Lett* (2015) 114:223901. doi:10.1103/PhysRevLett.114.223901
45. Peri V, Song Z-D, Serra-Garcia M, Engeler P, Queiroz R, Huang X, et al. Experimental characterization of fragile topology in an acoustic metamaterial. *Science* (2020) 367:797–800. doi:10.1126/science.aaz7654
46. He C, Ni X, Ge H, Sun X-C, Chen Y-B, Lu M-H, et al. Acoustic topological insulator and robust one-way sound transport. *Nat Phys* (2016) 12:1124–9. doi:10.1038/nphys3867
47. Du L, Liu Y, Li M, Ren H, Song K, Zhao X. Non-Trivial Transport Interface in a Hybrid Topological Material with Hexagonal Lattice Arrangement. *Front Phys* (2020) 8:595621. doi:10.3389/fphy.2020.595621
48. Lu L, Gao H, Wang Z. Topological one-way fiber of second Chern number. *Nat Commun* (2018) 9:5384. doi:10.1038/s41467-018-07817-3
49. Xiao M, Zhang ZQ, Chan CT. Surface Impedance and Bulk Band Geometric Phases in One-Dimensional Systems. *Phys Rev X* (2014) X4:021017. doi:10.1103/PhysRevX.4.021017
50. Kong X, Zhou Y, Xiao G, Sievenpiper DF. Spin-momentum locked modes on anti-phase boundaries in photonic crystals. *Opt Express* (2020) 28:2070. doi:10.1364/OE.379672
51. Ahn KH, Lookman T, Saxena A, Bishop AR. Electronic properties of structural twin and antiphase boundaries in materials with strong electron-lattice couplings. *Phys Rev B* (2005) 71:212102. doi:10.1103/PhysRevB.71.212102
52. Long Y, Ren J, Chen H. Intrinsic spin of elastic waves. *Proc Natl Acad Sci USA* (2018) 115:9951–5. doi:10.1073/pnas.1808534115
53. Shi C, Zhao R, Long Y, Yang S, Wang Y, Chen H, et al. Observation of acoustic spin. *Natl Sci Rev* (2019) 6:707–12. doi:10.1093/nsr/nwz059
54. Long Y, Zhang D, Yang C, Ge J, Chen H, Ren J. Realization of acoustic spin transport in metasurface waveguides. *Nat Commun* (2020) 11:4716. doi:10.1038/s41467-020-18599-y
55. Long Y, Ge H, Zhang D, Xu X, Ren J, Lu M-H, et al. Symmetry selective directionality in near-field acoustics. *Natl Sci Rev* (2020) 7:1024–35. doi:10.1093/nsr/nwaa040
56. Liu C-X, Zhang R-X, VanLeeuwen BK. Topological nonsymmorphic crystalline insulators. *Phys Rev B* (2014) 90:085304. doi:10.1103/PhysRevB.90.085304
57. Zhang P. Symmetry and degeneracy of phonon modes for periodic structures with glide symmetry. *J Mech Phys Sol* (2019) 122:244–61. doi:10.1016/j.jmps.2018.09.016
58. Xia Y, Cai X, Li G. Multitype Dirac fermions protected by orthogonal glide symmetries in a noncentrosymmetric system. *Phys Rev B* (2020) 102:041201. doi:10.1103/PhysRevB.102.041201
59. Tong S, Ren C. Directional acoustic emission via topological insulators based on cavity-channel networks. *Appl Phys Lett* (2020) 117:093504. doi:10.1063/5.0015591

60. Zhang X, Liu Z. Extremal Transmission and Beating Effect of Acoustic Waves in Two-Dimensional Sonic Crystals. *Phys Rev Lett* (2008) 101:264303. doi:10.1103/PhysRevLett.101.264303
61. Yu S-Y, Sun X-C, Ni X, Wang Q, Yan X-J, He C, et al. Surface phononic graphene. *Nat Mater* (2016) 15:1243–7. doi:10.1038/nmat4743

Conflict of Interest: The authors declare that the research was conducted in the absence of any commercial or financial relationships that could be construed as a potential conflict of interest.

Publisher's Note: All claims expressed in this article are solely those of the authors and do not necessarily represent those of their affiliated organizations, or those of the publisher, the editors and the reviewers. Any product that may be evaluated in this article, or claim that may be made by its manufacturer, is not guaranteed or endorsed by the publisher.

frontiers in Physics

REVIEW
published: 16 November 2021
doi: 10.3389/fphy.2021.771481

A Review of Topological Semimetal Phases in Photonic Artificial Microstructures

Boyang Xie[1†], Hui Liu[1†], Haonan Wang[1†], Hua Cheng[1], Jianguo Tian[1] and Shuqi Chen[1,2,3]**

[1]The Key Laboratory of Weak Light Nonlinear Photonics, Ministry of Education, Renewable Energy Conversion and Storage Center, School of Physics and TEDA Institute of Applied Physics, Nankai University, Tianjin, China, [2]The Collaborative Innovation Center of Extreme Optics, Shanxi University, Taiyuan, China, [3]Collaborative Innovation Center of Light Manipulations and Applications, Shandong Normal University, Jinan, China

In the past few years, the concept of topological matter has inspired considerable research in broad areas of physics. In particular, photonic artificial microstructures like photonic crystals and metamaterials provide a unique platform to investigate topologically non-trivial physics in spin-1 electromagnetic fields. Three-dimensional (3D) topological semimetal band structures, which carry non-trivial topological charges, are fundamental to 3D topological physics. Here, we review recent progress in understanding 3D photonic topological semimetal phases and various approaches for realizing them, especially with photonic crystals or metamaterials. We review topological gapless band structures and topological surface states aroused from the non-trivial bulk topology. Weyl points, 3D Dirac points, nodal lines, and nodal surfaces of different types are discussed. We also demonstrate their application in coupling spin-polarized electromagnetic waves, anomalous reflection, vortex beams generation, bulk transport, and non-Hermitian effects.

Keywords: topological photonics, metamaterials, photonic crystals, topological semimetals, Fermi arcs

OPEN ACCESS

Edited by:
Guancong Ma,
Hong Kong Baptist University, Hong Kong, SAR China

Reviewed by:
Xiao-Dong Chen,
Sun Yat-sen University, China
Yihao Yang,
Zhejiang University, China
Ruo-Yang Zhang,
Chern Institute of Mathematics, China

****Correspondence:***
Hua Cheng
hcheng@nankai.edu.cn
Shuqi Chen
schen@nankai.edu.cn

[†]These authors have contributed equally to this work

Specialty section:
This article was submitted to Optics and Photonics, a section of the journal Frontiers in Physics

Received: *06 September 2021*
Accepted: *30 September 2021*
Published: *16 November 2021*

Citation:
Xie B, Liu H, Wang H, Cheng H, Tian J and Chen S (2021) A Review of Topological Semimetal Phases in Photonic Artificial Microstructures. Front. Phys. 9:771481. doi: 10.3389/fphy.2021.771481

INTRODUCTION

In the last 2 decades, artificial microstructures including metamaterials and photonic crystals have attracted enormous interest because they provide great possibilities for manipulating optical waves. By judiciously modulating their structural parameters, novel physical phenomena and functionalities can be archived such as negative refractive index [1, 2], invisibility cloaks [3], and giant chiral response [4]. Optical metamaterials also promise an effective way for miniaturization and integration of optical devices. They have shown significant advantages in many practical application areas, such as optical holograms [5], sub-diffraction imaging [6], and the design of integrated multifunctional optical devices [7]. Over the last decade, the concept of topology has been extended from condensed matter physics to various systems including photonics, acoustics [8], mechanics [9, 10], and cold atoms [11]. As an optical dimension, topology characterizes the quantized global behavior of wave functions in contrast to other optical dimensions like amplitude, polarization, phase, or frequency. A topological phenomenon which does not change under continuous deformation can provide a robust way to control photons, yielding application in polarization control [12], lossless waveguides, lasers [13], and cavities. Based on the quantum Hall effect [14, 15], anomalous quantum Hall effect [16], quantum spin Hall effect [17], and valley Hall effect [18, 19], topological protected photonic waveguides have been proposed in the two-dimensional (2D) space, leading to the emerging research field of topological photonics [20–23].

With the development of research and experimental technique, topological photonics has further expanded to 3D [24]. Among the 3D topological states, topological semimetals have attracted much attention recently as the topological gapless phase, which possess topologically protected surface states and novel topological transport phenomena [25]. Gapless band structures such as Weyl points, spin-1 triple points, 3D Dirac points, and nodal lines or surfaces have been discussed in the photonic systems. The topological semimetal phase or gapless phase is fundamentally different from the 2D cases. Unlike the 2D Dirac points which can be easily removed if either time reversal symmetry (T) or inversion symmetry (P) is broken, the Weyl points as the fundamental band structure in 3D are stable in systems lacking T or P. Weyl points and other nodal points can carry non-trivial topological charge and give rise to topological Fermi arc surface states. Although there are a number of reviews covering the progress in topological photonics, approaches to photonic topological semimetals have been considered a minor subject of these reviews [26, 27]. Therefore, this review is focused on photonic topological semimetals and their applications.

In this review, we follow the fast progress in 3D topological photonic semimetal states. In the first part, we introduce the category of photonic semimetals, their topological invariant, and the condition to realize them. In the second part, we discuss the realization of photonic topological semimetals on approaches that use photonic crystals or metamaterials. Photonic Weyl points with T or P symmetry breaking, 3D Dirac points, nodal lines, and nodal surfaces are elucidated. In the last part, we introduce emerging applications including vector beam generation, chiral zero modes, and non-Hermitian effects.

3D TOPOLOGICAL SEMIMETAL PHASES

The milestone of topological physics dates back to the discovery of quantum Hall phases, where 2D electron gas under a perpendicular magnetic field has quantized Hall conductance [28]. Because the magnetic field broke T, electrons in the quantum Hall effect propagate one way along the boundary, generating the chiral current. Backscattering is not allowed even with large defects because the edge states are topologically protected. The quantized feature of the Hall conductance is originated from the topological Chern number as follows:

$$C_n = \frac{1}{2\pi}\int_{\mathrm{BZ}} \mathbf{F}_n d^2\mathbf{k}, \tag{1}$$

where $F_n = i\nabla \times \langle u_n(\mathbf{k})|\nabla_{\mathbf{k}}|u_n(\mathbf{k})\rangle$ is the Berry curvature of the nth band and u_n is the nth eigenstate. The number of gapless edge modes inside a bandgap is determined by the difference of gap Chern number, which is the summation of all band Chern numbers below the bandgap, also known as the bulk-edge correspondence. When T is broken with magnetic field, the photonic quantum Hall effect can also emerge in photonic crystals composed of magnetoelectric or gyromagnetic materials [14, 15, 28–30]. The magnetoelectric materials have cross-coupling between electric and magnetic fields, where the constitutive relations take the form of $\mathbf{D} = \hat{\epsilon}\mathbf{E} + \hat{\chi}\mathbf{H}$ and $\mathbf{B} = \hat{\mu}\mathbf{H} + \hat{\zeta}\mathbf{E}$. For example, Jacobs *et al.* demonstrated that non-trivial band topology can be realized in Tellegen photonic crystals with a diagonal magnetoelectric response [30]. In contrast, the gyromagnetic materials do not have cross-coupling between electric and magnetic fields [14], where the permeability tensor takes the form as $\hat{\mu} = \begin{bmatrix} \mu & i\kappa & 0 \\ -i\kappa & \mu & 0 \\ 0 & 0 & \mu_0 \end{bmatrix}$. Other photonic systems also use Floquet-like couple waveguides [31] and dynamic modulation [32] to mimic the quantum Hall effect.

Although the T-broken photonic systems have excellent one-way transport properties, it is difficult to realize or industrialize. Instead, T-invariant systems utilizing the quantum spin Hall effect have provided a solution without applying magnetic field or gyromagnetic materials. The quantum spin Hall state can be viewed as two copies of the quantum Hall state for each spin. Each spin is a lock to one helical edge state. Elections with spin up or spin down will generate an edge current of counterclockwise or clockwise, or vice versa. As the Chern number of each spin cancels with each other, the total Chern number of quantum spin Hall system is trivial. The topology in the quantum spin Hall effect is characterized by the Z_2 invariant [33], where the trivial and non-trivial Z_2 invariants are 0 and 1, respectively. The quantum spin Hall effect has been realized with 2D array of resonators [16], photonic crystals with crystalline symmetries [17], and bianisotropy-induced photonic topological insulators [34, 35].

Now, we introduce the 3D topological semimetals and show how they relate to the non-trivial topological invariant. Weyl points acting like relativistic fermionic particles with vanishing mass are featured as point degeneracies among two bands in the 3D momentum space. Linear dispersion around the Weyl point is governed by the Weyl Hamiltonian $H = v_x k_x \sigma_x + v_y k_y \sigma_y + v_z k_z \sigma_z$, where $v_{x,y,z}$ are group velocities and $\sigma_{x,y,z}$ are Pauli matrices. Weyl points as the most fundamental topological structure in 3D crystals, usually occurring in pairs and can be viewed as monopoles with quantized source of Berry flux. By integrating the Berry curvature in a 2D surface enclosing a Weyl point, the Chern number as the topological charge of Weyl point can be obtained. Weyl points are virtually indestructible against perturbations in a 3D momentum space, unless a pair of Weyl points with opposite topological charge annihilate with each other. The topological character of Weyl points is reflected in the appearance of topologically protected states on the surface. The equifrequency contours of the surface states are open arcs connecting the surface projections of Weyl points with opposite topological charges, which are known as the Fermi arcs, as shown in **Figure 1A**. Topologically protected surface states in topological semimetals are immune to a special kind of obstacles and defects, resulting in the non-reflective transmission of wave modes. For those systems with a momentum gap along the k_z direction, a line defect or obstruction which is translation invariant along the z direction can preserve the k_z wavenumber of the scattering waves, prohibiting the chiral surface modes from

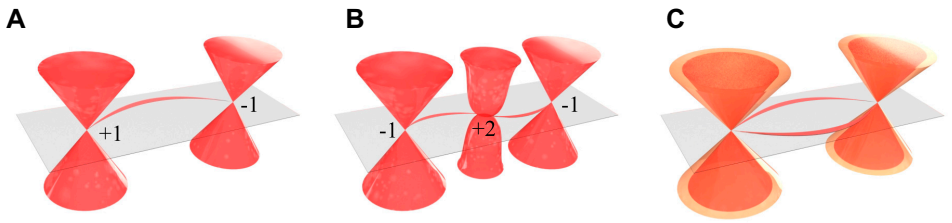

FIGURE 1 | (A) Pair of charge-1 Weyl points linked by a Fermi arc in the momentum space. The Weyl points have a cone-like linear dispersion. On equifrequency contour (gray plane), the surface states form an open arc linking the projection of Weyl points. **(B)** Charge-2 Weyl point **(middle)** linked with two charge-1 Weyl points. **(C)** A pair of 3D Dirac points as Z_2 monopoles linked by two branches of Fermi arcs.

scattering into the bulk or other surface modes inside different momentum gaps. As shown in **Figure 1B**, the topological charge of a bulk Weyl node can be reflected by the connectivity of Fermi arcs according to Nielsen-Ninomiya no-go theorem. For a charge-2 Weyl point with quadratic dispersion, there are two branches of Fermi arcs connecting the Weyl point. **Figure 1C** shows the fourfold 3D Dirac points which are symmetry-protected Z_2 monopoles in the 3D momentum space. Two branches of spin-polarized Fermi arcs can connect the Dirac point pair in the Brillouin zone. Other form of semimetal band structure has also been realized in photonics, such as nodal line [36, 37] and nodal surface [38]. The nodal line contains topological features as the Berry phase of π around the node. Recent studies have shown that nodal lines can carry a non-trivial Chern number as the Weyl points [37] or carry non-trivial Z_2 charge as the 3D Dirac points [28]. Nodal surfaces can also carry non-trivial Chern number in systems with non-symmorphic symmetries and T [39].

REALIZATION OF 3D PHOTONIC TOPOLOGICAL PHASES

Weyl Point With T-Breaking

Weyl points in 3D materials can be achieved by breaking either T or P. Here, we focus on the realization of photonic Weyl points achieved by the T-breaking approaches. For the Weyl points in electron systems with T-breaking, several novel topological properties are supported, such as axial anomaly [40], chiral anomaly [41, 42], gravitational anomaly [43], giant photocurrent [44], and quantum oscillation phenomena [45]. Lu *et al.* theoretically proposed that the breakthrough for achieving Weyl points with T- and/or P-breaking occurred in gyroid photonic crystals at infrared wavelengths. However, the realization of T-breaking in the photonic system usually relies on the magneto-optical effect, while the magneto-optical response of existing optical materials, such as ferromagnetic materials, is weak in the microwave frequencies and cannot cover the optical domain [46]. Although a considerably simple approach has been earlier proposed theoretically by Yang et al. in a magnetic tetrahedral photonic crystal [47], the experimental observation for the T-breaking Weyl point based on magnetic materials had not been realized until very recently due to the difficulty of fabricating the 3D structure in magnetic materials [48]. In addition, several theoretical works proposed recently that T could be broken in plasma [49, 50]. A new scheme shows that the plasma may support Weyl points in the T-breaking photonic system when an external magnetic field is applied [51]. Subsequently, Wang *et al.* experimentally observed photonic Weyl degeneracies in magnetized plasma at the terahertz regime, and the corresponding photonic Fermi arcs have also been demonstrated [52]. In this section, we review the main numerical and experimental schemes of 3D photonic topological Weyl points based on T-breaking system, including gyroid photonic crystals and magnetized plasmas.

The 3D photonic Weyl points with T-breaking were first theoretically predicted in double gyroid (DG) photonic crystals. The corresponding real-space structure in a unit cell consisting of a single gyroid (SG) and its inversion counterpart is shown in the **Figure 2A** [24]. The band structures of SG and DG photonic crystals are donated by red and blue lines, respectively, as shown in **Figure 2B**. The DG photonic crystal band structure exhibits a threefold quadratic nodal point as highlighted in green ellipses. When two air spheres are introduced in the DG photonic crystal without breaking P or T, the trivial threefold quadratic nodal point is transformed into a trivial twofold nodal ring. Starting with the twofold nodal ring, Weyl points are introduced by breaking P or T. P-breaking is done by adding an air sphere only in an SG, leading to the appearance of two pairs of Weyl points, as shown in the band structure plotted in **Figure 2C**. T-breaking is realized by adding an external magnetic field to the DG photonic crystal composed of a gyroelectric material. The band structure for only T-breaking is plotted in **Figure 2D** where only one pair of Weyl points appears in contrast to the P-breaking case. In the T-breaking system, P maps a Weyl point at $\mathbf{k}$ to $-\mathbf{k}$ with reversed chirality, while in the P-breaking system, T maps a Weyl point at $\mathbf{k}$ to $-\mathbf{k}$ with the same chirality. Because the net Berry flux integrated over the Brillouin zone must vanish, the net chirality of Weyl points must be zero. Therefore, a T-breaking system can only have one pair of Weyl points, while a P-breaking system should possess even pairs of Weyl points to neutralize the whole system. A single pair of photonic Weyl points with T broken was observed very recently based on a gyromagnetic photonic crystal operating at microwave frequencies [48]. The unit cell of the photonic crystal consisting of a gyromagnetic rod and a metallic plate perforated with holes is shown in **Figure 2E**. An external static magnetic field is applied along the z-axis to break T in the gyromagnetic photonic crystal. By increasing the strength of the external magnetic field, one pair of photonic Weyl points is generated and then annihilated, which

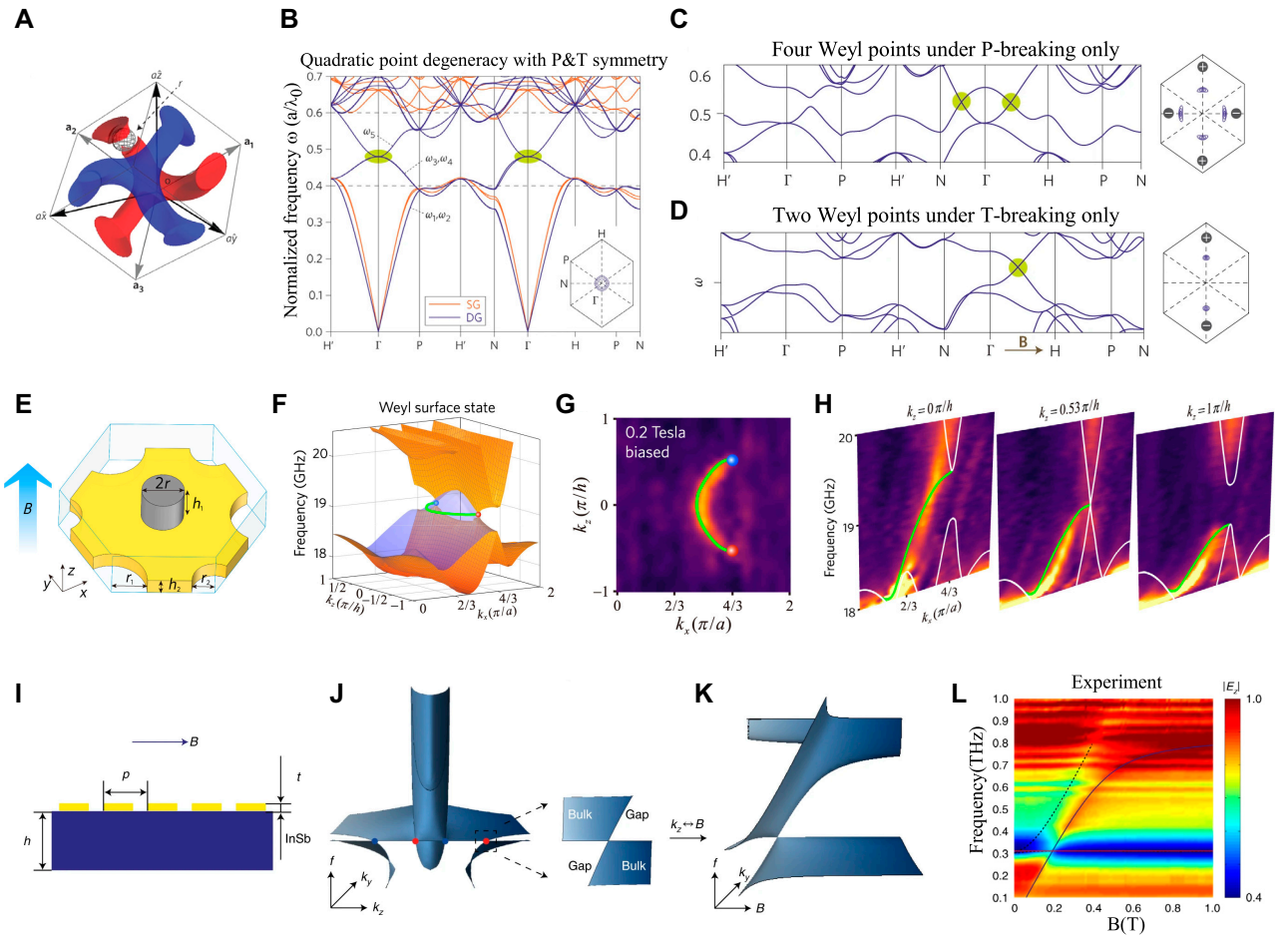

FIGURE 2 | 3D photonic Weyl semimetals by breaking *T* [24]. **(A)** The unit cell of double gyroid (DG) photonic crystals. **(B)** The band dispersion of original DG photonic crystal (blue line) and single gyroid (SG) photonic crystal (red line). **(C)** The band structure with only *P*-breaking by placing one air-sphere in only one gyroid, where two pairs of Weyl points appear. **(D)** The band structure with only *T*-breaking by applying a magnetic field to the DG photonic made of gyroelectric material, where one pair of Weyl points appears. **(E)** The unit cell of the gyromagnetic photonic crystal [48]. **(F)** Simulated band structure under a magnetic field of 0.2 T. The Fermi arc is donated by a green line. **(G)** Measured surface projections of single pair of Weyl points and the associated Fermi arc. **(H)** Measured surface dispersions on the front surface for $k_z = 0$, $k_z = 0.53\pi/h$, and $k_z = \pi/h$, respectively. **(I)** Schematics of the sample with a metal grating on the top of the InSb substrate [52]. **(J)** Simulated band structure of the magnetized plasma with $B = 0.19$ T. **(K)** Simulated band structure with k_z substituted by B. **(L)** Experimentally measured reflection spectra.

means the system transits into a topological semimetal phase and then the topological insulator phase. With a 0.2 T biasing magnetic field, the band structures of one pair of ideal Weyl points with opposite topological charge at the same frequency in Brillouin zone are shown in **Figure 2F**. The Fermi arc connecting the surface projections of this pair of Weyl points with opposite topological charges is measured experimentally, as shown in **Figure 2G**. With distinct k_z cases, the measured projected band structures corresponding to topological transition are shown in **Figure 2H**, where the Fermi arc exists only in the range of $k_z = 0$ to $k_z = 0.53\pi/h$.

Another experimental observation of Weyl points in the *T*-breaking photonic system was realized in magnetized plasma at the terahertz regime when an external magnetic field is applied. **Figure 2I** shows the sample with a metal grating to compensate for the phase mismatch on the top of the InSb substrate. For a semiconductor InSb, the band structure under a magnetic field strength of $B = 0.19$ T is plotted in **Figure 2J**. The band structure shows four Weyl points with opposite chiralities donated by red and blue spheres. The projected band structure around one Weyl point is shown on the right side of **Figure 2J**. Since magnetic field strength B behaves similarly with k_z in the effective Hamiltonian as well as in constructing the band structure of the Weyl points, a parameter space was constructed by scanning B, instead of k_z, in order to facilitate the observation. The band structure constructed in the synthetic parameter space $[k_x, k_y, B]$ is shown in **Figure 2K**, where linear dispersion demonstrates the presence of Weyl points. By varying the magnetic field strength from 0 to 1T, the reflection spectrum was measured, as shown in **Figure 2L**, which agrees well with the theoretical results in **Figure 2K**.

Weyl Points With P-breaking

P-breaking can be realized by specially designed structures, while an external or synthetic magnetic field is often required to break

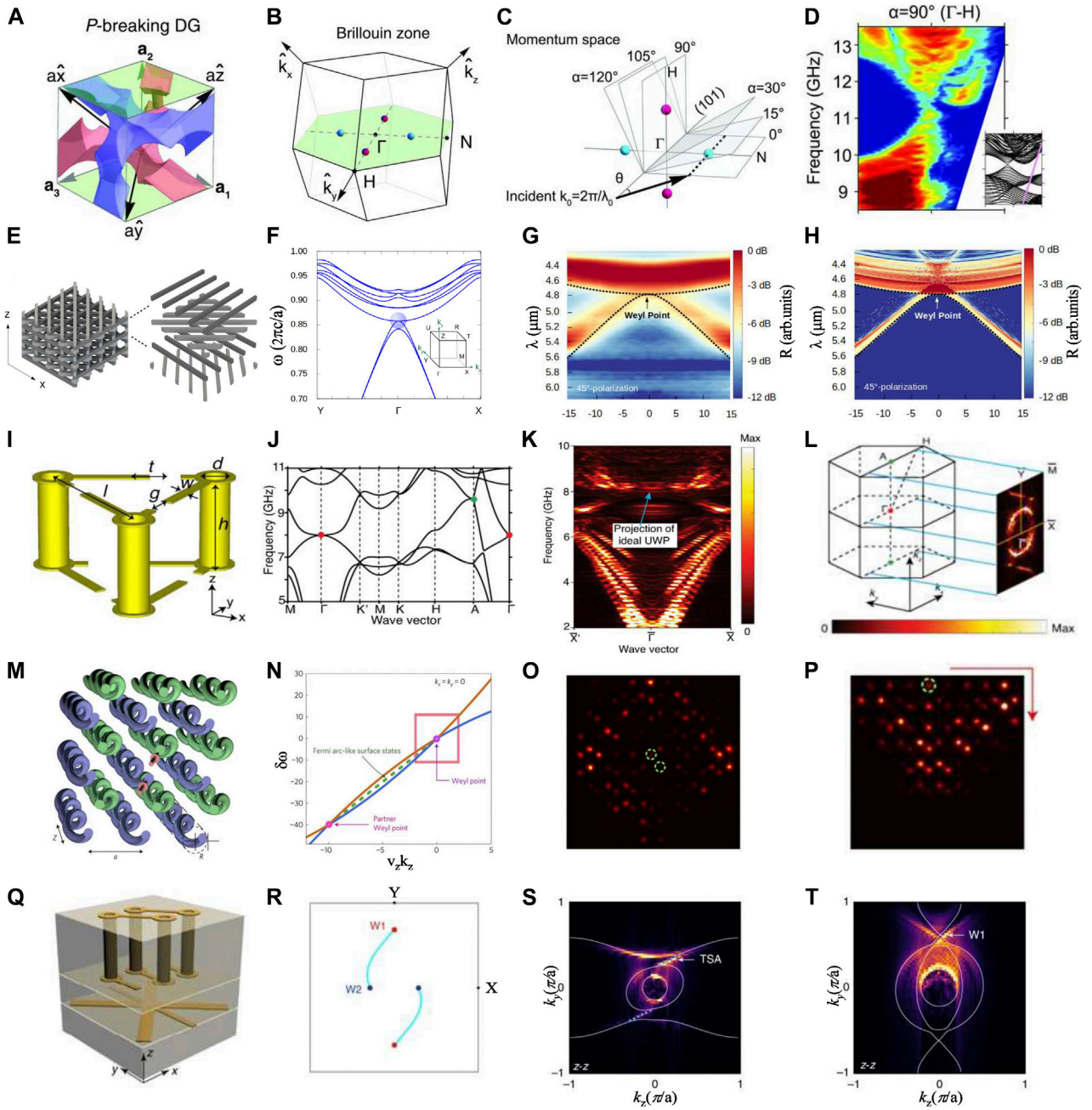

FIGURE 3 | (A) bcc cell of the *P*-breaking double gyroid photonic crystal [54]. **(B)** Two pairs of Weyl points are illustrated on the green (101) plane along *Γ*-*H* and *Γ*-*N* in the Brillouin zone. **(C)** The different bulk states can be excited by changing the incidence angle θ of the incident wave. **(D)** Experimental results of the Weyl point along the *Γ*-*H* direction. **(E)** Schematic diagram of the chiral woodpile structure [58]. **(F)** The band structure along the *Y*-*Γ*-*X* and the Weyl point is illustrated with a blue circle. **(G)** and **(H)** experimentally measured and simulated reflection spectra showing Weyl point for 45° polarizations, respectively. **(I)** The unit cell of the chiral metamaterial [63]. **(J)** Weyl points are denoted by red and green dots in the band structure. **(K)** Measured projected band diagram on the k_x–k_z plane. **(L)** Measured surface dispersion obtained by Fourier transformation. **(M)** Schematic diagram of the waveguide array structure [64]. **(N)** The dispersion diagram in the δk_x–δk_z plane when $\delta k_x = \delta k_y = 0$ shows the type-II Weyl points and Fermi arc–like surface states. **(O)** Experimental results of the intensity plots at the output facet at $a = 27$ μm, $\lambda = 1{,}525$ nm, and conical diffraction demonstrates the existence of type-II Weyl points. Green circles: position of input waveguides. **(P)** Experimental results of the intensity plots at the output facet at $a = 27$ μm, $\lambda = 1{,}500$ nm demonstrate the presence of Fermi arc–like surface states. Green circles: position of input waveguides. **(Q)** Schematic diagram of the unit cell of chiral hyperbolic metamaterials [71]. **(R)** Surface band structure on a varying frequency k_x–k_y map. **(S)** and **(T)** Experimental results of the topological surface-state arcs and type-II Weyl points in the momentum space at 5.46 GHz, respectively.

T. For example, using a periodic layered structure in the all-dielectric system can break only *P* to realize Weyl points [53]. In this section, we review Weyl points in photonic crystals and metamaterials by breaking *P*.

Weyl points were experimentally observed at microwave frequencies by using a 3D DG photonic crystal with broken *P* [54]. The *P*-breaking DG is shown in **Figure 3A**. Because *T* is preserved in the system, there are even pairs of Weyl points. **Figure 3B** shows two pairs of Weyl points in the (101) plane of the Brillouin zone. To observe the Weyl points, angle-resolved transmission measurement was used to probe the dispersions of the 3D bulk states. The bulk states of the *k* vectors can be excited with an incident wave with an incidence angle θ, as shown in **Figure 3C**. While maintaining the rotation angle of the samples $\alpha = 90^\circ$, the beam scans through the upper Weyl points along $\Gamma - H$. The experimental data and calculated band structures projected along the (101) plane clearly show a type-I Weyl point along $\Gamma - H$, as shown in **Figure 3D**. Type-I Weyl points have also been observed at optical frequencies in a photonic crystal coated with layered-composite nanometric materials [55].

If the Weyl system has additional spatial symmetries, Weyl points with higher topological charge can appear at high symmetry points in the Brillouin zone [51, 56]. Charge-2 Weyl points can exist in a chiral woodpile photonic crystal with screw symmetry [57]. Recently, a parity-breaking chiral woodpile photonic crystal fabricated by two-photon polymerization was constructed to observe a charge-2 Weyl point in the mid-infrared regime [58]. Each layer rotates 45° next to the neighboring layer, as shown in **Figure 3E**. The Weyl point with quadratic dispersion occurs at the Γ point, as shown in **Figure 3F**; **Figure 3G** shows the experimental observation of charge-2 Weyl points using the angle-resolved Fourier-transform infrared spectroscopy, in contrast to the simulated angle-resolved reflection spectra in **Figure 3H**. With a similar woodpile structure, not only Weyl points can be realized but also negative refraction can be observed in phononic crystals [59]. Weyl points with higher topological charge are also reported in metallic photonic crystals in microwave frequencies [60], acoustic structure [61], and transition-metal monosilicides [62].

Weyl points with higher topological charge exist not only in photonic crystal but also in chiral metamaterials [63]. Topological charge-2 ideal Weyl points were reported in the chiral microwave metamaterial which has C_3 rotational symmetry and time-reversal symmetry. The unit cell consists of three double-split ring resonators, as shown in **Figure 3I**. The Weyl points with a topological charge +2 at Γ point and −2 at A point are enforced by chiral symmetry. The band structure of the system is shown in **Figure 3J**. The measured projected band structure of the k_x–k_z plane along the high-symmetry line $\bar{X}'\bar{X}$ shows the ideal Weyl point, as depicted in **Figure 3K**. The crossing bands are quadratic in the k_x–k_y plane and linear in the k_z direction. Because the topological charge is 2, there are two Fermi arcs connecting the oppositely charged Weyl points, as shown in **Figure 3L**. Weyl points carrying higher topological charges have exotic topological properties; for instance, the Fermi arcs can extend over most of the Brillouin zone.

In addition to type-I Weyl points, type-II Weyl points are also observed in the experiment. The dispersion around type-II Weyl points is strongly tilted in contrast to type-I Weyl points, where the group velocities of the two crossing bands have the same sign along one direction [64]. Noh *et al.* observed type-II Weyl points at optical frequencies and Fermi arc–like surface states in a 3D photonic crystal structure of coupled single-mode waveguides [65]. The helical waveguides made by femtosecond direct laser writing are shown in **Figure 3M**. The partner Weyl point is associated with Fermi arc–like surface states, as shown in **Figure 3N**. When the lattice constant is $a = 27$ um, the conical diffraction pattern was clearly observed at the frequency of 1,525 nm, confirming the existence of type-II Weyl point, as shown in **Figure 3O**. The Fermi arc–like surface states in the experiment are shown in **Figure 3P**. Type-II Weyl points have also been found in acoustic systems [66, 67].

Another mechanism to break *P* is realized by combining chiral and hyperbolic properties in metamaterials [38, 68–70]. Yang *et al.* experimentally observed type-II Weyl points and photonic topological surface state arcs in a chiral hyperbolic metamaterial by near-field scanning measurements [71]. The cubic unit cell is shown in **Figure 3Q**. The unit cell has three layers as follows: the top layer is a chiral layer, the middle layer is a blank layer, and the bottom layer is a hyperbolic layer. Topological surface states connecting two pairs of Weyl points in the frequency-varying k_x–k_y plane are shown in **Figure 3R**. Topological surface state arcs and type-II Weyl points observed in the experiment are shown in **Figures 3S,T**, respectively. In addition, disorder in chiral hyperbolic metamaterials can induce topological state transition in the photonic Weyl system [72]. The combination of Weyl points and metamaterials has greatly enriched the field of the topological semimetal phase and brings new potential to the manipulation of electromagnetic and acoustic waves.

3D Dirac Point

Hosting a fourfold linear dispersion in the 3D momentum space, the 3D Dirac point represents the degeneracy of paired Weyl points with opposite chiralities. In photonics, fourfold degeneracy of the Dirac point can be achieved through additional symmetries, such as electromagnetic duality symmetry and space symmetries. While 3D Dirac points carry a trivial Chern number, they are Z_2 monopoles in the 3D momentum space [73]. Upon symmetry breaking, the band structure can transit into the Z_2 nodal ring, Weyl dipole, and topological bandgap supporting gapless surface states [74] or hinge states [75]. Recently, the transition from the 3D Dirac point to Weyl dipole is experimentally demonstrated in acoustics [76].

3D Dirac points can be classified into symmetry-enforced Dirac points and band inversion Dirac points according to the mechanism in forming the fourfold degeneracy. Symmetry-enforced Dirac points are unavoidable results of the non-symmorphic space group of a material. The first proposed photonic 3D Dirac photonic crystal has glide reflections in *x*, *y*, and *z* directions, as shown in **Figure 4A** [74]. The 3D Dirac points which host linear dispersions appear at high-symmetry P points of the Brillouin zone, as shown in **Figure 4B**. The glide

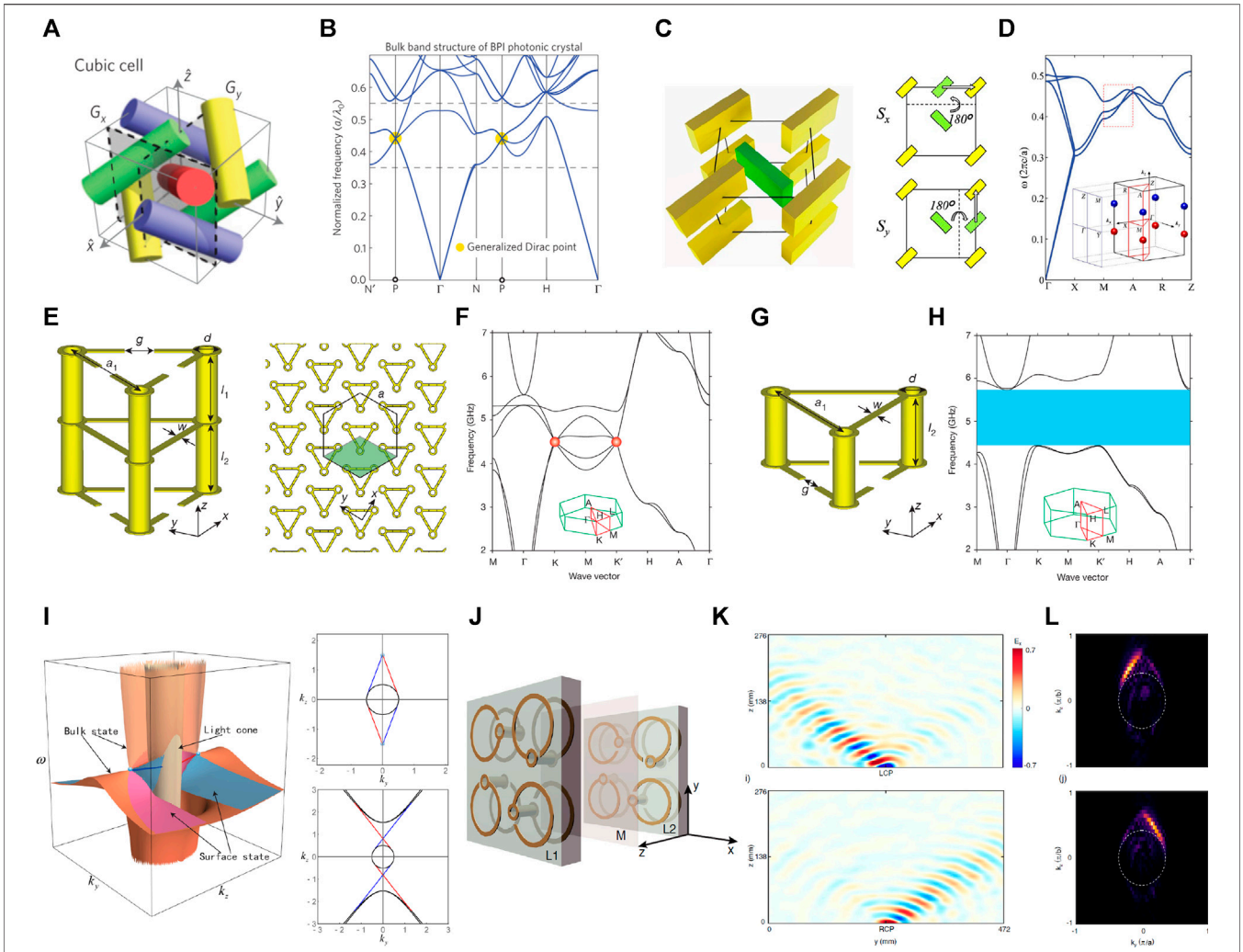

FIGURE 4 | (A) Photonic crystal with glide reflection in *x*, *y*, and *z* directions [74]. **(B)** Band structure with a single 3D Dirac point. **(C)** 3D Dirac photonic crystal with screw symmetries and **(D)** its photonic band structure [78]. **(E)** 3D array of metallic split-ring resonators with 3D Dirac point [79]. **(F)** Band structure of the photonic crystal with the unit cells in **(E)**. **(G)** Unit cell giving rise to a 3D topological bandgap through removing the top three split-ring resonators. **(H)** Band structure of the photonic topological insulator with the unit cells in **(G)**. **(I)** Bulk and surface state dispersions of a Dirac metamaterial with electromagnetic duality symmetry [81]. Equifrequency contour at above **(top-right)** and below **(bottom-right)** the Dirac point frequency. **(J)** Printed circuit board unit cell and spin-polarized topological surface states of a Dirac metamaterial **(K)** in the real and **(L)** momentum space [82].

symmetries together with time reversal symmetry not only stabilize the Dirac point but also prevent the anti-crossing of helicoid surface states, leading to the non-trivial band topology on the surface. As an example, quad-helicoid surface states are observed in acoustics [28, 77].

Meanwhile, band inversion 3D Dirac points have been discovered in photonics utilizing screw symmetries [78], hexagonal structures with C_3 or C_6 symmetry [79, 80], and electromagnetic duality symmetry [81, 82]. These 3D Dirac points lie on the generic momenta of an axis of rotation symmetry, always come in pairs, and can be eliminated through merging and pairwise annihilation. The locations of the band crossings can be continuously tuned as a function of the Hamiltonian control parameters. **Figure 4C** shows a type-II 3D Dirac photonic crystal with screw symmetries. Photonic Kramers double degeneracy of *p* and *d* states is generated by anti-unitary operators composed of the screw symmetry and *T*. The crossing of *p* and *d* states forms the fourfold degeneracy, as shown in **Figure 4D**. For hexagonal structures with C_3 symmetry (**Figure 4E**), the photonic band structure exhibits frequency-isolated 3D Dirac points for fine-tuned lattice parameters, as shown in **Figure 4F**. When removing the upper three split-ring resonators in the unit cell, the photonic metamaterial becomes a weak insulator (**Figures 4G,H**), which supports the robust interface state with cone dispersion. Overall, the band inversion Dirac points are formed with less symmetry elements and may provide an option to realize strongly anisotropic dispersion.

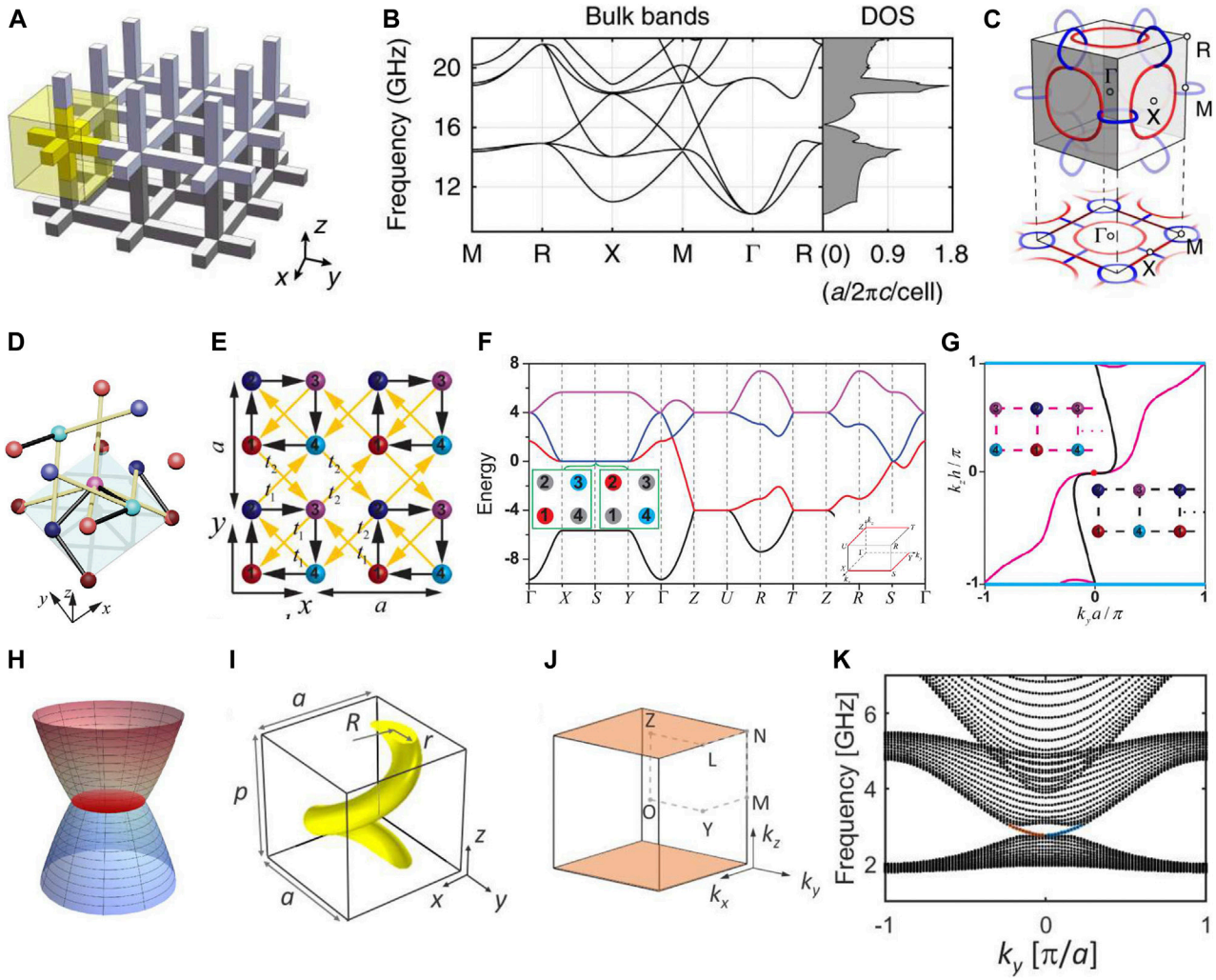

FIGURE 5 | (A) Schematic illustration for nodal chain photonic crystal [83]. **(B)** The bulk band structure and density of states. **(C)** The structure of nodal chains in the Brillouin zone. **(D)** Tight binding model for a charged nodal line [37]. **(E)** The projection of the tight binding model on the *x*–*y* plane. **(F)** The band structures with charged nodal lines are formed by geometric frustration. **(G)** Equifrequency contour on the k_y–k_z surface Brillouin zone. The red dot and cyan line represent the projection of the charged +2 Weyl point and the charged -2 nodal chain. **(H)** Schematics of a nodal surface [38]. **(I)** Schematic of a unit cell of the nodal surface photonic crystal. **(J)** Brillouin zone with the high-lighted nodal surface. **(K)** Surface state dispersion at $k_x = 0$ and $k_z = 0.5\pi/p$.

Electromagnetic duality symmetry is an internal symmetry of the electromagnetic field [81, 82]. The realization of this symmetry requires the proportionality between permittivity and permeability tensors, which indicates that metamaterials described by the effective medium theory are preferred. Due to the electromagnetic duality, circular polarizations are the eigenstates of the system. For left-handed circularly polarized (LCP) photons, one Dirac point behaves like a sink of Berry flux, while for right-handed circularly polarized (RCP) photons, it behaves like a source. As a result, two pairs of spin-polarized surface states appear at the interface between metamaterial and air, as shown in **Figure 4I**. In the experiment, fine-tuned metallic helical elements are used to introduce both electric and magnetic resonances in the microwave regime, as shown in **Figure 4J**. The spin-polarized topological surface states in the real and momentum space were experimentally demonstrated in **Figure 4K** and **Figure 4L**, respectively. This spin–orbit coupling character may bring about a unique advantage in the manipulation of light.

Nodal Line and Nodal Surface

Nodal lines protected by *P* and *T* symmetries are treated as the 3D extrusion of 2D Dirac points. They share the same local Hamiltonian $H(\mathbf{k}) = k_x\sigma_x + k_z\sigma_z$. The Berry phase around the nodal line is π. Due to the periodicity of the Brillouin zone, a single nodal line forms a closed ring. The Berry curvature vanishes under *P* and *T* symmetries, and the nodal line is not charged. The breaking of *P* or *T* in the nodal line can give rise to the phase transition to Weyl points [24]. Nodal rings can intersect and form nodal chains under the local chain Hamiltonian $H(\mathbf{k}) = k_x\sigma_x + (k_yk_z + m_z)\sigma_z$ when the mass term $m_z = 0$. Nodal chains are experimentally observed in a metallic mesh

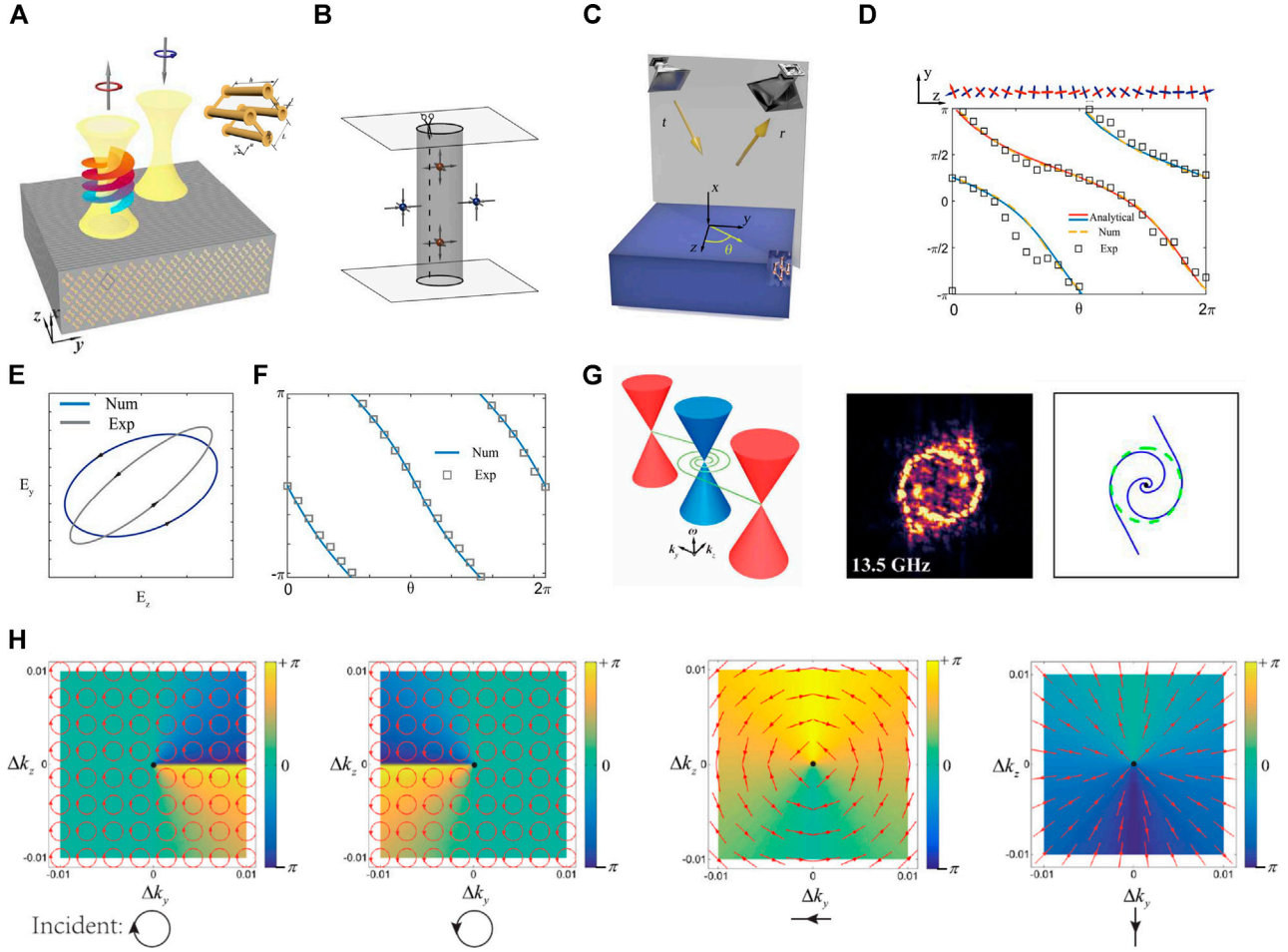

FIGURE 6 | (A) Vortical mirror in Weyl metamaterial is composed of metallic saddle-shaped structure, and an incident Gaussian beam can be reflected into a vortex beam [84]. **(B)** Weyl nodes with arrows indicating the directions of the Berry curvatures. Cylindrical surface enclosing the Weyl points has a topological charge of 2. **(C)** Reflection measurement setup in a microwave. **(D)** Reflection phases of the eigenstates and the eigenpolarizations of the Jones matrix for incident light. **(E)** An incident beam with the right-handed elliptical polarization state gives rise to **(F)** 4π phase winding, generating a vortex beam. **(G)** Spiral Fermi arcs formed by reflection between the Weyl metamaterial and perfect electric conductor. **(H)** Reflection spectrum around a 3D Dirac metamaterial [81].

photonic crystal [83], as shown in **Figure 5A**. These nodal chains are protected by mirror symmetry and have little frequency variation. The linear crossing of the third and fourth bands forms the line degeneracies of nodal chains, as shown in band structures in **Figures 5B,C**.

To obtain a charged nodal line, X. Meng *et al.* considered a simple Hamiltonian $H(\mathbf{k}) = k_x\sigma_x + k_z\sigma_z + k_\rho k_y\sigma_y$ [37], where $k_\rho = \sqrt{k_x^2 + k_z^2}$. The Hamiltonian possesses a nodal line along the y direction as the bands are degenerate at $k_\rho = 0$ and exhibits linear dispersion away from this nodal line. The quantized Berry charge carried by the nodal line is 1. The tight binding model of the charged nodal line is proposed using the concept of geometric frustration, as shown in **Figures 5D,E**. Two types of couplings are denoted as black and yellow bonds, respectively. Black bonds occur between adjacent layers, while yellow bonds occur between next adjacent layers. **Figure 5F** shows the band structure of this tight binding model, where perfect flat bands of nodal chains are found. The charged nodal chains give rise to the existence of chiral edge states, as shown in **Figure 5G**. In addition to the nodal line with a non-trivial Chern number, the Z_2 nodal line may exist in photonic crystals with glide reflection and T [28].

Nodal surfaces are degeneracies in two dimensions, as shown in **Figure 5H**. M. Kim *et al.* proposed a nodal surface metamaterial with twofold screw symmetry S_{2z} and T [38]. The metamaterial is composed of metallic helices, as shown in **Figure 5I**. The hyperbolicity and chirality of the metamaterial give rise to the topologically non-trivial phase; thus, the nodal surface carries a non-trivial topological charge of Chern number. The nodal surface is formed between the first and the second bands at $k_z = \pi/p$, as shown in **Figure 5J**. Surface modes exist according to the bulk–boundary correspondence, as shown in **Figure 5K** at $k_x = 0$ and $k_z = 0.5\pi/p$.

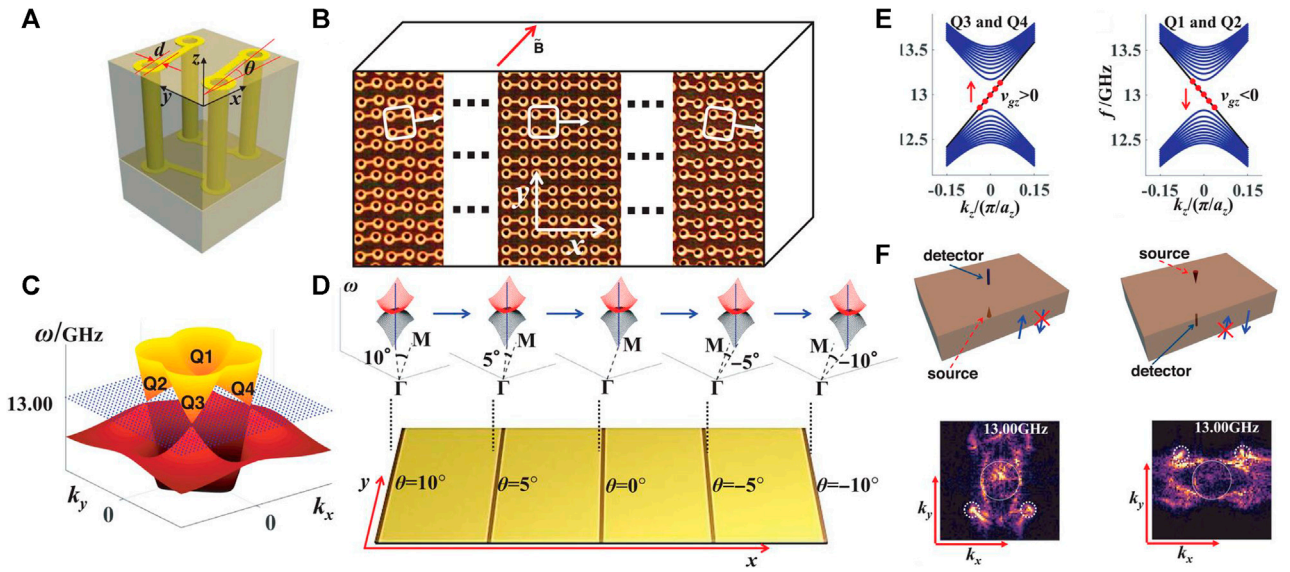

FIGURE 7 | (A) Saddle-shaped metallic coil with rotation about *z* axis [41]. **(B)** Top surface of the sample. Gradient of rotational angle along the *x* direction generates a synthetic magnetic field along the *z* direction. **(C)** Dispersion of the Weyl metamaterial with no rotation angle. **(D)** The position of the Weyl point Q1 shifts as the rotation angle varies linearly with *x*. **(E)** Band structures showing Landau levels for Weyl points. **(F)** Experimental result for up-going (down-going) chiral zero modes around Weyl points Q3 and Q4 (Q1 and Q2).

APPLICATION IN MANIPULATING LIGHT

Winding Phase and Vector Beams Generation

The non-trivial topology of photonic semimetals can be revealed not only by the surface states but also by the vortical phase profile in the reflection of spin-polarized electromagnetic waves. Cheng et al. demonstrate the vortical phase and the generation of vortex beam using the reflection property of Weyl metamaterials [84]. As shown in **Figure 6A**, an incident Gaussian beam with left-handed polarization can be reflected into a vortex beam with right-handed polarization. The Weyl metamaterial constructed by a metallic saddle-shaped connective coil has four ideal Weyl nodes in the Brillouin zone. When light is incident with a certain elevation angle φ and varies with an azimuthal angle θ, the winding number of the scattering matrix, which is 2 in 2π of phase, is equivalent to the projected topological charge enclosed by $k_0 \sin(\varphi)$ in the surface Brillouin zone, as shown in **Figure 6B**. To reveal the topological property of the reflected wave, a scattering matrix combined with four *s* and *p* polarizations is measured for varying azimuthal angle θ. It has been proven that the scattering matrix is topologically equivalent to the Hamiltonian. Two microwave horn antennas are used as a transmitter and a receiver, as shown in **Figure 6C**. The topological feature of the Weyl metamaterial is that each eigenstate's reflection phase winds 2π, and eigenpolarizations wind π for a full turn of rotation, as shown in **Figure 6D**. In an ideal case where the metamaterial and air are matched with the same impedance, the scattering matrix around the Weyl point is given as follows:

$$\hat{S} = e^{-i\theta}\begin{bmatrix} \cos\theta & \sin\theta \\ \sin\theta & -\cos\theta \end{bmatrix}. \quad (2)$$

The scattering matrix operated on the right-handed circular polarization state $|R\rangle$ is converted to the left-handed polarization state $|L\rangle$ with and an extra 2θ phase, while the conversion from $|L\rangle$ to $|R\rangle$ is without the extra phase. Therefore, a Gaussian beam with right-handed polarization would be converted in to a vortex beam with an orbital angular momentum of 2 upon reflection. In the experiment, a right-handed elliptical incident beam described in **Figure 6E** would give rise to a winding reflection phase of 4π, as shown in **Figure 6F**. The winding phase also gives rise to the spiral Fermi arc, as shown in **Figure 6G**.

The angle-resolved reflectance spectrum also shows how a Dirac node can be decomposed into two related Weyl points with opposite topological charge [81]. As shown in **Figure 6H**, an anticlockwise loop in the momentum space around the Dirac point with RCP or LCP incidence acquires a 2π or -2π reflection phase, when circular polarizations are the eigenstates of the system with electromagnetic duality. Moreover, symmetrical angular and radial vector beams are generated by a Gaussian beam incidence with TE and TM polarization states. In contrast to conventional vector beam generators that rely on spatially varying phase elements, Weyl and Dirac metamaterials which are alignment-free may establish a new way to generating vector and vortex beams.

Chiral Zero Mode for Bulk Transport

Owing to the chirality of Weyl points, the Weyl or 3D Dirac crystal can support one-way chiral zero modes under a strong magnetic field, which leads to non-conservation of chiral currents known as a chiral anomaly [85, 86]. The chiral zero mode is a one-way propagative bulk mode, which can be applied for the robust transport of photons in the bulk medium. In order to generate an effective field, shifting of the Weyl point positions is applied in the

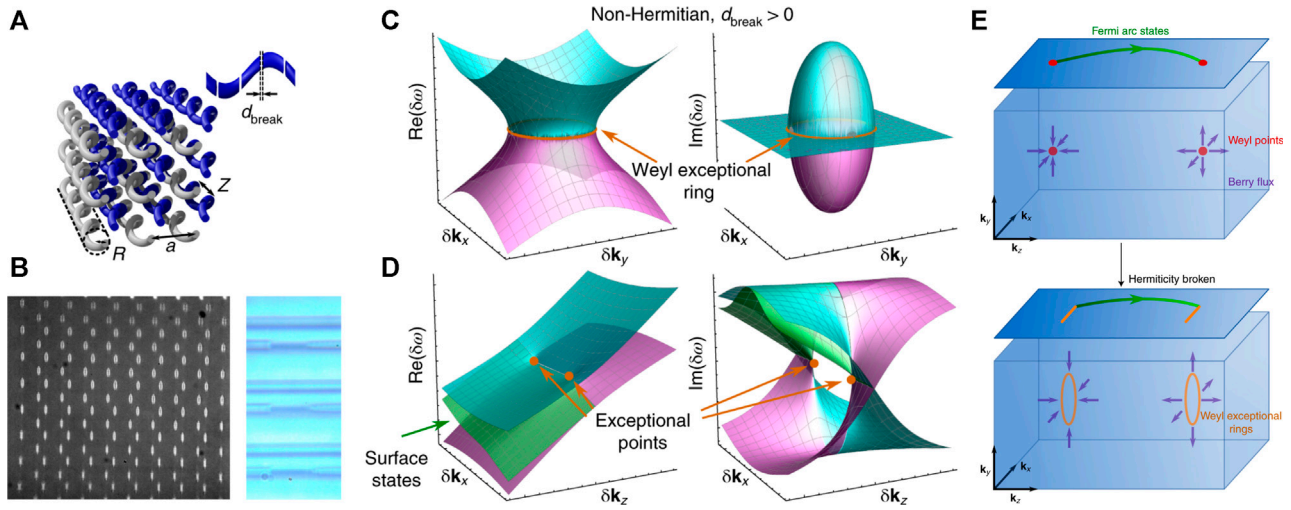

FIGURE 8 | (A) Bipartite helical waveguide array, where breaks have been added to one of the sublattices to remove the Hermiticity [90]. **(B)** Image of the output facet **(left)** and microscope image showing breaks added **(right)**. **(C)** Band structures in the $\delta k_x - \delta k_y$ plane possessing a Weyl nodal ring. **(D)** Band structures in the $\delta k_x - \delta k_z$ plane, exhibiting two exceptional points as the nodal ring intersects the plane twice. **(E)** Surface states convert to connecting the projection of Weyl exceptional rings with Hermiticity broken.

metamaterial [41], as shown in **Figures 7A,B**. The four Weyl points rotate around the *z* axis when rotating the metallic coil, as shown in **Figures 7C,D**, generating a pseudo-gauge field. The band structure is shown in **Figure 7E**, Landau levels for Weyl points with positive (negative) chirality support a chiral zero mode with a positive (negative) group velocity. This feature is observed in the Fourier transform results, as shown in **Figure 7F**, that zeroth Landau levels are up-propagating in Weyl points Q3 and Q4 while down-going in Q1 and Q2. Overall, the Weyl system provides a platform for examining the interesting features that appear under a magnetic field. It can also be applied for the robust transport of photons in the bulk medium. The mechanism to generate pseudo-gauge field in Weyl crystals has also been applied in acoustics [87].

Non-Hermitian Photonic Topological Semimetals

In the last few years, non-Hermiticity has been explored in topological materials such as topological insulators and Weyl semimetals [88, 89]. Photonic systems, which break Hermiticity through material absorption, gain, or radiative outcoupling, have a unique advantage to realize non-Hermiticity over the solid-state systems. Recently, the Weyl exceptional ring has been experimentally realized in a 3D photonic lattice composed of evanescently coupled helical waveguides [90], as shown in **Figures 8A,B**. The band structure of Weyl exceptional rings is shown in **Figures 8C,D**. To remove the Hermiticity of this system, periodic breaks are inserted into one of the two sublattices. The Weyl exceptional ring possesses quantized Berry charge–protected surface states, as shown in **Figure 8E**. The topological transition from Weyl points to Weyl exceptional rings is confirmed in the experiment by observing the appearance of Fermi arc surface states and the disappearance of conical diffraction for increasing break length. Various unconventional Weyl exceptional contours are also found in non-Hermitian chiral plasma, which can be achieved using metamaterials with effective constitutive parameters [91]. An unconventional Weyl point can transform into a quadratic Weyl exceptional circle, a type-I Weyl exceptional chain with one chain point, a type-II Weyl exceptional chain with two chain points, or other forms. Topological phase transition depending only on the strength of the non-Hermiticity allows for a new route to obtain tunable photonic topological materials [92].

PROSPECTIVE AND CONCLUSION

The study of photonic topological semimetal has been developed very rapidly. Great success has been achieved in finding new exotic features exploiting the spin-1 nature of photons. Having a great designability in structural design with composite materials, the photonic topological semimetal provides a unique platform to study the chirality or spin-related effects. The application of topology in photonic artificial microstructure also gives a new way to manipulate light. The application area may cover the robust transport, negative refraction, and vector beam generation. Based on the topological semimetal phase, the 3D topological insulator phase can be achieved through symmetry breaking. The design of photonic topological semimetal may further cover the non-linearity [93], non-Hermiticity [88], and more synthetic field or synthetic space [94]. Very recently, 3D higher order topological semimetals were proposed with topological

semimetals [95–99]. We believe that the photonic topological semimetals will continue to play an important role both in the theoretical study and application.

AUTHOR CONTRIBUTIONS

BX and SC conceived the idea. BX, HL, and HW prepared the draft. All authors contributed to the discussion and revision of the manuscript.

FUNDING

This work was supported by the National Key Research and Development Program of China (2016YFA0301102 and 2017YFA0303800), the National Natural Science Fund for Distinguished Young Scholar (11925403), the National Natural Science Foundation of China (12004198, 11974193, 91856101, and 11774186), Natural Science Foundation of Tianjin for Distinguished Young Scientists (18JCJQJC45700), and the China Postdoctoral Science Foundation (2020M680850).

REFERENCES

1. Shelby RA, Smith DR, Schultz S. Experimental Verification of a Negative Index of Refraction. *Science* (2001) 292:77–9. doi:10.1126/science.1058847
2. Smith DR, Pendry JB, Wiltshire MCK. Metamaterials and Negative Refractive index. *Science* (2004) 305:788–92. doi:10.1126/science.1096796
3. Pendry JB, Schurig D, Smith DR. Controlling Electromagnetic Fields. *Science* (2006) 312:1780–2. doi:10.1126/science.1125907
4. Cui Y, Kang L, Lan S, Rodrigues S, Cai W. Giant Chiral Optical Response from a Twisted-Arc Metamaterial. *Nano Lett* (2014) 14:1021–5. doi:10.1021/nl404572u
5. Wen D, Yue F, Li G, Zheng G, Chan K, Chen S, et al. Helicity Multiplexed Broadband Metasurface Holograms. *Nat Commun* (2015) 6:8241. doi:10.1038/ncomms9241
6. Fang N, Lee H, Sun C, Zhang X. Sub-diffraction-limited Optical Imaging with a Silver Superlens. *Science* (2005) 308:534–7. doi:10.1126/science.1108759
7. Chen S, Li Z, Liu W, Cheng H, Tian J. From Single-Dimensional to Multidimensional Manipulation of Optical Waves with Metasurfaces. *Adv Mater* (2019) 31:1802458. doi:10.1002/adma.201802458
8. Zhang X, Xiao M, Cheng Y, Lu M-H, Christensen J. Topological Sound. *Commun Phys* (2018) 1:97. doi:10.1038/s42005-018-0094-4
9. Huber SD. Topological Mechanics. *Nat Phys* (2016) 12:621–3. doi:10.1038/nphys3801
10. Ma G, Xiao M, Chan CT. Topological Phases in Acoustic and Mechanical Systems. *Nat Rev Phys* (2019) 1:281–94. doi:10.1038/s42254-019-0030-x
11. Cooper NR, Dalibard J, Spielman IB. Topological Bands for Ultracold Atoms. *Rev Mod Phys* (2019) 91:015005. doi:10.1103/RevModPhys.91.015005
12. Guo Y, Xiao M, Fan S. Topologically Protected Complete Polarization Conversion. *Phys Rev Lett* (2017) 119:1–5. doi:10.1103/PhysRevLett.119.167401
13. Zeng Y, Chattopadhyay U, Zhu B, Qiang B, Li J, Jin Y, et al. Electrically Pumped Topological Laser with valley Edge Modes. *Nature* (2020) 578:246–50. doi:10.1038/s41586-020-1981-x
14. Wang Z, Chong YD, Joannopoulos JD, Soljačić M. Reflection-Free One-Way Edge Modes in a Gyromagnetic Photonic Crystal. *Phys Rev Lett* (2008) 100:013905. doi:10.1103/PhysRevLett.100.013905
15. Wang Z, Chong Y, Joannopoulos JD, Soljačić M. Observation of Unidirectional Backscattering-Immune Topological Electromagnetic States. *Nature* (2009) 461:772–5. doi:10.1038/nature08293
16. Mittal S, Orre VV, Leykam D, Chong YD, Hafezi M. Photonic Anomalous Quantum Hall Effect. *Phys Rev Lett* (2019) 123:043201. doi:10.1103/PhysRevLett.123.043201
17. Wu L-H, Hu X. Scheme for Achieving a Topological Photonic Crystal by Using Dielectric Material. *Phys Rev Lett* (2015) 114:223901. doi:10.1103/PhysRevLett.114.223901
18. Liu J-W, Shi F-L, He X-T, Tang G-J, Chen W-J, Chen X-D, et al. Valley Photonic Crystals. *Adv Phys X* (2021) 6:1905546. doi:10.1080/23746149.2021.1905546
19. Dong J-W, Chen X-D, Zhu H, Wang Y, Zhang X. Valley Photonic Crystals for Control of Spin and Topology. *Nat Mater* (2017) 16:298–302. doi:10.1038/nmat4807
20. Lu L, Joannopoulos JD, Soljačić M, Soljačić M, Soljacic M. Topological Photonics. *Nat Photon* (2014) 8:821–9. doi:10.1038/nphoton.2014.248
21. Khanikaev AB, Shvets G. Two-dimensional Topological Photonics. *Nat Photon* (2017) 11:763–73. doi:10.1038/s41566-017-0048-5
22. Ozawa T, Price HM, Amo A, Goldman N, Hafezi M, Lu L, et al. Topological Photonics. *Rev Mod Phys* (2019) 91:15006. doi:10.1103/RevModPhys.91.015006
23. Liu H, Xie B, Cheng H, Tian J, Chen S. Topological Photonic States in Artificial Microstructures [Invited]. *Chin Opt Lett.* (2021) 19:052602. doi:10.3788/COL202119.052602
24. Lu L, Fu L, Joannopoulos JD, Soljačić M. Weyl Points and Line Nodes in Gyroid Photonic Crystals. *Nat Photon* (2013) 7:294–9. doi:10.1038/nphoton.2013.42
25. Armitage NP, Mele EJ, Vishwanath A. Weyl and Dirac Semimetals in Three-Dimensional Solids. *Rev Mod Phys* (2018) 90:015001. doi:10.1103/RevModPhys.90.015001
26. Xie B-Y, Wang H-F, Zhu X-Y, Lu M-H, Wang ZD, Chen Y-F. Photonics Meets Topology. *Opt Express* (2018) 26:24531. doi:10.1364/oe.26.024531
27. Kim M, Jacob Z, Rho J. Recent Advances in 2D, 3D and Higher-Order Topological Photonics. *Light Sci Appl* (2020) 9:130. doi:10.1038/s41377-020-0331-y
28. Cheng H, Sha Y, Liu R, Fang C, Lu L. Discovering Topological Surface States of Dirac Points. *Phys Rev Lett* (2020) 124:104301. doi:10.1103/PhysRevLett.124.104301
29. Raghu S, Haldane FDM. Analogs of Quantum-Hall-Effect Edge States in Photonic Crystals. *Phys Rev A* (2008) 78:033834. doi:10.1103/PhysRevA.78.033834
30. Jacobs DA, Miroshnichenko AE, Kivshar YS, Khanikaev AB. Photonic Topological Chern Insulators Based on Tellegen Metacrystals. *New J Phys* (2015) 17:125015. doi:10.1088/1367-2630/17/12/125015
31. Rechtsman MC, Zeuner JM, Plotnik Y, Lumer Y, Podolsky D, Dreisow F, et al..Photonic Floquet Topological Insulators. *Nature* (2013) 496:196–200. doi:10.1038/nature12066
32. Fang K, Yu Z, Fan S. Realizing Effective Magnetic Field for Photons by Controlling the Phase of Dynamic Modulation. *Nat Photon* (2012) 6:782–7. doi:10.1038/nphoton.2012.236
33. Fu L, Kane CL. Time Reversal Polarization and aZ2adiabatic Spin Pump. *Phys Rev B* (2006) 74:195312. doi:10.1103/PhysRevB.74.195312
34. Cheng X, Jouvaud C, Ni X, Mousavi SH, Genack AZ, Khanikaev AB. Robust Reconfigurable Electromagnetic Pathways within a Photonic Topological Insulator. *Nat Mater* (2016) 15:542–8. doi:10.1038/nmat4573
35. Chen W-J, Jiang S-J, Chen X-D, Zhu B, Zhou L, Dong J-W, et al..Experimental Realization of Photonic Topological Insulator in a Uniaxial Metacrystal Waveguide. *Nat Commun* (2014) 5:5782. doi:10.1038/ncomms6782
36. Burkov AA, Hook MD, Balents L. Topological Nodal Semimetals. *Phys Rev B* (2011) 84:235126. doi:10.1103/PhysRevB.84.235126
37. Xiao M, Sun X-Q, Fan S. Nodal Chain Semimetal in Geometrically Frustrated Systems. *Phys Rev B* (2019) 99:094206. doi:10.1103/PhysRevB.99.094206
38. Kim M, Lee D, Lee D, Rho J. Topologically Nontrivial Photonic Nodal Surface in a Photonic Metamaterial. *Phys Rev B* (2019) 99:235423. doi:10.1103/PhysRevB.99.235423
39. Yang Y, Xia J-p., Sun H-x, Ge Y, Jia D, Yuan S-q, et al. Observation of a Topological Nodal Surface and its Surface-State Arcs in an Artificial Acoustic crystal. *Nat Commun* (2019) 10:5185. doi:10.1038/s41467-019-13258-3
40. Liu C-X, Ye P, Qi X-L. Chiral Gauge Field and Axial Anomaly in a Weyl Semimetal. *Phys Rev B* (2013) 87:235306. doi:10.1103/PhysRevB.87.235306

41. Jia H, Zhang R, Gao W, Guo Q, Yang B, Hu J, et al. Observation of Chiral Zero Mode in Inhomogeneous Three-Dimensional Weyl Metamaterials. *Science* (2019) 363:148–51. doi:10.1126/science.aau7707
42. Kotetes P, Mercaldo MT, Cuoco M. Synthetic Weyl Points and Chiral Anomaly in Majorana Devices with Nonstandard Andreev-Bound-State Spectra. *Phys Rev Lett* (2019) 123:126802. doi:10.1103/PhysRevLett.123.126802
43. Gooth J, Niemann AC, Meng T, Grushin AG, Landsteiner K, Gotsmann B, et al. Experimental Signatures of the Mixed Axial-Gravitational Anomaly in the Weyl Semimetal NbP. *Nature* (2017) 547:324–7. doi:10.1038/nature23005
44. Kharzeev DE, Kikuchi Y, Meyer R, Tanizaki Y. Giant Photocurrent in Asymmetric Weyl Semimetals from the Helical Magnetic Effect. *Phys Rev B* (2018) 98:014305. doi:10.1103/PhysRevB.98.014305
45. O'Brien TE, Diez M, Beenakker CWJ. Magnetic Breakdown and Klein Tunneling in a Type-II Weyl Semimetal. *Phys Rev Lett* (2016) 116:236401. doi:10.1103/PhysRevLett.116.236401
46. Onbasli MC, Beran L, Zahradník M, Kučera M, Antoš R, Mistrík J, et al. Optical and Magneto-Optical Behavior of Cerium Yttrium Iron Garnet Thin Films at Wavelengths of 200-1770 Nm. *Sci Rep* (2016) 6:23640. doi:10.1038/srep23640
47. Yang Z, Xiao M, Gao F, Lu L, Chong Y, Zhang B. Weyl Points in a Magnetic Tetrahedral Photonic crystal. *Opt Express* (2017) 25:15772. doi:10.1364/OE.25.015772
48. Liu G-G, Gao Z, Zhou P, Wang Q, Hu Y, Wang M, et al. Observation of Weyl point Pair Annihilation in a Gyromagnetic Photonic Crystal. *arXiv* (2021). Available at: http://arxiv.org/abs/2106.02461 (Accessed June 03, 2021).
49. Jin D, Lu L, Wang Z, Fang C, Joannopoulos JD, Soljačić M, et al. Topological Magnetoplasmon. *Nat Commun* (2016) 7:7. doi:10.1038/ncomms13486
50. Zhang S, Xiong Y, Bartal G, Yin X, Zhang X. Magnetized Plasma for Reconfigurable Subdiffraction Imaging. *Phys Rev Lett* (2011) 106:243901. doi:10.1103/PhysRevLett.106.243901
51. Gao W, Yang B, Lawrence M, Fang F, Béri B, Zhang S. Photonic Weyl Degeneracies in Magnetized Plasma. *Nat Commun* (2016) 7:12435. doi:10.1038/ncomms12435
52. Wang D, Yang B, Gao W, Jia H, Yang Q, Chen X, et al. Photonic Weyl Points Due to Broken Time-Reversal Symmetry in Magnetized Semiconductor. *Nat Phys* (2019) 15:1150–5. doi:10.1038/s41567-019-0612-7
53. Bravo-Abad J, Lu L, Fu L, Buljan H, Soljačić M. Weyl Points in Photonic-crystal Superlattices. *2d Mater* (2015) 2:034013. doi:10.1088/2053-1583/2/3/034013
54. Lu L, Wang Z, Ye D, Ran L, Fu L, Joannopoulos JD, et al. Experimental Observation of Weyl Points. *Science* (2015) 349:622–4. doi:10.1126/science.aaa9273
55. Goi E, Yue Z, Cumming BP, Gu M. Observation of Type I Photonic Weyl Points in Optical Frequencies. *Laser Photon Rev* (2018) 12:1700271. doi:10.1002/lpor.201700271
56. Chang M-L, Xiao M, Chen W-J, Chan CT. Multiple Weyl Points and the Sign Change of Their Topological Charges in Woodpile Photonic Crystals. *Phys Rev B* (2017) 95:125136. doi:10.1103/PhysRevB.95.125136
57. Takahashi S, Oono S, Iwamoto S, Hatsugai Y, Arakawa Y. Circularly Polarized Topological Edge States Derived from Optical Weyl Points in Semiconductor-Based Chiral Woodpile Photonic Crystals, *J Phys Soc Jpn*, 87 (2018). 1234013–7. doi:10.7566/JPSJ.87.123401
58. Vaidya S, Noh J, Cerjan A, Jörg C, von Freymann G, Rechtsman MC. Observation of a Charge-2 Photonic Weyl Point in the Infrared. *Phys Rev Lett* (2020) 125:253902. doi:10.1103/PhysRevLett.125.253902
59. He H, Qiu C, Ye L, Cai X, Fan X, Ke M, et al. Topological Negative Refraction of Surface Acoustic Waves in a Weyl Phononic crystal. *Nature* (2018) 560:61–4. doi:10.1038/s41586-018-0367-9
60. Chen W-J, Xiao M, Chan CT. Photonic Crystals Possessing Multiple Weyl Points and the Experimental Observation of Robust Surface States. *Nat Commun* (2016) 7:13038. doi:10.1038/ncomms13038
61. He H, Qiu C, Cai X, Xiao M, Ke M, Zhang F, et al. Observation of Quadratic Weyl Points and Double-Helicoid Arcs. *Nat Commun* (2020) 11:1820. doi:10.1038/s41467-020-15825-5
62. Zhang T, Song Z, Alexandradinata A, Weng H, Fang C, Lu L, et al. Double-Weyl Phonons in Transition-Metal Monosilicides. *Phys Rev Lett* (2018) 120:016401. doi:10.1103/PhysRevLett.120.016401
63. Yang Y, Gao Z, Feng X, Huang Y-X, Zhou P, Yang SA, et al. Ideal Unconventional Weyl Point in a Chiral Photonic Metamaterial. *Phys Rev Lett* (2020) 125:143001. doi:10.1103/PhysRevLett.125.143001
64. Soluyanov AA, Gresch D, Wang Z, Wu Q, Troyer M, Dai X, et al. Type-II Weyl Semimetals. *Nature* (2015) 527:495–8. doi:10.1038/nature15768
65. Noh J, Huang S, Leykam D, Chong YD, Chen KP, Rechtsman MC. Experimental Observation of Optical Weyl Points and Fermi Arc-like Surface States. *Nat Phys* (2017) 13:611–7. doi:10.1038/nphys4072
66. Xie B, Liu H, Cheng H, Liu Z, Chen S, Tian J. Experimental Realization of Type-II Weyl Points and Fermi Arcs in Phononic Crystal. *Phys Rev Lett* (2019) 122:104302. doi:10.1103/PhysRevLett.122.104302
67. Yang Z, Zhang B. Acoustic Type-II Weyl Nodes from Stacking Dimerized Chains. *Phys Rev Lett* (2016) 117:224301. doi:10.1103/PhysRevLett.117.224301
68. Gao W, Lawrence M, Yang B, Liu F, Fang F, Béri B, et al. Topological Photonic Phase in Chiral Hyperbolic Metamaterials. *Phys Rev Lett* (2015) 114:037402. doi:10.1103/PhysRevLett.114.037402
69. Kim M, Gao W, Lee D, Ha T, Kim TT, Zhang S, et al. Extremely Broadband Topological Surface States in a Photonic Topological Metamaterial. *Adv Opt Mater.* (2019) 7:1900900. doi:10.1002/adom.201900900
70. Xiao M, Lin Q, Fan S. Hyperbolic Weyl Point in Reciprocal Chiral Metamaterials. *Phys Rev Lett* (2016) 117:057401. doi:10.1103/PhysRevLett.117.057401
71. Yang B, Guo Q, Tremain B, Barr LE, Gao W, Liu H, et al. Direct Observation of Topological Surface-State Arcs in Photonic Metamaterials. *Nat Commun* (2017) 8:97. doi:10.1038/s41467-017-00134-1
72. Liu C, Gao W, Yang B, Zhang S. Disorder-Induced Topological State Transition in Photonic Metamaterials. *Phys Rev Lett* (2017) 119:183901. doi:10.1103/PhysRevLett.119.183901
73. Yang B-J, Nagaosa N. Classification of Stable Three-Dimensional Dirac Semimetals with Nontrivial Topology. *Nat Commun* (2014) 5:4898. doi:10.1038/ncomms5898
74. Lu L, Fang C, Fu L, Johnson SG, Joannopoulos JD, Soljačić M. Symmetry-protected Topological Photonic crystal in Three Dimensions. *Nat Phys* (2016) 12:337–40. doi:10.1038/nphys3611
75. Yue C, Xu Y, Song Z, Weng H, Lu Y-M, Fang C, et al. Symmetry-enforced Chiral Hinge States and Surface Quantum Anomalous Hall Effect in the Magnetic Axion Insulator Bi2-xSmxSe3. *Nat Phys* (2019) 15:577–81. doi:10.1038/s41567-019-0457-0
76. Xie B, Liu H, Cheng H, Liu Z, Tian J, Chen S. Dirac Points and the Transition towards Weyl Points in Three-Dimensional Sonic Crystals. *Light Sci Appl* (2020) 9:201. doi:10.1038/s41377-020-00416-2
77. Cai X, Ye L, Qiu C, Xiao M, Yu R, Ke M, et al. Symmetry-enforced Three-Dimensional Dirac Phononic Crystals. *Light Sci Appl* (2020) 9:38. doi:10.1038/s41377-020-0273-4
78. Wang H-X, Chen Y, Hang ZH, Kee H-Y, Jiang J-H. Type-II Dirac Photons. *Npj Quant Mater* (2017) 2:54. doi:10.1038/s41535-017-0058-z
79. Yang Y, Gao Z, Xue H, Zhang L, He M, Yang Z, et al. Realization of a Three-Dimensional Photonic Topological Insulator. *Nature* (2019) 565:622–6. doi:10.1038/s41586-018-0829-0
80. Wang H, Xu L, Chen H, Jiang J-H. Three-dimensional Photonic Dirac Points Stabilized by point Group Symmetry. *Phys Rev B* (2016) 93:235155. doi:10.1103/PhysRevB.93.235155
81. Guo Q, Yang B, Xia L, Gao W, Liu H, Chen J, et al. Three Dimensional Photonic Dirac Points in Metamaterials. *Phys Rev Lett* (2017) 119:213901. doi:10.1103/PhysRevLett.119.213901
82. Guo Q, You O, Yang B, Sellman JB, Blythe E, Liu H, et al. Observation of Three-Dimensional Photonic Dirac Points and Spin-Polarized Surface Arcs. *Phys Rev Lett* (2019) 122:203903. doi:10.1103/PhysRevLett.122.203903
83. Yan Q, Liu R, Yan Z, Liu B, Chen H, Wang Z, et al. Experimental Discovery of Nodal Chains. *Nat Phys* (2018) 14:461–4. doi:10.1038/s41567-017-0041-4
84. Cheng H, Gao W, Bi Y, Liu W, Li Z, Guo Q, et al. Vortical Reflection and Spiraling Fermi Arcs with Weyl Metamaterials. *Phys Rev Lett* (2020) 125:093904. doi:10.1103/PhysRevLett.125.093904
85. Huang X, Zhao L, Long Y, Wang P, Chen D, Yang Z, et al. Observation of the Chiral-Anomaly-Induced Negative Magnetoresistance in 3D Weyl Semimetal TaAs. *Phys Rev X* (2015) 5:031023. doi:10.1103/PhysRevX.5.031023
86. Xiong J, Kushwaha SK, Liang T, Krizan JW, Hirschberger M, Wang W, et al. Evidence for the Chiral Anomaly in the Dirac Semimetal Na$_3$Bi. *Science* (2015) 350:413–6. doi:10.1126/science.aac6089
87. Peri V, Serra-Garcia M, Ilan R, Huber SD. Axial-field-induced Chiral Channels in an Acoustic Weyl System. *Nat Phys* (2019) 15:357–61. doi:10.1038/s41567-019-0415-x

88. El-Ganainy R, Makris KG, Khajavikhan M, Musslimani ZH, Rotter S, Christodoulides DN. Non-Hermitian Physics and PT Symmetry. *Nat Phys* (2018) 14:11–9. doi:10.1038/nphys4323
89. Bergholtz EJ, Budich JC, Kunst FK. Exceptional Topology of Non-hermitian Systems. *Rev Mod Phys* (2021) 93:15005. doi:10.1103/RevModPhys.93.015005
90. Cerjan A, Huang S, Wang M, Chen KP, Chong Y, Rechtsman MC. Experimental Realization of a Weyl Exceptional Ring. *Nat Photon* (2019) 13:623–8. doi:10.1038/s41566-019-0453-z
91. Yan Q, Chen Q, Zhang L, Xi R, Chen H, Yang Y. Unconventional Weyl Exceptional Contours in Non-hermitian Photonic Continua. *arXiv* (2021). Available at: http://arxiv.org/abs/2108.00841 (Accessed August 02, 2021).
92. Cerjan A, Xiao M, Yuan L, Fan S. Effects of Non-hermitian Perturbations on Weyl Hamiltonians with Arbitrary Topological Charges. *Phys Rev B* (2018) 97: 1–10. doi:10.1103/PhysRevB.97.075128
93. Zangeneh-nejad F, Fleury R. Nonlinear Second-Order Topological Insulators. *Phys Rev Lett* (2019) 123:53902. doi:10.1103/PhysRevLett.123.053902
94. Fan X, Qiu C, Shen Y, He H, Xiao M, Ke M, et al. Probing Weyl Physics with One-Dimensional Sonic Crystals. *Phys Rev Lett* (2019) 122:136802. doi:10.1103/PhysRevLett.122.136802
95. Ezawa M. Higher-Order Topological Insulators and Semimetals on the Breathing Kagome and Pyrochlore Lattices. *Phys Rev Lett* (2018) 120: 26801. doi:10.1103/PhysRevLett.120.026801
96. Lin M, Hughes TL. Topological Quadrupolar Semimetals. *Phys Rev B* (2018) 98:241103. doi:10.1103/PhysRevB.98.241103
97. Wieder BJ, Wang Z, Cano J, Dai X, Schoop LM, Bradlyn B, et al. Strong and Fragile Topological Dirac Semimetals with Higher-Order Fermi Arcs. *Nat Commun* (2020) 11:627. doi:10.1038/s41467-020-14443-5
98. Ezawa M. Second-order Topological Insulators and Loop-Nodal Semimetals in Transition Metal Dichalcogenides XTe2 (X = Mo, W). *Sci Rep* (2019) 9:5286. doi:10.1038/s41598-019-41746-5
99. Wang H-X, Lin Z-K, Jiang B, Guo G-Y, Jiang J-H. Higher-Order Weyl Semimetals. *Phys Rev Lett* (2020) 125:146401. doi:10.1103/PhysRevLett.125.146401

Conflict of Interest: The authors declare that the research was conducted in the absence of any commercial or financial relationships that could be construed as a potential conflict of interest.

Publisher's Note: All claims expressed in this article are solely those of the authors and do not necessarily represent those of their affiliated organizations, or those of the publisher, the editors, and the reviewers. Any product that may be evaluated in this article, or claim that may be made by its manufacturer, is not guaranteed or endorsed by the publisher.

frontiers in Physics

ORIGINAL RESEARCH
published: 11 January 2022
doi: 10.3389/fphy.2021.825643

Topological One-Way Edge States in an Air-Hole Honeycomb Gyromagnetic Photonic Crystal

Chaoqun Peng[1†], *Jianfeng Chen*[1*†], *Qiumeng Qin*[1] *and Zhi-Yuan Li*[1,2*]

[1]School of Physics and Optoelectronics, South China University of Technology, Guangzhou, China, [2]State Key Laboratory of Luminescent Materials and Devices, South China University of Technology, Guangzhou, China

Topological one-way edge states have attracted increasing attention because of their intriguing fundamental physics and potential applications, particularly in the realm of photonics. In this paper, we present a theoretical and numerical demonstration of topological one-way edge states in an air-hole honeycomb gyromagnetic photonic crystal biased by an external magnetic field. Localized horizontally to the edge and confined in vertical direction by two parallel metallic plates, these unique states possess robust one-way propagation characteristics. They are strongly robust against various types of defects, imperfections and sharp corners on the path, and even can unidirectionally transport along the irregular edges of arbitrary geometries. We further utilize the one-way property of edge states to overcome entirely the issue of back-reflections and show the design of topological leaky wave antennas. Our results open a new door towards the observation of nontrivial edge states in air-hole topological photonic crystal systems, and offer useful prototype of robust topological photonic devices, such as geometry-independent topological energy flux loops and topological leaky wave antennas.

Keywords: topological one-way edge state, robust one-way propagation, geometry-independent topological energy flux loop, topological leaky wave antenna, gyromagnetic photonic crystal

OPEN ACCESS

Edited by:
Cuicui Lu,
Beijing Institute of Technology, China

Reviewed by:
Yiqi Zhang,
Xi'an Jiaotong University, China
Yulan Fu,
Beijing University of Technology, China

****Correspondence:***
Zhi-Yuan Li
phzyli@scut.edu.cn
Jianfeng Chen
phjfchen@mail.scut.edu.cn

†These authors have contributed equally to this work

Specialty section:
This article was submitted to Optics and Photonics, a section of the journal Frontiers in Physics

Received: *30 November 2021*
Accepted: *21 December 2021*
Published: *11 January 2022*

Citation:
Peng C, Chen J, Qin Q and Li Z-Y (2022) Topological One-Way Edge States in an Air-Hole Honeycomb Gyromagnetic Photonic Crystal. Front. Phys. 9:825643. doi: 10.3389/fphy.2021.825643

INTRODUCTION

Topological physics is flourishing as an active field, which has drawn extensive attention in both fundamental research and applied science [1]. Topological insulator commonly features the striking phenomenon of topologically protected one-way transport, exhibiting edge states or surface states that are strongly robust against defects, disorders, obstacles, sharp corners and so on [2, 3]. Inspired from the discovery of condensed quantum Hall effect, many studies have shown that topological states show essentially single-particle behavior of electrons and one can establish an analogy relationship with photon behaviors called topological photonic state (or topological one-way edge state) [4–7]. Topological one-way edge state provides a powerful platform for novel photonic devices with nontrivial functionalities and excellent performances, such as one-way waveguide [8–12], topological laser [13–17], rainbow trapping phenomenon [18–21], dispersionless slow light [22–24], topological fibre [25–27].

One feasible way to produce topological one-way edge states is to immerse a gyromagnetic photonic crystal (GPC) in an external static magnetic field to break the time-reversal symmetry [28–34]. When this symmetry is broken, truly one-wave edge states emerge, allowing the electromagnetic (EM) wave and light propagate forward smoothly when impinging on defects or propagating in disordered media, or even tanking sharp turns at arbitrary angles. To date, plenty of

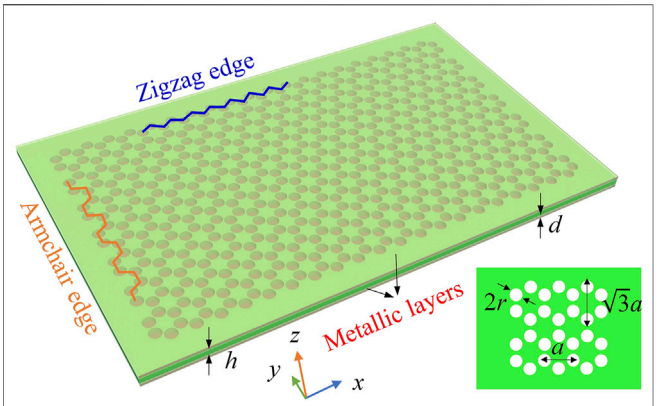

FIGURE 1 | Oblique-view of a rectangular air-hole honeycomb gyromagnetic photonic crystal. There exist two zigzag edges (blue) and two armchair edges (orange) along the x and y directions, respectively. The lattice constant along the zigzag edge is a, but that along the armchair edge is $\sqrt{3}a$. The thickness of this air-hole GPC is $h = 0.1a = 0.3$ cm, and the radius of air-hole is $r = 0.8$ cm. The lower right panel is a partial schematic diagram.

topological one-way edge states are focused on the two-dimensional cylinder-type GPC systems, which are consisted of an array of gyromagnetic cylinders immersed in air [30–34]. In contrast, little of them touch the air-hole-type GPC formed by an array of air holes in a gyromagnetic slab [35]. Yet, previous works in dielectric photonic crystals have shown that usually the transport behaviors of EM wave and light in cylinder-type photonic crystals are very different from that in air-hole-type photonic crystals [36–38]. So, it is interesting to examine the transport property of EM wave and light in an air-hole GPC, and it is also very worthwhile to explore the potential applications and devices of air-hole topological photonic system.

In this paper, we investigate, theoretically and numerically, topological one-way edge states in an air-hole GPC of a honeycomb lattice of air holes drilled in a gyromagnetic slab surrounded by two parallel metallic plates in vertical direction. We systematically study the projected band structures of edge states at both zigzag and armchair edges and analyze their eigenmodal fields. We demonstrate the one-way property of these special edge states, and also verify their transport robustness against various types of defects, imperfections, sharp corners, and even the irregular edges of arbitrary geometries. We further utilize the one-way property of edge states to overcome entirely the issue of back-reflections and show the design of topological leaky wave antennas. Our results open a new door towards the observation of nontrivial edge states in air-hole topological photonic systems, and show the prototype of robustly topological photonic devices.

TOPOLOGICAL ONE-WAY EDGE STATES AT ZIGZAG AND ARMCHAIR EDGES

We first design a rectangular air-hole GPC with 140 honeycomb lattices, where the lengths along the x and y directions are seven and twenty lattices respectively, as illustrated in **Figure 1**. The lattice constants of honeycomb lattice along the zigzag edge (x direction) and armchair edge (y direction) are $a = 3.0$ cm and $\sqrt{3}a$ respectively. Each air hole has a radius $r = 0.8$ cm and a height of $h = 0.1a$. In our simulations, this air-hole GPC is sandwiched between two parallel metallic layers with a thickness of $d = 0.15$ cm in vertical direction (z direction), as illustrated in **Figure 1**. The relative permittivity and permeability of the air are $\varepsilon_1 = 1$ and $\mu_1 = 1$ respectively. The gyromagnetic slab is composed of the commercial available yttrium-iron-garnet (YIG). In the absence of external static magnetic field, the relative permittivity and permeability of YIG is $\varepsilon_2 = 15.26$ and $\mu_2 = 1$ respectively. When an external static magnetic field is applied along + z direction, strong gyromagnetic anisotropy will be induced in YIG material, and its permeability can be given by [39–41].

$$\hat{\mu}_2 = \begin{pmatrix} 0.78 & -0.93i & 0 \\ 0.93i & 0.78 & 0 \\ 0 & 0 & 1 \end{pmatrix}. \quad (1)$$

These constitutive parameters correspond to those of YIG at 6.0 GHz with an external magnetic field of 500 Oe and a saturation magnetization of 1884 Gauss [39–41]. All the simulations are calculated by using the commercial software COMSOL MULTIPHYSICS with RF module in frequency domain, and only E polarization (where the electric field E is parallel to z-axis direction) is considered.

Next, we calculate the projected band structure of air-hole GPC along the zigzag edge, by adopting a supercell consisting of seven honeycomb lattices in one column, and the lattice constant is $a = 3.0$ cm. The projected band structures of the zigzag edges displayed in **Figure 2A** show that two dispersion curves (colored in red and blue respectively) appear inside the bandgap (green region) ranging from 5.52 to 6.21 GHz. The eigenmodal fields of points 1 and 2 at a frequency of $f_s = 5.90$ GHz depicted in **Figure 2B** reveal that there exist two edge states at two parallel zigzag edges. This phenomenon indicates that the YIG material shows the bandgap property that forbids the transport of EM waves in the YIG material, as a result, the one-way energy fluxes can be strongly localized at the zigzag interfaces between the air-hole GPC and the YIG material. As the slope signs of the red and blue dispersion curves are positive and negative respectively, the lower and upper zigzag edges will support right-propagating (red arrow) and left-propagating (blue arrow) one-way edge states respectively, as shown in **Figure 2B**. To exhibit the transport behaviors of one-way edge states, we use a configuration illustrated in **Figure 2C**. Two line sources (white stars) oscillating at a frequency of $f_s = 5.90$ GHz are placed at the center of upper and lower zigzag edges. The energy of line sources are confined at the upper and lower zigzag edges and unidirectionally propagate leftwards and rightwards respectively, in exactly agreement with the calculated results of **Figures 2A,B**.

Then, we calculate the projected band structure of air-hole GPC along the armchair edges, whose lattice constant is $\sqrt{3}a$. Their dispersions are calculated by adopting a supercell consisting of eight honeycomb lattices in one column, as plotted in **Figure 2E**. On the one hand, the calculated results illustrated in **Figure 2D** show that there exist two red and blue

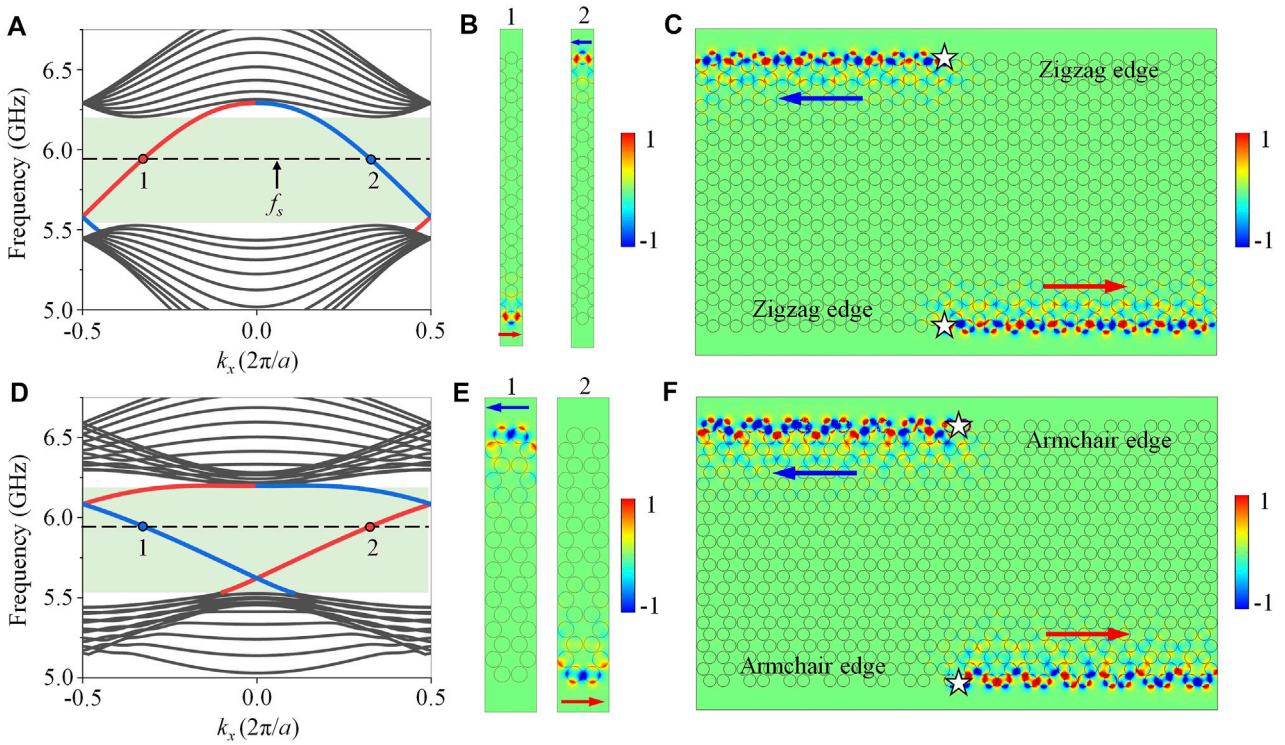

FIGURE 2 | Topological one-way edge states at zigzag and armchair edges of a rectangular air-hole honeycomb GPC. **(A–C)** Zigzag edges. **(D–F)** Armchair edges. **(A, D)** Projected band structures. **(B, E)** Eigenmodal fields. **(C, F)** Electric field distributions. Blue and red arrows indicate the left- and right-propagating one-way edge states respectively, and white stars represent the line sources oscillating at a frequency of f_s = 5.90 GHz. The frequency at the black dotted lines is f_s = 5.90 GHz, and the bandgap are marked as the greed region with a frequency range of 5.52 ~ 6.21 GHz.

dispersion curves dwelling the bandgap (green region) with a frequency range of 5.52~6.21 GHz, and their slopes are opposite. On the other hand, **Figure 2E** exhibits that the electric fields of eigenmodes 1 and 2 are concentrated at the armchair edges. Thus, there also exist two counter-propagating one-way edge states at the two parallel armchair edges. When two line sources oscillating at f_s = 5.90 GHz are placed at the upper and lower armchair interfaces, the left- and right-propagating one-way edge states can be excited respectively, as seen in **Figure 2F**. Consequently, these numerical simulations exhibit that both zigzag and armchair edges of air-hole honeycomb GPC support the one-way edge states in the green region with a frequency range of 5.52 ~ 6.21 GHz (their bandwidth is about 11.8%).

TOPOLOGICAL ENERGY FLUX LOOPS OF ARBITRARY GEOMETRIES

We have demonstrated the one-way transmission property of edge states existing at both zigzag and armchair edges. Now, we proceed to show the transport robustness of these one-way edge states in the presence of various types of defects, imperfections and sharp corners on the path. We must note that in our simulations, there exist two parallel perfect electric conductors clamping the air-hole GPC along the vertical direction (z direction) to avoid energy fluxes radiating into air. The line source (white star) oscillating at f_s = 5.90 GHz is placed at the lower zigzag interface. **Figure 3A** shows the simulated result of one-way edge states in a perfect rectangular air-hole honeycomb GPC without any imperfections. The one-way edge states propagate along the zigzag and armchair interfaces to form a counterclockwise energy flux loop. Then, an imperfection interface can be created by moving a line of five air holes at the lower zigzag edge along the y direction with a distance of $0.55a$, and the original positions of the moved air-holes are marked as five dotted circles, as plotted in **Figure 3B**. The electric field distribution shown in **Figure 3B** reveals that this imperfect interface still allows the EM wave propagating in one direction and forbidding backscattering. **Figure 3C** exhibits another common defected interface that can be constructed by replacing a honeycomb lattice of six air holes with six YIG cylinders of same size. As illustrated in **Figure 3C**, a new one-way interface between the air-hole GPC and the YIG material can be created, so that the edge states can turn around the defects without any back-reflection. We proceed to consider a regular right-angled trapezoid air-hole GPC including three types of sharp corners (60°–turn, 90°–turn and 120°–turn) and two types of edges (zigzag and armchair edges), as illustrated in **Figure 3D**. The schematic diagram of the partial structure (black dotted rectangle) is shown on the right panel of **Figure 3D**. It is a very common configuration in the previous works to be usually used to verify the transport robustness of

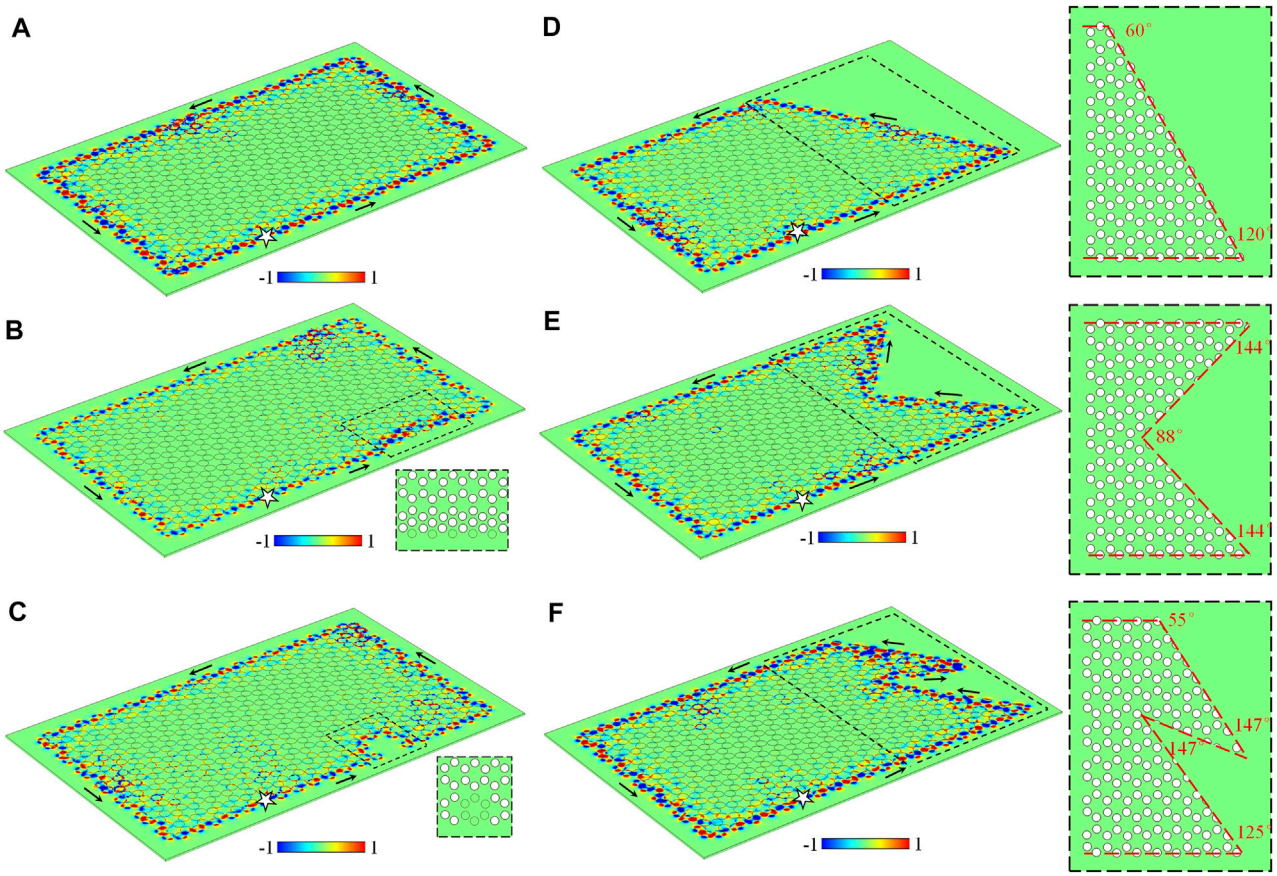

FIGURE 3 | Topological one-way edge states in air-hole GPCs of various geometries. **(A)** A perfect rectangular honeycomb GPC. **(B)** An imperfect zigzag interface is created by moving a line of five air holes at the lower zigzag edge along the *y* direction with a distance of 0.55*a*. **(C)** A defected zigzag interface is constructed by replacing a honeycomb lattice of six air holes with six YIG cylinders of same size. **(D–F)** Three irregular air-hole GPCs of various geometries. The angle of sharp corner is marked near the corner and the transport interfaces are marked as the red dotted lines.

topological edge states against the sharp corners. The simulated electric field distribution shows that the energy fluxes are strongly confined in the zigzag and armchair interfaces of trapezoid air-hole GPC. They can transport along the lower zigzag edge, climb over the 120° sharp corner, continue to transport along the tilt zigzag edge, pass through the 60°–turn to the upper zigzag edge, bypass the left armchair edge, turn around the 90°–turn at the bottom left, and finally go back to the source to form a counterclockwise energy flux loop.

In addition to creating the common defects, imperfections and sharp corners to demonstrate the transport robustness of one-way edge states, we proceed to calculate the electric field distributions in two configurations of irregular interfaces and unusual sharp corners. Notably, a configurable, controllable and efficient way to construct these special structures is to fill the YIG material into the air holes as required. It can be seen that the EM waves can robustly transport along the atypical zigzag and armchair edges, and smoothly bypass a 88°–turn and two 144°–turns in a reflection-free way, as shown in **Figure 3E**. More intriguingly, the simulated electric field distributions shown in **Figure 3F** exhibit that the energy fluxes can almost perfectly transmit from the lower zigzag edge to the upper edge although there exist the irregular edges (not the zigzag and armchair edges) and unusual sharp corners (such as 55°–turn, 125°–turn, and 147°–turn).

We have verified that the topological one-way edge states are extremely robust against the backscattering from the defects, imperfections and unusual sharp corners at both regular and irregular edges outside the air-hole GPCs. Beyond the robust transport, these results also imply the possibility of implementing deformed topological energy flux loop of arbitrary geometries. So we further investigate the transport behaviors of EM waves in the energy flux loops of arbitrary geometries inside the air-hole GPCs, including E-shaped, Heart-shaped and Lightning-shaped energy flux loops, as illustrated in **Figures 4A1–C1**. The excitation frequency of line source (white star) is f_s = 5.90 GHz. The electric field distribution shown in **Figure 4A2** shows that the energy fluxes are strongly confined at the interface of E-shaped loop and travel unidirectionally along the inside contour of air-hole GPC to form a counterclockwise energy flux loop. Again, both the contours of Heart-shaped and Lightning shaped energy flux loop also can be lighted by the line

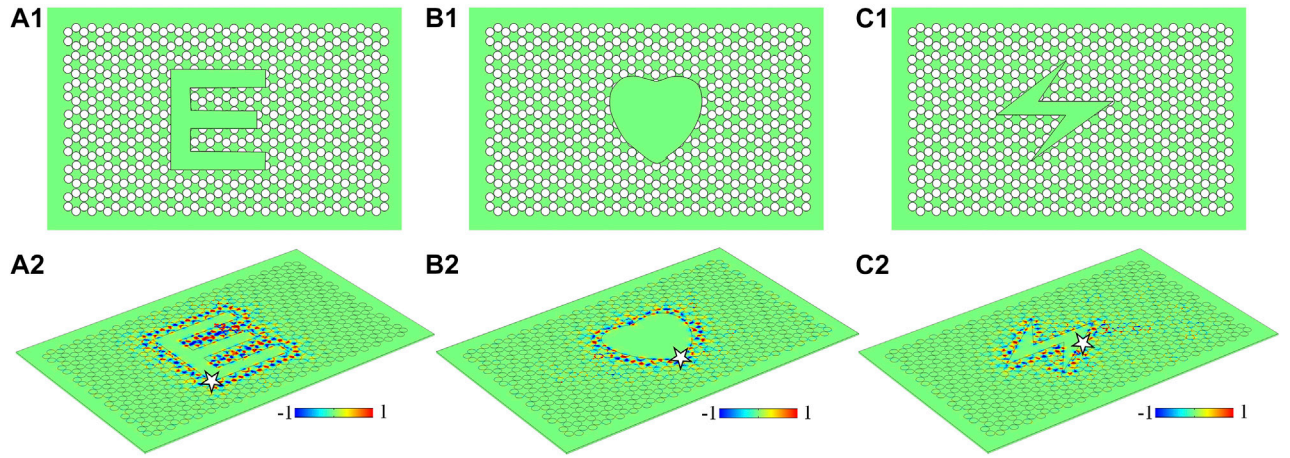

FIGURE 4 | Geometry-independent topological energy flux loop. **(A)** E-shaped loop. **(B)** Heart-shaped loop. **(C)** Lightning-shaped loop. **(A1–C1)** Schematic diagrams. **(A2–C2)** Electric field distributions.

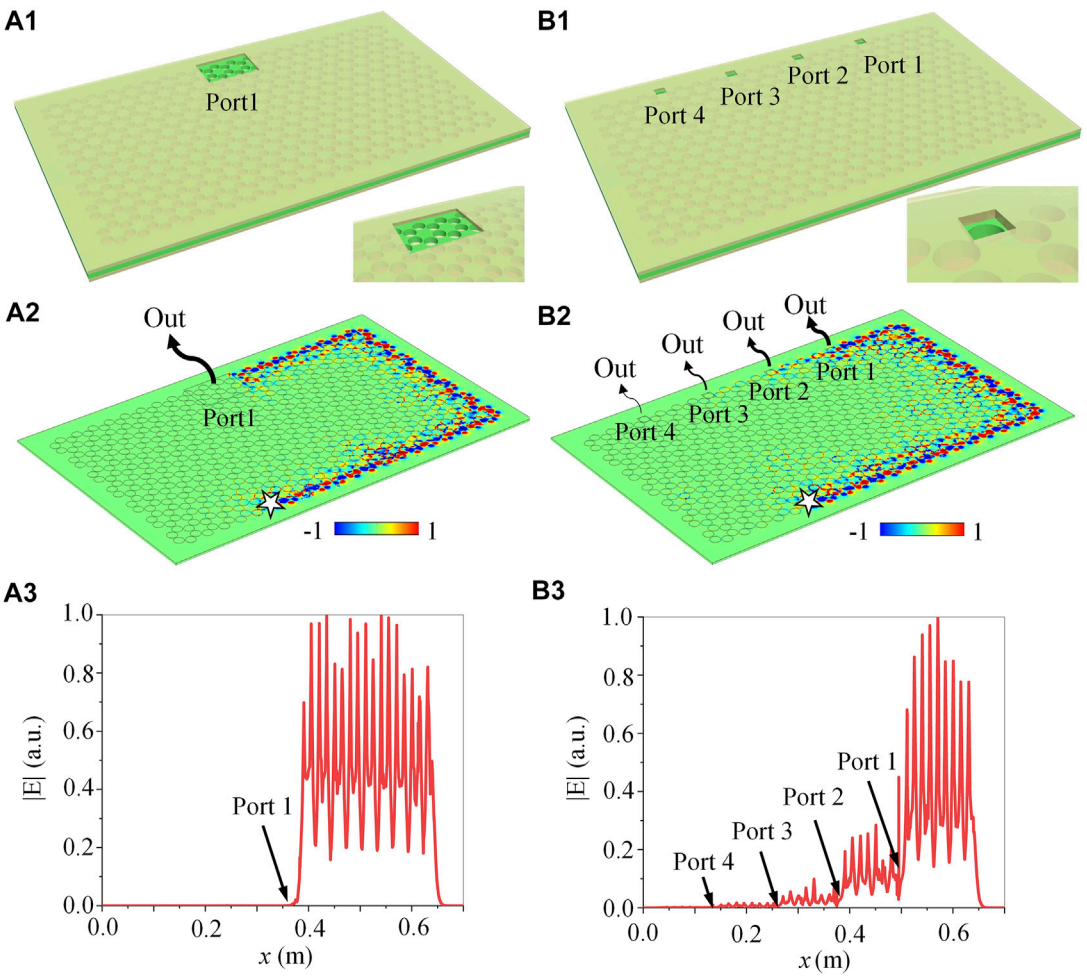

FIGURE 5 | Topological leaky wave antennas. **(A)** Single port antenna. **(B)** Four ports antenna. **(A1, B1)** Oblique-view. **(A2, B2)** Electric field distribution. **(A3, B3)** Amplitude of electric field along the upper zigzag interface.

source due to the excitation of one-way edge states, as seen in **Figures 4B2,C2**. These simulated results exhibit that the geometry-independent topological energy flux loops can be created in the air-hole GPCs, which may provide the great opportunity to develop complex topological circuitry of arbitrary geometries for the robust transport of photons in classical wave regimes.

TOPOLOGICAL LEAKY WAVE ANTENNA

We have mentioned above that when the metallic plates of air-hole GPC in vertical direction are removed, EM waves will leak into air. When the propagating wave is leaked out in air through a opened port, a leaky wave antenna will be formed [42, 43]. Utilizing this peculiar property, we can introduce small holes (or ports) in metallic plates (yellow) to allow EM waves to radiate outwards, thus, to achieve topological leaky wave antenna. It should be noted that one-way edge state in the rectangular air-hole GPC system shown in **Figure 3A** is a closed energy flux loop surrounding entire system. To suppress one-way energy fluxes making a full round trip to affect the energy of line source, holes or ports we introduced should be guaranteed that all electric field amplitudes are released before making a full round trip.

We first consider a topological leaky wave antenna with a simple configuration. Only one antenna port (Port 1) of a size of 9.0×6.3 cm above the upper zigzag edge is opened, and its schematic diagrams are illustrated in **Figure 5A1**. The simulated results displayed in **Figure 5A2** show that when the one-way energy fluxes reach Port 1, all of them directly leak into the air. As a result, no energy fluxes continue to propagate forwards to form a closed energy flux loop. The electric field amplitude distributions along the upper zigzag edge shown in **Figure 5A3** also exhibit that when EM wave meets Port 1, the amplitude of its electric field sharply drops to zero, exactly in agreement with our expectations. It should be noted that attributed to the one-way nature of edge states, the output port does not backscatter any EM wave to affect the radiation property of line source. In contrast, in the conventional trivial leaky wave antennas, the energy fluxes backscattered from the output port will reflect back to the previous transport channel and even transmit back to the line source, thereby affecting the energy transmission and radiation efficiency in the whole antenna system. Therefore, the one-way property of edge states can overcome entirely the issue of back-reflections and simplify the design of the leaky wave antenna.

On the other hand, we proceed to investigate the design of a topological leaky wave antenna array, made by cascading four antenna ports in the top metallic plate one after the other, as plotted in **Figure 5B1**. The size of these antenna ports is 1.6×1.6 cm, and the distance between the neighboring ports is 12.0 cm. As seen in **Figure 5B2**, when the energy fluxes reach Port 1, about 75% of them are released into air, and the rest continues to propagate forwards along the upper zigzag edge. All of energy fluxes will be completely leaked into air until they reach Port 4, as shown in **Figure 5B3**. Certainly, one can change the energy radiation ratio by modifying the size of each port and the distance between the neighboring ports. Similarly, because the backscattering of the topological one-way edge states is forbidden, the antenna ports do not scatter back any EM waves, so that the second port with further downstream will not affect the output properties of the first port. However, for the conventional trivial leaky wave antennas, the energy fluxes will be scattered back from the second port and transmitted backward through the first port, so that the backscattering of output port has a significant influence on the energy transmission and radiation efficiency in the whole antenna system. Notably, this backscattering has also significant consequences in many other systems, specifically those systems seeded by a master oscillator whose performance may be strongly affected by reflected signals. It should be emphasized that by introducing the irregular edges of arbitrary geometries into the air-hole GPCs, the geometry-independent topological leaky wave antenna can also be realized.

CONCLUSION

In summary, we have demonstrated that the topological one-way edge states could exist in a rectangular air-hole honeycomb GPC biased by an external magnetic field. We have studied the projected band structures of zigzag and armchair edges and they both exhibited the transport behaviors of the topological one-way edge states. Besides, we have demonstrated that these unique states are not only strongly robust against various types of defects, imperfections and sharp corners, but also can unidirectionally transport along irregular edges of arbitrary geometries. Moreover, we have utilized the one-way property of edge states to overcome entirely the issue of back-reflections and provided the design of topological leaky wave antennas. Our findings open a new door towards the observation of nontrivial edge states in the air-hole topological photonic systems, and show the prototype of robustly topological photonic devices, such as geometry-independent topological energy flux loops and topological leaky wave antennas.

DATA AVAILABILITY STATEMENT

The raw data supporting the conclusions of this article will be made available by the authors, without undue reservation.

AUTHOR CONTRIBUTIONS

All authors contributed extensively to this work. CP, JC, and QQ performed the simulation. CP and JC drew the figures. JC, CP, and Z-YL wrote the manuscript. Z-YL supervised the project. All authors participated in discussions and reviewed the manuscript.

FUNDING

The authors are grateful for the financial support from the National Natural Science Foundation of China (11974119), Science and Technology Project of Guangdong (2020B010190001), Guangdong Innovative and Entrepreneurial Research Team Program (2016ZT06C594), National Key R&D Program of China (2018YFA 0306200).

REFERENCES

1. Hasan MZ, Kane CL, Tse WK. Colloquium: Topological Insulators. *Rev Mod Phys* (2010) 82(4):3045–67. doi:10.1103/revmodphys.82.3045
2. Nadeem M, Hamilton AR, Fuhrer MS, Wang X. Quantum Anomalous Hall Effect in Magnetic Doped Topological Insulators and Ferromagnetic Spin-Gapless Semiconductors—A Perspective Review. *Small* (2020) 16(42): 1904322. doi:10.1002/smll.201904322
3. Cayssol J, Fuchs JN. Topological and Geometrical Aspects of Band Theory. *J Phys Mater* (2021) 4(3):034007. doi:10.1088/2515-7639/abf0b5
4. Xie BY, Wang HF, Zhu XY, Lu MH, Wang ZD, Chen YF. Photonics Meets Topology. *Opt Express* (2018) 26(19):24531–50. doi:10.1364/oe.26.024531
5. Ozawa T, Price HM, Amo A. Topological Photonics. *Rev Mod Phys* (2019) 91(1):015006. doi:10.1103/revmodphys.91.015006
6. Liu JW, Shi FL, He XT, Tang GJ, Chen WJ, Chen XD, et al. Valley Photonic Crystals. *Adv Phys X* (2021) 6(1):1905546. doi:10.1080/23746149.2021.1905546
7. Chen J, Liang W, Li ZY. Progress of Topological Photonic State in Magneto-Optical Photonic Crystal. *Acta Optic* (2021) 41(8):0823015. doi:10.3788/aos202141.0823015
8. Chen J, Liang W, Li ZY. Antichiral One-Way Edge States in a Gyromagnetic Photonic Crystal. *Phys Rev B* (2020) 101(21):214102. doi:10.1103/physrevb.101.214102
9. Zhuang S, Chen J, Liang W, Li ZY. Zero GVD Slow-Light Originating from a Strong Coupling of One-Way Modes in Double-Channel Magneto-Optical Photonic Crystal Waveguides. *Opt Express* (2021) 29(2):2478–87. doi:10.1364/oe.412460
10. Tasolamprou AC, Kafesaki M, Soukoulis CM, Economou EN, Koschny T. Chiral Topological Surface States on a Finite Square Photonic Crystal Bounded by Air. *Phys Rev Appl* (2021) 16(4):044011. doi:10.1103/physrevapplied.16.044011
11. Mann SA, Alù A. Broadband Topological Slow Light through Brillouin Zone Winding. *Phys Rev Lett* (2021) 127(12):123601. doi:10.1103/physrevlett.127.123601
12. Wang M, Zhang RY, Zhang L, Wang D, Guo Q, Zhang ZQ, et al. Topological One-Way Large-Area Waveguide States in Magnetic Photonic Crystals. *Phys Rev Lett* (2021) 126(6):067401. doi:10.1103/PhysRevLett.126.067401
13. Bahari B, Ndao A, Vallini F, El Amili A, Fainman Y, Kanté B. Nonreciprocal Lasing in Topological Cavities of Arbitrary Geometries. *Science* (2017) 358(6363):636–40. doi:10.1126/science.aao4551
14. Bandres MA, Wittek S, Harari G, Parto M, Ren J, Segev M, et al. Topological Insulator Laser: Experiments. *Science* (2018) 359(6381):eaar4005. doi:10.1126/science.aar4005
15. Shao ZK, Chen HZ, Wang S, Mao XR, Yang ZQ, Wang SL, et al. A High-Performance Topological Bulk Laser Based on Band-Inversion-Induced Reflection. *Nat Nanotechnol* (2020) 15(1):67–72. doi:10.1038/s41565-019-0584-x
16. Zeng Y, Chattopadhyay U, Zhu B, Qiang B, Li J, Jin Y, et al. Electrically Pumped Topological Laser with Valley Edge Modes. *Nature* (2020) 578(7794): 246–50. doi:10.1038/s41586-020-1981-x
17. Dikopoltsev A, Harder TH, Lustig E, Egorov OA, Beierlein J, Wolf A, et al. Topological Insulator Vertical-Cavity Laser Array. *Science* (2021) 373(6562): 1514–7. doi:10.1126/science.abj2232
18. Chen J, Liang W, Li ZY. Switchable Slow Light Rainbow Trapping and Releasing in Strongly Coupling Topological Photonic Systems. *Photon Res* (2019) 19(9):091075. doi:10.1364/prj.7.001075
19. Chen J, Qin Q, Peng C, Liang W, Li ZY. Slow Light Rainbow Trapping in a Uniformly Magnetized Gyromagnetic Photonic crystal Waveguide. *Front Mater* (2021) 8:728991. doi:10.3389/fmats.2021.728991
20. Zhang H, Qian L, Wang C, Ji CY, Liu Y, Chen J, et al. Topological Rainbow Based on Graded Topological Photonic Crystals. *Opt Lett* (2021) 46(6): 1237–40. doi:10.1364/ol.419271
21. Lu C, Wang C, Xiao M, Zhang ZQ, Chan CT. Topological Rainbow Concentrator Based on Synthetic Dimension. *Phys Rev Lett* (2021) 126(11): 113902. doi:10.1103/physrevlett.126.113902
22. Chen J, Liang W, Li ZY. Strong Coupling of Topological Edge States Enabling Group-Dispersionless Slow Light in Magneto-Optical Photonic Crystals. *Phys Rev B* (2019) 99(1):014103. doi:10.1103/physrevb.99.014103
23. Chen J, Liang W, Li ZY. Broadband Dispersionless Topological Slow Light. *Opt Lett* (2020) 45(18):4964–7. doi:10.1364/ol.401650
24. Shi FL, Cao Y, Chen XD, Liu JW, Chen WJ, Chen M, et al. Distortionless Pulse Transmission in Valley Photonic Crystal Slab Waveguide. *Phys Rev Appl* (2021) 15(2):024002. doi:10.1103/physrevapplied.15.024002
25. Lu L, Gao H, Wang Z. Topological One-Way Fiber of Second Chern Number. *Nat Commun* (2018) 9(1):5384. doi:10.1038/s41467-018-07817-3
26. Lin H, Lu L. Dirac-Vortex Topological Photonic Crystal Fibre. *Light Sci Appl* (2020) 9(1):202–7. doi:10.1038/s41377-020-00432-2
27. Zhang Z, Lu J, Liu T, Gan J, Heng X, Wu M, et al. Azimuthally and Radially Polarized Orbital Angular Momentum Modes in valley Topological Photonic crystal Fiber. *Nanophotonics* (2021) 10(16):4067–74. doi:10.1515/nanoph-2021-0395
28. Raghu S, Haldane FDM. Analogs of Quantum-Hall-Effect Edge States in Photonic Crystals. *Phys Rev A* (2008) 78(3):033834. doi:10.1103/physreva.78.033834
29. Haldane FD, Raghu S. Possible Realization of Directional Optical Waveguides in Photonic Crystals with Broken Time-Reversal Symmetry. *Phys Rev Lett* (2008) 100(1):013904. doi:10.1103/PhysRevLett.100.013904
30. Wang Z, Chong YD, Joannopoulos JD, Soljacić M. Reflection-Free One-Way Edge Modes in a Gyromagnetic Photonic Crystal. *Phys Rev Lett* (2008) 100(1): 013905. doi:10.1103/PhysRevLett.100.013905
31. Wang Z, Chong Y, Joannopoulos JD, Soljačić M. Observation of Unidirectional Backscattering-Immune Topological Electromagnetic States. *Nature* (2009) 461(7265):772–5. doi:10.1038/nature08293
32. Ao X, Lin Z, Chan CT. One-Way Edge Mode in a Magneto-Optical Honeycomb Photonic Crystal. *Phys Rev B* (2009) 80(3):033105. doi:10.1103/physrevb.80.033105
33. Fu JX, Liu RJ, Li ZY. Robust One-Way Modes in Gyromagnetic Photonic Crystal Waveguides with Different Interfaces. *Appl Phys Lett* (2010) 97(4): 041112. doi:10.1063/1.3470873
34. Poo Y, Wu RX, Lin Z, Yang Y, Chan CT. Experimental Realization of Self-Guiding Unidirectional Electromagnetic Edge States. *Phys Rev Lett* (2011) 106(9):093903. doi:10.1103/PhysRevLett.106.093903
35. Liu K, Shen L, He S. One-Way Edge Mode in a Gyromagnetic Photonic Crystal Slab. *Opt Lett* (2012) 37(19):4110–2. doi:10.1364/ol.37.004110
36. Wu LH, Hu X. Scheme for Achieving a Topological Photonic Crystal by Using Dielectric Material. *Phys Rev Lett* (2015) 114(22):223901. doi:10.1103/physrevlett.114.223901
37. Anderson PD, Subramania G. Unidirectional Edge States in Topological Honeycomb-Lattice Membrane Photonic Crystals. *Opt Express* (2017) 25(19):23293–301. doi:10.1364/oe.25.023293
38. Zhu X, Wang HX, Xu C, Lai Y, Jiang JH, John S. Topological Transitions in Continuously Deformed Photonic Crystals. *Phys Rev B* (2018) 97(8):085148. doi:10.1103/physrevb.97.085148
39. Lu J-C, Chen X-D, Deng W-M, Chen M, Dong J-W. One-Way Propagation of Bulk States and Robust Edge States in Photonic Crystals with Broken Inversion and Time-Reversal Symmetries. *J Opt* (2018) 20(7):075103. doi:10.1088/2040-8986/aac3a1
40. Pozar DM. *Microwave Engineering*. New York: Wiley (1998). p. 497–517.
41. Wohlfarth E. *Handbook of Magnetic Materials*. New York: Elsevier (1980). p. 293.
42. Lumer Y, Engheta N. Topological Insulator Antenna Arrays. *ACS Photon* (2020) 7(8):2244–51. doi:10.1021/acsphotonics.0c00797
43. Shen Q, You Y, Xu J, Shen Y, Deng X, Wang Z, et al. Mechanically Scanned Leaky-Wave Antenna Based on a Topological One-Way Waveguide. *Front Phys* (2020) 15(3):33601. doi:10.1007/s11467-020-0953-9

Conflict of Interest: The authors declare that the research was conducted in the absence of any commercial or financial relationships that could be construed as a potential conflict of interest.

frontiers in Physics

ORIGINAL RESEARCH
published: 20 January 2022
doi: 10.3389/fphy.2022.844417

Multiple One-Way Edge Modes in Sonic Crystals With Large Chern Numbers

Han Zhao[1], *Tian Zhang*[1], *Xiujuan Zhang*[1]*, *Ming-Hui Lu*[1,2,3]* and *Yan-Feng Chen*[1,3]

[1]National Laboratory of Solid State Microstructures and Department of Materials Science and Engineering, Nanjing University, Nanjing, China, [2]Jiangsu Key Laboratory of Artificial Functional Materials, Nanjing, China, [3]Collaborative Innovation Center of Advanced Microstructures, Nanjing University, Nanjing, China

The quantum Hall effect (QHE) associated with Chern insulators reveals the non-trivial topological properties of two-dimensional electronic systems subject to strong magnetic field, which features finite Chern number C and chiral edge states. The latter promise robust electron transport and have received tremendous attention in both the condensed matter physics and classical systems including photonics and acoustics. In acoustics, circulating air flow has been introduced to create an effective gauge magnetic field, which breaks the time-reversal symmetry and leads to chiral edge states for acoustic waves. While the robust edge states may offer possible routes towards acoustic devices yielding unidirectional sound propagation, e.g., acoustic diodes, the mode density at the interfaces is limited by small Chern numbers of ± 1. Here, we realize acoustic Chern insulators with large Chern numbers, i.e., $|C| \geq 1$ ($|C| = 1, 2, 3, 4$). The system is based on circulating air flow in a sonic crystal (SC) with fourfold rotational symmetry. The large Chern numbers are obtained by breaking multiple accidental degeneracies at (non-)high-symmetric points. Based on these Chern insulators, acoustic diodes are realized by joining structures of different Chern numbers. Up to eight propagation modes are supported on the interfaces, greatly improving the mode density and hence the propagation efficiency. Our design offers possible routes towards high-efficient and topologically robust acoustic diodes, which may further inspire acoustic non-reciprocal devices based on topological Chern insulators. Experimentally, our proposals can be realized based on angular-momentum-biased resonator arrays.

Keywords: large chern numbers, one-way edge states, quantum hall effect, acoustic diodes, topological protection

OPEN ACCESS

Edited by:
Guancong Ma,
Hong Kong Baptist University, Hong Kong SAR, China

Reviewed by:
Meng Xiao,
Hong Kong University of Science and Technology, Hong Kong SAR, China
Biao Yang,
National University of Defense Technology, China

***Correspondence:**
Xiujuan Zhang
xiujuanzhang@nju.edu.cn
Ming-Hui Lu
luminghui@nju.edu.cn

Specialty section:
This article was submitted to Optics and Photonics, a section of the journal Frontiers in Physics

Received: *28 December 2021*
Accepted: *10 January 2022*
Published: *20 January 2022*

Citation:
Zhao H, Zhang T, Zhang X, Lu M-H and Chen Y-F (2022) Multiple One-Way Edge Modes in Sonic Crystals With Large Chern Numbers. Front. Phys. 10:844417. doi: 10.3389/fphy.2022.844417

INTRODUCTION

The concept of topology has generated great research interest in the last few decades [1–10]. It was first introduced into the field of condensed matter physics to explain many phenomena beyond the scope of the traditional Landau symmetry breaking theory [11], for example, the QHE with broken time-reversal symmetry [12–15] and the quantum spin Hall effect based on spin-orbit coupling [16–19]. Thouless *et al.* found that band structures of certain materials, determined by the wave vector $\boldsymbol{k}$ in momentum space, have nontrivial topological properties, and materials in different topological phases cannot change smoothly into one another [20]. At their interfaces, topological interface states emerge where the electrons can only propagate at the interfaces and do not enter the bulk [21]. Such interface states exhibit the characteristics of robustness, immunity to defects, and

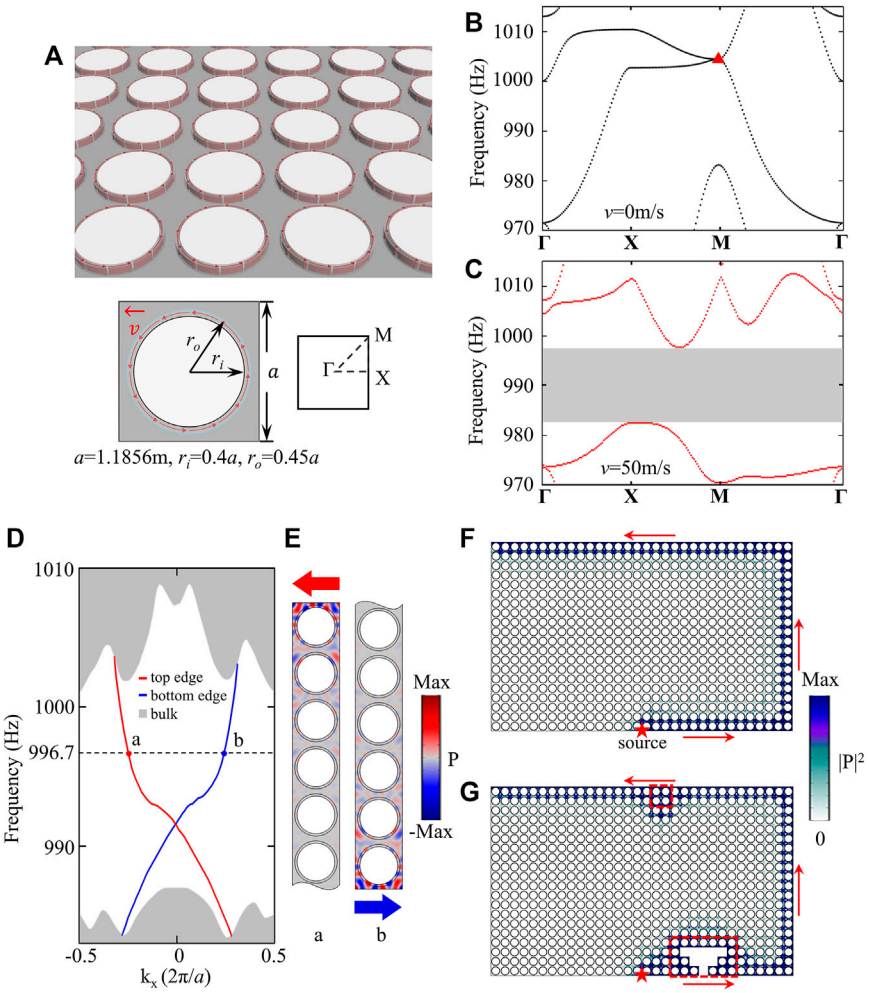

FIGURE 1 | An acoustic Chern insulator with $C = 1$. **(A)** Schematics of the proposed SC with C_{4v} symmetry. The anticlockwise air flow is depicted by red arrows in each unit cell. The inset in the lower right corner is the first Brillion zone (BZ). Geometric parameters for the SC are also listed. **(B)** Bulk band structure of the SC without air flow, showing one quadratic degeneracy at the M point (marked by a red triangle). **(C)** The same as **(B)**, only with a non-zero anticlockwise air flow ($\vec{v}$ = 50 m/s). The quadratic degeneracy is lifted and a full band gap is opened ranging from 982.5 to 997.75 Hz, as indicated by the grey shading. **(D)** Projected band structure of a ribbon supercell of the SC enclosed in the lower and upper directions by rigid boundaries. **(E)** Pressure field distributions of the lower and upper edge modes at 996.7 Hz, corresponding to those marked in **(D)**. Note that for the sake of clarity, only partial of the supercell is presented. The red and blue arrows indicate the opposite directions of the energy flow for these two edge modes. **(F)** The intensity field distributions of the one-way edge modes excited at 996.7 Hz by a point source. The red star indicates the position of the source and the red arrows indicate the propagation direction. **(G)** The same as **(F)**, only with local perturbations deliberately introduced on the edges (as highlighted by the red dashed boxes).

one-way transport, and therefore promise unprecedented applications in dissipationless electronics [22]. Later, the band topology theory was introduced into the fields of photonics and phononics, and quickly became a hot topic in recent years [23–36]. In electronics and photonics, external magnetic fields are applied to break the time-reversal symmetry. However, in acoustics, due to the lack of interactions between sound waves and magnetic fields, breaking the time-reversal symmetry faces considerable challenges. Recently, it was proposed that circulating air flow can act as an equivalent magnetic field for sound and therefore provides an effective technique to break the time-reversal symmetry in acoustics [37]. By using this technique, acoustic Chen insulators are realized, as an analogy of the QHE, supporting robust and unidirectional interface states for sound [27, 28, 30, 31].

The Chern number (denoted as C), a type of topological invariants, is often used to describe the topological properties of the QHE systems [38, 39]. When the Chern number is non-zero, the system is topologically nontrivial and can be referred to as a Chern insulator. The value of the Chen number determines the number of the one-way edge modes. In the previous studies for QHE, the Chern number has been limited to $|C| = 1$, while realizing large Chern numbers has many practical meanings, such as increasing the mode density to reduce the contact resistance of circuit interconnections and to improve the coupling efficiency, in a similar way as reducing the potential for traffic congestion by

expanding the roadways. In acoustics, similar properties are required for unidirectional sound control with large mode density and high efficiency. However, Chern insulators with Chern number lager than one were only discussed in electronic materials [40–45] and photonic crystals [46–48]. In acoustics, such an advance has been absent.

In this work, we realize acoustic Chern insulators with large Chern numbers up to four in a SC with circulating air flow. Our system has a fourfold rotational symmetry. Such a reduced symmetry from the previously adopted C_{6v} symmetry of the graphene-like honeycomb lattices [28] offers a more efficient way to construct multiple linear (Dirac) and quadratic degeneracies. By applying air flow, these degeneracies can be simultaneously lifted, leading to band gaps with large Chern numbers. By tuning the geometric parameters, we realize multiple Chern insulators with $|C| \geq 1$ ($|C| = 1, 2, 3, 4$). Based on these Chern insulators, acoustic diodes with large mode density are realized by joining structures of different Chern numbers, forming a diode network, where up to eight unidirectional sound "roadways" are obtained for each diode channel.

DESIGNS AND RESULTS

Acoustic Chern Insulators With Circulating Air Flow

The proposed SC is schematically shown in **Figure 1A**. Each unit cell with a lattice constant a consists of a rigid cylinder of radius r_i at its center. A ring cavity of $r_i < r < r_o$ is filled with an anticlockwise circulating air flow and outside the cavity (i.e., $r > r_o$) is the stationary air. The ring cavity and the outside region are separated by a thin impedance-matched layer at radius r_o. This layer has two functions. One is to avoid the interaction between fluids in different regions, and the other is to guarantee full sound transmission from the cavity to the outside region and vice versa [30].

As discussed above, in electronics and photonics, external magnetic fields break the time-reversal symmetry, while in acoustics, circulating air flow acts as an equivalent magnetic field to break the time-reversal symmetry for sound, which leads to band gaps of non-zero Chern numbers. To see this, we first present in **Figure 1B** the band structure of the SC in **Figure 1A** (here, we refer to it as SC1), without air flow. A quadratic degeneracy is observed at the high symmetric point M (marked by a red triangle), which, upon introducing the air flow with a velocity of $\vec{v} = 50$ m/s, is lifted and a full band gap is opened, as shown by the grey shading in **Figure 1C**. This gap carries a Chern number of $C = 1$ (as will be further discussed later). The non-zero Chern number promises robust one-way edge states at interfaces between materials of different topological phases, i.e., materials with different Chern numbers. As shown in **Figure 1D**, the projected band structures of a ribbon supercell of SC1 consisting of 1×20 unit cells are presented. The upper and lower boundaries of the supercell are enclosed by hard boundaries which can be considered as topologically trivial with $C = 0$. It can be seen from the figure that two dispersion curves emerge in the band gap, connecting the lower and upper bulk states. These dispersion curves correspond to the one-way edge states, which counter-propagate at the bottom (blue) and upper (red) boundaries, as exemplified by the pressure field distributions for two marked modes (**Figure 1E**).

A smoking-gun feature of the edge states in QHE systems is their unidirectionality and topologically protection. In **Figure 1F**, we conduct simulations on the propagation of the edge states in a finite structure made of 32×20 SC1 unit cells, which are enclosed by hard boundaries in the lower, upper and right directions while the left boundary is imposed by an absorbing boundary. The excitation is launched by a point source at the center of the lower boundary (denoted by the red star) with a frequency of 996.7 Hz (the same frequency as the marked eigen-states in **Figure 1D**). It is seen that despite the central position, the point source only excites the rightward edge states, which travel anticlockwise, consistent with the unidirectionality identified in **Figures 1D,E**. To further see the robustness of the one-way edge states, some local perturbations, including defects with several missing cells and disorders of reversed air flow, are deliberately introduced on the propagation route of the edge states. Surprisingly, it is shown that the edge states can go around these perturbations, as well as the sharp bends of 90°, and maintain their propagation without backscattering (**Figure 1G**).

Multiple Degeneracies at Non-High-Symmetric Points and Large Chern Numbers

The calculation of Chern numbers relies on the integration of Berry curvature over the entire BZ and has been a well-developed technique in studying the QHE systems [49–51]. Here, instead of conducting such a calculation, we can obtain the Chern numbers for each acoustic band gap intuitively from the bulk band structures. Specifically, for the linear degeneracies (i.e., the Dirac points), each of the two upper and lower bands connecting a pair of Dirac points can acquire a non-zero quantized Berry flux when gapped by breaking the time-reversal symmetry, i.e., one Dirac point contributes a π Berry flux and a pair sums to 2π [38, 47]. A 2π Berry flux change across the band gap indicates a Chern number of ± 1. This means when n ($n \geq 1$) pairs of Dirac degeneracies are gapped by the circulating air flow, the Chern numbers of the target gap is n or $-n$, depending on the air flow direction (an anticlockwise air flow induces positive Chern numbers while the clockwise air flow induces negative Chern numbers). For the quadratic degeneracies, since each quadratic point consists of two Dirac points [52], it singly contributes a Chern number of ± 1. Take the example in **Figures 1B,C**, where a quadratic point at the high-symmetric point M (at the BZ corner) is gapped by the air flow. Considering its distribution over the entire BZ, four $\frac{1}{4}$-quadratic points count to one complete quadratic point, giving rise to $C = 1$ for anticlockwise air flow and $C = -1$ for clockwise air flow.

From above analyses, it is seen that in order to obtain large Chern numbers, a straightforward way is to construct as many degenerate points as possible. In the following, we demonstrate that this can be realized in our system by tuning the geometric parameters, which can help to construct degenerate points not

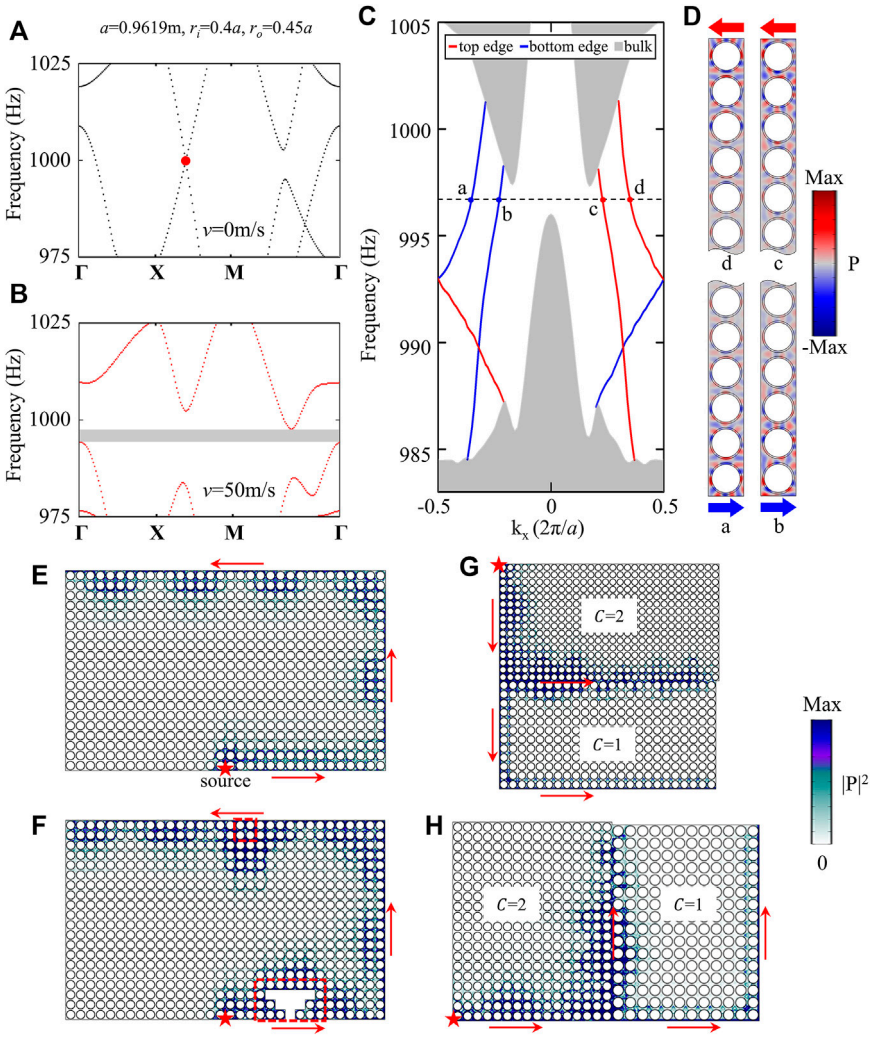

FIGURE 2 | Band structures and one-way edge modes in SC2 with $C = 2$. SC2 has the same design as SC1, only that the geometric parameters are slightly changed (as listed in the figure). **(A,B)** Bulk band structures of the SC2 with and without air flow. The red circle marks a Dirac point on the XM line. The grey region indicates the band gap for SC2, ranging from 994.25 to 997.5 Hz. **(C)** Projected band structure of a ribbon supercell of SC2 enclosed in the lower and upper directions by rigid boundaries. **(D)** Mode profiles for the eigen-states marked in **(C)** at 996.7 Hz. **(E)** The intensity field distributions of the one-way edge modes for $C = 2$ excited at 996.7 Hz. **(F)** The same as **(E)**, only with local perturbations. **(G,H)** Edge modes propagation in structures joined by SC1 with $C = 1$ and SC2 with $C = 2$.

only at high-symmetric points but also at non-high-symmetric points. In **Figure 2**, we show the Chern insulator with $C = 2$. The SC (referred to in the following as SC2) still has the same design as that in **Figure 1A**, only the geometric parameters are slightly changed. As a result, a linear Dirac point on the XM line is formed, as shown in **Figure 2A** where the Dirac point is marked by a red circle. After introducing air flow, this degeneracy is lifted and a full band gap is opened (**Figure 2B**). Applying the rule that we discussed above, eight $\frac{1}{2}$-Dirac points on the BZ boundary count to four complete Dirac points, suggesting a Chern number of ± 2. The projected band structures for a ribbon supercell enclosed in the lower and upper directions by rigid walls indeed provide evidence. As shown in **Figure 2C**, there are two pairs of edge states emerging in the band gap, with each corresponding to the lower or upper edge. The mode profiles of the pressure field distributions in **Figure 2D** further show that one of the two pairs is localized on the lower boundary with an energy flow in the forward direction while the other pair is localized on the upper boundary with an energy flow in the backward direction, consistent with the predictions.

We also conduct simulations to verify the one-way propagation for the edge states and their robustness against local perturbations. As shown in **Figure 2E**, a finite structure made of SC2 with 32×20 unit cells and enclosed by rigid walls is constructed where a point source is placed at the center of the lower boundary. The excitation is launched at 996.7 Hz. Similar as the edge states for $C = 1$, only the rightward propagation is excited, indicating the unidirectional properties. Differently, in this structure, due to the increased Chern number, each edge supports two edge modes with a broader "roadway" than that in

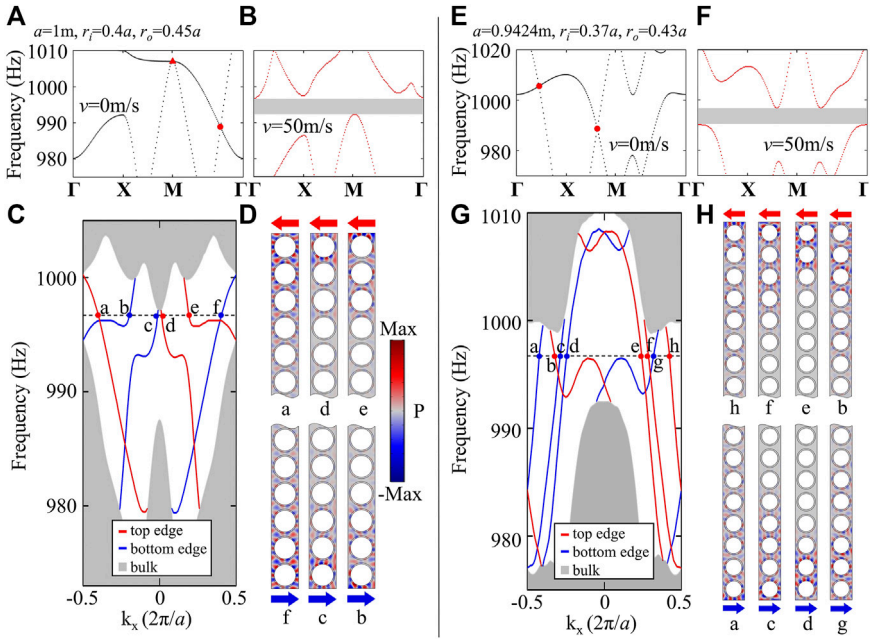

FIGURE 3 | Band structures and one-way edge modes in SC3 with $C = 3$ and SC4 with $C = 4$. **(A–D)** Respectively the bulk band structures for SC3 without air flow, with air flow, the projected band structure of the ribbon supercell and the associated mode profiles of the one-way edge modes. The geometric parameters for SC3 are listed in **(A)**. **(E–H)** The same as that in **(A–D)**, only for SC4 with $C = 4$. The geometric parameters of SC4 are listed in **(E)**. All marked edge modes are at 996.7 Hz.

Figure 1F. This can be seen from the apparently widened mode profiles in the perpendicular (to the propagation direction) direction. Further simulations on the edge state propagation with the presence of local perturbations also confirm that the edge modes for $C = 2$ are robust (**Figure 2F**).

As mentioned above, the number of edge states on an interface made of different materials is determined by the difference between their Chern numbers. This, combined with the unidirectionality, suggests by joining different Chern insulators, the edge modes can be effectively controlled for how many edge modes can be supported and which direction the edge modes propagate. For example, when we join a Chern insulator with $C = 2$ to the one with $C = 1$, at their interface, there will be $2 - 1 = 1$ edge mode. Depending on different joining directions, the edge mode also propagates in different directions. As shown in **Figures 2G,H**, where two Chern insulators with $C = 1$ and 2 are glued respectively in the y-direction and in the x-direction, they present interesting propagation behaviors. When the gluing is in the y-direction (**Figure 2G**), a point source from the upper-left port-entrance launches downward edge modes carrying two sound channels. Upon reaching to the gluing interface, these two channels are split into two directions, with one continuous in the downward direction while the other propagating in the rightward direction. When the gluing is in the x-direction (**Figure 2H**), signals from the lower-left port-entrance initially travel in the two rightward "roadways" and after a distance, they partially continue travelling rightward with the rest split into the upward "roadway".

The above results demonstrate that using insulators with large Chern numbers, versatile unidirectional sound control can be realized, which motivates us to search for even larger Chern numbers. In the following, we report the realization of Chern insulators of $C = 3$ (referred to as SC3) and $C = 4$ (referred to as SC4). **Figure 3A** presents the bulk band structure for SC3 without air flow, showing a quadratic point (red triangle) at the high symmetric point M and a linear Dirac point (red circle) on the M Γ line, which are simultaneously gapped upon introduction of air flow (**Figure 3B**). According to the rule to determine the Chern number, these degenerate points lead to $C = 3$. The projected band structures for the ribbon supercell in **Figure 3C** and the corresponding mode profiles in **Figure 3D** indicate that indeed a Chern insulator with three edge states on each boundary is realized. In **Figures 3E–H**, similar studies as that in **Figures 3A–D** are conducted, only the geometric parameters are again modulated, giving rise to two Dirac points (red circles in **Figure 3E**) at the BZ boundaries, which contribute a Chern number of $C = 4$ in SC4. The projected band structures for the ribbon supercell and the associated mode profiles verify the existence of four one-way edge modes on each boundary in this type of Chern insulator.

Here, we briefly discuss the non-Hermitian properties in the systems with circulating air flow. In general, there are two sources that can introduce non-Hermiticity into the system. One is the viscous dissipation induced by the friction between the acoustic waves and the high-speed circulating air flow. The other comes from the energy exchange between the system and the environment that drives the circulating motions [53]. In our studies, we neglect the viscous dissipation for simplicity (which

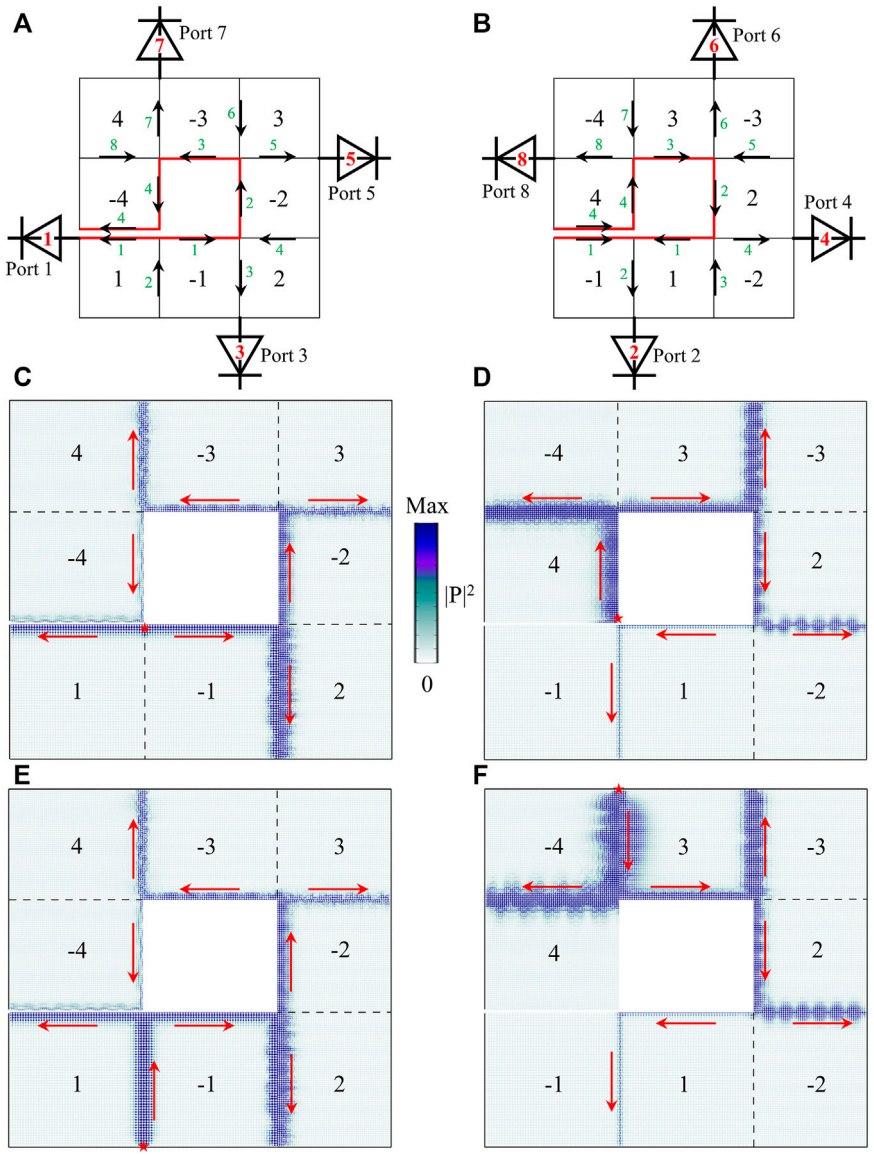

FIGURE 4 | Acoustic diode networks constructed by joining structures of different *C*. **(A,B)** Schematics of the acoustic diode networks. Numbers in black indicate the Chern number for each Sudoku section and the green numbers illustrate the number of edge modes in each channel. Black arrows depict the unidirectionality for the sound propagation. Thick red lines represent rigid walls while the rest boundaries are imposed by absorbing boundaries. The output ports are marked by the diode icons with the red thick numbers inside them indicating how many modes are outputted from the corresponding port. **(C,D)** Acoustic intensity field distributions for point source excitations in the diode networks shown in **(A,B)**. The source locations are marked by red stars and the excitation frequency is chosen as 996.25 Hz **(E,F)** The same as **(C,D)**, only that the excitations are launched by two outside-coming signals (indicated by red stars).

essentially is another form of energy exchange, i.e., that of sound and heat). For the latter source, the aerodynamics is adopted to characterize the energy exchange, which is implemented by the Aeroacoustics module in the commercial finite element software COMSOL. We find that the one-way edge states exhibit interesting behaviors. It is shown that the edge-state bands can be folded and consequently the edge states within the same band can have two opposite propagation directions (**Figure 3C**). Such a band folding, according to Ref. [53], is resulted from the anti-resonances induced by the circulating air flow. This phenomenon becomes especially visible when the filling fraction of the air flow gets larger and the edge states can be folded more than once, as shown in **Figure 3G**. These results offer an interesting perspective on active non-Hermiticity (i.e., non-Hermiticity induced by sources, external fields, external motions, etc.,) and its possible novel phenomena, yielding further explorations.

Acoustic Diodes Created by Joining Structures of Different Chern Numbers

As discussed above, the sign of *C* can be changed when the air flow is reversed. This means with our designs, there are up to eight types of

Chern insulators with $C = \pm 1, \pm 2, \pm 3, \pm 4$, where the four positive numbers are enabled by the anticlockwise air flow while the four negative numbers are induced by the clockwise air flow. By joining these Chern insulators, we realize an acoustic diode network containing multiple interface channels and ports that support various types of "roadways" with different "lanes". As schematically illustrated in **Figures 4A,B**, the diode network consists of a Sudoku-like structure with the outer eight sections filled with the Chern insulators with $C = \pm 1, \pm 2, \pm 3, \pm 4$ while the center section is a rigid void offering rigid walls for the outer sections (the rigid walls are highlighted by the thick red lines). The number labeled in each section represents the corresponding Chern number and the green numbers on the interfaces indicate the "lane" numbers. Eight output ports are created, which provide versatile unidirectionalities with different channel directions and up to 8 "lanes" (as indicated by the diode nodes and the red thick numbers labeled in each diode).

To visualize how this diode network works, we conduct excitation simulations. In **Figure 4C**, a point source is placed at the interface between $C = 1$ and -1 (indicated by a red star), which excites both leftward and rightward edge modes. The leftward one directly goes to the Port 1 while the energy carried by the rightward edge mode splits into two directions upon reaching to the interface between $C = 2$ and -1, with a substantial amount of energy flowing into the downward output channel (to Port 3) as it supports three edge modes and can carry more energy. The upward energy continuously flows, eventually going out from Port 5 when reaching to the interface between $C = 3$ and -2 and from Port 7 when reaching to the interface between $C = 4$ and -3. When we reverse the air flow direction, on the other hand, different functions can be obtained. As shown in **Figure 4D**, the point source is located at the lower-right corner of the section with $C = 4$. Its excitation now travels upwards and sends substantial amount of energy into the output channel of Port 8 which carries 8 "lanes" and is a considerably wide "roadway" for energy flowing. The rest energy is split into the rightward direction and successively goes out from Port 6, Port 4 and Port 2.

In addition to the excitations from a point source inside the network, these eight unidirectional sound channels can be launched from outside signals. As shown in **Figures 4E,F**, the input signals from the bottom of the −1/1 interface (**Figure 4E**) and from the top of the −4/3 interface (**Figure 4F**) also excite similar unidirectional one-way edge modes as that in **Figures 4C,D**, which eventually also go out from the Port 1 to Port 8. By further controlling the input signals, we can also turn off certain output ports. For example, if we have an input signal from the right of the −2/2 interface in **Figure 4A**, the Port 1 will be disabled as no energy is allowed in the left direction due to the unidirectionality. Similarly, if the input signal is from the right of the −3/2 interface in **Figure 4B** (with reversed air flow), the Port 8 will be disabled. Using similar ways, a flexible topological switch for these unidirectional diodes can be realized.

It should be pointed out that within each port, the multiple one-way edge transport suffers certain mode beating effect, i.e., different modes can crosstalk with each other via interferences. A direct evidence is the change of modal pattern. As shown in **Figure 2E**, when the launched edge states from the bottom edge go across the lower-right 90° bend into the right edge, the modal pattern changes. When the edge states go into the upper edge, the modal pattern changes again. This is different from the single edge state propagation shown in **Figure 1F** where the modal pattern maintains the same across the bottom, right and upper edges. This beating effect also exists in the acoustic diodes with multiple propagation channels, as shown in **Figures 4C–F**. This is a common phenomenon when multi-modes are travelling in close proximity to each other [54]. While the mode beating analysis is out the scope of this work, it can be performed using several methods, e.g., interferometry [55], correlation filtering [56] and spectral imaging [57]. By implementing these methods, how each mode in a multiple-modal system contributes to its neighbors in terms of profiles and weights, as well as their relative phases that determine the output focal spots, can be determined.

CONCLUSION AND DISCUSSION

In conclusion, we have realized acoustic Chern insulators with large Chern numbers in SCs based on circulating air flow. We identify a simple rule to obtain large Chern numbers, which relies on the number and type of dispersion degeneracies in the bulk bands. More degenerate points suggest larger Chern number. Based on such a rule, we tune the geometric parameters of our SCs to construct multiple degenerate points, which accordingly give rise to large Chern numbers up to 4. This rule is universal in QHE systems and therefore can guide the designs of large Chern numbers in other systems. By joining structures of different Chern numbers, we design an acoustic diode network, which, further facilitated by controlling air flows, exhibits robust and versatile unidirectionalities with controllable directions and up to 8 flowing "lanes" that can carry great amount of energy due to the high mode density. Our results demonstrate the high potential of Chern insulators with large Chern numbers, which can inspire a wide range of applications in nonreciprocal (integrated) acoustics and photonics, such as diodes, unidirectional sound/light control and directional topological lasing. These results can be experimentally tested in angular-momentum-biased resonator arrays, which recently are found to be experimentally feasible [58].

DATA AVAILABILITY STATEMENT

The original contributions presented in the study are included in the article/Supplementary Material, further inquiries can be directed to the corresponding authors.

AUTHOR CONTRIBUTIONS

M-HL conceived the idea. XZ proposed the acoustic diodes. HZ and TZ conducted the numerical simulations. XZ and HZ wrote

the manuscript. All authors have given approval to the final version of the manuscript.

FUNDING

This work is supported by the National Key R&D Program of China (2017YFA0303702, 2018YFA0306200), the National Natural Science Foundation of China (Grant Numbers 51902151, 11625418, and 51732006), and the Natural Science Foundation of Jiangsu Province (Grant Number BK20190284).

ACKNOWLEDGMENTS

The authors would like to thank Xu Ni, who has left academic employments, for his hard work to obtain the preliminary results of this research.

REFERENCES

1. Zak J. Berry's Phase for Energy Bands in Solids. *Phys Rev Lett* (1989) 62: 2747–50. doi:10.1103/PhysRevLett.62.2747
2. Yao W, Xiao D, Niu Q. Valley-dependent Optoelectronics from Inversion Symmetry Breaking. *Phys Rev B* (2008) 77:235406. doi:10.1103/PhysRevB.77.235406
3. Zhang H, Liu C-X, Qi X-L, Dai X, Fang Z, Zhang S-C. Topological Insulators in Bi2Se3, Bi2Te3 and Sb2Te3 with a Single Dirac Cone on the Surface. *Nat Phys* (2009) 5:438–42. doi:10.1038/nphys1270
4. Hasan MZ, Kane CL. Colloquium: Topological Insulators. *Rev Mod Phys* (2010) 82:3045–67. doi:10.1103/RevModPhys.82.3045
5. Qi X-L, Zhang S-C. Topological Insulators and Superconductors. *Rev Mod Phys* (2011) 83:1057–110. doi:10.1103/RevModPhys.83.1057
6. Wan X, Turner AM, Vishwanath A, Savrasov SY. Topological Semimetal and Fermi-Arc Surface States in the Electronic Structure of Pyrochlore Iridates. *Phys Rev B* (2011) 83:205101. doi:10.1103/PhysRevB.83.205101
7. Asorey M. Space, Matter and Topology. *Nat Phys* (2016) 12:616–8. doi:10.1038/nphys3800
8. He C, Sun X-C, Liu X-P, Lu M-H, Chen Y, Feng L, et al. Photonic Topological Insulator with Broken Time-Reversal Symmetry. *Proc Natl Acad Sci USA* (2016) 113:4924–8. doi:10.1073/pnas.1525502113
9. Zhang X, Xiao M, Cheng Y, Lu M-H, Christensen J. Topological Sound. *Commun Phys* (2018) 1:97. doi:10.1038/s42005-018-0094-4
10. Zhang X, Wang H-X, Lin Z-K, Tian Y, Xie B, Lu M-H, et al. Second-order Topology and Multidimensional Topological Transitions in Sonic Crystals. *Nat Phys* (2019) 15:582–8. doi:10.1038/s41567-019-0472-1
11. Kosterlitz JM, Thouless DJ. Ordering, Metastability and Phase Transitions in Two-Dimensional Systems. *J Phys C: Solid State Phys* (1973) 6:1181–203. doi:10.1088/0022-3719/6/7/010
12. Klitzing Kv., Dorda G, Pepper M. New Method for High-Accuracy Determination of the Fine-Structure Constant Based on Quantized Hall Resistance. *Phys Rev Lett* (1980) 45:494–7. doi:10.1103/PhysRevLett.45.494
13. Haldane FDM. Model for a Quantum Hall Effect without Landau Levels: Condensed-Matter Realization of the "Parity Anomaly". *Phys Rev Lett* (1988) 61:2015–8. doi:10.1103/PhysRevLett.61.2015
14. Novoselov KS, Geim AK, Morozov SV, Jiang D, Katsnelson MI, Grigorieva IV, et al. Two-dimensional Gas of Massless Dirac Fermions in Graphene. *Nature* (2005) 438:197–200. doi:10.1038/nature04233
15. Zhang Y, Tan Y-W, Stormer HL, Kim P. Experimental Observation of the Quantum Hall Effect and Berry's Phase in Graphene. *Nature* (2005) 438:201–4. doi:10.1038/nature04235
16. Kane CL, Mele EJ. Z2Topological Order and the Quantum Spin Hall Effect. *Phys Rev Lett* (2005) 95:146802. doi:10.1103/PhysRevLett.95.146802
17. Kane CL, Mele EJ. Quantum Spin Hall Effect in Graphene. *Phys Rev Lett* (2005) 95:226801. doi:10.1103/PhysRevLett.95.226801
18. Bernevig BA, Hughes TL, Zhang S-C. Quantum Spin Hall Effect and Topological Phase Transition in HgTe Quantum wells. *Science* (2006) 314: 1757–61. doi:10.1126/science.1133734
19. Bernevig BA, Zhang S-C. Quantum Spin Hall Effect. *Phys Rev Lett* (2006) 96: 106802. doi:10.1103/PhysRevLett.96.106802
20. Thouless DJ, Kohmoto M, Nightingale MP, den Nijs M. Quantized Hall Conductance in a Two-Dimensional Periodic Potential. *Phys Rev Lett* (1982) 49:405–8. doi:10.1103/PhysRevLett.49.405
21. Hatsugai Y. Chern Number and Edge States in the Integer Quantum Hall Effect. *Phys Rev Lett* (1993) 71:3697–700. doi:10.1103/PhysRevLett.71.3697
22. Castro Neto AH, Guinea F, Peres NMR, Novoselov KS, Geim AK. The Electronic Properties of Graphene. *Rev Mod Phys* (2009) 81:109–62. doi:10.1103/RevModPhys.81.109
23. Haldane FDM, Raghu S. Possible Realization of Directional Optical Waveguides in Photonic Crystals with Broken Time-Reversal Symmetry. *Phys Rev Lett* (2008) 100:013904. doi:10.1103/PhysRevLett.100.013904
24. Wang Z, Chong YD, Joannopoulos JD, Soljačić M. Reflection-free One-Way Edge Modes in a Gyromagnetic Photonic crystal. *Phys Rev Lett* (2008) 100: 013905. doi:10.1103/PhysRevLett.100.013905
25. Wang Z, Chong Y, Joannopoulos JD, Soljačić M. Observation of Unidirectional Backscattering-Immune Topological Electromagnetic States. *Nature* (2009) 461:772–5. doi:10.1038/nature08293
26. Khanikaev AB, Hossein Mousavi S, Tse W-K, Kargarian M, MacDonald AH, Shvets G. Photonic Topological Insulators. *Nat Mater* (2013) 12:233–9. doi:10.1038/nmat3520
27. Khanikaev AB, Fleury R, Mousavi SH, Alù A. Topologically Robust Sound Propagation in an Angular-Momentum-Biased Graphene-like Resonator Lattice. *Nat Commun* (2015) 6:8260. doi:10.1038/ncomms9260
28. Ni X, He C, Sun X-C, Liu X-p., Lu M-H, Feng L, et al. Topologically Protected One-Way Edge Mode in Networks of Acoustic Resonators with Circulating Air Flow. *New J Phys* (2015) 17:053016. doi:10.1088/1367-2630/17/5/053016
29. Wu L-H, Hu X. Scheme for Achieving a Topological Photonic Crystal by Using Dielectric Material. *Phys Rev Lett* (2015) 114:223901. doi:10.1103/PhysRevLett.114.223901
30. Yang Z, Gao F, Shi X, Lin X, Gao Z, Chong Y, et al. Topological Acoustics. *Phys Rev Lett* (2015) 114:114301. doi:10.1103/PhysRevLett.114.114301
31. Chen Z-G, Wu Y. Tunable Topological Phononic Crystals. *Phys Rev Appl* (2016) 5:054021. doi:10.1103/PhysRevApplied.5.054021
32. He C, Ni X, Ge H, Sun X-C, Chen Y-B, Lu M-H, et al. Acoustic Topological Insulator and Robust One-Way Sound Transport. *Nat Phys* (2016) 12:1124–9. doi:10.1038/nphys3867
33. Chen C, Ding X, Qin J, He Y, Luo Y-H, Chen M-C, et al. Observation of Topologically Protected Edge States in a Photonic Two-Dimensional Quantum Walk. *Phys Rev Lett* (2018) 121:100502. doi:10.1103/PhysRevLett.121.100502
34. Ozawa T, Price HM, Amo A, Goldman N, Hafezi M, Lu L, et al. Topological Photonics. *Rev Mod Phys* (2018) 91:015006. doi:10.1103/RevModPhys.91.015006
35. Chen H, Yao LY, Nassar H, Huang GL. Mechanical Quantum Hall Effect in Time-Modulated Elastic Materials. *Phys Rev Appl* (2019) 11:044029. doi:10.1103/PhysRevApplied.11.044029
36. Chen Z-G, Zhu W, Tan Y, Wang L, Ma G. Acoustic Realization of a Four-Dimensional Higher-Order Chern Insulator and Boundary-Modes Engineering. *Phys Rev X* (2021) 11:011016. doi:10.1103/PhysRevX.11.011016
37. Fleury R, Sounas DL, Sieck CF, Haberman MR, Alù A. Sound Isolation and Giant Linear Nonreciprocity in a Compact Acoustic Circulator. *Science* (2014) 343:516–9. doi:10.1126/science.1246957
38. Raghu S, Haldane FDM. Analogs of Quantum-Hall-Effect Edge States in Photonic Crystals. *Phys Rev A* (2008) 78:033834. doi:10.1103/PhysRevA.78.033834
39. Lu L, Joannopoulos JD, Soljačić M. Topological Photonics. *Nat Photon* (2014) 8:821–9. doi:10.1038/nphoton.2014.248

40. Yang S, Gu Z-C, Sun K, Das Sarma S. Topological Flat Band Models with Arbitrary Chern Numbers. *Phys Rev B* (2012) 86:241112. doi:10.1103/PhysRevB.86.241112
41. Wang J, Lian B, Zhang H, Xu Y, Zhang S-C. Quantum Anomalous Hall Effect with Higher Plateaus. *Phys Rev Lett* (2013) 111:136801. doi:10.1103/PhysRevLett.111.136801
42. Fang C, Gilbert MJ, Bernevig BA. Large-Chern-number Quantum Anomalous Hall Effect in Thin-Film Topological Crystalline Insulators. *Phys Rev Lett* (2014) 112:046801. doi:10.1103/PhysRevLett.112.046801
43. Xiong T-S, Gong J, An J-H. Towards Large-Chern-Number Topological Phases by Periodic Quenching. *Phys Rev B* (2016) 93:184306. doi:10.1103/PhysRevB.93.184306
44. Chen G, Sharpe AL, Fox EJ, Zhang Y-H, Wang S, Jiang L, et al. Tunable Correlated Chern Insulator and Ferromagnetism in a Moiré Superlattice. *Nature* (2020) 579:56–61. doi:10.1038/s41586-020-2049-7
45. Ge J, Liu Y, Li J, Li H, Luo T, Wu Y, et al. High-Chern-number and High-Temperature Quantum Hall Effect without Landau Levels. *Natl Sci Rev* (2020) 7:1280–7. doi:10.1093/nsr/nwaa089
46. Skirlo SA, Lu L, Soljačić M. Multimode One-Way Waveguides of Large Chern Numbers. *Phys Rev Lett* (2014) 113:113904. doi:10.1103/PhysRevLett.113.113904
47. Skirlo SA, Lu L, Igarashi Y, Yan Q, Joannopoulos J, Soljačić M. Experimental Observation of Large Chern Numbers in Photonic Crystals. *Phys Rev Lett* (2015) 115:253901. doi:10.1103/PhysRevLett.115.253901
48. Chan H-C, Guo G-Y. Tuning Topological Phase Transitions in Hexagonal Photonic Lattices Made of Triangular Rods. *Phys Rev B* (2018) 97:045422. doi:10.1103/PhysRevB.97.045422
49. Berry MV. Quantal Phase Factors Accompanying Adiabatic Changes. *Proc R Soc Lond A* (1984) 392:45–57. doi:10.1098/rspa.1984.0023
50. Wang H-X, Guo G-Y, Jiang J-H. Band Topology in Classical Waves: Wilson-loop Approach to Topological Numbers and Fragile Topology. *New J Phys* (2019) 21:093029. doi:10.1088/1367-2630/ab3f71
51. Wang C, Zhang H, Yuan H, Zhong J, Lu C. Universal Numerical Calculation Method for the Berry Curvature and Chern Numbers of Typical Topological Photonic Crystals. *Front Optoelectron* (2020) 13:73–88. doi:10.1007/s12200-019-0963-9
52. Chong YD, Wen X-G, Soljačić M. Effective Theory of Quadratic Degeneracies. *Phys Rev B* (2008) 77:349–54. doi:10.1103/PhysRevB.77.235125
53. Zhao D, Wang Y-T, Fung K-H, Zhang Z-Q, Chan CT. Acoustic Metamaterials with Spinning Components. *Phys Rev B* (2020) 101:054107. doi:10.1103/PhysRevB.101.054107
54. Travagnin M, Sartori F, Ruzzier M. Mode Beating Analysis by Sample Stretching and Wavelength Sweeping in a Few-Mode Fiber. *J Lightwave Technol* (2014) 32:494–504. doi:10.1109/JLT.2013.2294475
55. Fontaine NK, Ryf R, Mestre MA, Guan B, Palou X, Randel S, et al. *Optical Fiber Communication Conference and Exposition and the National Fiber Optic Engineers Conference (OFC/NFOEC), 2013*. Anaheim, CA, United States (2013). doi:10.1364/OFC.2013.OW1K.2Characterization of Space-Division Multiplexing Systems Using a Swept-Wavelength Interferometer
56. Kaiser T, Flamm D, Schröter S, Duparré M. Complete Modal Decomposition for Optical Fibers Using CGH-Based Correlation Filters. *Opt Express* (2009) 17:9347–56. doi:10.1364/OE.17.009347
57. Nicholson JW, Yablon AD, Ramachandran S, Ghalmi S. Spatially and Spectrally Resolved Imaging of Modal Content in Large-Mode-Area Fibers. *Opt Express* (2008) 16:7233–43. doi:10.1364/OE.16.007233
58. Ding Y, Peng Y, Zhu Y, Fan X, Yang J, Liang B, et al. Experimental Demonstration of Acoustic Chern Insulators. *Phys Rev Lett* (2019) 122:014302. doi:10.1103/PhysRevLett.122.014302

Conflict of Interest: The authors declare that the research was conducted in the absence of any commercial or financial relationships that could be construed as a potential conflict of interest.

Publisher's Note: All claims expressed in this article are solely those of the authors and do not necessarily represent those of their affiliated organizations, or those of the publisher, the editors and the reviewers. Any product that may be evaluated in this article, or claim that may be made by its manufacturer, is not guaranteed or endorsed by the publisher.

frontiers in Physics

REVIEW
published: 25 January 2022
doi: 10.3389/fphy.2022.845579

Recent Progress in Chiral Topological Quantum Interface

Ping Jiang, Na Ma, Xiaozhen Qiao and Hui Zhang*

College of Science, China University of Petroleum (East China), Qingdao, China

Chiral quantum optics and Topological photonics are both emerging field of research, which have attracted great attention in recent years. Chiral quantum optics provides a new approach to achieve full quantum control of light-matter interaction in a novel manner, which has potential possibility for the implementation of complex quantum information networks. Meanwhile, topological photonics provides a novel route for designing and realizing optical device with unprecedented functionality, such as robust light propagation, the immunity to various structural imperfection, back-scattering suppression as well as unidirectional transmission. The application of topological photonics in chiral quantum optics will promote the whole performance of integrated quantum device with topological protection. In this review, we summarize the progress of chiral quantum optics and topological photonics firstly. Then, we mainly focus on the research of topological chiral edge states based on photonic quantum spin-Hall effect and photonic quantum valley-Hall effect. Furthermore, we introduce the recent work of chiral topological quantum interface formed by embedding quantum dot into the interface between two topologically distinct photonic crystal structures. At last, we give short outlook on the future development direction and prospect for application of topological chiral quantum interface.

Keywords: chiral quantum optics, topological photonics, chiral topological quantum interfaces, integrated quantum devices, quantum dot

OPEN ACCESS

Edited by:
Cuicui Lu,
Beijing Institute of Technology, China

Reviewed by:
Hongu Zhang,
Beijing Institute of Technology, China
Sayed Elshahat,
Beijing Institute of Technology, China

****Correspondence:***
Ping Jiang
pjiang@upc.edu.cn

Specialty section:
This article was submitted to Optics and Photonics, a section of the journal Frontiers in Physics

Received: *30 December 2021*
Accepted: *10 January 2022*
Published: *25 January 2022*

Citation:
Jiang P, Ma N, Qiao X and Zhang H (2022) Recent Progress in Chiral Topological Quantum Interface. Front. Phys. 10:845579. doi: 10.3389/fphy.2022.845579

INTRODUCTION

A single photon interacting with a single quantum emitter is the canonical setting of quantum optics, while the central goal of which is to develop techniques for complete control of light–matter interaction at single quanta level [1]. Chiral interfaces provide a new approach to quantum control of light–matter interaction. The coupling between light and emitter depends on the propagation direction of light and the polarization of the transition dipole moment of the emitter. Then the photon–emitter interaction becomes non-reciprocal, which means that forward- and backward-propagating photons interact differently with the emitter. The photon emission and absorption even becomes unidirectional in the most extreme case [1]. By suppressing the decoherence caused by the surrounding environment, it has potential possibility for the implementation of quantum many-body systems that promotes the speedy development of complex quantum information networks [2]. Many research groups have paid great attention to chiral quantum optics and started to explore intrinsic correlations relating to spin-momentum locking and unidirectional propagation [3–8]. Although numerous efforts have been made, several limitations still exist in this research area which seriously restrict the further development of on-chip integrated quantum networks and information processing. Quantum systems are more susceptible to changes of surrounding environment including external disturbance and internal structural imperfection, especially for more complex multi-body system. Fortunately, the advent of topological photonics provides new strategy for

addressing the awkward problems and promoting the whole performance of integrated quantum device with topological protection.

Topological photonics has attracted extensive attention recently due to the unique optical behaviors, including robust light propagation, the immunity to various structural imperfection, back-scattering suppression as well as unidirectional transmission [9–16]. Most remarkably, chiral edge states with topological protection exist in the interface between two topologically distinct regions, allowing for the robust and directional propagation of light along the interface. Robust propagation of light in chiral edge states protected by topology is first demonstrated both theoretically and experimentally in Ref. [16] and then all kinds of intriguing physic phenomena based on photonic quantum Hall effect [18, 19], photonic quantum spin-Hall effect [20–23], and photonic quantum valley-Hall effect [24, 25] have been observed in different designed topological structures. Combining of chiral quantum optics with topological photonics to form chiral topological quantum interfaces promotes the further development of high-performance quantum integrated circuits and complex cascaded quantum systems [26, 27].

Herein, we review the recent progress in chiral topological quantum interface. Firstly, we provide a brief introduction of chiral quantum optics and topological photonics in *Progress in Chiral Quantum Interface and Topological Photonics*. Then we focus on chiral topological quantum interface combined with quantum emitters in *Realization of Chiral Topological Quantum Interface*. At last, we give a conclusion and a brief discussion for potential prospect in quantum integrated networks in *Conclusion*.

PROGRESS IN CHIRAL QUANTUM INTERFACE AND TOPOLOGICAL PHOTONICS

Chiral quantum optics as an emerging research field has attracted substantial attention. Some exotic physic phenomena in this field cannot be explained by conventional quantum optics. The advent of chiral quantum optics explains the intrinsic relationship between the unidirectional propagation of light and polarization of the emitter, which opens an intriguing research area and provides an in-depth understanding of light generation, propagation, and manipulation. If light with spin-momentum-locking can be coupled to the emitter with polarization-dependent dipole transition, the propagation direction of light will be determined even in some extreme case. Furthermore, propagation-direction-dependent emission, scattering, and absorption of photons from quantum emitters will be also obtained, which is a non-reciprocal process and a basic operation principle of chiral quantum optics [28, 29]. This chiral feature tends to appear in some specially designed nanostructures due to tightly transverse confinement of light, such as waveguides and nanobeams which will connect polarization property of the emitter and propagation direction of light due to spin-orbit coupling [30–32].

In recent years, chiral quantum optics has been investigated extensively and this spin-momentum-locked unidirectional propagation of light has been experimentally demonstrated in various dielectric [6, 8, 33–35] and plasmonic [36–39] photonic nanostructures. In these nanostructures, the strong transverse confinement of light, which is perpendicular to the propagation direction, naturally leads to a longitudinal component of the electric field. The transverse and longitudinal components of electric field produce π radian oscillations out of phase with each other, leading to an elliptically polarized electric field with spin angular momentum. The sign generated in this process determines the propagation direction of light which is forward or backward. Thus, the propagation direction of light reverses with the inversion of this sign. Considering the interaction between spin-momentum-locked light and quantum emitter, only when the polarization of transition dipole moment of the emitter is matched with local polarization of propagation direction of light, can the directional emission be appearing at this point. Some exactly engineered photonic crystal waveguides and nanocavities have been demonstrated as a promising platform to tailor interaction between light and matter due to their ability to lock polarization of photons to their propagation direction and realize unidirectional transmission of emitted photons [40–43]. For example, a broken-symmetry glide-plane waveguide can provide circularly polarized field mode at the maximum of field intensity, which cannot be observed in other conventional waveguides [44]. A number of associated experiments have been implemented. Besides, this chiral light-matter interaction between photonic nanostructure and quantum emitter has also been realized in other structures, such as nanobeam waveguides [34, 45], optical resonators [46, 47], and metamaterials [48]. Here, more details about systematic theoretical research and applications for chiral quantum interface in conventional nanostructures have been reviewed in Ref. [49].

A well-defined chiral quantum interface can not only enhance chiral light-matter interaction but also suppress massive transport loss. But disappointingly, the back-scattering loss and imperfect directionality caused by inherent fabrication impurities and disorders have negative influences on operation efficiency and information fidelity of quantum photonic circuits, which become extremely worse for long transmission length. Fortunately, topological photonic structures have great ability to solve these problems owing to their immunity to structural imperfections and robust propagation of light.

In 2005, Haldane and Raghu introduced the concept of topology to the realm of photonics [50, 51]. Then a new class of research perspective named topological photonics is opened up, which enables the massive potential possibility for realizing various functional integrated photonic devices and on-chip integrated photonic circuits with built-in protection. Topological photonics has attracted widespread interest once proposed as it provides a new paradigm in the further development of various robust photonic devices for integrated quantum photonic circuits and quantum computing [9–13]. The robust edge states protected by band topology enable the highly potential possibility for chiral light-matter interaction [52–55],

which have been observed in various photonic systems, including 1D photonic structures based on SSH model and AAH model [56, 57], 2D topological photonic structures based on metamaterials, synthetic gauge field and ring resonator arrays [58–61] as well as complicated higher dimensional photonic structures [62]. Nevertheless, some limitations existing in these topological structures impose serious restrictions on the further development of topological photonic devices and cannot satisfy on-chip integration requirements. Firstly, some structures made of gyromagnetic or bianisotropic materials in photonic quantum Hall systems with time-reversal broken can only exhibit unidirectional edge states under a strong magnetic field and cannot be applied in the optical range due to weak magnetic response [17–19, 59, 63, 64]. Besides, some special designs such as synthetic gauge field and ring resonator arrays are so complicated with huge difficulty in nanofabrication and on-chip integration, which is not similarly compatible with other photonic devices [60, 61, 65–70].

Two-dimensional semiconductor photonic crystal structures are promising candidates to solve these problems, as they are easier to achieve robust topological edge states with unidirectional transmission and anti-back-scattering and are less stringent about current nanofabrication techniques. Moreover, multiple defects and disorders can be introduced by deforming the shape and size of individual cells to investigate and verify some robust characteristics [71, 72]. Additionally, various operating wavelengths like telecommunication wavelength or even optical regime and different band structures can be simply realized by engineering structural parameters like lattice constant, air hole's radius, and dielectric cylinders [73–79]. Therefore, these 2D photonic crystal structures are known as extremely infusive platform to achieve various integrated photonic devices for on-chip integrated photonic circuits, like topological circulators [80], on-chip channel filters [71], and slow-light waveguides [81].

Here we just give a brief introduction to topological photonics. Next, we mainly focus on the progress of chiral topological quantum interface based on photonic quantum spin-Hall effect and photonic quantum valley-Hall effect. More details about the recent progress and applications of topological photonics have been reviewed in Refs. [11, 16, 82].

REALIZATION OF CHIRAL TOPOLOGICAL QUANTUM INTERFACE

An interface formed by connecting two topologically distinct photonic structures supports chiral edge state with directional propagation and immunity to back-scattering, which is easy to constitute chiral topological quantum interface when combined with quantum emitters like quantum dots (QDs). The prerequisite for implementing this chiral quantum interface in topological photonic is the appearance of chiral topological edge states with spin-momentum locking and directional transmission. The topological semiconductor photonic crystal structures have successfully aroused immense attention due to their compatibility with nano-manufacturing technology and ease of implementation for on-chip integrated photonic device [20]. Moreover, these structures can be directly integrated with quantum emitters such as quantum dots (QDs) to constitute chiral topological quantum interface with robustness to some structural imperfection, which enables to immensely improve the whole performance of integrated photonic devices and quantum networks [73, 83]. In this section, we will review the two-dimensional semiconductor photonic crystal structures and the polarization properties of chiral edge states in the photonic quantum spin-Hall systems and photonic quantum valley-Hall systems, respectively. Furthermore, we will introduce the recent work of chiral topological quantum interfaces formed by embedding quantum dots into the interface between two topologically distinct photonic crystal structures.

Chiral Topological Quantum Interface Based on Photonic Quantum Spin-Hall Effect

Chiral edge states can be realized in two-dimensional photonic crystal structures based on photonic quantum spin-Hall effect. These edge states protected by band topology can propagate in opposite directions at the interface between two kinds of topological distinct photonic crystals. In 2015, Wu et al. provided the theoretical basis of chiral topological edge states in a photonic quantum spin-Hall system and proposed the concept of pseudo time-reversal symmetry for the first time [84]. The considered honeycomb lattice with rotational symmetry composed of six-sites unit cells can fold two Dirac cones at K and K' points into doubly degenerate Dirac cones at Γ point in the first Brillouin zone. A topological nontrivial bandgap with nonzero Z_2 topology invariant can be opened by simply deforming the honeycomb while maintaining the hexagonal clusters and C_6 rotational symmetry unchanged, as shown in **Figures 1A,B**. Simultaneously, the photonic band dispersion experience an opened state, a closed state, and a reopened state when generally changing lattice constant from larger to smaller, which directly results in a topological phase transition and a band inversion identified as p± and d± states. When an interface consisting of two regions with different band topology is considered, two cross-bands connecting the upper and bottom bulk band lead to two pseudo spin states with opposite group velocities appearing within the bandgap as shown in **Figure 1C**. These in-gap edge states can be well located at the interface and exponentially decay into the bulk. Moreover, it is explicitly concluded from energy flow represented by Poynting vector shown in **Figure 1D** that these two pseudo spin-up and spin-down states respectively correspond to the left-hand and right-hand circular polarizations of in-plane magnetic fields for TM mode and also have a one-to-one correspondence with the propagation direction of electromagnetic energy, which is the fundamental of photonic quantum spin-Hall effect [85, 86].

After that, various semiconductor photonic crystal structures with C_6 rotation symmetry and pseudo time-reversal symmetry that support chiral edge states at the interface have been intensively investigated both theoretically and experimentally

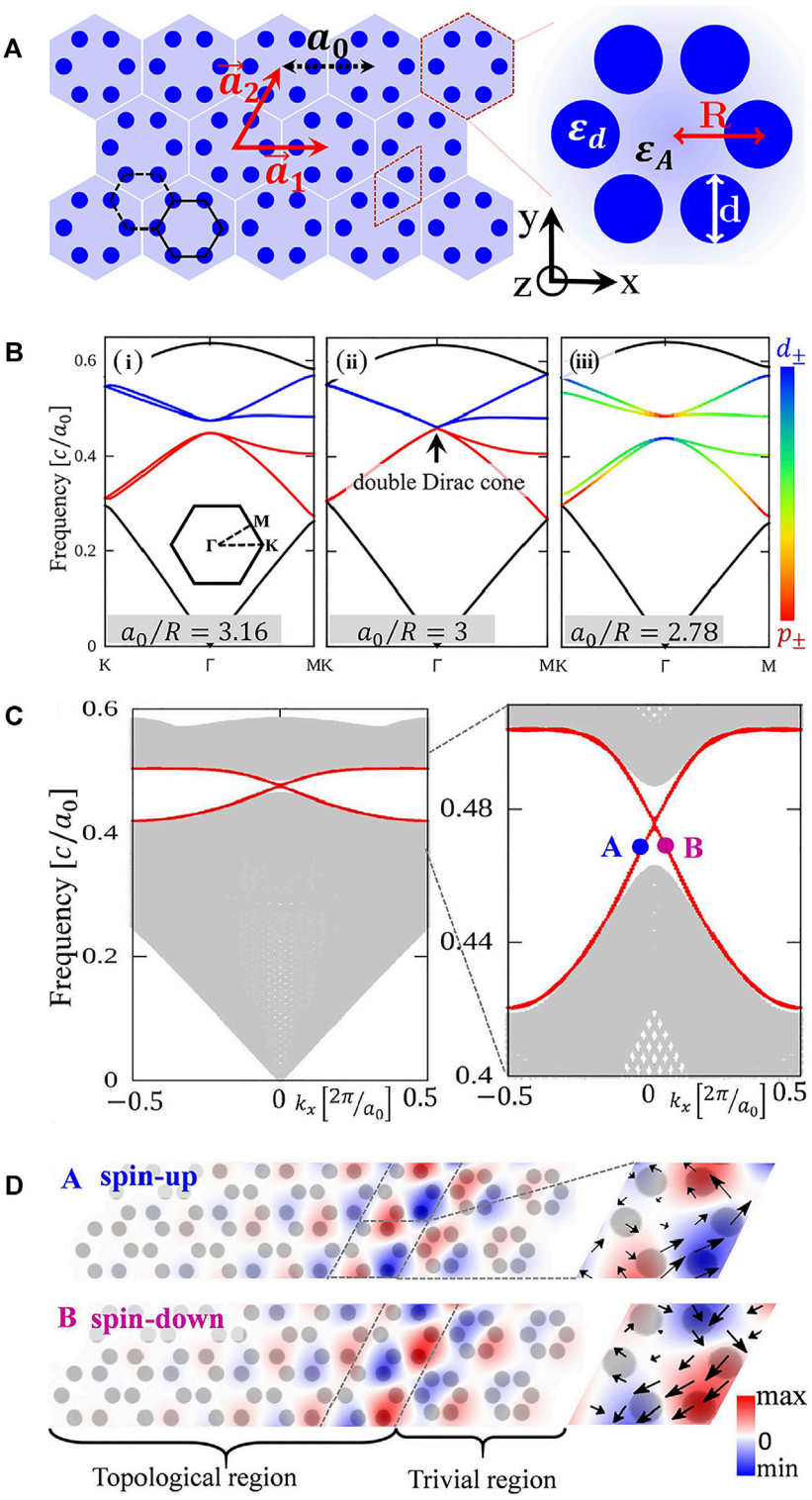

FIGURE 1 | (A) Topological photonic crystal structure with honeycomb lattice composed of six cylindrical pillars in each unit cell [84]. **(B)** Band structure in the first Brillouin zone for transverse electromagnetic mode with expanding or shrinking the honeycomb lattice. **(C)** Dispersion relation in the topological interface. The gray regions indicate bulk modes and the red curves indicate topological edge states within the bandgap. **(D)** Distribution of electric field intensity E_z at A and B points marked in **(C)**.

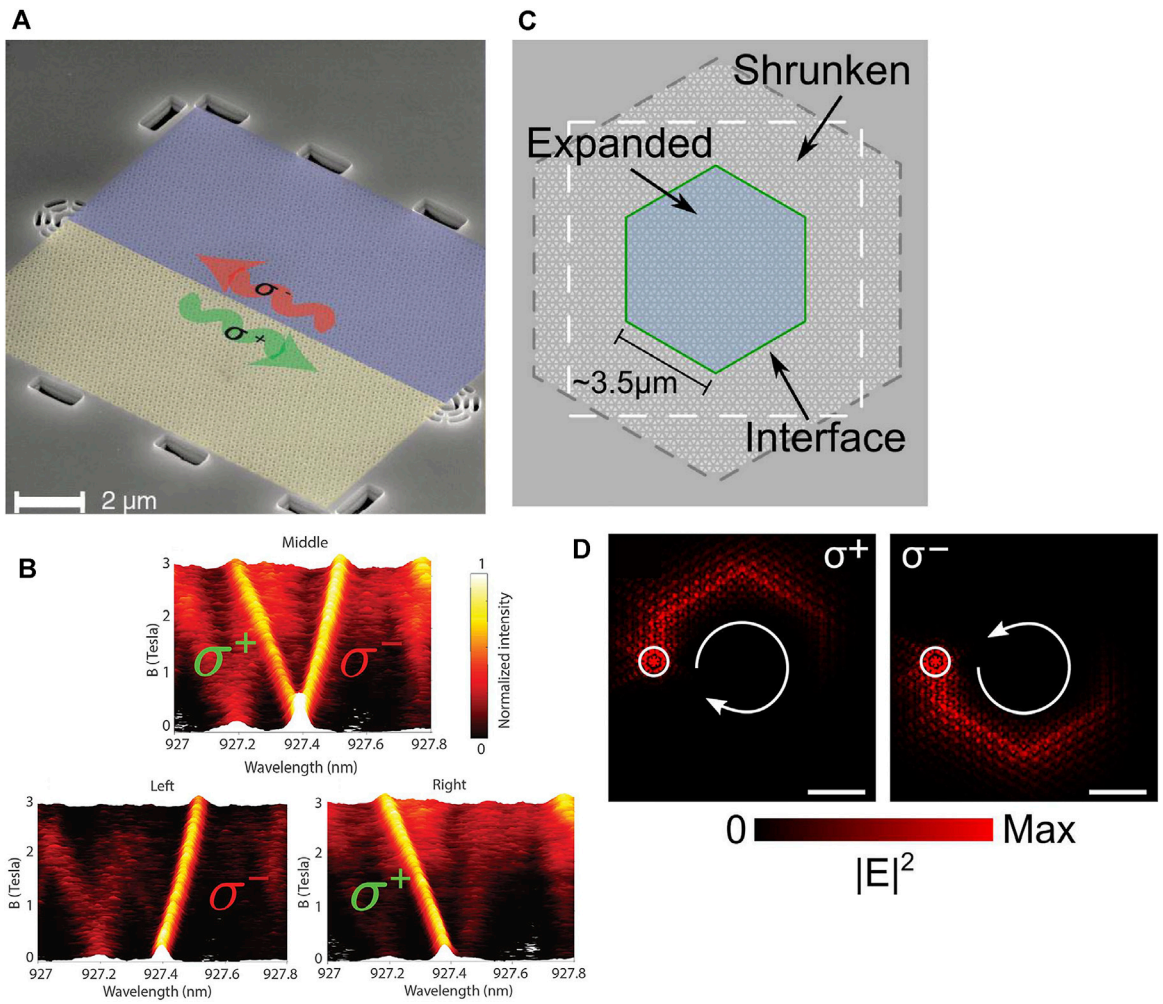

FIGURE 2 | (A) Schematic of the chiral quantum interface formed by connecting two photonic crystal structures with different band topologies indicated by blue and yellow [83]. **(B)** Emission and transmission spectrum collected from the position of a quantum dot, left and right grating output couplers as a function of the magnetic field, respectively. **(C)** Schematic of the ring resonator constituted by embedding a topological nontrivial region of hexagonal shape with expanded honeycomb lattice (blue area) in the center of the topological trivial region with shrunk honeycomb lattice (grey area). The green solid line indicates the interface between two topologically distinct photonic crystal regions [72]. **(D)** The electric field intensity distribution of two pseudo spin edge modes with opposite polarization excited by inversely polarized dipole sources represented by the white open circle.

[87–89]. Nanostructures based on cylindrical pillars made of Si or Al_2O_3 materials in the air have been demonstrated experimentally to realize two opposite pseudo spin edge states and unidirectional propagation of edge states [21, 90]. Although their operating wavelength can be extended to near-infrared or even visible range, several limitations still exist just as the cylinder structures are difficult to achieve in-plane transverse confinement of light. The above problems can be solved well by adding metallic plates. However, the enormous metal loss seriously deteriorates the performance of the photonic devices [84]. Moreover, nano-manufacturing technology and integration with other topological devices are challenging. Another simpler design approach has also been proposed to constitute all-dielectric topological photonic crystal structures with honeycomb lattice via etching air hole array on a dielectric slab, which is highly desirable for chip-scale integration devices [20, 91, 92].

With deformed honeycomb lattices topological photonic crystal structures, Barik et al. experimentally explored the chiral topological quantum interface for the first time in photonic quantum spin-Hall system, as shown in **Figure 2A** [83]. Emitted polarization-dependent photons from quantum dots coupled to two opposite pseudo spin edge states, exhibiting directional propagation and robust characteristic even in the presence of a 60° sharp bend. Chiral emission is achieved as shown in **Figure 2B**. Moreover, the single-photon behaviors at such topological interface have been experimentally demonstrated. Subsequently, Jalali et al. proposed theoretically and investigated experimentally GaAs topological ring resonator combined with InGaAs quantum dots, in which topological nontrivial photonic structure of hexagonal array with expanded lattice is surrounded by topological trivial photonic structure with shrunk lattice as in **Figure 2C** [72]. As shown in

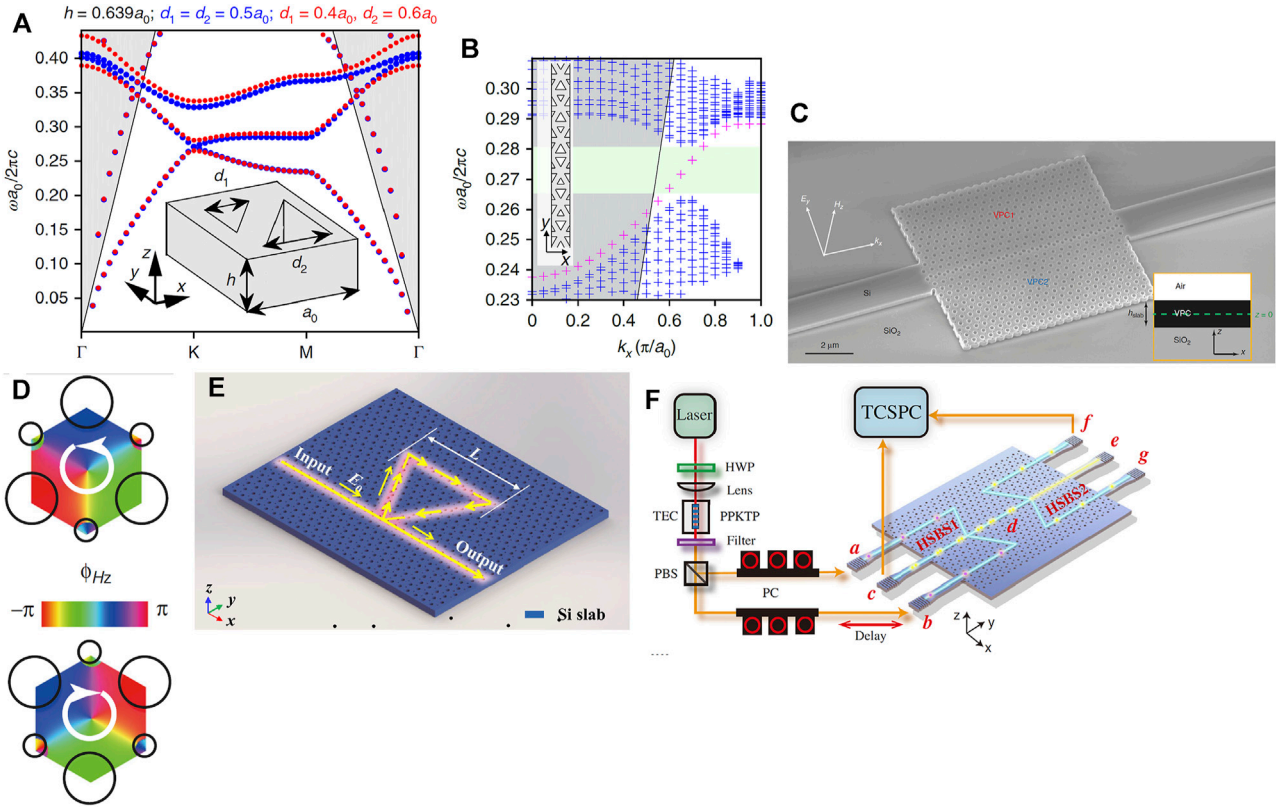

FIGURE 3 | (A) Band structures of the valley photonic crystal slab with triangular air holes. The inset represents the unit cell structure composed of two unequal triangular air holes [95]. **(B)** Band diagram of edge states in the interface between two distinct valley photonic crystals. The magenta curve indicates the edge state. The green and blue regions indicate the bandgap and bulk bands, respectively. **(C)** Schematic of the topological chiral interface by connecting two topologically distinct valley photonic crystal regions marked by "VPC1" and "VPC2" [99]. **(D)** Calculated phase distribution of Hz field for differently perturbed honeycomb lattice. **(E)** Schematic of the topological notch filter containing a triangular-loop ring resonator, in which only one edge state propagates forward and then directionally coupled to the ring resonator mode due to valley-polarization locking [71]. **(F)** Experimental setup and structural image of a complex topological structure with two harpoon-shaped beam splitters [100].

Figure 2D, the chiral emission is clearly observed via the electric field intensity distribution and the propagation direction of edge modes is closely associated with the polarization property of dipole sources. Moreover, the mode structures of the optical ring resonator remain unchanged when the location of the excitation point is changed in the vicinity of the interface. Therefore, this kind of topological ring resonator embedded with quantum dots can be effectively coupled with a bus waveguide to form some novel photonic device like add-drop filter, which represents an important building block for integrated quantum photonics.

Additionally, a new class of topologically engineered photonic crystal waveguides have been proposed and demonstrated recently, the guided modes of which have been identified as both chiral [6, 11] and resistant to back-scattering in 60-degree bends [71, 81, 93–95]. Quantum chiral-light matter interface has been demonstrated based on the quantum spin-Hall effect [96].

Chiral Topological Quantum Interface Based on Photonic Quantum Valley-Hall Effect

Another promising platform for realizing chiral quantum interface in topological photonics is valley photonic crystal (VPhC) based on the photonic analogous of quantum valley-Hall effect. This kind of valley photonic crystal is originally proposed in an all-Si photonic crystal platform with triangular lattices made of Si rods [97]. An interface or an edge constituted by two perturbed structures with a triangular Si rod in the hexagonal unit cell supports highly confined robust edge wave with immunity to back-scattering, which has the ability for realizing photonic topological insulator (PTI) and has immense potential for developing robust optical delay line with arbitrary-shape cavity. Subsequently, Chen et al. discussed the unidirectional excitation of valley bulk state with intrinsic chirality and topological phase transition in a valley photonic crystal platform with honeycomb lattice of circular Si rods [75]. In addition, other types of valley photonic crystals have been proposed with some special structural designs, such as staggered bianisotropic response with different bianisotropic coefficients but identical rod radii [98], valley surface-wave photonic crystals on a single metal surface made of metallic rods with different height [76], topological edge states along the armchair and zigzag domain walls composed of topologically distinct honeycomb lattices [79].

In the photonic valley-Hall system, the topological invariant used to characterize band topology of differently perturbed lattices is referred to the valley Chern number with the

definition of $C^{K/K'} = \frac{1}{2\pi} \int_{HBZ_{K/K'}} \Omega(k) d^2(k) = \pm \frac{1}{2}$, which is the integration of Berry curvature over half of the first Brillouin zone at K or K' points and is quantified as ±1/2. The difference between the valley Chern numbers determines the number of edge state at each valley. According to the bulk-edge correspondence and the difference of valley Chern numbers, only one helical edge state crosses the whole bandgap region between the first and second bulk band at the single valley, shown in **Figures 3A,B**. Another edge state with opposite group velocity and opposite helicity exists at the other valley due to time-reversal symmetry and the symmetry of band structure with respect to wave vector (k_x) in the momentum space. It is different from that of photonic quantum spin-Hall system in that photonic bands of these edge states are both below the light line, which directly ensures highly efficient in-plane confinement of light and reflection-free propagation.

Shalaev et al. experimentally demonstrated planar silicon photonic crystal structure with topological protection in telecommunication wavelength [95]. The honeycomb lattice with rhombic unit cell of two equilateral triangular air holes is considered in this work. When the sides of two triangular holes are equal and have C_6 symmetry, a Dirac zone for TE mode appears at K and K' points in the momentum space, which is protected by time- and spatial-reversal symmetry. When perturbing the unit cell by changing the side length of these two triangular air holes to break the spatial inversion symmetry, the degeneracy around the Dirac points is lifted and a controllable photonic bandgap is opened resulting in the presence of a topological valley phase. Besides, this type of photonic crystal structure possesses a nonzero Berry curvature with opposite signs at K and K' points. When the size of two triangular holes in the same unit cell is exchanged, the sign of Berry curvature is simultaneously flipped. A similar work that validates robust propagation of light is also implemented by constructing three various topological interfaces with flat-, Z-, and Ω-shape [99]. The experimental and simulation results illustrate that the high transmission spectra within the bandgap region are maintained flat-top, which means that broadband robust transportation can be achieved due to the suppression of inter-valley scattering [99]. More importantly, the selective excitation of valley-chirality-locked edge states existing an interface between two topologically distinct valley photonic crystals is demonstrated experimentally in this work, as shown in **Figure 3C**. The unit cell of these two different structures, consisting of two nonequivalent circular air holes, directly breaks the inversion symmetry and opens a photonic bandgap for TE-like polarization. It is shown from simulated Hz phase distribution in **Figure 3D** that the vortex phase increases clockwise or anticlockwise by 2π around the center of the unit cell for different photonic crystal structures, which directly corresponds to right- or left-handedness circular polarization and simultaneously has a straightforward relationship with valley pseudo spin, that is, valley degree of freedom (DOF). Thus, the valley-polarization-dependent edge state is selectively excited by controlling the chirality of light and highly efficient unidirectional coupling is expected to be achieved via vortex fields of chiral edge states.

Apart from the topological waveguide with straight interface or several sharp bends, other complicated topological photonic devices including circulators are also investigated. Gu et al. both theoretically and experimentally proposed a ring resonator with topological protection, which is constituted by a closed triangular-shape topological edge formed by two topologically distinct photonic crystal structures [71]. Due to valley-polarization locking, only one edge mode propagates forward along the straight interface and propagates clockwise along the ring resonator, as shown in **Figure 3E**. Besides, Chen et al. experimentally demonstrated a topological harpoon-shaped beam splitters (HSBS) with 50/50 splitting ratio in valley photonic crystal fabricated on SOI wafer [100]. Two-photon quantum interference based on Hong-Ou-Mandel is realized with a high visibility of 0.956. This kind of device is also verified to possess outstanding scalability and feasibility because it can combine two or even more above harpoon-shaped beam splitters to constitute more complex quantum networks as shown in **Figure 3F**. Moreover, topological slow-light waveguides made of Si valley photonic crystals are theoretically and experimentally demonstrated [101, 102]. The light propagation with topological protection and back-scattering-free in the slow light regime possesses widespread application prospects ranging from enhancing optical gain to nonlinearity for realizing active topological photonic devices and photonic integrated circuits [103, 104].

Although considerable efforts in Si-based valley photonic crystal slabs have been achieved both theoretically and experimentally with a wide range of application prospects in integrated Si photonics, it is challenging for chiral topological quantum interfaces combined with quantum emitters such as quantum dots. The III-V compound semiconductor materials provide incomparable superiority because they are convenient to directly integrate with various quantum emitters and enable the implementation of chiral emission and transmission of photons from quantum emitters. In 2019, Yamaguchi et al. experimentally realized a valley photonic crystal waveguide on a GaAs slab with embedded InAs quantum dot, as shown in **Figure 4A**. The embedded InAs quantum dot acts as an internal light source used not only for characterizing guiding mode of edge state at the topological interface between two topologically distinct regions with different modulated honeycomb lattices, but also for emitting single photons to realize directional emission and coupling with edge mode [105]. A bright radiation spot appearing at output port of the non-trivial interface is observed in **Figure 4B** by the micro-photoluminescence measurements, which indicates that light emitted from quantum dots can propagate along the topological interface. And the high transmittance from output port also suggests the robust propagation of light within the bandgap. The high confinement of light at the interface is also verified by changing excitation positions relative to the center of the interface. Even in the presence of sharp bends, the light only from the emission of quantum dot can propagate along the Z-shaped interface without any back-scattering. These crucial results lay the foundation for realizing chiral emission and directional coupling between edge mode and quantum

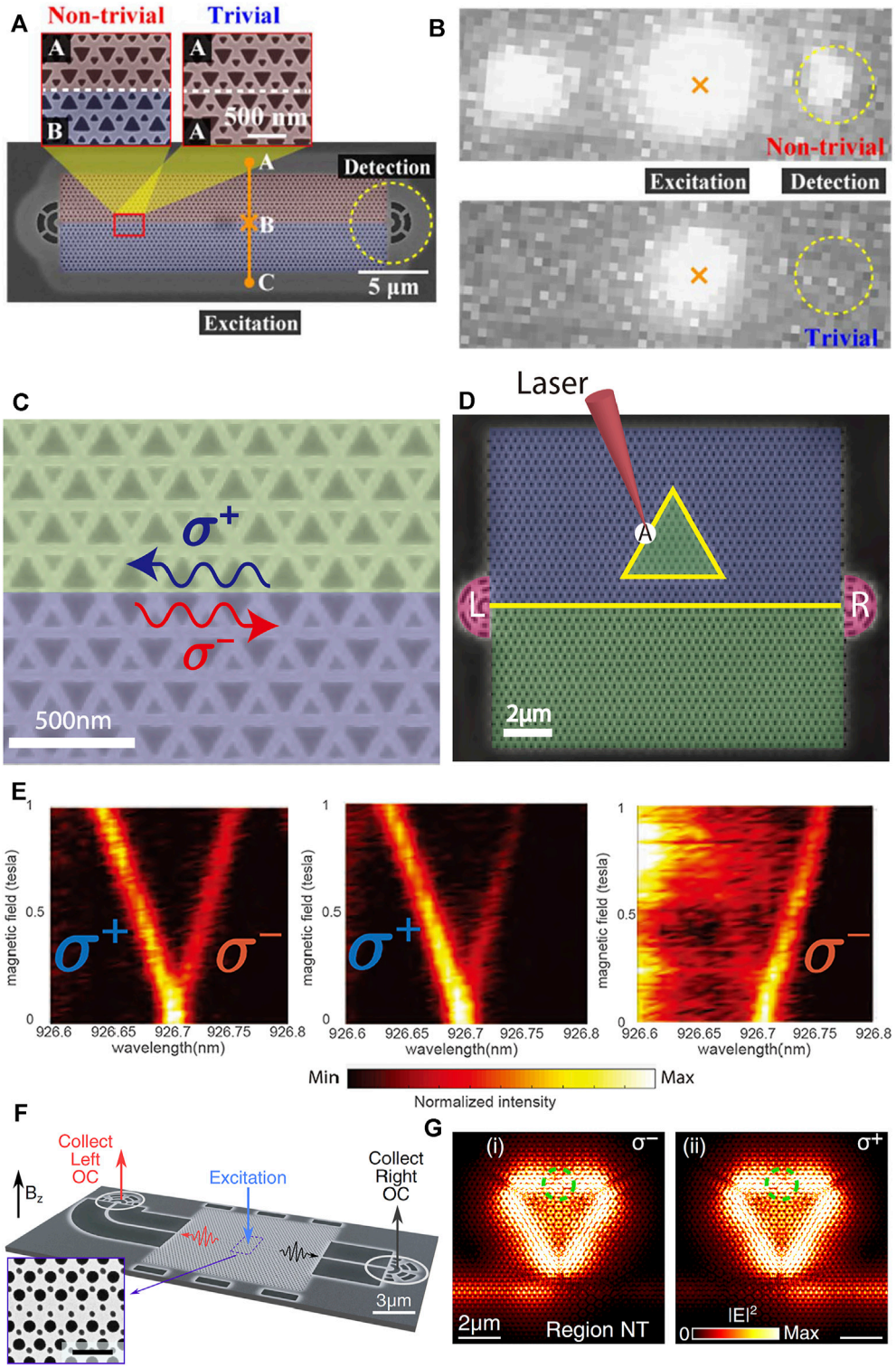

FIGURE 4 | (A) Schematic of a Z-shaped valley photonic crystal waveguide with two grating output couplers at the two ends [105]. **(B)** Measured photoluminescence images of non-trivial and trivial interfaces. **(C)** Schematic of the topological interface formed by two valley photonic crystals with the same bulk band but different topology properties, supporting two various edge states with opposite chirality [106]. **(D)** Structural image of the topological ring resonator composed of a triangular loop and a straight waveguide terminated by two grating output couplers marked by "L" and "R". The mark of "A" indicates the position of excitation. **(E)** Measured photoluminescence spectra from A position, left grating, and right grating, respectively. **(F)** Schematic of the topological ring resonator (RR) with triangular shape coupled to a straight waveguide (WG), terminated by two nanobeam waveguides and two grating output couplers [94]. **(G)** Calculated electric field profile of the topological ring resonator when excited by a dipole source with opposite circular polarization of σ- and σ+.

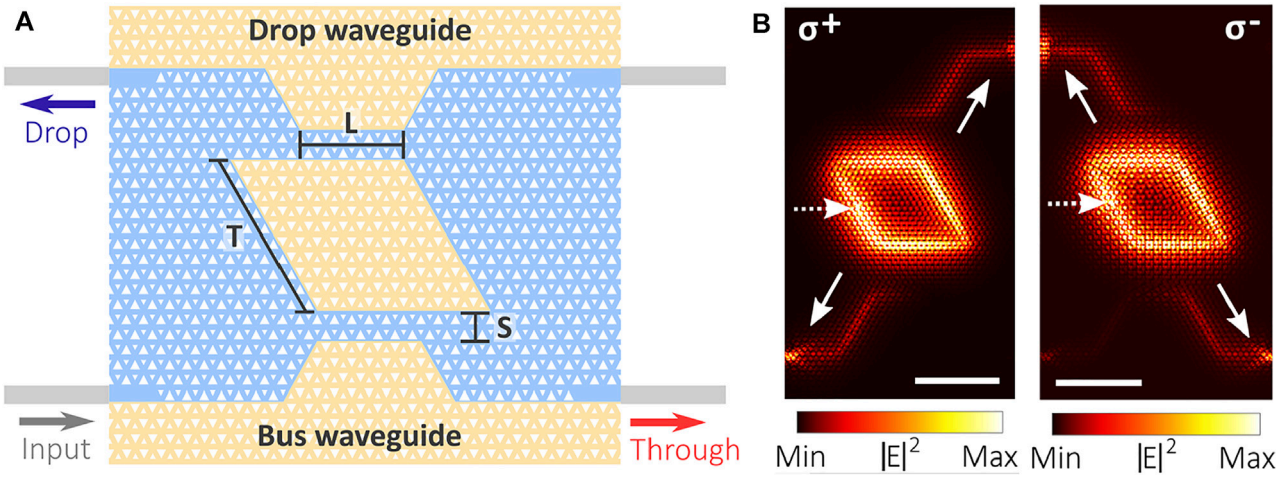

FIGURE 5 | (A) Schematic of a topological add-drop filter containing a rhombus-shaped ring resonator and a pair of access waveguides with the output ports marked by "Through" and "Drop" [80]. **(B)** Calculated electric field intensity distribution when the device is excited by a dipole source with σ+ and σ- polarization.

emitter as well as for exploring the chiral quantum ring resonator with topological protection.

Recently, Barik et al. experimentally constituted a topological ring resonator composed of chiral interface between two differently perturbed valley photonic crystal regions on a GaAs slab with embedded InAs quantum dots, as shown in **Figure 4C** [106]. The unidirectional coupling between quantum emitter and the resonator modes is observed in the simulation and experimental results. It is displayed in **Figure 4D** that the formed topological interface support two counter-propagating edge modes with opposite helicity, which leads to the emergence of resonator modes with opposite circular polarization. The light within the photonic bandgap can be highly confined at the boundary. And there is not any back-scattering at the three sharp corners owing to topological protection. It is observed from the calculated Poynting vector that when the ring resonator is excited by the dipole with right circular polarization (σ-), the electric field propagates clockwise along the triangular loop and then couples to the right part of the straight waveguide while the ring resonator is excited by the dipole with left circular polarization (σ+), the electric field propagates counterclockwise around the triangular loop and then couples to the left part of the straight waveguide. The reason is that the same band topology of the region below the straight waveguide and inside the triangular loop results in the same chirality at the interface. When applying a magnetic field on quantum dot, the two spectrally resolved branches with different transition dipole moments are formed due to Zeeman splitting, which corresponds to the opposite circular polarization, as displayed in **Figure 4E**. Moreover, when the emission lines of the quantum dot are resonant with resonator modes, the Purcell enhancement factor of 3.4 is obtained and thus the emission from thequantum dot is significantly enhanced. This work opens a new paradigm to engineer the chiral light-matter interaction in valley photonic crystal platforms. Various intriguing phenomena containing the generation of entangled spin states, photonic clusters states, and superradiant are supposed to be achieved in a new manner [107–109].

After that, Mehrabad et al. also experimentally demonstrated a chiral ring resonator in valley photonic crystal of honeycomb lattice on GaAs slab with an embedded layer of InGaAs quantum dots [94]. The topological structure with a bearded-shaped interface is displayed in **Figure 4F**. The light with σ-state couples to the left part of the topological waveguide and the light with σ+ state couples to the other part, which indicates that the propagation direction of light at the bearded-shape interface is determined by the chirality of the circular polarization of photons from quantum dot. Chiral emission and unidirectional coupling with topologically nontrivial guiding modes are simultaneously achieved. Based on robust propagation of light around sharp bends, a triangular-loop ring resonator with a straight topological waveguide below is constituted, the high Q factors of which can reach 12,500 and 4,000 in simulation and experimental results, respectively. It is shown as the simulation results in **Figure 4G** that a dipole with opposite circular polarization placed at the highly chiral point on the ring resonator interface excites different polarized resonator modes and the generated light field couples evanescently to the bus topological waveguide, in which the propagation of light is dependent on the chirality of the dipole polarization. These works have demonstrated the feasibility of chiral coupling for topological ring resonators and facilitated the further development of chiral light-matter interaction for various spinful photonic devices.

Besides the chiral ring resonators with topological protection combined with quantum emitters being essential components for integrated quantum networks, other topological integrated devices such as filters with quantum characteristics are also in urgent need of exploration. Mehrabad et al. proposed a topological add-drop filter composed of a rhombus-shaped ring resonator and a pair of access waveguides named as "through" and "drop" waveguides, as shown in **Figure 5A**

[80]. When the quantum dot at the interface is excited, the photons with various transition dipole momentum are coupled to different output ports under a nonzero magnetic field, which demonstrates chiral behavior and directional coupling between the ring resonator and quantum dot. Simulated results in **Figure 5B** demonstrate the chiral behavior again, enabling the realization of a bidirectional chiral router. Additionally, the second-order correlation function of $g^{(2)}(0) = 0.14$ indicates that the single-photon property of the single quantum dot emission can be well preserved during the whole propagating and coupling process of photons. Consequently, these kinds of valley photonic crystal structures combined with quantum emitters reveal the inherent mechanism of chiral control of light-matter interaction at the single-photon level and possess a widespread application for high-performance on-chip topological filters and circulators with in-built protection against structural imperfections and arbitrary-shape bending, which promote the future development of chiral integrated quantum photonic circuits [110].

CONCLUSION

On-chip chiral quantum light-matter interface provides a promising platform for efficient spin-photon coupling, non-reciprocal photonic elements, and quantum logic architectures. In this review, we mainly focus on the topological chiral quantum interfaces based on photonic quantum spin-Hall effect and photonic quantum valley-Hall effect. Various integrated devices including topological quantum ring resonators and filters are discussed concretely.

At present, the quantum chiral edge state has been realized both numerically and experimentally. But the experimental work on the topological quantum chiral interface with quantum emitter is still deficient. Therefore, relevant experimental research will be the focus in the near future. Besides, the combined quantum emitters are not solely limited to quantum dots, which can be extended to other types of quantum emitters such as defects in two-dimensional materials and color defects in diamonds. Furthermore, the application prospects based on topological quantum chiral interfaces will be the important development directions. Various ring resonators based on the topologically protected interface are formed with arbitrary shapes owing to robustness against various sharp bends, which can leave more space for high-density integrated quantum networks. Considering the spin-orbit interaction and more complex information-carrying capacity, the light beams with multiple degrees of freedom are in urgent need of development for the future implementation of high-speed and more secure multi-dimensional information communications and quantum teleportation systems.

At last, we would like to give a short discuss on the applications prospect of topological chiral interface. The platform of topologically robust and chiral interface between a photonic resonator and a quantum emitter could provide a robust and scalable pathway to engineer chiral light-matter interaction between multiple emitters coupled to a single resonator, without fine tuning of system parameters. The combination of quantum emitters and chiral topological interfaces can not only constitute various functional photonic devices, but also facilitate the development of effective single photon sources. The preeminent characteristics of these topological edge states especially topological ring resonators improve the light-emitting properties of quantum emitters themselves and the single photon behaviors can be well preserved during the whole robust propagation of light, leading to the effective and efficient coupling to other quantum devices. This undoubtedly increases the possibility of the on-chip quantum circuit implementation. Furthermore, various nanophotonic devices containing ultracompact filters and circulators with excellent performance based on topological quantum chiral interfaces will experience rapid development in the future, which are basic elements for achieving compact quantum integrated circuits. Although the photonic devices consisting of a single ring resonator have been intensely investigated, more complex photonic devices with diverse functionality based on multiple ring resonators possess enormous application prospects for complicated and changeable quantum computing and quantum information processing. In a chiral waveguide, photon-matter interactions between emitters are location-independent [110], which could promote the coupling of multiple solid-state emitters via photons while overcoming scalability issues associated with random emitter position, enabling large-scale super-radiant states and spin-squeezing. Finally, a versatile platform to explore many-body quantum physics at a topological edge, create chiral spin networks, and realize fractional quantum Hall states of light can be developed [111], which provide a new approach to study QED in a new regime.

AUTHOR CONTRIBUTIONS

PJ conceived the idea. PJ, NM, XQ, and HZ prepared the draft. All authors contributed to the discussion and revision of the manuscript.

FUNDING

This work was funded by the Central University Basic Research Fund (19CX02056A).

REFERENCES

1. Lodahl P, Mahmoodian S, Stobbe S, Rauschenbeutel A, Schneeweiss P, Volz J, et al. Chiral Quantum Optics. *Nature* (2017) 541:473–80. doi:10.1038/nature21037
2. Eisert J, Friesdorf M, Gogolin C. Quantum many-body Systems Out of Equilibrium. *Nat Phys* (2015) 11:124–30. doi:10.1038/nphys3215
3. Shomroni I, Rosenblum S, Lovsky Y, Bechler O, Guendelman G, Dayan B. All-optical Routing of Single Photons by a One-Atom Switch Controlled by a Single Photon. *Science* (2014) 345:903–6. doi:10.1126/science.1254699
4. Sayrin C, Junge C, Mitsch R, Albrecht B, O'Shea D, Schneeweiss P, et al. Nanophotonic Optical Isolator Controlled by the Internal State of Cold Atoms. *Phys Rev X* (2015) 5:041036. doi:10.1103/PhysRevX.5.041036
5. Rosenblum S, Bechler O, Shomroni I, Lovsky Y, Guendelman G, Dayan B. Extraction of a Single Photon from an Optical Pulse. *Nat Photon* (2016) 10:19–22. doi:10.1038/nphoton.2015.227
6. Mitsch R, Sayrin C, Albrecht B, Schneeweiss P, Rauschenbeutel A. Quantum State-Controlled Directional Spontaneous Emission of Photons into a Nanophotonic Waveguide. *Nat Commun* (2014) 5:1–5. doi:10.1038/ncomms6713
7. Junge C, O'Shea D, Volz J, Rauschenbeutel A. Strong Coupling between Single Atoms and Nontransversal Photons. *Phys Rev Lett* (2013) 110:213604. doi:10.1103/PhysRevLett.110.213604
8. Luxmoore IJ, Wasley NA, Ramsay AJ, Thijssen ACT, Oulton R, Hugues M, et al. Interfacing Spins in an InGaAs Quantum Dot to a Semiconductor Waveguide Circuit Using Emitted Photons. *Phys Rev Lett* (2013) 110:037402. doi:10.1103/PhysRevLett.110.037402
9. Lu L, Joannopoulos JD, Soljačić M. Topological Photonics. *Nat Photon* (2014) 8:821–9. doi:10.1038/nphoton.2014.248
10. Khanikaev AB, Shvets G. Two-dimensional Topological Photonics. *Nat Photon* (2017) 11:763–73. doi:10.1038/s41566-017-0048-5
11. Wu Y, Li C, Hu X, Ao Y, Zhao Y, Gong Q. Applications of Topological Photonics in Integrated Photonic Devices. *Adv Opt Mater* (2017) 5:1700357. doi:10.1002/adom.201700357
12. Xie B-Y, Wang H-F, Zhu X-Y, Lu M-H, Wang ZD, Chen Y-F. Photonics Meets Topology. *Opt Express* (2018) 26:24531–50. doi:10.1364/OE.26.024531
13. Ozawa T, Price HM, Amo A, Goldman N, Hafezi M, Lu L, et al. Topological Photonics. *Rev Mod Phys* (2019) 91:015006. doi:10.1103/RevModPhys.91.015006
14. Rider MS, Palmer SJ, Pocock SR, Xiao X, Arroyo Huidobro P, Giannini V. A Perspective on Topological Nanophotonics: Current Status and Future Challenges. *J Appl Phys* (2019) 125:120901. doi:10.1063/1.5086433
15. Kim M, Jacob Z, Rho J. Recent Advances in 2D, 3D and Higher-Order Topological Photonics. *Light Sci Appl* (2020) 9:1–30. doi:10.1038/s41377-020-0331-y
16. Iwamoto S, Ota Y, Arakawa Y. Recent Progress in Topological Waveguides and Nanocavities in a Semiconductor Photonic crystal Platform [Invited]. *Opt Mater Express* (2021) 11:319–37. doi:10.1364/OME.415128
17. Wang Z, Chong Y, Joannopoulos JD, Soljačić M. Observation of Unidirectional Backscattering-Immune Topological Electromagnetic States. *Nature* (2009) 461:772–5. doi:10.1038/nature08293
18. Ma T, Khanikaev AB, Mousavi SH, Shvets G. Guiding Electromagnetic Waves Around Sharp Corners: Topologically Protected Photonic Transport in Metawaveguides. *Phys Rev Lett* (2015) 114:127401. doi:10.1103/PhysRevLett.114.127401
19. Bahari B, Ndao A, Vallini F, El Amili A, Fainman Y, Kanté B. Nonreciprocal Lasing in Topological Cavities of Arbitrary Geometries. *Science* (2017) 358:636–40. doi:10.1126/science.aao4551
20. Parappurath N, Alpeggiani F, Kuipers L, Verhagen E. Direct Observation of Topological Edge States in Silicon Photonic Crystals: Spin, Dispersion, and Chiral Routing. *Sci Adv* (2020) 6:eaaw4137. doi:10.1126/sciadv.aaw4137
21. Xie B, Su G, Wang H-F, Liu F, Hu L, Yu S-Y, et al. Higher-order Quantum Spin Hall Effect in a Photonic crystal. *Nat Commun* (2020) 11:1–8. doi:10.1038/s41467-020-17593-8
22. Bliokh KY, Smirnova D, Nori F. Quantum Spin Hall Effect of Light. *Science* (2015) 348(6242):1448–51. doi:10.1126/science.aaa9519
23. Guo K, Wu J, Chen F, Zhou K, Liu S, Guo Z. Second Harmonic Generation Enhancement and Directional Emission from Topological Corner State Based on the Quantum Spin Hall Effect. *Opt Express* (2021) 29:26841–50. doi:10.1364/OE.432660
24. Bleu O, Solnyshkov DD, Malpuech G. Quantum valley Hall Effect and Perfect valley Filter Based on Photonic Analogs of Transitional Metal Dichalcogenides. *Phys Rev B* (2017) 95:235431. doi:10.1103/PhysRevB.95.235431
25. Yang Y, Yamagami Y, Yu X, Pitchappa P, Webber J, Zhang B, et al. Terahertz Topological Photonics for On-Chip Communication. *Nat Photon* (2020) 14:446–51. doi:10.1038/s41566-020-0618-9
26. Carmichael HJ. Quantum Trajectory Theory for Cascaded Open Systems. *Phys Rev Lett* (1993) 70:2273–6. doi:10.1103/PhysRevLett.70.2273
27. Gardiner CW. Driving a Quantum System with the Output Field from Another Driven Quantum System. *Phys Rev Lett* (1993) 70:2269–72. doi:10.1103/PhysRevLett.70.2269
28. Mitsch R, Sayrin C, Albrecht B, Schneeweiss P, Rauschenbeutel A. Directional Nanophotonic Atom-Wwaveguide Interface Based on Spin-Oorbit Interaction of Light (2014). arXivAvailable at: https://arxiv.org/abs/1406.0896 (Accessed December 13, 2021).
29. Coles RJ, Price DM, Dixon JE, Royall B, Clarke E, Kok P, et al. Chirality of Nanophotonic Waveguide with Embedded Quantum Emitter for Unidirectional Spin Transfer. *Nat Commun* (2016) 7:1–7. doi:10.1038/ncomms11183
30. Bliokh KY, Nori F. Transverse and Longitudinal Angular Momenta of Light. *Phys Rep* (2015) 592:1–38. doi:10.1016/j.physrep.2015.06.003
31. Bliokh KY, Rodríguez-Fortuño FJ, Nori F, Zayats AV. Spin-orbit Interactions of Light. *Nat Photon* (2015) 9:796–808. doi:10.1038/nphoton.2015.201
32. Aiello A, Banzer P, Neugebauer M, Leuchs G. From Transverse Angular Momentum to Photonic Wheels. *Nat Photon* (2015) 9:789–95. doi:10.1038/nphoton.2015.203
33. Luxmoore IJ, Wasley NA, Ramsay AJ, Thijssen ACT, Oulton R, Hugues M, et al. Optical Control of the Emission Direction of a Quantum Dot. *Appl Phys Lett* (2013) 103:241102. doi:10.1063/1.4845975
34. Petersen J, Volz J, Rauschenbeutel A. Chiral Nanophotonic Waveguide Interface Based on Spin-Orbit Interaction of Light. *Science* (2014) 346:67–71. doi:10.1126/science.1257671
35. Rodríguez-Fortuño FJ, Barber-Sanz I, Puerto D, Griol A, Martínez A. Resolving Light Handedness with an On-Chip Silicon Microdisk. *ACS Photon* (2014) 1:762–7. doi:10.1021/ph500084b
36. Lee S-Y, Lee I-M, Park J, Oh S, Lee W, Kim K-Y, et al. Role of Magnetic Induction Currents in Nanoslit Excitation of Surface Plasmon Polaritons. *Phys Rev Lett* (2012) 108:213907. doi:10.1103/PhysRevLett.108.213907
37. Lin J, Mueller JPB, Wang Q, Yuan G, Antoniou N, Yuan X-C, et al. Polarization-controlled Tunable Directional Coupling of Surface Plasmon Polaritons. *Science* (2013) 340:331–4. doi:10.1126/science.1233746
38. Rodríguez-Fortuño FJ, Marino G, Ginzburg P, O'Connor D, Martínez A, Wurtz GA, et al. Near-field Interference for the Unidirectional Excitation of Electromagnetic Guided Modes. *Science* (2013) 340:328–30. doi:10.1126/science.1233739
39. O'Connor D, Ginzburg P, Rodríguez-Fortuño FJ, Wurtz GA, Zayats AV. Spin-orbit Coupling in Surface Plasmon Scattering by Nanostructures. *Nat Commun* (2014) 5:1–7. doi:10.1038/ncomms6327
40. Coles RJ, Prtljaga N, Royall B, Luxmoore IJ, Fox AM, Skolnick MS. Waveguide-coupled Photonic crystal Cavity for Quantum Dot Spin Readout. *Opt Express* (2014) 22:2376–85. doi:10.1364/OE.22.002376
41. Arcari M, Söllner I, Javadi A, Lindskov Hansen S, Mahmoodian S, Liu J, et al. Near-unity Coupling Efficiency of a Quantum Emitter to a Photonic crystal Waveguide. *Phys Rev Lett* (2014) 113:093603. doi:10.1103/PhysRevLett.113.093603
42. Fong CF, Ota Y, Arakawa Y, Iwamoto S, Kato YK. Chiral Modes Near Exceptional Points in Symmetry Broken H1 Photonic crystal Cavities. *Phys Rev Res* (2021) 3:043096. doi:10.1103/PhysRevResearch.3.043096
43. Mahmoodian S, Prindal-Nielsen K, Söllner I, Stobbe S, Lodahl P. Engineering Chiral Light-Matter Interaction in Photonic crystal Waveguides with Slow Light. *Opt Mater Express* (2017) 7:43–51. doi:10.1364/OME.7.000043

44. Söllner I, Mahmoodian S, Hansen SL, Midolo L, Javadi A, Kiršanskė G, et al. Deterministic Photon-Emitter Coupling in Chiral Photonic Circuits. *Nat Nanotech* (2015) 10:775–8. doi:10.1038/nnano.2015.159
45. Xiao S, Wu S, Xie X, Yang J, Wei W, Shi S, et al. Position-dependent Chiral Coupling between Single Quantum Dots and Cross Waveguides. *Appl Phys Lett* (2021) 118:091106. doi:10.1063/5.0042480
46. Martin-Cano D, Haakh HR, Rotenberg N. Chiral Emission into Nanophotonic Resonators. *Acs Photon* (2019) 6:961–6. doi:10.1021/acsphotonics.8b01555
47. Tang L, Tang J, Zhang W, Lu G, Zhang H, Zhang Y, et al. On-chip Chiral Single-Photon Interface: Isolation and Unidirectional Emission. *Phys Rev A* (2019) 99:043833. doi:10.1103/PhysRevA.99.043833
48. Yadav RK, Liu W, Indukuri SRKC, Vasista AB, Kumar GVP, Agarwal GS, et al. Observation of Photonic Spin-Momentum Locking Due to Coupling of Achiral Metamaterials and Quantum Dots. *J Phys Condens Matter* (2020) 33:015701. doi:10.1088/1361-648X/abb650
49. Lodahl P, Mahmoodian S, Stobbe S, Rauschenbeutel A, Schneeweiss P, Volz J, et al. Chiral Quantum Optics. *Nature* (2017) 541:473–80. doi:10.1038/nature21037
50. Haldane FDM, Raghu S. Possible Realization of Directional Optical Waveguides in Photonic Crystals with Broken Time-Reversal Symmetry. *Phys Rev Lett* (2008) 100:013904. doi:10.1103/PhysRevLett.100.013904
51. Raghu S, Haldane FDM. Analogs of Quantum-Hall-Effect Edge States in Photonic Crystals. *Phys Rev A* (2008) 78:033834. doi:10.1103/PhysRevA.78.033834
52. Yan B, Xie J, Liu E, Peng Y, Ge R, Liu J, et al. Topological Edge State in the Two-Dimensional Stampfli-triangle Photonic Crystals. *Phys Rev Appl* (2019) 12:044004. doi:10.1103/PhysRevApplied.12.044004
53. Cao T, Fang L, Cao Y, Li N, Fan Z, Tao Z. Dynamically Reconfigurable Topological Edge State in Phase Change Photonic Crystals. *Sci Bull* (2019) 64:814–22. doi:10.1016/j.scib.2019.02.017
54. El-Ganainy R, Levy M. Optical Isolation in Topological-Edge-State Photonic Arrays. *Opt Lett* (2015) 40:5275–8. doi:10.1364/OL.40.005275
55. Ji C-Y, Liu G-B, Zhang Y, Zou B, Yao Y. Transport Tuning of Photonic Topological Edge States by Optical Cavities. *Phys Rev A* (2019) 99:043801. doi:10.1103/PhysRevA.99.043801
56. Gong Y, Guo L, Wong S, Bennett AJ, Oh SS. Tailoring Topological Edge States with Photonic crystal Nanobeam Cavities. *Sci Rep* (2021) 11:1–9. doi:10.1038/s41598-020-79915-6
57. Ke Y, Qin X, Mei F, Zhong H, Kivshar YS, Lee C. Topological Phase Transitions and Thouless Pumping of Light in Photonic Waveguide Arrays. *Laser Photon Rev* (2016) 10:995–1001. doi:10.1002/lpor.201600119
58. Chen W-J, Jiang S-J, Chen X-D, Zhu B, Zhou L, Dong J-W, et al. Experimental Realization of Photonic Topological Insulator in a Uniaxial Metacrystal Waveguide. *Nat Commun* (2014) 5:1–7. doi:10.1038/ncomms6782
59. Cheng X, Jouvaud C, Ni X, Mousavi SH, Genack AZ, Khanikaev AB. Robust Reconfigurable Electromagnetic Pathways within a Photonic Topological Insulator. *Nat Mater* (2016) 15:542–8. doi:10.1038/nmat4573
60. Bandres MA, Wittek S, Harari G, Parto M, Ren J, Segev M, et al. Topological Insulator Laser: Experiments. *Science* (2018) 359:359. doi:10.1126/science.aar4005
61. Fang K, Yu Z, Fan S. Realizing Effective Magnetic Field for Photons by Controlling the Phase of Dynamic Modulation. *Nat Photon* (2012) 6:782–7. doi:10.1038/nphoton.2012.236
62. Lu L, Joannopoulos JD, Soljačić M. Topological States in Photonic Systems. *Nat Phys* (2016) 12:626–9. doi:10.1038/nphys3796
63. Wang Z, Chong YD, Joannopoulos JD, Soljačić M. Reflection-free One-Way Edge Modes in a Gyromagnetic Photonic crystal. *Phys Rev Lett* (2008) 100:013905. doi:10.1103/PhysRevLett.100.013905
64. Khanikaev AB, Hossein Mousavi S, Tse W-K, Kargarian M, MacDonald AH, Shvets G. Photonic Topological Insulators. *Nat Mater* (2013) 12:233–9. doi:10.1038/nmat3520
65. Rechtsman MC, Zeuner JM, Tünnermann A, Nolte S, Segev M, Szameit A. Strain-induced Pseudomagnetic Field and Photonic Landau Levels in Dielectric Structures. *Nat Photon* (2013) 7:153–8. doi:10.1038/nphoton.2012.302
66. Tzuang LD, Fang K, Nussenzveig P, Fan S, Lipson M. Non-reciprocal Phase Shift Induced by an Effective Magnetic Flux for Light. *Nat Photon* (2014) 8:701–5. doi:10.1038/nphoton.2014.177
67. Hafezi M, Mittal S, Fan J, Migdall A, Taylor JM. Imaging Topological Edge States in Silicon Photonics. *Nat Photon* (2013) 7:1001–5. doi:10.1038/nphoton.2013.274
68. Mittal S, Fan J, Faez S, Migdall A, Taylor JM, Hafezi M. Topologically Robust Transport of Photons in a Synthetic Gauge Field. *Phys Rev Lett* (2014) 113:087403. doi:10.1103/PhysRevLett.113.087403
69. Mittal S, Goldschmidt EA, Hafezi M. A Topological Source of Quantum Light. *Nature* (2018) 561:502–6. doi:10.1038/s41586-018-0478-3
70. Hafezi M, Demler EA, Lukin MD, Taylor JM. Robust Optical Delay Lines with Topological protection. *Nat Phys* (2011) 7:907–12. doi:10.1038/nphys2063
71. Gu L, Yuan Q, Zhao Q, Ji Y, Liu Z, Fang L, et al. A Topological Photonic Ring-Resonator for On-Chip Channel Filters. *J Lightwave Technol* (2021) 39:5069–73. doi:10.1109/JLT.2021.3082558
72. Jalali Mehrabad M, Foster AP, Dost R, Clarke E, Patil PK, Farrer I, et al. A Semiconductor Topological Photonic Ring Resonator. *Appl Phys Lett* (2020) 116:061102. doi:10.1063/1.5131846
73. Slobozhanyuk AP, Khanikaev AB, Filonov DS, Smirnova DA, Miroshnichenko AE, Kivshar YS. Experimental Demonstration of Topological Effects in Bianisotropic Metamaterials. *Sci Rep* (2016) 6:1–7. doi:10.1038/srep22270
74. Wu X, Meng Y, Tian J, Huang Y, Xiang H, Han D, et al. Direct Observation of valley-polarized Topological Edge States in Designer Surface Plasmon Crystals. *Nat Commun* (2017) 8:1–9. doi:10.1038/s41467-017-01515-2
75. Chen X-D, Zhao F-L, Chen M, Dong J-W. Valley-contrasting Physics in All-Dielectric Photonic Crystals: Orbital Angular Momentum and Topological Propagation. *Phys Rev B* (2017) 96:020202. doi:10.1103/PhysRevB.96.020202
76. Gao Z, Yang Z, Gao F, Xue H, Yang Y, Dong J, et al. Valley Surface-Wave Photonic crystal and its Bulk/edge Transport. *Phys Rev B* (2017) 96:201402. doi:10.1103/PhysRevB.96.201402
77. Gao F, Xue H, Yang Z, Lai K, Yu Y, Lin X, et al. Topologically Protected Refraction of Robust Kink States in valley Photonic Crystals. *Nat Phys* (2018) 14:140–4. doi:10.1038/nphys4304
78. Rechtsman MC, Zeuner JM, Plotnik Y, Lumer Y, Podolsky D, Dreisow F, et al. Photonic Floquet Topological Insulators. *Nature* (2013) 496:196–200. doi:10.1038/nature12066
79. Noh J, Huang S, Chen KP, Rechtsman MC. Observation of Photonic Topological valley Hall Edge States. *Phys Rev Lett* (2018) 120:063902. doi:10.1103/PhysRevLett.120.063902
80. Mehrabad MJ, Foster A, Martin N, Dost R, Clarke E, Patil P, et al. A Chiral Topological Add-Drop Filter for Integrated Quantum Photonic Circuits (2021). arXivAvailable at: https://ui.adsabs.harvard.edu/abs/2021arXiv211007277J (Accessed December 16, 2021).
81. Xie X, Yan S, Dang J, Yang J, Xiao S, Wang Y, et al. Topological Cavity Based on Slow-Light Topological Edge Mode for Broadband Purcell Enhancement. *Phys Rev Appl* (2021) 16:014036. doi:10.1103/PhysRevApplied.16.014036
82. Yan Q, Hu X, Fu Y, Lu C, Fan C, Liu Q, et al. Quantum Topological Photonics. *Adv Opt Mater.* (2021) 9:2001739. doi:10.1002/adom.202001739
83. Barik S, Karasahin A, Flower C, Cai T, Miyake H, DeGottardi W, et al. A Topological Quantum Optics Interface. *Science* (2018) 359:666–8. doi:10.1126/science.aaq0327
84. Wu L-H, Hu X. Scheme for Achieving a Topological Photonic crystal by Using Dielectric Material. *Phys Rev Lett* (2015) 114:223901. doi:10.1103/PhysRevLett.114.223901
85. Hasan MZ, Kane CL. Colloquium: Topological Insulators. *Rev Mod Phys* (2010) 82:3045–67. doi:10.1103/RevModPhys.82.3045
86. Qi X-L, Zhang S-C. Topological Insulators and Superconductors. *Rev Mod Phys* (2011) 83:1057–110. doi:10.1103/RevModPhys.83.1057
87. Yang Y, Hang ZH. Topological Whispering Gallery Modes in Two-Dimensional Photonic crystal Cavities. *Opt Express* (2018) 26:21235–41. doi:10.1364/OE.26.021235
88. Sauer E, Vasco JP, Hughes S. Theory of Intrinsic Propagation Losses in Topological Edge States of Planar Photonic Crystals. *Phys Rev Res* (2020) 2:043109. doi:10.1103/PhysRevResearch.2.043109

89. Gorlach MA, Ni X, Smirnova DA, Korobkin D, Zhirihin D, Slobozhanyuk AP, et al. Far-field Probing of Leaky Topological States in All-Dielectric Metasurfaces. *Nat Commun* (2018) 9(1):1–8. doi:10.1038/s41467-018-03330-9
90. Yang Y, Xu YF, Xu T, Wang H-X, Jiang J-H, Hu X, et al. Visualization of a Unidirectional Electromagnetic Waveguide Using Topological Photonic Crystals Made of Dielectric Materials. *Phys Rev Lett* (2018) 120:217401. doi:10.1103/PhysRevLett.120.217401
91. Anderson PD, Subramania G. Unidirectional Edge States in Topological Honeycomb-Lattice Membrane Photonic Crystals. *Opt Express* (2017) 25: 23293–301. doi:10.1364/OE.25.023293
92. Barik S, Miyake H, DeGottardi W, Waks E, Hafezi M. Two-dimensionally Confined Topological Edge States in Photonic Crystals. *New J Phys* (2016) 18: 113013. doi:10.1088/1367-2630/18/11/113013
93. Arregui G, Gomis-Bresco J, Sotomayor-Torres CM, Garcia PD. Quantifying the Robustness of Topological Slow Light. *Phys Rev Lett* (2021) 126:027403. doi:10.1103/PhysRevLett.126.027403
94. Jalali Mehrabad M, Foster AP, Dost R, Clarke E, Patil PK, Fox AM, et al. Chiral Topological Photonics with an Embedded Quantum Emitter. *Optica* (2020) 7:1690–6. doi:10.1364/OPTICA.393035
95. Shalaev MI, Walasik W, Tsukernik A, Xu Y, Litchinitser NM. Robust Topologically Protected Transport in Photonic Crystals at Telecommunication Wavelengths. *Nat Nanotech* (2019) 14:31–4. doi:10.1038/s41565-018-0297-6
96. Hauff N, Hughes S, Jeannic HL, Lodahl P, Rotenberg N. Chiral Quantum Optics in Broken-Symmetry and Topological Photonic crystal Waveguides (2021). arXivAvailable at: https://arxiv.org/abs/2111.02828 (Accessed December 8, 2021).
97. Ma T, Shvets G. All-Si valley-Hall Photonic Topological Insulator. *New J Phys* (2016) 18:025012. doi:10.1088/1367-2630/18/2/025012
98. Dong J-W, Chen X-D, Zhu H, Wang Y, Zhang X. Valley Photonic Crystals for Control of Spin and Topology. *Nat Mater* (2017) 16:298–302. doi:10.1038/nmat4807
99. He X-T, Liang E-T, Yuan J-J, Qiu H-Y, Chen X-D, Zhao F-L, et al. A Silicon-On-Insulator Slab for Topological valley Transport. *Nat Commun* (2019) 10: 1–9. doi:10.1038/s41467-019-08881-z
100. Chen Y, He X-T, Cheng Y-J, Qiu H-Y, Feng L-T, Zhang M, et al. Topologically Protected valley-dependent Quantum Photonic Circuits. *Phys Rev Lett* (2021) 126:230503. doi:10.1103/PhysRevLett.126.230503
101. Yoshimi H, Yamaguchi T, Katsumi R, Ota Y, Arakawa Y, Iwamoto S. Experimental Demonstration of Topological Slow Light Waveguides in valley Photonic Crystals. *Opt Express* (2021) 29:13441–50. doi:10.1364/OE.422962
102. Yoshimi H, Yamaguchi T, Ota Y, Arakawa Y, Iwamoto S. Slow Light Waveguides in Topological valley Photonic Crystals. *Opt Lett* (2020) 45: 2648–51. doi:10.1364/OL.391764
103. Ek S, Lunnemann P, Chen Y, Semenova E, Yvind K, Mork J. Slow-light-enhanced Gain in Active Photonic crystal Waveguides. *Nat Commun* (2014) 5:1–8. doi:10.1038/ncomms6039
104. Corcoran B, Monat C, Grillet C, Moss DJ, Eggleton BJ, White TP, et al. Green Light Emission in Silicon through Slow-Light Enhanced Third-Harmonic Generation in Photonic-crystal Waveguides. *Nat Photon* (2009) 3:206–10. doi:10.1038/nphoton.2009.28
105. Yamaguchi T, Ota Y, Katsumi R, Watanabe K, Ishida S, Osada A, et al. GaAs valley Photonic crystal Waveguide with Light-Emitting InAs Quantum Dots. *Appl Phys Express* (2019) 12:062005. doi:10.7567/1882-0786/ab1cc5
106. Barik S, Karasahin A, Mittal S, Waks E, Hafezi M. Chiral Quantum Optics Using a Topological Resonator. *Phys Rev B* (2020) 101:205303. doi:10.1103/PhysRevB.101.205303
107. Sipahigil A, Evans RE, Sukachev DD, Burek MJ, Borregaard J, Bhaskar MK, et al. An Integrated diamond Nanophotonics Platform for Quantum-Optical Networks. *Science* (2016) 354:847–50. doi:10.1126/science.aah6875
108. Bhatti D, Schneider R, Oppel S, von Zanthier J. Directional Dicke Subradiance with Nonclassical and Classical Light Sources. *Phys Rev Lett* (2018) 120:113603. doi:10.1103/PhysRevLett.120.113603
109. Pichler H, Choi S, Zoller P, Lukin MD. Universal Photonic Quantum Computation via Time-Delayed Feedback. *Proc Natl Acad Sci USA* (2017) 114:11362–7. doi:10.1073/pnas.1711003114
110. Pichler H, Ramos T, Daley AJ, Zoller P. Quantum Optics of Chiral Spin Networks. *Phys Rev A* (2015) 91:042116. doi:10.1103/PhysRevA.91.042116
111. Barik S. *Chiral Quantum Optics Using Topological Photonics*. [PhD's thesis]. Maryland: University of Maryland (2020).

Conflict of Interest: The authors declare that the research was conducted in the absence of any commercial or financial relationships that could be construed as a potential conflict of interest.

Publisher's Note: All claims expressed in this article are solely those of the authors and do not necessarily represent those of their affiliated organizations, or those of the publisher, the editors and the reviewers. Any product that may be evaluated in this article, or claim that may be made by its manufacturer, is not guaranteed or endorsed by the publisher.

frontiers in Physics

ORIGINAL RESEARCH
published: 03 February 2022
doi: 10.3389/fphy.2022.831203

Bidirectional Rainbow Trapping in 1-D Chirped Topological Photonic Crystal

Sayed Elshahat[1,2] *and Cuicui Lu*[1,3]*

[1]*Key Laboratory of Advanced Optoelectronic Quantum Architecture and Measurements of Ministry of Education, Beijing Key Laboratory of Nanophotonics and Ultrafine Optoelectronic Systems, School of Physics, Beijing Institute of Technology, Beijing, China,* [2]*Physics Department, Faculty of Science, Assiut University, Assiut, Egypt,* [3]*Collaborative Innovation Center of Light Manipulations and Applications, Shandong Normal University, Jinan, China*

The rainbow trapping effect has attracted gathering attention due to its potential application in data processing, energy storage, and light-matter interaction enhancement. The interest has increased recently with the advent of topological photonic crystals (PCs), as the topological PC affords a robust platform for nanophotonic devices. We proposed a chirped one-dimensional (1D) PC as a sandwiched trapped between two1D topological PCs to realize two topological edge states (TESs) for topological protection and trap the formed rainbow. Through graded the thickness of dielectric layers of the chirped 1D PC, light of different wavelengths components localizes and stores at different spatial positions leading to rainbow trapping formation. Unidirectional rainbow trapping can be observed by progressively increasing the thicknesses of the chirped PC. Nonetheless, changing increasingly one of its thicknesses and solidifying the other leads to bidirectional rainbow trapping. Achieving bidirectional rainbow trapping will reduce the footprint of nanophotonic devices in the future. This work brings inspiration to the realization of the rainbow trapping effect and provides a way to design topological nanophotonic devices.

Keywords: rainbow trapping, topological photonic crystal, nanophotonic devices, chirped photonic crystal, topological edge state

OPEN ACCESS

Edited by:
Yiqi Zhang,
Xi'an Jiaotong University, China

Reviewed by:
Xiao-Dong Chen,
Sun Yat-sen University, China
Chen Shen,
Rowan University, United States
Fangwei Ye,
Shanghai Jiao Tong University, China

****Correspondence:***
Cuicui Lu
cuicuilu@bit.edu.cn

Specialty section:
This article was submitted to Optics and Photonics, a section of the journal Frontiers in Physics

Received: *08 December 2021*
Accepted: *10 January 2022*
Published: *03 February 2022*

Citation:
Elshahat S and Lu C (2022) Bidirectional Rainbow Trapping in 1-D Chirped Topological Photonic Crystal. Front. Phys. 10:831203. doi: 10.3389/fphy.2022.831203

INTRODUCTION

Photonics is principally concerned with the wave properties of frequency, wavevector, and polarization, representing the degrees of freedom of essential information for any optical system. Frequency plays an instrumental part in integrated photonic devices. In particular, it has been shown that in a tapered metamaterial structure, light can be trapped and slowed down in exact positions depending on its frequency [1]. This phenomenon is named a trapped rainbow, just as sunlight is scattered in a continuous color spectrum through a prism (hence the name is rainbow). The effect can also be considered as the spatial separation of the frequency components of the propagating wave. The appearance of rainbow trapping offers a novel technique for frequency routing of slow light [1]. After the formation of the first theoretical work, many successive methods were presented to realize rainbow trapping, such as metamaterials [1, 2], metasurfaces [3], plasmonic structures [4–6], phononic crystals in one-dimensional (1D) [7] and two-dimensional (2D) [8], and photonic crystals (PCs), in 1D [9], 2D [10, 11] and three-dimensional (3D) [12]. Most of the mentioned methods depend on either metallic or dielectric materials. However, metallic materials are lossy at optical wavelengths. Thus, the fully dielectric structure (PCs) is an excellent alternative to realizing rainbow trapping.

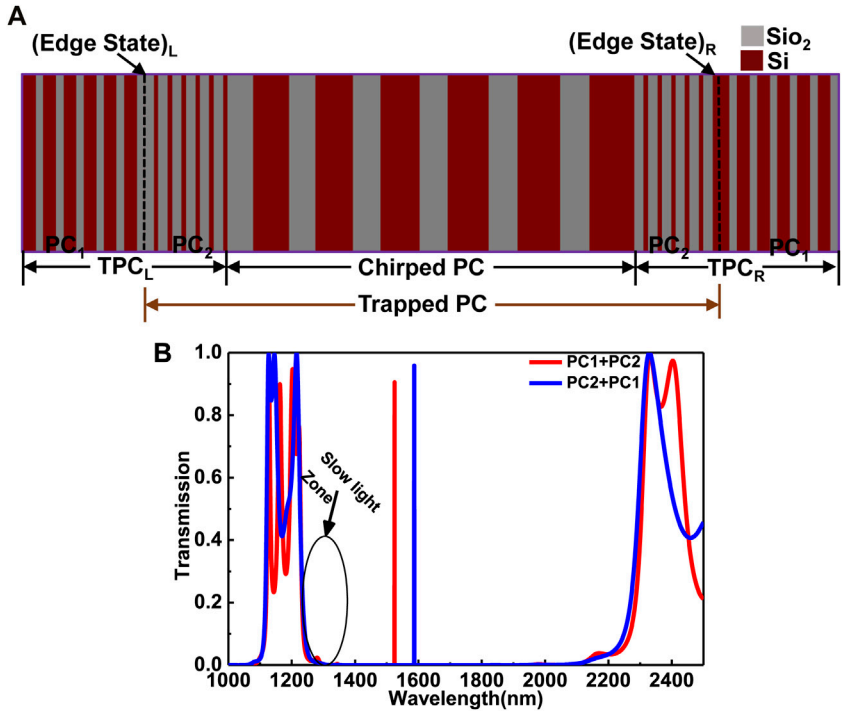

FIGURE 1 | (A) Schematic diagram of 1D PC heterostructure; **(B)** the transmission spectrum of TPC_L andTPC_R.

The rainbow trapping effect has attracted attention due to its potential applications in data processing, energy storage, and light-matter interaction enhancement. The interest has increased recently with the advent of topological PCs, which affords a robust platform for optical devices. Consequently, the combination of topology and rainbow can make possible new potentials designing topologically protected photonic devices. Due to the complex design and manufacturing structure of 2D and 3D PCs, topological PCs are preferred in the 1D structure for the advantages of simple design and ease of fabrication.

In this paper, the proposed structure is based on two-1D topological PCs to realize two topological edge states (TESs) for topological protection and trap the formed rainbow. A chirped 1D PC is inserted as a sandwiched between the two-1D topological PCs. The way to achieve the rainbow is to set the structure (or chirp) statically through one or more basic structural parameters such as position, size, and refractive index that gradually change along the direction of propagation. Through graded the thickness of dielectric layers of the chirped 1D PC, light of different wavelengths components localizes and stores at different spatial positions leading to rainbow trapping formation. The interesting observation is bidirectional rainbow trapping, increasing the thickness of one layer kind progressively and solidifying a different kind. Thus, the light propagates and localizes in both directions in the trapped area between the two TESs. Then, different frequencies can be segregated at different positions in both directions. To the best of our knowledge, this type of rainbow trapping has not been observed in topological photonics. Achieving bidirectional rainbow trapping will reduce the footprint of the nanophotonic device in the future. It is possible for this type of rainbow trapping to have numerous applications, for example, a bidirectional optical filter, a bidirectional laser, etc.

Designs and Results

The topological heterostructure of PC is based on two topological PCs, namely TPC_L and TPC_R as shown in **Figure 1A**. TPC_L is composed of two PCs (PC_1 and PC_2), from the same dielectric materials of silicon *Si* and silicon dioxide SiO_2 with refractive indices $n_{Si} = 3.48$ and $n_{SiO_2} = 1.45$, respectively. TPC_R, is composed of two PCs (PC_2 and PC_1), is the mirror image of TPC_L. PC_1 consists of six consecutive layers from *Si* and SiO_2 of layer thicknesses $d_{1Si} = 350$nm, and $d_{1SiO_2} = 225$nm, respectively, and the lattice constant of PC_1 is $a_1 = 575$nm. The thicknesses of PC_2, are evaluated based on [13], are $d_{2SiO_2} = 276$nm and $d_{2Si} = 115$nm and consists of six consecutive layers from SiO_2 and *Si*, respectively with $a_2 = 391$nm. The TESs can exist in $TPC_L\,(PC_1 + PC_2)$ and $TPC_R\,(PC_2 + PC_1)$ at the heterostructure interface because the two PCs possess bandgaps in the same wavelength range with different topological properties [14]. The transmission spectrum of TPC_L and TPC_R is shown in **Figure 1B** using the finite element method (FEM), solver package of COMSOL Multiphysics, with perfect matched layer boundary condition (PML). Two TESs formed at the left and right interfaces with a high resonated transmission peak between the two stacked PCs. The two TESs areas appeared inside the bandgap, allowing two areas of slow light zones near the bandgap edges. Whereas the two edge states work as a topological cavity to trap the light inside the

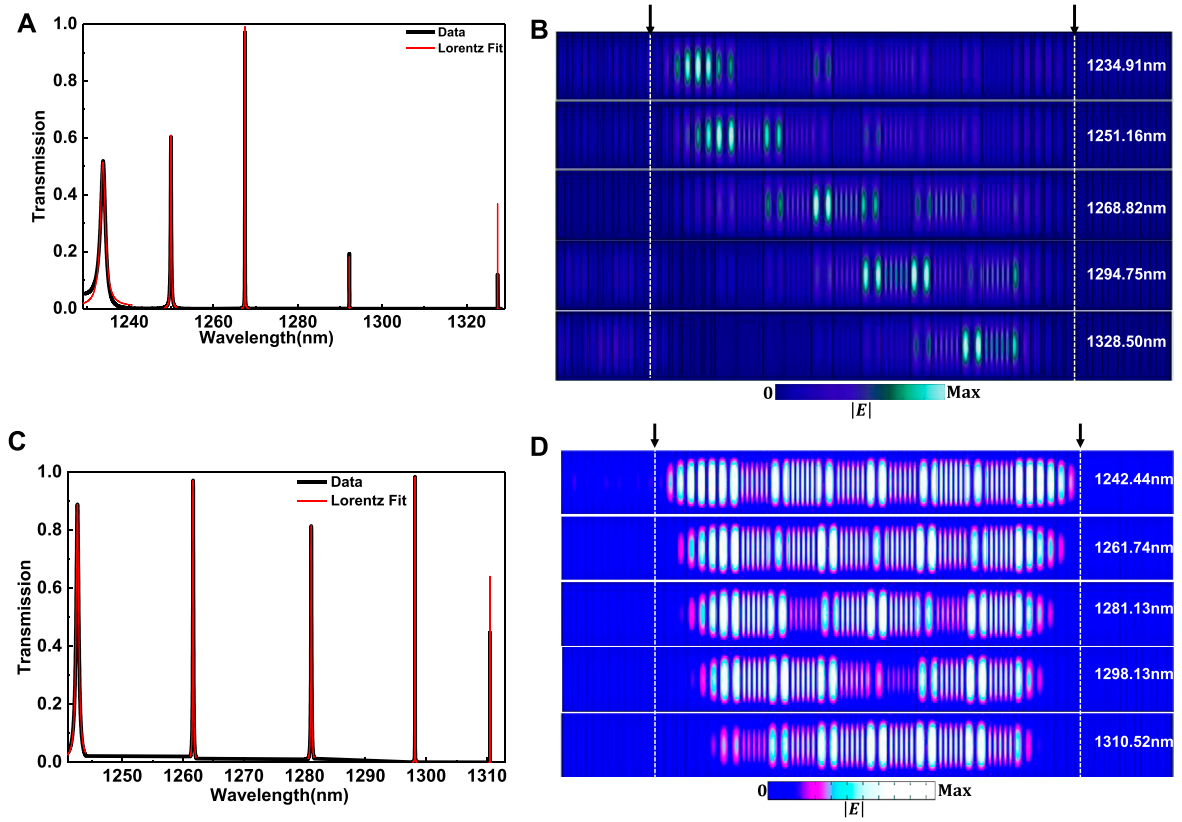

FIGURE 2 | (A) The transmission spectrum of the unidirectional rainbow trapping structure with the Lorentzian-fitting curves when d_{SiO_2} is varying from 740 to 765 nm and d_{Si} from 1,000 to 1,100 nm; **(B)** the electric field |E| intensity distribution of the unidirectional rainbow trapping at wavelengths 1234.91, 1251.16, 1268.82, 1294.75, and 1328.50 by nm; **(C)** the transmission spectrum of the bidirectional rainbow trapping structure with the Lorentzian-fitting curves of d_{SiO_2} varying from 740 to 765 nm and d_{Si} is fixed at 1,060 nm; **(D)** the |E| intensity distribution of the bidirectional rainbow trapping at wavelengths 1242.44, 1261.74, 1281.13, 1298.13, and 1310.52 by nm.

chirped structure, which may enhance the field localization and quality factor.

A linearly chirped 1D PC is inserted as a sandwiched between the two-1D topological PCs. The chirped 1D PC is composed of six consecutive layers from SiO_2 and Si. It started from SiO_2 to avoid the edge states between PC_2 and the chirped one. Consequently, PC_2, chirped PC and PC_2 formed a trapped PC, and the formed rainbow trapping will be topologically protected by the two TESs as shown in **Figure 1A**. The possibility for the light entering the trapped PC to escape is slight because the two edge states work like topological cavities. The thicknesses of SiO_2 and Si layers are d_{SiO_2} and d_{Si} respectively. Through graded d_{SiO_2} linearly from 740 to 765 nm and d_{Si} from 1,000 nm to 1,100 nm, the light can be trapped and slowed down in exact position depending on its frequency, forming a rainbow trapping effect.

Unidirectional and Bidirectional Rainbow Trapping

As mentioned above, achieving rainbow trapping is to set the structure statically through one or more basic structural parameters that gradually change along the propagation direction. Unidirectional rainbow trapping can be observed by gradually increasing d_{SiO_2} and d_{Si} of the chirped PC sandwiched between the two topological PCs. d_{SiO_2} is varying from 740 to 765 nm with an increment of 5 nm and d_{Si} from 1,000 to 1,100 nm with an increment of 20 nm. **Figure 2A** shows the transmission spectrum of the proposed structure with the fitting curves, which are symmetric in the representative Lorentzian-line shape. The resonated transmission peaks at nm wavelengths are 1234.91, 1251.16, 1268.82, 1294.75, and 1328.50, with the full width at half maximum ($FWHM$) by nm is 1.41444, 0.23029, 0.05598, 0.01136, and 5.86×10^{-4} respectively. The quality factor (Q), which is the ratio of the resonant wavelength to $FWHM$, at each resonated transmission peak is 873.07, 5.43×10^3, 2.26×10^4, 1.13×10^5, and 2.26×10^6 respectively. The high Q-factor due to the robust field localization between the two TES, which led to robust optical localization in the chirped area.

To show the formed unidirectional rainbow trapping, the electric field $|E|$ intensity distribution is calculated as shown in **Figure 2B**. Consequently, multi-modes are excited at the desired

wavelengths due to coupling light and the chirped structure. The $|E|$ intensity distributions point out the propagation of light inside the chirped PC. The $|E|$ intensity rises at the localization points. With gradually increasing the thicknesses of the chirped PC in the propagation direction and light propagates from left to right. In principle, the light will gradually slow down and eventually approach the "stop". The light of different wavelengths localizes at different spatial positions leading to rainbow trapping in the slow light zone near the left bandgap edge. The property of the bandgap rises when the wavelength of the incident light is in the order of the structure periodicity [15]. The left/right side of the chirped PC is composed of smaller $(740nm\,(d_{SiO_2}) + 1000\text{nm}\,(d_{\text{Si}})$ /larger $(765nm\,(d_{SiO_2}) + 1100\text{nm}\,(d_{\text{Si}})$ periodicity. This, in turn, affects the shorter/longer wavelengths to be trapped in the appropriate positions. As with increasing the wavelength, the trapped light moves to the right side. The lowest wavelength of 1,234.91 nm is localized near the left TES at the smaller periodicity. With increasing the wavelength, the $|E|$ intensity distributions move to the right till the right TES at the wavelength of 1,328.50 nm. The rainbow trapping bandwidth changed from 1,234.91 to 1,328.50 nm. We find that the formed rainbow is trapped between the two TESs, which act as a strong cavity and enhance the field localization and Q-factor.

The work can extend to construct bidirectional rainbow trapping by progressively increasing one of its thicknesses and solidifying the other. d_{SiO_2} is varying from 740 to 765 nm with an increment of 5 nm and d_{Si} can be fixed at any value from 1,000 to 1,100 nm. The results of fixing d_{Si} at 1060 nm is only shown. **Figure 2C** shows the transmission spectrum of the bidirectional rainbow trapping structure with the Lorentzian-fitting curves. The resonated transmission peaks that appear at wavelengths by nm are 1242.44, 1261.74, 1281.13, 1298.13, and 1310.52 with $FWHM$ by nm is 0.50719, 0.13104, 0.12927, 0.01949, and 0.00327, respectively. The Q-factor at each resonated transmission peak is 2.45×10^3, 9.77×10^3, 9.76×10^3, 6.66×10^4, and 4.00×10^5, respectively. The $|E|$ intensity distribution is shown in **Figure 2D**. The field localization is observed in both directions near the two TESs with a smaller wavelength. The two TESs work as a cavity to trap the light inside the chirped PC and make the possibility of light escaping slightly. With increasing the wavelength value, filed localization is shrinking into the chirped PC to form a unidirectional rainbow in both directions simultaneously. Accordingly, the different wavelengths from the wave packet can be segregated spatially at different positions in both directions, and bidirectional rainbow trapping is realized clearly. To the best of our knowledge, this kind of rainbow has not been observed yet in topological photonics. It may possess numerous applications, such as bidirectional devices. Realizing bidirectional rainbow trapping will diminish the footprint of nanophotonic devices in the future.

With increasing the number of alternative layers of the chirped PC, a higher Q-factor and multi-localized modes are obtained. Unidirectional and bidirectional rainbow trapping can be realized by considering ten periods of the chirped PC sandwiched between the two topological PCs. Through the same manner, unidirectional rainbow trapping is detected by gradually increasing d_{SiO_2} and d_{Si} of the chirped PC. d_{SiO_2} is varying from 740 to 785 nm with an increment of 5 nm and d_{Si} from 1,000 to 1,180 nm with an increment of 20 nm. Multi-modes are increased and excited at the desired wavelengths due to coupling light and the increased chirped PC. **Figure 3A** shows only three localized modes of the |E| intensity distribution of the formed unidirectional rainbow at 1233.58, 1305.83, and 1410.54 by nm. Different wavelengths localize in different spatial locations. Whereas the wavelength increases, the locations where the light is trapped move to the right side, as shown in **Figure 3A**. For the bidirectional rainbow trapping, it can be created by gradually thickening d_{SiO_2} and anchoring d_{Si}. A bidirectional rainbow is observed for fixing d_{Si} at any value from 1,000 to 1,180 nm with d_{SiO_2} is varying from 740 nm to 785 nm. **Figure 3B** shows the results of fixing d_{Si} at 1060 nm of the |E| intensity distribution of the bidirectional rainbow trapping at 1239.93, 1277.23, and 1308.64 by nm. It seen clearly from **Figure 3B**, as the wavelength value increases, the localization deposited in the chirped PC shrinks to form a unidirectional rainbow in both directions simultaneously. Hence, the bidirectional rainbow can be achieved. Summing up, as the number of periods increases, the transmittance remains high due to both TESs serving as a light-trapping cavity within the chirped PC, but with a very fine meshing and a small step size. It should be noted that increasing the number of periods will increase the manufacturing effort and cost. The less of the periods, the smaller size of the structures, and it is better for the integration of nanophotonic devices. We use six smaller periods for both topological PCs and chirped PC; thus, the trapped PC is 18 periods under the premise of good performance.

FDTD Validation

The proposed PC heterostructure was modeled by the finite-difference-time-domain (FDTD) method to validate the propagation properties. A high resolution (grid size for each dimension) of $30/\boldsymbol{a}_1$ is used, which is small enough to resolve a minor feature in the fields and structure during the simulation. A PML boundary is added to the edge of the domain of about $\boldsymbol{a}_1$ to absorb all incident energy without producing reflections. A Gaussian source was launched for FDTD calculation and placed in the middle of the trapped PC, as shown in **Figure 4A**. During the simulation, two monitors are introduced to study the spectral characteristics of the structure at specific wavelength/frequency values and used to measure the steady-state properties for the field distribution. The first and second monitors (M1 and M2) are placed at the trapped PC's beginning and ending, respectively. **Figures 4B,C** show the electric field intensity amplitude $(\boldsymbol{E}_z^2)$ along the propagation (z) of unidirectional and bidirectional rainbow trapping, respectively, at the center point of the x-y-plane.

In the case of unidirectional rainbow trapping of $\boldsymbol{d_{SiO_2}}$ linearly varies from 740 to 765 nm with $\boldsymbol{d_{Si}}$ from 1,000 to 1,100 nm, and based on the above explanation, at low wavelengths, M1 records the highest amplitude of the electric field intensity indicating the field localization, and the amplitude is minimized at M2 simultaneously. When the wavelength increases, the intensity begins to decrease at M1

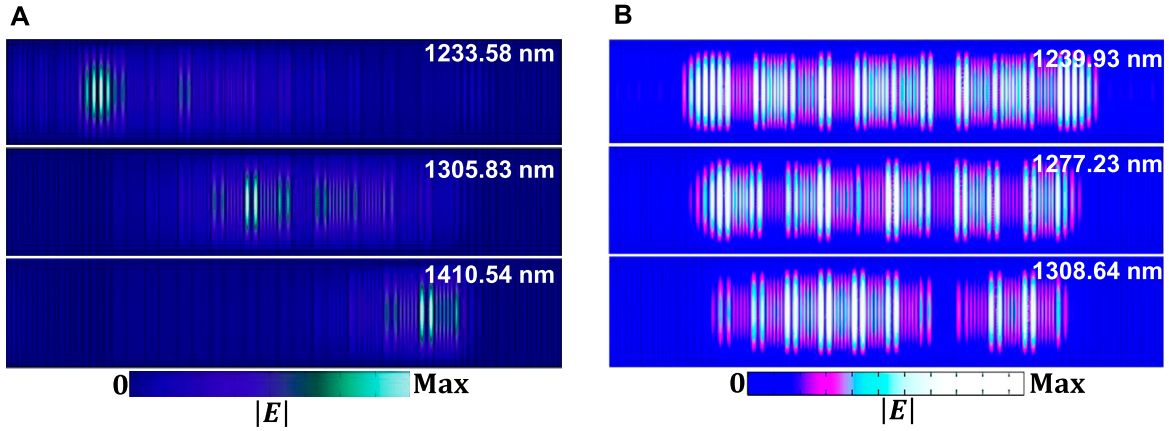

FIGURE 3 | (A) The |E| intensity distribution of the unidirectional rainbow trapping at wavelengths 1233.58, 1305.83, and 1410.54 by nm when d_{SiO_2} is varying from 740 nm to 785 nm with an increment of 5 nm and d_{Si} from 1000 nm to 1180 nm with an increment of 20 nm; **(B)** the |E| intensity distribution of the bidirectional rainbow trapping at wavelengths 1239.93, 1277.23, and 1308.64 by nm, when d_{SiO_2} is varying from 740 nm to 785 nm with an increment of 5 nm and d_{Si} is fixed at 1060 nm.

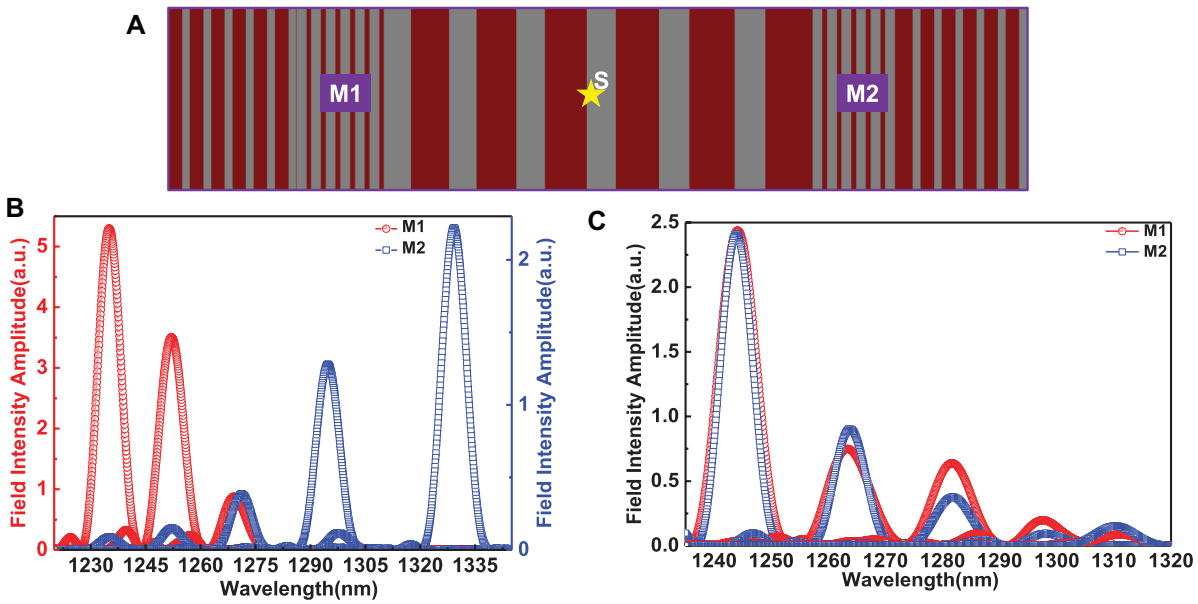

FIGURE 4 | (A) FDTD set up of grid size $30/a_1$ with placing a Gaussian source in the middle of the trapped PC and two monitors (M1, M2) to the left and right, respectively; The electric field intensity amplitude (E_z^2) of **(B)** unidirectional **(C)** bidirectional rainbow trapping.

gradually and vice versa at M2 because the field localization moves progressively from left to right with increasing the wavelength, which is illustrated in **Figure 4B**. A complete agreement with the previous section's results as shown in **Figure 2B**. However, there is a minor disparity in the values of wavelengths between FEM and FDTD methods, principally originating from the limited discretization of grid size in FDTD and the number of mesh points for FEM calculations.

Then, to verify bidirectional rainbow trapping, the same above condition are fixed but with d_{SiO_2} is varying from 740 to 765 nm and d_{Si} is fixed at 1,060 nm. The highest field intensity of M1 is located sequentially in the trapped PC from the left side (with the smallest wavelength) to the right side (with the largest wavelength). On the contrary, for M2, the highest field intensity is located sequentially in the trapped PC from the right side (with the smallest wavelength) to the left side (with the largest wavelength), as shown in **Figure 4C**, confirming the results in **Figure 2D**. The two TESs works as a cavity which cases exchange with transfer the energy flow between the two cavities of the forward and backward propagation. Meanwhile, rainbow

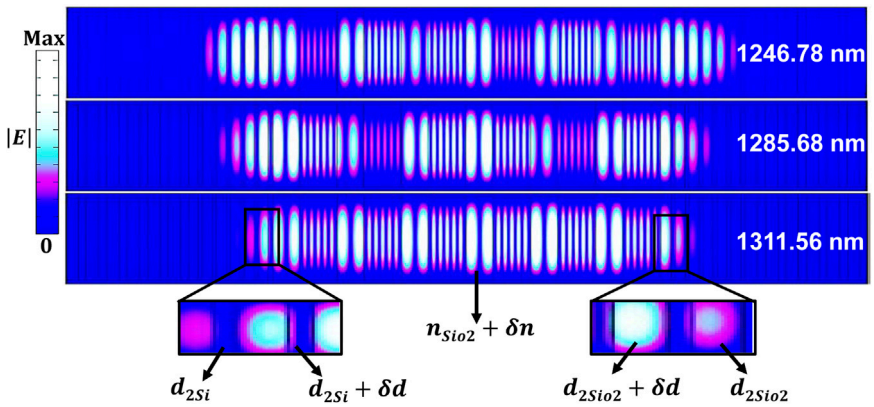

FIGURE 5 | Bidirectional rainbow trapping realization with disordering of some parameters, the inset shows the deformation in last and first layers of PC_2 from TPC_L and TPC_R respectively.

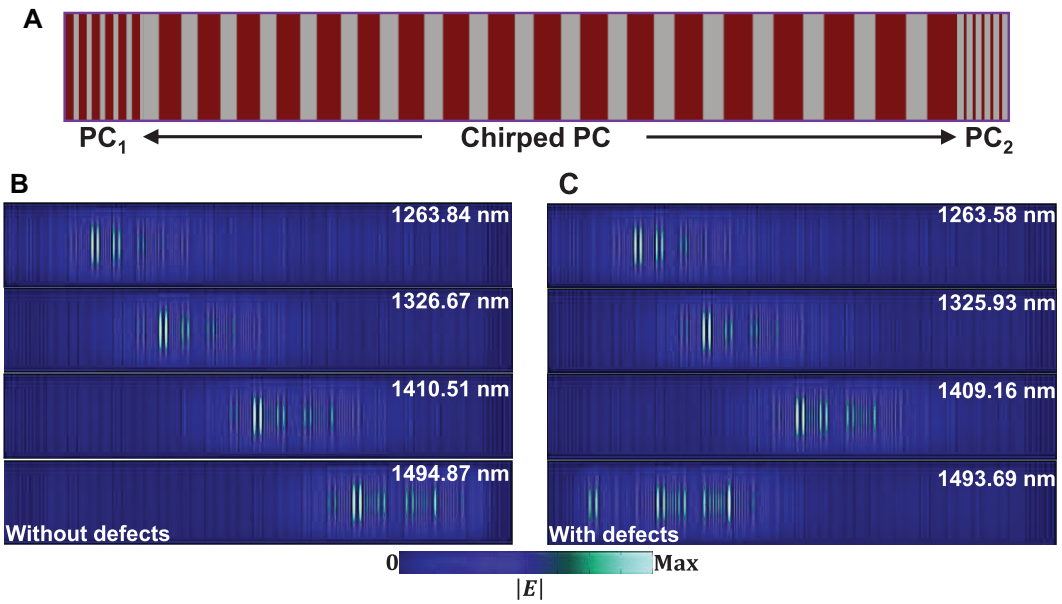

FIGURE 6 | (A) Schematic diagram of the chirped PC sandwiched between two PCs. The |E| intensity distribution of the trivial unidirectional rainbow trapping of 18 periods of the trapped chirped PC between PC_1 and PC_2 **(B)** without defects; **(C)** with defects by the disordering of some parameters (deformation in last and first layers of PC_1 and PC_2 respectively).

trapping is observed in both FEM and FDTD methods, which confirms our simulation results.

Immune to Defects

The critical step is to confirm that the formed rainbow is robust and topologically protected from disorders by the two TESs on both sides. Some disorders are introduced in the trapped PC (PC_2, chirped PC and PC_2) between the two TESs through changing thickness or refractive index of some layers. Three cases are considered; the last layer of PC_2 (d_{2Si}) from the TPC_L is deformed by $\delta d = \pm 0.05a_2$. Via the same amount of deformation ($\pm 0.05a_2$) is applied on the first layer of PC_2 (d_{2Si}) from the TPC_R. The last case is changing the refractive index of the middle SiO_2 in the chirped PC by $\delta n = \pm 0.01$. By applying each case individually or combined, rainbow tapping is achieved with a slight shifting in the wavelength. **Figure 5** shows the realization of bidirectional rainbow trapping with disordering of all deformed cases together. We can see clearly, the |E| intensity distribution is highly localized in the trapped PC due to topological protection by the two TESs even in the presence of disorders. Bidirectional rainbow trapping is still observed on both sides but with slight shifting in

wavelengths. Accordingly, the formed rainbow is robust and immune to disorders.

Trivial Rainbow Trapping

Trivial rainbow trapping is realized through the same modality by introducing a chirped PC as a trapped structure between two conventional PCs. In the exact mechanism as mentioned above, introducing a chirped PC as a sandwiched between two topological PCs (TPC_L and TPC_R). Under the same conditions and variables, values of PC_1 and PC_2 are setups, and the chirped PC consists of 18 periods from SiO_2 and Si as shown in **Figure 6A**. The bidirectional trivial rainbow trapping as in the content of the topological case cannot be formed when d_{Si} is fixed at any value from 1,000 to 1,340 nm and d_{SiO_2} is varying from 740 to 825 nm. This is because the two TESs act as a cavity to transfer the energy flow between the two cavities of the forward and backward propagation and make the possibility of light escaping slightly. Therefore, the formed bidirectional rainbow may occur in the topological case.

Unidirectional trivial rainbow trapping can be formed with the same conditions for topological cases. When d_{SiO_2} is varying from 740 to 825 nm with an increment of 5 nm and d_{Si} from 1,000 to 1,340 nm with an increment of 20 nm, as shown in **Figure 6B**. The trivial unidirectional rainbow trapping is observed but lacks highly field localization and light confinement compared with the topological case due to the robust field localization between the two TES, which resulted in a robust optical localization in the chirped region. Some disorders are introduced. The last and the first layer of PC_1 and PC_2 (d_{2SiO_2}) on the left and right sides respectively are deformed by $\delta d = \pm 0.05a_2$ with changing the refractive index of the middle SiO_2 in the chirped PC by $\delta n = \pm 0.01$. **Figure 6C** shows the formed trivial rainbow trapping with disordering. Two points are observed clearly between the two cases; some localized modes occurred at the same wavelengths, and others slightly shifted. However, the case of 1,493.69 nm is localized at a different position without defects.

CONCLUSIONS

In conclusion, a unidirectional and bidirectional rainbow trapping have been investigated. The main idea is based on trapping a chirped PC as a sandwich between two edge states. At the same time, the two edge states work as a cavity to trap the light inside the chirped structure and can be propagated in both directions. Consequently, different frequencies from the wave packet segregate at different positions in both directions. Moreover, the propagation properties are validated using FDTD by measuring the electric field intensity amplitude. In addition, we confirmed that the formed rainbow is robust and topologically protected even in the presence of disorders. Bidirectional rainbow trapping will open a feasible way for numerous applications, e.g., multichannel wavelength demultiplexers, bidirectional optical filter, and bidirectional laser.

DATA AVAILABILITY STATEMENT

The original contributions presented in the study are included in the article/Supplementary Material, further inquiries can be directed to the corresponding author.

AUTHOR CONTRIBUTIONS

SE conceived the idea, performed the numerical simulations, and wrote the draft of the manuscript. CL checked the simulation results and revised the manuscript. CL supervised the project.

FUNDING

National Natural Science Foundation of China (91850117, 11654003); Beijing Institute of Technology Research Fund Program for Young Scholars.

REFERENCES

1. Tsakmakidis KL, Boardman AD, Hess O. 'Trapped Rainbow' Storage of Light in Metamaterials. *Nature* (2007) 450(7168):397–401. doi:10.1038/nature06285
2. Hu H, Ji D, Zeng X, Liu K, Gan Q. Rainbow Trapping in Hyperbolic Metamaterial Waveguide. *Sci Rep* (2013) 3(1):1249. doi:10.1038/srep01249
3. Xu Z, Shi J, Davis RJ, Yin X, Sievenpiper DF. Rainbow Trapping with Long Oscillation Lifetimes in Gradient Magnetoinductive Metasurfaces. *Phys Rev Appl* (2019) 12(2):024043. doi:10.1103/PhysRevApplied.12.024043
4. Gan Q, Ding YJ, Bartoli FJ. "Rainbow" Trapping and Releasing at Telecommunication Wavelengths. *Phys Rev Lett* (2009) 102(5):056801. doi:10.1103/PhysRevLett.102.056801
5. Chen L, Wang GP, Gan Q, Bartoli FJ. Rainbow Trapping and Releasing by Chirped Plasmonic Waveguides at Visible Frequencies. *Appl Phys Lett* (2010) 97(15):153115. doi:10.1063/1.3502487
6. Schuller JA, Barnard ES, Cai W, Jun YC, White JS, Brongersma ML. Plasmonics for Extreme Light Concentration and Manipulation. *Nat Mater* (2010) 9(3):193–204. doi:10.1038/nmat2630
7. Chaplain GJ, De Ponti JM, Aguzzi G, Colombi A, Craster RV. Topological Rainbow Trapping for Elastic Energy Harvesting in Graded Su-Schrieffer-Heeger Systems. *Phys Rev Appl* (2020) 14(5):054035. doi:10.1103/PhysRevApplied.14.054035
8. Ungureanu B, Makwana MP, Craster RV, Guenneau S. Localizing Elastic Edge Waves via the Topological Rainbow Effect. *Phys Rev Appl* (2021) 15(1):014057. doi:10.1103/PhysRevApplied.15.014057
9. Shen Y, Fu J, Yu G. Rainbow Trapping in One-Dimensional Chirped Photonic Crystals Composed of Alternating Dielectric Slabs. *Phys Lett A* (2011) 375(43): 3801–3. doi:10.1016/j.physleta.2011.08.023
10. Lu C, Wang C, Xiao M, Zhang ZQ, Chan CT. Topological Rainbow Concentrator Based on Synthetic Dimension. *Phys Rev Lett* (2021) 126(11): 113902. doi:10.1103/PhysRevLett.126.113902
11. Zhang H, Qian L, Wang C, Lu C., Liu Y, Chen J, et al. Topological Rainbow Based on Graded Topological Photonic Crystals. *Opt Lett* (2021) 46(6): 1237–40. doi:10.1364/OL.419271
12. Hayran Z, Kurt H, Staliunas K. Rainbow Trapping in a Chirped Three-Dimensional Photonic crystal. *Sci Rep* (2017) 7(1):3046. doi:10.1038/s41598-017-03454-w

13. Elshahat S, Abood I, Esmail MSM, Ouyang Z, Lu C. One-Dimensional Topological Photonic Crystal Mirror Heterostructure for Sensing. *Nanomaterials* (2021) 11(8):1940. doi:10.3390/nano11081940
14. Dal Lago V, Atala M, Foa Torres LEF. Floquet Topological Transitions in a Driven One-Dimensional Topological Insulator. *Phys Rev A* (2015) 92(2): 023624. doi:10.1103/PhysRevA.92.023624
15. Kurt H, Yilmaz D. Rainbow Trapping Using Chirped All-Dielectric Periodic Structures. *Appl Phys B* (2013) 110(3):411–7. doi:10.1007/s00340-012-5270-8

Conflict of Interest: The authors declare that the research was conducted in the absence of any commercial or financial relationships that could be construed as a potential conflict of interest.

Publisher's Note: All claims expressed in this article are solely those of the authors and do not necessarily represent those of their affiliated organizations, or those of the publisher, the editors and the reviewers. Any product that may be evaluated in this article, orclaim that may be made by its manufacturer, is not guaranteed or endorsed by the publisher.

frontiers in Physics

REVIEW
published: 08 February 2022
doi: 10.3389/fphy.2022.845624

Hermitian and Non-Hermitian Dirac-Like Cones in Photonic and Phononic Structures

Jie Luo[1,2] *and Yun Lai*[3]*

[1]School of Physical Science and Technology, Soochow University, Suzhou, China, [2]Institute of Theoretical and Applied Physics, Soochow University, Suzhou, China, [3]National Laboratory of Solid State Microstructures, School of Physics and Collaborative Innovation Center of Advanced Microstructures, Nanjing University, Nanjing, China

Accidental degeneracy plays an important role in the generation of novel band dispersions. Photonic structures that exhibit an accidental Dirac-like conical dispersion at the center of the Brillouin zone can behave like a zero-index material at the Dirac-point frequency, leading to a number of unique features, such as invariant phase in space, wave tunneling, photonic doping and anti-doping, etc. Such a phenomenon has been explored in on-chip structures or three dimensions recently. The introduction of non-Hermiticity into the system *via* loss or gain could transform the accidental Dirac-like cone into a spawning ring of exceptional points, a complex Dirac-like cone or other unique dispersions. Similar Dirac-like cones and related physics are also observed in phononic structures. This review presents an overview of the accidental-degeneracy-induced Dirac-like cones at the center of the Brillouin zone in both photonic and phononic structures, including the fundamental physics, effective-medium description and experimental demonstration, as well as current challenges and future directions.

Keywords: zero refractive index, photonic/phononic band structure, metamaterials, Dirac/Dirac-like cones, non-Hermitian optics

OPEN ACCESS

Edited by:
Xiaoyong Hu,
Peking University, China

Reviewed by:
Meng Xiao,
Hong Kong University of Science and Technology, Hong Kong SAR, China
Qiuchen Yan,
Peking University, China

***Correspondence:**
Yun Lai
laiyun@nju.edu.cn

Specialty section:
This article was submitted to Optics and Photonics, a section of the journal Frontiers in Physics

Received: *30 December 2021*
Accepted: *19 January 2022*
Published: *08 February 2022*

Citation:
Luo J and Lai Y (2022) Hermitian and Non-Hermitian Dirac-Like Cones in Photonic and Phononic Structures. Front. Phys. 10:845624. doi: 10.3389/fphy.2022.845624

INTRODUCTION

Dirac cones or conical dispersions are unique features in some electronic band structures that describe unusual electron transport properties of materials like graphene. The electronic band structure of graphene near the Fermi level can be described by the massless Dirac equation near the six corners of the two-dimensional (2D) hexagonal Brillouin zone at the K and K' points [1, 2]. The linear dispersion can be visualized as two cones meeting at the Fermi level at the Dirac point, and the conical dispersion near the Dirac point is usually referred to as Dirac cones. Due to this unusual conical dispersion, graphene exhibits intriguing transport properties [1, 2], such as abnormal quantum Hall effect, Zitterbewegung, Klein tunneling, anti-localization, etc.

Dirac cone dispersions can also be observed in classical wave periodic structures such as photonic crystals (PhCs) [3, 4] and phononic crystals (PnCs) [5–8]. As photonic/acoustic analogue of graphene, 2D triangular/honeycomb PhCs [9–24] and PnCs [23, 25–28] have been demonstrated to possess Dirac cones near the K and K' points. This type of Dirac cones of double degeneracy are usually stable to the material parameters as long as the system exhibits the perfect symmetry (e.g., $C_{3(v)}$ and $C_{6(v)}$, and time reversal) [28].

Besides the structural symmetry, Dirac cones can also be created by accidental degeneracy through engineering the material and geometrical parameters [29–31]. In 2011, Huang et al.

demonstrated a Dirac cone at the center of the Brillouin zone, i.e., the Γ point with $\mathbf{k} = 0$, of a square lattice of 2D dielectric PhC [32]. The physical origin of this Dirac cone is different from the symmetry-protected Dirac cones occurring at high-symmetry points (i.e., K and K' points of a triangular/honeycomb lattice). The symmetry-protected Dirac cone is a result of double degeneracy and carries a π Berry phase. While the Dirac cone at the center of the Brillouin zone is a result of triple degeneracy, i.e., accidental degeneracy of a doubly degenerate mode and a single mode. The linear dispersions created by triply degenerate modes cannot be mapped into the Dirac Hamiltonian and carry no Berry phase. Therefore, the conical linear dispersions with triple degeneracy at the Brillouin zone center induced by accidental degeneracy instead of structural symmetry is called Dirac-like cones [23].

The presence or absence of Dirac-like cones is determined by the combination of mode symmetries [33, 34]. We should emphasize that accidental degeneracy can also lead to Dirac cones of double degeneracy in periodic systems without structural symmetry and at almost any k point in the Brillouin zone [35], i.e. beyond the Brillouin zone center, edges and high-symmetry lines. Such accidental-degeneracy-induced Dirac cones in general can be achieved by closing band gaps at a desired k point with a band engineering method [35] or other optimization techniques [36–40].

The PhC possessing a Dirac-like cone at the Γ point is of particular interest, because it offers an effective refractive index of zero at the Dirac-point frequency. It was discovered that such a PhC behaves like an impedance-matched zero index material (ZIM) [41–43] with $\varepsilon_{\text{eff}} = \mu_{\text{eff}} = 0$ at the Dirac-point frequency, and the linear dispersions could be understood from the effective medium perspective [32]. In this sense, this type of PhCs is an important class of dielectric metamaterials [44]. Possessing an infinite effective wavelength and zero spatial phase change, ZIMs exhibit extraordinary physical properties that enable many applications including directive emission [45–47], tunneling waveguides [48–50], energy flux control [51–56], photonic doping [57–61], cloaking and anti-doping [62–65], transmission and scattering manipulation [65–74], perfect absorption [59, 60, 75–80] and nonlinearity enhancement [81–85], etc. To date, the ZIMs have become an important class of artificial electromagnetic materials with potential applications in the wide spectrum from microwaves to optical frequencies. The dielectric PhCs with a Dirac-like cone at the center of the Brillouin zone provide a feasible and promising route towards ultralow-loss ZIMs.

The PhC with a Dirac-like cone has attracted significant research interest [23, 33, 35, 40, 59, 60, 64, 86–121]. Extensive investigations revealed many unique and interesting features. For instance, double Dirac cones, as a pair of two identical and overlapping Dirac cones, were observed at the Γ point of by utilizing a fourfold accidental degeneracy in triangular PhCs [100, 122, 123]. The double Dirac cones can also be obtained through folding the Dirac cones at the K and K' points in a honeycomb PhC to the Γ point [124–126]. Dual-polarization Dirac-like cones, i.e., the existence of Dirac-like cones for both transverse electric and magnetic polarizations in 2D PhC, have been proposed [39, 127, 128]. Semi-Dirac cones, which exhibit linear-parabolic dispersion, were created by the accidental degeneracy of two modes with a linear dispersion in one direction but a quadratic dispersion in the other direction [129–134]. The PhC with a semi-Dirac cone behaves as an intriguing class of anisotropic ZIM with $\varepsilon_{\text{eff}} = \mu_{\text{eff}} = 0$ along only one direction.

The Dirac cone system has been extended from the original 2D to on-chip platform or the bound state in continuum (BIC) [22, 135–147] and three-dimension (3D) [148–150], and from the original Hermitian (lossless) to non-Hermitian (lossy or gain) ones [136, 151–155]. It was discovered that the Dirac degeneracy can be straightforwardly linked to exceptional points (EPs) through the introduction of non-Hermiticity, i.e., material loss, gain, or open boundaries. The EP is a singularity in a non-Hermitian system where two or more eigenvalues and their associated eigenfunctions collapse into one eigenvalue or eigenfunction [156–158]. Besides photonic structures, the concept of Dirac-like cones has also been applied to other kinds of classical wave structures, including acoustic and elastic structures [23, 28, 148, 159–174].

This review presents an overview of Dirac-like cones from Hermitian and non-Hermitian systems in both photonic and phononic structures. We will introduce the fundamental physics, effective-medium description and experimental demonstration, as well as current challenges and potential directions of future research.

PHOTONIC CRYSTALS WITH A DIRAC-LIKE CONE AS ZERO INDEX MATERIALS

Figure 1A shows an example of a 2D PhC that exhibits a Dirac-like cone at the center of the Brillouin zone. The PhC consists of a square lattice of dielectric cylinders. The polarization is transverse-magnetic polarization, with electric field parallel to the cylinder axis. A Dirac-like cone, i.e., the triply-degenerate point, occurs at the Γ point. It comprises two linear bands that generate conical dispersions and an additional flat band. The two linear bands correspond to the accidental degeneracy of the electric monopole and magnetic dipole modes, whereas the flat band corresponds to the magnetic dipole mode in a rotated orientation, as shown by the right panel of **Figure 1A**. The doubly degenerate dipole modes correspond to the fields rotated by 90° with the wave vector perpendicular or parallel to the dipole moment (i.e., transverse or longitudinal dipole mode), as the result of C_{4v} symmetry of the PhC. The flat band is the consequence of the longitudinal dipole mode whose magnetic field is parallel to the wave vector, which is inaccessible from normal incidence.

In the vicinity of the Γ point where the in-plane wave vector $\mathbf{k}$ is small, the band structure of the PhC can be described by an effective Hamiltonian given by first-order degenerate perturbation theory [33, 136].

$$H_{\text{eff}} = \begin{pmatrix} \omega_D & v_g|\mathbf{k}| & 0 \\ v_g|\mathbf{k}| & \omega_D & 0 \\ 0 & 0 & \omega_D \end{pmatrix} \tag{1}$$

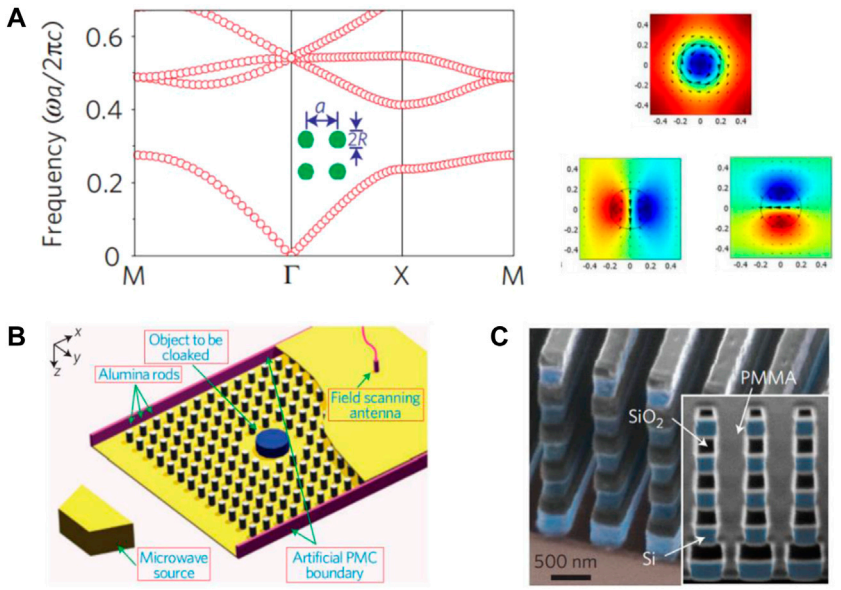

FIGURE 1 | (A) The band structure of a PhC consisting of a square lattice of dielectric rods. Two branches with linear dispersion intersect at a triply-degenerate point at the Γ point, forming a Dirac-like cone. The right panel shows the distributions of out-of-plane electric fields (color) and in-plane magnetic fields (arrows) of the eigenstates near the Dirac-like point. **(B)** The PhC with a Dirac-like cone was experimentally demonstrated in the microwave regime using a square array of alumina rods. Reproduced with permission from Ref. [32]. **(C)** A PhC consisting of horizontal square array of silicon bars was demonstrated to exhibit the Dirac-like cone in the infrared regime. Reproduced with permission from Ref. [91].

where ω_D is the Dirac-point frequency, v_g is the group velocity of the linear Dirac dispersion. The effective Hamiltonian has three eigenvalues as

$$\omega_1 = \omega_D + v_g|\mathbf{k}|,\ \omega_2 = \omega_D - v_g|\mathbf{k}|,\ \omega_3 = \omega_D \tag{2}$$

The first two eigenvalues indicate the conical linear dispersion in the vicinity of Dirac-point frequency, while third one is related to the intersecting flat band.

The experimental observation of the Dirac-like cone was realized in the microwave regime by Huang et al in 2011 [32] using a square array of alumina rods embedded within a parallel-plate waveguide, as schematically shown in **Figure 1B**. In the experimental implementation, the alumina rods have a finite height of 16 mm. To realize effective 2D PhC with infinite height, aluminum plates, as perfect electric conductor boundaries, are utilized to form a parallel plate waveguide. At the Dirac-point frequency, the PhC was found to behave like an impedance-matched ZIM with $\varepsilon_{\text{eff}} = \mu_{\text{eff}} = 0$. Experimental observation has clearly verified the ZIM-enabled cloaking and lensing effect with this PhC.

The optical PhC with a Dirac-like cone was demonstrated by Moitra et al in 2013 [91]. We note that the implementation at microwave frequencies cannot be directly transplanted to the optical frequencies because the dissipation loss of metal plates is dramatic. Therefore, an out-of-plane configuration by patterning horizontal square array of silicon bars was proposed instead (**Figure 1C**). The measured spectrum shows a ZIM-induced transmission peak at the wavelength of 1,409 nm, corresponding to the Dirac-like point. Furthermore, ZIM-enabled applications including angular selectivity of transmission and directional quantum dot emission were experimentally demonstrated.

It is noteworthy that the Dirac-like cone is a consequence of accidental degeneracy rather than structural symmetry. When the system parameters (e.g., cylinder radius or relative permittivity) are changed, the triple degenerate modes at the Dirac point will split into a single monopole mode and doubly degenerate dipole modes, forming a photonic band gap [32]. The band edge points at the Γ point are related to the zero effective parameters, because the phase accumulation on adjacent unit cell boundaries is zero. It is found that the zero permittivity, i.e., $\varepsilon_{\text{eff}} = 0$, originates from the electric monopole resonance, while the zero permeability, i.e., $\mu_{\text{eff}} = 0$, originates from the doubly degenerate magnetic dipole resonance [47]. However, due to the quadratic dispersions at band edges, the zero parameter leads to zero group velocity. Interestingly, the accidental degeneracy of the monopole and dipole modes turns the quadratic dispersion into a linearly conical dispersion with $\varepsilon_{\text{eff}} = \mu_{\text{eff}} = 0$, but with a non-zero group velocity. In addition, due to the ultralow-loss of the dielectric materials, the PhCs with a Dirac-like cone are excellent candidates for the ultralow-loss ZIMs.

ZIMs with a Dirac-like cone and a finite group velocity enable many intriguing applications. In the following, we give three examples of unique applications. The first one is the hybrid invisibility cloak based on the integration of metasurfaces and ZIM (**Figure 2A**) [64]. The key functionalities of wavefront tailoring with the metasurfaces and wave energy tunneling with the ZIM are combined together to achieve the invisibility cloak. The second one is

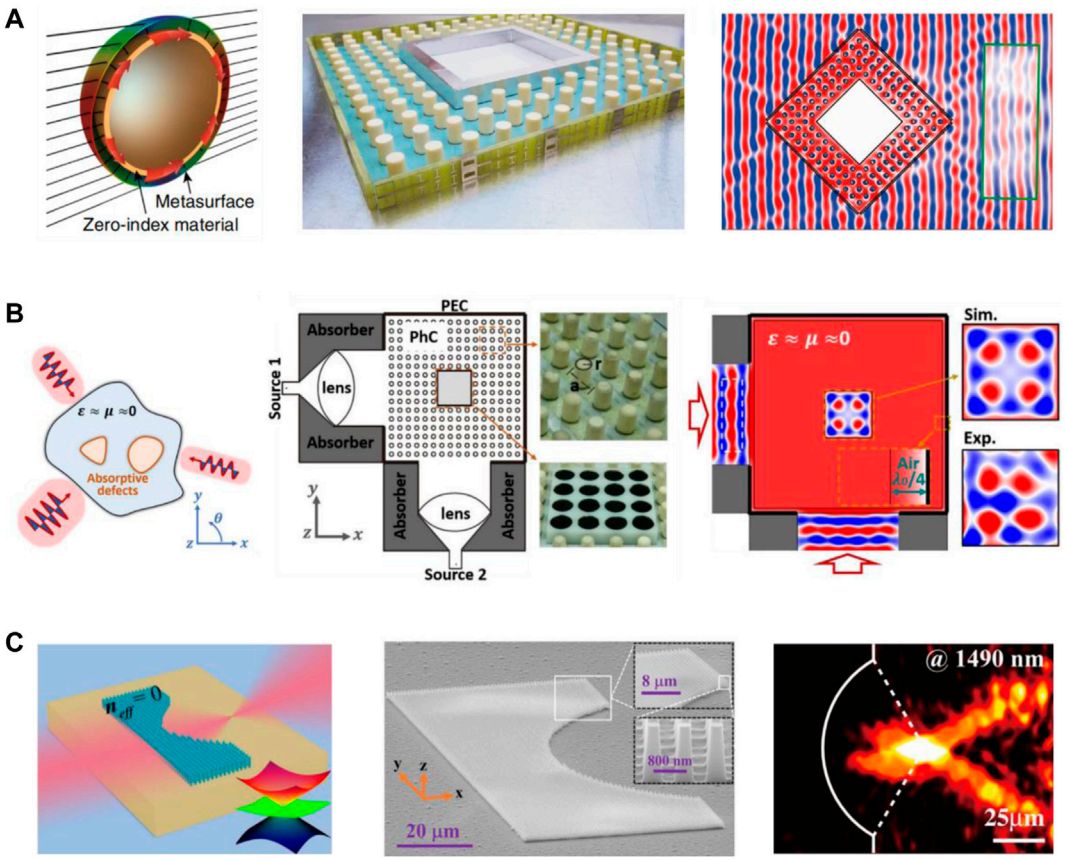

FIGURE 2 | (A) Left: schematic graph of a hybrid invisibility cloak based on the integration of metasurfaces and ZIM. Middle: picture of the fabricated microwave cloaking shell, which consists of a metasurface and a PhC with a Dirac-like cone. Right panel shows the electric-field distribution. The part inside the region marked by the green rectangle is measured in the experiment, and the other part is obtained by simulations. Reproduced with permission from Ref. [64]. **(B)** Left: illustration of the geometry-invariant coherent perfect absorber by using impedance-matched ZIM doped with absorptive defects. Middle panel shows the microwave experimental setup. A dielectric PhC with a Dirac-like cone is utilized to work as an effective impedance-matched ZIM. Right panel shows the measured electric-field distribution at the Dirac-point frequency. Reproduced with permission from Ref. [59]. **(C)** Left: schematic view of a plane-concave lens made of ZIM. Middle: scanning electron microscopy image of the fabricated lens consisting of silicon nanopillars on a silicon substrate. Right: optical microscope images of two incoherent beams passing through the lens, showing the focusing behavior at 1490 nm. Reproduced with permission from Ref. [139].

a geometry-invariant coherent perfect absorber via doping an impedance-matched ZIM with absorptive defects (**Figure 2B**) [59]. The behavior of coherent perfect absorption is independent of the size and shape of the ZIM and the position of the doping defects, because of the zero spatial phase change and uniform electric fields inside the ZIM. The third one is a plane-concave lens made of ZIM at near-infrared wavelengths (**Figure 2C**) [139]. Due to the zero spatial phase change across the ZIM, such a plane-concave lens can focus the incident plane wave with ultralow spherical aberration.

NON-HERMITIAN DIRAC-LIKE CONES AND EFFECTIVE MEDIUM DESCRIPTION

The abovementioned Dirac-like cone is based on the assumption of Hermitian PhC. It is reasonable, as the PhC are composed of low-loss dielectric materials. It is interesting to point out the band dispersion of the PhC could be drastically deformed if there exists loss/gain [24, 80, 136, 151–155, 175]. In 2015, Zhen et al experimentally demonstrated that in a photonic crystal slab the radiative loss-induced non-Hermitian perturbation can deform the Dirac-like cone into a 2D flat band enclosed by a ring of EPs [136]. The EP is a singularity in a non-Hermitian system where two or more eigenvalues and their associated eigenfunctions collapse into one eigenvalue or eigenfunction [156–158]. In the absence of loss, a Dirac-like cone as the result of accidental degeneracy of a doubly degenerate dipole mode and a single quadrupole mode dipole can be obtained at the Γ point. While in the presence of radiative loss, the Dirac-like cone is deformed into a flat band enclosed by a ring of EPs. As shown in **Figure 3A**, inside the ring of EPs, the real parts of the eigen-frequencies have degenerate flat dispersions, while the imaginary parts split into two branches. Outside the ring of EPs, the situations are just the opposite. The real parts split, while the imaginary parts tend to degeneracy.

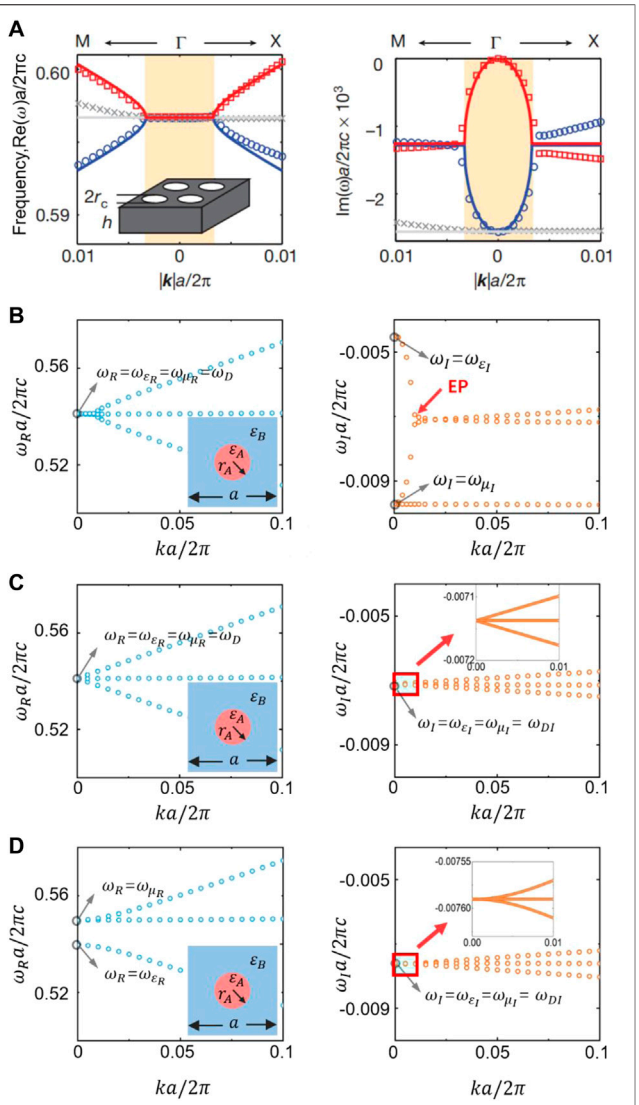

FIGURE 3 | (A) The real (left panel) and imaginary (right panel) parts of the eigen-frequencies of a PhC slab with finite thickness. By tuning the radius, accidental degeneracy in the real part can be achieved, but the Dirac-like cone is deformed into a 2D flat band enclosed by a ring of EPs. Reproduced with permission from Ref. [136] **[(B–D)]** The real (left) and imaginary (right) parts of the eigen-frequencies of a 2D non-Hermitian PhC consisting of a square lattice of cylindrical rods, showing **(B)** the ring of EPs, **(C)** complex Dirac-like cone with conical dispersions in both real and imaginary frequency spectra, and **(D)** the quadratic degeneracy. The relative permittivities of the rods (or background medium) are 12.5 + 0.5*i* (or 1) in **(B)**, 12.5 + 0.33*i* (or 1 + 0.0264*i*) in **(C)**, and 12 + 0.33*i* (or 1.04 + 0.02978*i*) in **(D)**. Reproduced with permission from Ref. [155].

These unique dispersion characteristics of the non-Hermitian PhC can also be described by an effective Hamiltonian as [33, 136].

$$H_{\text{eff}} = \begin{pmatrix} \omega_D & v_g|\mathbf{k}| & 0 \\ v_g|\mathbf{k}| & \omega_D - i\gamma_d & 0 \\ 0 & 0 & \omega_D - i\gamma_d \end{pmatrix} \tag{3}$$

with complex eigenvalues

$$\begin{aligned} \omega_1 &= \omega_D - i\frac{\gamma_d}{2} + v_g\sqrt{|\mathbf{k}|^2 - \left(\gamma_d/2v_g\right)^2},\ \omega_2 = \omega_1 \\ &= \omega_D - i\frac{\gamma_d}{2} - v_g\sqrt{|\mathbf{k}|^2 - \left(\gamma_d/2v_g\right)^2},\ \omega_3 = \omega_D - i\gamma_d \end{aligned} \tag{4}$$

where γ_d is induced by the radiative loss of the dipole modes. It is noted that the quadrupole mode does not radiate owing to its symmetry mismatch with plane waves in free space [136]. The first two eigenvalues indicate a ring of EPs appears at $|\mathbf{k}| = \gamma_d/2v_g$. Inside the ring, the real parts of eigenvalues are dispersionless and degenerate. While outside the ring, the imaginary parts are dispersionless and degenerate.

We note that the radiative loss from the PhC slab can be considered equivalent to the material loss in a 2D PhC. This provides us a simple way to investigate the non-Hermitian properties through engineering the losses in different constituents of the PhC. In 2021, Luo et al proposed a non-Hermitian 2D PhC composed of a square lattice of cylindrical rods [155]. The background medium and/or cylindrical rods contain material loss/gain. Through engineering the material loss/gain, it was discovered that besides the ring of EPs (**Figure 3B**), complex Dirac-like cone with conical dispersions in both real and imaginary frequency spectra (**Figure 3C**), and the quadratic degeneracy (**Figure 3D**) can be realized in non-Hermitian PhCs [155]. Such phenomena show the unique consequences of introducing loss/gain to the PhCs with Dirac-like cones.

Moreover, it was found that these non-Hermitian properties can be well explained from the effective medium point of view [155]. In a non-Hermitian PhC involving loss and/or gain, the eigen-frequency becomes a complex value as $\omega = \omega_R + i\omega_I$, and the effective permittivity $\varepsilon(\omega)$ and permeability $\mu(\omega)$ are generally complex and dispersive, which can be expressed as $\varepsilon(\omega) = \varepsilon_R(\omega) + i\varepsilon_I(\omega)$ and $\mu(\omega) = \mu_R(\omega) + i\mu_I(\omega)$. In a small frequency regime near the Γ point, linear relations between the effective parameters and the eigen-frequency can be assumed as:

$$\begin{cases} \varepsilon_R(\omega_R) = A_{\varepsilon_R} \times \left(\omega_R - \omega_{\varepsilon_R}\right) \\ \mu_R(\omega_R) = A_{\mu_R} \times \left(\omega_R - \omega_{\mu_R}\right) \\ \varepsilon_I(\omega_I) = A_{\varepsilon_I} \times \left(\omega_I - \omega_{\varepsilon_I}\right) \\ \mu_I(\omega_I) = A_{\mu_I} \times \left(\omega_I - \omega_{\mu_I}\right) \end{cases} \tag{5}$$

where A_{ε_R}, A_{μ_R}, A_{ε_I} and A_{μ_I} are unknown coefficients to be determined. When the loss/gain is small, we have $\omega_{\varepsilon_I} \approx \omega_{\mu_I} \approx 0$ and $\omega_{\varepsilon_R} \approx \omega_{\mu_R} \approx \omega_D$ with ω_D being the Dirac-point frequency in absence of loss/gain. In the complex frequency space, the dispersion relation can be expressed as,

$$(\omega_R + i\omega_I)^2(\varepsilon_R + i\varepsilon_I)(\mu_R + i\mu_I) = c^2\mathbf{k}^2 \tag{6}$$

where $\mathbf{k}$ is the in-plane wave vector, and c is the speed of light in free space. Based on the effective medium model with parameters and dispersion relation, besides the well explanation of the occurrence of the EP ring, other unique non-Hermitian phenomena like complex Dirac-like cone with conical dispersions in both real and imaginary frequency spectra, as well as the quadratic degeneracy were predicted [155], as summarized in **Table 1**. Moreover, we note that the flat band

TABLE 1 | Features of band structures of non-Hermitian PhCs.

	Characteristics of parameters		Features of band structures		Flat band
	$\omega_{\varepsilon_R}, \omega_{\mu_R}$	$\omega_{\varepsilon_I}, \omega_{\mu_I}$	Real parts	Imaginary parts	
Case 1 **Figure 3B**	$\omega_{\varepsilon_R} = \omega_{\mu_R} = \omega_D$	$\omega_{\varepsilon_I} \neq \omega_{\mu_I}$	Dispersion-less within EP ring	Ring of EPs	@$\begin{cases} \omega_R = \omega_D \\ \omega_I = \omega_{\mu_I} \end{cases}$
Case 2 **Figure 3C**	$\omega_{\varepsilon_R} = \omega_{\mu_R} = \omega_D$	$\omega_{\varepsilon_I} = \omega_{\mu_I} = \omega_{DI}$	Dirac-like cone	Dirac-like cone	@$\begin{cases} \omega_R = \omega_D \\ \omega_I = \omega_{DI} \end{cases}$
Case 3 **Figure 3D**	$\omega_{\varepsilon_R} \neq \omega_{\mu_R}$	$\omega_{\varepsilon_I} = \omega_{\mu_I} = \omega_{DI}$	Band gap	Quadratic degeneracy	@$\begin{cases} \omega_R = \omega_{\mu_R} \\ \omega_I = \omega_{DI} \end{cases}$

induced by the longitudinal electromagnetic mode in all scenarios can also be accurately predicted by using this non-Hermitian effective medium theory [155].

ON-CHIP APPLICATIONS WITH CLADDING AND BIC TECHNIQUES

For on-chip applications, the PhCs with a Dirac-like cone would suffer from large radiative losses in the out-of-plane direction, because the Dirac-cone dispersion resides above the light line and the transverse dipole mode forming the Dirac-like cone can couple to extended plane waves in free space [30, 31]. This would turn the PhC to be non-Hermitian, and hence the Dirac-like cone would disappear, hindering its applications as the ultralow-loss ZIM. In this sense, it is very important to solve the issue of radiative loss from real PhC chip structures with finite pillar height [22, 135–147]. In order to eliminate the out-of-plane radiative loss, two important classes of approaches have been proposed, that is, the utilization of claddings and BIC techniques.

A mirror cladding can reflect the leaky wave back down into the PhC slab, so as to eliminate the out-of-plane radiation. In 2015 Li et al fabricated an on-chip PhC slab cladded with gold films to avoid out-of-plane radiation, and a Dirac-like cone was observed at the wavelength of 1,590 nm (**Figure 4A**) [138]. However, such an implementation suffers propagation loss due to the conduction loss originating from the gold films. To reduce the conduction loss from the mirror, a dielectric Bragg reflector was proposed (**Figure 4B**) [30]. The Bragg reflector can reflect the leaky wave back down into the pillars, where it destructively interferes with the leaky wave below the array, thus eliminating the radiative loss.

Another technique is based on the concept of BIC, which is the photonic mode in the radiation continuum above the light line but is confined with an infinite quality factor [176]. With the BIC, it is possible to create resonances in a PhC slab with a Dirac-like cone that do not radiate [177]. Specifically, through engineering the height of the PhC slab, all the upward/downward out-of-plane radiation destructively interferes, thus forming a resonance-trapped BIC with a high quality factor (**Figure 4C**) [140]. Consequently, the radiative loss-induced EP ring would shrink into a Dirac-like cone [140, 145–147], which has been experimentally demonstrated at near-infrared wavelengths (**Figure 4D**) [147]. The Dirac-like cone is the consequence of the accidental degeneracy of a pair of dipole modes and a single quadrupole mode at the Γ point in [140, 147], while is formed due to the accidental degeneracy of a single monopole mode and doubly degenerate dipole modes in [145, 146] (**Figure 4E**). The low-order mode-based design can be better treated as a homogeneous ZIM.

We note that the monopole and higher-order modes besides the dipole modes at the Γ point do not have out-of-plane radiative loss because of their intrinsic mode symmetry. This suggests that it is possible to realize Dirac-like cone through harnessing the mode symmetry of the degenerate modes at the Dirac point. In 2018 minkov et al theoretically proposed a PhC slab with a hexagonal lattice described by the C_{6v} point group, in which a Dirac-like cone at the Γ point is achieved *via* the symmetry-protected BIC (**Figure 4F**) [144]. For a PhC slab with the C_{6v} symmetry, at the at the Γ point, modes that belong to the E_2 2D irreducible representation or a one-dimensional irreducible representation do not couple to plane waves in free space, that is, these modes are symmetry-protected BICs. Through engineering the structural parameters of the PhC slab, a Dirac-like cone as the result of accidental degeneracy of modes in the E_2 and the B_1 or B_2 irreducible representations can be obtained [144]. This theoretical prediction was experimentally demonstrated at near-infrared wavelengths recently (**Figure 4G**) [147].

THREE-DIMENSIONAL DIRAC-LIKE CONE AND THE ELECTROMAGNETIC VOID SPACE

Previously, Dirac-like cones due to accidental degeneracy are mostly investigated in 2D systems. 3D Dirac-like cones and ZIMs were rarely explored. Actually, the wave behaviors in 2D and 3D ZIM are inherently different as the former obey scalar wave equations while the latter follow vector wave equations. As a result, some physical effects observed in 2D ZIM, such as photonic doping [57–61], are absent in 3D ZIM. Instead, when a 3D impedance-matched ZIM contains random defects, unusual percolation of electromagnetic waves could appear [62]. In 2015 Luo et al theoretically demonstrated that there exists an unusual type of percolation threshold which, unlike normal percolation theory, is induced by the long-range connectivity of the defects in the transverse direction [62] (**Figure 5A**). It was discovered that below the percolation

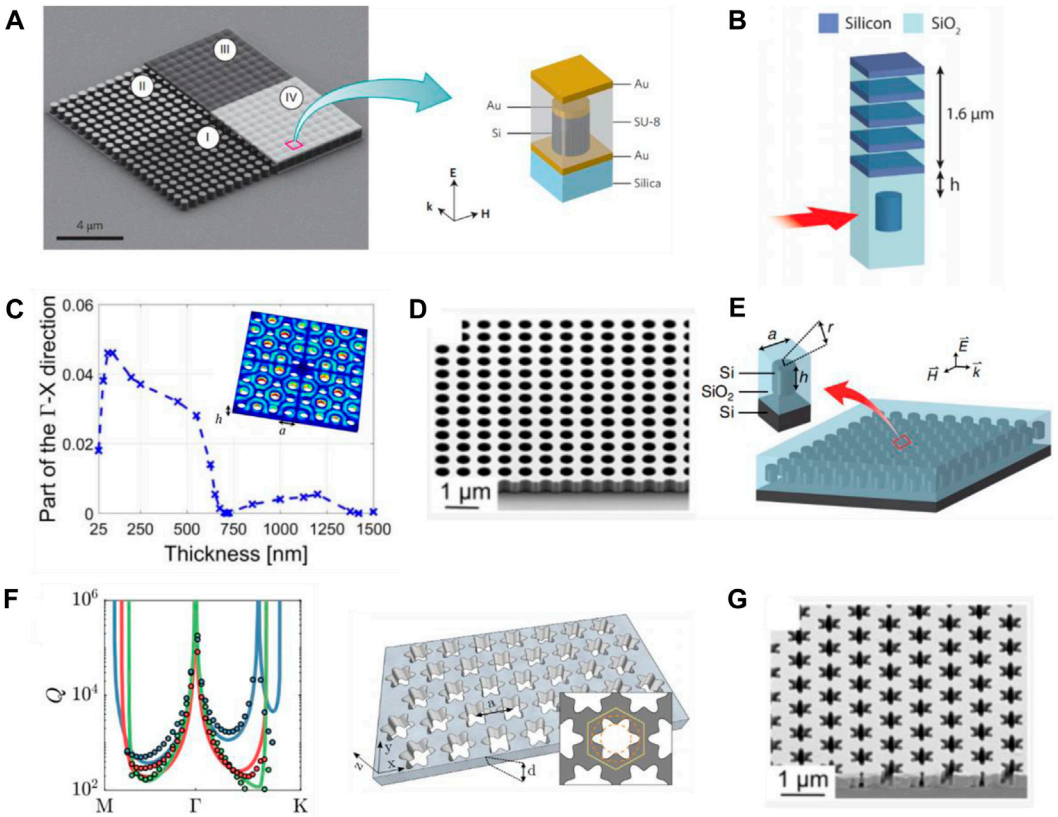

FIGURE 4 | (A) Scanning electron microscopy image of an on-chip PhC with a Dirac-like cone, and the schematic of unit cell. The cladding gold films are used to eliminate the out-of-plane radiation. Reproduced with permission from Ref. [138]. **(B)** Schematic of Bragg reflector design used to reflect the leaky wave back down into the pillars, where it destructively interferes with the leaky wave below the array. Reproduced with permission from Ref. [30]. **(C)** Extent of the ring of EPs in the ΓX direction versus the thickness of the PhC slab, which is illustrated by the inset. The radiative losses can be reduced using resonance-trapped BIC. Reproduced with permission from Ref. [140]. **(D)** Scanning electron microscopy images of a PhC slab with resonance-trapped BIC. A Dirac-like cone is formed due to the accidental degeneracy of a pair of dipole modes and a single quadrupole mode. Reproduced with permission from Ref. [147]. **(E)** Schematic of an on-chip PhC with resonance-trapped BIC. A Dirac-like cone is formed due to the accidental degeneracy of a single monopole mode and doubly degenerate dipole modes. Reproduced with permission from Ref. [146]. **(F)** Radiative quality factors for three photonic bands of a PhC slab illustrated by the right panel. A Dirac-like cone dispersion is obtained *via* symmetry-protected BIC without out-of-plane radiation. Reproduced with permission from Ref. [144]. **(G)** Scanning electron microscopy images of the PhC slab with symmetry-protected BIC. Reproduced with permission from Ref. [147].

threshold, the transmittance is always unity, irrespective of the material, shape and size of the embedded inclusions. The electromagnetic waves can squeeze through the gaps between random defects. While beyond the threshold, the transmittance will generally suffer a sharp reduction, and become strongly dependent on the configuration of defects (**Figure 5B**).

The 3D PhC with a Dirac-line cone dispersion offers a platform to explore the intriguing features of 3D ZIM. A theoretical design was investigated by Chan in 2012 [148]. The PhC consists of a simple cubic lattice of core-shell spheres. The core is a perfect electric conductor, and the shell is dielectric. From **Figure 5C** Dirac-like cone as the consequence of sixfold degenerate modes is observed at the Γ point. Both the effective permittivity and permeability are zero, i.e., $\varepsilon_{\text{eff}} = \mu_{\text{eff}} = 0$, at the Dirac-point frequency. However, the design is sensitive to the parameters and the fabrication is quite challenging. In 2021, Xu et al [150] experimentally realized the Dirac-like cone by employing another design of a 3D PhC composed of dielectric meshes. The dielectric meshes are orthogonally aligned along the x, y, and z directions, and intersect at the center of the unit cell (**Figure 5D**). At the Γ point, a sixfold accidental degeneracy of electric and magnetic dipole modes results in a Dirac-like cone. The microwave experiment demonstrated the near-perfect transmission of electromagnetic waves when there exist defects inside the PhC (i.e., effective 3D impedance-matched ZIM) below the percolation threshold. Such an extraordinary phenomenon that the transmission through an impedance-matched ZIM is independent of the embedded impurities may be referred to as an impurity-immunity or anti-doping effect [63, 150]. We emphasize that the 3D PhC of $\varepsilon_{\text{eff}} = \mu_{\text{eff}} = 0$ represents an interesting electromagnetic void space that is generated by expanding an infinitesimal point to a finite volume of space using transformation optics [178–180]. Such an electromagnetic

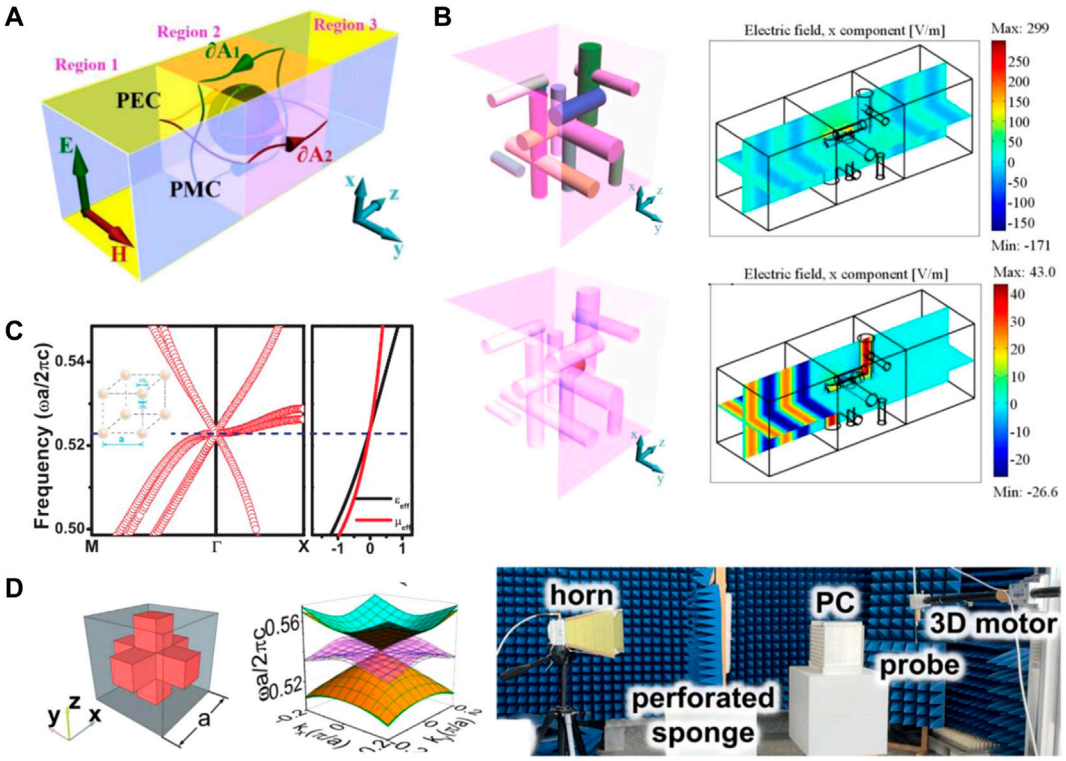

FIGURE 5 | (A) Schematic of unusual percolation of electromagnetic waves in a 3D impedance-matched ZIM host with defects. **(B)** Upper: schematic diagram of a 3D ZIM host embedded with random dielectric cylinders below the percolation threshold (left), and the simulated electric-field distribution, showing perfect transmission of electromagnetic waves (right). Lower: schematic diagram of the case beyond the percolation threshold (left), and the simulated electric-field distribution, showing near-zero transmission (right). Reproduced with permission from Ref. [62]. **(C)** A theoretical design of 3D ZIM using a 3D PhC consisting of a simple cubic lattice of core-shell spheres. A Dirac-like cone composed of sixfold degenerate modes is observed at the Γ point, and the effective parameters satisfy $\varepsilon_{eff} = \mu_{eff} = 0$ at the Dirac-point frequency. Reproduced with permission from Ref. [148]. **(D)** A microwave experimental realization of the 3D PhC with a Dirac-like cone for 3D ZIM. The PhC is composed of dielectric meshes. Reproduced with permission from Ref. [150].

void space has many interesting features that are absent in any other electromagnetic media.

DIRAC-LIKE CONES IN ACOUSTIC AND ELASTIC STRUCTURES

The concept of Dirac-like cones has also been developed in other kinds of classical wave structures including acoustic and elastic structures [23, 28, 148, 159–174].

In acoustics, the two key physical parameters that are essential for the propagation of the sound wave in materials are mass density and bulk modulus. Through carefully designing the two key physical parameters, microstructure and dimension parameters of PnCs, the Dirac-like cones at the center of the Brillouin zone can be obtained, also showing the effective zero refraction index property (i.e., simultaneous zero mass density and zero reciprocal bulk modulus). An experimental visualization of the Dirac-like cone in a 2D PnC was realized by Dubois et al in 2017 [166]. The PnC is a square lattice of blind holes (**Figure 6A**). Three bands are degenerate at the Dirac point, which correspond to a monopole mode and doubly degenerate dipole modes. Through measuring pressure field radiated by acoustic point source embedded in PnC, the directive emission enabled by zero refractive index was observed at the Dirac-point frequency. The 3D PnC exhibiting a Dirac-like cone was experimentally demonstrated by Xu et al in 2020 (**Figure 6B**) [174]. The unit cell of the PnC comprises three aluminum rods in air. A Dirac-like cone composed of fourfold degenerate modes occurs at the Γ point. The effective zero refractive index property at the Dirac-point frequency was demonstrated through investigating of wave tunneling effect in bending waveguides in both simulations and experiments, which is referred to as an acoustic "periscope".

In solids, both longitudinal and transverse waves exist, and the wave propagation properties are characterized by more parameters, such as the shear modulus. Through engineering the characteristic and dimension parameters, it is also possible to obtain Dirac cones in a PnC supporting both longitudinal and transverse waves. For example, Liu et al designed a 2D triangular-lattice PnC consisting of rubber cylinders embedded in silicon host, exhibiting a double Dirac cone at the Γ point as the consequence of fourfold degenerate modes (**Figure 6C**) [163]. Such a PnC possesses simultaneous zero effective refractive indices for both longitudinal and transverse waves at the Dirac

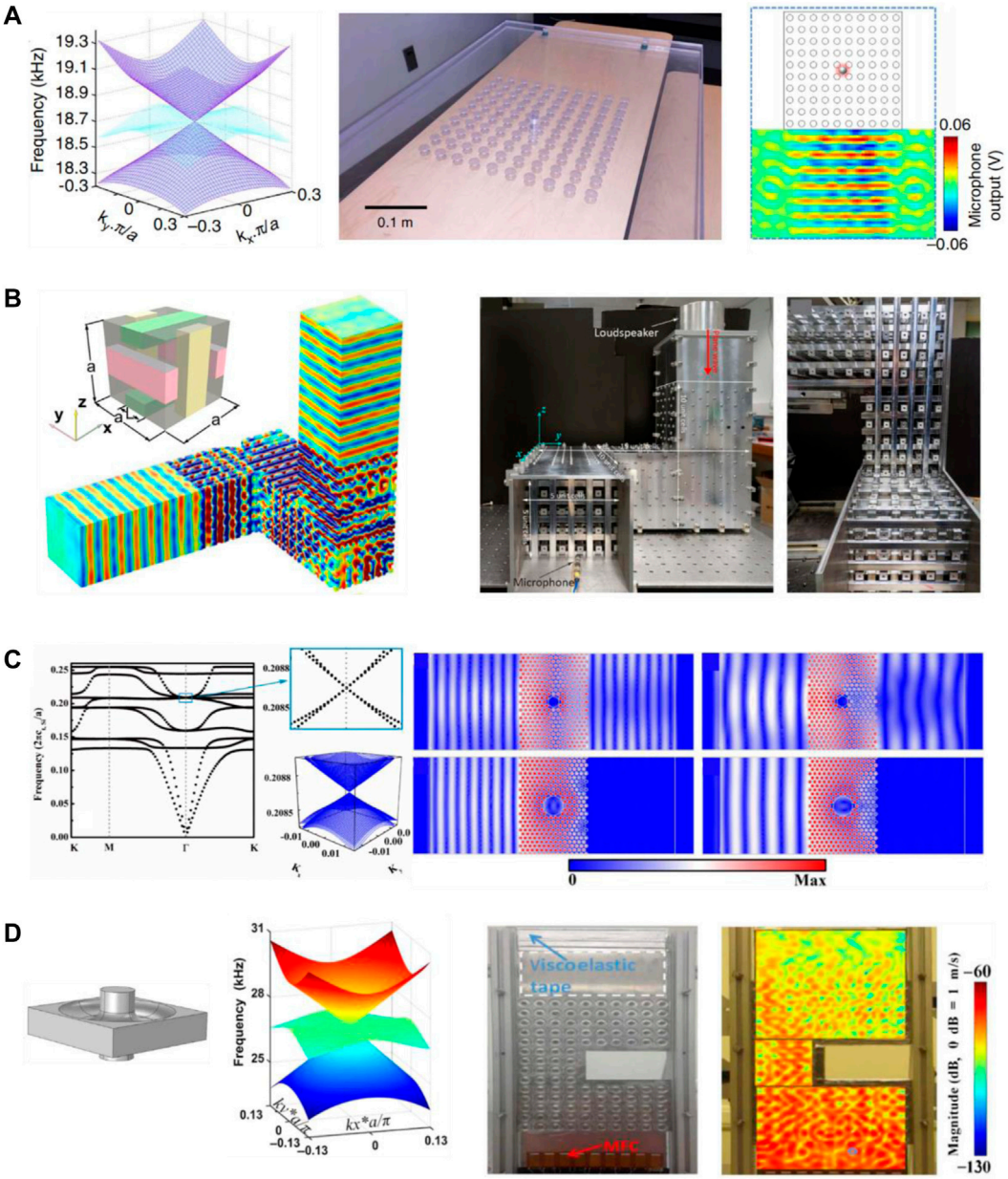

FIGURE 6 | (A) Left: enlarged view of dispersion surfaces near the Dirac-like cone of the PnC consisting of a square lattice of blind holes. Middle: photograph of the fabricated sample. Right: measured pressure field radiated by an acoustic point source embedded in PnC, showing the directive emission behavior at the Dirac-point frequency. Reproduced with permission from Ref. [166]. **(B)** Left: simulated pressure-field distribution when a bending waveguide is filled with 3D cubic-lattice PnC with a Dirac-like cone. The inset shows the unit cell comprising three aluminum rods in air. Right: photograph of the fabricated bending waveguide. Reproduced with permission from Ref. [174]. **(C)** Left: band structure for in-plane modes of a 2D triangular-lattice PnC consisting of rubber cylinders embedded in silicon host, and the enlarged view of the double Dirac cone. Right: simulated displacement-field distributions for the 2D PnC embedded with the steel cylinders to achieve transmission preserving plane wave characteristic (upper) and total reflection (lower). Different columns represent the incident longitudinal and transverse waves, respectively. Reproduced with permission from Ref. [163]. **(D)** Left: schematic of the tapered unit cell of a square-lattice PnC. Middle: enlarged view of dispersion surfaces near the Dirac-like cone. Right: photograph of U-shaped waveguide channel filled with the PnC, and measured amplitude of out-of-plane velocity at the Dirac-point frequency. Reproduced with permission from Ref. [165].

cone frequency, which can be utilized to prohibit the longitudinal-transverse mode conversion even in the presence of scattering objects. In 2017 Zhu et al experimentally realized simultaneous zero mass density and zero reciprocal shear modulus in an elastic waveguide filled with a square-lattice PnC with a Dirac-like cone. The unit cell consists of a square plate having an embedded elliptic torus-like taper and a resonating center mass (**Figure 6D**) [165]. Threefold

degenerate modes result in a Dirac-like cone at the Γ point. Numerical and experimental results confirmed the zero-refractive-index-enabled cloaking and super-coupling effects at the Dirac-point frequency.

SUMMARY AND OUTLOOK

We have reviewed the study of Dirac-like cones in both PhCs and PnCs, from Hermitian to non-Hermitian systems and from 2D to 3D. PhCs/PnCs with a Dirac-like cone at the center of the Brillouin zone behave as effective ZIM at the Dirac-point frequency, providing a remarkable platform for the ultralow-loss ZIMs and the ZIM-based applications. Due to this unique feature, the Dirac-like cones have attracted considerable attention from theoretical investigation of underlying physics to experimental verification and application exploration.

Despite the above advances, there are some remaining important open questions are worth exploring. For instance, the fast inverse design of Dirac-like cones at will is an interesting question. The inverse design problem, meaning the direct retrieval of the proper structure for the desired optical performance, requires exploration of a large degree of freedom in the design space, and hence is very challenging and time-consuming [36, 181]. Recently, topology optimization, as a large-scale computational technique employing powerful gradient-based numerical algorithms, has been applied to inversely design Dirac-like cones [36–40]. The topology optimization is a rule-based approach containing iterative searching steps in a case-by-case manner, usually relying on numerical simulations in each step to produce intermediate results that help to modify the searching strategy [181]. This process would be very time-consuming especially when dealing with complicated 3D structures. Deep learning, as a data-driven methodology, could overcome complicated design problems with growth of structural complexity and higher degree of freedom through training the artificial neural network [36, 181]. A trained neural network can be used as a fast, general purpose predictor of optical and electromagnetic responses of complicated 3D structures, and is particularly efficient in solving notoriously difficult inverse problems in nanophotonics [182–185]. Another way is the utilization of the systematic band engineering method that has realized Dirac cones at arbitrary k point in the Brillouin zone of PhCs without symmetry [35]. With such advanced designing techniques, customized Dirac and Dirac-like cones can realized in complex PhCs/PnCs.

Another interesting topic is the realization of Dirac-like cones or ZIMs at the deep-subwavelength scale. One of the most important features of PhCs/PnCs with Dirac-like cones is that they can mimic effective ZIM. However, most of the PhCs/PnCs are composed of periodic structures, whose lattice constant is in the half-wavelength scale. Such a bulky size hinders many applications that require deep-wavelength ZIM, including tunneling effect in deep-subwavelength channels [48–50] and arbitrary control of energy flux in the deep-subwavelength scale [52], etc. The realization of PhCs/PnCs with Dirac-like cones in the deep-subwavelength scale is important to expand their application scenarios.

AUTHOR CONTRIBUTIONS

YL and JL conceived the idea and wrote the draft of this review.

FUNDING

This work was supported by the National Key R&D Program of China (Grant Nos 2020YFA0211300, 2020YFA0211400, 2017YFA0303702) National Natural Science Foundation of China (Grant Nos 11974176, 12174188), China Postdoctoral Science Foundation (2021M702401), the Priority Academic Program Development of Jiangsu Higher Education Institutions (PAPD).

REFERENCES

1. Geim AK, Novoselov KS. The Rise of Graphene. *Nat Mater* (2007) 6:183–91. doi:10.1038/nmat1849
2. Castro Neto AH, Guinea F, Peres NMR, Novoselov KS, Geim AK. The Electronic Properties of Graphene. *Rev Mod Phys* (2009) 81:109–62. doi:10.1103/revmodphys.81.109
3. John S. Strong Localization of Photons in Certain Disordered Dielectric Superlattices. *Phys Rev Lett* (1987) 58:2486–9. doi:10.1103/physrevlett.58.2486
4. Yablonovitch E. Inhibited Spontaneous Emission in Solid-State Physics and Electronics. *Phys Rev Lett* (1987) 58:2059–62. doi:10.1103/physrevlett.58.2059
5. Sigalas MM, Economou EN. Elastic and Acoustic Wave Band Structure. *J Sound Vibration* (1992) 158:377–82. doi:10.1016/0022-460x(92)90059-7
6. Kushwaha MS, Halevi P, Dobrzynski L, Djafari-Rouhani B. Acoustic Band Structure of Periodic Elastic Composites. *Phys Rev Lett* (1993) 71:2022–5. doi:10.1103/physrevlett.71.2022
7. Martínez-Sala R, Sancho J, Sánchez JV, Gómez V, Llinares J, Meseguer F. Sound Attenuation by Sculpture. *Nature* (1995) 378:241. doi:10.1038/378241a0
8. Page JH, Sheng P, Schriemer HP, Jones I, Jing X, Weitz DA. Group Velocity in Strongly Scattering Media. *Science* (1996) 271:634–7. doi:10.1126/science.271.5249.634
9. Plihal M, Maradudin AA. Photonic Band Structure of Two-Dimensional Systems: The Triangular Lattice. *Phys Rev B* (1991) 44:8565–71. doi:10.1103/physrevb.44.8565
10. Peleg O, Bartal G, Freedman B, Manela O, Segev M, Christodoulides DN. Conical Diffraction and Gap Solitons in Honeycomb Photonic Lattices. *Phys Rev Lett* (2007) 98:103901. doi:10.1103/physrevlett.98.103901
11. Sepkhanov RA, Bazaliy YB, Beenakker CWJ. Extremal Transmission at the Dirac point of a Photonic Band Structure. *Phys Rev A* (2007) 75:063813. doi:10.1103/physreva.75.063813
12. Raghu S, Haldane FDM. Analogs of Quantum-Hall-Effect Edge States in Photonic Crystals. *Phys Rev A* (2008) 78:033834. doi:10.1103/physreva.78.033834
13. Sepkhanov RA, Nilsson J, Beenakker CWJ. Proposed Method for Detection of the Pseudospin-1/2 Berry Phase in a Photonic crystal with a Dirac Spectrum. *Phys Rev B* (2008) 78:045122. doi:10.1103/physrevb.78.045122
14. Zhang X. ObservingZitterbewegungfor Photons Near the Dirac Point of a Two-Dimensional Photonic Crystal. *Phys Rev Lett* (2008) 100:113903. doi:10.1103/physrevlett.100.113903

15. Haldane FD, Raghu S. Possible Realization of Directional Optical Waveguides in Photonic Crystals with Broken Time-Reversal Symmetry. *Phys Rev Lett* (2008) 100:013904. doi:10.1103/PhysRevLett.100.013904
16. Ochiai T, Onoda M. Photonic Analog of Graphene Model and its Extension: Dirac Cone, Symmetry, and Edge States. *Phys Rev B* (2009) 80:155103. doi:10.1103/physrevb.80.155103
17. Ao X, Lin Z, Chan C. One-way Edge Mode in a Magneto-Optical Honeycomb Photonic crystal. *Phys Rev B* (2009) 80:033105. doi:10.1103/physrevb.80.033105
18. Diem M, Koschny T, Soukoulis CM. Transmission in the Vicinity of the Dirac point in Hexagonal Photonic Crystals. *Physica B: Condensed Matter* (2010) 405:2990–5. doi:10.1016/j.physb.2010.01.020
19. Bittner S, Dietz B, Miski-Oglu M, Oria Iriarte P, Richter A, Schäfer F. Observation of a Dirac point in Microwave Experiments with a Photonic crystal Modeling Graphene. *Phys Rev B* (2010) 82:014301. doi:10.1103/physrevb.82.014301
20. Zandbergen SR, de Dood MJ. Experimental Observation of strong Edge Effects on the Pseudodiffusive Transport of Light in Photonic Graphene. *Phys Rev Lett* (2010) 104:043903. doi:10.1103/PhysRevLett.104.043903
21. Yu S-Y, Sun X-C, Ni X, Wang Q, Yan X-J, He C, et al. Surface Phononic Graphene. *Nat Mater* (2016) 15:1243–7. doi:10.1038/nmat4743
22. Collins MJ, Zhang F, Bojko R, Chrostowski L, Rechtsman MC. Integrated Optical Dirac Physics via Inversion Symmetry Breaking. *Phys Rev A* (2016) 94:063827. doi:10.1103/physreva.94.063827
23. Mei J, Wu Y, Chan CT, Zhang Z. First-principles Study of Dirac and Dirac-like Cones in Phononic and Photonic Crystals. *Phys Rev B* (2012) 86:035141. doi:10.1103/physrevb.86.035141
24. Szameit A, Rechtsman MC, Bahat-Treidel O, Segev M. PT-symmetry in Honeycomb Photonic Lattices. *Phys Rev A* (2011) 84:021806(R). doi:10.1103/physreva.84.021806
25. Zhang X, Liu Z. Extremal Transmission and Beating Effect of Acoustic Waves in Two-Dimensional Sonic Crystals. *Phys Rev Lett* (2008) 101:264303. doi:10.1103/physrevlett.101.264303
26. Torrent D, Sánchez-Dehesa J. Acoustic Analogue of Graphene: Observation of Dirac Cones in Acoustic Surface Waves. *Phys Rev Lett* (2012) 108:174301. doi:10.1103/physrevlett.108.174301
27. Torrent D, Mayou D, Sánchez-Dehesa J. Elastic Analog of Graphene: Dirac Cones and Edge States for Flexural Waves in Thin Plates. *Phys Rev B* (2013) 87:115143. doi:10.1103/physrevb.87.115143
28. Lu J, Qiu C, Xu S, Ye Y, Ke M, Liu Z. Dirac Cones in Two-Dimensional Artificial Crystals for Classical Waves. *Phys Rev B* (2014) 89:134302. doi:10.1103/physrevb.89.134302
29. Chan CT, Hang ZH, Huang X. Dirac Dispersion in Two-Dimensional Photonic Crystals. *Adv OptoElectronics* (2012) 2012:1–11. doi:10.1155/2012/313984
30. Vulis DI, Reshef O, Camayd-Muñoz P, Mazur E. Manipulating the Flow of Light Using Dirac-Cone Zero-index Metamaterials. *Rep Prog Phys* (2019) 82:012001. doi:10.1088/1361-6633/aad3e5
31. Li Y, Chan CT, Mazur E. Dirac-like Cone-Based Electromagnetic Zero-index Metamaterials. *Light Sci Appl* (2021) 10:203. doi:10.1038/s41377-021-00642-2
32. Huang X, Lai Y, Hang ZH, Zheng H, Chan CT. Dirac Cones Induced by Accidental Degeneracy in Photonic Crystals and Zero-Refractive-index Materials. *Nat Mater* (2011) 10:582–6. doi:10.1038/nmat3030
33. Sakoda K. Proof of the Universality of Mode Symmetries in Creating Photonic Dirac Cones. *Opt Express* (2012) 20:25181–94. doi:10.1364/oe.20.025181
34. Sakoda K. *Optical Properties of Photonic Crystals*. New York, USA: Springer (2005).
35. Chu H, Zhang Y, Luo J, Xu C, Xiong X, Peng R, et al. Band Engineering Method to Create Dirac Cones of Accidental Degeneracy in General Photonic Crystals without Symmetry. *Opt Express* (2021) 29:18070. doi:10.1364/oe.427389
36. Li W, Meng F, Chen Y, Li YF, Huang X. Topology Optimization of Photonic and Phononic Crystals and Metamaterials: A Review. *Adv Theor Simul.* (2019) 2:1900017. doi:10.1002/adts.201900017
37. Chen Y, Meng F, Jia B, Li G, Huang X. Inverse Design of Photonic Topological Insulators with Extra-wide Bandgaps. *Phys Status Solidi RRL* (2019) 13:1900175. doi:10.1002/pssr.201900175
38. Chen Y, Meng F, Li G, Huang X. Topology Optimization of Photonic Crystals with Exotic Properties Resulting from Dirac-like Cones. *Acta Materialia* (2019) 164:377–89. doi:10.1016/j.actamat.2018.10.058
39. Lin Z, Christakis L, Li Y, Mazur E, Rodriguez AW, Lončar M. Topology-optimized Dual-Polarization Dirac Cones. *Phys Rev B* (2018) 97:081408(R). doi:10.1103/physrevb.97.081408
40. Lin Z, Pick A, Lončar M, Rodriguez AW. Enhanced Spontaneous Emission at Third-Order Dirac Exceptional Points in Inverse-Designed Photonic Crystals. *Phys Rev Lett* (2016) 117:107402. doi:10.1103/physrevlett.117.107402
41. Liberal I, Engheta N. Near-zero Refractive index Photonics. *Nat Photon* (2017) 11:149–58. doi:10.1038/nphoton.2017.13
42. Liberal I, Engheta N. The Rise of Near-Zero-index Technologies. *Science* (2017) 358:1540–1. doi:10.1126/science.aaq0459
43. Niu X, Hu X, Chu S, Gong Q. Epsilon-near-zero Photonics: A New Platform for Integrated Devices. *Adv Opt Mater* (2018) 6:1701292. doi:10.1002/adom.201701292
44. Jahani S, Jacob Z. All-dielectric Metamaterials. *Nat Nanotech* (2016) 11:23–36. doi:10.1038/nnano.2015.304
45. Enoch S, Tayeb G, Sabouroux P, Guérin N, Vincent P. A Metamaterial for Directive Emission. *Phys Rev Lett* (2002) 89:213902. doi:10.1103/physrevlett.89.213902
46. Luo J, Xu P, Gao L. Directive Emission Based on One-Dimensional Metal Heterostructures. *J Opt Soc Am B* (2012) 29:35–9. doi:10.1364/josab.29.000035
47. Luo J, Lai Y. Epsilon-near-zero or Mu-Near-Zero Materials Composed of Dielectric Photonic Crystals. *Sci China Inf Sci* (2013) 56:1–10. doi:10.1007/s11432-013-5029-9
48. Silveirinha M, Engheta N. Tunneling of Electromagnetic Energy through Subwavelength Channels and Bends Usingε-Near-Zero Materials. *Phys Rev Lett* (2006) 97:157403. doi:10.1103/physrevlett.97.157403
49. Liu R, Cheng Q, Hand T, Mock JJ, Cui TJ, Cummer SA, et al. Experimental Demonstration of Electromagnetic Tunneling through an Epsilon-Near-Zero Metamaterial at Microwave Frequencies. *Phys Rev Lett* (2008) 100:023903. doi:10.1103/PhysRevLett.100.023903
50. Edwards B, Alù A, Young ME, Silveirinha M, Engheta N. Experimental Verification of Epsilon-Near-Zero Metamaterial Coupling and Energy Squeezing Using a Microwave Waveguide. *Phys Rev Lett* (2008) 100:033903. doi:10.1103/PhysRevLett.100.033903
51. Luo J, Xu P, Chen H, Hou B, Gao L, Lai Y. Realizing Almost Perfect Bending Waveguides with Anisotropic Epsilon-Near-Zero Metamaterials. *Appl Phys Lett* (2012) 100:221903. doi:10.1063/1.4723844
52. Luo J, Lu W, Hang Z, Chen H, Hou B, Lai Y, et al. Arbitrary Control of Electromagnetic Flux in Inhomogeneous Anisotropic media with Near-Zero index. *Phys Rev Lett* (2014) 112:073903. doi:10.1103/PhysRevLett.112.073903
53. Li Y, Jiang HT, Liu WW, Ran J, Lai Y, Chen H. Experimental Realization of Subwavelength Flux Manipulation in Anisotropic Near-Zero index Metamaterials. *Epl* (2016) 113:57006. doi:10.1209/0295-5075/113/57006
54. Luo J, Lai Y. Anisotropic Zero-index Waveguide with Arbitrary Shapes. *Sci Rep* (2014) 4:5875. doi:10.1038/srep05875
55. Zhang X, Wu Y. Effective Medium Theory for Anisotropic Metamaterials. *Sci Rep* (2015) 5:7892. doi:10.1038/srep07892
56. Ji W, Luo J, Lai Y. Extremely Anisotropic Epsilon-Near-Zero media in Waveguide Metamaterials. *Opt Express* (2019) 27:19463–73. doi:10.1364/oe.27.019463
57. Liberal I, Mahmoud AM, Li Y, Edwards B, Engheta N. Photonic Doping of Epsilon-Near-Zero media. *Science* (2017) 355:1058–62. doi:10.1126/science.aal2672
58. Liberal I, Li Y, Engheta N. Reconfigurable Epsilon-Near-Zero Metasurfaces via Photonic Doping. *Nanophotonics* (2018) 7:1117–27. doi:10.1515/nanoph-2018-0012
59. Luo J, Liu B, Hang ZH, Lai Y. Coherent Perfect Absorption via Photonic Doping of Zero-index media. *Laser Photon Rev.* (2018) 12:1800001. doi:10.1002/lpor.201800001
60. Wang D, Luo J, Sun Z, Lai Y. Transforming Zero-index media into Geometry-Invariant Coherent Perfect Absorbers via Embedded Conductive Films. *Opt Express* (2021) 29:5247. doi:10.1364/oe.416632

61. Coppolaro M, Moccia M, Castaldi G, Engheta N, Galdi V. Non-Hermitian Doping of Epsilon-Near-Zero media. *Proc Natl Acad Sci USA* (2020) 117: 13921–8. doi:10.1073/pnas.2001125117
62. Luo J, Hang ZH, Chan CT, Lai Y. Unusual Percolation Threshold of Electromagnetic Waves in Double-Zero Medium Embedded with Random Inclusions. *Laser Photon Rev* (2015) 9:523–9. doi:10.1002/lpor.201500083
63. Luo J, Li J, Lai Y. Electromagnetic Impurity-Immunity Induced by Parity-Time Symmetry. *Phys Rev X* (2018) 8:031035. doi:10.1103/physrevx.8.031035
64. Chu H, Li Q, Liu B, Luo J, Sun S, Hang ZH, et al. A Hybrid Invisibility Cloak Based on Integration of Transparent Metasurfaces and Zero-index Materials. *Light Sci Appl* (2018) 7:50. doi:10.1038/s41377-018-0052-7
65. Hao J, Yan W, Qiu M. Super-reflection and Cloaking Based on Zero index Metamaterial. *Appl Phys Lett* (2010) 96:101109. doi:10.1063/1.3359428
66. Silveirinha M, Engheta N. Design of Matched Zero-index Metamaterials Using Nonmagnetic Inclusions in Epsilon-Near-Zero media. *Phys Rev B* (2007) 75:075119. doi:10.1103/physrevb.75.075119
67. Tagviashvili M. $\varepsilon \rightarrow 0$ Limits in the Mie-Scattering Theory. *Phys Rev A* (2010) 81:045802. doi:10.1103/physreva.81.045802
68. Nguyen VC, Chen L, Halterman K. Total Transmission and Total Reflection by Zero index Metamaterials with Defects. *Phys Rev Lett* (2010) 105:233908. doi:10.1103/physrevlett.105.233908
69. Luo J, Xu P, Gao L, Lai Y, Chen H. Manipulate the Transmissions Using index-near-zero or Epsilon-Near-Zero Metamaterials with Coated Defects. *Plasmonics* (2012) 7:353–8. doi:10.1007/s11468-011-9314-4
70. Xu Y, Chen H. Total Reflection and Transmission by Epsilon-Near-Zero Metamaterials with Defects. *Appl Phys Lett* (2011) 98:113501. doi:10.1063/1.3565172
71. Wang T, Luo J, Gao L, Xu P, Lai Y. Hiding Objects and Obtaining Fano Resonances in index-near-zero and Epsilon-Near-Zero Metamaterials with Bragg-fiber-like Defects. *J Opt Soc Am B* (2013) 30:1878–84. doi:10.1364/josab.30.001878
72. Wang T, Luo J, Gao L, Xu P, Lai Y. Equivalent Perfect Magnetic Conductor Based on Epsilon-Near-Zero media. *Appl Phys Lett* (2014) 104:211904. doi:10.1063/1.4876918
73. Song J, Luo J, Lai Y. Side Scattering Shadow and Energy Concentration Effects of Epsilon-Near-Zero media. *Opt Lett* (2018) 43:1738–41. doi:10.1364/ol.43.001738
74. Yang Y, Jia Z, Xu T, Luo J, Lai Y, Hang ZH. Beam Splitting and Unidirectional Cloaking Using Anisotropic Zero-index Photonic Crystals. *Appl Phys Lett* (2019) 114:161905. doi:10.1063/1.5088837
75. Feng S, Halterman K. Coherent Perfect Absorption in Epsilon-Near-Zero Metamaterials. *Phys Rev B* (2012) 86:165103. doi:10.1103/physrevb.86.165103
76. Luo J, Li S, Hou B, Lai Y. Unified Theory for Perfect Absorption in Ultrathin Absorptive Films with Constant Tangential Electric or Magnetic fields. *Phys Rev B* (2014) 90:165128. doi:10.1103/physrevb.90.165128
77. Zhong S, Ma Y, He S. Perfect Absorption in Ultrathin Anisotropic ε-near-zero Metamaterials. *Appl Phys Lett* (2014) 105:023504. doi:10.1063/1.4890397
78. Bai P, Ding K, Wang G, Luo J, Zhang Z, Chan CT, et al. Simultaneous Realization of a Coherent Perfect Absorber and Laser by Zero-index media with Both Gain and Loss. *Phys Rev A* (2016) 94:063841. doi:10.1103/physreva.94.063841
79. Rensberg J, Zhou Y, Richter S, Wan C, Zhang S, Schöppe P, et al. Epsilon-near-zero Substrate Engineering for Ultrathin-Film Perfect Absorbers. *Phys Rev Appl* (2017) 8:014009. doi:10.1103/physrevapplied.8.014009
80. Xu C, Farhat M, Wu Y. Non-Hermitian Electromagnetic Double-Near-Zero index Medium in a Two-Dimensional Photonic crystal. *Appl Phys Lett* (2021) 119:224102. doi:10.1063/5.0073391
81. Vincenti MA, de Ceglia D, Ciattoni A, Scalora M. Singularity-driven Second- and Third-Harmonic Generation at ε-near-zero Crossing Points. *Phys Rev A* (2011) 84:063826. doi:10.1103/physreva.84.063826
82. Suchowski H, O'Brien K, Wong ZJ, Salandrino A, Yin X, Zhang X. Phase Mismatch-free Nonlinear Propagation in Optical Zero-index Materials. *Science* (2013) 342:1223–6. doi:10.1126/science.1244303
83. Alam MZ, De Leon I, Boyd RW. Large Optical Nonlinearity of Indium Tin Oxide in its Epsilon-Near-Zero Region. *Science* (2016) 352:795–7. doi:10.1126/science.aae0330
84. Alam MZ, Schulz SA, Upham J, De Leon I, Boyd RW. Large Optical Nonlinearity of Nanoantennas Coupled to an Epsilon-Near-Zero Material. *Nat Photon* (2018) 12:79–83. doi:10.1038/s41566-017-0089-9
85. Reshef O, De Leon I, Alam MZ, Boyd RW. Nonlinear Optical Effects in Epsilon-Near-Zero media. *Nat Rev Mater* (2019) 4:535–51. doi:10.1038/s41578-019-0120-5
86. Bittner S, Dietz B, Miski-Oglu M, Richter A. Extremal Transmission through a Microwave Photonic crystal and the Observation of Edge States in a Rectangular Dirac Billiard. *Phys Rev B* (2012) 85. doi:10.1103/physrevb.85.064301
87. Sakoda K. Universality of Mode Symmetries in Creating Photonic Dirac Cones. *J Opt Soc Am B* (2012) 29:2770. doi:10.1364/josab.29.002770
88. Fang K, Zhang Y, Li F, Jiang H, Li Y, Wang W, et al. Microwave Collimation Based on Zero index Metamaterials with Dirac point. *Opt Lett* (2012) 37: 4654–6. doi:10.1364/ol.37.004654
89. Antonakakis T, Craster RV, Guenneau S. High-frequency Homogenization of Zero-Frequency Stop Band Photonic and Phononic Crystals. *New J Phys* (2013) 15:103014. doi:10.1088/1367-2630/15/10/103014
90. Mattiucci N, Bloemer MJ, D'Aguanno G. All-optical Bistability and Switching Near the Dirac point of a 2-D Photonic crystal. *Opt Express* (2013) 21:11862. doi:10.1364/oe.21.011862
91. Moitra P, Yang Y, Anderson Z, Kravchenko II, Briggs DP, Valentine J. Realization of an All-Dielectric Zero-index Optical Metamaterial. *Nat Photon* (2013) 7:791–5. doi:10.1038/nphoton.2013.214
92. D Aguanno G, Mattiucci N, Conti C, Bloemer MJ. Field Localization and Enhancement Near the Dirac point of a Finite Defectless Photonic crystal. *Phys Rev B* (2013) 87:085135.
93. Sakoda K. Polarization-dependent Continuous Change in the Propagation Direction of Dirac-Cone Modes in Photonic-crystal Slabs. *Phys Rev A* (2014) 90:013835. doi:10.1103/physreva.90.013835
94. Mattiucci N, Bloemer MJ, D'Aguanno G. Phase-matched Second Harmonic Generation at the Dirac point of a 2-D Photonic crystal. *Opt Express* (2014) 22:6381. doi:10.1364/oe.22.006381
95. He W-Y, Chan CT. The Emergence of Dirac Points in Photonic Crystals with Mirror Symmetry. *Sci Rep* (2015) 5:8186. doi:10.1038/srep08186
96. Yu S-Y, Wang Q, Zheng L-Y, He C, Liu X-P, Lu M-H, et al. Acoustic Phase-Reconstruction Near the Dirac point of a Triangular Phononic crystal. *Appl Phys Lett* (2015) 106:151906. doi:10.1063/1.4918651
97. Ashraf MW, Faryad M. Dirac-like Cone Dispersion in Two-Dimensional Core-Shell Dielectric Photonic Crystals. *J Nanophoton* (2015) 9:093057. doi:10.1117/1.jnp.9.093057
98. Wang X, Jiang H, Li Y, Yan C, Deng F, Sun Y, et al. Transport Properties of Disordered Photonic Crystals Around a Dirac-like point. *Opt Express* (2015) 23:5126. doi:10.1364/oe.23.005126
99. Dong J-W, Chang M-L, Huang X-Q, Hang ZH, Zhong Z-C, Chen W-J, et al. Conical Dispersion and Effective Zero Refractive index in Photonic Quasicrystals. *Phys Rev Lett* (2015) 114:163901. doi:10.1103/physrevlett.114.163901
100. Li Y, Mei J. Double Dirac Cones in Two-Dimensional Dielectric Photonic Crystals. *Opt Express* (2015) 23:12089. doi:10.1364/oe.23.012089
101. Zhang P, Fietz C, Tassin P, Koschny T, Soukoulis CM. Numerical Investigation of the Flat Band Bloch Modes in a 2D Photonic crystal with Dirac Cones. *Opt Express* (2015) 23:10444. doi:10.1364/oe.23.010444
102. Ashraf MW, Faryad M. On the Mapping of Dirac-like Cone Dispersion in Dielectric Photonic Crystals to an Effective Zero-index Medium. *J Opt Soc Am B* (2016) 33:1008. doi:10.1364/josab.33.001008
103. Dong G, Zhou J, Yang X, Meng X. Precise Identification of Dirac-like point through a Finite Photonic crystal Square Matrix. *Sci Rep* (2016) 6:36712. doi:10.1038/srep36712
104. Nagai S, Sanada A. Γ-point Group Velocity of Lossy Dirac Cone Composite Right/left-Handed Metamaterials. *IEICE Electron Express* (2016) 13: 20160281. doi:10.1587/elex.13.20160281
105. Xu C, Lai Y. Configurable Dirac-like Conical Dispersions in Complex Photonic Crystals. *Phys Rev B* (2017) 95:045124. doi:10.1103/physrevb.95.045124
106. Qiu P, Qiu W, Lin Z, Chen H, Ren J, Wang J-X, et al. Investigation of Beam Splitter in a Zero-Refractive-index Photonic crystal at the Frequency of Dirac-like point. *Sci Rep* (2017) 7:9588. doi:10.1038/s41598-017-10056-z

107. Gao H, Zhou YS, Zheng ZY, Chen SJ, Dong JJ. Is the Photonic crystal with a Dirac Cone at its Γ point a Real Zero-index Material. *Appl Phys B* (2017) 123: 165. doi:10.1007/s00340-017-6738-3
108. Lou Q, Zhang Y, Poo Y, Ma H, Wu R. Realization of Unidirectional Transmission under Accidental Degenerated Dirac point. *Opt Commun* (2017) 389:58–62. doi:10.1016/j.optcom.2016.12.013
109. Xu T, Fang A, Jia Z, Ji L, Hang ZH. Realization of a complementary medium using dielectric photonic crystals. *Opt. Lett.* (2017) 42:4909. doi:10.1364/ol.42.004909
110. Dong G, Li Z, Zhou J, Qiao P, Yang X, Meng X. Precise Displacement Measurement in Single-Beam Interferometry Employing Photonic Metamaterial with Effective Zero-index. *Opt Express* (2017) 25:31509. doi:10.1364/oe.25.031509
111. Yves S, Berthelot T, Fink M, Lerosey G, Lemoult F. Measuring Dirac Cones in a Subwavelength Metamaterial. *Phys Rev Lett* (2018) 121:267601. doi:10.1103/physrevlett.121.267601
112. Xu B, Li T, Zhu S. Simulation of Massless Dirac Dynamics in Plasmonic Waveguide Arrays. *Opt Express* (2018) 26:13416. doi:10.1364/oe.26.013416
113. Hu L, Xie K, Hu Z, Mao Q, Xia J, Jiang H, et al. Experimental Observation of Wave Localization at the Dirac Frequency in a Two-Dimensional Photonic crystal Microcavity. *Opt Express* (2018) 26:8213. doi:10.1364/oe.26.008213
114. Reddy IVAK, Sukhotskiy V, Baev A, Liu K, Haus JW, Sakoda K, et al. Quasi-triply-degenerate States and Zero Refractive index in Two-Dimensional All-Dielectric Photonic Crystals. *Opt Express* (2020) 28:5548. doi:10.1364/oe.383589
115. Xu T, Zhu D, Hang ZH. Pulse Reshaping in Double-Zero-index Photonic Crystals with Dirac-Like-Cone Dispersion. *Sci Rep* (2020) 10:8416. doi:10.1038/s41598-020-65461-8
116. Xu C, Fang A, Chu H, Luo J, Chan CT, Hang ZH, et al. Angular Selection of Incident Waves by Photonic Crystals with Position-Varying Dirac Points at the Brillouin Zone Boundary. *Phys Rev B* (2016) 93:245116. doi:10.1103/physrevb.93.245116
117. Kim J, Yu S, Park N. Universal Design Platform for an Extended Class of Photonic Dirac Cones. *Phys Rev Appl* (2020) 13:044015. doi:10.1103/physrevapplied.13.044015
118. Hajian H, Ozbay E, Caglayan H. Enhanced Transmission and Beaming via a Zero-index Photonic crystal. *Appl Phys Lett* (2016) 109:031105. doi:10.1063/1.4959085
119. Li Y, Wu Y, Chen X, Mei J. Selection Rule for Dirac-like Points in Two-Dimensional Dielectric Photonic Crystals. *Opt Express* (2013) 21:7699. doi:10.1364/oe.21.007699
120. Indaleeb MM, Banerjee S. Simultaneous Dirac-like Cones at Two Energy States in Tunable Phononic Crystals: An Analytical and Numerical Study. *Crystals* (2021) 11:1528. doi:10.3390/cryst11121528
121. Shankhwar N, Kalra Y, Sinha RK. All Dielectric Zero-index Metamaterial for TE/TM Polarization. *J Opt* (2018) 20:115101. doi:10.1088/2040-8986/aae31c
122. Sakoda K. Double Dirac Cones in Triangular-Lattice Metamaterials. *Opt Express* (2012) 20:9925–39. doi:10.1364/oe.20.009925
123. Kim S, Kim S, Kee C. Photonic Crystals Composed of Virtual Pillars with Magnetic walls: Photonic Band Gaps and Double Dirac Cones. *Phys Rev B* (2016) 94: 085118. doi:10.1103/physrevb.94.085118
124. Wu L-H, Hu X. Scheme for Achieving a Topological Photonic crystal by Using Dielectric Material. *Phys Rev Lett* (2015) 114:223901. doi:10.1103/physrevlett.114.223901
125. Yang Y, Xu YF, Xu T, Wang H-X, Jiang J-H, Hu X, et al. Visualization of a Unidirectional Electromagnetic Waveguide Using Topological Photonic Crystals Made of Dielectric Materials. *Phys Rev Lett* (2018) 120:217401. doi:10.1103/physrevlett.120.217401
126. Lei L, Yu T, Liu W, Wang T, Liao Q. Dirac Cones with Zero Refractive Indices in Phoxonic Crystals. *Opt Express* (2022) 30:308. doi:10.1364/oe.446356
127. Wang J-R, Chen X-D, Zhao F-L, Dong J-W. Full Polarization Conical Dispersion and Zero-Refractive-Index in Two-Dimensional Photonic Hypercrystals. *Sci Rep* (2016) 6:22739. doi:10.1038/srep22739
128. Rodríguez JA, Wang B, Cappelli MA. Dual-polarization Dirac Cones in a Simple 2D Square Lattice Photonic crystal. *Opt Lett* (2020) 45:2486. doi:10.1364/ol.389163
129. Wu Y. A Semi-dirac point and an Electromagnetic Topological Transition in a Dielectric Photonic crystal. *Opt Express* (2014) 22:1906–17. doi:10.1364/oe.22.001906
130. He X-T, Zhong Y-N, Zhou Y, Zhong Z-C, Dong J-W. Dirac Directional Emission in Anisotropic Zero Refractive index Photonic Crystals. *Sci Rep* (2015) 5:13085. doi:10.1038/srep13085
131. Vertchenko L, DeVault C, Malureanu R, Mazur E, Lavrinenko A. Near-Zero Index Photonic Crystals with Directive Bound States in the Continuum. *Laser Photon Rev* (2021) 15:2000559. doi:10.1002/lpor.202000559
132. Yasa UG, Turduev M, Giden IH, Kurt H. Full Utilization of Semi-dirac Cones in Photonics. *Phys Rev B* (2018) 97:195131. doi:10.1103/physrevb.97.195131
133. Bor E, Turduev M, Yasa UG, Kurt H, Staliunas K. Asymmetric Light Transmission Effect Based on an Evolutionary Optimized Semi-dirac Cone Dispersion Photonic Structure. *Phys Rev B* (2018) 98:245112. doi:10.1103/physrevb.98.245112
134. Bor E, Gorkem Yasa U, Kurt H, Turduev M. Demonstration of Carpet Cloaking by an Anisotropic Zero Refractive index Medium. *Opt Lett* (2020) 45:2423. doi:10.1364/ol.388432
135. Chua S-L, Lu L, Bravo-Abad J, Joannopoulos JD, Soljačić M. Larger-area Single-Mode Photonic crystal Surface-Emitting Lasers Enabled by an Accidental Dirac point. *Opt Lett* (2014) 39:2072. doi:10.1364/ol.39.002072
136. Zhen B, Hsu CW, Igarashi Y, Lu L, Kaminer I, Pick A, et al. Spawning Rings of Exceptional Points Out of Dirac Cones. *Nature* (2015) 525:354–8. doi:10.1038/nature14889
137. Memarian M, Eleftheriades GV. Dirac Leaky-Wave Antennas for Continuous Beam Scanning from Photonic Crystals. *Nat Commun* (2015) 6:5855. doi:10.1038/ncomms6855
138. Li Y, Kita S, Muñoz P, Reshef O, Vulis DI, Yin M, et al. On-chip Zero-index Metamaterials. *Nat Photon* (2015) 9:738–42. doi:10.1038/nphoton.2015.198
139. He X-T, Huang Z-Z, Chang M-L, Xu S-Z, Zhao F-L, Deng S-Z, et al. Realization of Zero-Refractive-Index Lens with Ultralow Spherical Aberration. *ACS Photon* (2016) 3:2262–7. doi:10.1021/acsphotonics.6b00714
140. Kamiński PM, Taghizadeh A, Breinbjerg O, Mørk J, Arslanagić S. Control of Exceptional Points in Photonic crystal Slabs. *Opt Lett* (2017) 42:2866–9. doi:10.1364/OL.42.002866
141. Vulis DI, Li Y, Reshef O, Camayd-Muñoz P, Yin M, Kita S, et al. Monolithic CMOS-Compatible Zero-index Metamaterials. *Opt Express* (2017) 25: 12381–99. doi:10.1364/oe.25.012381
142. Kita S, Li Y, Camayd-Muñoz P, Reshef O, Vulis DI, Day RW, et al. On-chip All-Dielectric Fabrication-Tolerant Zero-index Metamaterials. *Opt Express* (2017) 25:8326. doi:10.1364/oe.25.008326
143. Reshef O, Camayd-Muñoz P, Vulis DI, Li Y, Lončar M, Mazur E. Direct Observation of Phase-free Propagation in a Silicon Waveguide. *ACS Photon* (2017) 4:2385–9. doi:10.1021/acsphotonics.7b00760
144. Minkov M, Williamson IAD, Xiao M, Fan S. Zero-index Bound States in the Continuum. *Phys Rev Lett* (2018) 121:263901. doi:10.1103/physrevlett.121.263901
145. Peng Y, Liao S. ZIM Laser: Zero-Index-Materials Laser. *IEEE J Multiscale Multiphys Comput Tech* (2019) 4:133–42. doi:10.1109/jmmct.2019.2905368
146. Dong T, Liang J, Camayd-Muñoz S, Liu Y, Tang H, Kita S, et al. Ultra-low-loss On-Chip Zero-index Materials. *Light Sci Appl* (2021) 10:10. doi:10.1038/s41377-020-00436-y
147. Tang H, DeVault C, Camayd-Muñoz SA, Liu Y, Jia D, Du F, et al. Low-Loss Zero-Index Materials. *Nano Lett* (2021) 21:914–20. doi:10.1021/acs.nanolett.0c03575
148. Chan CT, Huang X, Liu F, Hang ZH. Dirac Dispersion and Zero-index in Two Dimensional and Three Dimensional Photonic and Phononic Systems. *Prog Electromagn Res B* (2012) 44:164–90. doi:10.2528/pierb12082103
149. Sakoda K. Dirac Cone in Two- and Three-Dimensional Metamaterials. *Opt Express* (2012) 20:3898–917. doi:10.1364/oe.20.003898
150. Xu C, Chu H, Luo J, Hang ZH, Wu Y, Lai Y. Three-dimensional Electromagnetic Void Space. *Phys Rev Lett* (2021) 127:123902. doi:10.1103/physrevlett.127.123902
151. Cui X, Ding K, Dong J-W, Chan CT. Realization of Complex Conjugate media Using Non-PT-symmetric Photonic Crystals. *Nanophotonics* (2019) 9: 195–203. doi:10.1515/nanoph-2019-0389

152. Wang H, Xie B, Gupta SK, Zhu X, Liu L, Liu X, et al. Exceptional Concentric Rings in a Non-hermitian Bilayer Photonic System. *Phys Rev B* (2019) 100: 165134. doi:10.1103/physrevb.100.165134
153. Xue H, Wang Q, Zhang B, Chong YD. Non-Hermitian Dirac Cones. *Phys Rev Lett* (2020) 124:236403. doi:10.1103/physrevlett.124.236403
154. Wang N, Zhang R, Chan CT, Wang GP. Effective Medium Theory for a Photonic Pseudospin-1/2 System. *Phys Rev B* (2020) 102:094312. doi:10.1103/physrevb.102.094312
155. Luo L, Shao Y, Li J, Fan R, Peng R, Wang M, et al. Non-Hermitian Effective Medium Theory and Complex Dirac-like Cones. *Opt Express* (2021) 29: 14345. doi:10.1364/oe.425862
156. Miri MA, Alù A. Exceptional Points in Optics and Photonics. *Science* (2019) 363:eaar7709. doi:10.1126/science.aar7709
157. Özdemir SK, Rotter S, Nori F, Yang L. Parity-time Symmetry and Exceptional Points in Photonics. *Nat Mater* (2019) 18:783–98. doi:10.1038/s41563-019-0304-9
158. Gupta SK, Zou Y, Zhu XY, Lu MH, Zhang LJ, Liu XP, et al. Parity-Time Symmetry in Non-hermitian Complex Optical Media. *Adv Mater* (2019) 2019:1903639. doi:10.1002/adma.201903639
159. Liu F, Lai Y, Huang X, Chan CT. Dirac Cones at k=0 in Phononic Crystals. *Phys Rev B* (2011) 84:224113. doi:10.1103/physrevb.84.224113
160. Liu F, Huang X, Chan CT. Dirac Cones at k=0 in Acoustic Crystals and Zero Refractive index Acoustic Materials. *Appl Phys Lett* (2012) 100:071911. doi:10.1063/1.3686907
161. Chen Z-G, Ni X, Wu Y, He C, Sun X-C, Zheng L-Y, et al. Accidental Degeneracy of Double Dirac Cones in a Phononic crystal. *Sci Rep* (2014) 4: 4613. doi:10.1038/srep04613
162. Li Y, Wu Y, Mei J. Double Dirac Cones in Phononic Crystals. *Appl Phys Lett* (2014) 105:014107. doi:10.1063/1.4890304
163. Liu F, Liu Z. Elastic Waves Scattering without Conversion in Metamaterials with Simultaneous Zero Indices for Longitudinal and Transverse Waves. *Phys Rev Lett* (2015) 115:175502. doi:10.1103/physrevlett.115.175502
164. Wu S, Mei J. Flat Band Degeneracy and Near-Zero Refractive index Materials in Acoustic Crystals. *AIP Adv* (2016) 6:015204. doi:10.1063/1.4939847
165. Zhu H, Semperlotti F. Double-zero-index Structural Phononic Waveguides. *Phys Rev Appl* (2017) 8:064031. doi:10.1103/physrevapplied.8.064031
166. Dubois M, Shi C, Zhu X, Wang Y, Zhang X. Observation of Acoustic Dirac-like Cone and Double Zero Refractive index. *Nat Commun* (2017) 8:14871. doi:10.1038/ncomms14871
167. Dai H, Xia B, Yu D. Dirac Cones in Two-Dimensional Acoustic Metamaterials. *J Appl Phys* (2017) 122:065103. doi:10.1063/1.4998438
168. Dai H, Liu T, Jiao J, Xia B, Yu D. Double Dirac Cone in Two-Dimensional Phononic Crystals beyond Circular Cells. *J Appl Phys* (2017) 121:135105. doi:10.1063/1.4979852
169. Zhao W, Yang Y, Tao Z, Hang ZH. Tunable Transmission and Deterministic Interface States in Double-Zero-index Acoustic Metamaterials. *Sci Rep* (2018) 8:6311. doi:10.1038/s41598-018-24773-6
170. Hyun J, Choi W, Wang S, Park C-s., Kim M. Systematic Realization of Double-Zero-index Phononic Crystals with Hard Inclusions. *Sci Rep* (2018) 8:7288. doi:10.1038/s41598-018-25696-y
171. Indaleeb MM, Banerjee S, Ahmed H, Saadatzi M, Ahmed R. Deaf Band Based Engineered Dirac Cone in a Periodic Acoustic Metamaterial: A Numerical and Experimental Study. *Phys Rev B* (2019) 99:024311. doi:10.1103/physrevb.99.024311
172. Li B, Li Z, Christensen J, Tan KT. Dual Dirac Cones in Elastic Lieb-like Lattice Metamaterials. *Appl Phys Lett* (2019) 114:081906. doi:10.1063/1.5085782
173. Indaleeb MM, Ahmed H, Saadatzi M, Banerjee S. Deaf Band-Based Prediction of Dirac Cone in Acoustic Metamaterials. *J Appl Phys* (2020) 127:064903. doi:10.1063/1.5122297
174. Xu C, Ma G, Chen ZG, Luo J, Shi J, Lai Y, et al. Three-dimensional Acoustic Double-Zero-index Medium with a Fourfold Degenerate Dirac-like point. *Phys Rev Lett* (2020) 124:074501. doi:10.1103/PhysRevLett.124.074501
175. Makris KG, El-Ganainy R, Christodoulides DN, Musslimani ZH. Beam Dynamics in PT Symmetric Optical Lattices. *Phys Rev Lett* (2008) 100: 103904. doi:10.1103/physrevlett.100.103904
176. Hsu CW, Zhen B, Stone AD, Joannopoulos JD, Soljačić M. Bound States in the Continuum. *Nat Rev Mater* (2016) 1:16048. doi:10.1038/natrevmats.2016.48
177. Hsu CW, Zhen B, Lee J, Chua S-L, Johnson SG, Joannopoulos JD, et al. Observation of Trapped Light within the Radiation Continuum. *Nature* (2013) 499:188–91. doi:10.1038/nature12289
178. Pendry JB, Schurig D, Smith DR. Controlling Electromagnetic fields. *Science* (2006) 312:1780–2. doi:10.1126/science.1125907
179. Leonhardt U. Optical Conformal Mapping. *Science* (2006) 312:1777–80. doi:10.1126/science.1126493
180. Schurig D, Mock JJ, Justice BJ, Cummer SA, Pendry JB, Starr AF, et al. Metamaterial Electromagnetic Cloak at Microwave Frequencies. *Science* (2006) 314:977–80. doi:10.1126/science.1133628
181. Ma W, Liu Z, Kudyshev ZA, Boltasseva A, Cai W, Liu Y. Deep Learning for the Design of Photonic Structures. *Nat Photon* (2020) 15:77–90. doi:10.1038/s41566-020-0685-y
182. Peurifoy J, Shen Y, Jing L, Yang Y, Cano-Renteria F, DeLacy BG, et al. Nanophotonic Particle Simulation and Inverse Design Using Artificial Neural Networks. *Sci Adv* (2018) 4:eaar4206. doi:10.1126/sciadv.aar4206
183. Malkiel I, Mrejen M, Nagler A, Arieli U, Wolf L, Suchowski H. Plasmonic Nanostructure Design and Characterization via Deep Learning. *Light Sci Appl* (2018) 7:60. doi:10.1038/s41377-018-0060-7
184. Liu Z, Zhu D, Rodrigues SP, Lee K-T, Cai W. Generative Model for the Inverse Design of Metasurfaces. *Nano Lett* (2018) 18:6570–6. doi:10.1021/acs.nanolett.8b03171
185. Luo J, Li X, Zhang X, Guo J, Liu W, Lai Y, et al. Deep-learning-enabled Inverse Engineering of Multi-Wavelength Invisibility-To-Superscattering Switching with Phase-Change Materials. *Opt Express* (2021) 29:10527. doi:10.1364/oe.422119

Conflict of Interest: The authors declare that the research was conducted in the absence of any commercial or financial relationships that could be construed as a potential conflict of interest.

frontiers in Physics

ORIGINAL RESEARCH
published: 18 February 2022
doi: 10.3389/fphy.2022.844049

Topological Engineering of the Iso-Frequency Contours in Connection-Type Metamaterials

*Zhao-Lin Liao, Wei-Min Deng, Ze-Liang Xiang, Wen-Jie Chen * and Jian-Wen Dong **

School of Physics and State Key Laboratory of Optoelectronic Materials and Technologies, Sun Yat-Sen University, Guangzhou, China

The topology of isofrequency surface governs the electromagnetic wave propagation and light–matter interaction in metamaterials. For most metamaterials with local medium description, the low-frequency isosurfaces are typical spheres or ellipsoids centered at zero momentum, which, to some extent, limits our manipulation ability on low-frequency wave. In this work, based on connection-type wire metamaterials, we propose a scheme to engineer the shapes of isofrequency surfaces. An equivalent circuit model is developed to analyze the low-frequency dispersion of connection-type metamaterials. It implies that the shape of index ellipsoids at quasistatic limit is determined by the equivalent inductances and capacitances of the metallic meshes. By adjusting these equivalent circuit parameters, we can achieve the isotropic or anisotropic index ellipsoids at quasistatic limit and, hence, a cruciform or bowtie-shaped isofrequency contours for the lowest-frequency band. Our results demonstrate a feasible platform for topological engineering of isofrequency surfaces, which may pave the way to novel devices for manipulating long-wavelength electromagnetic wave.

Keywords: metamaterials, metallic meshes, isofrequency contours, quasistatic limit, equivalent circuit

OPEN ACCESS

Edited by:
Guancong Ma,
Hong Kong Baptist University, Hong Kong SAR, China

Reviewed by:
Jie Luo,
Soochow University, China
Zi-Lan Deng,
Jinan University, China

***Correspondence:**
Wen-Jie Chen
chenwenj5@mail.sysu.edu.cn
Jian-Wen Dong
dongjwen@mail.sysu.edu.cn

Specialty section:
This article was submitted to Optics and Photonics, a section of the journal Frontiers in Physics

Received: *27 December 2021*
Accepted: *21 January 2022*
Published: *18 February 2022*

Citation:
Liao Z-L, Deng W-M, Xiang Z-L, Chen W-J and Dong J-W (2022) Topological Engineering of the Iso-Frequency Contours in Connection-Type Metamaterials. Front. Phys. 10:844049. doi: 10.3389/fphy.2022.844049

1 INTRODUCTION

The isofrequency surfaces (IFSs) of a medium play an important role in determining the electromagnetic (EM) wave propagation[1] and light–matter interactions [2, 3] inside the medium. For a natural material, the shape of IFSs depends on its microscopic atomic arrangement and is usually an isotropic sphere or an anisotropic ellipsoid in k space. Metamaterials (MMs) [4–10], artificially synthesized materials with subwavelength microstructures, can exhibit various types of closed/open IFSs with exotic topologies (concave sphere [11, 12], hyperboloid [2, 3, 13, 14], cuboid [15, 16], etc.), which lead to anomalous wave phenomena (negative refraction [1, 11, 12], subwavelength imaging [17–20], self-collimation [15, 16, 21, 22], etc.) alongside numerous engineering applications. However, since their unnatural responses rely on the EM resonance of metallic structures [4, 5, 10], these exotic IFSs and associated phenomena only occur near the resonant frequency, which limits their working bandwidth. Also, when the wave frequency approaches quasistatic limit, the IFSs of these artificial media usually deteriorate to an ordinary ellipsoid centered at a zero k-point.

It would be highly desirable if the shapes of low-frequency IFSs can be customized at will, then we could control the EM wave propagation behavior in a relatively broader bandwidth. It is well known that metallic wire medium [4, 23–40], such as disconnected wire arrays, can exhibit the strong spatial dispersion (nonlocal effect) even in long-wavelength limit [25, 26]. By incorporating two or more sets

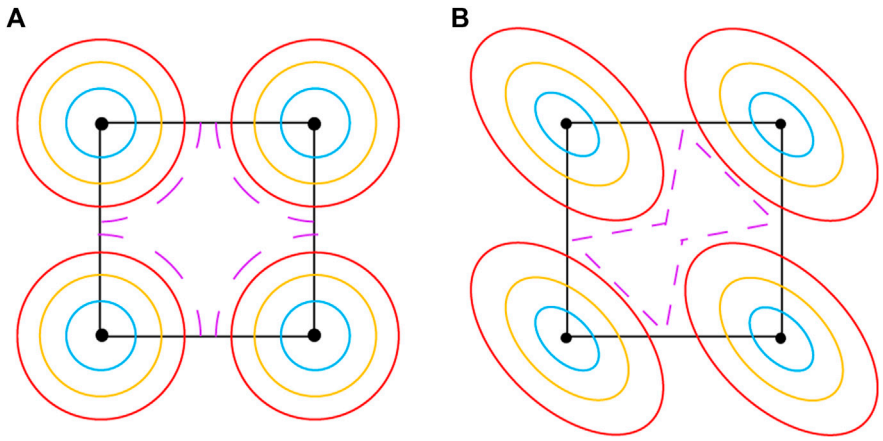

FIGURE 1 | Topological engineering of IFCs utilizing the degree of freedom of index ellipsoids at a nonzero *k*-point. While the centers of index ellipsoids are determined by the global connectivity of the metallic mesh, the shapes of index ellipsoids can be designed via the structural details of the mesh. **(A)** IFCs of the metamaterial with an isotropic index circle at the Brillouin zone corner. As the frequency increases, the four circles grow and shape into a cruciform. **(B)** IFCs of the MM with an anisotropic index ellipse at the Brillouin zone corner. As the frequency increases, the four ellipses grow and shape into a bowtie.

of metallic meshes, one can engineer the density of states at quasistatic limit [28, 32, 33]. The EM properties of these multiple interlocking meshes are governed by electric circuit equations [28, 29] rather than Maxwell equations [41]; they are, thus, called non-Maxwellian medium. Interestingly, researchers [33] found that the global connectivity of these metallic meshes can introduce a momentum shift of the low-frequency index ellipsoid away from the zero *k*-point. Recently, wire medium again attracted the attention of researchers, since it could serve as a new design degree of freedom to tailor the low-frequency dispersion [34–37] and associated wave properties [38–40] of MMs.

In this study, based on connection-type MMs [28, 32–34, 36] that support multiple quasistatic modes at a nonzero *k*-point, we propose a scheme to engineer the shapes of low-frequency IFSs. As frequency increases from zero, isotropic or anisotropic index ellipsoids emerge from these nonzero *k*-points. By properly shaping the index ellipsoids, one can, in principle, realize arbitrary-shaped isofrequency contours (IFCs) even for the lowest frequency band. The benefit of our method is that it may provide a novel way for manipulating long-wavelength EM wave. To illustrate our idea clearly, we focus on a 2D slab of connection-type MMs, instead of complex 3D MMs. We develop an equivalent circuit model for the connection-type MMs to describe their low-frequency EM behaviors. The model implies that the shape of index ellipsoids can be engineered via the equivalent inductances and capacitances of the metallic meshes, which are determined by the structural details of the meshes. By appropriately adjusting the metallic structure, we can achieve isotropic or anisotropic index ellipsoids with different group velocities, which agree well with our equivalent circuit model.

2 RESULTS

Connection-type MMs are a type of MMs composed of N sets of interpenetrating metallic meshes, which support $(N-1)$ quasistatic modes lying at a nonzero *k*-point. Their positions in k space are determined by the global connectivity of the meshes, rather than the structural detail of the meshes. For instance, 2D double-mesh MMs with square lattice [33] can support one quasistatic mode at the Brillouin zone corner (M point), as shown in **Figure 1**. In addition, this quasistatic mode is not an isolated solution at zero frequency. When frequency increases, the index ellipsoids turn into a circle or ellipse from an isolated point at M, which corresponds to a linear cone dispersion emerging from the M point. While the emerging point can be controlled by designing the mesh connectivity, the shapes of index ellipsoids or the group velocities of linear bands are determined by the structural details. Once we can engineer both the centers and the shapes of the low-frequency index ellipsoids, arbitrary-shaped IFCs can be achieved in principle. For the case in **Figure 1**, if the index ellipsoids emerging from the M point are a circle, then cruciform-shaped IFCs (dashed line in **Figure 1A**) would be expected for the midband frequency of band 1. Also, if the index ellipsoids emerging from the M point are an ellipse, bowtie-shaped IFCs (dashed line in **Figure 1B**) would be expected. Generally speaking, multiple zero-frequency modes would appear at multiple *k*-points when considering more sets of interlaced wire meshes. By engineering the shape of each ellipse via the equivalent inductances and capacitances between multiple meshes, arbitrary-shaped IFCs can, in principle, be realized in connection-type MMs.

To analyze the low-frequency index ellipsoids, we establish an equivalent circuit model which could serve as a guideline in designing connection-type MMs. Here, we consider a 2D double mesh arranged in a square lattice. Centered in its unit cell is a metallic block (height d and width w), whose top (bottom) end is connected to the adjacent unit cell via the metallic bar in the $\hat{\mathbf{u}}_1$ ($\hat{\mathbf{u}}_2$) direction (**Figure 2A**). When the unit cell is repeated in x and y directions (3 × 3 supercell in **Figure 2B**), it is actually composed of two disconnected meshes (colored in blue and red)

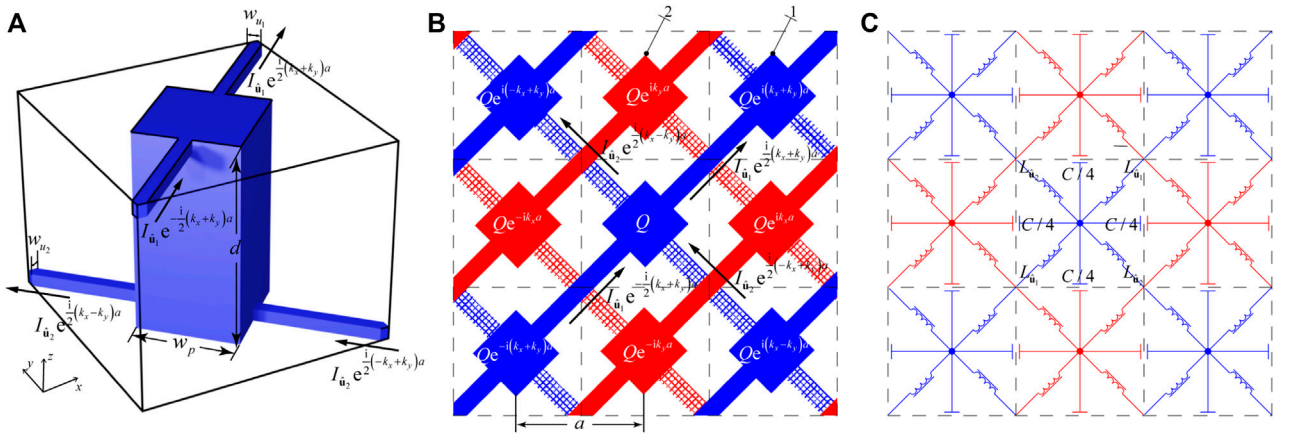

FIGURE 2 | 2D double-mesh MM. **(A)** Unit cell (lattice constant a = 1 *cm*). The metallic block (width w and height d) centered at the unit cell is connected to the adjacent blocks by two metallic wires (width $w_{\hat{\mathbf{u}}_n}$ and n = 1, 2) in $\hat{\mathbf{u}}_1$ and $\hat{\mathbf{u}}_2$ directions. The alternating currents on the wires crossing through the cell boundaries would lead to a time-varying charge Q accumulated on the block. **(B)** 3 × 3 supercell of the 2D double-mesh MM. It shows that the MM is composed of two disconnected metallic meshes (blue and red) with independent potentials. The potential difference for the central unit cell is assumed to be $\Delta\varphi$, and then, the potential differences elsewhere can be obtained using Bloch theorem. **(C)** Equivalent circuit model of the 2D double mesh.

arranged in a checkerboard manner. Since all the metallic components in this study are assumed to be a perfect electric conductor (PEC), blue and red colors just highlight the two sets of meshes with independent quasistatic potentials. According to the quasistatic potential analysis in [33], these 2D double-mesh MMs have one quasistatic mode lying at zone corner M.

We construct a circuit model for this structure to describe its Bloch modes at relatively low (but not zero) frequency. Note that the double-mesh MMs are a slab with finite thickness in the z-direction embedded in air background, and we only consider the EM modes with Bloch k near the M point. Since Bloch k lies below the light cone, the EM mode is guided in the slab and its leakage into air can be neglected. The EM field of Bloch mode would induce alternating currents on the metallic wires and charge accumulation. In **Figure 2A**, the total current passing through the top (bottom) wire along the $\hat{\mathbf{u}}_1$ ($\hat{\mathbf{u}}_2$) direction is assumed to be $I_{\hat{\mathbf{u}}_1}$ ($I_{\hat{\mathbf{u}}_2}$). Taking into consideration the Bloch boundary condition, the currents at the unit cell corners should be $I_{\hat{\mathbf{u}}_1}e^{\frac{i}{2}(k_x+k_y)a}$ and $I_{\hat{\mathbf{u}}_1}e^{-\frac{i}{2}(k_x+k_y)a}$ ($I_{\hat{\mathbf{u}}_2}e^{\frac{i}{2}(k_x-k_y)a}$ and $I_{\hat{\mathbf{u}}_2}e^{\frac{i}{2}(-k_x+k_y)a}$) along the $\hat{\mathbf{u}}_1$ ($\hat{\mathbf{u}}_2$) direction. Due to these alternating currents, a time-varying charge Q should accumulate on the metallic block, which satisfies the following equation:

$$i\omega Q = I_{\hat{\mathbf{u}}_1}e^{\frac{i}{2}(k_x+k_y)a} - I_{\hat{\mathbf{u}}_1}e^{-\frac{i}{2}(k_x+k_y)a} + I_{\hat{\mathbf{u}}_2}e^{\frac{i}{2}(k_x-k_y)a} - I_{\hat{\mathbf{u}}_2}e^{\frac{i}{2}(-k_x+k_y)a}. \tag{1}$$

Since we are dealing with the low-frequency Bloch modes at the k-point not far away from M, the charge on each block should be almost plus or minus alternatively in the square array. Also, as the two meshes serve as two conductors of a capacitor at quasistatic limit, the charge on one block should be proportional to the local potential difference between the two meshes and written as follows:

$$Q = C\Delta\varphi, \tag{2}$$

where $\Delta\varphi$ is the local potential difference between a metallic block and its nearest four neighboring blocks. On the other hand, the alternating currents flowing on the wires would induce alternating magnetic fields, which are here specified by vector potential field $\vec{A}(\vec{r})$. They satisfy the following relation:

$$\begin{bmatrix} A_{\hat{\mathbf{u}}_1} \\ A_{\hat{\mathbf{u}}_2} \end{bmatrix} = \begin{bmatrix} L_{\hat{\mathbf{u}}_1} & \\ & L_{\hat{\mathbf{u}}_2} \end{bmatrix} \begin{bmatrix} I_{\hat{\mathbf{u}}_1} \\ I_{\hat{\mathbf{u}}_2} \end{bmatrix}, \tag{3}$$

where $A_{\hat{\mathbf{u}}_n}$ (n = 1, 2) is a line integral of the vector potential on the path between two neighboring blocks (gray solid line in **Figure 3B**). The inductance matrix is a 2 × 2 matrix whose off-diagonal terms vanish due to the mirror symmetry of the structure. As we are considering the Bloch modes near the M point, $I_{\hat{\mathbf{u}}_1}$ in **Eq. (3)** represents a series of currents (**Figure 3A**), rather than a single line current, in an infinite square lattice. Meanwhile, $A_{\hat{\mathbf{u}}_1}$ represents the vector potential field (**Figure 3B**) induced by these collectively oscillating currents. Thus, the inductance $L_{\hat{\mathbf{u}}_1}$ is actually the ratio between the current array and its induced vector potentials, rather than the self-inductance or mutual inductance of a single wire.

For a perfect conductor, the microscopic electric field inside should vanish, and we have the following equation:

$$\begin{aligned} i\omega A_{\hat{\mathbf{u}}_1} &= \Delta\varphi e^{i(k_x+k_y)a} - \Delta\varphi, \\ i\omega A_{\hat{\mathbf{u}}_2} &= \Delta\varphi e^{i(-k_x+k_y)a} - \Delta\varphi. \end{aligned}, \tag{4}$$

where the local potential difference $\Delta\varphi$ satisfies Bloch theorem, and the voltage drop between two adjacent unit cells can be evaluated by the difference between the local potential differences of the two unit cells.

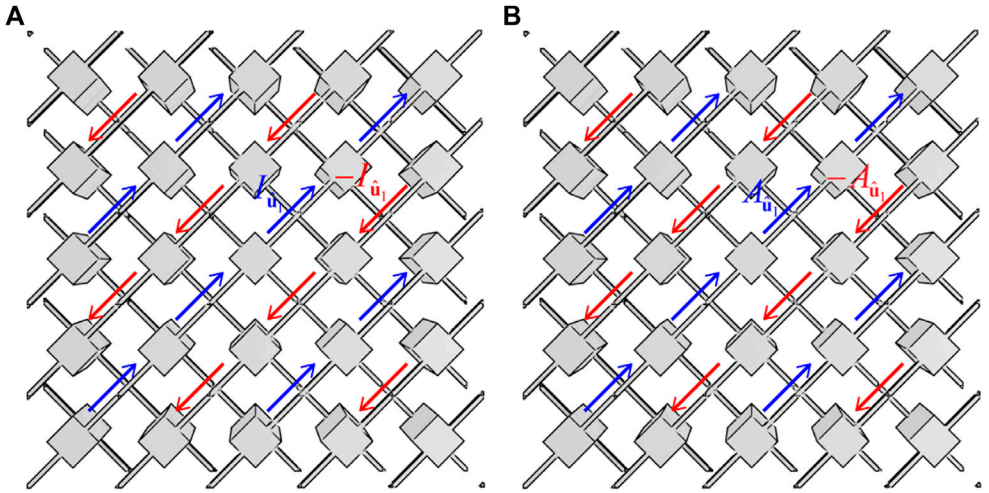

FIGURE 3 | Periodic distributions of **(A)** currents and **(B)** the current-induced vector potentials on the double-mesh MM. Since the quasistatic mode is located at Brillouin zone corner *M*, the electric currents on the two meshes are out of phase (blue and red) and so do the vector potentials they induce. The inductance $L_{\hat{\mathbf{u}}_1}$ is defined as the ratio between this vector potential distribution and the current distribution.

Combining **Eqs. 1–4**, we obtain the following generalized eigenvalue equation:

$$\begin{bmatrix} e^{\frac{i}{2}(k_x+k_y)a} - e^{-\frac{i}{2}(k_x+k_y)a} & e^{\frac{i}{2}(k_x-k_y)a} - e^{\frac{i}{2}(-k_x+k_y)a} & -i\omega C \\ -i\omega L_{\hat{\mathbf{u}}_1} & & e^{i(k_x+k_y)a} - 1 \\ & -i\omega L_{\hat{\mathbf{u}}_2} & e^{i(-k_x+k_y)a} - 1 \end{bmatrix} \begin{bmatrix} I_{\hat{\mathbf{u}}_1} \\ I_{\hat{\mathbf{u}}_2} \\ \Delta\varphi \end{bmatrix} = \begin{bmatrix} 0 \\ 0 \\ 0 \end{bmatrix}. \tag{5}$$

The equation has a nonzero eigenvector only when the determinant in **Eq. 5** vanishes; then, the low-frequency dispersion can be derived as follows:

$$\omega^2 = 4C^{-1}\left(L_{\hat{\mathbf{u}}_1}^{-1} \sin^2 \frac{(\delta k_x + \delta k_y)a}{2} + L_{\hat{\mathbf{u}}_2}^{-1} \sin^2 \frac{(\delta k_x - \delta k_y)a}{2} \right). \tag{6}$$

The band dispersion is controlled by two equivalent inductances and one equivalent capacitance mentioned above, which can be calculated in magnetostatic and electrostatic limits. Also, this model applies well for low frequencies, as long as the Bloch modes near the quasistatic mode (at the *M* point in this case) are considered (δk_x and δk_y are sufficiently small compared to the reciprocal vector). Although the equivalent circuit model would deteriorate as the frequency increases, it still gives a qualitative prediction on the IFCs at midband frequency and can serve as a guideline for MM design.

From **Eq. 6**, the group velocities in $\hat{\mathbf{u}}_1$ and $\hat{\mathbf{u}}_2$ directions are written as

$$\begin{aligned} v_{g,\hat{\mathbf{u}}_1} &= a\sqrt{2C^{-1}L_{\hat{\mathbf{u}}_1}^{-1}}, \\ v_{g,\hat{\mathbf{u}}_2} &= a\sqrt{2C^{-1}L_{\hat{\mathbf{u}}_2}^{-1}}. \end{aligned} \tag{7}$$

and can then be controlled by the equivalent capacitance and two equivalent inductances. Since the group velocities depend on the equivalent capacitance and inductances, the shape of the index ellipsoid can be controlled by adjusting the structural details of meshes, which determine the equivalent circuit parameters.

To investigate the dependence of group velocities on the structural parameters, we numerically calculate the equivalent inductances and capacitances of a series of double-mesh MMs. First, we alter the height of the metallic block centered at the unit cell while keeping other parameters unaltered (width $w_p = 0.4a$ and $w_{\hat{\mathbf{u}}_1} = w_{\hat{\mathbf{u}}_2} = 0.05a$). Results from electrostatic and magnetostatic simulations are shown in **Figure 4A**. It is found that the change of block height would mostly alter the equivalent capacitance C between the two meshes, rather than inductances $L_{\hat{\mathbf{u}}_1}$ and $L_{\hat{\mathbf{u}}_2}$. The reason is that the block height would increase the surface area of the meshes and, thus, the equivalent capacitance rises. On the other hand, the equivalent inductances are related to the width of the horizontal metallic wires and the distance between them [29]. The two inductances almost remain unchanged, as in **Figure 4A**. Hence, the group velocities at quasistatic limit along $\hat{\mathbf{u}}_1$ and $\hat{\mathbf{u}}_2$ directions should decrease as the block height changes. **Figure 4B** shows the results obtained from calculated band structures and the ones from equivalent parameters, which agreed well with each other.

In another case, we increase the $\hat{\mathbf{u}}_1$ wire width while keeping the other structural parameters unchanged (height $d = 0.8a$, width $w_p = 0.4a$, and $w_{\hat{\mathbf{u}}_2} = 0.05a$). The results are plotted in **Figures 4C,D**. In this case, the symmetry of the structure is reduced from S_4 to C_2, resulting in anisotropic inductances in $\hat{\mathbf{u}}_1$ and $\hat{\mathbf{u}}_2$ directions. The inductance $L_{\hat{\mathbf{u}}_1}$ (purple open circle in **Figure 4C**) decreases, while $L_{\hat{\mathbf{u}}_2}$ (blue solid circle in **Figure 4C**) remains almost unchanged. In the meantime, the equivalent capacitance slightly increases due to the surface area of the $\hat{\mathbf{u}}_1$ wire. To sum up, the group velocity $v_{g,\hat{\mathbf{u}}_1}$ becomes faster as $w_{\hat{\mathbf{u}}_2}$ increases while $v_{g,\hat{\mathbf{u}}_2}$ becomes somewhat slower, see the symbols

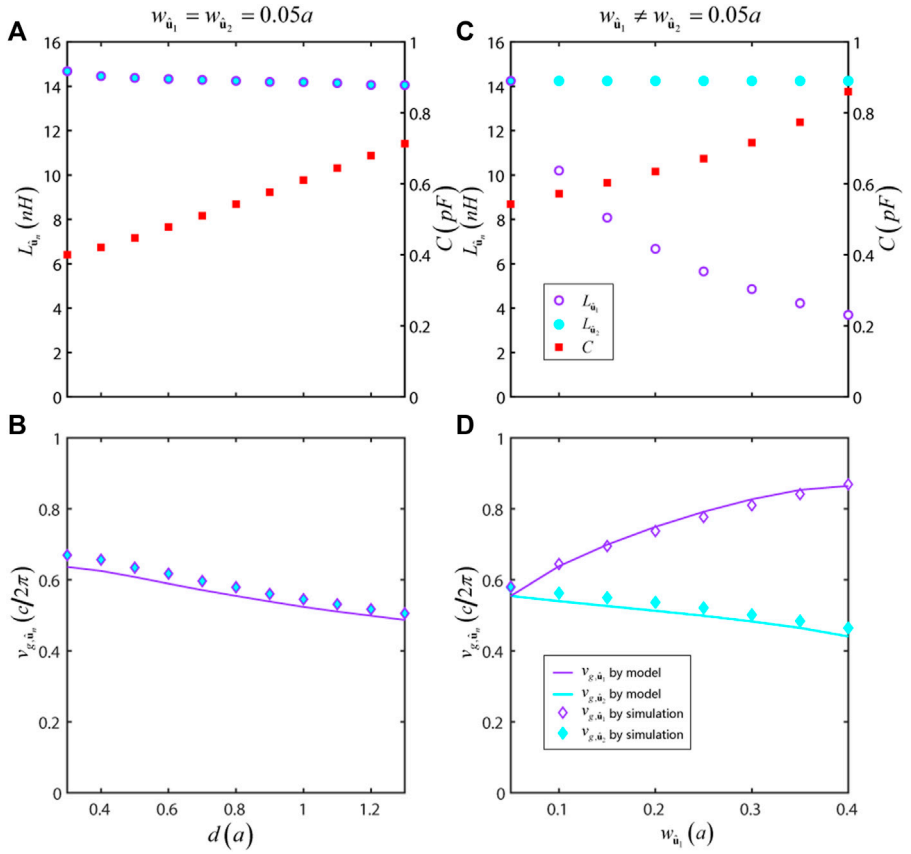

FIGURE 4 | Tuning the group velocities of index ellipsoids by the inductances $L_{\hat{\mathbf{u}}_n}$ and capacitance C of the double-mesh MM. **(A)** Parameter dependencies of the inductances and capacitance for the isotropic MM. Here, we change the metallic block's height while keeping the other parameters unchanged (width $w_p = 0.4a$ and $w_{\hat{\mathbf{u}}_1} = w_{\hat{\mathbf{u}}_2} = 0.05a$). **(B)** Group velocities of the index circle at quasistatic limit as a function of d. Solid lines are given by the equivalent circuit model, while symbols are given by the simulated band structure. **(C,D)** The same as panels A and B but for the anisotropic MM, where we change one of the bar widths $w_{\hat{\mathbf{u}}_1}$ instead of height d (height $d = 0.8a$, width $w_p = 0.4a$, and $w_{\hat{\mathbf{u}}_2} = 0.05a$).

(model) and lines (simulation) in **Figure 4D**. Here, the index ellipsoids are oriented in $\hat{\mathbf{u}}_1$ and $\hat{\mathbf{u}}_2$ directions. In principle, the index ellipsoids can be oriented in other directions by properly designing the widths of four horizontal wires in the unit cell.

To further see the applicability of our model, **Figures 5A,B** plot the numerically simulated band structure and index ellipsoids for isotropic double-mesh MMs (height $d = 0.8a$, width $w_p = 0.4a$, and $w_{\hat{\mathbf{u}}_1} = w_{\hat{\mathbf{u}}_2} = 0.05a$) while **Figure 5C** gives the index ellipsoids predicted by our model. They agree well with each other and validate our theory. In both results, the index ellipsoids gradually evolve from a circle to a squircle shape as the frequency increases, due to the two sinusoidal terms in **Eq. 6**.

To see the influence for different equivalent inductances in $\hat{\mathbf{u}}_1$ and $\hat{\mathbf{u}}_2$ directions, we increase the bar width of the metallic wire in the $\hat{\mathbf{u}}_1$ direction in order to weaken its inductance $L_{\hat{\mathbf{u}}_1}$. Meanwhile, all the other parameters remain unchanged (height $d = 0.8a$, width $w_p = 0.4a$, $w_{\hat{\mathbf{u}}_1} = 0.4a$, and $w_{\hat{\mathbf{u}}_2} = 0.05a$) (inset of **Figure 5E**). The group velocity in the $\hat{\mathbf{u}}_1$ direction of the first band becomes faster than that in the $\hat{\mathbf{u}}_2$ direction, leading to elliptical index ellipsoids simulated in **Figure 5F**. Also, as the frequency increases, the shape of index ellipsoids evolves gradually from an ellipse to a rounded rhombus. This is well predicted by our circuit model (**Figure 5G**).

According to our circuit model, we can achieve isotropic or anisotropic shape of index ellipsoids at quasistatic limit by adjusting the equivalent inductances in $\hat{\mathbf{u}}_1$ and $\hat{\mathbf{u}}_2$ directions. Then, the special-shaped IFCs can be achieved for midband frequencies of band 1, as proposed in **Figure 1**. For isotropic wire MM slabs in **Figure 2A** with appropriate structural parameters (height $d = 0.42a$, width $w_p = 0.4a$, and $w_{\hat{\mathbf{u}}_1} = w_{\hat{\mathbf{u}}_2} = 0.2a$), an index ellipsoid emerges from the M point due to the isotropic equivalent inductances. For midband frequencies ($f = 0.2$ (c/a) for example), the IFCs become cruciform shaped (**Figure 6A**). In another case, the index ellipsoid at M can be anisotropic when two equivalent

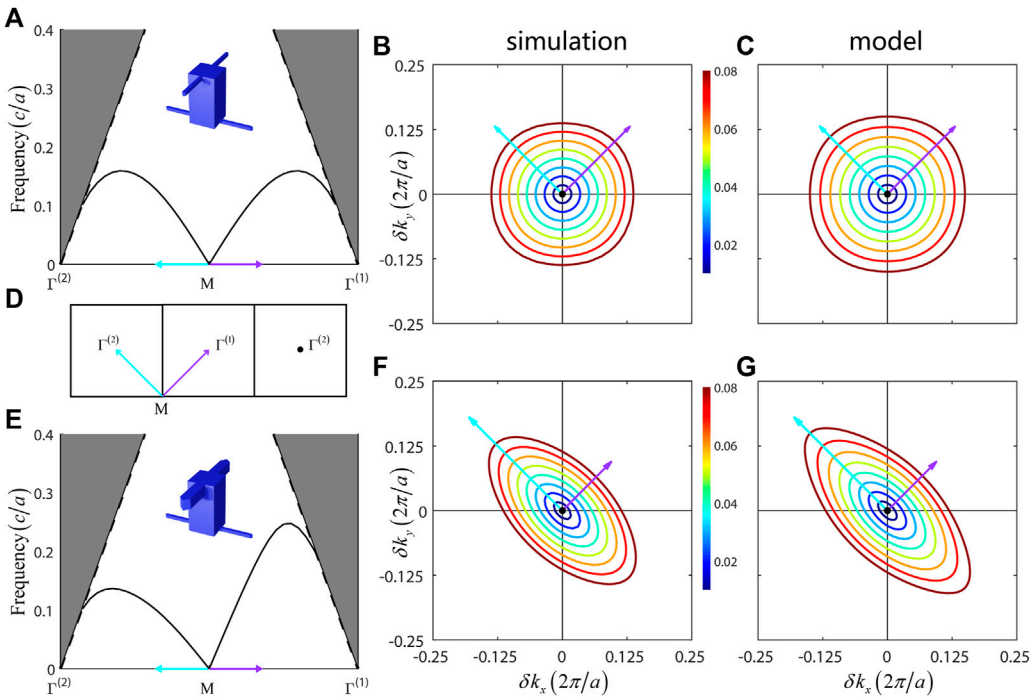

FIGURE 5 | Shaping the index ellipsoids by introducing anisotropic inductances. **(A)** Simulated band dispersion and **(B)** corresponding IFCs for the isotropic MM shown in **Figure 2A**. In this case, the two metallic wires have the same bar width (height $d = 0.8a$, width $w_p = 0.4a$, and $w_{\hat{\mathbf{u}}_1} = w_{\hat{\mathbf{u}}_2} = 0.05a$), leading to the isotropic inductances along $\hat{\mathbf{u}}_1$ and $\hat{\mathbf{u}}_2$ directions. **(C)** IFCs given by the equivalent circuit model. When the frequency increases, the index circle gradually evolves into a squircle shape, which agrees well with the simulated result in panel B. **(D)** First and second Brillouin zones. **(E)** Simulated band dispersion and **(F)** corresponding IFCs for an anisotropic metamaterial. In this case, the metallic wire in the $\hat{\mathbf{u}}_1$ direction has a thicker bar width than the one in the $\hat{\mathbf{u}}_2$ direction (height $d = 0.8a$, width $w_p = 0.4a$, $w_{\hat{\mathbf{u}}_1} = 0.4a$, and $w_{\hat{\mathbf{u}}_2} = 0.05a$), leading to anisotropic inductances and the index ellipse in panel F. **(G)** IFCs given by the equivalent circuit model.

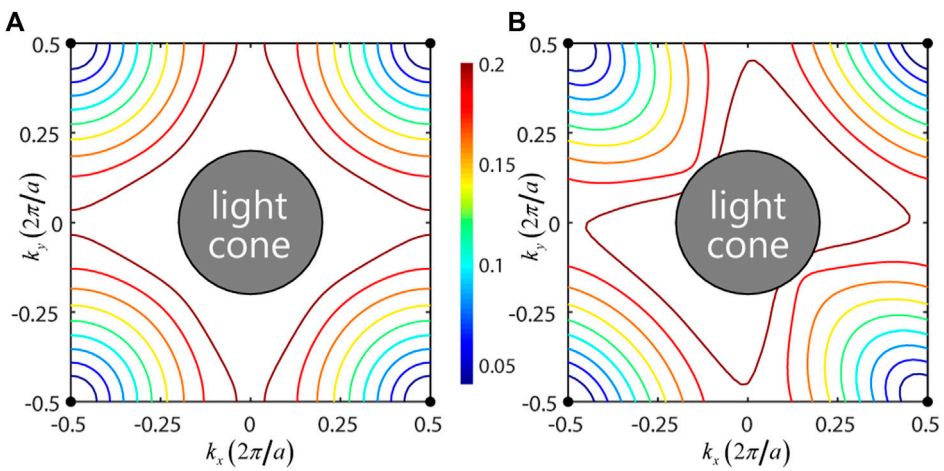

FIGURE 6 | MMs with **(A)** cruciform-shaped or **(B)** bowtie-shaped IFCs (simulation). Structural parameters: in **(A)**, height $d = 0.42a$, width $w_p = 0.4a$, and $w_{\hat{\mathbf{u}}_1} = w_{\hat{\mathbf{u}}_2} = 0.2a$; in **(B)**, height $d = 0.36a$, width $w_p = 0.4a$, $w_{\hat{\mathbf{u}}_1} = 0.3a$, and $w_{\hat{\mathbf{u}}_2} = 0.05a$.

inductance parameters are unequal. Considering the MM slabs with structural parameters (height $d = 0.36a$, width $w_p = 0.4a$, $w_{\hat{\mathbf{u}}_1} = 0.3a$, and $w_{\hat{\mathbf{u}}_2} = 0.05a$), we have bowtie-shaped IFCs at around $f = 0.2$ (c/a) (**Figure 6B**). In addition, the frequency range of special-shaped IFCs can be adjusted by the mutual capacitance between double meshes.

3 CONCLUSION

In conclusion, we propose an equivalent circuit model for connection-type MMs to analyze its low-frequency dispersion away from quasistatic limit, taking into account the mesh connectivity. The model implies that the low-frequency IFCs can be engineered via the equivalent inductances and capacitance of the metallic meshes. For instance, we adjust the metallic block height and the wire width according to the model and demonstrate the feasibility of shaping the low-frequency IFCs. Coupled with the degree of freedom of the quasistatic mode at an arbitrary *k*-point, one can, in principle, realize the arbitrary topology of IFCs and manipulate the EM propagation properties using an artificial medium.

DATA AVAILABILITY STATEMENT

The original contributions presented in the study are included in the article/supplementary material, and further inquiries can be directed to the corresponding authors.

AUTHOR CONTRIBUTIONS

WC and JD initiated and supervised the project. ZL and WC developed the theory. ZL performed the numerical simulations. ZL and WC wrote the draft. All authors contributed to the theoretical discussions, simulated data analysis, and manuscript writing.

FUNDING

This work was supported by the National Key R&D Program of China (Grant No. 2019YFA0706302), National Natural Science Foundation of China (Grant Nos. 62035016, 11874435, and 11904421), Natural Science Foundation of Guangdong Province (Grant No. 2018B030308005), Guangzhou Science, Technology, and Innovation Commission (Grant No. 201904010223), and Fundamental Research Funds for the Central Universities (Grant No. 20lgjc05 and 2021qntd27). ZX was supported by the National Science Foundation of China (Grant No. 11874432) and the National Key R&D Program of China (Grant No. 2019YFA0308200).

REFERENCES

1. Fang A, Koschny T, Soukoulis CM. Optical Anisotropic Metamaterials: Negative Refraction and Focusing. *Phys Rev B* (2009) 79:245127. doi:10.1103/PhysRevB.79.245127
2. Krishnamoorthy HNS, Jacob Z, Narimanov E, Kretzschmar I, Menon VM. Topological Transitions in Metamaterials. *Science* (2012) 336:205–9. doi:10.1126/science.1219171
3. Poddubny AN, Belov PA, Kivshar YS. Purcell Effect in Wire Metamaterials. *Phys Rev B* (2013) 87:035136. doi:10.1103/PhysRevB.87.035136
4. Pendry JB, Holden AJ, Stewart WJ, Youngs I. Extremely Low Frequency Plasmons in Metallic Mesostructures. *Phys Rev Lett* (1996) 76:4773–6. doi:10.1103/PhysRevLett.76.4773
5. Pendry JB, Holden AJ, Robbins DJ, Stewart WJ. Magnetism from Conductors and Enhanced Nonlinear Phenomena. *IEEE Trans Microwave Theor Techn.* (1999) 47:2075–84. doi:10.1109/22.798002
6. Smith DR, Padilla WJ, Vier DC, Nemat-Nasser SC, Schultz S. Composite Medium with Simultaneously Negative Permeability and Permittivity. *Phys Rev Lett* (2000) 84:4184–7. doi:10.1103/PhysRevLett.84.4184
7. Smith DR, Pendry JB, Wiltshire MCK. Metamaterials and Negative Refractive index. *Science* (2004) 305:788–92. doi:10.1126/science.1096796
8. Simovski CR. Material Parameters of Metamaterials (A Review). *Opt Spectrosc* (2009) 107:726–53. doi:10.1134/s0030400x09110101
9. Liu Y, Zhang X. Metamaterials: a New Frontier of Science and Technology. *Chem Soc Rev* (2011) 40:2494–507. doi:10.1039/C0CS00184H
10. Sakai O, Tachibana K. Plasmas as Metamaterials: a Review. *Plasma Sourc Sci. Technol.* (2012) 21:013001. doi:10.1088/0963-0252/21/1/013001
11. Shelby RA, Smith DR, Schultz S. Experimental Verification of a Negative index of Refraction. *Science* (2001) 292:77–9. doi:10.1126/science.1058847
12. Pendry J. Negative Refraction. *Contemp Phys* (2004) 45:191–202. doi:10.1080/00107510410001667434
13. Smith DR, Schurig D. Electromagnetic Wave Propagation in media with Indefinite Permittivity and Permeability Tensors. *Phys Rev Lett* (2003) 90:077405. doi:10.1103/PhysRevLett.90.077405
14. Poddubny A, Iorsh I, Belov P, Kivshar Y. Hyperbolic Metamaterials. *Nat Photon* (2013) 7:948–57. doi:10.1038/nphoton.2013.243
15. Chigrin D, Enoch S, Sotomayor Torres C, Tayeb G. Self-guiding in Two-Dimensional Photonic Crystals. *Opt Express* (2003) 11:1203–11. doi:10.1364/OE.11.001203
16. Yu X, Fan S. Bends and Splitters for Self-Collimated Beams in Photonic Crystals. *Appl Phys Lett* (2003) 83:3251–3. doi:10.1063/1.1621736
17. Luo C, Johnson SG, Joannopoulos JD, Pendry JB. Subwavelength Imaging in Photonic Crystals. *Phys Rev B* (2003) 68:045115. doi:10.1103/PhysRevB.68.045115
18. Wang X, Ren ZF, Kempa K. Unrestricted Superlensing in a Triangular Two Dimensional Photonic crystal. *Opt Express* (2004) 12:2919–24. doi:10.1364/OPEX.12.002919
19. Salandrino A, Engheta N. Far-field Subdiffraction Optical Microscopy Using Metamaterial Crystals: Theory and Simulations. *Phys Rev B* (2006) 74:075103. doi:10.1103/PhysRevB.74.075103
20. Silveirinha MG, Belov PA, Simovski CR. Subwavelength Imaging at Infrared Frequencies Using an Array of Metallic Nanorods. *Phys Rev B* (2007) 75:035108. doi:10.1103/PhysRevB.75.035108
21. Witzens J, Loncar M, Scherer A. Self-collimation in Planar Photonic Crystals. *IEEE J Select Top Quan Electron.* (2002) 8:1246–57. doi:10.1109/JSTQE.2002.806693
22. Noori M, Soroosh M, Baghban H. Self-collimation in Photonic Crystals: Applications and Opportunities. *Annalen der Physik* (2018) 530:1700049. doi:10.1002/andp.201700049
23. Maslovski SI, Tretyakov SA, Belov PA. Wire media with Negative Effective Permittivity: A Quasi-Static Model. *Microw Opt Technol Lett* (2002) 35:47–51. doi:10.1002/mop.10512
24. Belov PA, Tretyakov SA, Viitanen AJ. Dispersion and Reflection Properties of Artificial media Formed by Regular Lattices of Ideally Conducting Wires. *J Electromagn Waves Appl* (2002) 16:1153–70. doi:10.1163/156939302x00688
25. Belov PA, Marqués R, Maslovski SI, Nefedov IS, Silveirinha M, Simovski CR, et al. Strong Spatial Dispersion in Wire media in the Very Large Wavelength Limit. *Phys Rev B* (2003) 67:113103. doi:10.1103/PhysRevB.67.113103
26. Nefedov IS, Viitanen AJ, Tretyakov SA. Propagating and Evanescent Modes in Two-Dimensional Wire media. *Phys Rev E* (2005) 71:046612. doi:10.1103/PhysRevE.71.046612
27. Silveirinha MG. Nonlocal Homogenization Model for a Periodic Array Ofe-Negative Rods. *Phys Rev E* (2006) 73:046612. doi:10.1103/PhysRevE.73.046612
28. Shin J, Shen J-T, Fan S. Three-dimensional Electromagnetic Metamaterials that Homogenize to Uniform Non-maxwellian media. *Phys Rev B* (2007) 76:113101. doi:10.1103/PhysRevB.76.113101
29. Maslovski SI, Silveirinha MG. Nonlocal Permittivity from a Quasistatic Model for a Class of Wire media. *Phys Rev B* (2009) 80:245101. doi:10.1103/PhysRevB.80.245101
30. Maslovski SI, Morgado TA, Silveirinha MG, Kaipa CSR, Yakovlev AB. Generalized Additional Boundary Conditions for Wire media. *New J Phys* (2010) 12:113047. doi:10.1088/1367-2630/12/11/113047

31. Simovski CR, Belov PA, Atrashchenko AV, Kivshar YS. Wire Metamaterials: Physics and Applications. *Adv Mater* (2012) 24:4229–48. doi:10.1002/adma.201200931
32. Latioui H, Silveirinha MG. Light Tunneling Anomaly in Interlaced Metallic Wire Meshes. *Phys Rev B* (2017) 96:195132. doi:10.1103/PhysRevB.96.195132
33. Chen W-J, Hou B, Zhang Z-Q, Pendry JB, Chan CT. Metamaterials with index Ellipsoids at Arbitrary K-Points. *Nat Commun* (2018) 9:2086. doi:10.1038/s41467-018-04490-4
34. Powell AW, Mitchell-Thomas RC, Zhang S, Cadman DA, Hibbins AP, Sambles JR. Dark Mode Excitation in Three-Dimensional Interlaced Metallic Meshes. *ACS Photon* (2021) 8:841–6. doi:10.1021/acsphotonics.0c01811
35. Sakhno D, Koreshin E, Belov PA. Longitudinal Electromagnetic Waves with Extremely Short Wavelength. *Phys Rev B* (2021) 104:L100304. doi:10.1103/PhysRevB.104.L100304
36. Wang H, Chen Q, Zetterstrom O, Quevedo-Teruel O. Three-dimensional Broadband and Isotropic Double-Mesh Twin-Wire media for Meta-Lenses. *Appl Sci* (2021) 11:7153. doi:10.3390/app11157153
37. Sakhno D, Koreshin E, Belov PA. Quadraxial Metamaterial. *arXiv e-prints* (2021), arXiv:2111.02230.
38. Du L, Yang A, Zayats AV, Yuan X. Deep-subwavelength Features of Photonic Skyrmions in a Confined Electromagnetic Field with Orbital Angular Momentum. *Nat Phys* (2019) 15:650–4. doi:10.1038/s41567-019-0487-7
39. Kim M, Lee D, Nguyen TH-Y, Lee H-J, Byun G, Rho J. Total Reflection-Induced Efficiency Enhancement of the Spin Hall Effect of Light. *ACS Photon* (2021) 8:2705–12. doi:10.1021/acsphotonics.1c00727
40. Deng Z-L, Shi T, Krasnok A, Li X, Alù A. Observation of Localized Magnetic Plasmon Skyrmions. *Nat Commun* (2022) 13:8. doi:10.1038/s41467-021-27710-w
41. Smith DR, Pendry JB. Homogenization of Metamaterials by Field Averaging (Invited Paper). *J Opt Soc Am B* (2006) 23:391–403. doi:10.1364/JOSAB.23.000391

Conflict of Interest: The authors declare that the research was conducted in the absence of any commercial or financial relationships that could be construed as a potential conflict of interest.

Publisher's Note: All claims expressed in this article are solely those of the authors and do not necessarily represent those of their affiliated organizations, or those of the publisher, the editors, and the reviewers. Any product that may be evaluated in this article, or claim that may be made by its manufacturer, is not guaranteed or endorsed by the publisher.

frontiers in Physics

REVIEW
published: 28 March 2022
doi: 10.3389/fphy.2022.862962

Fundamentals and Applications of Topological Polarization Singularities

*Feifan Wang [1], Xuefan Yin[2], Zixuan Zhang[1], Zihao Chen[1], Haoran Wang[3], Peishen Li[1], Yuefeng Hu[3,4], Xinyi Zhou[1] and Chao Peng[1,3]**

[1]State Key Laboratory of Advanced Optical Communication Systems and Networks, School of Electronics and Frontiers Science Center for Nano-optoelectronics, Peking University, Beijing, China, [2]Department of Electronic Science and Engineering, Kyoto University, Kyoto, Japan, [3]Peng Cheng Laboratory, Shenzhen, China, [4]Peking University Shenzhen Graduate School, Shenzhen, China*

Radiations towards the continuum not only brings non-Hermicity to photonic systems but also provides observable channels for understanding their intrinsic physics underneath. In this article, we review the fundamental physics and applications of topological polarization singularities, which are defined upon the far-field radiation of photonic systems and characterized by topological charges as the winding numbers of polarization orientation around a given center. A brief summarizing of topological charge theory is presented. A series of applications related to topological polarization singularities are then discussed.

Keywords: topological charges, topological photonics, bound states in the continuum, optical singularities, non-Hermitian optics

OPEN ACCESS

Edited by:
Guancong Ma,
Hong Kong Baptist University, Hong Kong SAR, China

Reviewed by:
Cuicui Lu,
Beijing Institute of Technology, China
Yi Xu,
Guangdong University of Technology, China

****Correspondence:***
Chao Peng
pengchao@pku.edu.cn

Specialty section:
This article was submitted to Optics and Photonics, a section of the journal Frontiers in Physics

Received: *26 January 2022*
Accepted: *24 February 2022*
Published: *28 March 2022*

Citation:
Wang F, Yin X, Zhang Z, Chen Z, Wang H, Li P, Hu Y, Zhou X and Peng C (2022) Fundamentals and Applications of Topological Polarization Singularities. Front. Phys. 10:862962. doi: 10.3389/fphy.2022.862962

1 INTRODUCTION

Waves are ubiquitous phenomena in the nature. Serving as one of the most fundamental concepts in modern physics and applications, the examples range from electromagnetic waves, acoustic waves, to matter waves. Ever since the discovery of the transverse nature of some waves, the study of the polarization properties of those vector waves has attracted a great deal of attention, and varieties of novel mathematical concepts have been introduced. Among them, the most direct representation of polarization is the elliptically polarized state. For a generic plane wave, its field vector can be traced from the evolution of amplitudes and phases along two orthogonal directions, and correspondingly, the wave motion becomes a rotating vector that follows an ellipse path. In addition, the complicated polarization states can be projected onto the Poincaré sphere for better visualization, by using the Stokes' parameters [1]. Such a geometric representation shed lights upon deeper understanding of polarization from topological perspectives [2].

From a topological point of view, the objects of interest are some special points or regions on the Poincaré sphere, known as the singularities, such as lines where the polarization gets linear ("*L* lines"), points with circular polarization ("*C* points"), and centers of polarization vortices ("*V* points") [2–6]. At these regions, one or two components that compose the polarization, namely amplitude and phase, are ill-defined, so that the waves may exhibit some abnormal behavior, leading to exotic and potential useful physical phenomena. In particular, a special attention has been paid to the realization of singularities in optical domain [2, 6–9]. Examples include optical vortex beam generation [10–12], cylindrically polarized laser beams for tighter focusing [13–16], and the bound states in the continuum (BICs) [17–20]. It is noteworthy to highlight the BICs. Although the BICs have been developed from different contexts in history, their nature was found to be topological. Since first proposed in 1929 by von Neumann and Wigner [21], the BICs are understood as an

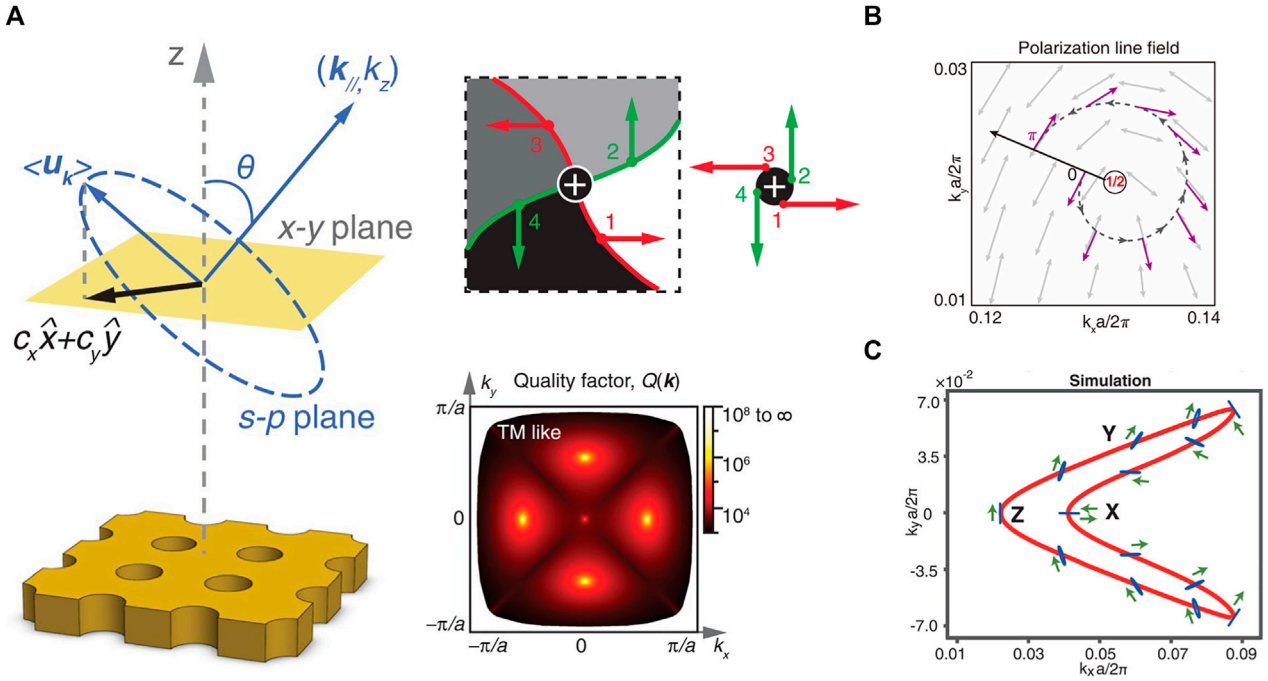

FIGURE 1 | Definitions and properties of different types of polarization singularities, **(A)** BICs [25] copyright American Physical Society; **(B)** a CP with charge +1/2 [43] copyright Springer Nature Ltd., and **(C)** a bulk Fermi arc connecting paried EPs [26] Copyright AAAS.

elimination of radiation in the case that radiation is allowed. After the first photonic realization [22], the BICs had been intensively investigated in various systems from a picture of destructive interference of waves [17, 18, 23, 24].

Later, the topological picture regarding BICs was established: they are interpreted as the vortex centers in far-field polarization orientation field where the polarization is ill-defined and all the radiation is forbidden [25]. In other words, BICs are a type of *V*-points in *k*-momentum space. By counting on the winding times of polarization direction around a specific center in momentum space, a conserved quantity called "topological charge" was defined, which was proved to be a topological invariant. It is found that the BICs possess integer topological charges [25]. Besides, the circularly-polarized states (CPs) carry half-integer topological charges, as a type of *C*-points. Furthermore, the topological charges defined on polarization are connected to the non-trivial band topology of non-Hermitian systems: half charges have been observed from a bulk Fermi arc encircling paired exceptional points (EPs) [26]. These findings built a framework to understand the polarization singularities, and utilize them for many applications.

In this article, we review the fundamental physics and applications of the research field of topological polarization singularities. We start from briefly summarizing the general principles and theory framework, and then present a comprehensive review on a series of applications related to polarization singularities. At last, we give our prospect and summary.

2 PRINCIPLES AND THEORY

The concept of optical singularities provide vivid and useful representations to understand the exotic phenomena of light, and thus they are applied in a series of investigation for different purposes. To keep the review focused, we concentrate on topological polarization singularities in this article. Specifically, we review the theoretical framework of polarization topological charges in this section, including their definitions, origins, and the methods for manipulating them. More information and connections regarding related topics can be found in other review articles, including topological photonics [27–29], singular optics [2, 6, 7], non-Hermitian topology [30–36], BICs [37–39], and orbital angular momentum of light (OAM) [40–42].

2.1 Theory of Polarization Topological Charges

Polarization topological charge was firstly proposed to depict the topological nature of BICs. In 2014, Zhen et al. [25] pointed out that the BICs are *V*-points in the far-field polarization vector field, carrying integer topological charges in momentum space. At the vortex center, the radiation is eliminated since the far-field polarization cannot be defined. **Figure 1A** illustrates the basic concepts of BICs. A resonance turns into a BIC if and only if $c_x = c_y = 0$, where (c_x, c_y) is the projection on the x-y plane of electric field $< u_k >$ of the radiative wave. The polarization field winds according to the topological charge, and *Q* diverges at BICs. An

explicit definition of the polarization topological charge is given by:

$$q = \frac{1}{2\pi}\oint_C d\mathbf{k} \cdot \nabla_{\mathbf{k}}\phi(\mathbf{k}) \quad (1)$$

in which $\phi(k)$ is the angle of the polarization vector arg $[c_x(\mathbf{k}) + ic_y(\mathbf{k})]$ describing the orientation of polarization major axis, $\mathbf{k}$ is the in-plane wavevector, and C is a closed simple path in momentum space that goes around a specific point along the counterclockwise direction. **Eq. 1** describes the number of times that the polarization vector winds around the specific point in momentum space. Encircling the BICs, namely the vortex centers, the polarization vector has to come back to itself after travelling through a closed loop, upon which the topological charge q must be an integer. Besides, according to the definition, we readily check that the CPs carry half-integer charges as $q = \pm 1/2$ from a topological view. **Figure 1B** gives a possible configuration of the polarization field near a CP, giving rise to a topological charge $q = +1/2$. Both the BICs and CPs are types of topological polarization singularities.

Note that the polarization topological charge is defined upon the far-field polarization in momentum space, which may connect, or say project the intrinsic band topology to the radiation field. For example, half-integer charges was observed around the bulk Fermi arc (**Figure 1C**), as a direct consequence of paired EPs [26] revealing the non-Hermitian topology of the bulk bands. However, the connection between band topology and radiation topology may not be obvious. For instance, the BICs and CPs are polarization singularities in radiation field, but they are topologically trivial upon the energy band. Further explorations are for sure interesting topics.

As a topological invariant, topological charges are conserved quantities: they continuously evolve in the momentum space and cannot suddenly disappear unless one charge drops out of the light cone or annihilates with another charge with the opposite sign. Besides, a pair of half charges can merge to an integer charge, or annihilate to nothing according to their signs. Consequently, the topological charge evolution offers an abstract but essential view to understand the radiation characteristics, as well as new methods to manipulate it. Examples and consequences of charge evolution will be presented in the following section.

Topological charge is actually a quite general concept that can quantitatively depict the winding of any arbitrary attributes. Although sharing the same terminology, the term "topological charge" are not only defined on the polarization, but also on phase, or other attributes of wave, in the real space, momentum space or parameter space. It is worthy to pay extra attention to distinguish the definitions. For instance, the term has been applied to phase singularities [44–51] that are related to vortex beam generations, and singularities on transmissions or reflections [52–55]. Other definitions utilizing the concept of winding are also reported in electromagnetic [19, 56–58], phononic [59] and mechanical systems [60].

2.2 Origins of Integer Topological Charge

The BICs, which are polarization singularities carrying integer charges, have been an attractive topic for several decades. The history, origins and results of BICs have been comprehensively reviewed by Hsu et al. [37] in 2016. In this section, we will summarize the new advances and understandings developed in recent years. Given that the investigations upon the BICs are diverse and extensive, we organize our review from different aspects.

From the aspect of physics origins, Friedrich and Wintgen presented a fundamental picture of interfering resonances to create the BICs [61]. Their original work pointed out that, the coupling between any two or more leaky resonances could eliminate the radiation of particular hybridized resonances, if the coupling strengths were well chosen. Although the term "FW BIC" is currently usually specialized to a BIC raised from interband coupling, other types of BICs can also be interpreted from Friedrich and Wintger's picture, if one appropriately defines the "resonances". For instance, for a photonic crystal (PhC) slab or gratings system, such resonances are guided-mode resonances [62–67]; for nanoparticles, dielectric spheres or tight-binding metasurfaces, the resonances are Mie resonances or other localized states [68–70]; for metallic systems, they are plasmonics resonances [20, 71]. Accordingly, BICs can be explained as the hybridization of different bases (i.e. unperturbed resonances) equivalently from a mathematical point of view. Examples include the coupled-wave theory that uses quasi-plane waves as the bases in periodic structures [17, 23, 24], and the multipole-expansion theory for Mie resonances in which the shape of a single resonator matters [72–74].

From the aspect of system symmetry, the BICs are classified into "symmetry-protected BICs", and "symmetry-incompatible BICs" [17, 37]. Since the radiation elimination originates from the high symmetry, the symmetry-protected BICs usually reside at the symmetry center in momentum space (for instance the Γ point). It is noteworthy that the symmetry-protected BICs have been independently developed in different photonic fields in history and described by different terminologies, such as band-edge modes in distributed-feedback lasers (DFB) [75–79], and photonic-crystal surface emitting lasers (PCSELs) [78, 80–83]. On the other hand, the symmetry-incompatible BICs also have many alias names, such as tunable BICs [24], off-Γ BICs [23], resonance trapping BICs [84], and topology-protected BICs [25, 85]. Since the creation of symmetry-incompatible BICs doesn't rely on the in-plane symmetry, they can move off the symmetry center in momentum space, which is distinguishable from the symmetry-protected ones.

From the aspect of platforms, the BICs are realized in both periodic and non-periodic structures. PhC is an easy-to-fabricate, optical-friendly platform to investigate BICs and other polarization singularities, in which the lattice periodicity offers naturally well-defined Bloch bases to depict the wave interactions [20, 86, 87]. Compared with PhCs, metasurfaces [68–70], coupled arrays of rods [19, 88, 89] and spheres [85, 90] share some similarities in their geometries: both of them are periodic and planar. The major difference might be—while the PhC supports long-range interactions, the wave interactions in metasurfaces are likely short-ranged and dominated by a few of adjacent unit cells. Alternatively, another type of systems is single resonators [18, 91, 92]. Although in principle a perfect BIC cannot be realized in a

three-dimensional compact volume [37, 93], the single resonators can support quasi-BICs with considerably high-Q and extremely small modal volume V, thus they are promising for nonlinear optic application and sensing.

It is noteworthy that, the BICs with high-order topological charges $|q| > 1$ are also reported. The vortices with $q = -2$ were found in a triangular latticed PhC slab [20] owing to the high in-plane symmetry of the lattice at the high-order Γ point although not been explicitly mentioned. In 2020, Yoda et al. [94] reported a symmetry-protected BIC with charge $q = -2$ in a C_6 symmetric lattice. It was found that two BICs each with $q = -1$ spawned from the $q = -2$ charge when the in-plane symmetries were broken from C_6 to C_2.

Another interesting fact is, although the BICs are usually isolated points, they can appear as a line in momentum space when involving extra dimensions. In 2019, Cerjan et al. [95] proposed a method called the environmental design for this purpose, in which the environment worked as new degree of freedom. Recently, this line of BICs was observed in a slab by altering the surrounding radiative environment with a 3D PhC [96].

Moreover, the topological polarization singularities are found in other systems such as disordered or quasi-crystal systems, and parity-time-symmetric (PT-symmetric) systems. In 2019, De Angelis et al. [97] reported the random vortices in a chaotic cavity composed of 2D PhCs. In 2021, Che et al. [98] experimentally observed the quasi-BICs in 2D photonic quasi-crystals. In 2020, Song et al. [99] reported the emergence of two types of modes with divergence of Q in a PT-symmetric system, named as a "PT-BIC" and a "lasing threshold mode".

2.3 Emergence of Half-Integer Topological Charge

Another type of polarization singularities, namely CPs, can also emerge in momentum space by tuning material or structural parameters. According to the definition of topological charges, the CPs carry half-integer charges that obey the conservation law of topological charge together with the integer charges. Several methods are reported to create these half charges.

One method is to split integer charges to paired half charges following the conservation law, for instance $q = 1 \rightarrow 1/2 + 1/2$, by breaking the in-plane symmetry. As reported by Liu et al. [100], it was observed that a symmetry-protected BIC split into a pair of CPs with opposite helicity but carrying topological charges of the same sign. Similar phenomenon was observed by Chen et al. [71]. The CPs can also originate from symmetry-incompatible BICs. For instance, Ye et al. [101] reported two CPs with identical topological charges of $q = -1/2$ but different handedness originating from a BIC with charge $q = -1$ at the K point in a honeycomb-lattice PhC. As mentioned above, Yoda et al. [94] showed that the BIC with high order charge $q = -2$ split to integer charges following $q = -2 \rightarrow (-1) + (-1)$ by breaking the symmetry from C_6 to C_2. By further breaking the C_2 symmetry, the integer charge split to paired half charges as $q = -1 \rightarrow (-1/2) + (-1/2)$. It is noteworthy that all the evolution followed the conservation law.

An alternative method for creating half charges is to spawn the CPs from trivial polarization field, namely $q = 0$. Recently, Zeng et al. [102] built a two-layered 1D PhC with an offset between the layers. Two CPs emerged from a given k point where the far-field polarization is trivial, carrying opposite signed half charges as $q = 0 \rightarrow 1/2 + (-1/2)$. Apparently, the conservation law still held.

Besides, polarization half charges are related to another important type of singularities in non-Hermitian system, namely EPs. In 2018, Zhou et al. [26] reported a pair of EPs connected by so-called bulk Fermi arc. A flip of the polarization major axis was observed in experiment along one closed loop around the EP pair connected by bulk Fermi arc, showing a clear signature of polarization half charge. It is noteworthy that the EPs belonged to the singularities upon the non-Hermitian band, while the polarization half charges represented the singularities upon the radiation. It is still vague that how the band topology connects to the radiation topology. Nevertheless, as reported by Chen et al. [103], a conservation law of global charge was still valid.

2.4 Consequences of Topological Charge Evolution

The conservation law of topological charges allows the continuous evolution of charges in momentum space, namely moving, merging, splitting and annihilating with the summation of all charge numbers remaining constant. Since the topological charges are related to the far-field radiation characteristics, it was found that interesting and useful consequences could be obtained from the topological charge evolution.

One of the example is the merging of multiple integer topological charges, i.e. the BICs, which strongly suppresses the out-of-plane scattering and leads to a class of robust ultra-high-Q resonances. Although the BICs completely forbid the radiation and own infinite photon lifetime in theory, their experimental realizations had suffered from a limited Q in a level of 10^4 [17], due to the energy leakage from the inevitable out-of-plane scattering originated from fabrication imperfections. To address this problem, Jin et al. [104] reported a method of merging BICs in a C_4 symmetric PhC slab where existed eight off-Γ BICs with $q = \pm 1$ charges around one symmetry-protected BIC at the Γ point. By continuously tuning the lattice periodicity a, the eight BICs kept moving until merging at Γ, and further annihilated into one isolated BIC with charge $q = +1$. (**Figure 2A**).

As mentioned, the configuration of topological charges implies the radiation capabilities of nearby resonances, and further determines the observable Qs in samples by taking into account the scattering losses. Near an isolated BIC with charge $q = \pm 1$, the Q scales quadratically ($1/k^2$) as the distance k away from the BIC. However, the scaling law dramatically changes to $1/k^6$ when nine BICs just merge, as shown in Jin's work. As a result, the scattering loss was significantly suppressed, and a record-high Q of 4.9×10^5 was experimentally observed.

Recently, Kang et al. [105] took a further step and realized a merging BIC at off-high symmetry points, namely the merging

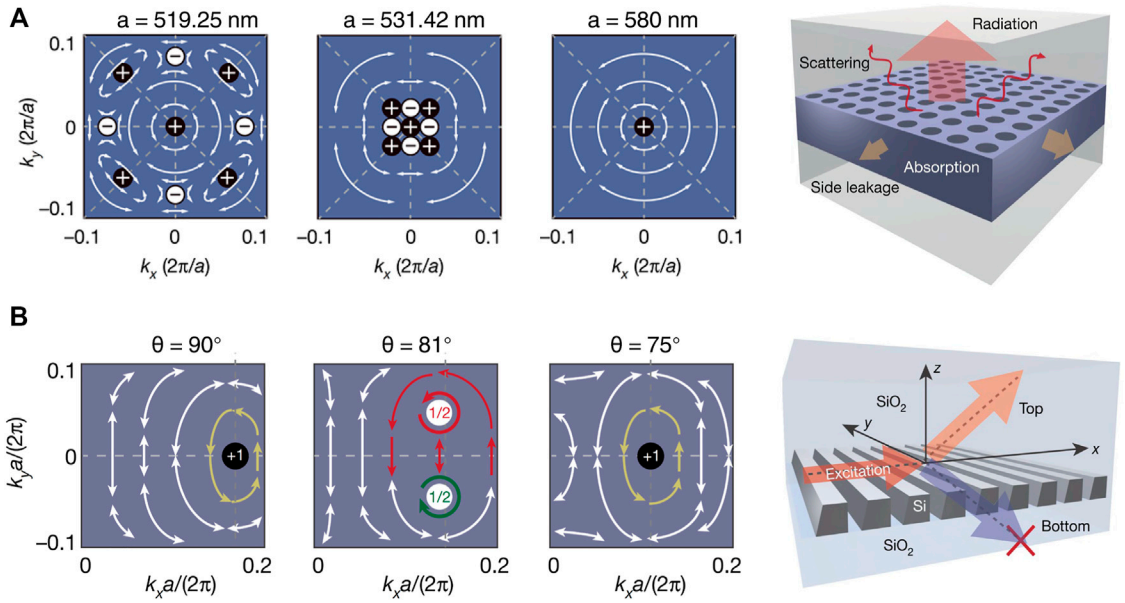

FIGURE 2 | Consequences of topological charge evolution. **(A)** A high-*Q* cavity robust of out-of-plane scatterings constructed by the merging of multiple integer charges [104]. **(B)** The merged half-charges in downward radiation leading to a unidirectional radiation [43]. Copyright Springer Nature Ltd.

behavior of integer charges were not restricted to the Brillouin zone (BZ) center. The in-plane C_4 and mirror symmetries were broken, resulting in the merging of an FW-BIC and a tunable-BIC at a nearly arbitrary point in momentum space.

Another example of topological charge evolution is related to an interplay with half charges and integer charges, leading to the realization of unidirectional guided resonances (UGRs) (**Figure 2B**), reported by Yin et al. [43]. The evolution started from an off-Γ BIC in a 1D silicon PhC slab, carrying a topological charge of $q = +1$ upon both up- and downwards radiation. By tilting the sidewall that broke the in-plane C_2 symmetry and up-down mirror symmetry simultaneously, the BIC split into a pair of CPs carrying $q = +1/2$ upon both the top and bottom sides of the slab. Further, paired CPs evolved following different trajectories in the upward and downward radiation fields due to the breaking of up-down mirror symmetry. At a specific angle, the paired CPs in downward radiation merged into an integer charge while upward CPs remained departing. Therefore, the downward radiation was totally eliminated while the upward radiation channel was still open, thus generating a resonance with directional emission named UGR. The experimental results demonstrated 99.8% of the energy radiated through the upward channel at UGR.

Recently, Zeng et al. [102] reported a similar phenomenon from theory in a two-layered 1D PhC with an offset between the two layers which broke the up-down-mirror symmetry. Two pairs of CPs with $q = \pm 1/2$: one left-handed pair and another right-handed pair, emerged at a specific value of the offset. By continuously varying the offset, the CPs evolved in momentum space, and merged to integer charges at different k points upon up- and downward radiation, which created two UGRs.

3 APPLICATIONS

Topological charge provides not only a convenient mathematical tool in theory, but also flexible and rich methods for manipulating lights, thus paving the way to a variety of applications. In particular, topological charges can be tuned to selectively eliminate or suppress the radiation, which leads to the realization of optical modes with ultra-long lifetime and desired radiation patterns in intensity, phase and polarization. Consequently, topological charges have been applied in many scenarios, boosting the development of light trapping, lasing, light-matter interaction enhancement, nonlinear optics, wavefront control, polarization conversion, photonic integration and others. In this section, we review the recent progresses of applications related to the topological charges.

3.1 Trapping of Light and Optical High-*Q* Cavities

From a scientific or technological point of view, the importance of light-trapping is self-evident. The BICs are interpreted as vortices in far-field polarization, thus providing novel methods for light-trapping other than conventional optical cavities such as bound states under light-cone [108–110].

Early efforts was paid to inhibit out-of-plane radiations in large-area 2D systems. In 2012, Lee et al. [106] reported observation of a unique high-*Q* resonance near zero wavevector in large-area 2D PhC slab by using angular resolved analysis. *Q* of 1×10^4 was found near the symmetry-protected BIC at Γ point (**Figure 3A**). In 2013, Hsu et al. [17] reported the off-Γ BICs for the first time, in which the *Q*s of resonances diverge to infinity at seemly insignificant wavevectors

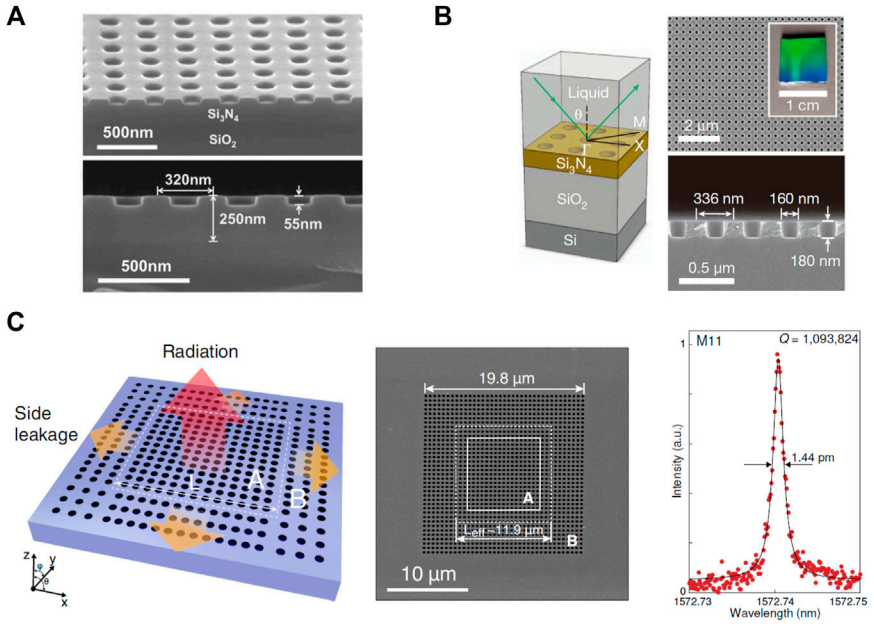

FIGURE 3 | (A) Macroscopic photonic crystal [106] for observing symmetry-protected BICs, copyright American Physical Society. **(B)** The observation of symmetry-incompatible off-Γ BICs [17], copyright Springer Nature Ltd. **(C)** Miniaturized BICs [107], copyright Science China Press.

on certain bands. The structure is shown in **Figure 3B**. A radiative quality factor Q_r of 1×10^6 was measured at a direction angle ~ 35° of the reflection. Such BICs can stably exist in a general class of geometries and can move to a different k point by continuously tuning the system parameters.

Subsequently, Zhen et al. [25] proposed the topological interpretation of the BICs in 2014 as elaborated in previous sections. The BICs' capability of trapping light are further promoted. In 2019, Jin et al. [104] proposed and realized a class of ultra-high-Q resonances by merging multiple off-Γ BICs carrying topological charges towards the center of Brillouin zone (BZ). As a direct consequence of topological charge manipulation, Qs as high as 4.9×10^5 were observed in an SOI PhC slab, as mentioned in **Section 2.4**. The merging-BIC designs strongly suppressed out-of-plane-scattering losses caused by fabrication imperfections, thus paved the way to realistic applications of BICs.

Strictly speaking, all the above examples belong to high-Q resonances but not high-Q cavities. According to the continuity of electromagnetic field, it was proved that fully 3D compact BIC does not exist in theory [37, 93]. In addition, the periodic conditions of PhC imply that the structure extends infinitely in the lateral direction, which is not practically feasible. The high-Q resonances in PhC slabs only localize in the vertical direction but remain de-localized in transverse direction across the slab.

The most straightforward method for achieving 3D light-trapping is to simply truncate the PhC slab laterally. Such method reduces modal volume V but also drastically degrades the quality factor Q because it introduces leakage in both lateral and vertical directions. A common relationship between Q and V for truncated BICs was derived [111] and verified experimentally [112]. In 2019, Liu et al. [69] observed a truncated BIC with Q of 18,511 and footprint of $19 \times 19\,\mu m^2$. In 2021, a long-lifetime mode with Q of 7,300 was reported in InGaAsP PhC slab for low-threshold lasing in a footprint of $22.4 \times 22.4\,\mu m^2$ [113]. In addition to simply truncating the PhC, the light can be confined transversely by applying lateral hetero-structures as reflective perimeters. For example, a mode with Q of 2×10^4 has been measured in footprint of $215\,\mu m^2$ [114]. In these designs, although the hetero-structure suppress the lateral energy leakage effectively, the leakage toward out-of-plane direction raised by truncation remains unresolved.

Recently, Chen et al. [107] reported a new method of light trapping combining lateral mirrors and BIC in a cooperative way (**Figure 3C**). Light was confined in the vertical direction by manipulating the constellation of topology charges, matching them with the finite-size radiation channel. In the transverse direction, the light was trapped by the near-perfectly reflective photonic bandgap of the lateral hetero-structure, with the radiative and scattering losses of the boundary region being greatly suppressed, at the same time, the radiation in cavity region becomes highly directional. The coworking of the topological-charges covered a larger area in momentum space that protects the scattered waves from radiation. Since the boundary region shared similar geometries with the cavity region, they also benefit from the protection of topological constellation for a smaller radiation loss. As a result, light-trapping in all three dimensions was achieved. Miniaturized BICs with Qs of 1.09×10^6 was measured experimentally with a footprint of ~ 20 μm × 20 μm. Benefiting from the protection of topological constellations that are composed by topological

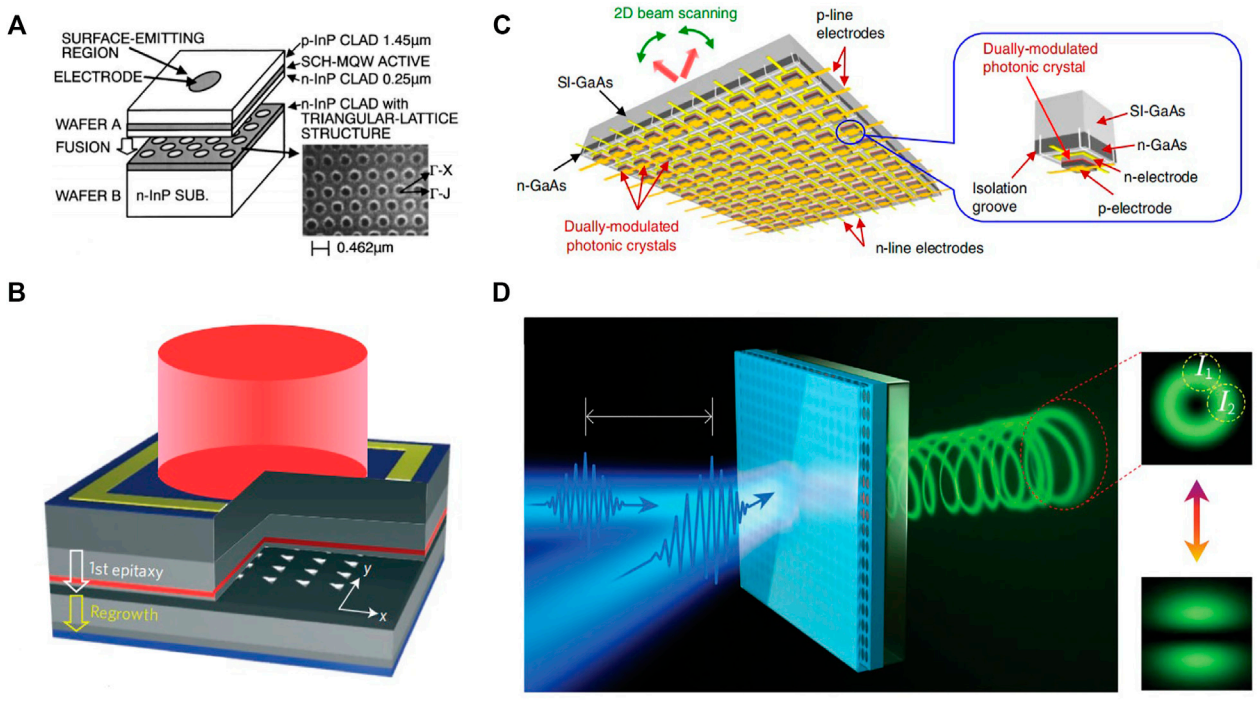

FIGURE 4 | (A) Early PCSEL based on wafer fusion technique [80], copyright AIP publishing. **(B)** A W-class high-power PCSEL [82], copyright Springer Nature Ltd. **(C)** The on-chip beam scanning laser [123], copyright Springer Nature Ltd. **(D)** All-optical switching from the vortex microlaser [124], copyright AAAS.

charges, the microcavity exhibited excellent robustness to fabrication imperfections.

3.2 Lasing and Vortex Beam Generation

Since the integer topological charges carried by BICs are good candidates for realizing high-Q resonances, their most direct application is for lasing. Historically, the band-edge modes were widely adopted for semiconductor lasers such as DFB lasers [75–79] and distributed Bragg reflector (DBR) lasers [115–117]. Although it is not explicitly mentioned, the grating modes that operate at the band-edge of second-order Γ point are actually the symmetry-protected BICs. Later, the periodicity of one-dimensional gratings was extended to two-dimensional PhC slabs, leading to the invention of photonic-crystal surface-emitting lasers (PCSELs) [80]. The PCSELs also operate near the band edge residing in the continuum, supporting coherent oscillations in large areas. In the case that the periodic lattice and unit cells of PCSELs respect C_2 or higher in-plane symmetry, the lasing band-edge modes are found to be symmetry-protected BICs, too [118, 119].

In the past two decades, PCSELs have experienced dramatically developments and become a promising laser architecture as the successor of DFB lasers which had already made tremendous successes in industry. With a comprehensive review of PCSELs presented elsewhere [120], here we just list several major milestones: the first lasing action of PCSELs was observed in 1999 [80], as illustrated in **Figure 4A**; room-temperature, continuous-wave operation, current-injected lasing was achieved in 2004 [81]. Later, the abilities of tailoring beam patterns were reported in 2006 [121]; the lasing wavelength was extended to blue-violet region in 2008 [78]; a beam-steering functionality was demonstrated in 2010 [118]. What's more, much efforts have been paid to promote the lasing power, and watt-class lasing was achieved (shown in **Figure 4B**) in 2014 [82] and 10-W-class lasing in 2019 [83]. Recently, PCSELs with a peak power of 20 *W* and pulse width of 35 *ps* were realized [122] and on-chip beam scanning lasers were first achieved [123] as illustrated in **Figure 4C**. It is noteworthy that, in the early age of PCSELs, circular shaped holes were adopted to pattern the PhC, so that the lasing modes were the BICs with infinite Qs in theory. Although the high Q factor lowered the lasing threshold, it was not good for high-efficient power extraction which was critical for high-power lasers. Therefore, the in-plane C_2 symmetries were broken on purpose, which turned the BICs with infinite Qs to quasi-BICs with high but finite Q values in carefully controlled manners [82, 83].

Besides the PCSELs, the lasing action utilizing the BICs have also been developed in a parallel lane motivated from physics curiosity. In 2017, Kodigala et al. [84] demonstrated the optical-pumped lasing in an array of suspended cylindrical nanoresonators consisting of $In_xGa_{1-x}As_yP_{1-y}$ multiple quantum wells, claimed as the first lasing action of the BICs. In 2018, Ha et al. [125] reported directional lasing in resonant semiconductor nanoantenna arrays, that is, arrays of GaAs nanopillars. On the other hand, lasing action has been reported in Mie-resonant BICs, too. For instance, combining colloidal CdSe/CdZnS core-shell nanoplatelets with square-

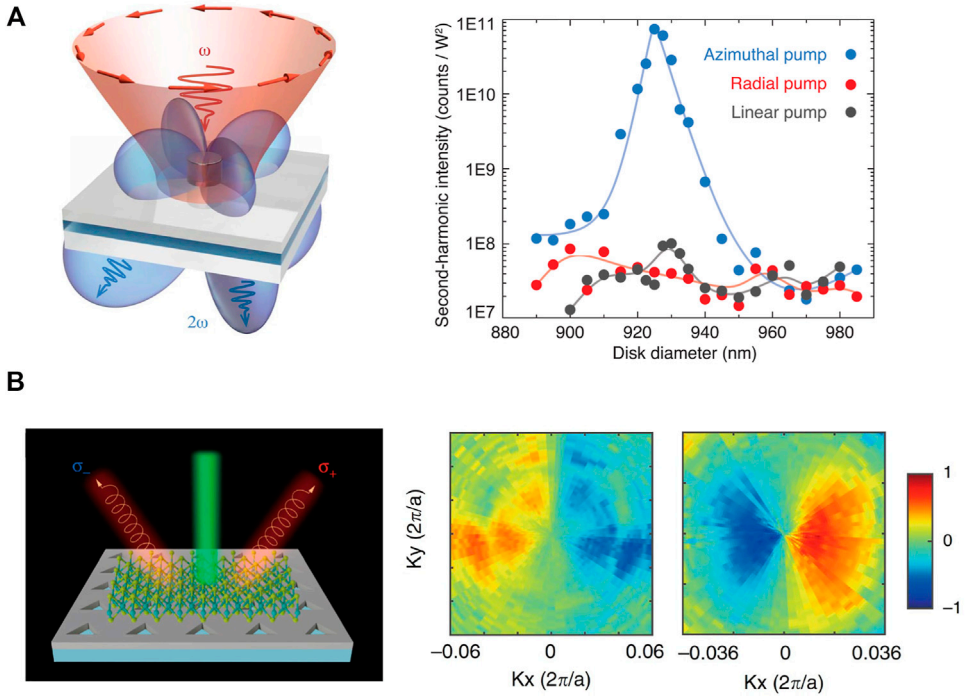

FIGURE 5 | Light-matter interaction enhancement and nonlinear optics. **(A)** SHG in an isolated antenna, the SH intensity vs nano-resonator diameter was measured at different pump polarizations [18], copyright AAAS. **(B)** Routing of valley photons with different chiralities by coupling to CPs, measured valley polarization in momentum space at 615 *nm* (left) and 628 *nm* (right) [129], copyright Springer Nature Ltd.

latticed TiO_2 nanocylinders, Wu et al. [126] reported the lasing from in-phased out-of-plane magnetic dipoles in 2020.

It is worthy to mention that, the polarization singularities accompanied with the BICs can be adopted to generate rich and exotic beam patterns. Some early experiments of PCSELs showed such possibility of creating tailored vectorial beams [121]. Recently, vortex beam generation has attracted huge attention, particularly owing to its great potentials in escalating the optical communication systems to higher level of multiplexing. In 2020, Wang et al. [12] reported optical vortex generation in a PhC slab with i-fold ($i > 2$) rotational symmetry related to the BICs, in which spin-to-orbit angular momentum conversion was realized and the vortex beam was proved to be a diffraction resistant high-order quasi-Bessel beam. Also in 2020, Huang et al. [124] reported that the BICs enabled ultra-fast control of vortex micro-lasers based on a perovskite metasurface, as shown in **Figure 4D**. Through modifying the two-beam-pumping configuration, ultra-fast switching between a vortex beam and regular linearly polarized beam was demonstrated with a transition time of only 1.5 ps.

3.3 Light-Matter Interaction Enhancement and Nonlinear Optics

As elaborated in **Section 3.1**, ultra-high Qs and small modal volume Vs can be achieved by arranging the topological charges, leading to dramatic enhancement of Purcell effect that favors the light-matter interactions and nonlinear optics. In 2019, Xu et al. [127] experimentally demonstrated third-harmonic generation (THG) in silicon metasurfaces and observed a conversion efficiency of 5×10^6 at $100\,mW$. Later, Liu et al. [69] promoted the Q to a record-high value of 18,511 in the metasurface, and reported that the THG conversion efficiency was five orders of magnitude higher than the former silicon metasurfaces. Even the second-harmonic generation (SHG) was also observed in silicon in their work. Moreover, Kang et al. [128] observed the high-order vortices, namely, high-order topological charges upon the harmonic waves generated from optical nonlinearity.

To enhance the efficiency of the nonlinear processes, several considerations were taken into account. Firstly, the excitation and emission of the resonances under critical-coupling condition would maximize the field strength in the cavity. As reported, by slightly breaking the in-plane symmetry that shifted the resonance away from the complete dark BIC, the energy exchange between the external excitation and the resonance became more efficient, thus promoting the conversion efficiency [127, 130]. Besides, the process benefited a lot from a doubly-resonant design, namely both the excitation and its harmonics were resonances supported by the same cavity. For example, Wang et al. [114] realized a GaN photonic cavity from this concept, in which the fundamental frequency matched with a

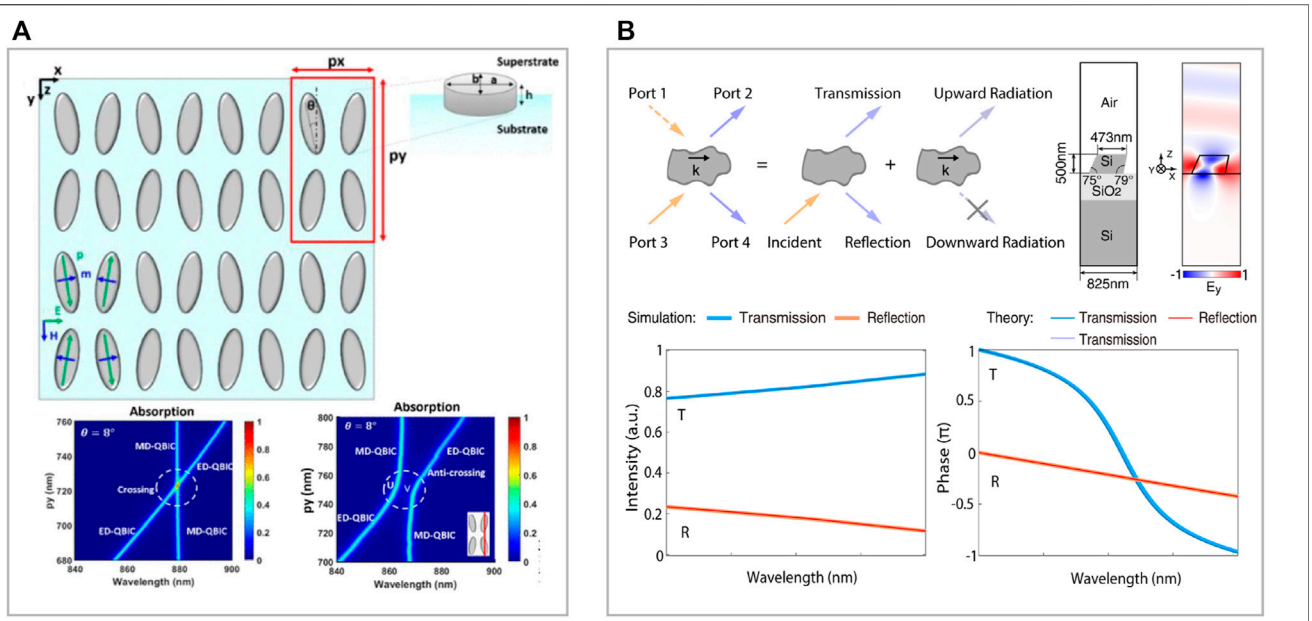

FIGURE 6 | Light manipulation in intensity and phase. **(A)** High-*Q* silicon metasurface and its absorption spectra [134], copyright American Chemical Society. **(B)** Intensity flatten phase shifting based on the unidirectional radiation resonance [135], copyright De Gruyter.

defect mode and its second-harmonics operated upon a quasi-BIC. As a result, the intrinsic conversion efficiency was 10 times larger than singly resonant cavities with similar materials.

Besides the periodic structures including PhCs and metasurfaces, single Mie resonators provide another promising platform for nonlinear optics. Although the *Q*s of single resonators are lower than that of periodic structures, single resonators have particular advantages in small modal volume *V* to promote the strength of light-matter interaction. In 2018, Carletti et al. [91] predicted that the conversion efficiency of SHG in an isolated AlGaAs nano-antenna could be two orders of magnitude stronger than that in conventional designs. In 2020, Koshelev et al. [18] experimentally implemented such design, as illustrated in **Figure 5A**. They found a quasi-BIC in a particle with a diameter of 930 *nm* and height of 635 *nm*. Owing to the mutual interference of several Mie modes, *Q* of 188 was realized. Combining with doubly-resonant strategy, two orders of magnitude higher conversion efficiency was achieved as expected.

In addition to those dielectric nonlinear materials, thin-film materials such as 2D transitional metal dichalcogenides (TMDCs) were specifically cooperated with the BICs to investigate the light-matter interaction. In 2018, Koshelev et al. [131] achieved a strongly-coupled exciton-photon system in which PhC was covered by a WSe_2 monolayer. Two years later, Kravtsov et al. [132] demonstrated a BIC-based polaritonic excitation with $MoSe_2$ upon PhCs, in which strong exciton-fraction-dependent optical nonlinearities were exhibited. Besides, as reported by Yu et al. [133], the decoupling from the continuum could confine light in a low-dielectric waveguide upon high-dielectric substrate, which contributed to new graphene device designs.

Besides the *V*-points (BICs), the *C* points (CPs) can also be involved in the light-matter interactions since they provide extra selectivity in chirality. In 2020, Wang et al. [129] generated paired CPs with different chirality. Owing to the valley-dependent selection rules in WSe_2, the photons radiated from inequivalent valleys could couple to the two CPs, as illustrated in **Figure 5B**. Accordingly, a maximum degree of valley polarization over 80% was observed.

3.4 Intensity and Phase Modulation

Amplitudes and phases are fundamental attributes depicting the characteristics of light. By cooperating with the resonances associated with topological charges, these attributes can be manipulated thus leading to a series of applications.

As a directly-observable attribute, the intensity of light can be controlled for a variety of purposes. Specifically, in 2019, Yu et al. [133] realized a BIC-waveguide-integrated modulator in which the electro-absorption effect of graphene was adopted and a bandwidth of 5 *GHz* was achieved. In 2020, Tian et al. [134] theoretically proposed that a near-unity absorption could happen on an all-dielectric metasurface with quasi-BICs, when the material absorption rate matched with the radiative decay rate (**Figure 6A**). Dai et al. [53] proposed a mechanism for perfect reflection called coherent perfect reflection (CPR), which was raised from interband coupling between two propagating modes so the forward transmission of light could be eliminated under appropriate complex coupling coefficients. Besides, Wong et al. [55] conceived an idea for perfect isolation of light from topological theory, upon a nonreciprocal metasurface composed of dimer unit cells interacting with a static magnetic field.

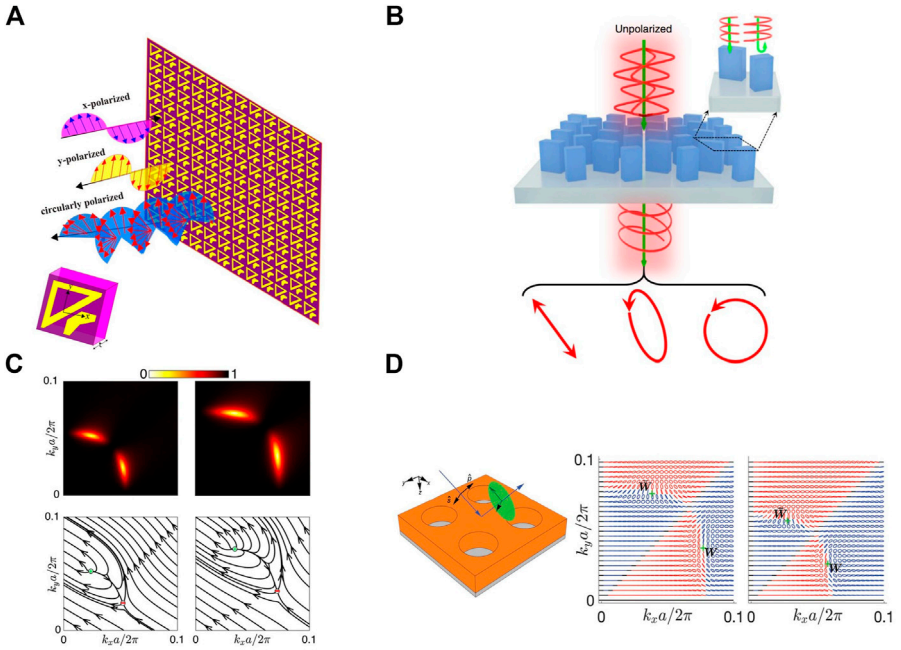

FIGURE 7 | (A) fish-like metasurface converting linear polarization to orthogonal-linear and circular polarization [142], copyright Springer Nature Ltd. **(B)** Dimerized nanopillars generating linear, elliptical and circular polarization regardless of input polarization [145], copyright Springer Nature Ltd. **(C)** Maps of reflection coefficient and vector field of reflection in momentum space in the polarization conversion [52], copyright American Physical Society. **(D)** PhC slab manipulating incident polarization to arbitrary polarization in reflection [146], copyright Wiley-VCH GmbH, Weinheim.

Besides, phase is also a key attribute of light that plays important roles in many scenarios. The modulation of phase is as straightforward as intensity, since both of them are related to the tuning of the resonances themselves. As an example, a thermo-optic phase-shifter utilizing the high-Q quasi-BICs was reported [136]. However, phase-only modulation, namely the phase modulation without the change of intensity, is even more important for applications ranging from three-dimensional video projection, flat metalens optics, to optical phased arrays and light detection and ranging.

Although perfect phase-only modulation is difficult, much effort was devoted for intensity-flatten phase modulation, with the key concept of making the resonance operating under over-coupled status. For instance, Kwon et al. [137] experimentally demonstrated nano-electromechanical tuning of gratings associated with quasi-BICs in the telecom wavelength. They realized a spectral shift over 5 nm, with absolute intensity modulation over 40%, modulation speed exceeding 10 kHz, and a phase shift of 144° with a bias of 4 V. Salary et al. [138] proposed an electro-optically tunable all-dielectric metasurface composed of elliptical silicon nanodisks for the same purpose. By applying bias voltage, the electro-optical driven Huygens mode produced a dynamic phase span of 240° while maintaining an average transmission amplitude of 0.77, giving rise to a unevenness of about 25%.

Recently, it was reported by Zhang et al. [135] that perfect phase-only modulation was possible in theory with the assistance of the UGRs (**Figure 6B**). As mentioned, UGRs are connected to single-sided topological polarization singularities. A UGR mandates the light transmitting to only one out-going port without other choices, which creates perfect phase-shifting upon the transmission if nonradiative loss is negligible. The unevenness of transmission intensity could be lower than 10% with nonradiative Q > 8,000 which was feasible in state-of-art fabrication process.

3.5 Polarization Conversion

Polarization is a critical and fundamental attribute of electromagnetic waves and the polarization control has been widely used in optical communications [139], nonlinear optics [140], imaging [141], etc. Besides cascading polarizers and waveplates to regulate the polarization, periodic structures including the metasurfaces and PhC slabs are promising platforms to achieve the polarization conversion [52, 139, 142–146], by manipulating the polarization singularities in radiation.

To be specific, Khan et al. [142] reported a single-layer, mirror-symmetric anisotropic metasurface constructed of fish-like unit cells to demonstrate both the linear cross-polarization conversion and linear-to-circular polarization conversion in X-band, as illustrated by **Figure 7A**. Besides, broadband linear-to-circular polarization conversion in the terahertz region with almost unity conversion efficiency was demonstrated by Chang et al. [144] based on the birefringent metasurface. In 2021, Wang et al. [145] proposed a monolayer all-dielectric metasurface composed of dimerized nanopillars shown in **Figure 7B**, which generated arbitrary polarization on the Poincaré sphere from the unpolarized input light. This effect was equivalent to an

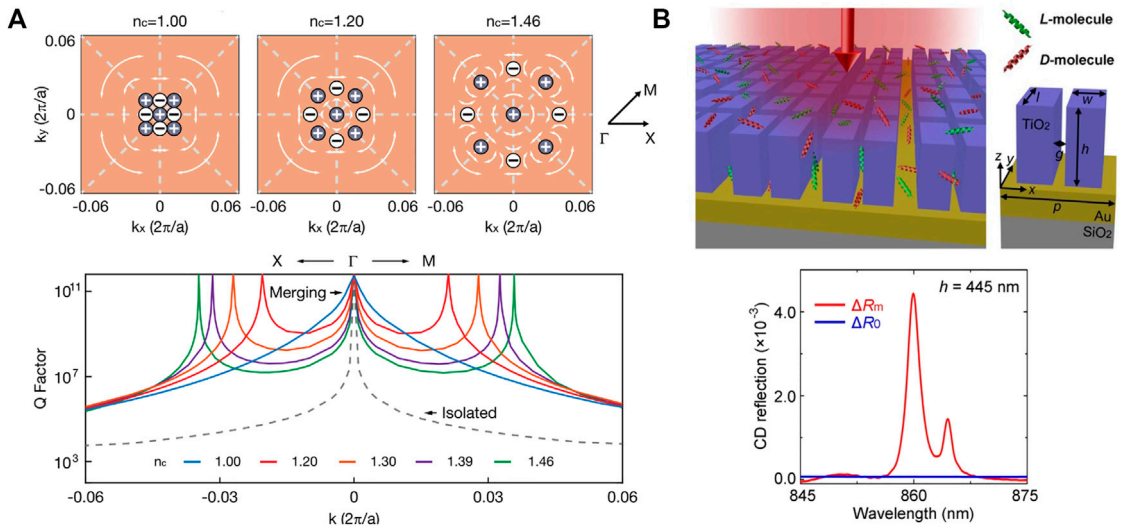

FIGURE 8 | Refractive index and chiral sensing applications. **(A)** Topological charge evolution of merging BICs and the Qs with refractive index variation [159], copyright IEEE. **(B)** Comparison of CD reflection spectrum of the BICs metasurface enhanced chiral layer and the bare chiral layer [160], copyright American Chemical Society.

"all-in-one" full Poincaré sphere polarizer. In addition, Yu et al. [143] reported a dynamic control of polarization conversion depending on the metasurfaces with electrically tunable refractive indices for the metasurface antennas.

Recently, 2D PhC slab structures were employed to manipulate the polarization without tuning the structural parameters [52, 146]. In particular, Guo et al. [52] achieved complete polarization conversion between linear polarizations, indicating the full energy exchange between *p*- and *s*-polarized incident lights; in addition, they proved such polarization conversion was topologically protected owing to the winding vector of the complex reflection coefficient. Complete polarization conversion happened at the vortex center, where a nonzero winding number (+1 or −1) in momentum space gave rise to a zero reflection coefficient, which is shown in **Figure 7C**. More interestingly, they revealed the relationship between the complete polarization conversion and the integer topological charges, namely the BICs. Given that the BICs correspond to the vanishing points of out-going coupling coefficients, they always appeared on the curves that supported complete polarization conversion in momentum space, thus bridging the phenomena with topological singularities.

Furthermore, arbitrary polarization conversion was proposed in a lossless 2D PhC slab [146]. Namely, by tuning the incident light with any given polarization towards a given direction that fell into a wide range of frequency, the polarization of the reflected light could cover the whole Poincaré sphere. **Figure 7D** shows the result of the reflected polarization under *s*-polarized incidence for frequency $0.402 \times 2\pi c/a$ and $0.405 \times 2\pi c/a$, in which a is the lattice constant. Complete polarization conversion occurred at W point where all the *s*-polarized incidence converted to *p*-polarized, related with the topological property of the scattering matrix [52]. Moreover, with losses, the 2D PhC slab system could still generate arbitrary output polarization if the input was *p*- or *s*-polarized.

3.6 Spectral and Chiral Sensing

Given that topological polarization singularities possess exotic characteristics upon the radiation fields, it is reasonable to utilize them for sensing the surrounding environment. In particular, the high-*Q* nature of integer charges (BICs), and the chiral responses of half charges (CPs) are two promising features. In a perturbated environment, the ideal BICs transform to quasi-BICs with shifted resonance wavelengths while remaining considerably high *Q*s, thus providing the capability of sensing small refractive-index changes from spectral observation. High sensitivity refractive index (RI) sensing in chemical and biological processes has been realized in many high-*Q* resonators [147–157]. The RI sensors based on BICs realized by dielectric metasurfaces and PhC slabs have also shown promising performances in figure-of-merit (FOM) and detection-limit (DL) [158, 159]. On the other hand, since chiral responses observed from the reflected or transmitted light can be used to distinguish the chirality of targets, chiral sensing were realized accordingly [160]. In addition, although not directly utilizing the polarization singularities, it is noteworthy to mention a class of novel methods that use the EPs to improve sensing performance [161–170], given by the underlying connections to the polarization singularities.

For instance, in 2017, Liu et al. [158] experimentally demonstrated RI sensing in a wavelength range of 1,400, –, 1,600 *nm* by applying the BICs in PhCs, which showed great potential for label-free optical biosensors. To further promote the sensing performance, it was important to suppress the out-of-

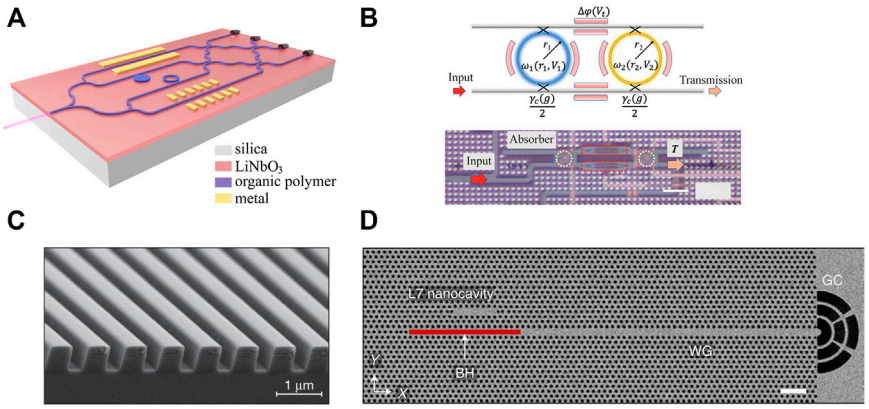

FIGURE 9 | BIC-based photonic integrated components, including **(A)** photonic circuit where low-refractive index material was patterned on a high-refractive-index substrate. Adapted with permission from [178] copyright The Optical Society, **(B)** filter [179], copyright American Physical Society. **(C)** Grating coupler [43], copyright Springer Nature Ltd. and **(D)** laser [180], copyright Springer Nature Ltd.

plane scattering loss caused by fabrication imperfections to improve the *Q*s. Following this strategic, Lv et al. [159] adopted the merging BIC design to RI sensing, which significantly promoted the DL performances in practice owing to the higher *Q*s (**Figure 8A**). However, the sensitivity of RI sensors are also related to the field overlap between the optical resonances and the targets embedded in surrounding environment. Methods such as breaking the in-plane symmetry or using low-contrast materials have been developed on PhC slabs [171] and metasurfaces [172] platforms for high-sensitivity hyper-spectral bio-molecular detection.

On the other hand, chiral sensing is desired in medical and biological applications. Since many biochemical compounds are chiral in nature, circular dichroism (CD) spectroscopy is utilized for the enantiomer-specific analysis of chiral samples. It is noteworthy that certain resonant nanostructures can significantly enhance the circular dichroism responses and improve the sensitivity of spectroscopy as well as photochemical, and thus ehannce the sensitivity of chiral sensing [173]. In 2019, Koshelev et al. [174] investigated the effect of detuning between the electrical and magnetic dipole resonances in silicon nano-cylinders in which the optical chirality at the nanoscale could be greatly enhanced. Later in 2020, Chen et al. [160] demonstrated the acquisition of CD spectrum and molar concentration over an individual metasurface with a high sensitivity (**Figure 8B**). Owing to the high-*Q* resonances, a hyperchiral field enhancement of the CD signal by a factor of 59 was observed, together with a large FOM of 80.6 in the detection of molar concentration, and thus it became a promising mythology in food industry, medical diagnostics, and drug development.

The EPs belong to a type of topologically non-trivial diabolic points. In 2017, for the first time, Chen et al. [170] proposed the scheme of using the micro-cavities operated at non-Hermitian spectral degeneracies for sensing. Owing to the complex-square-root dependency near an EP, the frequency splitting scaled as the square root of the perturbation strength, and hence, led to larger responses from small perturbation than that from traditional dispersion relations. This method paved the way for the sensors with unprecedented sensitivity. It is noteworthy that as mentioned in **Section 2.1**, the EPs are accompanied with polarization singularities, namely half-charges. Although not reported yet, we are optimistic to see the polarization singularity raised from EPs being utilized for sensing in the future.

3.7 Photonic Integration

Topological polarization singularities provide a vivid picture for light manipulation, which is useful in eliminating radiations, suppressing scatterings, and creating directional emitting, and thus shed light on the possibilities of photonic integration. Specifically, the superior photon confinement ability of the BICs leads to the ultra-high *Q*, ultra-narrow linewidth and low propagation loss, and the merging of half charges upon a single-side may boost the applications requiring unidirectional emission. Hereby we introduce some devices as examples, including waveguides [175–178], filters [179], couplers [43] and lasers [180].

By using BICs to confine light vertically, Zhang et al. [176] and Lin et al. [177] demonstrated waveguiding in PhC slabs. These works demonstrated the possibility to manipulate the radiation lifetime and spatial dispersion of BIC in a cooperative way. The BIC-based in-plane waveguiding was also utilized in the topological edge state in Zhang et al.'s work [175].

Recently, a new photonic platform with a low-refractive index material (Polymer) patterned on a high-refractive-index substrate ($LiNbO_3$) was demonstrated for integrated BIC-based devices including waveguides, microcavities, directional couplers, and modulators [178, 181]. This platform overcame the challenge of fabricating nano-scale structures upon high-refractive-index dielectric materials. The schematic of the platform in [178] is shown in **Figure 9A**. Specifically, the waveguide width was optimized and a BIC was observed by tuning the coupling strength between the TM bound mode and TE continuous mode. Benefiting from the BIC, the propagation loss of a straight waveguide was reduced to almost zero. For bent

waveguides, the bending loss was suppressed in a similar way by changing the bend radius and waveguide width. Besides, the BICs also provided an ultra-high Q, showing an intrinsic Q over 10^6 in microdisk cavities.

Gong et al. [179] implemented a BIC filter based on silicon photonic integrated circuits (PICs). The BIC filter was composed of two cascaded ring resonators side-coupled to two bus waveguides, as illuatrated in **Figure 9B**, with the two resonance frequencies $\omega_1$and ω_2 both tunable. By tuning the phase delay between the two rings to a multiple of π, the working state approached a near-FP-BIC [37] point, resulting in a filter performance with a near-unity transmission at $\omega_0 = \frac{\omega_1+\omega_2}{2}$ and a near-zero transmission at ω_1 and ω_2.

On the other hand, unidirectional guided resonances (UGRs) proposed by Yin et al. [43] paves the way to energy-efficient grating couplers. The UGRs only radiate toward one side of the PhC slab with the radiation at the other side eliminated (**Figure 9C**). The asymmetry ratio of the directional radiation reached 27.7 *dB* which indicated 99.8% of the power radiated toward the target direction. Moreover, the effect was maintained within a reasonably broad bandwidth (over 90% within a 26 *nm* bandwidth), and was proved to be effective for a coupling angle ranging from 5 to 11°.

The ultra-narrow linewidth of the BICs also facilitates the on-chip integrated lasers. Yu et al. experimentally an demonstrated a Fano BIC laser with a 5.8 *MHz* linewidth based on InP PhC slab buried within Si wafer [180](**Figure 9D**). Fano interference occurred between the discrete mode of a nanocavity and the continuum modes of a waveguide. The propagating modes in the waveguide destructively interfered with the nanocavity mode at the BIC wavelength, thereby turning the ordinary leaky mode into a BIC. Assuming an ideal BIC, a Fano mirror with total reflection would be formed in the waveguide region. Therefore, the light would be confined in the nanocavity and the region within the Fano mirror. The Q of the Fano BIC was significantly increased because photons were generated in the active region but stored in the passive region. Furthermore, the long lifetimes of the photons in the passive area can offset part of the quantum fluctuations caused by spontaneous radiation in the active area. The Fano BIC laser showed good mode selectivity and its lasing linewidth met the requirement of coherent optical communication.

4 DISCUSSION

In previous sections, we have reviewed the fundamentals and applications of polarization singularities that are defined upon the far-field radiations. As elaborated, the polarization singularities are topological in nature, with their existence and continuous evolution robust in the momentum space. From the view of science, polarization singularities reflect the "inside information" of a system which becomes observable since the escaping photons carry it out. On the other hand, polarization singularities establish abstract and primitive concepts for depicting, and further manipulating lights, and then pave the way to many applications as discussed.

For an outlook, several points might be noteworthy. From theoretical point of view, it is essential to build up a comprehensive connection between radiation topology, where polarization singularities are defined, and non-Hermitian topology, where generic topological band theory is developed upon. Given that radiation raises non-Hermiticity, it is expected that non-trivial intrinsic band topology might lead to observable manifestation in radiation field, that bridges to polarization singularities. Given that many exotic phenomena were discovered in non-Hermitian systems, it is necessary to study how the radiation raises and represents unique topology landscapes for deeper understanding of the physics. For instance, both the BICs and EPs carry topological charges in their far-field radiation, but only the latter are associated with nontrivial Chern numbers. Besides, from the view of technology, there's still much to explore about extending the idea of polarization singularity manipulation to more materials, devices, scenarios and applications. We are optimistic to foresee that the utilization of polarization singularities will be boosted by the methodology of topological photonics, thus bring essential promotion to many key applications, including optical communication, LIDAR, AR/VR, and bio-sensing.

AUTHOR CONTRIBUTIONS

CP organized the article. FW, CP, and XY composed Section 1, 2, and 4. All the authors contributed to Section 3.

FUNDING

This work was supported by the National Natural Science Foundation of China (Grant Nos. 61922004 and 62135001), China Postdoctoral Science Foundation funded project (Grant No. 2021M690239), National Key Research and Development Program of China (2020YFB1806405), and Major Key Project of PCL (PCL2021A14, PCL2021A04).

REFERENCES

1. Poincaré H. *Théorie mathématique de la lumière: cours de Physique Mathématique*. Paris: Georges Carré Editeur (1889).
2. Soskin MS, Vasnetsov MV. Singular Optics. *Prog Opt* (2001) 42:219–76. doi:10.1016/S0079-6638(01)80018-4
3. Nye JF. Lines of Circular Polarization in Electromagnetic Wave fields. *Proc R Soc Lond A* (1983) 389:279–90. doi:10.1098/rspa.1983.0109
4. Nye JF. Polarization Effects in the Diffraction of Electromagnetic Waves: the Role of Disclinations. *Proc R Soc Lond A* (1983) 387:105–32. doi:10.1098/rspa.1983.0053
5. Berry MV. Geometry of Phase and Polarization Singularities Illustrated by Edge Diffraction and the Tides. In: MS Soskin MV Vasnetsov, editors. *Second International Conference on Singular Optics (Optical Vortices): Fundamentals and Applications*, 4403. Crimea: International Society for Optics and Photonics (2001). p. 1–12. doi:10.1117/12.428252

6. Dennis MR, O'Holleran K, Padgett MJ. Chapter 5 Singular Optics: Optical Vortices and Polarization Singularities. *Prog Opt* (2009) 53:293–363. doi:10.1016/S0079-6638(08)00205-9
7. Gbur GJ. *Singular Optics*. Boca Raton: CRC Press (2016).
8. Berry M. *A Half-century of Physical Asymptotics and Other Diversions: Selected Works by Michael Berry*. Singapore: World Scientific (2017).
9. Wang Q, Tu C-H, Li Y-N, Wang H-T. Polarization Singularities: Progress, Fundamental Physics, and Prospects. *APL Photon* (2021) 6:040901. doi:10.1063/5.0045261
10. Allen L, Barnett SM, Padgett MJ. *Optical Angular Momentum*. Boca Raton: CRC Press (2016).
11. Desyatnikov AS, Torner L, Kivshar YS. *Optical Vortices and Vortex Solitons* (2005). *arXiv preprint nlin/0501026*.
12. Wang B, Liu W, Zhao M, Wang J, Zhang Y, Chen A, et al. Generating Optical Vortex Beams by Momentum-Space Polarization Vortices Centred at Bound States in the Continuum. *Nat Photon* (2020) 14:623–8. doi:10.1038/s41566-020-0658-1
13. Tovar AA. Production and Propagation of Cylindrically Polarized Laguerre-Gaussian Laser Beams. *J Opt Soc Am A* (1998) 15:2705–11. doi:10.1364/JOSAA.15.002705
14. Youngworth KS, Brown TG. Focusing of High Numerical Aperture Cylindrical-Vector Beams. *Opt Express* (2000) 7:77–87. doi:10.1364/OE.7.000077
15. Zhan Q, Leger J. Focus Shaping Using Cylindrical Vector Beams. *Opt Express* (2002) 10:324–31. doi:10.1364/OE.10.000324
16. Dorn R, Quabis S, Leuchs G. Sharper Focus for a Radially Polarized Light Beam. *Phys Rev Lett* (2003) 91:233901. doi:10.1103/PhysRevLett.91.233901
17. Hsu CW, Zhen B, Lee J, Chua S-L, Johnson SG, Joannopoulos JD, et al. Observation of Trapped Light within the Radiation Continuum. *Nature* (2013) 499:188–91. doi:10.1038/nature12289
18. Koshelev K, Kruk S, Melik-Gaykazyan E, Choi J-H, Bogdanov A, Park H-G, et al. Subwavelength Dielectric Resonators for Nonlinear Nanophotonics. *Science* (2020) 367:288–92. doi:10.1126/science.aaz3985
19. Bulgakov EN, Sadreev AF. Bound States in the Continuum with High Orbital Angular Momentum in a Dielectric Rod with Periodically Modulated Permittivity. *Phys Rev A* (2017) 96:013841. doi:10.1103/PhysRevA.96.013841
20. Zhang Y, Chen A, Liu W, Hsu CW, Wang B, Guan F, et al. Observation of Polarization Vortices in Momentum Space. *Phys Rev Lett* (2018) 120:186103. doi:10.1103/PhysRevLett.120.186103
21. von Neuman J, Wigner E. Über merkwürdige diskrete eigenwerte. Uber das verhalten von eigenwerten bei adiabatischen prozessen. *Physikalische Z* (1929) 30:467–70.
22. Plotnik Y, Peleg O, Dreisow F, Heinrich M, Nolte S, Szameit A, et al. Experimental Observation of Optical Bound States in the Continuum. *Phys Rev Lett* (2011) 107:183901. doi:10.1103/PhysRevLett.107.183901
23. Yang Y, Peng C, Liang Y, Li Z, Noda S. Analytical Perspective for Bound States in the Continuum in Photonic crystal Slabs. *Phys Rev Lett* (2014) 113:037401. doi:10.1103/PhysRevLett.113.037401
24. Ni L, Wang Z, Peng C, Li Z. Tunable Optical Bound States in the Continuum beyond In-Plane Symmetry protection. *Phys Rev B* (2016) 94:245148. doi:10.1103/PhysRevB.94.245148
25. Zhen B, Hsu CW, Lu L, Stone AD, Soljačić M. Topological Nature of Optical Bound States in the Continuum. *Phys Rev Lett* (2014) 113:257401. doi:10.1103/PhysRevLett.113.257401
26. Zhou H, Peng C, Yoon Y, Hsu CW, Nelson KA, Fu L, et al. Observation of Bulk Fermi Arc and Polarization Half Charge from Paired Exceptional Points. *Science* (2018) 359:1009–12. doi:10.1126/science.aap9859
27. Lu L, Joannopoulos JD, Soljačić M. Topological Photonics. *Nat Photon* (2014) 8:821–9. doi:10.1038/nphoton.2014.248
28. Khanikaev AB, Shvets G. Two-dimensional Topological Photonics. *Nat Photon* (2017) 11:763–73. doi:10.1038/s41566-017-0048-5
29. Ozawa T, Price HM, Amo A, Goldman N, Hafezi M, Lu L, et al. Topological Photonics. *Rev Mod Phys* (2019) 91:015006. doi:10.1103/revmodphys.91.015006
30. Parto M, Liu YGN, Bahari B, Khajavikhan M, Christodoulides DN. Non-Hermitian and Topological Photonics: Optics at an Exceptional point. *Nanophotonics* (2020) 10:403–23. doi:10.1515/nanoph-2020-0434
31. Feng L, El-Ganainy R, Ge L. Non-Hermitian Photonics Based on Parity-Time Symmetry. *Nat Photon* (2017) 11:752–62. doi:10.1038/s41566-017-0031-1
32. El-Ganainy R, Makris KG, Khajavikhan M, Musslimani ZH, Rotter S, Christodoulides DN. Non-Hermitian Physics and PT Symmetry. *Nat Phys* (2018) 14:11–9. doi:10.1038/nphys4323
33. Ghatak A, Das T. New Topological Invariants in Non-hermitian Systems. *J Phys Condens Matter* (2019) 31:263001. doi:10.1088/1361-648x/ab11b3
34. Ashida Y, Gong Z, Ueda M. Non-Hermitian Physics. *Adv Phys* (2020) 69:249–435. doi:10.1080/00018732.2021.1876991
35. Yin X, Peng C. Manipulating Light Radiation from a Topological Perspective. *Photon Res* (2020) 8:B25. doi:10.1364/prj.403444
36. Peng C. Trapping Light in the Continuum - from Fantasy to Reality. *Sci Bull* (2020) 65:1527–32. doi:10.1016/j.scib.2020.05.009
37. Hsu CW, Zhen B, Stone AD, Joannopoulos JD, Soljačić M. Bound States in the Continuum. *Nat Rev Mater* (2016) 1:16048. doi:10.1038/natrevmats.2016.48
38. Koshelev K, Bogdanov A, Kivshar Y. Meta-optics and Bound States in the Continuum. *Sci Bull* (2019) 64:836–42. doi:10.1016/j.scib.2018.12.003
39. Azzam SI, Kildishev AV. Photonic Bound States in the Continuum: From Basics to Applications. *Adv Opt Mater*. (2021) 9:2001469. doi:10.1002/adom.202001469
40. Allen L, Padgett MJ, Babiker M. IV the Orbital Angular Momentum of Light. In: E Wolf, editor. *Progress in Optics*, 39. New York: Elsevier (1999). p. 291–372. doi:10.1016/S0079-6638(08)70391-3.ISSN:0079-6638
41. Franke-Arnold S, Allen L, Padgett M. Advances in Optical Angular Momentum. *Laser Photon Rev* (2008) 2:299–313. doi:10.1002/lpor.200810007
42. Padgett MJ. Orbital Angular Momentum 25 Years on [Invited]. *Opt Express* (2017) 25:11265. doi:10.1364/oe.25.011265
43. Yin X, Jin J, Soljačić M, Peng C, Zhen B. Observation of Topologically Enabled Unidirectional Guided Resonances. *Nature* (2020) 580:467–71. doi:10.1038/s41586-020-2181-4
44. Kravets VG, Schedin F, Jalil R, Britnell L, Gorbachev RV, Ansell D, et al. Singular Phase Nano-Optics in Plasmonic Metamaterials for Label-free Single-Molecule Detection. *Nat Mater* (2013) 12:304–9. doi:10.1038/nmat3537
45. Ramezani H, Li H-K, Wang Y, Zhang X. Unidirectional Spectral Singularities. *Phys Rev Lett* (2014) 113:263905. doi:10.1103/PhysRevLett.113.263905
46. Sreekanth KV, Sreejith S, Han S, Mishra A, Chen X, Sun H, et al. Biosensing with the Singular Phase of an Ultrathin Metal-Dielectric Nanophotonic Cavity. *Nat Commun* (2018) 9:369. doi:10.1038/s41467-018-02860-6
47. Li Y, Argyropoulos C. Exceptional Points and Spectral Singularities in Active Epsilon-Near-Zero Plasmonic Waveguides. *Phys Rev B* (2019) 99:075413. doi:10.1103/PhysRevB.99.075413
48. Shen Y, Wang X, Xie Z, Min C, Fu X, Liu Q, et al. Optical Vortices 30 Years on: OAM Manipulation from Topological Charge to Multiple Singularities. *Light Sci Appl* (2019) 8:90. doi:10.1038/s41377-019-0194-2
49. Han Z, Ohno S, Minamide H. Spectral Phase Singularity in a Transmission-type Double-Layer Metamaterial. *Optica* (2020) 7:1721. doi:10.1364/OPTICA.404090
50. Ni J, Huang C, Zhou L-M, Gu M, Song Q, Kivshar Y, et al. Multidimensional Phase Singularities in Nanophotonics. *Science* (2021) 374:eabj0039. doi:10.1126/science.abj0039
51. Liu M, Zhao C, Zeng Y, Chen Y, Zhao C, Qiu C-W. Evolution and Nonreciprocity of Loss-Induced Topological Phase Singularity Pairs. *Phys Rev Lett* (2021) 127:266101. doi:10.1103/PhysRevLett.127.266101
52. Guo Y, Xiao M, Fan S. Topologically Protected Complete Polarization Conversion. *Phys Rev Lett* (2017) 119:167401. doi:10.1103/PhysRevLett.119.167401
53. Dai S, Liu L, Han D, Zi J. From Topologically Protected Coherent Perfect Reflection to Bound States in the Continuum. *Phys Rev B* (2018) 98:081405. doi:10.1103/PhysRevB.98.081405
54. Sweeney WR, Hsu CW, Stone AD. Theory of Reflectionless Scattering Modes. *Phys Rev A* (2020) 102:063511. doi:10.1103/PhysRevA.102.063511
55. Wong WC, Wang W, Yau WT, Fung KH. Topological Theory for Perfect Metasurface Isolators. *Phys Rev B* (2020) 101:121405. doi:10.1103/PhysRevB.101.121405
56. Mukherjee S, Gomis-Bresco J, Pujol-Closa P, Artigas D, Torner L. Topological Properties of Bound States in the Continuum in Geometries

with Broken Anisotropy Symmetry. *Phys Rev A* (2018) 98:063826. doi:10.1103/PhysRevA.98.063826
57. Song AY, Catrysse PB, Fan S. Broadband Control of Topological Nodes in Electromagnetic fields. *Phys Rev Lett* (2018) 120:193903. doi:10.1103/PhysRevLett.120.193903
58. Xiao Y-X, Ding K, Zhang R-Y, Hang ZH, Chan CT. Exceptional Points Make an Astroid in Non-hermitian Lieb Lattice: Evolution and Topological protection. *Phys Rev B* (2020) 102:245144. doi:10.1103/PhysRevB.102.245144
59. Tong H, Liu S, Zhao M, Fang K. Observation of Phonon Trapping in the Continuum with Topological Charges. *Nat Commun* (2020) 11:5216. doi:10.1038/s41467-020-19091-3
60. Ilic O, Kaminer I, Zhen B, Miller OD, Buljan H, Soljačić M. Topologically Enabled Optical Nanomotors. *Sci Adv* (2017) 3:9. doi:10.1126/sciadv.1602738
61. Friedrich H, Wintgen D. Interfering Resonances and Bound States in the Continuum. *Phys Rev A* (1985) 32:3231–42. doi:10.1103/physreva.32.3231
62. Huang MCY, Zhou Y, Chang-Hasnain CJ. A Surface-Emitting Laser Incorporating a high-index-contrast Subwavelength Grating. *Nat Photon* (2007) 1:119–22. doi:10.1038/nphoton.2006.80
63. Zhou Y, Huang MCY, Chang-Hasnain CJ. Large Fabrication Tolerance for VCSELs Using High-Contrast Grating. *IEEE Photon Technol Lett* (2008) 20:434–6. doi:10.1109/LPT.2008.916969
64. Huang MCY, Zhou Y, Chang-Hasnain CJ. Single Mode High-Contrast Subwavelength Grating Vertical Cavity Surface Emitting Lasers. *Appl Phys Lett* (2008) 92:171108. doi:10.1063/1.2917447
65. Ye Zhou Y, Huang MCY, Chase C, Karagodsky V, Moewe M, Pesala B, et al. High-index-contrast Grating (HCG) and its Applications in Optoelectronic Devices. *IEEE J Select Top Quan Electron.* (2009) 15:1485–99. doi:10.1109/JSTQE.2009.2021145
66. Wang Z, Zhang H, Ni L, Hu W, Peng C. Analytical Perspective of Interfering Resonances in high-index-contrast Periodic Photonic Structures. *IEEE J Quan Electron.* (2016) 52:1–9. doi:10.1109/JQE.2016.2568763
67. Lee S-G, Magnusson R. Band Flips and Bound-State Transitions in Leaky-Mode Photonic Lattices. *Phys Rev B* (2019) 99:045304. doi:10.1103/PhysRevB.99.045304
68. Koshelev K, Lepeshov S, Liu M, Bogdanov A, Kivshar Y. Asymmetric Metasurfaces with High- Q Resonances Governed by Bound States in the Continuum. *Phys Rev Lett* (2018) 121:193903. doi:10.1103/PhysRevLett.121.193903
69. Liu Z, Xu Y, Lin Y, Xiang J, Feng T, Cao Q, et al. High- Q Quasibound States in the Continuum for Nonlinear Metasurfaces. *Phys Rev Lett* (2019) 123:253901. doi:10.1103/PhysRevLett.123.253901
70. Yesilkoy F, Arvelo ER, Jahani Y, Liu M, Tittl A, Cevher V, et al. Ultrasensitive Hyperspectral Imaging and Biodetection Enabled by Dielectric Metasurfaces. *Nat Photon* (2019) 13:390–6. doi:10.1038/s41566-019-0394-6
71. Chen A, Liu W, Zhang Y, Wang B, Liu X, Shi L, et al. Observing Vortex Polarization Singularities at Optical Band Degeneracies. *Phys Rev B* (2019) 99:180101. doi:10.1103/PhysRevB.99.180101
72. Chen W, Chen Y, Liu W. Line Singularities and Hopf Indices of Electromagnetic Multipoles. *Laser Photon Rev* (2020) 14:2000049. doi:10.1002/lpor.202000049
73. Chen W, Chen Y, Liu W. Singularities and Poincaré Indices of Electromagnetic Multipoles. *Phys Rev Lett* (2019) 122:153907. doi:10.1103/PhysRevLett.122.153907
74. Sadrieva Z, Frizyuk K, Petrov M, Kivshar Y, Bogdanov A. Multipolar Origin of Bound States in the Continuum. *Phys Rev B* (2019) 100:115303. doi:10.1103/PhysRevB.100.115303
75. Streifer W, Scifres D, Burnham R. Analysis of Grating-Coupled Radiation in GaAs:GaAlAs Lasers and Waveguides - I. *IEEE J Quan Electron.* (1976) 12:422–8. doi:10.1109/JQE.1976.1069175
76. Kim M, Kim CS, Bewley WW, Lindle JR, Canedy CL, Vurgaftman I, et al. Surface-emitting Photonic-crystal Distributed-Feedback Laser for the Midinfrared. *Appl Phys Lett* (2006) 88:191105. doi:10.1063/1.2203234
77. Lu T-C, Chen S-W, Lin L-F, Kao T-T, Kao C-C, Yu P, et al. GaN-based Two-Dimensional Surface-Emitting Photonic crystal Lasers with AlN/GaN Distributed Bragg Reflector. *Appl Phys Lett* (2008) 92:011129. doi:10.1063/1.2831716
78. Matsubara H, Yoshimoto S, Saito H, Jianglin Y, Tanaka Y, Noda S. GaN Photonic-crystal Surface-Emitting Laser at Blue-Violet Wavelengths. *Science* (2008) 319:445–7. doi:10.1126/science.1150413
79. Chassagneux Y, Colombelli R, Maineult W, Barbieri S, Beere HE, Ritchie DA, et al. Electrically Pumped Photonic-crystal Terahertz Lasers Controlled by Boundary Conditions. *Nature* (2009) 457:174–8. doi:10.1038/nature07636
80. Imada M, Noda S, Chutinan A, Tokuda T, Murata M, Sasaki G. Coherent Two-Dimensional Lasing Action in Surface-Emitting Laser with Triangular-Lattice Photonic crystal Structure. *Appl Phys Lett* (1999) 75:316–8. doi:10.1063/1.124361
81. Ohnishi D, Okano T, Imada M, Noda S. Room Temperature Continuous Wave Operation of a Surface-Emitting Two-Dimensional Photonic crystal Diode Laser. *Opt Express* (2004) 12:1562. doi:10.1364/OPEX.12.001562
82. Hirose K, Liang Y, Kurosaka Y, Watanabe A, Sugiyama T, Noda S. Watt-class High-Power, High-Beam-Quality Photonic-crystal Lasers. *Nat Photon* (2014) 8:406–11. doi:10.1038/nphoton.2014.75
83. Yoshida M, De Zoysa M, Ishizaki K, Tanaka Y, Kawasaki M, Hatsuda R, et al. Double-lattice Photonic-crystal Resonators Enabling High-Brightness Semiconductor Lasers with Symmetric Narrow-Divergence Beams. *Nat Mater* (2019) 18:121–8. doi:10.1038/s41563-018-0242-y
84. Kodigala A, Lepetit T, Gu Q, Bahari B, Fainman Y, Kanté B. Lasing Action from Photonic Bound States in Continuum. *Nature* (2017) 541:196–9. doi:10.1038/nature20799
85. Bulgakov EN, Maksimov DN. Topological Bound States in the Continuum in Arrays of Dielectric Spheres. *Phys Rev Lett* (2017) 118:267401. doi:10.1103/PhysRevLett.118.267401
86. Doeleman HM, Monticone F, den Hollander W, Alù A, Koenderink AF. Experimental Observation of a Polarization Vortex at an Optical Bound State in the Continuum. *Nat Photon* (2018) 12:397–401. doi:10.1038/s41566-018-0177-5
87. Wang Z, Liang Y, Beck M, Scalari G, Faist J. Topological Charge of Finite-Size Photonic crystal Modes. *Phys Rev B* (2020) 102:045122. doi:10.1103/PhysRevB.102.045122
88. Bulgakov EN, Pichugin KN, Sadreev AF. All-optical Light Storage in Bound States in the Continuum and Release by Demand. *Opt Express* (2015) 23:22520. doi:10.1364/OE.23.022520
89. Bulgakov EN, Maksimov DN. Bound States in the Continuum and Polarization Singularities in Periodic Arrays of Dielectric Rods. *Phys Rev A* (2017) 96:063833. doi:10.1103/PhysRevA.96.063833
90. Bulgakov EN, Sadreev AF. Light Trapping above the Light Cone in a One-Dimensional Array of Dielectric Spheres. *Phys Rev A* (2015) 92:023816. doi:10.1103/PhysRevA.92.023816
91. Carletti L, Koshelev K, De Angelis C, Kivshar Y. Giant Nonlinear Response at the Nanoscale Driven by Bound States in the Continuum. *Phys Rev Lett* (2018) 121:033903. doi:10.1103/PhysRevLett.121.033903
92. Rybin MV, Koshelev KL, Sadrieva ZF, Samusev KB, Bogdanov AA, Limonov MF, et al. High- Q Supercavity Modes in Subwavelength Dielectric Resonators. *Phys Rev Lett* (2017) 119:243901. doi:10.1103/PhysRevLett.119.243901
93. Silveirinha MG. Trapping Light in Open Plasmonic Nanostructures. *Phys Rev A* (2014) 89:023813. doi:10.1103/physreva.89.023813
94. Yoda T, Notomi M. Generation and Annihilation of Topologically Protected Bound States in the Continuum and Circularly Polarized States by Symmetry Breaking. *Phys Rev Lett* (2020) 125:053902. doi:10.1103/PhysRevLett.125.053902
95. Cerjan A, Hsu CW, Rechtsman MC. Bound States in the Continuum through Environmental Design. *Phys Rev Lett* (2019) 123:023902. doi:10.1103/PhysRevLett.123.023902
96. Cerjan A, Jörg C, Vaidya S, Augustine S, Benalcazar WA, Hsu CW, et al. Observation of Bound States in the Continuum Embedded in Symmetry Bandgaps. *Sci Adv* (2021) 7:eabk1117. doi:10.1126/sciadv.abk1117
97. De Angelis L, Bauer T, Alpeggiani F, Kuipers L. Index-symmetry Breaking of Polarization Vortices in 2D Random Vector Waves. *Optica* (2019) 6:1237. doi:10.1364/OPTICA.6.001237
98. Che Z, Zhang Y, Liu W, Zhao M, Wang J, Zhang W, et al. Polarization Singularities of Photonic Quasicrystals in Momentum Space. *Phys Rev Lett* (2021) 127:043901. doi:10.1103/PhysRevLett.127.043901
99. Song Q, Hu J, Dai S, Zheng C, Han D, Zi J, et al. Coexistence of a New Type of Bound State in the Continuum and a Lasing Threshold Mode Induced by Pt Symmetry. *Sci Adv* (2020) 6:eabc1160. doi:10.1126/sciadv.abc1160
100. Liu W, Wang B, Zhang Y, Wang J, Zhao M, Guan F, et al. Circularly Polarized States Spawning from Bound States in the Continuum. *Phys Rev Lett* (2019) 123:116104. doi:10.1103/PhysRevLett.123.116104

101. Ye W, Gao Y, Liu J. Singular Points of Polarizations in the Momentum Space of Photonic crystal Slabs. *Phys Rev Lett* (2020) 124:153904. doi:10.1103/PhysRevLett.124.153904
102. Zeng Y, Hu G, Liu K, Tang Z, Qiu C-W. Dynamics of Topological Polarization Singularity in Momentum Space. *Phys Rev Lett* (2021) 127:176101. doi:10.1103/PhysRevLett.127.176101
103. Chen W, Yang Q, Chen Y, Liu W. Evolution and Global Charge Conservation for Polarization Singularities Emerging from Non-hermitian Degeneracies. *Proc Natl Acad Sci USA* (2021) 118:e2019578118. doi:10.1073/pnas.2019578118
104. Jin J, Yin X, Ni L, Soljačić M, Zhen B, Peng C. Topologically Enabled Ultrahigh-Q Guided Resonances Robust to Out-Of-Plane Scattering. *Nature* (2019) 574:501–4. doi:10.1038/s41586-019-1664-7
105. Kang M, Zhang S, Xiao M, Xu H. Merging Bound States in the Continuum at Off-High Symmetry Points. *Phys Rev Lett* (2021) 126:117402. doi:10.1103/PhysRevLett.126.117402
106. Lee J, Zhen B, Chua S-L, Qiu W, Joannopoulos JD, Soljačić M, et al. Observation and Differentiation of Unique High-QOptical Resonances Near Zero Wave Vector in Macroscopic Photonic Crystal Slabs. *Phys Rev Lett* (2012) 109:067401. doi:10.1103/PhysRevLett.109.067401
107. Chen Z, Yin X, Jin J, Zheng Z, Zhang Z, Wang F, et al. Observation of Miniaturized Bound States in the Continuum with Ultra-high Quality Factors. *Sci Bull* (2022) 67:359–66. doi:10.1016/j.scib.2021.10.020
108. Akahane Y, Asano T, Song B-S, Noda S. High-*Q* Photonic Nanocavity in a Two-Dimensional Photonic crystal. *Nature* (2003) 425:944–7. doi:10.1038/nature02063
109. Song B-S, Noda S, Asano T, Akahane Y. Ultra-high-*Q* Photonic Double-Heterostructure Nanocavity. *Nat Mater* (2005) 4:207–10. doi:10.1038/nmat1320
110. Deotare PB, McCutcheon MW, Frank IW, Khan M, Lončar M. High Quality Factor Photonic crystal Nanobeam Cavities. *Appl Phys Lett* (2009) 94:121106. doi:10.1063/1.3107263
111. Chua S-L, Chong Y, Stone AD, Soljacic M, Bravo-Abad J. Low-threshold Lasing Action in Photonic crystal Slabs Enabled by Fano Resonances. *Opt Express* (2011) 19:1539. doi:10.1364/OE.19.001539
112. Liang Y, Peng C, Sakai K, Iwahashi S, Noda S. Three-dimensional Coupled-Wave Analysis for Square-Lattice Photonic crystal Surface Emitting Lasers with Transverse-Electric Polarization: Finite-Size Effects. *Opt Express* (2012) 20:15945. doi:10.1364/OE.20.015945
113. Hwang M-S, Lee H-C, Kim K-H, Jeong K-Y, Kwon S-H, Koshelev K, et al. Ultralow-threshold Laser Using Super-bound States in the Continuum. *Nat Commun* (2021) 12:4135. doi:10.1038/s41467-021-24502-0
114. Wang J, Clementi M, Minkov M, Barone A, Carlin J-F, Grandjean N, et al. Doubly Resonant Second-Harmonic Generation of a Vortex Beam from a Bound State in the Continuum. *Optica* (2020) 7:1126. doi:10.1364/OPTICA.396408
115. Shyh Wang S. Principles of Distributed Feedback and Distributed Bragg-Reflector Lasers. *IEEE J Quan Electron.* (1974) 10:413–27. doi:10.1109/jqe.1974.1068152
116. Reinhart FK, Logan RA, Shank CV. GaAs-AlxGa1-xAs Injection Lasers with Distributed Bragg Reflectors. *Appl Phys Lett* (1975) 27:45–8. doi:10.1063/1.88262
117. Hasnain G, Tai K, Yang L, Wang YH, Fischer RJ, Wynn JD, et al. Performance of Gain-Guided Surface Emitting Lasers with Semiconductor Distributed Bragg Reflectors. *IEEE J Quan Electron.* (1991) 27:1377–85. doi:10.1109/3.89954
118. Kurosaka Y, Iwahashi S, Liang Y, Sakai K, Miyai E, Kunishi W, et al. On-chip Beam-Steering Photonic-crystal Lasers. *Nat Photon* (2010) 4:447–50. doi:10.1038/nphoton.2010.118
119. Peng C, Liang Y, Sakai K, Iwahashi S, Noda S. Three-dimensional Coupled-Wave Theory Analysis of a Centered-Rectangular Lattice Photonic crystal Laser with a Transverse-electric-like Mode. *Phys Rev B* (2012) 86:035108. doi:10.1103/physrevb.86.035108
120. Ishizaki K, Zoysa MD, Noda S. Progress in Photonic-crystal Surface-Emitting Lasers. *Photonics* (2019) 6:96. doi:10.3390/photonics6030096
121. Miyai E, Sakai K, Okano T, Kunishi W, Ohnishi D, Noda S. Lasers Producing Tailored Beams. *Nature* (2006) 441:946. doi:10.1038/441946a
122. Morita R, Inoue T, De Zoysa M, Ishizaki K, Noda S. Photonic-crystal Lasers with Two-Dimensionally Arranged Gain and Loss Sections for High-Peak-Power Short-Pulse Operation. *Nat Photon* (2021) 15:311–8. doi:10.1038/s41566-021-00771-5
123. Sakata R, Ishizaki K, De Zoysa M, Fukuhara S, Inoue T, Tanaka Y, et al. Dually Modulated Photonic Crystals Enabling High-Power High-Beam-Quality Two-Dimensional Beam Scanning Lasers. *Nat Commun* (2020) 11:3487. doi:10.1038/s41467-020-17092-w
124. Huang C, Zhang C, Xiao S, Wang Y, Fan Y, Liu Y, et al. Ultrafast Control of Vortex Microlasers. *Science* (2020) 367:1018–21. doi:10.1126/science.aba4597
125. Ha ST, Fu YH, Emani NK, Pan Z, Bakker RM, Paniagua-Domínguez R, et al. Directional Lasing in Resonant Semiconductor Nanoantenna Arrays. *Nat Nanotech* (2018) 13:1042–7. doi:10.1038/s41565-018-0245-5
126. Wu M, Ha ST, Shendre S, Durmusoglu EG, Koh W-K, Abujetas DR, et al. Room-Temperature Lasing in Colloidal Nanoplatelets via Mie-Resonant Bound States in the Continuum. *Nano Lett* (2020) 20:6005–11. doi:10.1021/acs.nanolett.0c01975
127. Xu L, Zangeneh Kamali K, Huang L, Rahmani M, Smirnov A, Camacho-Morales R, et al. Dynamic Nonlinear Image Tuning through Magnetic Dipole Quasi-BIC Ultrathin Resonators. *Adv Sci* (2019) 6:1802119. doi:10.1002/advs.201802119
128. Kang L, Wu Y, Ma X, Lan S, Werner DH. High-Harmonic Optical Vortex Generation from Photonic Bound States in the Continuum. *Adv Opt Mater* (2021) 10:2101497. doi:10.1002/adom.202101497
129. Wang J, Li H, Ma Y, Zhao M, Liu W, Wang B, et al. Routing valley Exciton Emission of a WS2 Monolayer via Delocalized Bloch Modes of In-Plane Inversion-Symmetry-Broken Photonic crystal Slabs. *Light Sci Appl* (2020) 9:148. doi:10.1038/s41377-020-00387-4
130. Koshelev K, Tang Y, Li K, Choi D-Y, Li G, Kivshar Y. Nonlinear Metasurfaces Governed by Bound States in the Continuum. *ACS Photon* (2019) 6:1639–44. doi:10.1021/acsphotonics.9b00700
131. Koshelev KL, Sychev SK, Sadrieva ZF, Bogdanov AA, Iorsh IV. Strong Coupling between Excitons in Transition Metal Dichalcogenides and Optical Bound States in the Continuum. *Phys Rev B* (2018) 98:161113. doi:10.1103/PhysRevB.98.161113
132. Kravtsov V, Khestanova E, Benimetskiy FA, Ivanova T, Samusev AK, Sinev IS, et al. Nonlinear Polaritons in a Monolayer Semiconductor Coupled to Optical Bound States in the Continuum. *Light Sci Appl* (2020) 9:56. doi:10.1038/s41377-020-0286-z
133. Yu Z, Wang Y, Sun B, Tong Y, Xu JB, Tsang HK, et al. Hybrid 2D-Material Photonics with Bound States in the Continuum. *Adv Opt Mater.* (2019) 7:1901306. doi:10.1002/adom.201901306
134. Tian J, Li Q, Belov PA, Sinha RK, Qian W, Qiu M. High-Q All-Dielectric Metasurface: Super and Suppressed Optical Absorption. *ACS Photon* (2020) 7:1436–43. doi:10.1021/acsphotonics.0c00003
135. Zhang Z, Yin X, Chen Z, Wang F, Hu W, Peng C. Observation of Intensity Flattened Phase Shifting Enabled by Unidirectional Guided Resonance. *Nanophotonics* (2021) 10:4467–75. doi:10.1515/nanoph-2021-0393
136. Lv J, Yin X, Jin J, Zhang H, Zhao C, Peng C, et al. Demonstration of a Thermo-Optic Phase Shifter by Utilizing High-Q Resonance in high-index-contrast Grating. *Opt Lett* (2018) 43:827. doi:10.1364/OL.43.000827
137. Kwon H, Zheng T, Faraon A. Nano-electromechanical Tuning of Dual-Mode Resonant Dielectric Metasurfaces for Dynamic Amplitude and Phase Modulation. *Nano Lett* (2021) 21:2817–23. doi:10.1021/acs.nanolett.0c04888
138. Salary MM, Mosallaei H. Tunable All-Dielectric Metasurfaces for Phase-Only Modulation of Transmitted Light Based on Quasi-Bound States in the Continuum. *ACS Photon* (2020) 7:1813–29. doi:10.1021/acsphotonics.0c00554
139. Xiong W, Hsu CW, Bromberg Y, Antonio-Lopez JE, Amezcua Correa R, Cao H. Complete Polarization Control in Multimode Fibers with Polarization and Mode Coupling. *Light Sci Appl* (2018) 7:54. doi:10.1038/s41377-018-0047-4
140. Li G, Chen S, Pholchai N, Reineke B, Wong PWH, Pun EYB, et al. Continuous Control of the Nonlinearity Phase for Harmonic Generations. *Nat Mater* (2015) 14:607–12. doi:10.1038/nmat4267
141. Rubin NA, D'Aversa G, Chevalier P, Shi Z, Chen WT, Capasso F. Matrix Fourier Optics Enables a Compact Full-Stokes Polarization Camera. *Science* (2019) 365:eaax1839. doi:10.1126/science.aax1839
142. Khan MI, Khalid Z, Tahir FA. Linear and Circular-Polarization Conversion in X-Band Using Anisotropic Metasurface. *Sci Rep* (2019) 9:4552. doi:10.1038/s41598-019-40793-2

143. Yu P, Li J, Liu N. Electrically Tunable Optical Metasurfaces for Dynamic Polarization Conversion. *Nano Lett* (2021) 21:6690–5. doi:10.1021/acs.nanolett.1c02318
144. Chang C-C, Zhao Z, Li D, Taylor AJ, Fan S, Chen H-T. Broadband Linear-To-Circular Polarization Conversion Enabled by Birefringent Off-Resonance Reflective Metasurfaces. *Phys Rev Lett* (2019) 123:237401. doi:10.1103/PhysRevLett.123.237401
145. Wang S, Deng Z-L, Wang Y, Zhou Q, Wang X, Cao Y, et al. Arbitrary Polarization Conversion Dichroism Metasurfaces for All-In-One Full Poincaré Sphere Polarizers. *Light Sci Appl* (2021) 10:24. doi:10.1038/s41377-021-00468-y
146. Guo Y, Xiao M, Zhou Y, Fan S. Arbitrary Polarization Conversion with a Photonic crystal Slab. *Adv Opt Mater.* (2019) 7:1801453. doi:10.1002/adom.201801453
147. Dorfner D, Zabel T, Hürlimann T, Hauke N, Frandsen L, Rant U, et al. Photonic crystal Nanostructures for Optical Biosensing Applications. *Biosens Bioelectron* (2009) 24:3688–92. doi:10.1016/j.bios.2009.05.014
148. Huang M, Yanik AA, Chang T-Y, Altug H. Sub-wavelength Nanofluidics in Photonic crystal Sensors. *Opt Express* (2009) 17:24224–33. doi:10.1364/OE.17.024224
149. Kang C, Phare CT, Vlasov YA, Assefa S, Weiss SM. Photonic crystal Slab Sensor with Enhanced Surface Area. *Opt Express* (2010) 18:27930–7. doi:10.1364/OE.18.027930
150. Lai W-C, Chakravarty S, Zou Y, Guo Y, Chen RT. Slow Light Enhanced Sensitivity of Resonance Modes in Photonic crystal Biosensors. *Appl Phys Lett* (2013) 102:041111. doi:10.1063/1.4789857
151. Lee MR, Fauchet PM. Two-dimensional Silicon Photonic crystal Based Biosensing Platform for Protein Detection. *Opt Express* (2007) 15:4530–5. doi:10.1364/OE.15.004530
152. Nicolaou C, Lau WT, Gad R, Akhavan H, Schilling R, Levi O. Enhanced Detection Limit by Dark Mode Perturbation in 2D Photonic crystal Slab Refractive index Sensors. *Opt Express* (2013) 21:31698–712. doi:10.1364/OE.21.031698
153. Sun Y, Fan X. Analysis of Ring Resonators for Chemical Vapor Sensor Development. *Opt Express* (2008) 16:10254–68. doi:10.1364/OE.16.010254
154. Tu X, Chen S-L, Song C, Huang T, Guo LJ. Ultrahigh Q Polymer Microring Resonators for Biosensing Applications. *IEEE Photon J.* (2019) 11:1–10. doi:10.1109/jphot.2019.2899666
155. Vollmer F, Arnold S. Whispering-gallery-mode Biosensing: Label-free Detection Down to Single Molecules. *Nat Methods* (2008) 5:591–6. doi:10.1038/nmeth.1221
156. Wang S, Liu Y, Zhao D, Yang H, Zhou W, Sun Y. Optofluidic Fano Resonance Photonic crystal Refractometric Sensors. *Appl Phys Lett* (2017) 110:091105. doi:10.1063/1.4977563
157. Xiao Y-F, Zou C-L, Li B-B, Li Y, Dong C-H, Han Z-F, et al. High-QExterior Whispering-Gallery Modes in a Metal-Coated Microresonator. *Phys Rev Lett* (2010) 105:153902. doi:10.1103/PhysRevLett.105.153902
158. Liu Y, Zhou W, Sun Y. Optical Refractive Index Sensing Based on High-Q Bound States in the Continuum in Free-Space Coupled Photonic Crystal Slabs. *Sensors* (2017) 17:1861. doi:10.3390/s17081861
159. Lv J, Chen Z, Yin X, Zhang Z, Hu W, Peng C. High-sensitive Refractive index Sensing Enabled by Topological Charge Evolution. *IEEE Photon J.* (2020) 12:1–10. doi:10.1109/jphot.2020.3017806
160. Chen Y, Zhao C, Zhang Y, Qiu C-w. Integrated Molar Chiral Sensing Based on High-Q Metasurface. *Nano Lett* (2020) 20:8696–703. doi:10.1021/acs.nanolett.0c03506
161. Heiss WD. Repulsion of Resonance States and Exceptional Points. *Phys Rev E* (2000) 61:929–32. doi:10.1103/PhysRevE.61.929
162. Berry MV. Physics of Nonhermitian Degeneracies. *Czechoslovak J Phys* (2004) 54:1039–47. doi:10.1023/B:CJOP.0000044002.05657.04
163. Dembowski C, Gräf H-D, Harney HL, Heine A, Heiss WD, Rehfeld H, et al. Experimental Observation of the Topological Structure of Exceptional Points. *Phys Rev Lett* (2001) 86:787–90. doi:10.1103/PhysRevLett.86.787
164. Lee S-B, Yang J, Moon S, Lee S-Y, Shim J-B, Kim SW, et al. Observation of an Exceptional point in a Chaotic Optical Microcavity. *Phys Rev Lett* (2009) 103:134101. doi:10.1103/PhysRevLett.103.134101
165. Zhu J, Özdemir ŞK, He L, Yang L. Controlled Manipulation of Mode Splitting in an Optical Microcavity by Two Rayleigh Scatterers. *Opt Express* (2010) 18:23535–43. doi:10.1364/OE.18.023535
166. Peng B, Özdemir ŞK, Liertzer M, Chen W, Kramer J, Yılmaz H, et al. Chiral Modes and Directional Lasing at Exceptional Points. *Proc Natl Acad Sci USA* (2016) 113:6845–50. doi:10.1073/pnas.1603318113
167. Choi Y, Kang S, Lim S, Kim W, Kim J-R, Lee J-H, et al. Quasieigenstate Coalescence in an Atom-Cavity Quantum Composite. *Phys Rev Lett* (2010) 104:153601. doi:10.1103/PhysRevLett.104.153601
168. Zhen B, Hsu CW, Igarashi Y, Lu L, Kaminer I, Pick A, et al. Spawning Rings of Exceptional Points Out of Dirac Cones. *Nature* (2015) 525:354–8. doi:10.1038/nature14889
169. Gao T, Estrecho E, Bliokh KY, Liew TCH, Fraser MD, Brodbeck S, et al.Observation of Non-hermitian Degeneracies in a Chaotic Exciton-Polariton Billiard. *Nature* (2015) 526:554–8. doi:10.1038/nature15522
170. Chen W, Kaya Özdemir Ş, Zhao G, Wiersig J, Yang L. Exceptional Points Enhance Sensing in an Optical Microcavity. *Nature* (2017) 548:192–6. doi:10.1038/nature23281
171. Romano S, Lamberti A, Masullo M, Penzo E, Cabrini S, Rendina I, et al. Optical Biosensors Based on Photonic Crystals Supporting Bound States in the Continuum. *Materials* (2018) 11:526. doi:10.3390/ma11040526
172. Romano S, Mangini M, Penzo E, Cabrini S, De Luca AC, Rendina I, et al. Ultrasensitive Surface Refractive index Imaging Based on Quasi-Bound States in the Continuum. *ACS Nano* (2020) 14:15417–27. doi:10.1021/acsnano.0c06050
173. Solomon ML, Saleh AAE, Poulikakos LV, Abendroth JM, Tadesse LF, Dionne JA. Nanophotonic Platforms for Chiral Sensing and Separation. *Acc Chem Res* (2020) 53:588–98. doi:10.1021/acs.accounts.9b00460
174. Koshelev K, Jahani Y, Tittl A, Altug H, Kivshar Y. Enhanced Circular Dichroism and Chiral Sensing with Bound States in the Continuum. In: *CLEO: QELS_Fundamental Science*. San Jose: Optical Society of America (2019). p. 6. FTh4C. doi:10.1364/CLEO\\text{_}QELS.2019.FTh4C.610.1364/cleo_qels.2019.fth4c.6
175. Zhang Z, Lan Z, Xie Y, Chen MLN, Sha WEI, Xu Y. Bound Topological Edge State in the Continuum for All-Dielectric Photonic Crystals. *Phys Rev Appl* (2021) 16:064036. doi:10.1103/physrevapplied.16.064036
176. Zhang Z, Qin F, Xu Y, Fu S, Wang Y, Qin Y. Negative Refraction Mediated by Bound States in the Continuum. *Photon Res* (2021) 9:1592. doi:10.1364/prj.427094
177. Lin Y, Feng T, Lan S, Liu J, Xu Y. On-chip Diffraction-free Beam Guiding beyond the Light Cone. *Phys Rev Appl* (2020) 13:064032. doi:10.1103/physrevapplied.13.064032
178. Yu Z, Xi X, Ma J, Tsang HK, Zou C-L, Sun X. Photonic Integrated Circuits with Bound States in the Continuum. *Optica* (2019) 6:1342. doi:10.1364/OPTICA.6.001342
179. Gong Z, Serafini J, Yang F, Preble S, Yao J. Bound States in the Continuum on a Silicon Chip with Dynamic Tuning. *Phys Rev Appl* (2021) 16:024059. doi:10.1103/PhysRevApplied.16.024059
180. Yu Y, Sakanas A, Zali AR, Semenova E, Yvind K, Mørk J. Ultra-coherent Fano Laser Based on a Bound State in the Continuum. *Nat Photon* (2021) 15:758–64. doi:10.1038/s41566-021-00860-5
181. Yu Z, Tong Y, Tsang HK, Sun X. High-dimensional Communication on Etchless Lithium Niobate Platform with Photonic Bound States in the Continuum. *Nat Commun* (2020) 11:2602. doi:10.1038/s41467-020-15358-x

Conflict of Interest: The authors declare that the research was conducted in the absence of any commercial or financial relationships that could be construed as a potential conflict of interest.

frontiers | Frontiers in Physics

REVIEW
published: 28 April 2022
doi: 10.3389/fphy.2022.866552

A Short Review of All-Dielectric Topological Photonic Crystals

Hai-Xiao Wang[1]* *and Jian-Hua Jiang*[2]*

[1]School of Physical Science and Technology, Guangxi Normal University, Guilin, China, [2]School of Physical Science and Technology and Collaborative Innovation Center of Suzhou Nano Science and Technology, Soochow University, Suzhou, China

Topological photonics is an emergent field at the cross of photonics and topological physics which opens our eyes to novel topological phenomena and versatile photonic effects. Photonic crystals (PhCs) are the optical analogs of conventional crystals that have proven to be an excellent photonic platform to explore topological physics. Here, we present a brief review of the all-dielectric topological PhCs by focusing on several prominent milestones of topological phases, such as the Su-Schrieffer–Heeger model, topological insulators, topological semimetals, and higher order topological phases. For each topological phase, the topological invariants and the intriguing topological properties as well as the potential applications are discussed. We conclude with the current challenge and the prospect of all-dielectric topological PhCs.

Keywords: all-dielectric, photonic crystals, crystalline symmetry, topological phases, higher-order topology

OPEN ACCESS

Edited by:
Xiaoyong Hu,
Peking University, China

Reviewed by:
Xiaoxiao Wang,
Xiaoyong Hu, China
Qi Huixin,
Peking University, China

***Correspondence:**
Hai-Xiao Wang
hxwang@gxnu.edu.cn
Jian-Hua Jiang
jianhuajiang@suda.edu.cn

Specialty section:
This article was submitted to Optics and Photonics, a section of the journal Frontiers in Physics

Received: *31 January 2022*
Accepted: *23 March 2022*
Published: *28 April 2022*

Citation:
Wang H-X and Jiang J-H (2022) A Short Review of All-Dielectric Topological Photonic Crystals. Front. Phys. 10:866552. doi: 10.3389/fphy.2022.866552

INTRODUCTION

Photonic crystals (PhCs), originally proposed by Yablonovitch [1] and John [2], are periodic structures of electromagnetic materials in which the electromagnetic wave propagates in a similar way as electrons move inside the conventional crystals (**Figures 1A–C**). Actually, many natural structures, such as the colorful wings of butterflies (**Figures 1D, E**) [3, 4] and the skin of chameleons (**Figures 1F,G**) [5], have PhC origins. PhCs not only decorate nature brilliantly but also provide a powerful means to manipulate and control the propagation of light. For example, PhCs with complete band gaps, which serve as light semiconductors, are highly desirable in controlling and manipulating light [6–8]. Thanks to the Bloch band theory for the periodic systems, the photonic band structure can be designed and tuned conveniently, making PhCs a key platform for studying a broad spectrum of energy band-related physics [9].

The past decades also witnessed the birth of various topological phases of electrons in condensed matter systems, such as topological insulators, superconductors, and semimetals [10–12]. One of the well-known topological phases is the integer quantum Hall effect (IQHE), which is a quantized version of the Hall effect discovered by Klitzing [13]. He found that two-dimensional (2D) electron gas in a strong magnetic field with low temperatures has a quantized Hall conductance. The most significant feature of IQHE is that electrons are localized in the bulk but unidirectionally propagate along the boundaries without any backscattering, even in the presence of large defects. An invariant called Chern number (or TKNN number) is employed to characterize the topological property of IQHE [14, 15]. Haldane [16] later on proposed a toy model based on the honeycomb lattice for supporting IQHE and demonstrated that the essential element to obtain IQHE is not a net magnetic field but the breaking of time-reversal symmetry (T), which paves a way to realize IQHE in the periodic lattice systems. Moreover, because the nontrivial topological phases can survive in the non-interacting systems, the topology studies later on transferred to the photonics and directly led to the birth of topological photonics [17–23]. Generally, topological photonics aims to explore the physics

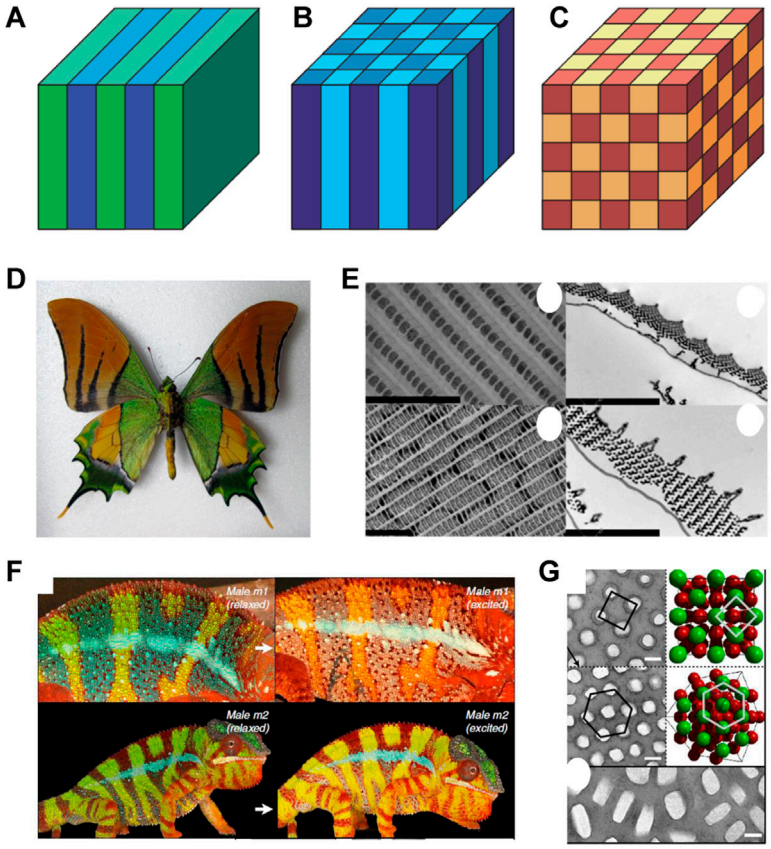

FIGURE 1 | All-dielectric PhCs in nature [3–5, 9]. Schematic model of **(A)** one-dimensional (1D), **(B)** two-dimensional (2D), and **(C)** three-dimensional (3D) PhCs Reproduced permission from Ref. [9]. **(D)** Image of butterfly. **(E)** Electron micrographs of the scale on the wings of the butterfly, which exhibit long-range order. Reproduced Permission from Ref. 3. **(F)** Reversible color change in chameleons. **(G)** Transmission electron microscopy images of guanine nanocrystals and the 3D PhC model. Reproduced permission from Ref. 5.

of topological phases of matter, which was originally discovered in condensed matter physics, in a novel optical context. The first case of topological photonics is proposed by Haldane and Raghu [24, 25], who transferred IQHE to the realm of photonics in PhCs made with nonreciprocal media. Subsequently, Haldane and Raghu's idea was experimentally demonstrated by Wang et al. [26, 27] in the gyromagnetic PhCs in the microwave regime. In the literature, the photonic analogs of IQHE with nonzero Chern number and unidirectional and backscattering immunity edge states (also known as chiral edge states) are generically termed photonic Chern insulators (PCIs).

Although chiral edge states featured with unidirectional and backscattering immunity are highly desirable in light guiding, the use of PCIs in optical devices remains a challenge mainly because magneto-optical responsive materials hardly exist in the optical frequency. It is natural to explore the photonic analog of the quantum spin Hall insulator (QSHI) [also known as a photonic topological insulator (PTI)] with T, which makes it more suitable for practical applications. In the context of condensed matter physics, the QSHI can be regarded as two copies of Chern insulators with opposite spin, where the spin-up and spin-down electrons propagate in opposite directions [28–31]. Therefore, a topological invariant named spin Chern number can be employed to characterize the QSHI in some situations. The sign of the group velocity of the edge states is locked by the spin. The edge states featured with spin–momentum locking are termed helical edge states. Thanks to the Kramers theorem, the edge states of spin-up and spin-down cross each other at $k = 0$ without opening a gap, making it a pair of topologically protected edge states. However, the Kramers theorem is no longer valid in photonics due to the distinct nature between electrons and photons. Therefore, to realize the photonic Kramers degeneracy is at the heart of the design of PTIs. At the early stage of the development of topological photonics, the optical polarization such as TE/TM [32, 33], TE + TM/TE-TM [34], and LCP/RCP [35] are utilized to act as the spin degree of freedom (DoF) in realizing PTIs. Nevertheless, these schemes extremely rely on the metamaterial with special electromagnetic properties, such as the electromagnetic duality, which hardly exist in the optical frequency. It was not until 2015 that Wu et al. [36] proposed a scheme of PTI *via* crystalline symmetry, which goes beyond the material limitation and largely promotes the development of the all-dielectric topological photonics.

In addition, it is also deserved to mention the photonic analog of valley Hall insulator that preserve T but lacks the parity inversion symmetry (P). In the context of electronics, the valley labels the degenerate energy extrema of bands in the momentum space, which can be employed to process information in modern electronic devices. By employing the valley DoF, a number of intriguing phenomena such as valley filters [37] and valley-selective Hall transport [38, 39] have been achieved due to the valley-contrasting physics. Taking the honeycomb lattice as an example, gapping the Dirac point *via* staggering the sublattice potential results in the K and K' valleys. Electrons at different valleys (K and K') propagate along the boundaries in the opposite directions. Similar to the helical edge states in QSHI, the edge states dispersion of a valley Hall insulator exhibits opposite signs of the group velocity. In the view of topological physics, the Berry curvature around $K(K')$ is nonzero, giving rise to the valley-dependent edge state as local topological effects. However, the Berry curvature at K and K' is of opposite value, which leads to a total Chern number of zero. Inspired by the valley Hall effect in the valleytronics, Ma et al. [40] first bring the valley DoF into photonic realms, leading to the studies of photonic valley Hall insulators (PVHIs).

Very recently, a new class of topological insulators, called the higher-order topological insulators (HOTIs) that are characterized by higher-order bulk-boundary correspondence, were discovered [41–44]. The higher-order topology manifests itself with nontrivial boundary states that are more than one dimension lower than bulk states. For example, a 2D HOTI hosts one-dimensional (1D) edge states at the edge boundaries as well as zero-dimensional (0D) corner states at the corner boundaries. Prototype HOTIs include quadrupole and octupole topological insulators [41, 45, 46], three-dimensional (3D) HOTIs in electronic systems with topological hinge states [42, 47–49], and HOTIs with quantized Wannier centers [43]. Although the concept of HOTI was first proposed in electronics, the experimental confirmations of most HOTIs are still absent. By contrast, HOTIs and the emergent higher-order topological states have been realized in acoustic and photonic systems, thanks to their versatile performance. To the best of our knowledge, Li et al. [50] first reported the photonic HOTI in the kagome lattice that exhibits topological bulk polarization.

In addition to the aforementioned 2D topological systems, it is also deserved to pay attention to other topological systems associated with their photonic counterparts. For example, the 1D Su-Schrieffer–Heeger (SSH) model, originally proposed for polyacetylene [51], describes spinless fermions hopping on a diatomic chain with staggered hopping amplitude. Remarkably, exchanging the hopping amplitudes within a unit cell yields two topologically distinct phases. A topological invariant named Zak phase [62] for the SSH model can be defined, which is an integer related to the ratio of the two hopping amplitudes. The study of the 1D SSH model also attracts much attention since it provides a concise physical picture to understand the topological phenomena [52–54]. To the best of our knowledge, Xiao et al. [55] first studied the photonic analog of the SSH model based on 1D all-dielectric PhCs. For 3D topological systems, both topological gapless and topological gapped systems should be highlighted, where the former includes the Dirac semimetal, Weyl semimetal, nodal line semimetal, and so on, while the latter includes 3D topological insulators and 3D HOTIs. It is natural to extend QSHI to 3D version, which led to the study of 3D topological insulators. However, the 3D topological gapless phase has no 2D counterpart. A typical 3D topological gapless phase is the Weyl semimetal, of which the band structure contains Weyl points that corresponding to the solution of the massless Dirac equations. The topological invariant of a Weyl point is called topological charge (or chirality), which can be obtained by integrating the Berry curvature over a small sphere enclosing the Weyl point. When two Weyl points with opposite signs of chirality merge, a 3D Dirac point featured with Z_2 topological charge appeared [12]. As a manifestation of topology, the surface dispersion of Weyl (Dirac) semimetal map to helicoid (double-helicoid) structure, of which the isoenergy contours are Fermi arcs [56, 57]. To the best of our knowledge, the 3D all-dielectric topological insulator are initially proposed by Lu et al. [58] and Slobozhanyuk et al. [59], respectively, while the first report of topological semimetal is implemented by Lu et al. [60, 61] in the all-dielectric gyroid PhCs.

In this review, we focus on the topological photonics that is made of all-dielectric PhCs. We first review various topological phases and point out the initial proposals of the all-dielectric topological photonics. Then, we introduce several milestones of topological phases based on all-dielectric topological photonics, from 1D to 3D, by discussing topological invariants, intriguing properties, and potential applications. Finally, we conclude by providing the outlooks for the future development direction of the all-dielectric topological photonics.

1D ALL-DIELECTRIC TOPOLOGICAL PHOTONIC CRYSTALS AND THEIR INTERFACE STATES

We start from the 1D all-dielectric topological photonics based on the SSH model. The topological invariant for the SSH model is the Zak phase [62], which is defined as follows:

$$\theta = \int_{-\pi}^{\pi} dk \Lambda_{n,k}, \tag{1}$$

where $\Lambda_{n,k} = i\langle \psi_{n,k}(r) | \nabla_k \psi_{n,k}(r) \rangle$ is the Berry connection for the nth band and $\psi_{n,k}(r)$ is the periodic part of the k-dependent Bloch wavefunction. Note that we set the lattice constant to be unity in **Eq. 1**.

In systems with P, the Zak phase can only be 0 (trivial) or π (nontrivial). The integral of the Berry connection can be obtained by dividing the Brillouin zone (BZ) into many small segments and approximating the integral as the summation of the contribution from each small segment. For example, if the BZ is divided into N segments, then the Zak phase is given by [63].

$$\theta = i \ln \prod_{i=1}^{N} \langle \psi_{n,k_i} | \psi_{n,k_{i+1}} \rangle. \tag{2}$$

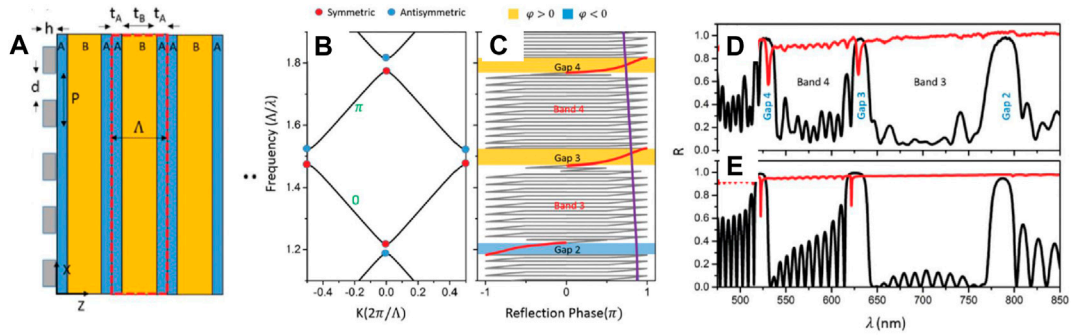

FIGURE 2 | One-dimensional all-dielectric topological PhCs [65]. **(A)** Schematic structure of the silver films/PhC systems. (B, C) Inner connection between Zak phase and the sign of reflection phase, where **(B)** gives the photonic band structure with Zak phase and **(C)** displays the reflection phases of the 1D PhCs. **(D)** Experimental and **(E)** numerical reflection spectra of the PhC (black line) and the silver film/PhC (red line). Reproduced permission with Ref. 65.

The aforementioned method to calculate the Zak phase is termed the Wilson loop approach, which is a gauge invariant and compatible with numerical implementations [63, 64]. In addition, in the systems with P, the bulk states at the high symmetry points are either even or odd. Therefore, the Zak phase can also be determined *via* the parity inversion picture, which is given by

$$\frac{\theta}{\pi} = \frac{1}{2}\left[\xi\left(k=0\right) - \xi\left(k=\pi\right)\right]: \, mod\, 2, \tag{3}$$

where $\xi(k=0)$ and $\xi(k=\pi)$ are the parity at $k=0$ and π, respectively. The nontrivial Zak phase manifested itself in the topological edge mode as the most significant feature of the SSH model. Therefore, it is expected that the interface states exist when the Zak phase of the occupied band on the one side of 1D PhCs is different from that on the other side. In 2014, Xiao et al. [55] theoretically demonstrated a rigorous relation between the surface impedance of a 1D PhC and the Zak phases of the bulk bands, which is given by

$$\exp\left(i\theta_n\right) = -sgn\left(\phi_n\right)/sgn\left(\phi_{n-1}\right). \tag{4}$$

Here, θ_n is the Zak phase of the nth bulk band, and φ_n and φ_{n-1} are the reflection phase of the nth gap and $(n-1)$th gap, respectively. Soon after this work, Wang et al. [65] experimentally demonstrated **Eq. 4** by implementing a reflection measurement. **Figure 2A** presents the structure of the measurement setups, which are composed of a silver film and a binary PhC. The values of the Zak phases can be acquired *via* either numerical calculation or the parity inversion picture, which are labeled in **Figure 2B**. In particular, the numerically calculated reflection phase in **Figure 2C** shows that the Zak phase of a specific band depends on the ratio of the reflection phase of its upper and lower band gaps, which is in good agreement with **Eq. 4**. Moreover, in **Figure 2D**, the experimental reflection spectra of the PhCs (black lines) and silver/PhCs (red) reveal that interface state only exists in the band gap with the nontrivial Zak phase, which matches well with the numerical simulation in **Figure 2E**. Remarkably, **Eq. 4** unveils an inner connection between the topology and optical property of a 1D PhC, which provides an effective method to calculate the Zak phase in order to avoid the cumbersome calculation [66], as well as to generate PhC interface states for various applications [67]. Note that **Eq. 4** is even applicable to explain the origin of some geometric-induced interface states, such as 2D PhC possessing Dirac-like cone at $k = 0$ [68], mutually inverted PhCs [69], and self-complementary checkerboard PhCs [70].

2D TOPOLOGICAL GAPPED PHASES BASED ON ALL-DIELECTRIC PHOTONIC CRYSTALS

Photonic Analog of Chern Insulator

As a landmark of topological photonics, Wang et al. [27] first experimentally demonstrated unidirectional electromagnetic wave featured with backscattering immunity in the 2D magneto-optical square-lattice PhCs that made of yttrium iron garnet (YIG). When an external DC magnetic field is applied, the YIG produces strong magnetic anisotropy, making the PhC a magnetic insulator. The breaking of T *via* an external applied magnetic field is essential to realize the PCI. **Figure 3A** presents the band structure of PhCs with T breaking adopted from Wang's scheme. The primitive unit cell is shown in the inset. The nontrivial band topology can be demonstrated *via* the first-principle calculation of band Chern number, which can be implemented through the integral of Berry curvature in the discretized Brillouin zone [71] or the Wilson loop approach [63]. Here, we introduce the main idea of the Wilson loop approach to calculate the band Chern number. Note that the Chern number that is related to the Berry phase can be calculated using the following relations [72]:

$$\begin{aligned} 2\pi C_n &= -\int_{-\pi}^{\pi}\int_{-\pi}^{\pi} dk_x dk_y \left(\partial k_x \Lambda_{n,k}^{(y)} - \partial k_y \Lambda_{n,k}^{(x)}\right) \\ &= \int_{-\pi}^{\pi} dk_y \, \partial k_y \left[\int_{-\pi}^{\pi} dk_x \Lambda_{n,k}^{(x)}\right] \\ &\equiv \int_{-\pi}^{\pi} d\theta_{n,k_y}, \end{aligned} \tag{5}$$

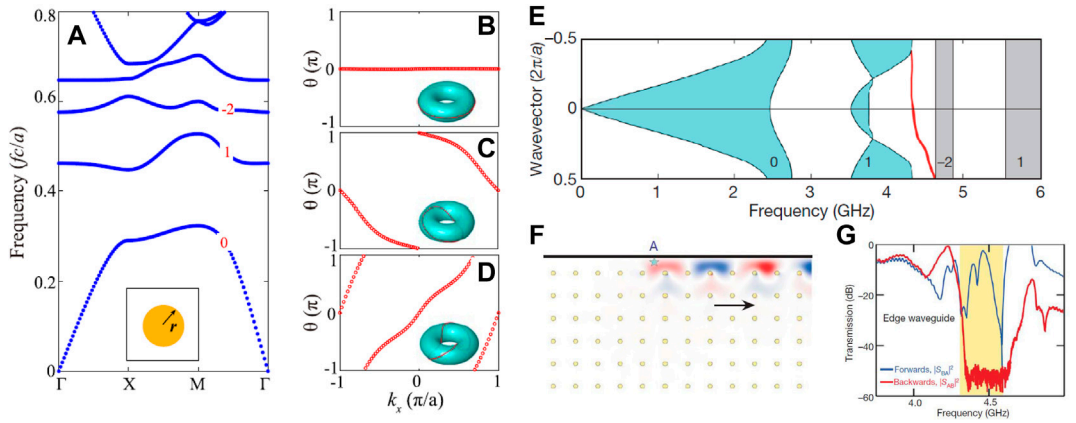

FIGURE 3 | Photonic analog of Chern insulators [27, 63]. **(A)** Photonic band structure with applied magnetic field. The Chern number of each band is labeled in red. (B–D) The evolution of the Berry phase of **(B)** the first, **(C)** the second, and **(D)** the third photonic band as the functions of k_x. The winding number of the Berry phase gives the Chern number. Reproduced permission from Ref. 27. **(E)** Calculated projected photonic band structure with the chiral edge state exits at the interface between the metal cladding and the PhC. **(F)** Chiral edge state field distribution, which radiates only to the right along metal cladding. **(G)** Measure transmission spectra of the chiral edge states. Reproduced permission from Ref. 63.

where

$$\theta_{n,k_y} \equiv \int_{-\pi}^{\pi} dk_x \Lambda_{n,k}^{(x)} \tag{6}$$

is the Berry phase for the nth band along the loop $k_x \in [-\pi,\pi]$ for a fixed k_y which is obtained by the integration over the Berry connection through **Eq. 2** for the Wilson loop along k_x. Note that the 2D BZ is equivalent to a torus under the periodic boundary condition for the Bloch states. Therefore, in numerical calculations, the Chern number C_n is obtained by counting the winding phase of when k_y goes from $-\pi$ to π. The Chern numbers of the first three bands are determined by plotting the Berry phase $\theta_{n,kx}$ (n = 1, 2, *and* 3) as functions of k_x. For the first photonic band, the Berry phase remains zero for all k_x, leading to a zero Chern number, while for the second (third) photonic band, the Berry phase has a winding number of 1 (-2), corresponding to a Chern number $C_2 = 1(C_3 = -2)$, as shown in **Figures 3B–D**. The Chern numbers calculated here from the Wilson loop approach agree with the Chern numbers inferred from the chiral edge states in using the bulk-edge correspondence [73]. As shown in **Figure 3E**, the projected band structure (light blue areas) with a chiral edge state (red line) is calculated in finite systems. A typical field distribution of the chiral edge state is also displayed in **Figure 3F**. To characterize the chiral edge states, the transmission measurement is implemented. From **Figure 3G**, it is shown that a strong forward transmission with the second band gap approximately 50 dB greater than the backward transmission at frequencies was observed at mid-gap frequencies. After this milestone of work, a series of work related to the PCIs made of gyromagnetic PhCs are implemented, such as cladding-free guiding of topologically protected edge states [74, 75], steering of multiple edge states along domain walls with large Chern numbers [76, 77], designing of one-way slow-light PhC waveguide [78–81], and antichiral edge states [82, 83]. It is evident that the unidirectional backscattering immunity edge states are expected to have a deep impact on the designing of new optical devices. However, owing to the weak magnetic response in optical materials and the difficulty in device integration, the use of PCIs in optical devices remains a challenge. To date, there is an urgent need to achieve one-way waveguides at optical wavelength.

Photonic Analog of Quantum Spin-Hall Insulator

In 2015, Wu et al. [36] proposed a scheme for achieving PTI by using the all-dielectric PhC, which paves a way for the practical application of PTI. In their seminal work, they start with an expanded cell of photonic honeycomb lattice. Based on the band folding mechanism, the well-known Dirac cone at K and K' points are folded at Γ point, giving rise to the deterministic double Dirac cone. By either stretching or compressing the expanded unit cell, the double Dirac cone lifted into a trivial or nontrivial band gap. Such a scheme for realizing PTI was later demonstrated by observing the momentum–pseudospin locking in the microwave experiment [84]. Inspired by Wu's work, a large number of studies of all-dielectric PTI are implemented based on the photonic honeycomb lattice [85–96] and other specific PhC structures, such as core–shell PhCs [97], Stampfli-triangle PhCs [98], and moon-shaped PhCs [99].

Actually, to construct all-dielectric PTI, two issues should be highlighted: one is to create the fourfold-degeneracy double Dirac cone, which is the mother state of PTI, the other one is to find out the photonic analog spin–orbit coupling terms. Guided by these two principles, Xu et al. [97] systematically studied accidental band degeneracy in an all-dielectric core–shell PhC (**Figure 4A**), where the Mie resonance can be regarded as atomic orbits for photonic bands [100]. Those atomic orbits can be of s, p, d, and f nature and have well-defined parities at Γ point [see a typical band structure of the core–shell PhCs in **Figure 4B**]. Note that due to the C_6 crystalline symmetry, both the photonic p-orbit and

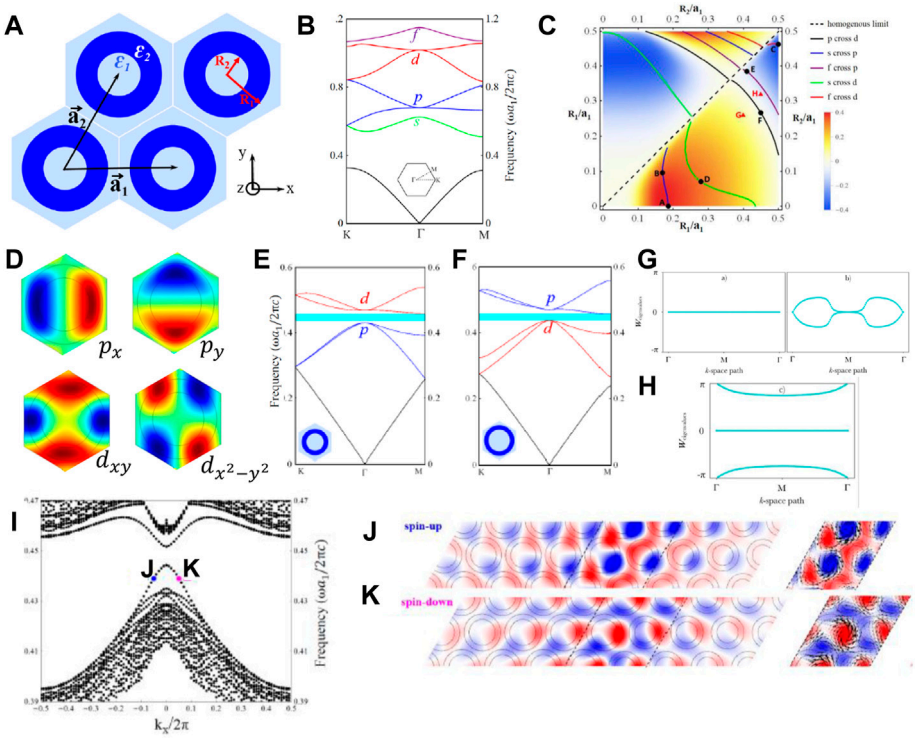

FIGURE 4 | Photonic analog of quantum spin Hall insulator [97, 101]. **(A)** Schematic configuration of a triangular PhC using core–shell dielectric. **(B)** Typical band structure of the core–shell PhCs, where the photonic-like orbits are labeled. **(C)** Phase diagram of the *p* – *d* inversion induced photonic topological insulator in the geometric parameter spaces. **(D)** Eigen modes of *p* doublets (p_x, p_y) and *d* doublets (d_{xy}, dx^2–y^2), which served as the photonic pseudospin DoF. (E, F) Band structure of core–shell PhCs with **(E)** trivial and **(F)** nontrivial band gaps. (G, H) Wannier center positions of the bands below the **(G)** trivial and **(H)** nontrivial band gap. Reproduced permission from Ref. 101. **(I)** Projected band structure of two PhCs with helical edge states. **(J)** and **(K)** are the E_z field pattern in (I). Reproduced permission from Ref. 97.

d-orbit are double degenerate. **Figure 4C** gives the electric field patterns of the *p* doublets (p_x and p_y) and *d* doublets (d_{xy} and dx^2–y^2). In particular, these four states can be linearly combined into $p\pm = (p_x \pm ip_y)/\sqrt{2}$ and $d\pm = (dx^2\text{–}y^2 \pm id_{xy})/\sqrt{2}$, where subscript + (−) refers to pseudospin-up (pseudospin-down). Apparently, the spin DoF here is synthesized by the orbital angular momentum [89]. By tuning the inner and outer radii of the core–shell PhCs, the phase diagram with multiple accidental degeneracies can be acquired (**Figure 4D**).

Importantly, the double Dirac cone formed by the *p* and *d* doublets plays a vital role in the phase transition between PTI and a normal insulator. When the *p* band is below the *d* band (**Figure 4E**), the gap exhibits a trivial phase, while flipping the order of the *p* and *d* photonic bands results in a nontrivial band gap (**Figure 4F**). Such a parity inversion (also known as *p*-*d* inversion) picture is at the heart of the quantum spin Hall effect in electronic systems [31]. The topological invariant of PTI can be also acquired *via* the Wilson loop approach [63]. Considering the Berry phase calculation for multiple bands, the inner product $\langle\psi_{k_i}|\psi_{k_{i+1}}\rangle$ in **Eq. 2** should be replaced by matrix $M^{ki,ki+1}$ of which the matrix elements are given.

$$M_{nn'}^{k_i,k_{i+1}} = \langle\psi_{n,k_i}\big|\psi_{n',k_{i+1}}\rangle, n,n' \in 1\ldots N, \tag{7}$$

where the band indices *n* and *n*′ go over all the bands below the concerned band gaps. Then, the Berry phase for a loop in the BZ can be obtained by the matrix product of the Berry connection matrix through the following form,

$$\hat{W} = \prod_{i=1}^{N} \hat{M}^{k_i,k_{i+1}}. \tag{8}$$

To evaluate the topological invariant, one needs the eigenvalues of the above Berry phase matrix, which can be written as follows:

$$\theta_n \equiv -\Im[\log(w_n)], n = 1,\ldots,N, \tag{9}$$

where w_n is the *n*th eigenvalues of the matrix $\hat{W}$.

Typical Berry phase calculations for a trivial insulator and PTI *via* the Wilson loop approach are displayed in **Figures 4G,H**. For the trivial case, the Wilson loop of the first band has a constant value equal to 0 (see left panel in **Figure 4G**), while that of the set of the second and third bands does not exhibit any winding properties (see right panel in **Figure 4G**). For the nontrivial case, it is necessary to take the three lowest bands as a set since there is a band crossing between the first and second bands. As shown in **Figure 4H**, there is no winding but the Wannier centers are localized at the edge of the unit cell, in contrast to that in the trivial case. In the literature, such a topological insulator with non-winding values of Wilson loop is called the photonic

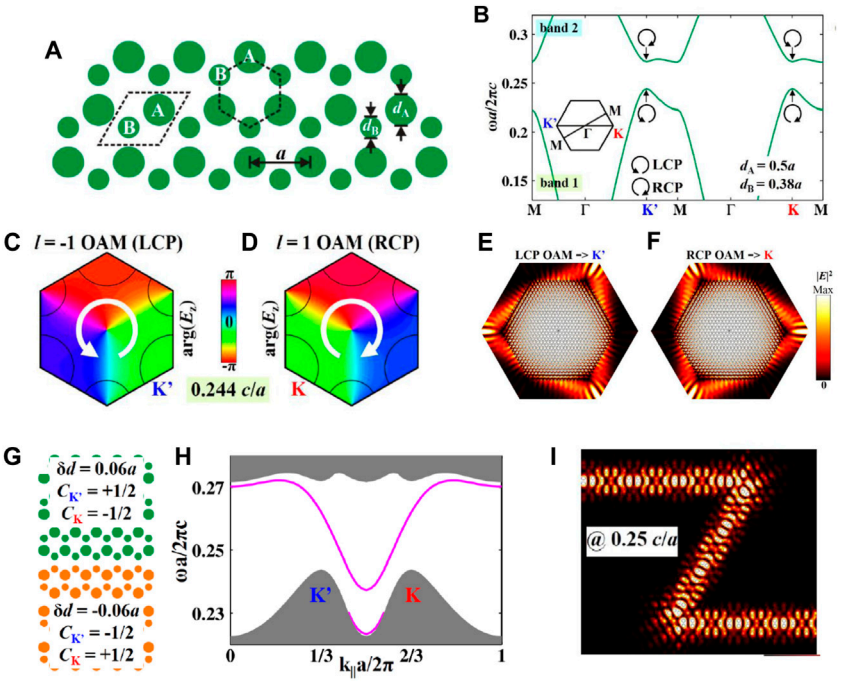

FIGURE 5 | Photonic analog of valley Hall insulator [119]. **(A)** Schematic of valley PhCs based on honeycomb lattice, where the radii of the two rods are different in a unit cell. **(B)** Photonic band structure for transverse magnetic modes, in which four valley states are marked. **(C,D)** Valley-contrasting chiral orbital angular momentum and the phase distributions of E_z at K and K' valleys. (E, F) Electric intensity of the excited. **(E)** K' and **(F)** K valley states. **(G)** Schematic of the edge constructed by two distinct valley PhCs. **(H)** Valley-dependent edge states. **(I)** Electric field intensity at a specific frequency, illustrating the smooth propagating wave through the Z sharp corners. Reproduced permission from Ref. 119.

obstructed atomic limit [101, 102], which is easily confusing with the concept of fragile topological insulator [96, 99, 102, 103]. Parallel to the topological invariant calculation, a typical calculation of the edge state using two PhCs with distinct topology is presented in **Figure 4I**. Note that the helical edge states are gapped, which originate from the C_6 symmetry breaking at the boundary between the two different PhCs. The size of the gap depends on the strength of the perturbation induced by the symmetry breaking. However, the helical feature of the edge states is still clearly demonstrated. As shown in **Figures 4J,K**, the edge states at the J(K) point are mostly pseudospin-down (pseudospin-up) as recognized from the real space distribution of the Poynting vector with the negative (positive) group velocity.

Utilizing the robust transport properties of the topological PhC interface, many intriguing physical systems are explored, including unidirectional electromagnetic waveguide [84], topological all-optical logic gates [104], topological whispering gallery modes [105], coupled cavity-waveguide system [106], topological converter [95], topological bulk laser [93], Dirac vortex cavity [107], and Dirac vortex fiber [108]. Additionally, all-dielectric PTIs also open an avenue to quantum optics. In 2018, Barik et al. [86] proposed an all-dielectric topological PhC slab with 2D helical edge states confined in a dielectric slab, which is highly desirable to achieve out-of-plane confinement without the use of metal [85, 86, 90, 94]. They also demonstrate the strong interface between the single quantum emitters and topological photonic states [94]. Since all-dielectric PTIs take full advantage of crystalline symmetry and thus go beyond the material limitation, more in-depth research based on all-dielectric PTIs is foreseen.

Photonic Analog of Valley Hall Insulator

Another kind of topology-related gapped systems with T is PVHIs [40, 109–135]. Following the idea of valleytronics in the graphene, Chen et al. [119] proposed a PVHI based on the modified honeycomb PhCs, as shown in **Figure 5A**, where the radii of the two rods are different in a unit cell. Note that most PVHI studies are based on the modified honeycomb lattice [110, 111, 113, 116, 117, 119, 122, 123] since it provides a concise physical picture. Other proposals, including detuning the refractive index [124, 125] and specific geometric designs without P [40, 109, 112, 114, 115, 118, 120, 121, 126], are also adopted to study valley physics. From the point of view of the symmetry, these PVHIs broke the C_6 symmetry of the structure while preserved the C_3 symmetry. A typical band structure of PVHI is presented in **Figure 5B**, where two inequivalent but T valleys (K and K') with vortex-valley locking (**Figures 5C,D**) are observed.

Using the valley as a binary DoF, the unidirectional excitation of the valley chirality bulk states can be realized either by sources carrying orbital angular momentum with proper chirality (**Figures 5E,F**) [119] or by a point-like chiral source based on the azimuthal phase matching condition [120]. Similar to the pseudospin–momentum locking effect in PTIs, there also exist valley pseudospin–momentum locking edge states at the interface

of two valley Hall PhCs (**Figures 5G,H**). Most studies hold that the different valley topological index between two of the valley Hall PhCs gives a nonzero valley Chern number and lead to the emergence of the valley-dependent edge states. However, the valley Chern number cannot be used as a topological invariant because it is not a quantized value. Yang et al. [117] addressed that the chiral vortex-valley locking plays a fundamental role in the emergence of the valley-dependent edge states, rather than the valley Chern number. Thanks to the chiral vortex-valley locking, valley PhCs with valley-dependent edge states exhibit robust transportation against sharp corners (**Figure 5I**).

For applications, many intriguing photonic devices, including energy beam splitters [127, 131, 132, 135], logic gates [127], switches [132], fiber [134], and filter [132] are created *via* PVHIs [131, 132]. Based on valley edge states, the electrically pumped terahertz quantum cascade laser is also realized [128]. Xie et al. [133] constructed a topological cavity based on slow-light valley Hall edge states, which exhibit a greatly enhanced Purcell factor. Moreover, it is also desirable to realize PVHIs with a large Chern number, which can support multimode topological transmission [114, 118].

Photonic Higher-Order Topological Insulators

The recent advances in higher-order topology deepen our knowledge of the topology physics. The first HOTI proposed by Benalcazar et al. [41] is a quadrupole topological insulator (QTI), in which the bulk dipole is absent while the quantized, fractional electric multipole moments emerged in the bulk. The key to realize a QTI is to generate both positive and negative nearest-neighbor couplings in a single physical system. In order to meet such requirements, Chen et al. [136] proposed a scheme to realize QTI in plasmon-polaritonic systems by utilizing the sign-reversal mechanism for the coupling between the plasmon-polaritonic cavities. In addition, He et al. [137] extended the idea of QTI from tight-binding models to continuum theories. They demonstrated that the quadrupole topological phase survived in a gyromagnetic PhC, of which the quadrupole moment is quantized by the simultaneous presence of crystalline symmetry and broken T. Since the realization of photonic QTI is limited to some specific systems, most studies focus on the photonic HOTIs with quantized Wannier centers. In 2018, Ezawa [43] constructed a tight-binding model on the breathing kagome lattice, in which both gapped edge states and corner states are observed. In his proposal, the bulk polarization is served as a topological index, which can be defined as the integral of the Berry connection. Intuitively, the bulk polarization characterizes the displacement of the average position of the Wannier center from the center of the unit cell, giving rise to the emergence of corner states in a finite system.

Inspired by Ezawa's proposal, the studies on the HOTI based on the kagome lattice are later transferred to various classical systems [50, 138–143]. In particular, all-dielectric PhCs provide an excellent platform to study HOTI with quantized Wannier centers and thus have been extensively studied [50, 144–154]. Wang et al. [154] systematically studied the multiple higher-order phase transition in a 2D hexagonal PhC with C_3 symmetry, where each unit cell consists of three dielectric rods, as illustrated in **Figure 6A**. By moving the three dielectric rods along three symmetry lines, the PhCs undergo a continuous geometry transformation that includes three triangular lattice configurations and three kagome lattice configurations. Typical band structures for the triangular and kagome lattices are presented in **Figures 6B,C**. Accompanying with the geometry transformation, the first photonic band experiences multiple phase transitions (**Figure 6D**). To characterize the higher order topology, one can calculate the bulk polarization (Wannier center positions) *via* the Wilson loop approach, as depicted in **Figures 6E–G**, or use the symmetry indicators [155], which can be achieved from C_3 eigenvalues at high symmetry points.

As a direct manifestation of the higher-order band topology, one may expect that corner states appear in a finite system with C_3 symmetry. However, the emergence of corner states also depends on the geometric configurations [141, 156]. We remark that often the photonic bands do not have the chiral symmetry and the corner states may shift into the bulk continuum and disappear without the chiral symmetry. To avoid this, it is necessary to place two all-dielectric PhCs with distinct higher topological phases together in a finite system. Along with the geometry transformation, various cases of the calculated supercell are realized, where outside PhCs are of trivial phase, while the insider PhCs are dependent. Several prototype geometries of the calculated supercell are presented in **Figure 6H**. The eigen solutions are displayed systematically in **Figure 6I**. **Figures 6J,K** give the electric field $|E_z|$ distributions of the eigenstates of the corner and edge states. In particular, two types of corner states emerge, as revealed in Refs. 50, 142, 154: type-I corner states due to the nearest neighbor couplings and type-II corner states originating from the next nearest-neighbor coupling.

In addition to the kagome lattice with C_3 symmetry, the nontrivial bulk polarization and corner states can also appear in the expanded C_4 symmetric lattice. A typical case is the 2D Su-Schrieffer–Heeger model, which has been extensively studied [151–153]. The 2D Zak phase is employed to characterize the higher-order topology. The photonic HOTIs have been found promising applications in high-quality nanocavities [157], cavity quantum electrodynamics [158], topological nanolasers [159, 160], and multi-channel system fibers [161]. Since HOTIs set up examples with multidimensional topological physics going beyond the bulk-edge correspondence in conventional topological insulators and semimetals, it opens a new avenue toward exploring novel topological phenomena and optical device applications.

Before proceeding, let us comment on the 1D and 2D all-dielectric topological PhCs. Since all-dielectric PhCs are the optical analogs of conventional crystals, it is natural to explore different topological phases as well as to find the potential applications based on all-dielectric PhCs. For 1D topological photonics, the 1D PhC consists of a dielectric AB layered structure that is regarded as a photonic analog of the SSH model. Since the 1D binary PhC supports the Tamm mode, which originates from the lack of translation symmetry, there is a need to clarify the difference as well as a connection between the topological interface states and Tamm modes [162]. For 2D cases,

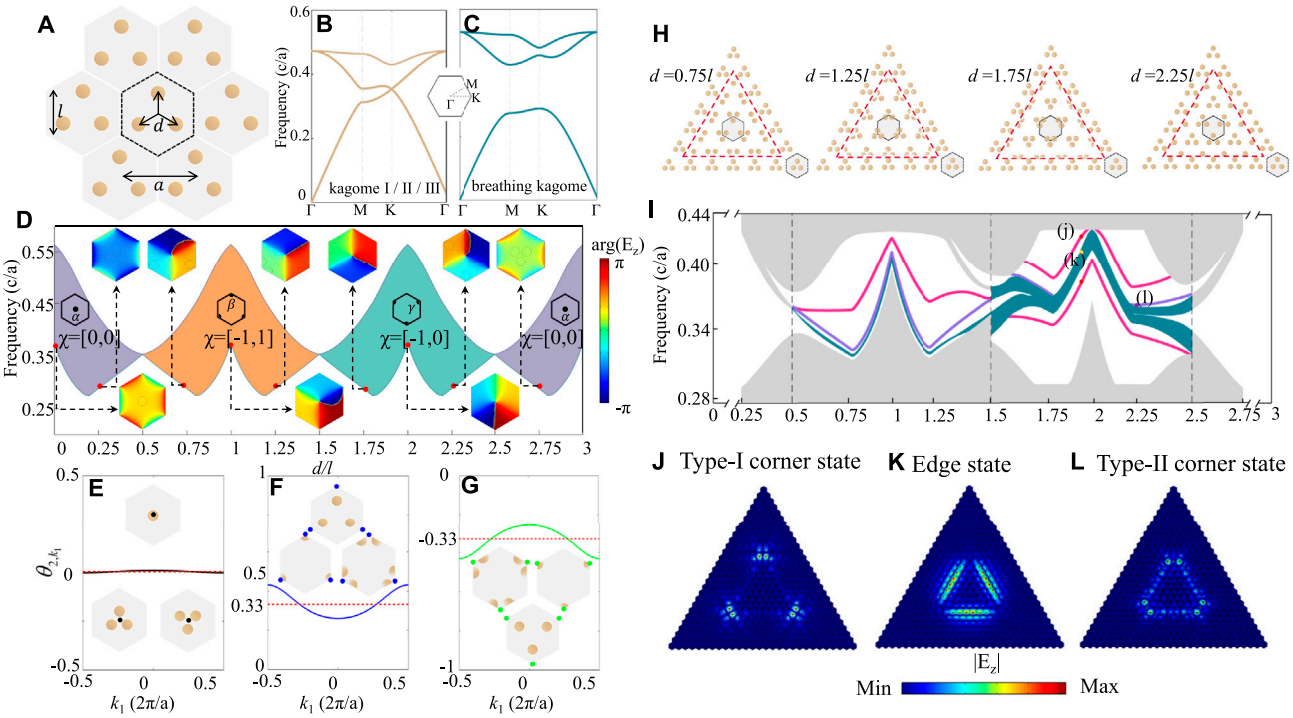

FIGURE 6 | Photonic higher order topological insulator [154]. **(A)** 2D PhCs with C_3 symmetry, where the primitive cell is indicated by hexagonal dotted lines. (B, C) Typical band structure for **(B)** triangular PhCs and **(C)** kagome lattice. **(D)** Eigenfrequencies of the first and second photonic bands at the *K* point as a function of geometric parameter *d*. (E–G) The calculated Berry phase for PhCs with **(E)** the phase [0,0], **(F)** the phase [−1,1], and **(G)** the phase [−1,0]. The bulk polarization is shown in red dots. The corresponding Wannier center configuration is also displayed in the insets. **(H)** Schematic illustration of large triangular supercell with two types of PhCs with distinct higher order topology. **(I)** Eigenfrequencies of the photon as functions of the geometric parameter *d*. (J–L) Typical electric field pattern for **(J)** type-I corner state, **(K)** edge state, and **(L)** type-II corner state. Reproduced permission from Ref. 154.

topological phases in all-dielectric PhCs are more diverse, including PCI, PTI, PVHI, and HOTI. We notice that most studies focus on the topological phase transition between trivial and nontrivial phases, while that between two nontrivial phases is very few [163–165]. It is expected that all-dielectric PhCs will become more versatile if two topological phases coexist in a single system. In addition, it is also interesting to introduce other ingredients into the all-dielectric PhCs, such as layer DoF [111, 166].

3D TOPOLOGICAL PHASES BASED ON ALL-DIELECTRIC PHOTONIC CRYSTALS

In the previous sections, we have reviewed the 2D topological phases. It is natural to extend 2D topological phases to 3D cases. In what follows, we give a brief review on several milestone works of 3D topological insulators and topological semimetals that are made of all-dielectric PhCs.

3D All-Dielectric Photonic Topological Insulator

Generally, 3D topological insulators can be realized in both T-broken and T-invariant system. A typical T-broken case is the 3D quantum Hall phase [also known as a strong topological insulator (STI)], which can be regarded as a 3D extended version of the 2D quantum Hall phase. To the best of our knowledge, Lu et al. [58] first proposed the photonic analog of 3D STI by using PhCs composed of ferrimagnetic materials (**Figure 7A**). A magnetic field bias breaks T and produces a nontrivial band gap that hosts a single-surface Dirac cone (**Figures 7B,C**), which is protected by the nonsymmorphic glide reflections. Such a gapless surface state is fully robust against the random disorder of any type. The evolution of Wannier centers is calculated *via* the Wilson loop approach to characterize the bulk topological invariant (**Figure 7D**).

Similarly, the 3D quantum spin Hall phase [also known as a weak topological insulator (WTI)] can be viewed as a generalization of the 2D quantum spin Hall phase and corresponds to the T-invariant case. In 2011, Yannopapas [167] proposed a scheme for realizing a 3D photonic analog of WTI. A tetragonal lattice of uniaxial dielectric cavities in a lossless metallic host was investigated using a coupled dipole method, which is the photonic counterpart of topological crystalline insulators in an electronic system [168]. This system with T and point-group symmetry exhibit a complete 3D band gap and gapless topological surface states. Topological photonics with 3D band gaps also have been proposed by using 3D bianisotropic structures [59, 169]. As shown in **Figure 7E** a stacked layer of triangular arrays of mirror-symmetry-broken dielectric rods

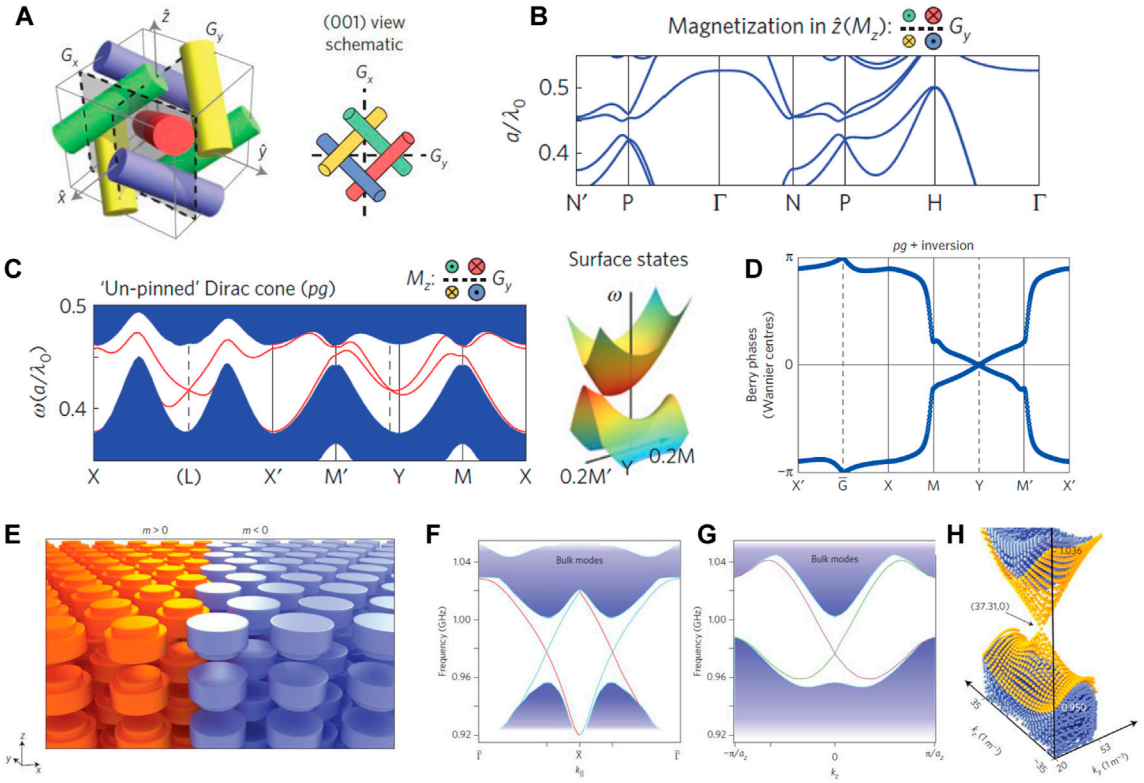

FIGURE 7 | Three-dimensional photonic topological insulators [58, 59]. **(A)** Three-dimensional all-dielectric PhCs with topological band gap. **(B)** Bulk band structure when magnetization is applied. **(C)** Single-surface Dirac cone in the $M' - M$ line. **(D)**) Gapless hybrid Wannier centers corresponding to the nontrivial surface states in **(C)**. **(E)** Schematics of the domain wall formed by the two 3D PTIs. (F, G) Band diagrams of topological surface states supported by the domain wall in **(E)** with 2D cut-planes **(F)** ω-$k_{||}$ and **(G)** ω-k_z, respectively. **(H)** Conical Dirac-like dispersion of the surface states. Reproduced permission from Refs. 58, 59.

(**Figure 7F**) supports a conical dispersion of topological surface states (**Figures 7G,H**) and backscattering immunity propagation of the surface modes. The scheme for achieving 3D photonic WTI paves a way to various optical devices, such as topological lasers and circuits in previously inaccessible 3D geometries.

3D All-Dielectric Photonic Topological Semimetals

As one of the earliest studies of topological semimetals, Lu et al. theoretically [60] and experimentally [61] demonstrated the existence of Weyl points in gyroid PhCs. The Weyl point refers to the 3D linear point between two bands, of which the dispersions are governed by the Weyl Hamiltonian. Unlike the 2D Dirac point, which is protected by PT symmetry, the 3D Weyl point only exists on the systems that lack T or P or both [170–176]. Such a character makes a single Weyl point absolutely robust to any perturbations. The only way to eliminate and create Weyl points is through pair annihilations and pair generations of Weyl points with opposite chirality. It seems the emergence of Weyl points is somehow accidental, nevertheless, one can have a 3D topological phase with symmetry protection first and then have the Weyl points by symmetry reduction (**Figure 8A**) [170–173]. From this point of view, Wang et al. [170, 171] systematically studied the 3D Z_2 Dirac point, which can be viewed as a pair of Weyl points with opposite chirality, based on all-dielectric PhCs. Usually, the 3D Dirac points are unstable when two Weyl points annihilate each other and form a gap. Nevertheless, Wang et al. [170, 171] pointed out that 3D Z_2 Dirac can survive stably *via* certain crystalline symmetry, and split into the Weyl points when the P is broken.

As an illustration, **Figure 8B** presents a kind of 3D all-dielectric PhCs with nonsymmorphic symmetry. In each unit cell, there are two dielectric blocks of the same shape and permittivity, which are connected *via* screw symmetry S_x and S_y (**Figure 8C**). To realize the Z_2 photonic Dirac point, both Kramers double degeneracy and parity-inversion should be synthesized, in which the crystalline symmetry plays a key role in realizing these two elements. On the one hand, anti-unitary operators that combine the screw symmetry with T symmetry are created to simulate the photonic Kramers degenerate pairs. On the other hand, the eigenvalue of a two-fold rotation symmetry operator is employed to define the parity of photonic states. The distribution of 3D Z_2 Dirac points in the BZ is displayed in **Figure 8D**.

The 3D Dirac point emerges from the band crossing of two doublets with distinct parities (**Figures 8E,F**). The spit–orbit physics of the Dirac points can be understood *via* a symmetry-

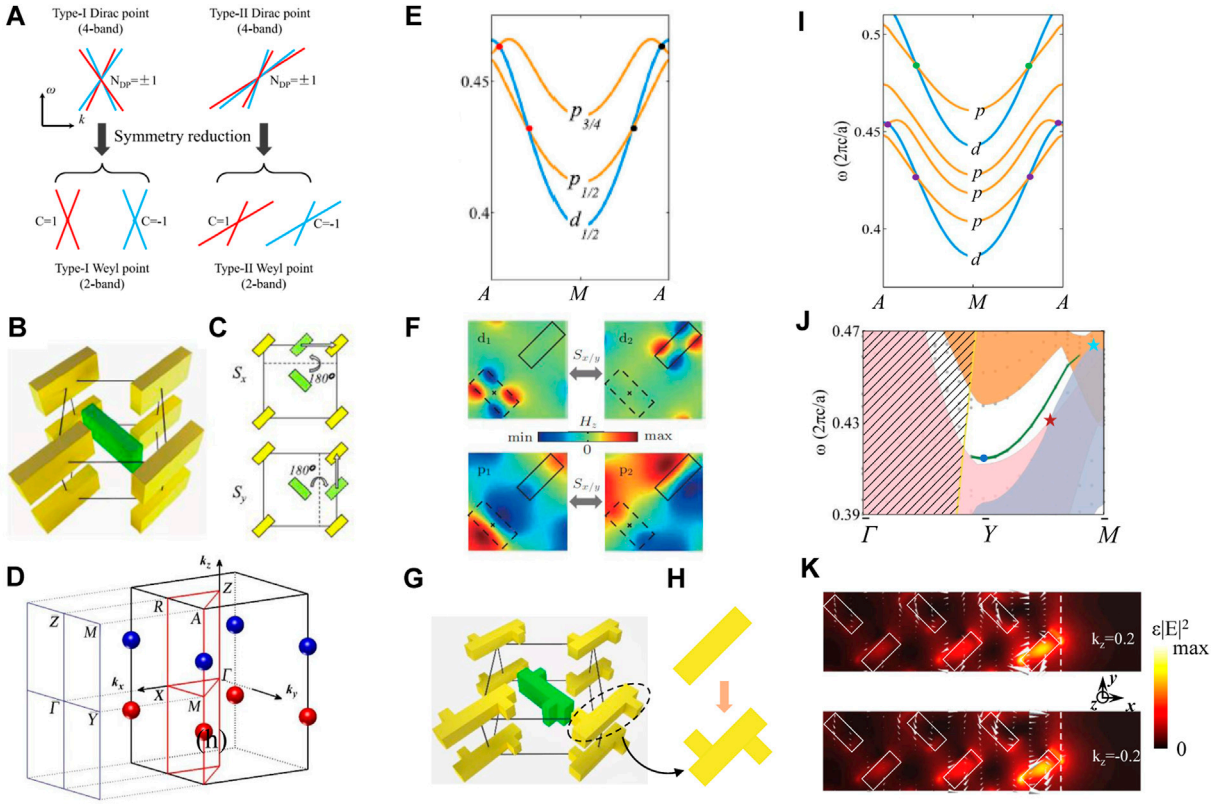

FIGURE 8 | Photonic topological semimetals [171]. **(A)** Relationship between type-I/type-II Dirac points and Weyl points. **(B)** Three-dimensional structure of a unit cell, where the boundaries are indicated by black lines. **(C)** Illustration of the two screw symmetry S_x and S_y in top-down view. **(D)** The bulk and surface Brillouin zone, with the distribution of the Dirac points. **(E)** Parity inversion induced type-I and type-II Dirac points on the MA line. **(F)** Magnetic field profiles of the *p*- and *d*-wave doublets, $p_{1/2}$ and $d_{1/2}$, respectively. The doubly degenerate states are connected by the screw symmetries. **(G)** Unit cell structure of the symmetry-broken PhCs. **(H)** Three-dimensional view with zoom-in illustration of structure deformations. **(I)** Band structure on the MA line for part of the first six photonic bands indicates, which the crossings are identified as type-I and type-II Weyl points. **(J)** Surface band and projected bulk band on PhC–air surface. **(K)** Energy density and Poynting vector profiles for the topological surface states at two opposite wavevectors. Reproduced permission from Ref. 171.

TABLE 1 | Summary of various all-dielectric photonic topological systems mentioned in this review.

Dimensionality	topological system	Topological invariant	Significant feature	Potential applications
1D	Photonic SSH	Zak phase	Interface states	Generate specific interface states
2D	PCI	Chern number	Chiral edge states	Unidirectional and backscattering immunity waveguide
2D	PQSHI	Spin Chern number	Helical edge states	Whisper gallery waveguide, all-logic gates, and lasers
2D	PVHI	Vortex chirality	Valley-dependent edge states	Energy beam splitter, all-logic gates, fiber, and filter
2D	HOTI	Polarization	1D gapped edge states and 0D corner states	Nanocavity, nanolaser, and fibers
3D	STI	Z_2 invariant	Single-surface Dirac cone	Optical diodes
3D	WTI	Z_2 invariant	Two-surface Dirac cone with spin locking	High-power laser, optical diodes, and photonic computer chips
3D	Weyl semimetal	Topological charge	Helicoid surface states	Anomalous refraction
3D	Dirac semimetal	Z_2 topological charge	Doubled-helicoid surface states	Open cavity and anomalous refraction

based ˜$k{\cdot}p$ ~ theory. When the space symmetry is reduced, it is expected that the Dirac point will split into Weyl points. As shown in **Figures 8G,H**, by transforming the dielectric blocks into other shapes, namely, breaking the screw symmetry while keeping the two-fold rotation symmetry, the crossing between the band with distinct parities (i.e., *p* and *d* bands) result in Weyl points (**Figure 8I**). Following this idea, the Weyl point is also realized in the metasurface [172] and twisted 1D dielectric PhCs [173]. Because the 3D Dirac point acts as the mother state of the Weyl points, it is interesting to explore the properties of surface states according to the bulk-edge correspondence principle. **Figure 8J** shows a gapless surface band traversing the projected photonic

band gap. The topological surface states carry finite total angular momentum as indicated in **Figure 8K** by the winding profile of the Poynting vectors. The sign of the photonic total angular moment is changed when the wavevector is reversed. This property is similar to the "spin–wavevector locking" on the edges of topological insulators. Based on such a salient feature, one can further study frequency-, angle-, wavevector-, and angular momentum-selective transmission in Weyl/Dirac PhCs. In addition, note that the topological surface states are below the light-line and hence can form cavity states on the PhC–air interfaces with no need for additional cladding. Last but not least, the conical dispersions in Dirac/Weyl all-dielectric PhCs provide a new mechanism to realize unconventional optical properties, such as anomalous refraction [171].

CONCLUSION AND OUTLOOK

The past decade has witnessed the rapid development of topological photonics, which is beneficial for both electronics and photonics. Although many exotic topological phenomena have been demonstrated, the aid of metamaterials hinders the application of topological photonics. Therefore, it is highly desirable to realize all-dielectric topological PhCs, which take full advantage of the crystalline symmetry and get rid of the limitation of the material. In this review, we give a brief review on several milestones of all-dielectric topological PhCs by discussing their topological invariants, intriguing properties, and potential applications. A summary of all-dielectric topological PhCs mentioned in this review is provided in **Table 1**. We conclude that all-dielectric PhCs served as a common photonic system have achieved great success in both emulating various topological phases and finding potential application in light manipulation.

All-dielectric topological PhCs will continue to evolve in the coming years, as in the past decade. The scope of all-dielectric topological PhCs is becoming diverse and can be further expanded by combing nonlinearity [177–181], non-hermiticity [182–186], real space topology (such as dislocation [187] and disinclination [188–190]), and synthesis dimension [196–206]. In particular, it was reported recently that non-hermiticity fundamentally changes the topological band theory, leading to exotic phenomena like non-Hermitian skin effect, as confirmed in the 1D SSH model [191–195]. By adding gain and loss into the all-dielectric PhCs, one can study non-Hermitian topological photonics in a direct way [182–185]. Alternatively, as an open system, topological waveguide-cavity coupled structure made of all-dielectric, offers an excellent platform to study non-Hermitian topological physics [186]. In addition to non-hermiticity, it also deserves to study the all-dielectric topological PhCs with the ingredient of synthesis dimension. It is generally believed that the dimension of a physical system cannot be larger than its geometric dimensionality. However, with the introduction of synthetic frequency dimension, and combined with the intrinsic geometric dimension, one can investigate higher dimensional physics. These studies may sustain further developments of all-dielectric topological photonics and offer novel methods for light manipulations.

AUTHOR CONTRIBUTIONS

H-XW conceived the idea and prepared the draft. All authors contributed to the discussion and revision of the manuscript.

FUNDING

This work was supported by the National Natural Science Foundation of China (11904060, 12074279, and 12125504).

REFERENCES

1. Yablonovitch E. Inhibited Spontaneous Emission in Solid-State Physics and Electronics. *Phys Rev Lett* (1987) 58:2059–62. doi:10.1103/physrevlett.58.2059
2. John S. Strong Localization of Photons in Certain Disordered Dielectric Superlattices. *Phys Rev Lett* (1987) 58:2486–9. doi:10.1103/physrevlett.58.2486
3. Biró LP, Kertész K, Vértesy Z, Márk GI, Bálint Z, Lousse V, et al. Living Photonic Crystals: Butterfly Scales - Nanostructure and Optical Properties. *Mater Sci Eng C* (2007) 27:941–6. doi:10.1016/j.msec.2006.09.043
4. Proietti Zaccaria R. Butterfly wing Color: A Photonic crystal Demonstration. *Opt Lasers Eng* (2016) 76:70–3. doi:10.1016/j.optlaseng.2015.04.008
5. Teyssier J, Saenko SV, van der Marel D, Milinkovitch MC. Photonic Crystals Cause Active Colour Change in Chameleons. *Nat Commun* (2015) 6:6368. doi:10.1038/ncomms7368
6. Ishizaki K, Noda S. Manipulation of Photons at the Surface of Three-Dimensional Photonic Crystals. *Nature* (2009) 460:367–70. doi:10.1038/nature08190
7. Ma T-X, Wang Y-S, Zhang C. Photonic and Phononic Surface and Edge Modes in Three-Dimensional Phoxonic Crystals. *Phys Rev B* (2018) 97:134302. doi:10.1103/PhysRevB.97.134302
8. Cersonsky RK, Antonaglia J, Dice BD, Glotzer SC. The Diversity of Three-Dimensional Photonic Crystals. *Nat Commun* (2021) 12:2543. doi:10.1038/s41467-021-22809-6
9. JD Joannopoulos, editor. *Photonic Crystals: Molding the Flow of Light*. 2nd ed. Princeton: Princeton University Press (2008).
10. Qi X-L, Zhang S-C. Topological Insulators and Superconductors. *Rev Mod Phys* (2011) 83:1057–110. doi:10.1103/RevModPhys.83.1057
11. Hasan MZ, Kane CL. Colloquium: Topological Insulators. *Rev Mod Phys* (2010) 82:3045–67. doi:10.1103/RevModPhys.82.3045
12. Armitage NP, Mele EJ, Vishwanath A. Weyl and Dirac Semimetals in Three-Dimensional Solids. *Rev Mod Phys* (2018) 90:015001. doi:10.1103/RevModPhys.90.015001
13. Klitzing Kv., Dorda G, Pepper M. New Method for High-Accuracy Determination of the fine-structure Constant Based on Quantized Hall Resistance. *Phys Rev Lett* (1980) 45:494–7. doi:10.1103/physrevlett.45.494
14. Thouless DJ, Kohmoto M, Nightingale MP, den Nijs M. Quantized Hall Conductance in a Two-Dimensional Periodic Potential. *Phys Rev Lett* (1982) 49:405–8. doi:10.1103/PhysRevLett.49.405
15. Kohmoto M. Topological Invariant and the Quantization of the Hall Conductance. *Ann Phys* (1985) 160:343–54. doi:10.1016/0003-4916(85)90148-4
16. Haldane FDM. Model for a Quantum Hall Effect without Landau Levels: Condensed-Matter Realization of the "Parity Anomaly". *Phys Rev Lett* (1988) 61:2015–8. doi:10.1103/physrevlett.61.2015

17. Lu L, Joannopoulos JD, Soljačić M. Topological Photonics. *Nat Photon* (2014) 8:821–9. doi:10.1038/nphoton.2014.248
18. Khanikaev AB, Shvets G. Two-dimensional Topological Photonics. *Nat Photon* (2017) 11:763–73. doi:10.1038/s41566-017-0048-5
19. Wu Y, Li C, Hu X, Ao Y, Zhao Y, Gong Q. Applications of Topological Photonics in Integrated Photonic Devices. *Adv Opt Mater* (2017) 5:1700357. doi:10.1002/adom.201700357
20. Xie B-Y, Wang H-F, Zhu X-Y, Lu M-H, Wang ZD, Chen Y-F. Photonics Meets Topology. *Opt Express* (2018) 26:24531. doi:10.1364/OE.26.024531
21. Ozawa T, Price HM, Amo A, Goldman N, Hafezi M, Lu L, et al. Topological Photonics. *Rev Mod Phys* (2019) 91:015006. doi:10.1103/RevModPhys.91.015006
22. Kim M, Jacob Z, Rho J. Recent Advances in 2D, 3D and Higher-Order Topological Photonics. *Light Sci Appl* (2020) 9:130. doi:10.1038/s41377-020-0331-y
23. Liu H, Xie B, Cheng H, Tian J, Chen S. Topological Photonic States in Artificial Microstructures [Invited]. 中国光学快报 (2021) 19:052602. doi:10.3788/COL202119.052602
24. Raghu S, Haldane FDM. Analogs of Quantum-Hall-Effect Edge States in Photonic Crystals. *Phys Rev A* (2008) 78:033834. doi:10.1103/PhysRevA.78.033834
25. Haldane FDM, Raghu S. Possible Realization of Directional Optical Waveguides in Photonic Crystals with Broken Time-Reversal Symmetry. *Phys Rev Lett* (2008) 100:013904. doi:10.1103/physrevlett.100.013904
26. Wang Z, Chong YD, Joannopoulos JD, Soljacić M. Reflection-free One-Way Edge Modes in a Gyromagnetic Photonic crystal. *Phys Rev Lett* (2008) 100:013905. doi:10.1103/PhysRevLett.100.013905
27. Wang Z, Chong Y, Joannopoulos JD, Soljačić M. Observation of Unidirectional Backscattering-Immune Topological Electromagnetic States. *Nature* (2009) 461:772–5. doi:10.1038/nature08293
28. Kane CL, Mele EJ. Quantum Spin Hall Effect in Graphene. *Phys Rev Lett* (2005) 95:226801. doi:10.1103/PhysRevLett.95.226801
29. Kane CL, Mele EJ. Z2Topological Order and the Quantum Spin Hall Effect. *Phys Rev Lett* (2005) 95:146802. doi:10.1103/PhysRevLett.95.146802
30. Bernevig BA, Zhang S-C. Quantum Spin Hall Effect. *Phys Rev Lett* (2006) 96:106802. doi:10.1103/PhysRevLett.96.106802
31. Bernevig BA, Hughes TL, Zhang S-C. Quantum Spin Hall Effect and Topological Phase Transition in HgTe Quantum Wells. *Science* (2006) 314:1757–61. doi:10.1126/science.1133734
32. Chen W-J, Jiang S-J, Chen X-D, Zhu B, Zhou L, Dong J-W, et al. Experimental Realization of Photonic Topological Insulator in a Uniaxial Metacrystal Waveguide. *Nat Commun* (2014) 5:5782. doi:10.1038/ncomms6782
33. Ma T, Khanikaev AB, Mousavi SH, Shvets G. Guiding Electromagnetic Waves Around Sharp Corners: Topologically Protected Photonic Transport in Metawaveguides. *Phys Rev Lett* (2015) 114:127401. doi:10.1103/physrevlett.114.127401
34. Khanikaev AB, Hossein Mousavi S, Tse W-K, Kargarian M, MacDonald AH, Shvets G. Photonic Topological Insulators. *Nat Mater* (2013) 12:233–9. doi:10.1038/nmat3520
35. He C, Sun X-C, Liu X-P, Lu M-H, Chen Y, Feng L, et al. Photonic Topological Insulator with Broken Time-Reversal Symmetry. *Proc Natl Acad Sci U.S.A* (2016) 113:4924–8. doi:10.1073/pnas.1525502113
36. Wu L-H, Hu X. Scheme for Achieving a Topological Photonic Crystal by Using Dielectric Material. *Phys Rev Lett* (2015) 114:223901. doi:10.1103/PhysRevLett.114.223901
37. Rycerz A, Tworzydło J, Beenakker CWJ. Valley Filter and valley Valve in Graphene. *Nat Phys* (2007) 3:172–5. doi:10.1038/nphys547
38. Xiao D, Yao W, Niu Q. Valley-contrasting Physics in Graphene: Magnetic Moment and Topological Transport. *Phys Rev Lett* (2007) 99:236809. doi:10.1103/PhysRevLett.99.236809
39. Yao W, Xiao D, Niu Q. Valley-dependent Optoelectronics from Inversion Symmetry Breaking. *Phys Rev B* (2008) 77:235406. doi:10.1103/PhysRevB.77.235406
40. Ma T, Shvets G. All-Si valley-Hall Photonic Topological Insulator. *New J Phys* (2016) 18:025012. doi:10.1088/1367-2630/18/2/025012
41. Benalcazar WA, Bernevig BA, Hughes TL. Quantized Electric Multipole Insulators. *Science* (2017) 357:61–6. doi:10.1126/science.aah6442
42. Schindler F, Cook AM, Vergniory MG, Wang Z, Parkin SSP, Bernevig BA, et al. Higher-order Topological Insulators. *Sci Adv* (2018) 4:eaat0346. doi:10.1126/sciadv.aat0346
43. Ezawa M. Higher-Order Topological Insulators and Semimetals on the Breathing Kagome and Pyrochlore Lattices. *Phys Rev Lett* (2018) 120. doi:10.1103/PhysRevLett.120.026801
44. Xie B, Wang H-X, Zhang X, Zhan P, Jiang J-H, Lu M, et al. Higher-order Band Topology. *Nat Rev Phys* (2021) 3:520–32. doi:10.1038/s42254-021-00323-4
45. Benalcazar WA, Bernevig BA, Hughes TL. Electric Multipole Moments, Topological Multipole Moment Pumping, and Chiral Hinge States in Crystalline Insulators. *Phys Rev B* (2017) 96:245115. doi:10.1103/PhysRevB.96.245115
46. Franca S, van den Brink J, Fulga IC. An Anomalous Higher-Order Topological Insulator. *Phys Rev B* (2018) 98:201114. doi:10.1103/PhysRevB.98.201114
47. Langbehn J, Peng Y, Trifunovic L, von Oppen F, Brouwer PW. Reflection-Symmetric Second-Order Topological Insulators and Superconductors. *Phys Rev Lett* (2017) 119:246401. doi:10.1103/PhysRevLett.119.246401
48. Song Z, Fang Z, Fang C. (d−2) -Dimensional Edge States of Rotation Symmetry Protected Topological States. *Phys Rev Lett* (2017) 119:246402. doi:10.1103/PhysRevLett.119.246402
49. Schindler F, Wang Z, Vergniory MG, Cook AM, Murani A, Sengupta S, et al. Higher-order Topology in Bismuth. *Nat Phys* (2018) 14:918–24. doi:10.1038/s41567-018-0224-7
50. Li M, Zhirihin D, Gorlach M, Ni X, Filonov D, Slobozhanyuk A, et al. Higher-order Topological States in Photonic Kagome Crystals with Long-Range Interactions. *Nat Photon* (2019) 14:89. doi:10.1038/s41566-019-0561-9
51. Su WP, Schrieffer JR, Heeger AJ. Soliton Excitations in Polyacetylene. *Phys Rev B* (1980) 22:2099–111. doi:10.1103/physrevb.22.2099
52. Lang L-J, Cai X, Chen S. Edge States and Topological Phases in One-Dimensional Optical Superlattices. *Phys Rev Lett* (2012) 108:220401. doi:10.1103/PhysRevLett.108.220401
53. Li L, Xu Z, Chen S. Topological Phases of Generalized Su-Schrieffer-Heeger Models. *Phys Rev B* (2014) 89:085111. doi:10.1103/PhysRevB.89.085111
54. Chen H-T, Chang C-H, Kao H-c. Connection between the Winding Number and the Chern Number. *Chin J Phys* (2021) 72:50–68. doi:10.1016/j.cjph.2020.12.025
55. Xiao M, Zhang ZQ, Chan CT. Surface Impedance and Bulk Band Geometric Phases in One-Dimensional Systems. *Phys Rev X* (2014) 4:021017. doi:10.1103/PhysRevX.4.021017
56. Fang C, Lu L, Liu J, Fu L. Topological Semimetals with Helicoid Surface States. *Nat Phys* (2016) 12:936–41. doi:10.1038/nphys3782
57. Yang B, Guo Q, Tremain B, Liu R, Barr LE, Yan Q, et al. Ideal Weyl Points and Helicoid Surface States in Artificial Photonic crystal Structures. *Science* (2018) 359:1013–6. doi:10.1126/science.aaq1221
58. Lu L, Fang C, Fu L, Johnson SG, Joannopoulos JD, Soljačić M. Symmetry-protected Topological Photonic crystal in Three Dimensions. *Nat Phys* (2016) 12:337–40. doi:10.1038/nphys3611
59. Slobozhanyuk A, Mousavi SH, Ni X, Smirnova D, Kivshar YS, Khanikaev AB. Three-dimensional All-Dielectric Photonic Topological Insulator. *Nat Photon* (2017) 11:130–6. doi:10.1038/nphoton.2016.253
60. Lu L, Fu L, Joannopoulos JD, Soljačić M. Weyl Points and Line Nodes in Gyroid Photonic Crystals. *Nat Photon* (2013) 7:294–9. doi:10.1038/nphoton.2013.42
61. Lu L, Wang Z, Ye D, Ran L, Fu L, Joannopoulos JD, et al. Experimental Observation of Weyl Points. *Science* (2015) 349:622–4. doi:10.1126/science.aaa9273
62. Zak J. Berry's Phase for Energy Bands in Solids. *Phys Rev Lett* (1989) 62:2747–50. doi:10.1103/physrevlett.62.2747
63. Wang H-X, Guo G-Y, Jiang J-H. Band Topology in Classical Waves: Wilson-loop Approach to Topological Numbers and Fragile Topology. *New J Phys* (2019) 21:093029. doi:10.1088/1367-2630/ab3f71
64. Yu R, Qi XL, Bernevig A, Fang Z, Dai X. Equivalent Expression ofZ2topological Invariant for Band Insulators Using the Non-abelian Berry Connection. *Phys Rev B* (2011) 84:075119. doi:10.1103/PhysRevB.84.075119

65. Wang Q, Xiao M, Liu H, Zhu S, Chan CT. Measurement of the Zak Phase of Photonic Bands through the Interface States of a Metasurface/photonic crystal. *Phys Rev B* (2016) 93:041415. doi:10.1103/physrevb.93.041415
66. Gao WS, Xiao M, Chan CT, Tam WY. Determination of Zak Phase by Reflection Phase in 1D Photonic Crystals. *Opt Lett* (2015) 40:5259. doi:10.1364/ol.40.005259
67. Gao W, Xiao M, Chen B, Pun EYB, Chan CT, Tam WY. Controlling Interface States in 1D Photonic Crystals by Tuning Bulk Geometric Phases. *Opt Lett* (2017) 42:1500. doi:10.1364/OL.42.001500
68. Huang X, Xiao M, Zhang ZQ, Chan CT. Sufficient Condition for the Existence of Interface States in Some Two-Dimensional Photonic Crystals. *Phys Rev B* (2014) 90:075423. doi:10.1103/physrevb.90.075423
69. Huang X, Yang Y, Hang ZH, Zhang Z-Q, Chan CT. Geometric Phase Induced Interface States in Mutually Inverted Two-Dimensional Photonic Crystals. *Phys Rev B* (2016) 93:085415. doi:10.1103/PhysRevB.93.085415
70. Chen X-D, Zhao D, Zhu X-S, Shi F-L, Liu H, Lu J-C, et al. Edge States in Self-Complementary Checkerboard Photonic Crystals: Zak Phase, Surface Impedance, and Experimental Verification. *Phys Rev A* (2018) 97:013831. doi:10.1103/PhysRevA.97.013831
71. Fukui T, Hatsugai Y, Suzuki H. Chern Numbers in Discretized Brillouin Zone: Efficient Method of Computing (Spin) Hall Conductances. *J Phys Soc Jpn* (2005) 74:1674–7. doi:10.1143/JPSJ.74.1674
72. Weng H, Yu R, Hu X, Dai X, Fang Z. Quantum Anomalous Hall Effect and Related Topological Electronic States. *Adv Phys* (2015) 64:227–82. doi:10.1080/00018732.2015.1068524
73. Hatsugai Y. Chern Number and Edge States in the Integer Quantum Hall Effect. *Phys Rev Lett* (1993) 71:3697–700. doi:10.1103/PhysRevLett.71.3697
74. Ao X, Lin Z, Chan CT. One-way Edge Mode in a Magneto-Optical Honeycomb Photonic crystal. *Phys Rev B* (2009) 80:033105. doi:10.1103/physrevb.80.033105
75. Poo Y, Wu R-x., Lin Z, Yang Y, Chan CT. Experimental Realization of Self-Guiding Unidirectional Electromagnetic Edge States. *Phys Rev Lett* (2011) 106:093903. doi:10.1103/physrevlett.106.093903
76. Skirlo SA, Lu L, Soljačić M. Multimode One-Way Waveguides of Large Chern Numbers. *Phys Rev Lett* (2014) 113:113904. doi:10.1103/physrevlett.113.113904
77. Skirlo SA, Lu L, Igarashi Y, Yan Q, Joannopoulos J, Soljačić M. Experimental Observation of Large Chern Numbers in Photonic Crystals. *Phys Rev Lett* (2015) 115:253901. doi:10.1103/physrevlett.115.253901
78. Yang Y, Poo Y, Wu R-x., Gu Y, Chen P. Experimental Demonstration of One-Way Slow Wave in Waveguide Involving Gyromagnetic Photonic Crystals. *Appl Phys Lett* (2013) 102:231113. doi:10.1063/1.4809956
79. Chen J, Liang W, Li ZY. Strong Coupling of Topological Edge States Enabling Group-Dispersionless Slow Light in Magneto-Optical Photonic Crystals. *Phys Rev B* (2019) 99:014103. doi:10.1103/physrevb.99.014103
80. Chen J, Liang W, Li Z-Y. Switchable Slow Light Rainbow Trapping and Releasing in Strongly Coupling Topological Photonic Systems. *Photon Res* (2019) 7:1075. doi:10.1364/PRJ.7.001075
81. Chen J, Liang W, Li Z-Y. Broadband Dispersionless Topological Slow Light. *Opt Lett* (2020) 45:4964. doi:10.1364/OL.401650
82. Chen J, Liang W, Li Z-Y. Antichiral One-Way Edge States in a Gyromagnetic Photonic crystal. *Phys Rev B* (2020) 101:214102. doi:10.1103/PhysRevB.101.214102
83. Zhou P, Liu G-G, Yang Y, Hu Y-H, Ma S, Xue H, et al. Observation of Photonic Antichiral Edge States. *Phys Rev Lett* (2020) 125:263603. doi:10.1103/PhysRevLett.125.263603
84. Yang Y, Xu YF, Xu T, Wang H-X, Jiang J-H, Hu X, et al. Visualization of a Unidirectional Electromagnetic Waveguide Using Topological Photonic Crystals Made of Dielectric Materials. *Phys Rev Lett* (2018) 120:217401. doi:10.1103/PhysRevLett.120.217401
85. Zhu X, Wang H-X, Xu C, Lai Y, Jiang J-H, John S. Topological Transitions in Continuously Deformed Photonic Crystals. *Phys Rev B* (2018) 97:085148. doi:10.1103/physrevb.97.085148
86. Barik S, Miyake H, DeGottardi W, Waks E, Hafezi M. Two-dimensionally Confined Topological Edge States in Photonic Crystals. *New J Phys* (2016) 18:113013. doi:10.1088/1367-2630/18/11/113013
87. Huang H, Huo S, Chen J. Reconfigurable Topological Phases in Two-Dimensional Dielectric Photonic Crystals. *Crystals* (2019) 9:221. doi:10.3390/cryst9040221
88. Jin M-C, Gao Y-F, Ma Q-L, Zhang W, Song H, Sun J-P. Regularly Multiple Double Dirac Cones in Photonic Bands and Topological Transitions of All-Dielectric Photonic Crystals. *Phys Rev Mater* (2021) 5:024204. doi:10.1103/PhysRevMaterials.5.024204
89. Deng W-M, Chen X-D, Zhao F-L, Dong J-W. Transverse Angular Momentum in Topological Photonic Crystals. *J Opt* (2018) 20:014006. doi:10.1088/2040-8986/aa9b06
90. Parappurath N, Alpeggiani F, Kuipers L, Verhagen E. Direct Observation of Topological Edge States in Silicon Photonic Crystals: Spin, Dispersion, and Chiral Routing. *Sci Adv* (2020) 6. doi:10.1126/sciadv.aaw4137
91. Gorlach MA, Ni X, Smirnova DA, Korobkin D, Zhirihin D, Slobozhanyuk AP, et al. Far-field Probing of Leaky Topological States in All-Dielectric Metasurfaces. *Nat Commun* (2018) 9. doi:10.1038/s41467-018-03330-9
92. Slobozhanyuk A, Shchelokova AV, Ni X, Hossein Mousavi S, Smirnova DA, Belov PA, et al. Near-field Imaging of Spin-Locked Edge States in All-Dielectric Topological Metasurfaces. *Appl Phys Lett* (2019) 114:031103. doi:10.1063/1.5055601
93. Shao Z-K, Chen H-Z, Wang S, Mao X-R, Yang Z-Q, Wang S-L, et al. A High-Performance Topological Bulk Laser Based on Band-Inversion-Induced Reflection. *Nat Nanotechnol* (2020) 15:67–72. doi:10.1038/s41565-019-0584-x
94. Barik S, Karasahin A, Flower C, Cai T, Miyake H, DeGottardi W, et al. A Topological Quantum Optics Interface. *Science* (2018) 359:666–8. doi:10.1126/science.aaq0327
95. Kagami H, Amemiya T, Okada S, Nishiyama N, Hu X. Topological Converter for High-Efficiency Coupling between Si Wire Waveguide and Topological Waveguide. *Opt Express* (2020) 28:33619. doi:10.1364/OE.398421
96. Wei Y, Yan B, Peng Y, Shi A, Zhao D, Peng R, et al. Fragile Topology in Double-Site Honeycomb Lattice Photonic crystal. *Opt Lett* (2021) 46:3941. doi:10.1364/OL.434502
97. Xu L, Wang H-X, Xu Y-D, Chen H-Y, Jiang J-H. Accidental Degeneracy in Photonic Bands and Topological Phase Transitions in Two-Dimensional Core-Shell Dielectric Photonic Crystals. *Opt Express* (2016) 24:18059. doi:10.1364/OE.24.018059
98. Yan B, Xie J, Liu E, Peng Y, Ge R, Liu J, et al. Topological Edge State in the Two-Dimensional Stampfli-Triangle Photonic Crystals. *Phys Rev Appl* (2019) 12:044004. doi:10.1103/physrevapplied.12.044004
99. Li Z, Chan H-C, Xiang Y. Fragile Topology Based Helical Edge States in Two-Dimensional Moon-Shaped Photonic Crystals. *Phys Rev B* (2020) 102:245149. doi:10.1103/PhysRevB.102.245149
100. Lidorikis E, Sigalas MM, Economou EN, Soukoulis CM. Tight-binding Parametrization for Photonic Band gap Materials. *Phys Rev Lett* (1998) 81:1405–8. doi:10.1103/PhysRevLett.81.1405
101. Blanco de Paz M, Devescovi C, Giedke G, Saenz JJ, Vergniory MG, Bradlyn B, et al. Tutorial: Computing Topological Invariants in 2D Photonic Crystals. *Adv Quan Tech* (2020) 3:1900117. doi:10.1002/qute.201900117
102. de Paz MB, Vergniory MG, Bercioux D, García-Etxarri A, Bradlyn B. Engineering Fragile Topology in Photonic Crystals: Topological Quantum Chemistry of Light. *Phys Rev Res* (2019) 1:032005. doi:10.1103/physrevresearch.1.032005
103. Alexandradinata A, Höller J, Wang C, Cheng H, Lu L. Crystallographic Splitting Theorem for Band Representations and Fragile Topological Photonic Crystals. *Phys Rev B* (2020) 102:115117. doi:10.1103/PhysRevB.102.115117
104. He L, Zhang WX, Zhang XD. Topological All-Optical Logic gates Based on Two-Dimensional Photonic Crystals. *Opt Express* (2019) 27:25841. doi:10.1364/oe.27.025841
105. Yang Y, Hang ZH. Topological Whispering Gallery Modes in Two-Dimensional Photonic crystal Cavities. *Opt Express* (2018) 26:21235. doi:10.1364/OE.26.021235
106. Ji C-Y, Liu G-B, Zhang Y, Zou B, Yao Y. Transport Tuning of Photonic Topological Edge States by Optical Cavities. *Phys Rev A* (2019) 99:043801. doi:10.1103/PhysRevA.99.043801
107. Gao X, Yang L, Lin H, Zhang L, Li J, Bo F, et al. Dirac-vortex Topological Cavities. *Nat Nanotechnol* (2020) 15:1012–8. doi:10.1038/s41565-020-0773-7
108. Lin H, Lu L. Dirac-vortex Topological Photonic crystal Fibre. *Light Sci Appl* (2020) 9:202. doi:10.1038/s41377-020-00432-2

109. Deng W-M, Chen X-D, Chen W-J, Zhao F-L, Dong J-W. Vortex index Identification and Unidirectional Propagation in Kagome Photonic Crystals. *Nanophotonics* (2019) 8:833–40. doi:10.1515/nanoph-2019-0009
110. He X-T, Liang E-T, Yuan J-J, Qiu H-Y, Chen X-D, Zhao F-L, et al. A Silicon-On-Insulator Slab for Topological valley Transport. *Nat Commun* (2019) 10: 872. doi:10.1038/s41467-019-08881-z
111. Chen XD, He XT, Dong JW. All-Dielectric Layered Photonic Topological Insulators. *Laser Photon Rev* (2019) 13:1900091. doi:10.1002/lpor.201900091
112. Wong S, Saba M, Hess O, Oh SS. Gapless Unidirectional Photonic Transport Using All-Dielectric Kagome Lattices. *Phys Rev Res* (2020) 2:012011. doi:10.1103/PhysRevResearch.2.012011
113. Xu Z, Kong X, Davis RJ, Bisharat Da., Zhou Y, Yin X, et al. Topological valley Transport under Long-Range Deformations. *Phys Rev Res* (2020) 2:013209. doi:10.1103/physrevresearch.2.013209
114. Xi X, Ye K-P, Wu R-X. Topological Photonic crystal of Large valley Chern Numbers. *Photon Res* (2020) 8:B1. doi:10.1364/prj.396872
115. Tang G-J, Chen X-D, Shi F-L, Liu J-W, Chen M, Dong J-W. Frequency Range Dependent Topological Phases and Photonic Detouring in valley Photonic Crystals. *Phys Rev B* (2020) 102:174202. doi:10.1103/PhysRevB.102.174202
116. Arora S, Bauer T, Barczyk R, Verhagen E, Kuipers L. Direct Quantification of Topological protection in Symmetry-Protected Photonic Edge States at Telecom Wavelengths. *Light Sci Appl* (2021) 10:9. doi:10.1038/s41377-020-00458-6
117. Yang J-K, Hwang Y, Oh SS. Evolution of Topological Edge Modes from Honeycomb Photonic Crystals to Triangular-Lattice Photonic Crystals. *Phys Rev Res* (2021) 3:L022025. doi:10.1103/physrevresearch.3.l022025
118. Yan B, Peng Y, Xie J, Peng Y, Shi A, Li H, et al. Multifrequency and Multimode Topological Waveguides in Stampfli-triangle Photonic crystal with Large valley Chern Numbers. *arXiv:2104.14142[physics]* (2021).
119. Chen X-D, Zhao F-L, Chen M, Dong J-W. Valley-contrasting Physics in All-Dielectric Photonic Crystals: Orbital Angular Momentum and Topological Propagation. *Phys Rev B* (2017) 96. doi:10.1103/PhysRevB.96.020202
120. Ye L, Yang Y, Hong Hang Z, Qiu C, Liu Z. Observation of valley-selective Microwave Transport in Photonic Crystals. *Appl Phys Lett* (2017) 111: 251107. doi:10.1063/1.5009597
121. Han Y, Fei H, Lin H, Zhang Y, Zhang M, Yang Y. Design of Broadband All-Dielectric valley Photonic Crystals at Telecommunication Wavelength. *Opt Commun* (2021) 488:126847. doi:10.1016/j.optcom.2021.126847
122. Yang Y, Jiang H, Hang ZH. Topological Valley Transport in Two-Dimensional Honeycomb Photonic Crystals. *Sci Rep* (2018) 8. doi:10.1038/s41598-018-20001-3
123. Chen XD, Shi FL, Liu H, Lu JC, Deng WM, Dai JY, et al. Tunable Electromagnetic Flow Control in Valley Photonic Crystal Waveguides. *Phys Rev Appl* (2018) 10:044002. doi:10.1103/physrevapplied.10.044002
124. Wu Y, Hu X, Gong Q. Reconfigurable Topological States in valley Photonic Crystals. *Phys Rev Mater* (2018) 2:122201. doi:10.1103/PhysRevMaterials.2.122201
125. Noh J, Huang S, Chen KP, Rechtsman MC. Observation of Photonic Topological Valley Hall Edge States. *Phys Rev Lett* (2018) 120:063902. doi:10.1103/PhysRevLett.120.063902
126. Chan H-C, Guo G-Y. Tuning Topological Phase Transitions in Hexagonal Photonic Lattices Made of Triangular Rods. *Phys Rev B* (2018) 97:045422. doi:10.1103/physrevb.97.045422
127. He L, Ji HY, Wang YJ, Zhang XD. Topologically Protected Beam Splitters and Logic gates Based on Two-Dimensional Silicon Photonic crystal Slabs. *Opt Express* (2020) 28:34015. doi:10.1364/OE.409265
128. Zeng Y, Chattopadhyay U, Zhu B, Qiang B, Li J, Jin Y, et al. Electrically Pumped Topological Laser with valley Edge Modes. *Nature* (2020) 578: 246–50. doi:10.1038/s41586-020-1981-x
129. He L, Zhang H, Zhang W, Wang Y, Zhang X. Topologically Protected Vector Edge States and Polarization Beam Splitter by All-Dielectric valley Photonic crystal Slabs. *New J Phys* (2021) 23:093026. doi:10.1088/1367-2630/ac20eb
130. Ji C-Y, Zhang Y, Zou B, Yao Y. Robust Fano Resonance in the Photonic valley Hall States. *Phys Rev A* (2021) 103:023512. doi:10.1103/PhysRevA.103.023512
131. Makwana M, Craster R, Guenneau S. Topological Beam-Splitting in Photonic Crystals. *Opt Express* (2019) 27:16088. doi:10.1364/OE.27.016088
132. Makwana MP, Craster RV. Designing Multidirectional Energy Splitters and Topological valley Supernetworks. *Phys Rev B* (2018) 98:235125. doi:10.1103/PhysRevB.98.235125
133. Xie X, Yan S, Dang J, Yang J, Xiao S, Wang Y, et al. Topological Cavity Based on Slow-Light Topological Edge Mode for Broadband Purcell Enhancement. *Phys Rev Appl* (2021) 16:014036. doi:10.1103/PhysRevApplied.16.014036
134. Makwana M, Wiltshaw R, Guenneau S, Craster R. Hybrid Topological Guiding Mechanisms for Photonic crystal Fibers. *Opt Express* (2020) 28: 30871. doi:10.1364/oe.398559
135. Makwana MP, Chaplain G. Tunable Three-Way Topological Energy-Splitter. *Sci Rep* (2019) 9:18939. doi:10.1038/s41598-019-55485-0
136. Chen Y, Lin Z-K, Chen H, Jiang J-H. Plasmon-polaritonic Quadrupole Topological Insulators. *Phys Rev B* (2020) 101:041109. doi:10.1103/PhysRevB.101.041109
137. He L, Addison Z, Mele EJ, Zhen B. Quadrupole Topological Photonic Crystals. *Nat Commun* (2020) 11:3119. doi:10.1038/s41467-020-16916-z
138. Ezawa M. Higher-order Topological Electric Circuits and Topological Corner Resonance on the Breathing Kagome and Pyrochlore Lattices. *Phys Rev B* (2018) 98:201402. doi:10.1103/PhysRevB.98.201402
139. Yang H, Li Z-X, Liu Y, Cao Y, Yan P. Observation of Symmetry-Protected Zero Modes in Topolectrical Circuits. *Phys Rev Res* (2020) 2:022028. doi:10.1103/PhysRevResearch.2.022028
140. Xue H, Yang Y, Gao F, Chong Y, Zhang B. Acoustic Higher-Order Topological Insulator on a Kagome Lattice. *Nat Mater* (2019) 18:108–12. doi:10.1038/s41563-018-0251-x
141. Ni X, Weiner M, Alù A, Khanikaev AB. Observation of Higher-Order Topological Acoustic States Protected by Generalized Chiral Symmetry. *Nat Mater* (2019) 18:113–20. doi:10.1038/s41563-018-0252-9
142. Shen S-l., Li C, Wu J-F. Investigation of Corner States in Second-Order Photonic Topological Insulator. *Opt Express* (2021) 29:24045. doi:10.1364/OE.426691
143. Wakao H, Yoshida T, Araki H, Mizoguchi T, Hatsugai Y. Higher-order Topological Phases in a spring-mass Model on a Breathing Kagome Lattice. *Phys Rev B* (2020) 101:094107. doi:10.1103/PhysRevB.101.094107
144. Phan HT, Liu F, Wakabayashi K. Valley-dependent Corner States in Honeycomb Photonic Crystals without Inversion Symmetry. *Opt Express* (2021) 29:18277. doi:10.1364/OE.427222
145. Wu S, Jiang B, Liu Y, Jiang J-H. All-dielectric Photonic crystal with Unconventional Higher-Order Topology. *Photon Res* (2021) 9:668. doi:10.1364/PRJ.418689
146. Yang Y, Jia Z, Wu Y, Xiao R-C, Hang ZH, Jiang H, et al. Gapped Topological Kink States and Topological Corner States in Honeycomb Lattice. *Sci Bull* (2020) 65:531–7. doi:10.1016/j.scib.2020.01.024
147. Proctor M, Huidobro PA, Bradlyn B, de Paz MB, Vergniory MG, Bercioux D, et al. Robustness of Topological Corner Modes in Photonic Crystals. *Phys Rev Res* (2020) 2:042038. doi:10.1103/physrevresearch.2.042038
148. Liu F, Deng H-Y, Wakabayashi K. Helical Topological Edge States in a Quadrupole Phase. *Phys Rev Lett* (2019) 122:086804. doi:10.1103/PhysRevLett.122.086804
149. Li M, Wang Y, Lu M, Sang T. Two Types of Corner States in Two-Dimensional Photonic Topological Insulators. *J Appl Phys* (2021) 129: 063104. doi:10.1063/5.0039586
150. Chen Y, Meng F, Kivshar Y, Jia B, Huang X. Inverse Design of Higher-Order Photonic Topological Insulators. *Phys Rev Res* (2020) 2:023115. doi:10.1103/PhysRevResearch.2.023115
151. Xie B-Y, Wang H-F, Wang H-X, Zhu X-Y, Jiang J-H, Lu M-H, et al. Second-order Photonic Topological Insulator with Corner States. *Phys Rev B* (2018) 98:205147. doi:10.1103/PhysRevB.98.205147
152. Xie B-Y, Su G-X, Wang H-F, Su H, Shen X-P, Zhan P, et al. Visualization of Higher-Order Topological Insulating Phases in Two-Dimensional Dielectric Photonic Crystals. *Phys Rev Lett* (2019) 122:233903. doi:10.1103/PhysRevLett.122.233903
153. Chen X-D, Deng W-M, Shi F-L, Zhao F-L, Chen M, Dong J-W. Direct Observation of Corner States in Second-Order Topological Photonic Crystal Slabs. *Phys Rev Lett* (2019) 122:233902. doi:10.1103/PhysRevLett.122.233902
154. Wang H-X, Liang L, Jiang B, Hu J, Lu X, Jiang J-H. Higher-order Topological Phases in Tunable C3 Symmetric Photonic Crystals. *Photon Res* (2021) 9: 1854. doi:10.1364/PRJ.433188
155. Benalcazar WA, Li T, Hughes TL. Quantization of Fractional Corner Charge in Cn -symmetric Higher-Order Topological Crystalline Insulators. *Phys Rev B* (2019) 99:245151. doi:10.1103/physrevb.99.245151

156. Chen Z-G, Wang L, Zhang G, Ma G. Chiral Symmetry Breaking of Tight-Binding Models in Coupled Acoustic-Cavity Systems. *Phys Rev Appl* (2020) 14:024023. doi:10.1103/PhysRevApplied.14.024023
157. Ota Y, Liu F, Katsumi R, Watanabe K, Wakabayashi K, Arakawa Y, et al. Photonic crystal Nanocavity Based on a Topological Corner State. *Optica* (2019) 6:786. doi:10.1364/OPTICA.6.000786
158. Xie X, Zhang W, He X, Wu S, Dang J, Peng K, et al. Cavity Quantum Electrodynamics with Second-Order Topological Corner State. *Laser Photon Rev* (2020) 14:1900425. doi:10.1002/lpor.201900425
159. Kim H-R, Hwang M-S, Smirnova D, Jeong K-Y, Kivshar Y, Park H-G. Multipolar Lasing Modes from Topological Corner States. *Nat Commun* (2020) 11:5758. doi:10.1038/s41467-020-19609-9
160. Zhang W, Xie X, Hao H, Dang J, Xiao S, Shi S, et al. Low-threshold Topological Nanolasers Based on the Second-Order Corner State. *Light Sci Appl* (2020) 9:109. doi:10.1038/s41377-020-00352-1
161. Gong R, Zhang M, Li H, Lan Z. Topological Photonic crystal Fibers Based on Second-Order Corner Modes. *Opt Lett* (2021) 46:3849. doi:10.1364/ol.430579
162. Henriques JCG, Rappoport TG, Bludov YV, Vasilevskiy MI, Peres NMR. Topological Photonic Tamm States and the Su-Schrieffer-Heeger Model. *Phys Rev A* (2020) 101:043811. doi:10.1103/physreva.101.043811
163. Chen Z-G, Mei J, Sun X-C, Zhang X, Zhao J, Wu Y. Multiple Topological Phase Transitions in a Gyromagnetic Photonic crystal. *Phys Rev A* (2017) 95: 043827. doi:10.1103/PhysRevA.95.043827
164. Chen MLN, Jiang LJ, Lan Z, Sha WEI. Coexistence of Pseudospin- and valley-Hall-like Edge States in a Photonic crystal with C3v Symmetry. *Phys Rev Res* (2020) 2:043148. doi:10.1103/PhysRevResearch.2.043148
165. Liu G-G, Zhou P, Yang Y, Xue H, Ren X, Lin X, et al. Observation of an Unpaired Photonic Dirac point. *Nat Commun* (2020) 11:1873. doi:10.1038/s41467-020-15801-z
166. Wu X, Li Z, Chen J, Li X, Tian J, Huang Y, et al. Interlayer Topological Transport and Devices Based on Layer Pseudospins in Photonic Valley-Hall Phases. *Adv Opt Mater.* (2019) 7:1900872. doi:10.1002/adom.201900872
167. Yannopapas V. Gapless Surface States in a Lattice of Coupled Cavities: A Photonic Analog of Topological Crystalline Insulators. *Phys Rev B* (2011) 84. doi:10.1103/PhysRevB.84.195126
168. Fu L. Topological Crystalline Insulators. *Phys Rev Lett* (2011) 106:106802. doi:10.1103/physrevlett.106.106802
169. Ochiai T. Gapless Surface States Originating from Accidentally Degenerate Quadratic Band Touching in a Three-Dimensional Tetragonal Photonic crystal. *Phys Rev A* (2017) 96:043842. doi:10.1103/physreva.96.043842
170. Wang H, Xu L, Chen H, Jiang J-H. Three-dimensional Photonic Dirac Points Stabilized by point Group Symmetry. *Phys Rev B* (2016) 93:235155. doi:10.1103/PhysRevB.93.235155
171. Wang H-X, Chen Y, Hang ZH, Kee H-Y, Jiang J-H. Type-II Dirac Photons. *Npj Quant Mater* (2017) 2:54. doi:10.1038/s41535-017-0058-z
172. Guo Q, Yang B, Xia L, Gao W, Liu H, Chen J, et al. Three Dimensional Photonic Dirac Points in Metamaterials. *Phys Rev Lett* (2017) 119:213901. doi:10.1103/PhysRevLett.119.213901
173. Chen Y, Wang H-X, Bao Q, Jiang J-H, Chen H. Ideal Type-II Weyl Points in Twisted One-Dimensional Dielectric Photonic Crystals. *Opt Express* (2021) 29:40606. doi:10.1364/OE.444780
174. Bravo-Abad J. Weyl Points in Photonic-crystal Superlattices. *2D Mater* (2015) 8:034013. doi:10.1088/2053-1583/2/3/034013
175. Chang ML, Xiao M, Chen WJ, Chan CT. Multiple Weyl Points and the Sign Change of Their Topological Charges in Woodpile Photonic Crystals. *Phys Rev B* (2017) 95. doi:10.1103/physrevb.95.125136
176. Wang L, Jian S-K, Yao H. Topological Photonic crystal with Equifrequency Weyl Points. *Phys Rev A* (2016) 93:061801. doi:10.1103/PhysRevA.93.061801
177. Jürß C, Bauer D. High-harmonic Generation in Su-Schrieffer-Heeger Chains. *Phys Rev B* (2019) 99:195428. doi:10.1103/PhysRevB.99.195428
178. Smirnova D, Kruk S, Leykam D, Melik-Gaykazyan E, Choi D-Y, Kivshar Y. Third-Harmonic Generation in Photonic Topological Metasurfaces. *Phys Rev Lett* (2019) 123:103901. doi:10.1103/PhysRevLett.123.103901
179. Smirnova DA, Smirnov LA, Leykam D, Kivshar YS. Topological Edge States and Gap Solitons in the Nonlinear Dirac Model. *Laser Photon Rev* (2019) 13: 1900223. doi:10.1002/lpor.201900223
180. Lan Z, You JW, Panoiu NC. Nonlinear One-Way Edge-Mode Interactions for Frequency Mixing in Topological Photonic Crystals. *Phys Rev B* (2020) 101: 155422. doi:10.1103/PhysRevB.101.155422
181. Smirnova D, Leykam D, Chong Y, Kivshar Y. Nonlinear Topological Photonics. *Appl Phys Rev* (2020) 7:021306. doi:10.1063/1.5142397
182. Jiang J-R, Chen W-T, Chern R-L. Parity-time Phase Transition in Photonic Crystals with $$C_{6v}$$ Symmetry. *Sci Rep* (2020) 10:15726. doi:10.1038/s41598-020-72716-x
183. Zhou X, Wu J, Wu Y. Topological Corner States in Non-hermitian Photonic Crystals. *Opt Commun* (2020) 466:125653. doi:10.1016/j.optcom.2020.125653
184. Chen MLN, Jiang LJ, Zhang S, Zhao R, Lan Z, Sha WEI. Comparative Study of Hermitian and Non-hermitian Topological Dielectric Photonic Crystals. *Phys Rev A* (2021) 104:033501. doi:10.1103/PhysRevA.104.033501
185. Jiang J, Yan B, Peng Y, Xie J, Shi A, Liu J. Multiband Topological States in Non-hermitian Photonic Crystals. *Opt Lett* (2022) 47:437. doi:10.1364/ol.449733
186. Dong J, Hu Q, Ji C-Y, Zou B, Zhang Y. Exceptional Points in a Topological Waveguide-Cavity Coupled System. *New J Phys* (2021) 23:113025. doi:10.1088/1367-2630/ac3441
187. Li F-F, Wang H-X, Xiong Z, Lou Q, Chen P, Wu R-X, et al. Topological Light-Trapping on a Dislocation. *Nat Commun* (2018) 9. doi:10.1038/s41467-018-04861-x
188. Liu Y, Leung S, Li F-F, Lin Z-K, Tao X, Poo Y, et al. Bulk-disclination Correspondence in Topological Crystalline Insulators. *Nature* (2021) 589: 381–5. doi:10.1038/s41586-020-03125-3
189. Wang Q, Xue H, Zhang B, Chong YD. Observation of Protected Photonic Edge States Induced by Real-Space Topological Lattice Defects. *Phys Rev Lett* (2020) 124:243602. doi:10.1103/physrevlett.124.243602
190. Peterson CW, Li T, Jiang W, Hughes TL, Bahl G. Trapped Fractional Charges at Bulk Defects in Topological Insulators. *Nature* (2021) 589:376–80. doi:10.1038/s41586-020-03117-3
191. Yao S, Wang Z. Edge States and Topological Invariants of Non-hermitian Systems. *Phys Rev Lett* (2018) 121:086803. doi:10.1103/PhysRevLett.121.086803
192. Imura K-I, Takane Y. Generalized Bulk-Edge Correspondence for Non-hermitian Topological Systems. *Phys Rev B* (2019) 100:165430. doi:10.1103/PhysRevB.100.165430
193. Yokomizo K, Murakami S. Non-Bloch Band Theory of Non-hermitian Systems. *Phys Rev Lett* (2019) 123:066404. doi:10.1103/PhysRevLett.123.066404
194. Helbig T, Hofmann T, Imhof S, Abdelghany M, Kiessling T, Molenkamp LW, et al. Generalized Bulk-Boundary Correspondence in Non-hermitian Topolectrical Circuits. *Nat Phys* (2020) 16:747–50. doi:10.1038/s41567-020-0922-9
195. Zhang K, Yang Z, Fang C. Correspondence between Winding Numbers and Skin Modes in Non-hermitian Systems. *Phys Rev Lett* (2020) 125:126402. doi:10.1103/physrevlett.125.126402
196. Yuan L, Fan S. Bloch Oscillation and Unidirectional Translation of Frequency in a Dynamically Modulated Ring Resonator. *Optica* (2016) 3:1014. doi:10.1364/OPTICA.3.001014
197. Yuan L, Shi Y, Fan S. Photonic Gauge Potential in a System with a Synthetic Frequency Dimension. *Opt Lett* (2016) 41:741. doi:10.1364/OL.41.000741
198. Lin Q, Xiao M, Yuan L, Fan S. Photonic Weyl point in a Two-Dimensional Resonator Lattice with a Synthetic Frequency Dimension. *Nat Commun* (2016) 7. doi:10.1038/ncomms13731
199. Lin Q, Sun X-Q, Xiao M, Zhang S-C, Fan S. A Three-Dimensional Photonic Topological Insulator Using a Two-Dimensional Ring Resonator Lattice with a Synthetic Frequency Dimension. *Sci Adv* (2018) 4:eaat2774. doi:10.1126/sciadv.aat2774
200. Ozawa T, Price HM, Goldman N, Zilberberg O, Carusotto I. Synthetic Dimensions in Integrated Photonics: From Optical Isolation to Four-Dimensional Quantum Hall Physics. *Phys Rev A* (2016) 93:043827. doi:10.1103/PhysRevA.93.043827
201. Yuan L, Xiao M, Lin Q, Fan S. Synthetic Space with Arbitrary Dimensions in a Few Rings Undergoing Dynamic Modulation. *Phys Rev B* (2018) 97:104105. doi:10.1103/PhysRevB.97.104105

202. Yuan L, Lin Q, Zhang A, Xiao M, Chen X, Fan S. Photonic Gauge Potential in One Cavity with Synthetic Frequency and Orbital Angular Momentum Dimensions. *Phys Rev Lett* (2019) 122:083903. doi:10.1103/PhysRevLett.122.083903
203. Qin C, Wang B, Wong ZJ, Longhi S, Lu P. Discrete Diffraction and Bloch Oscillations in Non-hermitian Frequency Lattices Induced by Complex Photonic Gauge fields. *Phys Rev B* (2020) 101:064303. doi:10.1103/PhysRevB.101.064303
204. Qin C, Yuan L, Wang B, Fan S, Lu P. Effective Electric-Field Force for a Photon in a Synthetic Frequency Lattice Created in a Waveguide Modulator. *Phys Rev A* (2018) 97:063838. doi:10.1103/physreva.97.063838
205. Qin C, Liu Q, Wang B, Lu P. Photonic Weyl Phase Transition in Dynamically Modulated brick-wall Waveguide Arrays. *Opt Express* (2018) 26:20929–43. doi:10.1364/oe.26.020929
206. Qin C, Zhou F, Peng Y, Sounas D, Zhu X, Wang B, et al. Spectrum Control through Discrete Frequency Diffraction in the Presence of Photonic Gauge Potentials. *Phys Rev Lett* (2018) 120:133901. doi:10.1103/PhysRevLett.120.133901

Conflict of Interest: The authors declare that the research was conducted in the absence of any commercial or financial relationships that could be construed as a potential conflict of interest.

frontiers | Frontiers in Physics

ORIGINAL RESEARCH
published: 03 June 2022
doi: 10.3389/fphy.2022.902533

Multiport Routing of Topologically Optical Transport Based on Merging of Valley-Dependent Edge States and Second-Order Corner States

Meng-Yu Li, Wen-Jie Chen, Xin-Tao He and Jian-Wen Dong**

School of Physics and State Key Laboratory of Optoelectronic Materials and Technologies, Sun Yat-sen University, Guangzhou, China

Topological photonics provide a novel platform to robustly manipulate the flow of light and design high-performance nanophotonic devices. To do this, a fundamental mechanism is the flexible control of optical transport based on topological boundary states on edges or corners. In this work, we design a multiport device to route the topologically optical transport by using both valley-dependent edge states (VDESs) and second-order corner states (SOCSs). The VDESs are derived from sublattice symmetry breaking in a honeycomb lattice, while SOCSs are induced by the lattice deformation of Kagome lattice. In terms of unit cell, we find that both configurations can be reconsidered as the same triangular-lattice photonic crystal, which consists of a hexagon-profile air hole array in silicon background. Therefore, a four-port device is designed based on the two configurations. In simulation, we observe the frequency-dependent routing effect of the topologically optical transport by merging of VDESs and SOCSs. This work not only shows a novel platform to explore various topological phases in the photonic system but also provides guidance in the development of topological photonic integrated circuits with mode division multiplexing.

Keywords: topological photonics, photonic crystals (PCs), topological edge states, corner states, multiport routing

OPEN ACCESS

Edited by:
Xiaoyong Hu,
Peking University, China

Reviewed by:
Qiuchen Yan,
Peking University, China
Xiaoxiao Wang,
Xiaoyong Hu, China

****Correspondence:***
Xin-Tao He
hext9@mail.sysu.edu.cn
Jian-Wen Dong
dongjwen@mail.sysu.edu.cn

Specialty section:
This article was submitted to Optics and Photonics, a section of the journal Frontiers in Physics

Received: *23 March 2022*
Accepted: *25 April 2022*
Published: *03 June 2022*

Citation:
Li M-Y, Chen W-J, He X-T and Dong J-W (2022) Multiport Routing of Topologically Optical Transport Based on Merging of Valley-Dependent Edge States and Second-Order Corner States. Front. Phys. 10:902533. doi: 10.3389/fphy.2022.902533

INTRODUCTION

Topology, a concept of mathematics that studies the invariant global properties under continuous deformation, has been introduced into the physics systems to explore the intriguing band structures in the momentum space [1, 2]. Due to tunable geometric structures and controllable band dispersions, photonic crystals (PCs) arouse a wide range of research interest to implement the topological concept in photonic systems [3–7]. The topological PCs have been used to demonstrate many topological physics with nontrivial phases, such as quantum Hall effect, quantum spin Hall effect, quantum valley Hall effect (QVHE), and 2D Zak phase [8–15, 42, 43]. By using the topologically protected states, topological PCs also provide a platform to design intriguing devices in integrated optics and nanophotonics [16–25].

For example, the QVHE of light can be demonstrated by a honeycomb-lattice PC with sublattice symmetry breaking, namely, valley photonic crystal (VPC) [19, 20, 26–29]. When two topologically distinct VPCs are placed side-by-side to form an interface, valley-dependent edge states (VDESs) will emerge and robustly propagate along the interface with backscattering-suppressed electromagnetic features. On the other hand, by lattice deformation in a Kagome-lattice PC, one can implement a

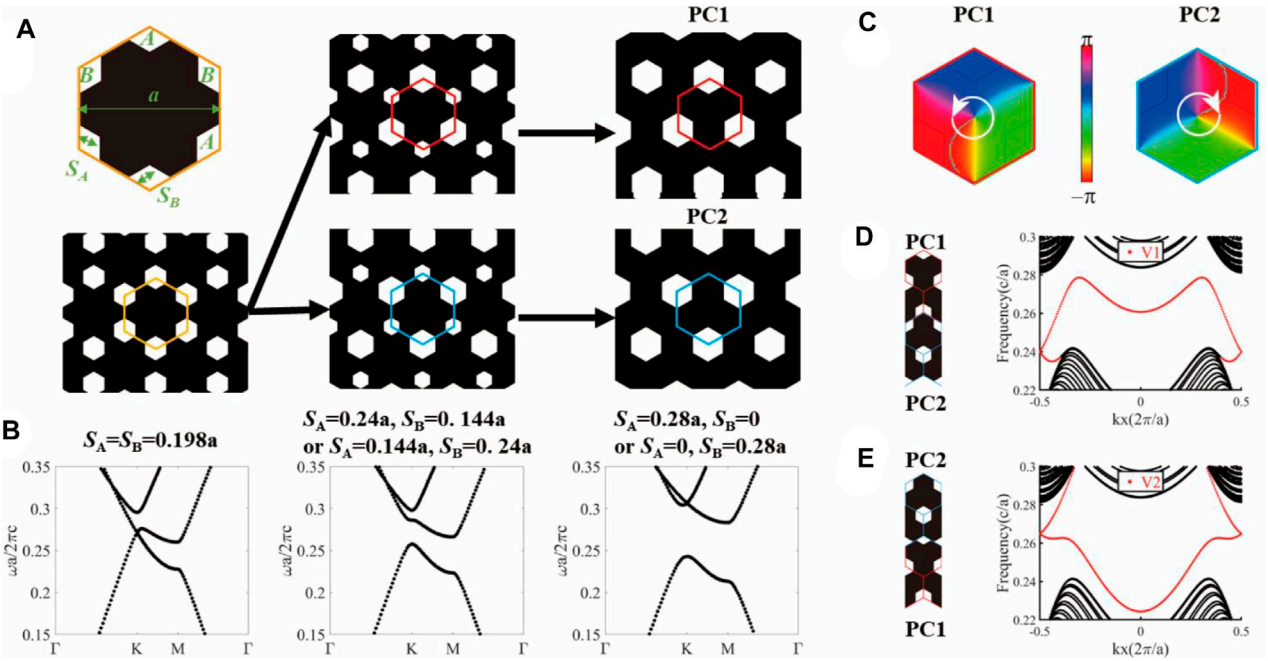

FIGURE 1 | Design of valley photonic crystal in a honeycomb lattice. **(A)** The evolution of honeycomb-lattice photonic crystals (PCs) and **(B)** the corresponding TE-polarized band structures. The unit cell of honeycomb-lattice PC with lattice constant *a* consists of two hexagon-profile air holes at the corners, where the side length of hole A (or hole B) is S_A (or S_B). When the two air holes have equivalent side length that $S_A = S_B = 0.198a$ (left panel), the TE-polarized photonic bands possess a Dirac cone around the K point. The spatial inversion symmetry of honeycomb PC is broken when $S_A \neq S_B$, and thus the degenerate states at the K point are lifted to open a common TE band gap. Finally, we have two specific cases, i.e., PC1 with $S_A = 0$ and $S_B = 0.28a$ and PC2 with $S_A = 0.28a$ and $S_B = 0$. **(C)** Phase distribution of H_z eigenfields of the first TE bulk band at the K point. For PC1 (or PC2), we can observe that the phase vortex increases counterclockwise (or clockwise) by 2π around the center of unit cell, indicating the valley Chern index $C_K = -1/2$ (or $C_K = +1/2$). **(D,E)** Schematics of two types of valley-dependent interfaces and their edge dispersions (labeled as V1 and V2). The red points represent the edge states, while the black points represent bulk states.

second-order topological photonic crystal (SOTPC) with the nontrivial 2D Zak phase [30–34]. Such SOTPC supports in-plane-localized 0D state, i.e., second-order corner state (SOCS), which is derived from the topological nontrivial phase of 2D insulating bulk states. Based on those topological boundary states on edges or corners, optical transport can be controlled flexibly and various prototypes of novel photonic devices have been successfully demonstrated [19, 35, 36], such as topological photonic routing, slow light waveguide, and PC mirrors. Furthermore, it is interesting to merge different types of topological boundary states in a single PC platform [37, 38], which can be potential to develop mode-division multiplexing in the topological photonic integrated circuits.

In this work, we apply both VDESs and SOCSs to construct a frequency-dependent routing platform in a multiport device. For one, by breaking the sublattice symmetry in a honeycomb-lattice PC, the VDESs can be acquired in an interface between two topologically distinct VPCs. For another, the SOTPCs are designed by the lattice deformation of Kagome-lattice PC, and the localized SOCSs can be induced at the intersection of the interface between two SOTPCs with different 2D Zak phases. The unit cells for both configurations consist of hexagon-profile air holes in a triangular lattice, and the geometry of air holes has the same size. Therefore, both configurations can be reconsidered as a same triangular-lattice photonic crystal in silicon background. Therefore, a four-port device is designed based on the two configurations. By merging of VDESs and SOCSs, the simulation results of the four-port device demonstrate the frequency-dependent routing effect of topologically optical transport, which is potential for the mode-division multiplexing in the development of topological photonic integrated circuits.

Design of Valley Photonic Crystals in Honeycomb Lattice

To design a valley photonic crystal, we construct a two-dimensional honeycomb-lattice photonic crystal, whose unit cell contains two types of hexagon-profile air holes at the corners, i.e., hole A and hole B. As shown in **Figure 1A**, the air holes are embedded in the dielectric background (shaded in black) with a relative permittivity ε_{eff}. The side length of hole A (or B) is S_A (or S_B), and the lattice constant is *a*. Here, $\varepsilon_{eff} = 8.12$ is the effective permittivity of the dielectric background based on the TE_0 mode index of silicon slab with $0.55a$ thickness (corresponding to a 220-nm-thickness silicon slab when the operation wavelength is around 1,550 nm). When the two air holes have an equivalent side length that $S_A = S_B = 0.198a$, the transverse-electric (TE) photonic bands of honeycomb-lattice PC [left panel of **Figure 1B**] possess a Dirac cone around the K/K′

point due to the C_{3v} point group symmetry of the lattice. Note that the photonic bands and their eigenmodes in this work are calculated by the MIT photonic band (MPB) package [39]. If we increase (reduce) S_A and reduce (increase) S_B, the spatial inversion symmetry of honeycomb PC will be broken and thus a common TE-polarized band gap is opened, which is derived from the lift up and down of degenerate states at the K/K' point. These configurations are both valley photonic crystals (VPCs), as described and demonstrated in previous works [19, 20, 28]. Note that the filling ratio of air holes maintains constant during the evolution, which ensures that the band structures of PCs do not change much in frequency.

As shown in the right panel of **Figure 1A**, we consider two specific configurations, i.e., PC1 that $S_A = 0.28a$ and $S_B = 0$ and PC2 that $S_A = 0$ and $S_B = 0.28a$. Such a configuration can be reconsidered as a simple triangular-lattice PC with a hexagon-profile air hole at the corners. Both PC1 and PC2 possess the same band structures and a 15.2% band gap from 0.243 c/a to 0.283 c/a. Here, the band-gap size is expressed as a percentage of the gap-midgap ratio $\Delta\omega/\omega_m$, where $\Delta\omega$ is the frequency width of the band gap and ω_m is the frequency at the middle of the gap. It is a general and useful characterization, which is independent of the scale of PCs.

Although PC1 and PC2 have the same bulk band structures [i.e., the band structures in the right panel of **Figure 1B**], their topological properties are distinct and characterized by different valley Chern indices $C_{K/K'}$. For valley-contrasting physics [40–42], the valley Chern index is defined as

$$C_{K/K'} = \tau_z \mathrm{sgn}(\Delta)/2, \tag{1}$$

where τ_z is the z component of the Pauli matrix that $\tau_z = +1$ at the K valley and $\tau_z = -1$ at the K′ valley. 2Δ denotes the frequency difference between two valley bulk modes. For another, modes at the two inequivalent valleys K/K′ are a pair of pseudospins, so they carry valley-dependent magnetic momentum,

$$m(K, K') = \tau_z \mu_B^*, \tag{2}$$

where μ_B^* is the effective Bohr magneton at the bottom band and $sgn(\mu_B^*) = sgn(\Delta)$ [40]. With regard to a PC, the effective "magnetic" momentum is related to the phase vortex of electromagnetic fields around the center of unit cell. When the phase vortex increases clockwise or counterclockwise by 2π, we can have $\tau_z sgn(\mu_B^*) = +1$ or -1. In other words, by observing the phase vortex of bulk modes at different valleys, it is easy to determine the valley Chern index. **Figure 1C** gives the phase distribution of H_z eigenfields of the first TE bulk band at K point. For PC1 (or PC2), we can observe that the phase vortex increases counterclockwise (or clockwise) by 2π around the center of the unit cell, indicating the valley Chern index $C_K = -1/2$ (or $C_K = +1/2$). Therefore, though one part of air holes (A or B) vanishes, PC1 and PC2 still maintain the topologically distinct features of valley-contrasting physics in a manner.

As band gaps of PC1 and PC2 are topologically distinct, the valley-dependent edge states (VDESs) can be obtained at the interface of domain walls between two VPCs with different valley indices. In **Figures 1D,E**, we show two types of interfaces (i.e., V1 and V2) constructed by PC1 and PC2 and their edge dispersions. The V1 case is PC1 at the upper domain and PC2 at the bottom, while V2 is PC2 at the upper domain and PC1 at the bottom. We calculate the edge dispersions for both two types of interfaces. The black points and red points represent bulk states and VDESs, respectively. The edge dispersions of V1-type and V2-type interfaces cover over the frequency range of the bulk band gap. Note that the group velocity direction of the V1-type (V2-type) VDES at the K valley is positive (negative) and vice versa for the K' valley. It is in agreement with the bulk-edge correspondence, for example, that the difference of the valley-dependent topological index at the K valley crossing the domain wall of the V1-type interface (i.e., $C_K^{bottom} - C_K^{top}$) is +1.

Design of Second-Order Topological Photonic Crystals in Kagome Lattice

Except for VDES, another kind of topological boundary state in this work is the second-order corner state (SOCS). To implement SOCS, we will firstly design the second-order topological PC in Kagome lattice. As shown in **Figure 2A**, the unit cell is the assignment of Δ-shape cluster, consisting of three rhombic-profile air holes in a dielectric background. The side length of the rhombic hole $d = 0.28a$, where a is the lattice constant of Kagome PC. L_1 is the distance from the center of the rhombic hole to the center of the unit cell, such that the coupling length of the intra-cell cluster is $\sqrt{3}\,L_1$. L_2 is the distance from the center of the rhombic hole to the vertex of the unit cell, and thus the coupling length of the inter-cell cluster is $\sqrt{3}\,L_2$.

To approximately describe the topological properties of such PC, we can use the 2D Su–Schrieffer–Heeger (SSH) model [14, 15], which is determined by the relationship between L_1 and L_2. When $L_1 = L_2$, the strength of the intra-cluster coupling is equal to that of inter-cluster coupling, and there is a degeneracy point around the K point in the band structure, as shown in the left panel of **Figure 2B**. When we shrink the clusters with the decrease of L_1 (or expand the clusters with the increase of L_1), the balance of intra-coupling and inter-coupling is broken and thus open a TE-polarized band gap [as shown in the middle and right panels of **Figure 2B**]. The expanded case (i.e., red border with $L_1 > L_2$) shown in the top panel of **Figure 2A** is majorly dependent on inter-cluster coupling, while the shrunken structure (i.e., green border with $L_1 < L_2$) shown in the bottom panel of **Figure 2A** is dominant for intra-cluster coupling. For the specific condition that $L_1 = 0.5d$ (or $L_2 = 0.5d$), the intra- (or inter) clusters can be reconsidered as a new hexagon hole with side length equal to d. In this case, there is a 15.2% TE-polarized band gap from 0.243 c/a to 0.283 c/a for both PC1 and PC3. Based on the second-order topological physics [43, 44], it is easy to obtain the expanded PC that has a non-trivial phase and the shrunken PC that has a trivial phase. On the other hand, when we consider a ▽-shaped cluster as shown in **Figure 2C**, the shrunken case also changes to be PC3 (green border) and the expanded case can have another nontrivial second-order TPC (i.e., PC2 labeled as a blue border). More details about the discussions of the topological properties will be shown in the next section.

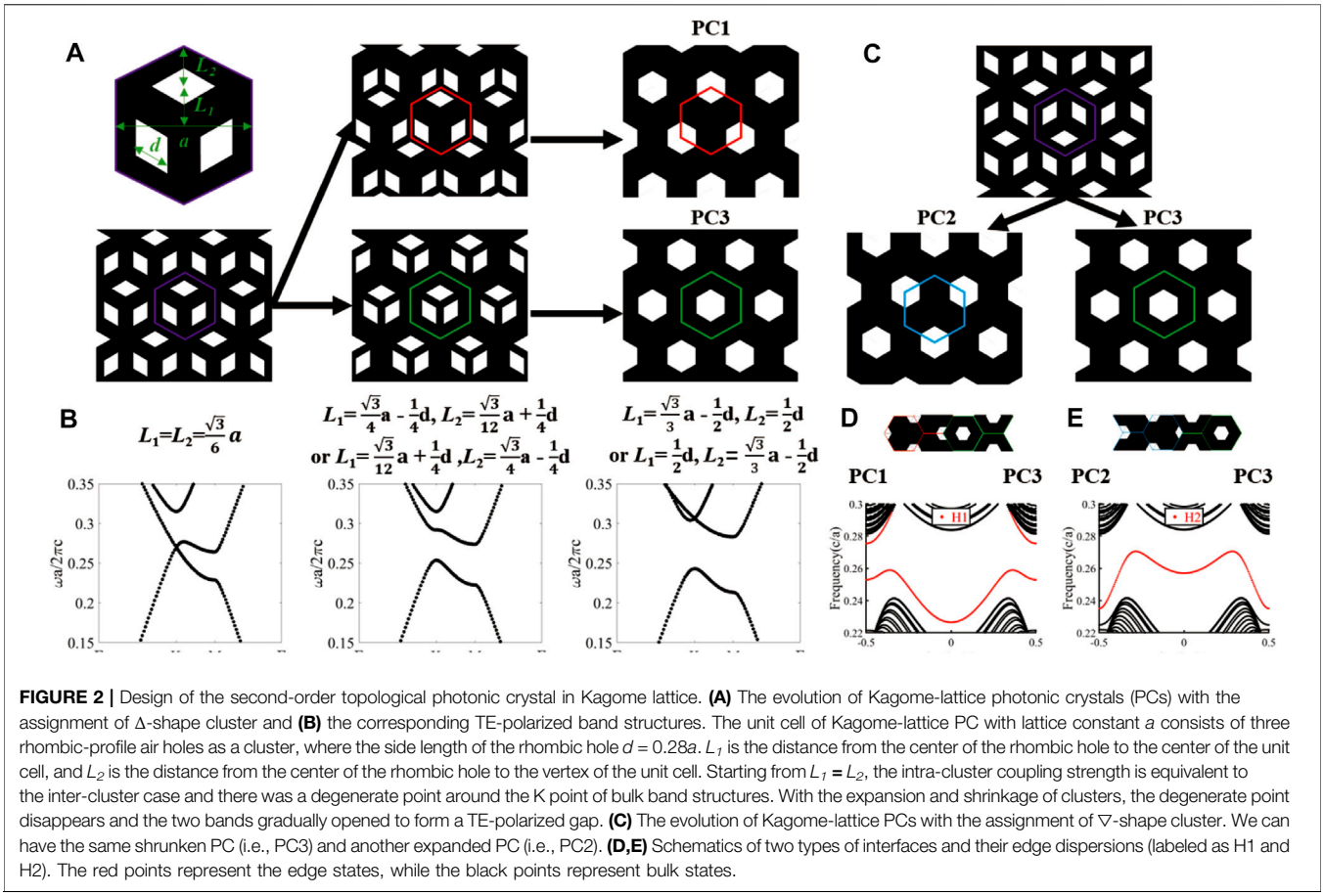

FIGURE 2 | Design of the second-order topological photonic crystal in Kagome lattice. **(A)** The evolution of Kagome-lattice photonic crystals (PCs) with the assignment of Δ-shape cluster and **(B)** the corresponding TE-polarized band structures. The unit cell of Kagome-lattice PC with lattice constant *a* consists of three rhombic-profile air holes as a cluster, where the side length of the rhombic hole $d = 0.28a$. L_1 is the distance from the center of the rhombic hole to the center of the unit cell, and L_2 is the distance from the center of the rhombic hole to the vertex of the unit cell. Starting from $L_1 = L_2$, the intra-cluster coupling strength is equivalent to the inter-cluster case and there was a degenerate point around the K point of bulk band structures. With the expansion and shrinkage of clusters, the degenerate point disappears and the two bands gradually opened to form a TE-polarized gap. **(C)** The evolution of Kagome-lattice PCs with the assignment of ∇-shape cluster. We can have the same shrunken PC (i.e., PC3) and another expanded PC (i.e., PC2). **(D,E)** Schematics of two types of interfaces and their edge dispersions (labeled as H1 and H2). The red points represent the edge states, while the black points represent bulk states.

There are six types of the interfaces formed by two of these three PCs, and we have discussed two of them (i.e., V1 and V2) in the last section. Here, we show two types of second-order interfaces formed by the second-order topologically nontrivial case (i.e., PC1 or PC2) and the second-order topologically trivial case (i.e., PC3), which will be applied to design the multiport routing device in the following discussion. As shown in **Figure 2D**, one is the H1-type interface between PC1 in the left and PC3 in the right. The edge dispersion shows that there is an "edge" band gap between the edge states (red dots) that does not support any bulk and edge state. As shown in **Figure 2E**, another one is the H2-type interface between PC2 in the left and PC3 in the right. There is an "edge" band gap between the bulk states (black dots) and edge states (red dots). The second-order corner states we are interested in will fall in these "edge" band gaps.

Two Types of Second-Order Corner States in the Topological Interfaces

To characterize the topological phases of the expanded and shrunken PCs in Kagome lattice, one can extract the bulk polarization $P = (p_1, p_2)$, where p_m is the bulk polarization component in the direction of the reciprocal vector $\mathbf{b}_m$ and m represents 1 or 2. In particular, the Kagome-lattice PCs have C_3 symmetry that constrains on $\mathbf{P}$, so $p_1 = p_2$ and we can extract a simple form of the bulk polarization with respect to the parities at high-symmetry wavevector points (i.e. Γ and K) [43–45],

$$p_m = \frac{-i}{2\pi}\ln\left[\prod_{n\in occ}\frac{\theta_m^n(K)}{\theta_m^n(\Gamma)}\right], \tag{3}$$

where

$$\theta_m^n(\mathrm{k}) = \langle u_n(\mathrm{k})|R_3|u_n(\mathrm{k})\rangle / \langle u_n(\mathrm{k})|u_n(\mathrm{k})\rangle, \tag{4}$$

is the expectation value of the three-fold symmetric operator R_3 in the $\mathbf{b}_m$ direction and $u_n(k)$ is the Bloch function of n-th-band eigenfields at a specific $\mathbf{k}$ point. The subscript "occ" in **Eq. 3** implies the summation over the bands below the band gap. Note that the Kagome-lattice PCs in this work only have one TE-polarized bulk band below the topological band gap. At Γ point, the bulk state of the first TE band is a zero-frequency mode, which is always homogeneous in real space such that $\theta_m^1(\Gamma) \equiv 1$. Thus, the expression of bulk polarization can be simplified as,

$$p_m = \frac{-i}{2\pi}\ln[\theta_m(K)], \tag{5}$$

Here, θ_m represents the expectation value of the threefold symmetric operator R_3 of the first band. In simulation, when we

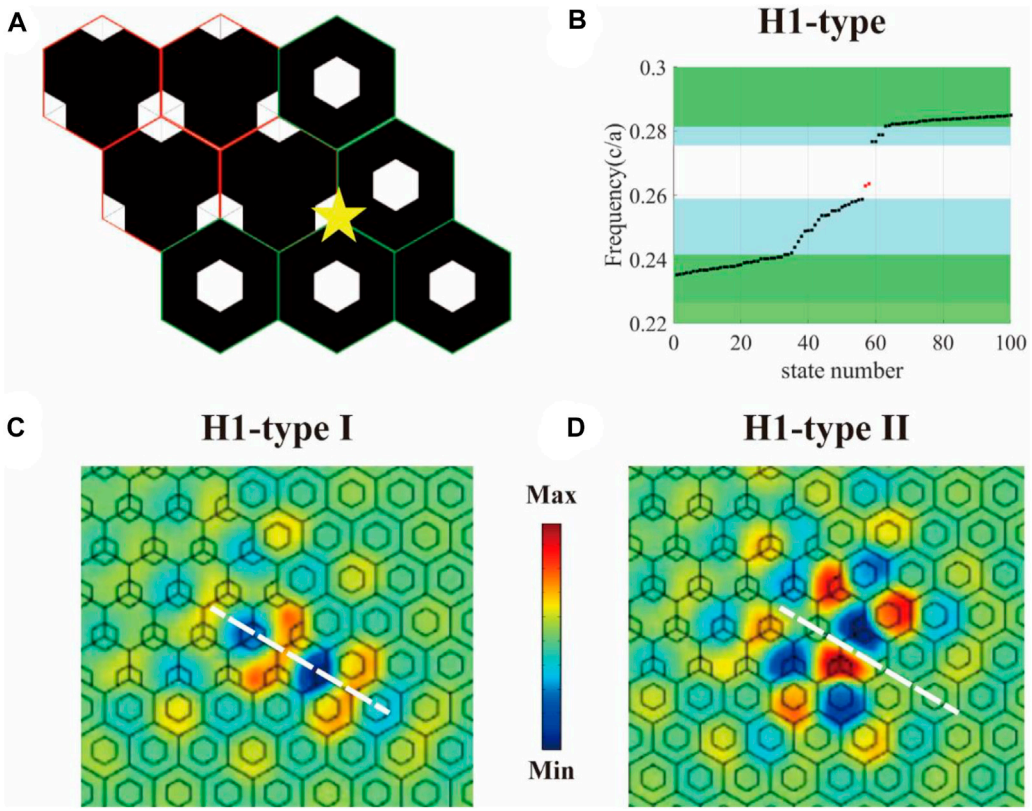

FIGURE 3 | Two types of second-order corner states (SOCSs) in H1-type topological interfaces. **(A)** Schematic view and **(B)** eigenmode spectrum of the H1-type topological interface with a 120-deg-bending geometry. The interface is constructed by PC1 and PC3. Green and blue regions indicate the frequency range of bulk states and edge states, respectively. There are two eigenmodes (marked by red point) falling in the band gap and isolating from bulk and edge states, i.e. two types of SOCSs. **(C)** and **(D)** Distributions of real-part H_z fields for the two SOCSs. The SOCS with even symmetry (around 0.262*c*/*a*) is the type I corner state (labeled as H1-type-I), while the SOCS with odd symmetry (around 0.263*c*/*a*) is the type II corner state (labeled as H1-type-II). We use dashed white lines marking the mirror plane.

introduce the distribution of the Bloch mode at K $u_n(K)$ into **Eq. 5**, the bulk polarization can be estimated to determine the second-order topological phase. For the two types of expanded PCs, the PC1 [labeled as a red border in **Figure 2A**] has a non-trivial phase with nonzero bulk polarization P = (-1/3,-1/3), while the PC2 [labeled as a blue border in **Figure 2C**] has another type of nontrivial phase with nonzero bulk polarization P = (1/3,1/3). And the shrunken PC3 has a trivial phase with zero bulk polarization P = (0,0).

When PC1 and PC3 are spliced together that the topological non-trivial lattice is surrounded by the topological trivial lattice, the two H1-type boundaries are intersected at a corner (marked by a yellow star) and thus form a 120-deg-bending interface, as shown in **Figure 3A**. Next, we will compute the eigenmode spectrum of the interface by using the frequency-domain eigenvalue solution of COMSOL, in order to better understand the optical behavior. The PC1 [red border] is arranged as a rhombus shape with a side length of 20*a*, and the outer region is terminated with the topologically trivial PC3 [green border]. In the simulated model, the computational cell is a rhombus with the total side length of 40*a* and covers with a scattering boundary. **Figure 3B** shows the eigenmode spectrum of the H1-type interface with a 120-deg-bending geometry. Green and blue regions indicate the frequency range of bulk states and edge states, respectively. There are two eigenmodes (marked by red point) falling in the band gap and isolating from bulk and edge states, i.e., two types of SOCSs. In **Figures 3C,D**, we show the real part of H_z-field distributions of the two isolated modes, i.e., H1-type I and H1-type II corner states. With respect to mirror symmetry (the mirror planes are marked as white dashed lines), the lower-frequency one (around 0.262*c*/*a*) is an even mode derived from the nearest-neighboring hopping of SOTPC, while the higher-frequency one (around 0.263*c*/*a*) is an odd mode under the consideration of the next-nearest-neighboring hopping of SOTPC [46].

Proposal for Topological Photonic Crystal Routing Platform

In this section, based on the VDESs with robust transport and localized SOCSs, we will show the design of a multiport topological routing platform for the flexible control of topologically optical transport. As shown in **Figure 4A**, the platform is rhombus with a side length of 55*a*. There are four domains in the topological routing platform, which is constructed by PC1, PC2, and PC3. The boundaries formed by these

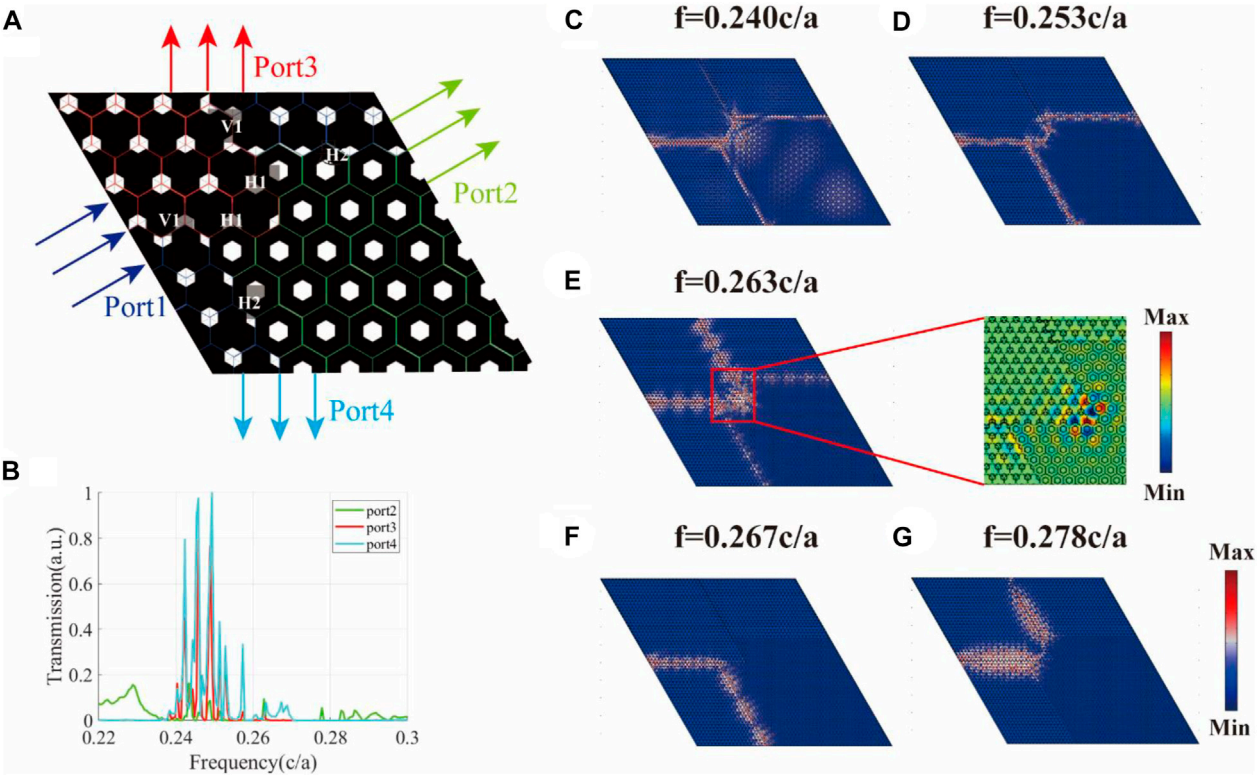

FIGURE 4 | Design of a four-port routing platform based on topological photonic crystals. **(A)** Schematics of the multiport topological routing platform. There are four domains on the platform constructed by PC1, PC2, and PC3. The boundaries of these different topological photonic crystals introduce three different edge states (V1, H1, and H2) and two corner states (H1 type) at the intersection point. **(B)** Transmission spectrum of the four-port device when light is incident from port 1. The transmission intensity of different paths obviously varies with frequency. **(C–G)** Electric-field intensity distributions at the frequencies 0.240*c*/*a*, 0.253*c*/*a*, 0.263*c*/*a*, 0.267*c*/*a*, and 0.278*c*/*a*, respectively. The inset of panel **(E)** shows the real part of H_z field distribution at a frequency of 0.263*c*/*a*, indicating the excitation of the H1-type II corner state. Through the frequency-dependent selective excitation of different types of topological boundary states, such a four-port device provides a novel way to route the optical transport with topologically protected robustness.

topological PCs introduce three different edge states (V1, H1, and H2) along the interfaces and two corner states (H1-type I and H1-type II) at the intersection point [marked by a yellow star in **Figure 3A**]. The merging of different types of those topological boundary states can realize the frequency-dependent selection of transmission path. For incidence, a 4*a*-width waveguide-mode source with TE polarization is placed at the input terminal of port 1, depicted as purple arrows of **Figure 4A**. The incident source has the same amplitude for different frequencies. Three detectors with 4*a* width are placed at the output ends of ports 2–4 to measure the transmittance, shown as green, red, and cyan arrows in **Figure 4A**, respectively. In **Figure 4B**, we calculate the transmission spectrum of the four-port device when light is incident from port 1. The transmission intensities are described as arbitrary unit (a.u.) and normalized by the maximum intensity. We can see that the transmission of different paths obviously varies with frequency. With the increase of frequency, the excited waves change from bulk states to edge states and output to a certain port dependent on the selective excitation of those topological boundary states. Port 4 has the highest transmittance (cyan line) because the propagation light from port 1 to port 4 only experiences the coupling of V1 to H2 with a 120-deg detouring angle. On the contrary, port 2 has the lowest transmittance (green line). The propagation light from port 1 to port 2 involves the coupling of three types of edge states and two different angles, so that the high transmission should meet criteria that the boundary states of V1, H1, and H2 are all excited simultaneously. As for port 3, the transmission should mainly rely on the VDES of the V1 interface, but there is another interface (i.e., H1) in the middle that has an effect on its transmission efficiency.

To visually demonstrate the routing characteristics with the variation of frequency, we also calculate the distributions of electric-field intensity at several representative frequencies, as shown in **Figures 4C–G**. In **Figure 4C**, since the operation frequency of 0.240*c*/*a* is below the bulk band gap, both bulk states and edge states are excited and the propagation waves leak to the bulk crystal. At a frequency of 0.253c/a [**Figure 4D**], the propagation waves have mainly splitted to both port 2 and port 4, so the platform can act as an optical power splitter in this case. Although there is a lack of edge states in the H1 interface at a frequency of 0.263c/a, most of the propagation waves can output to port 3 with the aid of SOCS, as shown in **Figure 4E**. The inset gives the real part of H_z fields with odd symmetry that confirm the

excitation of the type II corner state. Due to the absence of H1 edge states and SOCSs at a frequency of 0.267*c*/*a* [**Figure 4F**], the propagation waves incident from port 1 can only couple to the bottom-left H2 interface and output to port 4. At a frequency of 0.278*c*/*a* in **Figure 4G**, H2 edge states are absent but the channel supports both V1 and H1 edge states, so that the propagation waves can output to port 3. In a word, through the frequency-dependent selective excitation of different types of topological boundary states, such a four-port device provides a global method to route the optical transport with the topologically protected robustness. The global method means such robustness is one of the intrinsic properties of VDESs and SOCSs, which could be totally predicted by investigating the bulk topology, regardless of the local region around the corner. Therefore, some promising applications for light manipulation in topological nanophotonics (e.g., mode-division multiplexing) will benefit by the decrease of design complexity.

CONCLUSION

In summary, we have realized both VDESs and SOCSs based on two configurations of unit cell in the same triangular-lattice PC. The VDESs are derived from sublattice symmetry breaking in the honeycomb-lattice configuration, while SOCSs are induced by the lattice deformation of the Kagome-lattice configuration. We have designed a four-port device to selectively excite VDESs and SOCSs. Finally, the frequency-dependent routing effect of topological optical transport has been confirmed by simulation results. Our work explores various topological intriguing phases in a single photonic crystal platform, which will enrich the capability of light manipulation based on topological photonic systems. By merging of VDESs and SOCSs, the proposal of the multiport routing device provides a novel method to develop mode-division multiplexing in topological photonic integrated circuits.

DATA AVAILABILITY STATEMENT

The original contributions presented in the study are included in the article/Supplementary Material; further inquiries can be directed to the corresponding authors.

AUTHOR CONTRIBUTIONS

X-TH and J-WD initiated and supervised the project. M-YL and X-TH developed the theory. M-YL performed the numerical simulations. M-YL and X-TH wrote the draft. All authors contributed to the theoretical discussions, simulated data analysis, and article writing.

FUNDING

This work was supported by the National Key Research and Development Program of China (Grant No. 2019YFA0706302), the National Natural Science Foundation of China (Grant Nos. 62035016 and 11904421), the Basic and Applied Basic Research Foundation of Guangdong Province (Grant No. 2018B030308005), the Guangzhou Science, Technology and Innovation Commission (Grant No. 202002030322), and the Fundamental Research Funds for the Central Universities (Grant No. 20lgjc05).

REFERENCES

1. Hasan MZ, Kane CL. Colloquium: Topological Insulators. *Rev Mod Phys* (2010) 82:3045–67. doi:10.1103/RevModPhys.82.3045
2. Qi X-L, Zhang S-C. Topological Insulators and Superconductors. *Rev Mod Phys* (2011) 83:1057–110. doi:10.1103/RevModPhys.83.1057
3. Haldane FDM, Raghu S. Possible Realization of Directional Optical Waveguides in Photonic Crystals with Broken Time-Reversal Symmetry. *Phys Rev Lett* (2008) 100:013904. doi:10.1103/PhysRevLett.100.013904
4. Lu L, Joannopoulos JD, Soljačić M. Topological Photonics. *Nat Photon* (2014) 8:821–9. doi:10.1038/nphoton.2014.248
5. Khanikaev AB, Shvets G. Two-dimensional Topological Photonics. *Nat Photon* (2017) 11:763–73. doi:10.1038/s41566-017-0048-5
6. Ozawa T, Price HM, Amo A, Goldman N, Hafezi M, Lu L, et al. Topological Photonics. *Rev Mod Phys* (2019) 91:015006. doi:10.1103/RevModPhys.91.015006
7. Tang GJ, He XT, Shi FL, Liu JW, Chen XD, Dong JW. Topological Photonic Crystals: Physics, Designs, and Applications. *Laser Photon Rev* (2022) 16:2100300. doi:10.1002/lpor.202100300
8. Wang Z, Chong Y, Joannopoulos JD, Soljačić M. Observation of Unidirectional Backscattering-Immune Topological Electromagnetic States. *Nature* (2009) 461:772–5. doi:10.1038/nature08293
9. Khanikaev AB, Hossein Mousavi S, Tse W-K, Kargarian M, MacDonald AH, Shvets G. Photonic Topological Insulators. *Nat Mater* (2012) 12:233–9. doi:10.1038/nmat3520
10. Chen W-J, Jiang S-J, Chen X-D, Zhu B, Zhou L, Dong J-W, et al. Experimental Realization of Photonic Topological Insulator in a Uniaxial Metacrystal Waveguide. *Nat Commun* (2014) 5:5782. doi:10.1038/ncomms6782
11. Wu L-H, Hu X. Scheme for Achieving a Topological Photonic Crystal by Using Dielectric Material. *Phys Rev Lett* (2015) 114:223901. doi:10.1103/PhysRevLett.114.223901
12. Dong J-W, Chen X-D, Zhu H, Wang Y, Zhang X. Valley Photonic Crystals for Control of Spin and Topology. *Nat Mater* (2017) 16:298–302. doi:10.1038/nmat4807
13. Yang Y, Xu YF, Xu T, Wang H-X, Jiang J-H, Hu X, et al. Visualization of a Unidirectional Electromagnetic Waveguide Using Topological Photonic Crystals Made of Dielectric Materials. *Phys Rev Lett* (2018) 120:217401. doi:10.1103/PhysRevLett.120.217401
14. Liu F, Wakabayashi K. Novel Topological Phase with a Zero Berry Curvature. *Phys Rev Lett* (2017) 118:076803. doi:10.1103/PhysRevLett.118.076803
15. Xie B-Y, Wang H-F, Wang H-X, Zhu X-Y, Jiang J-H, Lu M-H, et al. Second-order Photonic Topological Insulator with Corner States. *Phys Rev B* (2018) 98:205147. doi:10.1103/PhysRevB.98.205147
16. Fu J-X, Lian J, Liu R-J, Gan L, Li Z-Y. Unidirectional Channel-Drop Filter by One-Way Gyromagnetic Photonic crystal Waveguides. *Appl Phys Lett* (2011) 98:211104. doi:10.1063/1.3593027
17. Bahari B, Ndao A, Vallini F, El Amili A, Fainman Y, Kanté B. Nonreciprocal Lasing in Topological Cavities of Arbitrary Geometries. *Science* (2017) 358:636–40. doi:10.1126/science.aao4551
18. Barik S, Karasahin A, Flower C, Cai T, Miyake H, DeGottardi W, et al. A Topological Quantum Optics Interface. *Science* (2018) 359:666–8. doi:10.1126/science.aaq0327
19. He X-T, Liang E-T, Yuan J-J, Qiu H-Y, Chen X-D, Zhao F-L, et al. A Silicon-On-Insulator Slab for Topological valley Transport. *Nat Commun* (2019) 10:872. doi:10.1038/s41467-019-08881-z

20. Shalaev MI, Walasik W, Tsukernik A, Xu Y, Litchinitser NM. Robust Topologically Protected Transport in Photonic Crystals at Telecommunication Wavelengths. *Nat Nanotech* (2019) 14:31–4. doi:10.1038/s41565-018-0297-6
21. Shao Z-K, Chen H-Z, Wang S, Mao X-R, Yang Z-Q, Wang S-L, et al. A High-Performance Topological Bulk Laser Based on Band-Inversion-Induced Reflection. *Nat Nanotechnol* (2020) 15:67–72. doi:10.1038/s41565-019-0584-x
22. Gao X, Yang L, Lin H, Zhang L, Li J, Bo F, et al. Dirac-vortex Topological Cavities. *Nat Nanotechnol* (2020) 15:1012–8. doi:10.1038/s41565-020-0773-7
23. Yang Y, Yamagami Y, Yu X, Pitchappa P, Webber J, Zhang B, et al. Terahertz Topological Photonics for On-Chip Communication. *Nat Photon* (2020) 14: 446–51. doi:10.1038/s41566-020-0618-9
24. Zeng Y, Chattopadhyay U, Zhu B, Qiang B, Li J, Jin Y, et al. Electrically Pumped Topological Laser with valley Edge Modes. *Nature* (2020) 578:246–50. doi:10.1038/s41586-020-1981-x
25. Chen Y, He X-T, Cheng Y-J, Qiu H-Y, Feng L-T, Zhang M, et al. Topologically Protected Valley-Dependent Quantum Photonic Circuits. *Phys Rev Lett* (2021) 126:230503. doi:10.1103/PhysRevLett.126.230503
26. Wu X, Meng Y, Tian J, Huang Y, Xiang H, Han D, et al. Direct Observation of valley-polarized Topological Edge States in Designer Surface Plasmon Crystals. *Nat Commun* (2017) 8:1304. doi:10.1038/s41467-017-01515-2
27. Gao F, Xue H, Yang Z, Lai K, Yu Y, Lin X, et al. Topologically Protected Refraction of Robust Kink States in valley Photonic Crystals. *Nat Phys* (2018) 14:140–4. doi:10.1038/nphys4304
28. Ma J, Xi X, Sun X. Topological Photonic Integrated Circuits Based on Valley Kink States. *Laser Photon Rev* (2019) 13:1900087. doi:10.1002/lpor.201900087
29. Han Y, Fei H, Lin H, Zhang Y, Zhang M, Yang Y. Design of Broadband All-Dielectric valley Photonic Crystals at Telecommunication Wavelength. *Opt Commun* (2021) 488:126847. doi:10.1016/j.optcom.2021.126847
30. Chen X-D, Deng W-M, Shi F-L, Zhao F-L, Chen M, Dong J-W. Direct Observation of Corner States in Second-Order Topological Photonic Crystal Slabs. *Phys Rev Lett* (2019) 122:233902. doi:10.1103/PhysRevLett. 122.233902
31. Xie B-Y, Su G-X, Wang H-F, Su H, Shen X-P, Zhan P, et al. Visualization of Higher-Order Topological Insulating Phases in Two-Dimensional Dielectric Photonic Crystals. *Phys Rev Lett* (2019) 122:233903. doi:10.1103/PhysRevLett. 122.233903
32. Ota Y, Liu F, Katsumi R, Watanabe K, Wakabayashi K, Arakawa Y, et al. Photonic crystal Nanocavity Based on a Topological Corner State. *Optica* (2019) 6:786–9. doi:10.1364/OPTICA.6.000786
33. Zhang W, Xie X, Hao H, Dang J, Xiao S, Shi S, et al. Low-threshold Topological Nanolasers Based on the Second-Order Corner State. *Light Sci Appl* (2020) 9: 109. doi:10.1038/s41377-020-00352-1
34. He X-T, Li M-Y, Qiu H-Y, Ruan W-S, Zhou L-D, Liu L, et al. In-plane Excitation of a Topological Nanophotonic Corner State at Telecom Wavelengths in a Cross-Coupled Cavity. *Photon Res* (2021) 9:1423. doi:10. 1364/prj.419569
35. Yoshimi H, Yamaguchi T, Ota Y, Arakawa Y, Iwamoto S. Slow Light Waveguides in Topological valley Photonic Crystals. *Opt Lett* (2020) 45: 2648–51. doi:10.1364/OL.391764
36. Yuan M, Xu T, Hang ZH. Construction of Optical Topological Cavities Using Photonic Crystals. *Front Phys* (2021) 9:9. doi:10.3389/fphy.2021.697719
37. Zhu X, Wang H-X, Xu C, Lai Y, Jiang J-H, John S. Topological Transitions in Continuously Deformed Photonic Crystals. *Phys Rev B* (2018) 97. doi:10.1103/ PhysRevB.97.085148
38. Yang Y, Jia Z, Wu Y, Xiao R-C, Hang ZH, Jiang H, et al. Gapped Topological Kink States and Topological Corner States in Honeycomb Lattice. *Sci Bull* (2020) 65:531–7. doi:10.1016/j.scib.2020.01.024
39. Johnson S, Joannopoulos J. Block-iterative Frequency-Domain Methods for Maxwell's Equations in a Planewave Basis. *Opt Express* (2001) 8:173–90. doi:10.1364/OE.8.000173
40. Xiao D, Yao W, Niu Q. Valley-contrasting Physics in Graphene: Magnetic Moment and Topological Transport. *Phys Rev Lett* (2007) 99:236809. doi:10. 1103/PhysRevLett.99.236809
41. Ma T, Shvets G. All-Si valley-Hall Photonic Topological Insulator. *New J Phys* (2016) 18:025012. doi:10.1088/1367-2630/18/2/025012
42. Chen X-D, Zhao F-L, Chen M, Dong J-W. Valley-contrasting Physics in All-Dielectric Photonic Crystals: Orbital Angular Momentum and Topological Propagation. *Phys Rev B* (2017) 96:020202. doi:10.1103/ PhysRevB.96.020202
43. Fang C, Gilbert MJ, Bernevig BA. Bulk Topological Invariants in Noninteracting point Group Symmetric Insulators. *Phys Rev B* (2012) 86: 86. doi:10.1103/PhysRevB.86.115112
44. Ni X, Weiner M, Alù A, Khanikaev AB. Observation of Higher-Order Topological Acoustic States Protected by Generalized Chiral Symmetry. *Nat Mater* (2019) 18:113–20. doi:10.1038/s41563-018-0252-9
45. Xue H, Yang Y, Gao F, Chong Y, Zhang B. Acoustic Higher-Order Topological Insulator on a Kagome Lattice. *Nat Mater* (2019) 18:108–12. doi:10.1038/ s41563-018-0251-x
46. Li M, Zhirihin D, Gorlach M, Ni X, Filonov D, Slobozhanyuk A, et al. Higher-order Topological States in Photonic Kagome Crystals with Long-Range Interactions. *Nat Photon* (2019) 14:89–94. doi:10.1038/s41566-019-0561-9

Conflict of Interest: The authors declare that the research was conducted in the absence of any commercial or financial relationships that could be construed as a potential conflict of interest.

Publisher's Note: All claims expressed in this article are solely those of the authors and do not necessarily represent those of their affiliated organizations, or those of the publisher, the editors, and the reviewers. Any product that may be evaluated in this article, or claim that may be made by its manufacturer, is not guaranteed or endorsed by the publisher.

Advantages of publishing in Frontiers

OPEN ACCESS
Articles are free to read for greatest visibility and readership

FAST PUBLICATION
Around 90 days from submission to decision

HIGH QUALITY PEER-REVIEW
Rigorous, collaborative, and constructive peer-review

TRANSPARENT PEER-REVIEW
Editors and reviewers acknowledged by name on published articles

Frontiers
Avenue du Tribunal-Fédéral 34
1005 Lausanne | Switzerland

Visit us: www.frontiersin.org
Contact us: frontiersin.org/about/contact

REPRODUCIBILITY OF RESEARCH
Support open data and methods to enhance research reproducibility

DIGITAL PUBLISHING
Articles designed for optimal readership across devices

FOLLOW US
@frontiersin

IMPACT METRICS
Advanced article metrics track visibility across digital media

EXTENSIVE PROMOTION
Marketing and promotion of impactful research

LOOP RESEARCH NETWORK
Our network increases your article's readership